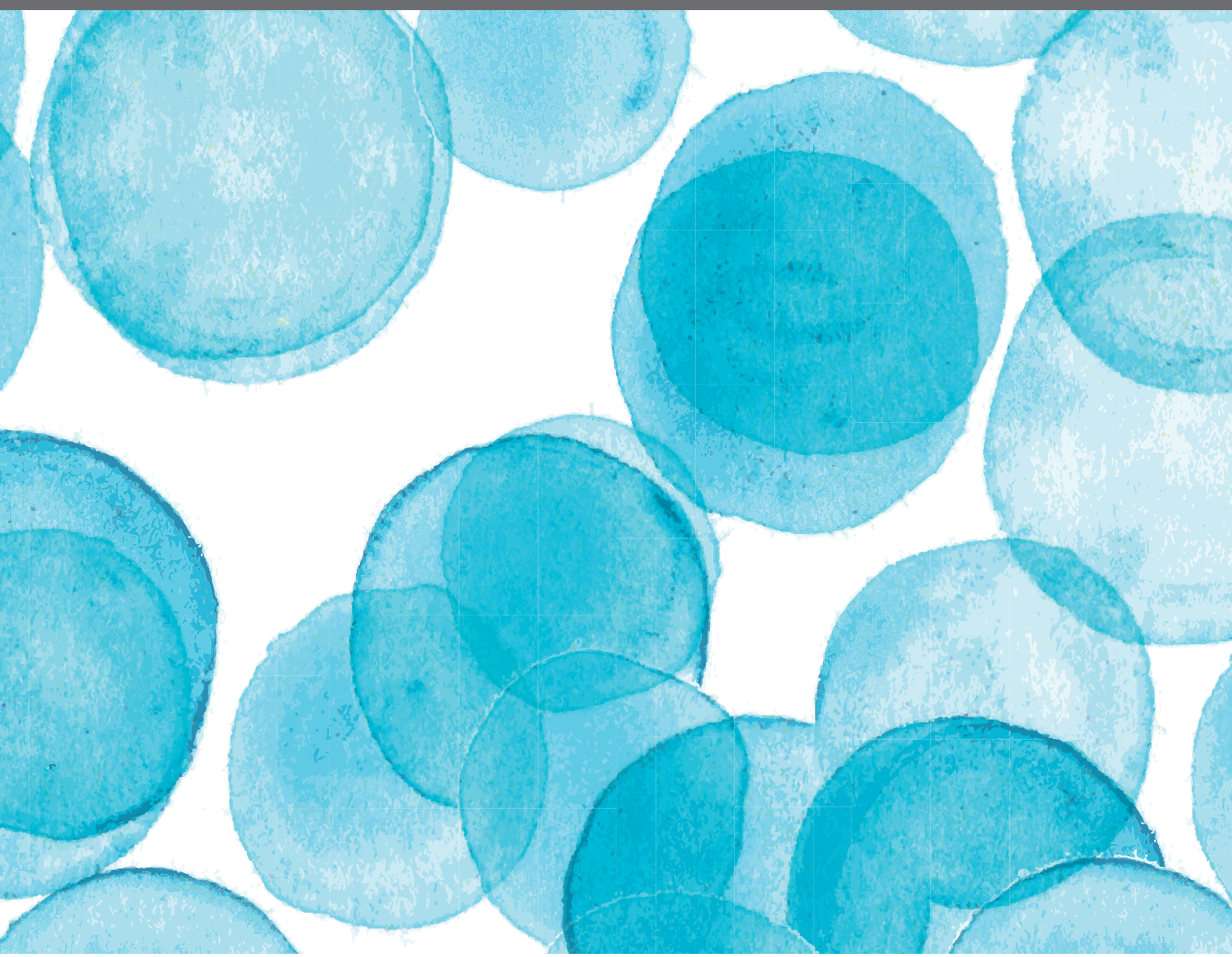
BIOLOGICAL ROTARY NANOMOTORS

EDITED BY: Michael Manson, Tom Duncan, Pushkar Lele, Jun Liu and Beiyan Nan

PUBLISHED IN: Frontiers in Microbiology



frontiers Research Topics

Frontiers eBook Copyright Statement

The copyright in the text of individual articles in this eBook is the property of their respective authors or their respective institutions or funders. The copyright in graphics and images within each article may be subject to copyright of other parties. In both cases this is subject to a license granted to Frontiers.

The compilation of articles constituting this eBook is the property of Frontiers.

Each article within this eBook, and the eBook itself, are published under the most recent version of the Creative Commons CC-BY licence. The version current at the date of publication of this eBook is CC-BY 4.0. If the CC-BY licence is updated, the licence granted by Frontiers is automatically updated to the new version.

When exercising any right under the CC-BY licence, Frontiers must be attributed as the original publisher of the article or eBook, as applicable.

Authors have the responsibility of ensuring that any graphics or other materials which are the property of others may be included in the CC-BY licence, but this should be checked before relying on the CC-BY licence to reproduce those materials. Any copyright notices relating to those materials must be complied with.

Copyright and source acknowledgement notices may not be removed and must be displayed in any copy, derivative work or partial copy which includes the elements in question.

All copyright, and all rights therein, are protected by national and international copyright laws. The above represents a summary only. For further information please read Frontiers' Conditions for Website Use and Copyright Statement, and the applicable CC-BY licence.

ISSN 1664-8714
ISBN 978-2-83250-555-7
DOI 10.3389/978-2-83250-555-7

About Frontiers

Frontiers is more than just an open-access publisher of scholarly articles: it is a pioneering approach to the world of academia, radically improving the way scholarly research is managed. The grand vision of Frontiers is a world where all people have an equal opportunity to seek, share and generate knowledge. Frontiers provides immediate and permanent online open access to all its publications, but this alone is not enough to realize our grand goals.

Frontiers Journal Series

The Frontiers Journal Series is a multi-tier and interdisciplinary set of open-access, online journals, promising a paradigm shift from the current review, selection and dissemination processes in academic publishing. All Frontiers journals are driven by researchers for researchers; therefore, they constitute a service to the scholarly community. At the same time, the Frontiers Journal Series operates on a revolutionary invention, the tiered publishing system, initially addressing specific communities of scholars, and gradually climbing up to broader public understanding, thus serving the interests of the lay society, too.

Dedication to Quality

Each Frontiers article is a landmark of the highest quality, thanks to genuinely collaborative interactions between authors and review editors, who include some of the world's best academicians. Research must be certified by peers before entering a stream of knowledge that may eventually reach the public - and shape society; therefore, Frontiers only applies the most rigorous and unbiased reviews.
Frontiers revolutionizes research publishing by freely delivering the most outstanding research, evaluated with no bias from both the academic and social point of view. By applying the most advanced information technologies, Frontiers is catapulting scholarly publishing into a new generation.

What are Frontiers Research Topics?

Frontiers Research Topics are very popular trademarks of the Frontiers Journals Series: they are collections of at least ten articles, all centered on a particular subject. With their unique mix of varied contributions from Original Research to Review Articles, Frontiers Research Topics unify the most influential researchers, the latest key findings and historical advances in a hot research area! Find out more on how to host your own Frontiers Research Topic or contribute to one as an author by contacting the Frontiers Editorial Office: frontiersin.org/about/contact

BIOLOGICAL ROTARY NANOMOTORS

Topic Editors:
Michael Manson, Texas A&M University, United States
Tom Duncan, Upstate Medical University, United States
Pushkar Lele, Texas A&M University, United States
Jun Liu, Yale University, United States
Beiyan Nan, Texas A&M University, United States

Citation: Manson, M., Duncan, T., Lele, P., Liu, J., Nan, B., eds. (2022). Biological Rotary Nanomotors. Lausanne: Frontiers Media SA.
doi: 10.3389/978-2-83250-555-7

Table of Contents

05 ***Editorial: Biological Rotary Nanomotors***
Michael D. Manson, Beiyan Nan, Pushkar P. Lele, Jun Liu and Thomas M. Duncan

INTRODUCTION TO BIOLOGICAL ROTARY NANOMOTORS

07 ***Rotary Nanomotors in the Rear View Mirror***
Michael D. Manson

14 ***A New Class of Biological Ion-Driven Rotary Molecular Motors With 5:2 Symmetry***
Martin Rieu, Roscislaw Krutyholowa, Nicholas M. I. Taylor and Richard M. Berry

THE BACTERIAL FLAGELLUM

34 ***Modeling Bacterial Flagellar Motor With New Structure Information: Rotational Dynamics of Two Interacting Protein Nano-Rings***
Yuansheng Cao, Tairan Li and Yuhai Tu

43 ***The Bacterial Flagellar Motor: Insights Into Torque Generation, Rotational Switching, and Mechanosensing***
Shuaiqi Guo and Jun Liu

53 ***Swimming Using a Unidirectionally Rotating, Single Stopping Flagellum in the Alpha Proteobacterium*** **Rhodobacter sphaeroides**
Judith P. Armitage

62 ***Dynamic Hybrid Flagellar Motors—Fuel Switch and More***
Kai M. Thormann

71 ***The Periplasmic Domain of the Ion-Conducting Stator of Bacterial Flagella Regulates Force Generation***
Michio Homma and Seiji Kojima

83 ***Bacterial Proprioception: Can a Bacterium Sense Its Movement?***
Rachit Gupta, Junhua Yuan and Pushkar P. Lele

92 ***Insight Into Distinct Functional Roles of the Flagellar ATPase Complex for Flagellar Assembly in*** **Salmonella**
Tohru Minamino, Miki Kinoshita and Keiichi Namba

GLIDING MOTORS

106 ***Flagellar Motor Transformed: Biophysical Perspectives of the*** **Myxococcus xanthus** ***Gliding Mechanism***
Jing Chen and Beiyan Nan

114 ***Design Principles of the Rotary Type 9 Secretion System***
Abhishek Trivedi, Jitendrapuri Gosai, Daisuke Nakane and Abhishek Shrivastava

COUPLING ROTATION TO PROCESSES IN THE OUTER MEMBRANE OF GRAM-NEGATIVE BACTERIA

124 ***The Ton Motor***
Anna C. Ratliff, Susan K. Buchanan and Herve Celia

132 ***Force-Generation by the Trans-Envelope Tol-Pal System***
Melissa N. Webby, Daniel P. Williams-Jones, Cara Press and Colin Kleanthous

THE ARCHAELLUM, A PROPULSIVE MOTOR DRIVEN BY ATP HYDROLYSIS

145 ***How Did the Archaellum Get Its Rotation?***
Davi Ortega and Morgan Beeby

151 ***Towards Elucidating the Rotary Mechanism of the Archaellum Machinery***
João Nuno de Sousa Machado, Sonja-Verena Albers and Bertram Daum

THE FOF1 ATP SYNTHASE

164 ***CryoEM Reveals the Complexity and Diversity of ATP Synthases***
Gautier M. Courbon and John L. Rubinstein

174 ***How Does F_1-ATPase Generate Torque?: Analysis From Cryo-Electron Microscopy and Rotational Catalysis of Thermophilic F_1***
Hiroyuki Noji and Hiroshi Ueno

181 ***F_1F_O ATP Synthase Molecular Motor Mechanisms***
Wayne D. Frasch, Zain A. Bukhari and Seiga Yanagisawa

211 ***Rotational Mechanism of F_O Motor in the F-Type ATP Synthase Driven by the Proton Motive Force***
Shintaroh Kubo and Shoji Takada

224 ***F_1-ATPase Rotary Mechanism: Interpreting Results of Diverse Experimental Modes With an Elastic Coupling Theory***
Sándor Volkán-Kacsó and Rudolph A. Marcus

frontiers | Frontiers in Microbiology

TYPE Editorial
PUBLISHED 21 September 2022
DOI 10.3389/fmicb.2022.1012681

Check for updates

OPEN ACCESS

EDITED AND REVIEWED BY
Marc Strous,
University of Calgary, Canada

*CORRESPONDENCE
Michael D. Manson
mike@bio.tamu.edu

SPECIALTY SECTION
This article was submitted to Microbial Physiology and Metabolism, a section of the journal Frontiers in Microbiology

RECEIVED 05 August 2022
ACCEPTED 29 August 2022
PUBLISHED 21 September 2022

CITATION
Manson MD, Nan B, Lele PP, Liu J and Duncan TM (2022) Editorial: Biological rotary nanomotors.
Front. Microbiol. 13:1012681.
doi: 10.3389/fmicb.2022.1012681

COPYRIGHT
© 2022 Manson, Nan, Lele, Liu and Duncan. This is an open-access article distributed under the terms of the Creative Commons Attribution License (CC BY). The use, distribution or reproduction in other forums is permitted, provided the original author(s) and the copyright owner(s) are credited and that the original publication in this journal is cited, in accordance with accepted academic practice. No use, distribution or reproduction is permitted which does not comply with these terms.

Editorial: Biological rotary nanomotors

Michael D. Manson[1]*, Beiyan Nan[1], Pushkar P. Lele[2], Jun Liu[3] and Thomas M. Duncan[4]

[1]Department of Biology, Texas A&M University, College Station, TX, United States, [2]Artie McFerrin Department of Chemical Engineering, Texas A&M University, College Station, TX, United States, [3]Microbial Sciences Institute, Department of Microbial Pathogenesis, Yale University, New Haven, CT, United States, [4]Department of Biochemistry & Molecular Biology, Upstate Medical University, Syracuse, NY, United States

KEYWORDS

rotary nanomotors, flagella, archaella, gliding, outer membrane transport, ATP synthase

Editorial on the Research Topic
Biological rotary nanomotors

This Research Topic of 20 review articles covers the incredible variety of molecular rotary nanomachines that have evolved over billions of years. The details of their molecular mechanisms are well-known for the Bacterial Flagellar Motor (BFM) and FoF1 ATP synthase/ATPase. They are inferred by analogy to the BFM for others: the 5:2 motors of gliding bacteria and the 5:2 motors of the Ton and Tol systems that govern events at the outer membrane of gram-negative bacteria. All of these systems couple a transmembrane ion motive force to useful work. Two additional articles consider the unique propulsion generator of the Archaea, the archaellum, which appears to be driven entirely by ATP hydrolysis and has an evolutionary history completely independent of those for the 5:2 motors and FoF1.

This Research Topic originated with Mike Manson, who was inspired by the recently published structures of 5:2 rotary motors and the desire to create a fitting tribute to Howard Berg, who introduced rotary motors into biology. The effort was augmented by recruitment of Tom Duncan, Pushkar Lele, Jun Liu, and Beiyan Nan, who possess the expertise to select the authors best able to tell the story of rotary nanomotors and to edit their contributions.

The Research Topic has six sections. The first two chapters serve as an introduction to the history, structure, and energetics of rotary motors driven by an ion motive force. The second of these provides a detailed consideration of the structure of 5:2 rotary motors and how their function and energetics compare with the Fo motor of ATP synthases, which has a gearing ratio ranging from 8:1 to 15:1 in different species. The next seven articles provide detailed reviews about different aspects and incarnations of BFMs. The following two articles discuss the function of ion-powered motors in gliding bacteria, which do not depend on flagella. Next, two reviews cover the Exb/Ton and Tol/Pal

systems, both of which are driven by 5:2-type motors. As a segue into the FoF1 motors that drive ATP synthesis, the next two articles cover the archaellum, a helical propeller like the bacterial flagellum, but one driven by ATP hydrolysis rather than an ion motive force and possessing a completely different evolutionary trajectory. The last five articles review different aspects of what is known about the FoF1 ATP synthase, a crucial and ubiquitous energy-transducing enzyme that couples two rotary motor devices.

The editors thank all 49 authors who generously agreed to put their collective knowledge about rotary nanomotors into words. They represent the leading research groups worldwide studying rotary molecular machines. The positive responses to our invitations were doubtless aided by the recognition that this was a tribute to the visionary insight of Howard Berg, whose paper with Robert Anderson in 1973 first declared that "Bacteria Swim by Rotating Helical Filaments."

We hoped that Howard would write an introduction to this Research Topic. Unfortunately, he passed away on December 30, 2021, just as it became clear that our vision was going to become reality. That sad event adds both poignancy and timeliness to this Research Topic. We also want to thank the four editors who supplemented the efforts of the five designated guest editors mentioned above and the 33 reviewers who, together with the guest editors, ensured that everything presented in the reviews was as clear, complete, and accurate as possible.

We hope this Research Topic serves as a fitting tribute to Howard Berg, the unconventional intellect whose insight ushered in an entire field of molecular biophysics: the study of rotary molecular motors. Savor what is presented here and anticipate the new revelations which doubtless await in the coming years.

Author contributions

All authors listed have made a substantial, direct, and intellectual contribution to the work and approved it for publication.

Acknowledgments

This effort was made possible by the original invitation from Ronan Conlon to Mike Manson to guest edit a Research Topic for Frontiers in Microbiology. The effort was capably facilitated by Ronan and Helene Jensen, the supervising editor for Frontiers in Microbiology. The cost of publication was partially underwritten by the Department of Biology at Texas A&M University in recognition of former Department Head Timothy C. Hall for his contribution to the Texas A&M Department of Biology and the career of the first author.

Conflict of interest

The authors declare that the research was conducted in the absence of any commercial or financial relationships that could be construed as a potential conflict of interest.

Publisher's note

All claims expressed in this article are solely those of the authors and do not necessarily represent those of their affiliated organizations, or those of the publisher, the editors and the reviewers. Any product that may be evaluated in this article, or claim that may be made by its manufacturer, is not guaranteed or endorsed by the publisher.

frontiers | Frontiers in Microbiology

REVIEW
published: 29 April 2022
doi: 10.3389/fmicb.2022.873573

Rotary Nanomotors in the Rear View Mirror

*Michael D. Manson**

Texas A&M University, College Station, TX, United States

Rotation is part of our everyday lives. For most of human history, rotation was considered a uniquely human invention, something beyond the anatomical capabilities of organisms. In 1973, Howard Berg made the audacious proposal that the common gut bacterium *Escherichia coli* swims by rotating helical flagellar filaments. In 1987, Paul Boyer suggested that the FoF1 ATP synthase of *E. coli* is also a rotary device. Now we know that rotating nanomachines evolved independently at least three times. They power a wide variety of cellular processes. Here, the study of flagellar rotation in *E. coli* is briefly summarized. In 2020, the Cryo-EM structure of the MotAB stator element of the bacterial flagellum was described. The structure strongly suggests that the MotAB stator rotates to drive flagellar rotation. Similar motors are coupled to other diverse processes. The following articles in this issue review the current knowledge and speculation about rotating biological nanomachines.

Keywords: flagellum, rotation, motor, ion motive force, Howard Berg

OPEN ACCESS

Edited by:
Stanley Brul,
University of Amsterdam, Netherlands

Reviewed by:
Marie-stephanie Aschtgen,
Karolinska Institutet (KI), Sweden
Daisuke Nakane,
The University
of Electro-Communications, Japan

***Correspondence:**
Michael D. Manson
mike@bio.tamu.edu

Specialty section:
This article was submitted to Microbial Physiology and Metabolism, a section of the journal Frontiers in Microbiology

Received: *11 February 2022*
Accepted: *28 February 2022*
Published: *29 April 2022*

Citation:
Manson MD (2022) Rotary Nanomotors in the Rear View Mirror. Front. Microbiol. 13:873573. doi: 10.3389/fmicb.2022.873573

INTRODUCTION

This article is intended as an introduction to an issue devoted to biological rotary nanomotors. It provides a historical perspective on the study of rotation of the bacterial flagellum, the first—and for more than 20 years the only—known biological rotary motor. It has recently become clear that rotary motors on a molecular scale are everywhere in nature. It is this realization that inspired the review and perspective articles that are compiled in this issue.

Rotation has some marvelous properties as a form of motion. It can be continuous in one direction as long as a constant force is applied to generate the torque required to balance the resistance. It is reversible, switching from clockwise to counterclockwise and back again (What did they call the two directions of rotation before we had clocks? Perhaps right-handed and left-handed screws). Rotation can be driven from torque applied by a central hub or axle, or it can be driven by an external current that supplies the energy for rotation about a hub or axle. It can generate or be driven by flows of wind, water, or electrical current. It is the ideal motion for conversion of potential energy into kinetic energy, and vice versa.

Rotation has been ubiquitous in our lives since the invention of the wheel, first as an aid to potters and only later as a convenient way to move heavy loads. Until 1973, we can be forgiven for thinking rotation was a uniquely human invention among living organisms. Examples of what superficially looked like rotation were illusions: the helical beat of the long, propulsive cilia of some protozoa; the seemingly circular beat of multiple, much-shorter cilia around the oral opening of a rotifer; the remarkably quick swiveling of an owl's head through nearly 360°.

Everyone agreed there was a good reason that there was no rotation in living organisms. How would connections be made across a rotating joint? Blood vessels, nerves, connective tissue would

all be twisted into an awful snarl, and any communication across the joint would be interrupted. Even at the microscopic level, filaments made of actin, myosin, tubulin, or any other polymerizing protein would become entangled. Another problem was how lubrication would be provided for parts rotating relative to one another.

The problem was that people were thinking too big. There is no need for a filamentous connection between the parts of a molecular motor. There is also no need for a lubricant.

The curtain that blocked our view of rotation in living organisms was raised in 1973. In a paper appearing in *Nature,* Howard Berg and Robert Anderson presented the idea that flagella, thin helical filaments used for motility by bacteria, propel the cells by rotating (Berg and Anderson, 1973). They reasoned from available information. The paper features one hand-drawn figure, thereby extending a precedent set by Watson and Crick 20 years earlier (Watson and Crick, 1953).

Berg and Anderson had two irrefutable pieces of evidence for rotation. A swimming *Escherichia coli* cell is pushed by a bundle of 4–6 flagellar filaments. The first evidence for rotation was provided by the observation that when divalent antibody prepared against flagellar filaments was added to swimming cells, the cells immediately stopped swimming. The interpretation was that their flagellar filaments became crosslinked and could no longer slide past one another as they must in a bundle of rotating filaments. When monovalent antibody raised against the filament was added, motility was retained. The interpretation was that the filaments became thicker when they bound the monovalent antibody but could still slide past one another as they rotated in a bundle.

The second piece of evidence was again provided by divalent antibody, but in a very different way. An extracellular structure called the proximal hook is found at the base of the filament. This hook acts as a universal joint to allow rotation perpendicular to the lateral surface of the cell to bend 90° to allow the filament to rotate parallel to the long axis of the cell (**Figure 1A**). Polyhook mutants make extra-long hooks and no filament. These mutants do not swim. When divalent antibody raised against the polyhooks was added to a dense suspension of polyhook mutant cells, it was seen that pairs of adjacent cells became attached to one another. These cells began to spin in opposite directions, as they would if they were now joined by two crosslinked polyhooks, each rotated from its base.

This pioneering and paradigm-breaking work was quickly confirmed by experiments from the laboratories of Mel Simon and Julius Adler. Their papers were published back-to-back in *Nature* just 6 months after the Berg and Anderson paper appeared. Both took advantage of the fact that, if the stub of a flagellar filament or the proximal hook is attached to a surface by antibody, rotation of what soon came to be called the motor at its base caused the "tethered" cell body to spin. The Simon lab found that the cells rotated both clockwise (CW) and counterclockwise (CCW). Because the cell bodies must rotate in the opposite direction as the flagellum, this demonstrated directly that flagella rotate both CCW and CW (Silverman and Simon, 1974). The Adler lab showed that when tethered cells are exposed to chemicals that they sense as attractants or repellents, they respond by changing their pattern of rotation (Larsen et al., 1974b). Attractants cause the cells to rotate exclusively CW for a time because they cause the flagellum to rotate CCW. Repellents cause the cell bodies to spin exclusively CCW, although for a shorter time, because they cause the flagellum to rotate CW. This switching in the direction of flagellar rotation is the basis for chemotaxis (see below).

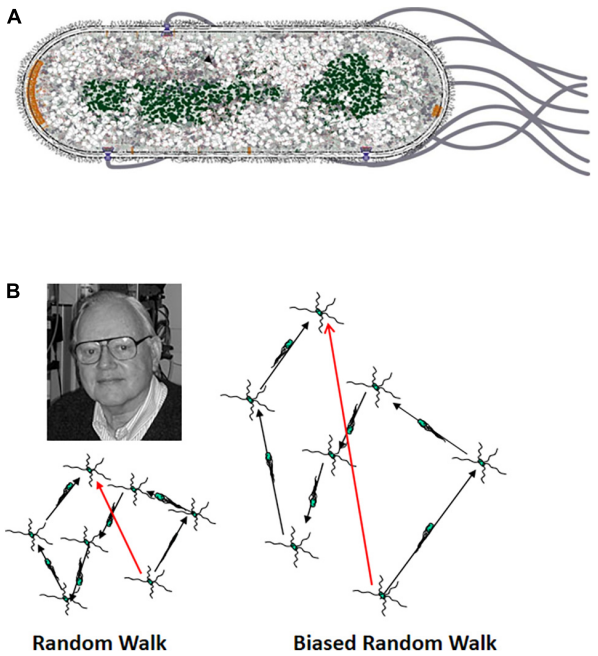


FIGURE 1 | (A) Diagram of an *E. coli* cell. *E. coli* is a rod-shaped, gram-negative bacterium. It has an inner and outer membrane with a thin but relatively rigid peptidoglycan (PG) cell wall in the periplasmic space between the two membranes. The four to six flagella arise at random points along lateral surface of the cell cylinder. The proximal hook serves as a universal joint to allow rotation of the flagellum perpendicular to the cell envelope to bend 90° so that the left-handed helical flagellar filaments can come together to form a bundle that pushes the cell. The nucleoid is shown in green, and the chemoreceptor patches at the cell poles are shown in orange. The patch at the old pole is larger. In this image it is at the leading end of the cell, although the old pole can be either at the leading or trailing end (Berg and Turner, 1995). **(B)** The three-dimensional random walk. The image at the left shows a two-dimensional projection of a cell that is running and tumbling in three dimensions. The image to the right shows a cell that is swimming in a gradient of an attractant chemical with a higher concentration at the top. The runs in the up-gradient direction are longer than in the image to the left, whereas the runs in the down-gradient direction are of the same length. The shorter runs in the absence of an attractant gradient provide space for Howard Berg to look on approvingly from the upper left.

These discoveries came just at the time that the behavior of swimming cells was being recorded automatically by the tracking microscope invented by Howard Berg (1971). The tracking microscope had been used to show that *E. coli* cells swim in a behavior first called running and twiddling (**Figure 1B**), with twiddles later being called tumbles (Berg and Brown, 1972). The cells swim on a path (the run) that is as straight as can be given the rotational diffusion of an object as small as an *E. coli* cell. They then go through a brief period of chaotic motion (the twiddle

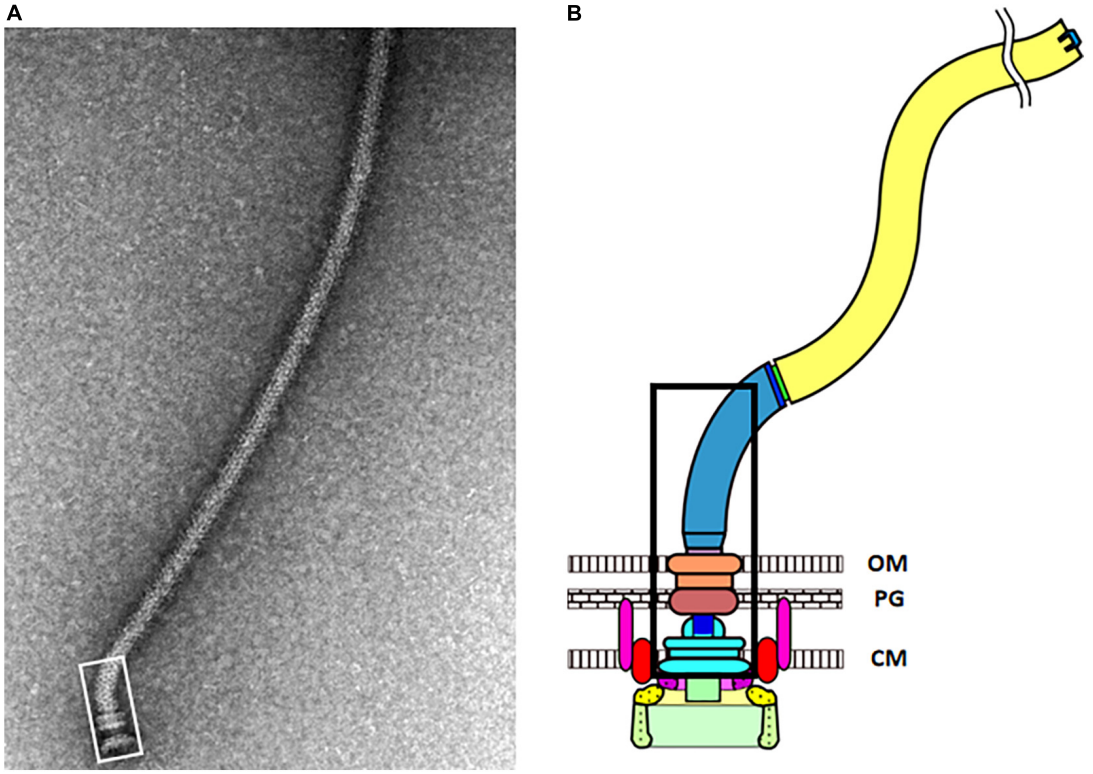


FIGURE 2 | (A) Electron micrograph of an isolated flagellum. The vast majority of the photo shows the long flagellar filament. The hook-basal body complex is outlined by the white rectangle at the lower left. It contains the MS-ring, the rod, the P-ring, the L-ring, and the proximal hook. The C-ring, the export apparatus, and the MotAB stators did not co-isolate with the hook-basal body complex. **(B)** Cartoon image of an *E. coli* flagellum. The portion of the hook-basal body outlined by the white rectangle in panel **(A)** is outlined by the black rectangle. Two MotAB stator units are shown, with MotA in red and MotB in pink. Below the MS-ring (light blue) is the export apparatus show in purple and as a green rectangle. FliG (yellow) is at the top of the C-ring, where it can interact with MotA. FliM and FliN (light green) are below FliG (Images kindly provided by Tohru Minamino, Osaka University).

or tumble) that reorients them before the onset of the next run. The average change in heading is about 68°, slightly biased in the direction the cell had been heading. Both runs and tumbles show an exponential length distribution, with the mean run lasting about 1 s and the mean tumble about 0.1 s. This behavior was aptly described as a 3-dimensional random walk.

The runs became longer when the cells swam up a concentration gradient of a chemical that was an attractant (Mesibov and Adler, 1972; Adler et al., 1973) or down a concentration gradient of a chemical that was a repellent (Tso and Adler, 1974). The data from the Adler lab with tethered cells made it clear that CCW flagellar rotation (viewed looking down the axis of the flagellar bundle toward the cell) propels runs and implies that CW flagellar rotation leads to tumbles. Cells swimming down an attractant gradient or up a repellent gradient do not change the length of their runs. This led Berg to conclude that *E. coli* is an optimist, happy when things are getting better and soldiering on unresponsively when things are getting worse. This differed from the classical idea that bacteria navigate by responding to negative stimuli with an avoidance response, the Schreckbewegung (shock reaction) described by Engelmann (1883).

The next major advance was the demonstration that flagellar rotation is powered by the ion motive force across the membrane. The Adler lab had shown as early as 1974 that an intermediate in oxidative phosphorylation, not ATP, was the driving force for flagellar rotation (Larsen et al., 1974a). In 1977, motility was induced in a suspension of non-motile de-energized cells of *Streptococcus* strain V4051 with a valinomycin-induced potassium diffusion potential or a transmembrane pH gradient (Manson et al., 1977). Thus, either the electrical or chemical component of the proton motive force (pmf) can drive flagellar rotation. Further confirmation of the role of the pmf in bacterial motility was provided by the Skulachev group (Glagolev and Skulachev, 1978).

Using de-energized tethered cells of the motile *Streptococcus*, it was demonstrated that the rotational speed of the flagellar motor operating at high load is directly proportional to either the electrical or chemical component of the pmf (Manson et al., 1980). In these experiments, the highest value of the pmf was −80 mV. Rotation was induced even when the sign of the pmf was reversed so that hydrogen ions flowed out of, rather than into, the cells.

A similar result was obtained using voltage-clamp experiments with giant *E. coli* cells (Fung and Berg, 1995). In this study, the linear dependence on pmf was extended to −150 mV, nearly the −170 mV pmf maintained by actively metabolizing

E. coli cells. It was also shown that an interior positive pmf drove CW rotation of a flagellum that rotated CCW in response to an inwardly directed proton flow. This result confirmed a conclusion reached earlier with tethered cells of a *Streptococcus* mutant whose flagella were locked in CCW rotation. Their flagella spun CW when an inside-positive potassium diffusion potential was induced with valinomycin in the presence of a high external KCl concentration (Berg et al., 1982).

The motile *Streptococcus* had one more contribution to make to our understanding of flagellar rotation. It was used to estimate the proton flux through the flagellar motor (Meister et al., 1987). The data suggested that about 1,200 protons were required per rotation of the flagellum. This result led to the conclusion that when the motor operates at high load, as in a tethered cell, it works with close to 100% efficiency. For rapidly spinning flagella, the efficiency is much lower, probably "due to dissipation by processes internal to the motor."

The bacterial flagellum is a complex machine (**Figure 2**). In *E. coli*, the products of about 40 genes (**Table 1**) are required to construct a fully functional flagellum. In other species, particularly those with very rapidly rotating flagella (e.g., *Vibrio* species) or internal periplasmic flagella (spirochetes), other

TABLE 1 | Proteins involved in the regulation, assembly, and structure of the *E. coli* flagellum.

Protein	Function	Component of mature flagellum	Operon	Map location (min)
FlgA	P-ring assembly	No	*flgA*	24
FlgB	Proximal rod	Yes	*flgB-J*	24
FlgC	Proximal rod	Yes	*flgB-J*	24
FlgD	Hook cap	No	*flgB-J*	24
FlgE	Hook protein	Yes	*flgB-J*	24
FlgF	Proximal rod	Yes	*flgB-J*	24
FlgG	Distal rod	Yes	*flgB-J*	24
FlgH	L-ring	Yes	*flgB-J*	24
FlgI	P-ring	Yes	*flgB-J*	24
FlgJ	Muramidase	No	*flgB-J*	24
FlgK	Hook-filament junction (at hook)	Yes	*flgKL*	25
FlgL	Hook-filament junction (at filament)	Yes	*flgKL*	25
FlgM	Inhibitor of σ^F	No	*flgMN*	24
FlgN	Chaperone for FlgK and FlgL	No	*flgMN*	24
FlhA	Protein export	Yes	*flhBAE*	42
FlhB	Protein export specificity	Yes	*flhBAE*	42
FlhC	Master transcriptional regulator	No	*flhDC*	42
FlhD	Master transcriptional regulator	No	*flhDC*	43
FlhE	Regulation of protein exporter	Yes	*flhBAE*	43
FliA	Sigma factor for late flagellar genes (σ^F)	No	*fliA*	43
FliC	Flagellin (polymerizes to form filament)	Yes	*fliC*	43
FliD	Filament cap (needed for FliC polymerization)	Yes	*fliDST*	43
FliE	MS-ring rod junction	Yes	*fliE-K*	43
FliF	MS-ring	Yes	*fliE-K*	43
FliG	C-ring, interacts with MotA	Yes	*fliE-K*	43
FliH	Protein export	Yes	*fliE-K*	43
FliI	Protein export (ATPase)	Yes	*fliE-K*	43
FliJ	Export chaperone	Yes	*fliE-K*	43
FliK	Hook-length control	No	*fliE-K*	43
FliL	Stability of flagellum	Yes	*fliL-R*	44
FliM	C-ring, switch component, binds CheY-P	Yes	*fliL-R*	44
FliN	C-ring, switch component	Yes	*fliL-R*	44
FliO	Scaffold for FliPQR assembly	No	*fliL-R*	44
FliP	Protein export	Yes	*fliL-R*	44
FliQ	Protein export	Yes	*fliL-R*	44
FliR	Protein export	Yes	*fliL-R*	44
FliS	FliC chaperone	No	*fliDST*	43
FliT	FliC chaperone	No	*fliDST*	43
MotA	Stator component, interacts with FliG	Yes	*motAB*[a]	43
MotB	Stator component, bind to PG cell wall	Yes	*motAB*[a]	43

[a] *The complete operon is motABcheAW.*

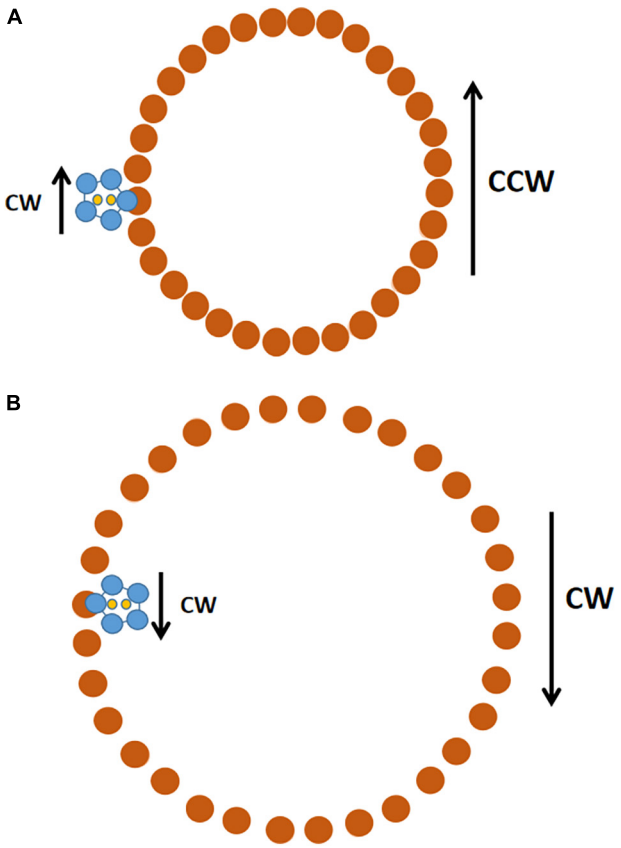


FIGURE 3 | Schematic of how a CW-rotating stator can drive both CCW and CW rotation of the C-ring. The view is looking down from the cell membrane toward the top of the C-ring. **(A)** The C-ring is in its compact conformation. In the stator unit (MotA pentamer in blue, MotB dimer in yellow), the MotA pentamer rotates CW around the MotB dimer, which is fixed in place by its attachment to the PG cell wall. The inner edge of the MotA ring contacts FliG (brown) in the C-ring and drives its CCW rotation. There are 34 FliG subunits in the C-ring (Hu et al., 2022); the cartoon shows 32 because it was easier to get 32 evenly spaced. **(B)** The C-ring is in the expanded conformation it assumes after binding of CheY-P to FliMN. The stator unit remains fixed in the same position, but now, when the MotA pentamer rotates CW, its outer edge makes contact with FliG and drives rotation of the C-ring in the CW direction. Only one stator unit is shown, but there is room for up to 11 stators to associate with the C-ring.

proteins are required, but the basic set of parts remains the same. Most of the gene products are designated as Flg, Flh, or Fli, depending on where on the chromosome the encoding genes are located. Four of these proteins are transcriptional regulators. Others are required only transiently during the assembly of the flagellum. Two of them, MotA and MotB, are not required to build a flagellum but are required for it to rotate. They are of special interest because they comprise a common element, presumably evolved from a common ancestral gene, that is found in several rotary motors discussed in this issue that are coupled to processes other than flagellar rotation.

The first part of the flagellum to assemble is the membrane-inserted MS-ring. It is composed of 26 copies of the FliF protein. The rod, the proximal hook, and the filament extend outward from the MS-ring. The C-ring, made up of the FliG, FliM, and FliN proteins, assembles on the cytoplasmic face of the MS-ring. FliM and FliN interact with the signaling protein CheY, which is converted into its active phosphorylated form at the chemoreceptor patch, to switch the direction of flagellar rotation from CCW to CW. FliG, which is attached firmly to FliF in the MS-ring, interacts with MotA, which supplies the force needed for rotation of the C-ring.

MotAB constitute the ion channel and form the stator component of the flagellar motor. They function as stators because the C-terminal portion of the MotB protein binds tightly to the peptidoglycan (PG) cell wall. Stators can be added to induce the rotation of paralyzed flagellar basal bodies that are already assembled but not functioning (Silverman et al., 1976). When the flagellar motor operates at high load, as in a tethered cell, the addition of each stator causes an equal step increase in rotation speed (Block and Berg, 1984). The original estimate was that up to 8 MotAB units could be added to a motor (Blair and Berg, 1988), but later work raised that estimate to a maximum of at least 11 stator units per motor (Reid et al., 2006). The flagellar motor can operate at low load with a single stator unit, but additional stators are recruited when increased load on the motor requires the production of higher torque (Lele et al., 2013; Tipping et al., 2013).

Charged residues in a cytoplasmic loop of the MotA subunit of the stator make electrostatic contact with charged residues in the C-terminal "motility" domain of the FliG protein to apply torque to the C-ring (Zhou et al., 1998a). In *E. coli*, the association of stator units with the flagellum is dynamic. There is a rapid exchange between motor-associated stator units and a pool of dissociated stator elements freely diffusing in the membrane (Leake et al., 2006). The dwell time of a stator unit on a motor in that study was about 30 s.

When the stator units are in the membrane and not associated with a flagellar motor, a plug in the MotB subunit blocks the flow of protons (Hosking et al., 2006). A radical refolding of the periplasmic domain of MotB occurs when a stator unit associates with the C-ring (Kojima et al., 2009). This conformational change does two things; it unplugs the ion-conducting channel in the stator, and it extends the PG-binding domain so that it can bind to the PG cell wall. Thus, anchoring of the stator and its activation as an ion channel are coupled events.

The stoichiometry of MotA and MotB was thought to be 4:2 (Kojima and Blair, 2004). It is striking how long that misconception persisted and perhaps delayed the discovery that the stator rotates. An aspartate residue near the cytoplasmic end of the membrane-spanning N-terminal segment of MotB is critical either as a site of protonation (Zhou et al., 1998b) or of Na^+-binding to the MotB homolog PotB in sodium-driven motors (Fukuoka et al., 2009). Transmembrane helices 3 and 4 of MotA and the single transmembrane helix of MotB form the ion-conducting channel (Braun et al., 2004). Most models for stator function envisioned the cytoplasmic loop of MotA swinging back and forth like the arm of a parent propelling children on a playground merry-go-round. That is how I described it in my bacterial physiology class. It remained a puzzle, however, why twice as many channel elements were present in MotA as in

MotB. Were two of the MotA proteins just loafing some of the time?

The original estimate of A to B subunit stoichiometry in the stator was based on biochemical analysis of purified stator complexes. However, carefully those experiment were carried out, they cannot match the accuracy of actually imaging the stator complexes with cryo electron microscopy. Two groups accomplished that in 2020 (Deme et al., 2020; Santiveri et al., 2020). Both studies agreed that the stoichiometry is 5 MotA to 2 MotB subunits rather than 4:2. The new 5:2 ratio suggested that only one effective ion-conducting channel exists at a time and led to immediate speculation that what must be happening is that the MotA pentamer rotates around the MotB dimer in a temporal series of 10 steps of 36° in a full rotation.

The contacts between MotA and FliG would allow rotation of the stator to drive rotation of the C-ring, and thus of the entire flagellum (Hu et al., 2022). The stators presumably rotate only CW, but they can drive the rotation of the C-ring in either direction (**Figure 3**). If the C-ring is in a compact configuration, the CW-rotating stators would make the C-ring rotate CCW. If the C-ring is in an expanded configuration, the CW-rotating stators would make the C-ring rotate CW.

This was one of those amazing moments in science when one discovery solves multiple problems. The first is how a flow of ions through the stator into the cell translates into rotation of the C-ring. The second is how flagella can rotate bidirectionally when the ion flow is normally always from outside the cytoplasm to inside. The third is why a flagellum that normally rotates only CCW reverses to CW rotation when the proton motive force is inside positive; if protons flow outward through the stator, it should rotate CCW and drive CW rotation of the C-ring fixed in the compact conformation.

It was the discovery of the rotating stator that provided the impetus for compiling an issue devoted to rotary nanomachines. Various aspects of flagella are the topics of seven articles. Four articles consider systems that operate with homologs of MotAB that are coupled to functions other than flagellar motility: movement over surfaces by gliding bacteria, transport of large substrates across the outer membrane of gram-negative bacteria, and cell division. Two articles consider a structure that superficially looks like a flagellum but is functionally and evolutionarily completely distinct: the ATP-hydrolysis-driven archaellum of the Archaea. Finally, seven articles discuss the rotary FoF1 ATP synthase. Evidence to support the idea that this enzyme in *E. coli* is a rotary device was presented by the laboratory of Paul Boyer in 1987 (Kandpal and Boyer, 1987) and demonstrated to be a rotary device by direct observation in 1997 (Noji et al., 1997). The energy for all of these rotary machines other than the archaellum is provided by a transmembrane ion motive force that drives the coupling ion down its potential energy gradient into the cell. This issue celebrates both rotary nanomachines and the life of Howard Berg, who departed us on December 30, 2021. Enjoy.

AUTHOR CONTRIBUTIONS

MM conceived and wrote the article.

REFERENCES

Adler, J., Hazelbauer, G. L., and Dahl, M. M. (1973). Chemotaxis toward sugars in *Escherichia coli*. *J. Bacteriol.* 115, 824–847.

Berg, H. C. (1971). How to track bacteria. *Rev. Sci. Instrum.* 42, 868–871. doi: 10.1063/1.1685246

Berg, H. C., and Anderson, R. A. (1973). Bacteria swim by rotating their flagellar filaments. *Nature* 245, 380–382. doi: 10.1038/245380a0

Berg, H. C., and Brown, D. A. (1972). Chemotaxis in *Escherichia coli* analysed by three-dimensional tracking. *Nature* 239, 500–504. doi: 10.1038/239500a0

Berg, H. C., Manson, M. D., and Conley, M. P. (1982). Dynamics and energetics of flagellar rotation in bacteria. *Symp. Soc. Exp. Bio.* 35, 1–31.

Berg, H. C., and Turner, L. (1995). Cells of *Escherichia coli* swim either end forward. *Proc. Natl. Acad. Sci. U. S. A* 92, 477–479. doi: 10.1073/pnas.92.2.477

Blair, D. F., and Berg, H. C. (1988). Restoration of torque in defective flagellar motors. *Science* 242, 1678–1681. doi: 10.1126/science.2849208

Block, S. M., and Berg, H. C. (1984). Successive incorporation of force-generating units in the bacterial rotary motor. *Nature* 309, 470–472. doi: 10.1038/309470a0

Braun, T. F., Al-Mawsawi, L. Q., Kojima, S., and Blair, D. F. (2004). Arrangement of core membrane segments in the MotA/MotB proton-channel complex of *Escherichia coli*. *Biochemistry* 43, 35–45. doi: 10.1021/bi035406d

Deme, J. C., Johnson, S., Vickery, O., Aron, A., Monkhouse, H., Griffiths, T., et al. (2020). Structures of the stator complex that drives rotation of the bacterial flagellum. *Nat. Microbiol.* 5, 1553–1564. doi: 10.1038/s41564-020-0788-8

Engelmann, T. W. (1883). Bacterium photometricum. Ein Beitrag zur vergleichenden Physiologie des Licht- und Farbsinnes. *Pflügers Arch. Gesamte Physiol. Menschen Thiere* 30, 95–124. doi: 10.1007/bf01674325

Fukuoka, H., Sowa, Y., Kojima, S., Ishijima, A., and Homma, M. (2009). Sodium-dependent dynamic assembly of membrane complexes in sodium-driven flagellar motors. *Mol. Microbiol.* 71, 825–835. doi: 10.1111/j.1365-2958.2008.06569.x

Fung, D. C., and Berg, H. C. (1995). Powering the flagellar motor of *Escherichia coli* with an external voltage source. *Nature* 375, 809–812. doi: 10.1038/375809a0

Glagolev, A. N., and Skulachev, V. P. (1978). The proton pump is a molecular engine of motile bacteria. *Nature* 272, 280–282. doi: 10.1038/272280a0

Hosking, E. R., Vogt, C., Bakker, E. P., and Manson, M. D. (2006). The *Escherichia coli* MotAB proton channel unplugged. *J. Mol. Biol.* 364, 921–937. doi: 10.1016/j.jmb.2006.09.035

Hu, H., Santiveri, M., Wadwha, N., Berg, H. C., Erhardt, M., Taylor, N. M. I., et al. (2022). Structural basis of torque generation in the bi-directional bacterial flagellar motor. *Trends Biochem. Sci.* 47, 160–172. doi: 10.1016/j.tibs.2021.06.005

Kandpal, R. P., and Boyer, P. D. (1987). *Escherichia coli* F1 ATPase is reversibly inhibited by intra- and intersubunit crosslinking: an approach to assess rotational catalysis. *Biochim. Biophys. Acta* 890, 97–105. doi: 10.1016/0005-2728(87)90073-9

Kojima, S., and Blair, D. F. (2004). Solubilization and purification of the MotA/MotB complex of Escherichia coli. *Biochemistry* 43, 26–34. doi: 10.1021/bi035405l

Kojima, S., Imada, K., Sakuma, M., Sudo, Y., Kojima, C., Minamino, T., et al. (2009). Stator assembly and activation mechanism of the flagellar motor by the periplasmic region of MotB. *Mol. Microbiol.* 73, 710–718. doi: 10.1111/j.1365-2958.2009.06802.x

Larsen, S. H., Reader, R. W., Kort, E. N., Tso, W. W., and Adler, J. (1974b). Change in direction of flagellar rotation is the basis of the chemotactic response in *Escherichia coli*. *Nature* 249, 74–77. doi: 10.1038/249074a0

Larsen, S. H., Adler, J., Gargus, J. J., and Hogg, R. W. (1974a). Chemomechanical coupling without ATP: the source of energy for motility and chemotaxis in

bacteria. *Proc. Natl. Acad. Sci. U. S. A.* 71, 1239–1243. doi: 10.1073/pnas.71.4.1239

Leake, M. C., Chandler, J. H., Wadhams, G. H., Bai, F., Berry, R. M., Armitage, J. P., et al. (2006). Stoichiometry and turnover in single, functioning membrane protein complexes. *Nature* 443, 355–358. doi: 10.1038/nature05135

Lele, P., Hosu, B. G., and Berg, H. C. (2013). Dynamics of mechanosensing in the bacterial flagellar motor. *Proc. Natl. Acad. Sci. U. S. A.* 110, 11839–11844. doi: 10.1073/pnas.1305885110

Manson, M. D., Tedesco, P., Berg, H. C., Harold, F. M., and Van der Drift, C. (1977). A protonmotive force drives bacterial flagella. *Proc. Natl. Acad. Sci. U. S. A.* 74, 3060–3064. doi: 10.1073/pnas.74.7.3060

Manson, M. D., Tedesco, P. M., and Berg, H. C. (1980). Energetics of flagellar rotation in bacteria. *J. Mol. Biol.* 138, 541–561. doi: 10.1016/s0022-2836(80)80017-9

Meister, M., Lowe, G., and Berg, H. C. (1987). The proton flux through the bacterial flagellar motor. *Cell* 49, 643–650. doi: 10.1016/0092-8674(87)90540-x

Mesibov, R., and Adler, J. (1972). Chemotaxis toward amino acids in *Escherichia coli*. *J. Bacteriol.* 112, 315–326. doi: 10.1128/jb.112.1.315-326.1972

Noji, N., Yasuda, R., Yoshida, M., and Kinosita, K. Jr. (1997). Direct observation of rotation of F1 ATPase. *Nature* 386, 299–302. doi: 10.1038/386299a0

Reid, S. W., Leake, M. C., Chandler, J. H., Lo, C. J., Armitage, J. P., Berry, R. M., et al. (2006). The maximum number of torque-generating units in the flagellar motor of *Escherichia coli* is at least 11. *Proc. Natl. Acad. Sci. U. S. A.* 103, 8066–8071. doi: 10.1073/pnas.0509932103

Santiveri, M., Roa-Eguiara, A., Kühne, D., Wadwha, N., Hu, H., Berg, H. C., et al. (2020). Structure and function of stator units of the bacterial flagellar motor. *Cell* 183, 244–257.e16. doi: 10.1016/j.cell.2020.08.016

Silverman, M., and Simon, M. (1974). Flagellar rotation and the mechanism of bacterial motility. *Nature* 249, 73–74.

Silverman, M., Matsumura, P., and Simon, M. (1976). The identification of the mot gene product with Escherichia coli-lambda hybrids. *Proc. Natl. Acad. Sci. U.S.A.* 73, 3126–3130. doi: 10.1073/pnas.73.9.3126

Tipping, M. J., Delalez, N. J., Lim, R., Berry, R. M., and Armitage, J. P. (2013). Load-dependent assembly of he bacterial flagellar motor. *Mbio* 4, e00551–13. doi: 10.1128/mBio.00551-13

Tso, W. W., and Adler, J. (1974). Negative chemotaxis in *Escherichia coli*. *J. Bacteriol.* 118, 560–576. doi: 10.1128/jb.118.2.560-576.1974

Watson, J. D., and Crick, F. H. (1953). Molecular structure of nucleic acids: a structure for deoxyribose nucleic acid. *Nature* 171, 737–738. doi: 10.1038/171737a0

Zhou, J., Lloyd, S. A., and Blair, D. F. (1998a). Electrostatic interactions between rotor and stator in the bacterial flagellar motor. *Proc. Natl. Acad. Sci. U. S. A.* 95, 6436–6341. doi: 10.1073/pnas.95.11.6436

Zhou, J., Sharp, L. L., Tang, H. L., Lloyd, S. A., Billings, S., Braun, T. F., et al. (1998b). Function of protonatable residues in the flagellar motor of *Escherichia coli*: a critical role for Asp 32 of MotB. *J. Bacteriol.* 180, 2729–2735. doi: 10.1128/JB.180.10.2729-2735.1998

Conflict of Interest: The author declares that the research was conducted in the absence of any commercial or financial relationships that could be construed as a potential conflict of interest.

Publisher's Note: All claims expressed in this article are solely those of the authors and do not necessarily represent those of their affiliated organizations, or those of the publisher, the editors and the reviewers. Any product that may be evaluated in this article, or claim that may be made by its manufacturer, is not guaranteed or endorsed by the publisher.

Copyright © 2022 Manson. This is an open-access article distributed under the terms of the Creative Commons Attribution License (CC BY). The use, distribution or reproduction in other forums is permitted, provided the original author(s) and the copyright owner(s) are credited and that the original publication in this journal is cited, in accordance with accepted academic practice. No use, distribution or reproduction is permitted which does not comply with these terms.

frontiers | Frontiers in Microbiology

TYPE Review
PUBLISHED 05 August 2022
DOI 10.3389/fmicb.2022.948383

Check for updates

OPEN ACCESS

EDITED BY
Michael Manson,
Texas A&M University, United States

REVIEWED BY
Tohru Minamino,
Osaka University, Japan
David Blair,
The University of Utah, United States

*CORRESPONDENCE
Richard M. Berry
Richard.Berry@physics.ox.ac.uk
Nicholas M. I. Taylor
nicholas.taylor@cpr.ku.dk

†These authors have contributed equally to this work

SPECIALTY SECTION
This article was submitted to Microbial Physiology and Metabolism, a section of the journal Frontiers in Microbiology

RECEIVED 19 May 2022
ACCEPTED 04 July 2022
PUBLISHED 05 August 2022

CITATION
Rieu M, Krutyholowa R, Taylor NMI and Berry RM (2022) A new class of biological ion-driven rotary molecular motors with 5:2 symmetry.
Front. Microbiol. 13:948383.
doi: 10.3389/fmicb.2022.948383

COPYRIGHT
© 2022 Rieu, Krutyholowa, Taylor and Berry. This is an open-access article distributed under the terms of the Creative Commons Attribution License (CC BY). The use, distribution or reproduction in other forums is permitted, provided the original author(s) and the copyright owner(s) are credited and that the original publication in this journal is cited, in accordance with accepted academic practice. No use, distribution or reproduction is permitted which does not comply with these terms.

A new class of biological ion-driven rotary molecular motors with 5:2 symmetry

Martin Rieu[1,2†], Roscislaw Krutyholowa[3†], Nicholas M. I. Taylor[4*] and Richard M. Berry[1,2*]

[1]Department of Physics, University of Oxford, Oxford, United Kingdom, [2]Kavli Institute for Nanoscience Discovery, Dorothy Crowfoot Hodgkin Building University of Oxford, Oxford, United Kingdom, [3]Department of Biology, Institute of Molecular Biology and Biophysics, ETH Zurich, Zurich, Switzerland, [4]Novo Nordisk Foundation Center for Protein Research, University of Copenhagen, Copenhagen, Denmark

Several new structures of three types of protein complexes, obtained by cryo-electron microscopy (cryo-EM) and published between 2019 and 2021, identify a new family of natural molecular wheels, the "5:2 rotary motors." These span the cytoplasmic membranes of bacteria, and their rotation is driven by ion flow into the cell. They consist of a pentameric wheel encircling a dimeric axle within the cytoplasmic membrane of both Gram-positive and gram-negative bacteria. The axles extend into the periplasm, and the wheels extend into the cytoplasm. Rotation of these wheels has never been observed directly; it is inferred from the symmetry of the complexes and from the roles they play within the larger systems that they are known to power. In particular, the new structure of the stator complex of the Bacterial Flagellar Motor, $MotA_5B_2$, is consistent with a "wheels within wheels" model of the motor. Other 5:2 rotary motors are believed to share the core rotary function and mechanism, driven by ion-motive force at the cytoplasmic membrane. Their structures diverge in their periplasmic and cytoplasmic parts, reflecting the variety of roles that they perform. This review focuses on the structures of 5:2 rotary motors and their proposed mechanisms and functions. We also discuss molecular rotation in general and its relation to the rotational symmetry of molecular complexes.

KEYWORDS

bacterial flagellar motility, molecular machine, cryo EM, structure function, rotary motor

Introduction

Nature has made very little use of the wheel for locomotion. On the macroscopic scale, there are good reasons for this. First, there is the problem of how to exchange nutrients and other metabolic necessities with a wheel that needs to be physically separate from the rest of the organism if it is to rotate. Furthermore, without flat roads, a wheel is not very effective for animal locomotion. Neither of these problems exists, however, for life on the micro- and nano-scales, where diffusion solves the nutrient transport problem and immersion in aqueous solutions makes "roads" irrelevant. The first-discovered natural wheel is the Bacterial Flagellar Motor (BFM), a rotary device that propels

swimming bacteria (Wadhwa and Berg, 2021). Rotation of the BFM was proposed in 1973 (Berg and Anderson, 1973), and much has been learned about it since then. Until 2020, the only other known wheels in nature were the family of F-, V- and A-type ATPases (Müller and Grüber, 2003; Kühlbrandt and Davies, 2016; Guo and Rubinstein, 2018). Rotation of the F_1-ATPase coupled to ATP hydrolysis was inferred from biochemical evidence (Duncan and Bulygin, 1995) and later observed directly in 1997 (Noji et al., 1997), and the rotational mechanism has been described in considerable detail (Noji et al., 1997; Sobti et al., 2021; Guo and Rubinstein, 2022; Noji and Ueno, 2022). In its native setting, the F_1 component of the F_1F_O ATP-synthase synthesizes ATP as F_O turns in response to the ion-motive force. In the reverse reaction, ATP hydrolysis by F_1 can drive the rotation of F_O in the opposite direction, leading to the pumping of ions out across the membrane. Rotation is also a component of the motion of other known molecular machines, including many that move relative to helical DNA molecules, usually coupled to ATP hydrolysis. But this class of motion is closer to a nut and bolt or screw than to a wheel.

Several new structures of three types of protein complexes, obtained by cryo-electron microscopy (cryo-EM) and published between 2019 and 2021, identify a new family of natural molecular wheels, the "5:2 rotary motors." These consist of a pentameric wheel encircling a dimeric axle within the cytoplasmic membrane of both Gram-positive and Gram-negative bacteria. The axles extend into the periplasm, and the wheels extend into the cytoplasm. Rotation of these wheels has never been observed directly; it is inferred from the symmetry of the complexes and from the roles they play within the larger systems that they are known to power. In particular, the new structure of the stator complex of the BFM, $MotA_5B_2$, is consistent with a "wheels within wheels" model of the BFM. To quote the late Howard Berg: "So, remarkably, the rotary flagellar motor is powered by an array of even smaller rotary motors. This represents a major shift in thinking about how the stator units operate" (Wadhwa and Berg, 2021). Other 5:2 rotary motors are believed to share the core rotary function and mechanism, driven by ion-motive force at the cytoplasmic membrane. Their structures diverge in their periplasmic and cytoplasmic parts, reflecting the variety of roles that they perform. This review focuses on general aspects of the structures of 5:2 rotary motors and their proposed mechanisms and functions.

We also discuss molecular rotation in general and its relation to the rotational symmetry of molecular complexes. Rotation is a natural way to achieve a repetitive process within a confined space. It is also an effective way to generate locomotion, similar to either a wheeled vehicle or the propellers of boats and aeroplanes. Any rotary machine is defined by the parts that rotate relative to each other. By convention, the part that is anchored to its surroundings is called the "stator," and the other is called the "rotor."

Because equivalent components in different 5:2 motors may be anchored in some cases and not in others, and because the entire $MotA_5B_2$ complex has long been identified as the BFM "stator unit," we will avoid using the terms "stator" and "rotor" for the parts of 5:2 motors and rotary complexes, reserving them for parts of the entire BFM. Instead, to avoid confusion, we will use "outer" to designate the part further from the rotation axis and "inner" for the other. Known rotary molecular motors can be characterized by symmetry mismatches between the inner and outer parts. These mismatches are thought to be intrinsic to their rotary mechanism. For example, the outer:inner symmetry ratio for F_1 is 3:1, and for F_O it is 1:n, where the c-ring rotational symmetry n ranges from 8 to 15 (Cheuk and Meier, 2021). Rotational symmetries in the BFM are large and variable: current rotor structures are 34- and 46-fold (other rotor symmetries may be discovered in future), and the number of stator units can vary between 1-fold and 18-fold (Chang et al., 2021). However, the discovery that the repeating unit of the BFM stator is a 5:2 rotary motor, which is now believed to be entirely responsible for torque generation, indicates that BFM symmetry mismatches are not intrinsic to its fundamental mechanism. The discovery of the family of 5:2 rotary motors raises the question of whether rotary motors with other symmetries remain to be discovered, and what considerations select for which symmetries. We address these and other symmetry-related questions in later parts of this article.

Structures of ion-driven 5:2 rotary motors

MotAB

Many species of bacteria utilize flagella to move. Flagella generate propulsion *via* clockwise (CW) or counterclockwise (CCW) rotation (as viewed, per convention, from outside the cell) of a helical extracellular filament stemming from the hook, which is attached to the BFM rotor (Armitage and Berry, 2020). The BFM is a circular transmembrane macromolecular assembly approximately 60 nm in diameter, depending on the species (Chang et al., 2020). In Gram-negative bacteria, it consists of obligatory L-, P-, MS- and C-ring structures that owe their names to their positions relative to the membrane (Zhu et al., 2017). Some species have additional, often large, stator structures (reviewed by Terashima et al., 2017), for example, the H- and T-rings that are hypothesized to be necessary in sodium-driven BFMs (Merino and Tomás, 2016; Zhu et al., 2017). In *Escherichia coli* and *Salmonella enterica*, rotation of the C-ring in either direction is driven by multiple independent $MotA_5B_2$ stator units, whose rotation is driven by H^+ influx across the cytoplasmic membrane, which is driven by the protonmotive force (PMF). In other species other ions replace H^+; for example, *Vibrio alginolyticus* has Na^+-driven stator units called $PomA_5B_2$. Stator units are now believed to rotate unidirectionally, pushing a ring of FliG on the periphery of the C-ring *via* either their proximal or distal parts (relative to the rotation axis of the entire BFM) to drive CCW or CW rotation, respectively (Carroll et al., 2020). The overall structure and mechanism of the BFM are discussed further

below and illustrated in Figure 1. The MS- and C-rings near the cytoplasmic membrane are parts of the rotor and are present in all BFMs, whereas the L- and P- rings are stationary bushings that transmit rotation through the outer membrane and are unique to Gram-negative bacteria.

BFM stator units are molecular assemblies of approximately 200 kDa encoded by the products of two genes from a single operon (Liu and Ochman, 2007). Each unit comprises a single "5:2 rotary motor," in which an outer part consisting of five transmembrane, predominantly alpha-helical, MotA subunits surrounds a cavity that accommodates an inner part consisting of the two N-terminal transmembrane helices of a MotB dimer (Figure 2A). Within the MotA protein, two domains can be clearly distinguished – a transmembrane domain, involved in proton-driven torque generation, and a cytoplasmic domain, which transfers mechanical energy to FliG in the C-ring. The crystal structure of the C-terminal domain of MotB revealed a peptidoglycan-binding domain that anchors the MotAB stator unit to the cell wall and restricts lateral in-membrane diffusion, keeping MotAB available for the C-ring. Several studies shed light on the structures of periplasmic domains of MotB from *Helicobacter pylori*, *S. enterica*, and PomB from *V. alginolyticus* (Kojima et al., 2009; Oneill et al., 2011; Zhu et al., 2014). The N-termini of the MotB dimer comprises an axle for MotA rotation, followed by a short helical plug that mechanically fixes the position of MotA relative to MotB, stopping rotation (Morimoto et al., 2010; Homma et al., 2021; Figure 2B). Genetic deletion of the plug reduces bacterial growth rates (Hosking et al., 2006) because the uncontrolled proton flow acidifies the cytoplasm.

It is likely that the periplasmic side of MotA contains narrow H^+ channels that allow protons to flow from the periplasm to a binding site at a conserved aspartate residue (D22 in *Campylobacter jejuni*, D32 in *E. coli* (Zhou et al., 1998) and D33 in *S. enterica*) mid-way across the membrane on MotB (Figure 2C). Proton binding neutralizes the otherwise negatively charged D22. This is mimicked by the mutation MotB D22N, which induces only very limited changes (in a structure from *C. jejuni*) – mainly a reorientation of one of the side chains of residue 22 when the structure of the unplugged wild-type stator is compared to the structure of the unplugged D22N stator. These observations, along with the 5:2 rotational symmetry, suggest a model for the mechanism of coupling proton flux to the rotation of MotAB and the other 5:2 rotary motors, which is described below.

Recently, cryo-EM-based atomic models have been built for the H^+-dependent stator units of *C. jejuni*, *Bacillus subtilis*, and *Clostridium sporogenes* (Deme et al., 2020; Santiveri et al., 2020). EM maps have also been obtained for the Na^+–driven *V. alginolyticus* and *Vibrio mimicus* PomAB and the H^+-driven *Shewanella oneidensis* MotAB. All of them share the same 5:2 stoichiometry and have a common subunit arrangement. However, there are some noticeable differences. For instance, the MotAB stator units from Gram-negative bacteria possess a slightly bigger periplasmic/extracellular part than their Gram-positive counterparts (Figures 3A,B). In addition, the MotA pentamer from Gram-negative *C. jejuni* organizes with near-perfect C5 symmetry, whereas the C5 symmetry

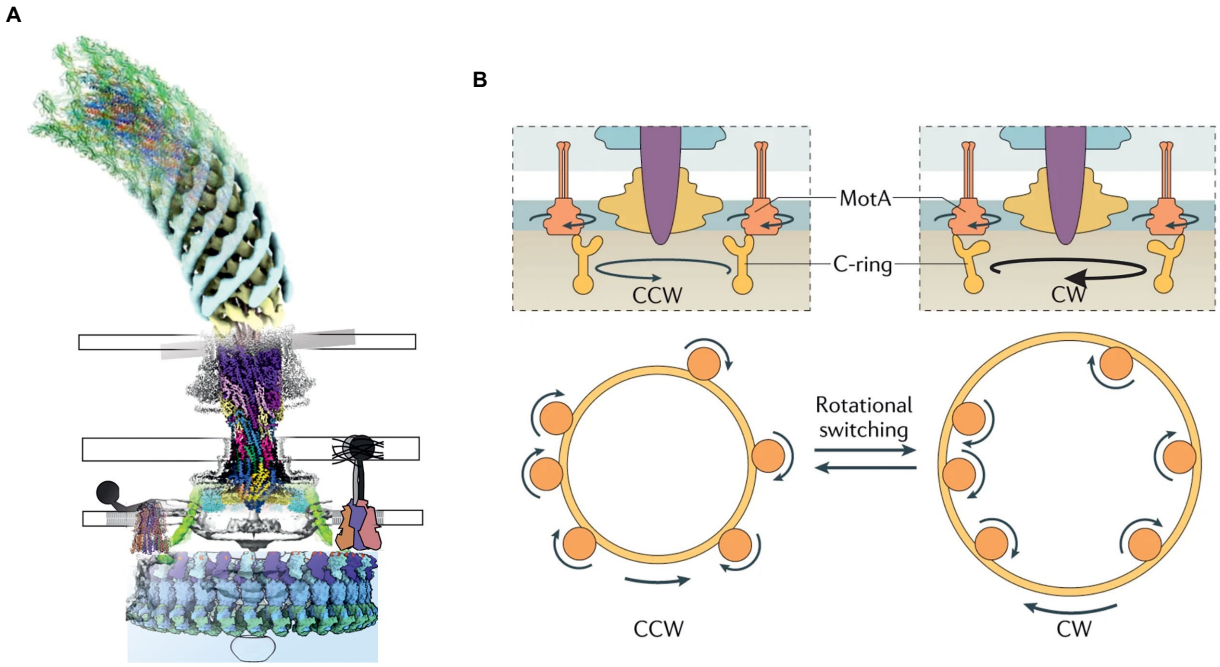


FIGURE 1
(A) A composite model of the bacterial flagellar motor based on the published structures. **(B)** The current model of rotation and switching of the BFM driven by the unidirectional rotation of MotAB. (**B** adapted from: https://www.nature.com/articles/s41579-021-00626-4).

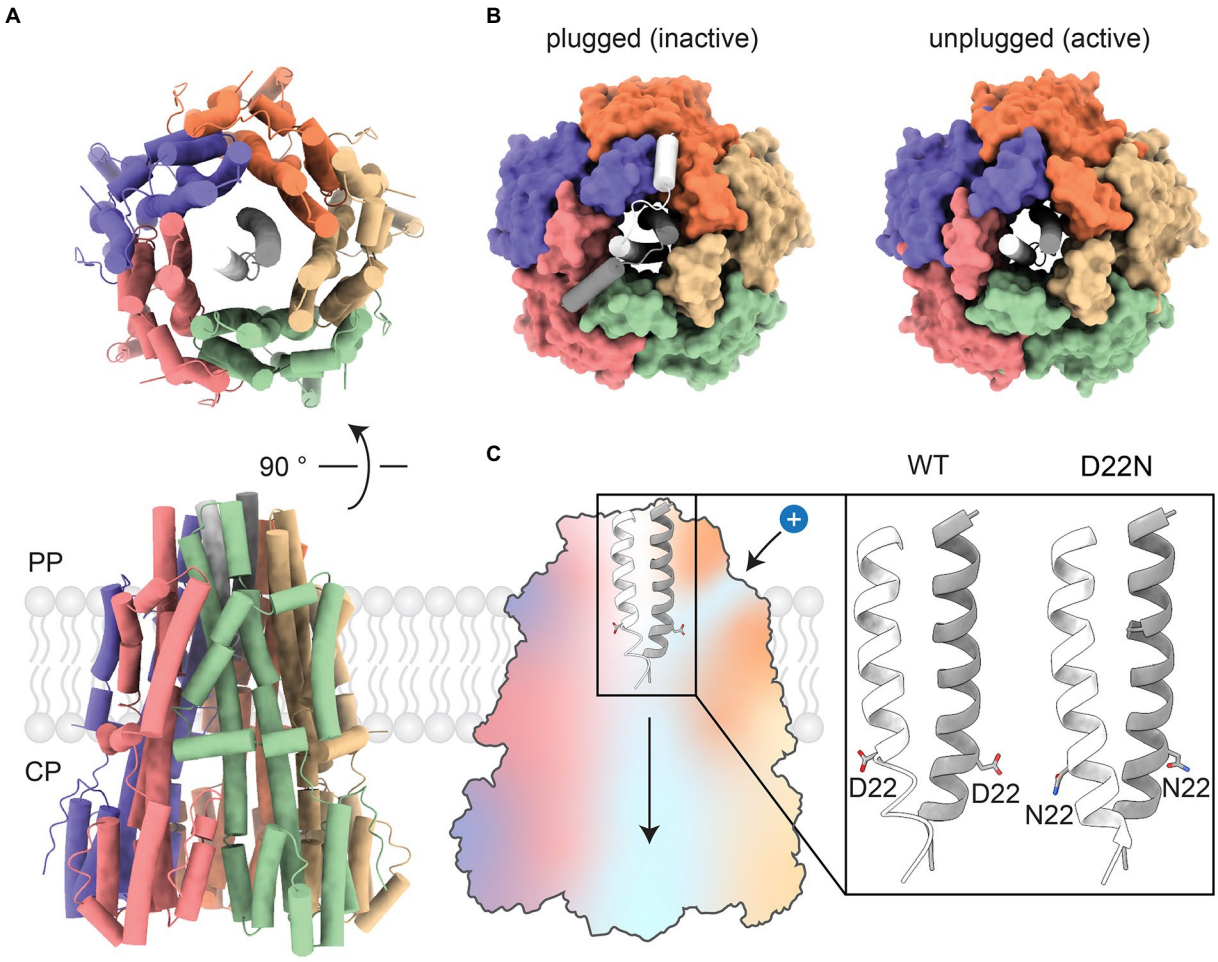


FIGURE 2
Overview of the *Cj*MotA/MotB complex. **(A)** Top and front views of the *Cj*MotA (colored)/*Cj*MotB (white and gray) protein complex in 5:2 stoichiometry (PDB ID:6YKP). **(B)** Comparison of plugged (left, inactive, PDB ID: 6YKM) and unplugged (right, active, PDB ID: 6YKP) complexes. Plugs mechanically block the rotation of the MotA pentamer relative to MotB. **(C)** (Left) Proton channels for proton influx and dissociation in MotA/B complex are shown as blue areas on the cross-section of the MotA/B complex. (Right) Close-up view of MotB helices with D22 highlighted. Unprotonated side chains of aspartic acid (D22) point upward, facing the proton inlet channel (PDB ID: 6YKP). The protonation-mimetic residue substitution D22N reorients the sidechain of residue 22 downward, enabling MotA/B movement (PDB ID: 6YKR).

of the MotA pentamer from a Gram-positive *C. sporogenes* is more distorted. The potential mechanistic causes of asymmetry in the case of *C. sporogenes* MotA have been discussed (Deme et al., 2020). However, it is not clear whether such a difference is systematic between Gram-positive and Gram-negative bacteria or whether it is observed due to enhanced stability of alternative or intermediate states captured by cryo-EM in particular species. The difference between a symmetric structure of *B. subtilis* MotAB and an asymmetric *C. sporogenes* MotAB, both Gram-positive, favor the stability-related hypothesis. Additional structures of Gram-positive and Gram-negative stators should resolve this issue.

ExbBD

Another example of a structurally characterized 5:2 rotary motor is the ExbBD complex, which is vital for the function of the Ton system responsible for the uptake of iron ions, vitamin B12, and biopolymers (Faraldo-Gómez and Sansom, 2003; Noinaj et al., 2010; Krewulak and Vogel, 2011; Celia et al., 2020). In Gram-negative bacteria, the ExbBD complex is located in the inner membrane (IM). It utilizes the PMF to activate transport at TonB-dependent receptors, over ~20 nm distant in the outer membrane (OM) (Du et al., 2014; Celia et al., 2020; Ratliff et al., 2021). The C-terminal domain of TonB interacts with TonB-dependent receptors and induces conformational changes which promote ligand uptake. Recent cryo-EM reconstructions of ExbBD from *E. coli* and *Serratia marcescens* reveal the familiar 5:2 arrangement (Figure 3D; Celia et al., 2019; Biou et al., 2021). As in MotAB, five transmembrane ExbB proteins surround two central ExbD helices. Unfortunately, existing cryo-EM reconstructions lack structural information on other parts of the complex that are important for its function: a relatively large cytoplasmic domain of ExbB and the periplasmic domain of

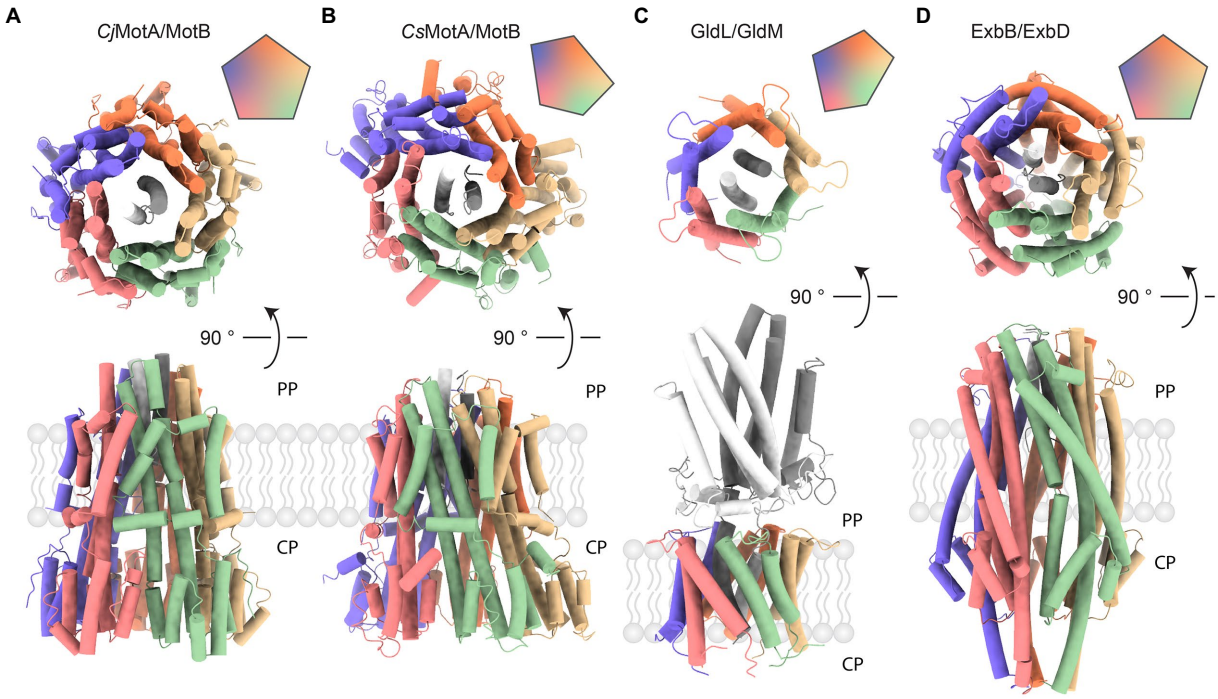


FIGURE 3
Comparison of complexes with 5:2 stoichiometry. Vertical (top) and horizontal (bottom) views of protein complexes with 5:2 stoichiometry. Assembly symmetry is represented by the top right insert. PP stands for periplasm, CP indicates cytoplasm. **(A)** MotA/B complex from a Gram-negative *Campylobacter jejuni* (PDB ID: 6YKP). **(B)** MotA/B complex from a Gram-positive *Clostridium sporogenes* (PDB ID: 6YSF). **(C)** GldL/M complex from a Gram-negative *Flavobacterium johnsoniae* (PDB ID: 6YS8). The periplasmic domain is shown in gray. **(D)** ExbB/D complex from a Gram-negative *Serratia marcescens* (PDB ID: 7AJQ). ExbB (colored) accommodates two helices from ExbD (shades of gray) that serve as a rotational axis.

ExbD. Other important parts of the TonB-ExbBD structure remain to be solved (Maki-Yonekura et al., 2018). Despite the fact that the C-terminal domain of TonB bound to several TonB-dependent receptors has been structurally characterized, the question of specificity and regulation of these interactions also remains largely unanswered (Pawelek et al., 2006; Josts et al., 2019). Cryo-EM studies from 2016 and 2018 observed several different stoichiometries of *E. coli* ExbB:D, which varied from 5:0, 5:1, 6:0, and 6:3, depending on pH and purification protocol (Figures 4A,B; Celia et al., 2016; Maki-Yonekura et al., 2018). It remains to be seen whether these forms have any physiological relevance or are artifacts of sample preparation.

GldLM

Gram-negative Bacteroidetes utilize another 5:2 motor, the GldLM complex, as a proton-driven engine for gliding motility on solid surfaces and to power type IX secretion systems (McBride, 2019; Wadhwa and Berg, 2021). A structure of the *Flavobacterium johnsoniae* GldLM complex (homologous to *Porphryomonas gingivalis* PorLM, for which a lower-resolution map was obtained) was determined recently using cryo-EM (Figure 3C; Hennell James et al., 2021). The composition of the type IX secretion system and putative functions of its individual parts are described in a recent review (Gorasia et al., 2020). Like MotAB, GldLM consists of proteins expressed from a single operon (Braun et al., 2005). GldL and GldM form the outer and inner parts, respectively, corresponding to MotA and MotB. Like MotB, the periplasmic domains of GldM dimerize. However, GldLM shares no obvious sequence homology with MotAB. While MotB binds peptidoglycan, anchoring the complex, the periplasmic part of GldM contains four domains, which upon dimerization form an 18 nm long shaft that may function to transfer mechanical energy to a proposed GldNK ring that is required for gliding motility and Type 9 protein secretion (Leone et al., 2018). Transmembrane GldL subunits are arranged in an asymmetric pentagon, similarly to MotA in Gram-positive bacteria (Figures 3B,C). Potential causes and effects of GldLM asymmetry have been discussed (Hennell James et al., 2021).

Phylogenetics

The evolution of proton-driven rotation appears to be functionally convergent between BFM stator units and rotary ATP synthases. These systems utilize the same principle of proton-driven rotation despite having separate evolutionary histories and

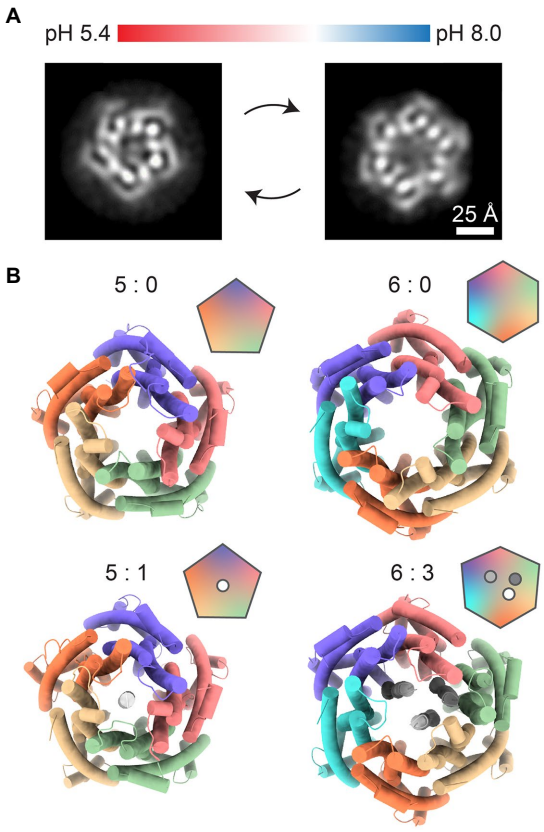


FIGURE 4
Other possible stoichiometries of the ExbB/D complex.
(A) Changes in pH shift the equilibrium between pentameric (left) and hexameric (right) ExbB/D complexes. Images represent relevant 2D class averages from Maki-Yonekura et al. (2018).
(B) Top views of previously solved ExbB/D complexes. Labels indicate the ExbB:ExbD ratio. The 5:0 complex (PDB ID: 5SV0) was published by Celia et al. (2016). The 5:1 (PDB ID: 5ZFV), 6:0 (PDB ID: 5ZFP) and 6:3 (PDB ID: 5ZFU) complexes were published by Maki-Yonekura et al. (2018).

seemingly unrelated amino acid and DNA sequences. However, within the 5:2 motors, divergence seems more likely, given the sequence and structural relationships between different systems. MotAB and ExbBD are known to be homologs (Marmon, 2013). MotAB and ExbBD and the other 5:2 motors TolQR and AglRQS, and GldLM not only serve different purposes; they also vary in how they are arranged within their larger systems. MotB, the inner part of the MotAB 5:2 motor, binds the peptidoglycan cell wall, anchoring the stator unit in place. By contrast, in current models of the function of GldLM, the inner GldM part rotates to pass mechanical energy to the rest of the gliding system. There is no direct evidence for anchoring of GldL, but without it rotation of the 5:2 motor could be wasted as the rotation of GldL in the membrane rather than transferred efficiently to the intended targets *via* GldM. It remains to be determined experimentally whether pentameric ExbB and GldL rotate in the membrane and, if not, which factors prevent them from doing so. Anchoring could be achieved either by binding an unknown protein partner, by alterations in local lipid composition, or even by lipid conjugation to the pentameric barrels. In the absence of structural information for TolQR and AglRQS, speculation as to their wider function is based on the assumption that they too are 5:2 rotary motors.

To explore the likely range and variation among 5:2 rotary motor complexes, we systematically queried UniProt database. First, we asked how many different bacterial species and strains possess individual MotA, MotB, ExbB, ExbD, GldL, and GldM annotated subunits. As expected, the majority of analyzed species contain InterPro family annotations for both complex-forming proteins (Figure 5A). In species that have 5:2 complexes with outer and inner proteins (overlapping circles in Figure 5A), some species contain multiple sets of outer proteins, which results in a greater number of proteins than species (Figure 5B). The number of species containing MotB is greater than those containing MotA (Figure 5A, top), and the number of MotBs in species containing both MotA and MotB is also larger (Figure 5B, top). This effect is absent, or even slightly reversed, for ExbBD and GldLM (Figures 5A,B, middle, bottom). This may simply be an artifact of poor protein family annotation (we examined five species with MotB but no MotA annotated, selected at random, and in all cases found a MotA gene candidate in the vicinity that might yield a protein product of high similarity to MotA). More interestingly, it may indicate various specialized MotA variants that assemble on-demand around a particular type of MotB protein that confines the stator to a particular molecular neighborhood. To our knowledge, there is no experimental evidence to corroborate or falsify this hypothesis.

To explore the variability of the proteins we identified, we analyzed the sequence-length distributions of proteins (Figure 5C). MotA proteins show two unequal, narrow peaks in the vicinity of 250 a.a. ExbB and GldL are very similar. The inner parts, MotB, ExbD, and GldM, each show a single peak, which is broad for MotB and narrow for the others. Unlike MotA, in which a relatively large portion of the protein is transmembrane, most of the polypeptide in the MotB family is periplasmic, and variation in the thickness of the periplasm between species may explain the broad sequence length distribution of MotB. ExbD is rather short compared to other inner proteins, and the distribution of sequence lengths of ExbD-like proteins shows a skewed single-peak distribution, which could be related to its interaction with TonB. GldM, by contrast, is much larger, which is consistent with its proposed function as a shaft spanning the periplasm.

Finally, we performed synteny (co-localization) analysis of genes encoding these 5:2 rotary molecular motors using GeCon T (Figure 5D; Martinez-Guerrero et al., 2008). The gene order appears to be well preserved in Bacteria, except for *Desulfovibrio magneticus* RS-1, in which MotB precedes MotA. Other interesting cases of the genomic context of stator unit genes are highlighted.

We tried to systematically check several model organisms for the existence of 5:2 rotary motor proteins using both annotations from UniProt database and protein BLAST to verify protein identity. Within our selected set of model species, MotA and MotB

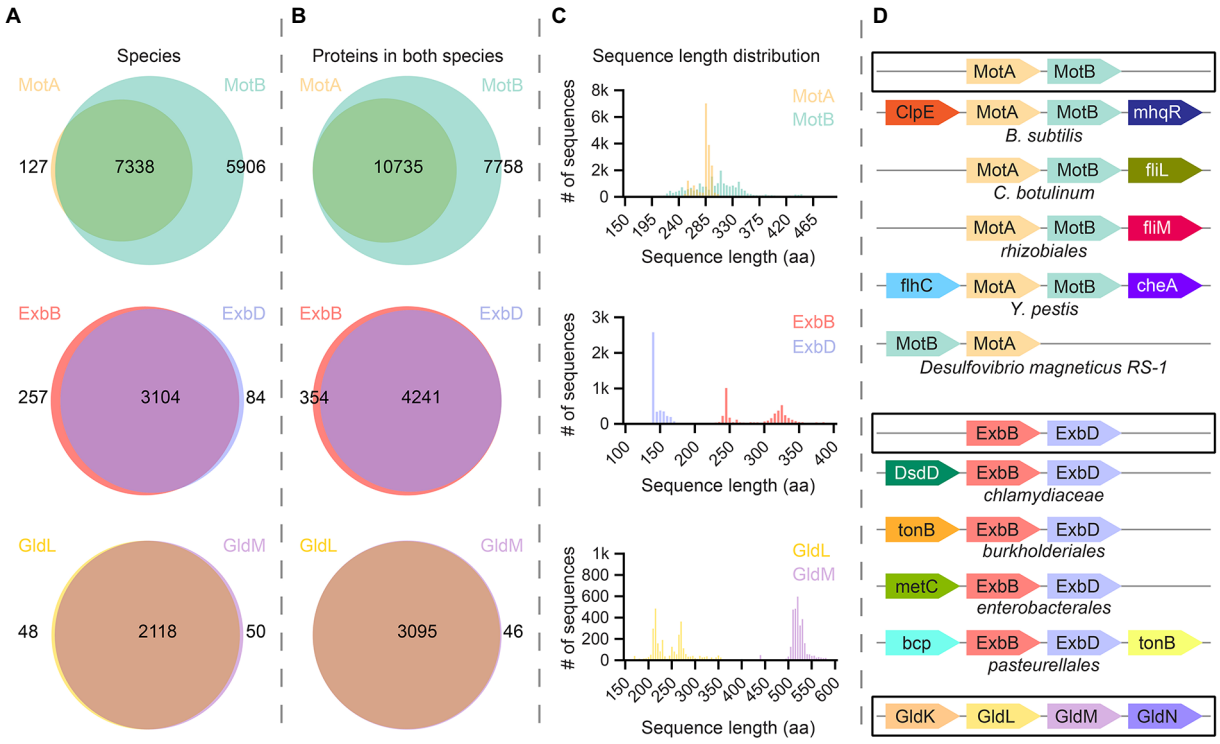


FIGURE 5
Bioinformatic analysis of bacterial proteins in the MotA/MotB family. **(A)** UniProt database were systematically screened for species that contain the MotA, MotB, ExbB, ExbD, GldL, or GldM proteins. In most cases, species contain annotations for both the transmembrane-barrel component and the rotational-axis component of a protein pair. **(B)** We analyzed the number of proteins in species that contain two elements of molecular motors [overlapping in **(A)**]. The number of annotated ExbB/D and GldL/M proteins is rather similar, whereas there are many more annotations for MotB than for MotA. **(C)** Sequence length distribution of all proteins described in **(B)**. Each histogram bin represents 5 amino acids. Proteins from the MotA family show a narrow two-peak distribution, whereas proteins from MotB family show more divergent lengths. ExbB and GldL proteins come in two length classes with normal distributions, while the size distribution of ExbD and GldM proteins is rather uniform. **(C)** The most prominent cases of synteny (co-localization) of genes encoding molecular machines. A typical scenario is highlighted by black rectangles. Functionally relevant or widespread genomic neighbors are shown. MotA-MotB synteny is broken only in the case of *Desulfovibrio magneticus RS-1*.

are present in all Gram-negatives and some Gram-positives. The ExbBD system is considered a property of Gram-negative bacteria, although there are several ExbB-family proteins annotated in *Staphylococcus aureus* and *C. sporogenes*. It remains to be tested experimentally whether, and if so how, some orthologs of the Ton system function in Gram-positive microorganisms with a thick cell wall and in the absence of the ExbD subunit. The GldLM system is present exclusively in Bacteroidetes.

A model for the rotary mechanism

Any molecular motor is defined by coupling directed mechanical motion, on a length scale similar to that of the entire motor, to an energy source such as a chemical reaction. Coupling consists of a "mechanochemical cycle" – a cyclic set of transitions between different states that both consume (electro) chemical free energy and generate directed movement (Berry, 2000). The mechanism is defined by these states and by the constraints imposed by the structure of the motor upon transitions between them. In particular, for ion-driven rotary motors, binding or unbinding of ions must change the freedom of one part to rotate relative to the other, and the rotation angle must in turn change the accessibility of the ion-binding sites from each side of the membrane. It is the interplay of these constraints that defines the mechanochemical cycle.

The new structures of 5:2 rotary motors provide strong evidence for a rotary mechanism in two ways. Most obviously, the 5:2 symmetry mismatch between outer and inner parts creates a 10-fold periodicity in the rotation angle: states separated by 1/10th of a revolution are identical except for the exchange of individual, nominally identical, subunits. Thus, the mechanochemical cycle is fully defined by a sub-cycle that describes a 36° rotation. Figure 6 shows the simplest and most general such cycle for any 5:2 rotary motor, a variant of the classic "turnstile" model (Berry, 2000) first proposed for the entire BFM in the 1980s (Mitchell, 1984) and now believed to apply to the rotation of F_O of the ATP-synthase (Pogoryelov et al., 2009). The model is based on the following two critical constraints.

1. It is impossible for a proton-binding site (e.g., MotB-D22 in *C. jejuni* MotB) to access both periplasm and cytoplasm in the

same mechanochemical state. Otherwise, protons could cross the membrane uncoupled from rotation – the motor would leak. Because 5 divided by 2 is not an integer, each proton-binding site contacts a different part of the inner cavity of the surrounding pentamer; allowing each to be accessible to different ionic "half-channels" in the pentamer. A half-channel has access to either the periplasm (e.g., Figure 2C) or cytoplasm. In the model presented in Figure 6, periplasmic and cytoplasmic half-channels are shown as thick blue and orange lines, respectively, and proton leakage is prevented by a rotational offset between the two sets of five channels. The offset angle is unknown, but for simplicity, Figure 6 shows the offset as 1/10th of a rev. The structures of the wild-type and protonation-mimicking D22N mutant MotAB (Figure 2C) suggest that motions of the side chain of D22 may also contribute to the separation of the cytoplasmic and periplasmic half-channels (Santiveri et al., 2020).

2. The central dimer (e.g., $MotB_2$) is free to rotate within the pentamer, through ~1/10th of a revolution (between states [H -] and [H -]′ in Figure 6), only in a sub-set of protonation states. In Figure 6, a suitable set of such rotation constraints arises from simple constraints on individual binding sites: charged sites can access only angles indicated by red "rails," whereas neutral protonated sites can access only angles indicated by gray rails. Santiveri et al.'s (2020) model based on details of the structure of MotAB imposes slightly different constraints, allowing rotation only when both MotB-D22-binding sites are protonated. A hydrophobic patch on MotA, which a charged site cannot pass, has been proposed as a possible structural explanation (Santiveri et al., 2020). The BFM is believed to work with a "power stroke" mechanism (Berry and Berg, 1999; Lo et al., 2013), which would be the case if the rotation transition releases free energy, for example by coupling proton motion across some part of the membrane voltage to rotation (Santiveri et al., 2020). In general, however, this rotation need not be directly coupled to proton motion in all 5:2 rotary motors.

Figure 6 illustrates the mechanochemical cycle that couples the net transport of one proton across the membrane to a rotation of 36°. Individual MotA subunits of the outer pentamer are identified by different colors, and the inner dimer molecules are shown in shades of gray and black. The transitions out of each state that are allowed are indicated by black arrows. The range of accessible rotation angles (gray pie-wedges) rotates by 36° when the protonated binding sites are swapped, between [H -] and [– H], in a direction that depends upon the direction of proton flow that achieved the swap. The heavy arrows in Figure 6 show the preferred directions with a typical PMF, which drives proton influx. The turnstile cycle can be understood by following the proton that binds to the "black" site from the periplasm in state [– H], rotates around the gray rail from a periplasmic half-channel to a cytoplasmic half-channel, i.e., from [H -] to [H -]′, and leaves to the cytoplasm. Protons on the gray site follow an equivalent path but are half a cycle out of phase. It is the net left-handed helicity of these paths that sets the direction of coupling between rotation and proton flux, in this instance coupling proton influx to CW rotation of the pentamer relative to the dimer, as viewed from outside the cell. Reversing the direction of proton flow to outward in non-switching chemotaxis mutants, either by setting up an interior-positive K^+-diffusion potential in *Streptococcus* strain V4051 (Berg et al., 1982), or by reversing the polarity of voltage-clamped giant *E. coli* cells (Fung and Berg, 1995), appears to reverse the direction of motor rotation.

There is currently no evidence as to whether the ion-binding sites (and channels) in GldLM are on the inner or outer components. The turnstile model can accommodate either possibility; it requires only that the half channels and binding sites are on different components and that they describe "helical" ion transit paths that include rotation between inner and outer components. It is not known in any 5:2 motor whether protonation swapping proceeds *via* doubly protonated [H H] or doubly charged [– –] states, or both, in part because current resolution of the obtained cryo-EM reconstructions does not allow visualization of protons.

The mechanochemical cycle of Figure 6 does not include a role for the experimentally observed broken C_2 symmetry of the MotB dimer within the entire 5:2 complex, nor for conformational changes within the dimer or pentamer (Kojima and Blair, 2001). However, the general scheme (Figure 6) still works in essentially the same way if the central dimer is allowed to have multiple conformations and to sit asymmetrically within the pentamer, for example, following the Santiveri et al. model (Santiveri et al., 2020; Supplementary Figure S1). The details of motor constraints should be revealed as new structures capture new states in the cycle and biophysical experiments constrain models according to their predicted patterns of flagellar rotation.

Various cations can replace H^+ as the coupling ion in the BFMs of different species. For example, some Na^+-driven stator units also work with Li^+ or Cs^+. With its high atomic number, Cs^+ is a good candidate for potential structural determination of the ionization states of the motor. Whatever details may be discovered in various 5:2 rotary motor mechanisms, 10-fold rotational symmetry is almost certain to be a universal feature.

The rotary model is very a natural inference from the structure of 5:2 motors. The present state of knowledge is comparable to that of F_1 ATPase after the first atomic structure of F_1 (Abrahams et al., 1994) showed 3:1 symmetry, with a 3-fold $\alpha_3\beta_3$ outer symmetry broken by the asymmetric inner γ-subunit, strongly suggestive of a rotary mechanism. Direct proof of the rotary mechanism by single-molecule biophysical experiments soon followed (Noji et al., 1997).

What does the rotary model of 5:2 motors predict for such experiments? First – rotation itself, confirming that defining feature of the mechanism. Second – the mechanochemical cycles described above couple the transit of 10 ions to each rotation of the motor. This sets an upper limit of $10ePMF/2\pi$ to the motor torque, *via* the principle of Conservation of Energy, where e is the unit charge and $ePMF$ is the free energy available per ion transit. Third – rotation is predicted to occur in 36° steps corresponding to transitions between symmetrically equivalent states ([– H] and [H -]′

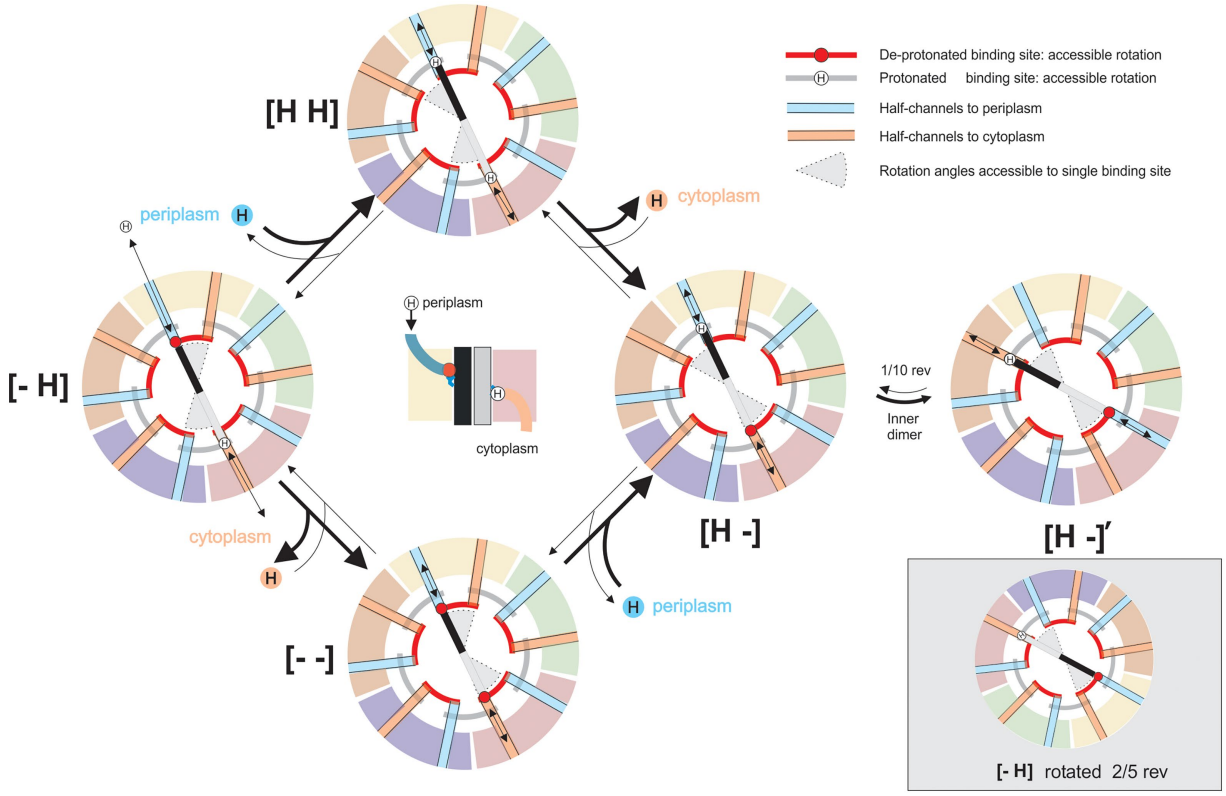


FIGURE 6
A model for the mechanistic basis for the function of 5:2 rotary motors. Schematic cross-sections of a 5:2 rotary motor in a membrane slice containing the proton-binding sites on the inner dimer. Different outer subunits are shown as arcs, distinguished by color, inner subunits are shown as black and gray bars. Deprotonated sites are negatively charged (red circles), protonated sites are neutral ("H"). "Half-channels" linking sites to the periplasm (blue) or cytoplasm (orange) are shown as colored radial lines. The location of half-channels relative to the boundaries between outer subunits is drawn from the MotAB structure (Santiveri et al., 2020), but it does not affect the mechanism and is speculative and illustrative only. Black arrows indicate transitions in the mechanochemical cycle, accessible from each state. Red and gray arcs indicate angles that a binding site can occupy when de-protonated or protonated, respectively. The central image shows a side view of state [– H], illustrating half-channels. In state [– H], the charged "black" binding site can bind a proton from the periplasm, and the "grey" site has a proton bound which can be released into the cytoplasm. Either of these transitions locks dimer rotation due to the constraints on individual binding sites (states [H H] or [– –]). After both transitions are completed the inner dimer is free to rotate counterclockwise (states [H -], [H -]'). States [– H] and [H -]' are equivalent: rotation of the entire complex and exchange of nominally identical subunits maps one onto the other (bottom right). The cycle is reversible, but it is biased by the PMF, which drives protons from the periplasm to the cytoplasm.

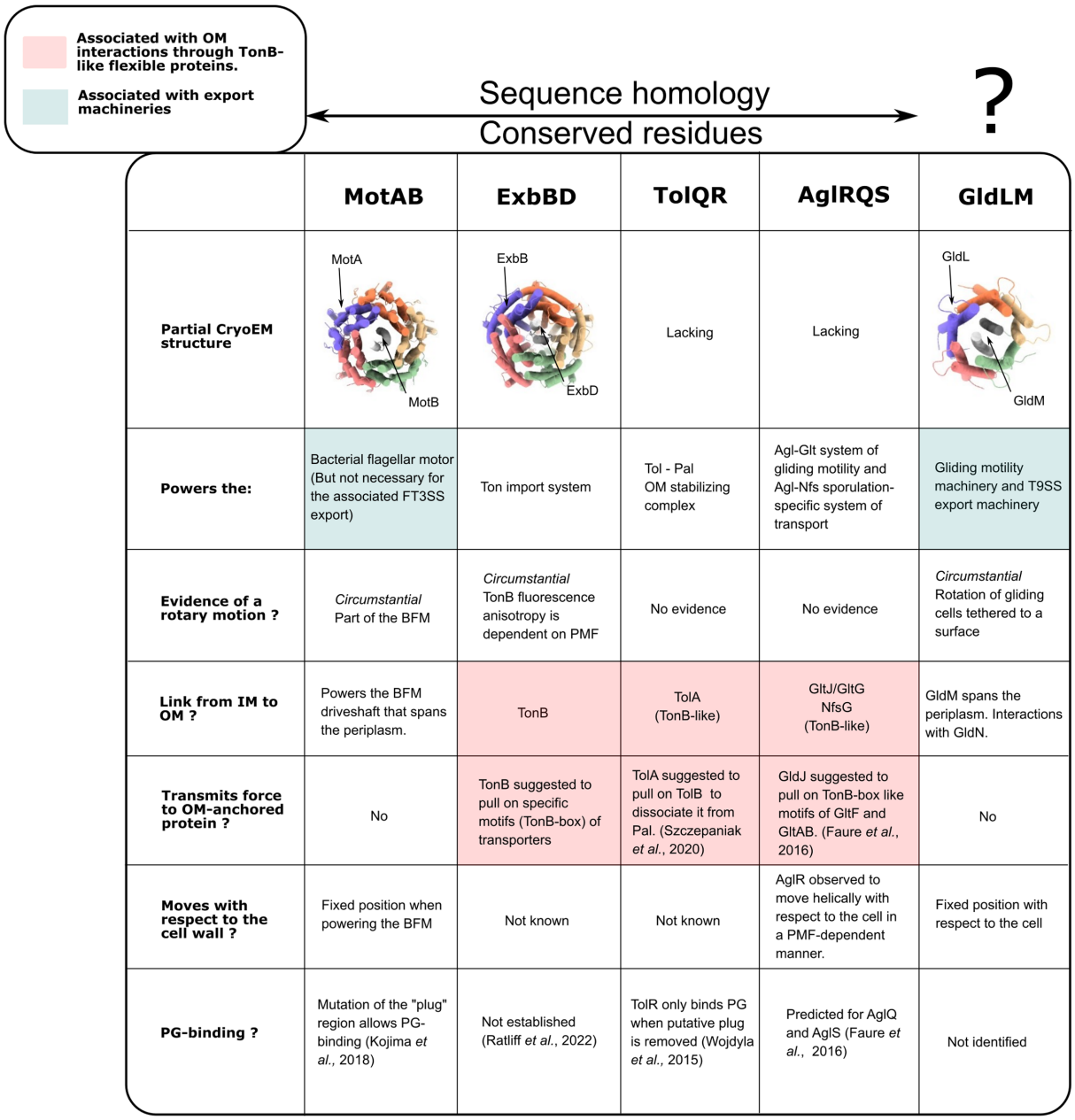
in Figure 6), one per ion transit. The symmetry between these equivalent motor states is broken if the 5:2 rotary motor interacts asymmetrically with an external component. For example, if the flagellar C-ring is to the left in Figure 6, then the two MotB chains are no longer equivalent. In the current model of the BFM, $MotA_5$ interacts with the C-ring at its proximal side during CCW rotation and at its distal side during CW rotation (although recent studies show that a smaller-diameter C-ring induces CW rotation (Sakai et al., 2019), questioning this model). If these interactions are very similar, the effects of C-ring-induced asymmetry may be minimal. Nonetheless, in the interactions with the C-ring, there are only 5 equivalent states per rotation, which may occur in five 72° steps or by "limping" with five pairs of 36° steps with different dwell times. If they could be measured, these patterns of rotation and their dependence upon external factors such as ion concentrations and ion motive force would allow confirmation and a full understanding of the rotary mechanism.

Functions as components of larger systems

To date, high-resolution structures of 5:2 rotary motors have been obtained in three different bacterial systems, and homologous proteins and lower-resolution structures are known in a further two systems (Figure 7). It is reasonable to assume that all share the same essential structural and mechanistic features. Here we discuss what is known, or can be speculated, about how the rotation of the 5:2 motor is coupled to its function in each system.

MotAB, bacterial flagellar motor

The BFM (Figure 1) is the best understood of these systems, and the only one in which rotation of any component (here, the BFM rotor) has been conclusively demonstrated.



	MotAB	ExbBD	TolQR	AglRQS	GldLM
Partial CryoEM structure	MotA / MotB	ExbB / ExbD	Lacking	Lacking	GldL / GldM
Powers the:	Bacterial flagellar motor (But not necessary for the associated FT3SS export)	Ton import system	Tol - Pal OM stabilizing complex	Agl-Glt system of gliding motility and Agl-Nfs sporulation-specific system of transport	Gliding motility machinery and T9SS export machinery
Evidence of a rotary motion ?	*Circumstantial* Part of the BFM	*Circumstantial* TonB fluorescence anisotropy is dependent on PMF	No evidence	No evidence	*Circumstantial* Rotation of gliding cells tethered to a surface
Link from IM to OM ?	Powers the BFM driveshaft that spans the periplasm.	TonB	TolA (TonB-like)	GltJ/GltG NfsG (TonB-like)	GldM spans the periplasm. Interactions with GldN.
Transmits force to OM-anchored protein ?	No	TonB suggested to pull on specific motifs (TonB-box) of transporters	TolA suggested to pull on TolB to dissociate it from Pal. (Szczepaniak *et al.*, 2020)	GldJ suggested to pull on TonB-box like motifs of GltF and GltAB. (Faure *et al.*, 2016)	No
Moves with respect to the cell wall ?	Fixed position when powering the BFM	Not known	Not known	AglR observed to move helically with respect to the cell in a PMF-dependent manner.	Fixed position with respect to the cell
PG-binding ?	Mutation of the "plug" region allows PG-binding (Kojima *et al.*, 2018)	Not established (Ratliff *et al.*, 2022)	TolR only binds PG when putative plug is removed (Wojdyla *et al.*, 2015)	Predicted for AglQ and AglS (Faure *et al.*, 2016)	Not identified

FIGURE 7
Functional comparisons of the PMF-dependent bacterial complexes with known 5:2 structures (MotAB, ExbBD, and GldLM) and their sequence homologs. PDB ID for CryoEM structures, from left to right: 6YKP, 7AJQ, 6YS8. GldLM is reported as lacking sequence homology with other 5:2 motors. However a pairwise sequence alignment using EMBOSS Needle and BLOSUM62 showed identity and similarity of ~15 and 31%, respectively, for MotA/GldL, 18 & 30% for MotB/GldM, indicating the possibility that they might be homologs.

The recent MotAB structures, along with cryo-electron tomography (ET) of entire BFMs *in situ* (Zhao et al., 2013; Carroll et al., 2020), have overturned previous ideas about how the BFM works. The new picture is that energy transduction from the ion motive force to torque occurs entirely within the MotAB stator units, which act as small wheels to rotate the much larger C-ring. The long-established rotation of the BFM is the main supporting evidence for the rotary model of 5:2 complexes. Further support is provided by recent structures of the entire flagellar motor of *Borrelia burgdorferi*, obtained *in situ* by cryo-ET (Chang et al., 2020). These images show that the C-ring contacts opposite sides of the stator units in flagellar motors that are believed to be rotating in opposite directions (Figure 1B). This would allow unidirectional rotation of the stator units to power rotation of the flagellar motor in either direction, explaining switching in the direction

of flagellar rotation, which is at the heart of bacterial chemotaxis. Considerable uncertainty remains as to the details of this model of flagellar switching. In *B. burgdorferi* (Chang et al., 2020), CW motor rotation is associated with increased radius at the top of the C-ring, implying CW rotation of $MotA_5$ (Figure 1B). But in *Vibrio alginolyticus* (Carroll et al., 2020), the change in C-ring radius associated with directional switching is too small to span $MotA_5$, as required by the *B. burgdorferi* model. Furthermore, a FliF-G fusion-deletion mutant of *Salmonella enterica*, with a C-ring of reduced diameter and no apparent space for interactions between FliG and the distal part of MotA (Sakai et al., 2019), rotates CW. Therefore, it remains possible that the details of the flagellar switch, and possibly even the direction of rotation of MotAB, may vary between species.

The MotAB structures show the MotB "plug" helices (Hosking et al., 2006) bent down, possibly closing the periplasmic ion channel and also blocking rotation of the MotB dimer within the MotA pentamer (Kojima et al., 2009, 2018; Li et al., 2011; Terahara et al., 2017; Figure 2B). Studies of single motors show that MotAB stator units in *E. coli* are mechanosensitive – the number of active units is greater when the BFM is working against a higher load (Lele et al., 2013). This has been modeled as a catch bond, which has a decreased off-rate for binding when a load is applied (Nord et al., 2017a). Estimates of the force dependence of the off-rate are consistent with a transition state for activation of tight binding that is shifted by 4 nm from the loosely-bound state (Wadhwa et al., 2021). By comparison, if the C-terminus of the structurally resolved plug helix was pulled to its maximum distance from the membrane without unfolding, it would move about 3 nm from its closed position.

Taken together, these observations suggest a molecular model for mechanosensing. Force generated at the MotA-FliG interface when the motor works under load is transferred to the cell-wall anchor along the length of MotB. This pulls on the C-terminus of the plug helix, opening the ion channel and activating the stator unit and the catch-bond. This model also explains the recent observation that the first stator unit takes longer to bind than subsequent units (Ito et al., 2021). When the first (still plugged) unit binds to both the rotor and the cell wall, there is no motor torque to pull on the plug to activate the unit and start motor rotation, so activation is relatively slow. Subsequent units bind a motor that is already rotating, which pulls the plug as soon as it binds the cell wall, activating these units more rapidly.

Nothing is yet known about the details of the rolling interface between the small and big wheels in the flagellar motor. We can, however, speculate that a likely mechanism is a form of cog-wheel, in which each of 5 MotA "teeth" engages a matching structure in the FliG component of the C-ring. This is supported by the fact that the ratio of FliG units in the C-ring and of MotA units in the stator element (34/5 = 6.80) in *S. enterica* is close to the ratio of the radius of the C-ring and the radius of the MotA pentamer ring (21–25 nm/3.5 nm = 6–7) (Thomas et al., 2006; Chen et al., 2011; Santiveri et al., 2020). Thus, the tangential distances between adjacent FliG and MotA monomers are very similar. This would allow FliG and MotA monomers to match up during rotation. Even if the interface is softer than a cog-wheel implies, tight coupling between rotations of the two wheels is a reasonable expectation, with a gear ratio set approximately by their relative sizes.

Because the C-rings of *E. coli* and *S. enterica* have a 34-fold symmetry (Kawamoto et al., 2021), the cog-wheel model predicts 34/5 revolutions of each MotAB stator unit per revolution of the C-ring. Ten ions per revolution of the MotA pentamer then correspond to $10 \times 34/5 = 68$ ions per MotAB stator unit per revolution of the flagellar motor. (By the same reasoning, in *B. burgdorferi* in which the larger C-ring has a 46-fold symmetry, there would be 92 ions per revolution per stator unit.) Biophysical measurements of torque and speed in single flagellar motors in *E. coli* find a maximum torque of 0.9 pN nm/mV/stator unit, from which energy conservation sets a lower limit of 39 ions per revolution per unit (Nord et al., 2017b). This is less than the above prediction of 68 ions per rev, as required by energy conservation, but the difference between the two numbers begs an explanation – if the experimental estimates are all accurate, the system is wasting energy somewhere. It is also possible that published torque estimates are too low because they were obtained using viscous drag coefficients of polystyrene beads without considering the possibility of contact friction with the cell surface. Alternatively, if there are systematic errors in the opposite direction, then the lower limit might be 34 rather than 39 ions per revolution, corresponding to 5 rather than 10 ions per revolution of MotAB. This would require an entirely new model for the mechanism by which 5:2 rotary motors operate.

The model of 5:2 rotary stator units also makes predictions about the stepping patterns in flagellar rotation. The 26-fold stepping previously reported in the BFM (Sowa et al., 2005) is now understood to be due to the passive bearing at the LP-ring/rod junction (Johnson et al., 2021; Yamaguchi et al., 2021) and not as a signature of the torque generating mechanism. Because the C-ring further breaks the symmetry of the 5:2 MotAB rotary motor, either 10- or 5-fold stepping rotation of MotAB might be observable, corresponding to 68- or 34-fold stepping of the flagellar motor. However, if the coupling is loose – either between ion transit and rotation of MotAB, or in the interface between MotAB and FliG, then very different or even no stepping patterns might be seen. Kinetics of 34-fold steps might contain a signature of underlying 68-fold symmetry, with two proton transits powering each 34-fold step; by direct analogy with unresolved transitions in the F_1 ATP-hydrolyis sub-step [first described as 30° (Yasuda et al., 2001), then revised to 40° (Ueno et al., 2005)]. These two sub-steps were later assigned to separate events in the ATP hydrolysis cycle. The BFM is reviewed elsewhere in this collection (Manson, 2022).

How does current biophysical knowledge of other 5:2 complexes accommodate a rotary model?

The rotary model of MotAB naturally matches its function, powering the rotary BFM. How the known functions of other 5:2 rotary motors (Figure 7) might be achieved by rotation is much less clear. Published biochemical and biophysical characterizations allow the formulation of some hypotheses, which we discuss here.

ExbBD, Ton import system

Fluorescence anisotropy measurements (Jordan et al., 2013) suggest that the ExbBD-bound protein TonB undergoes reorientation *in vivo* during the fluorescence lifetime of the labeling GFP, dependent upon PMF and ExbBD. This is weak evidence for rotation of ExbBD, given that *any* movement of the protein is likely to cause its reorientation. However, it confirms the motion of TonB in the IM coupled through ExbBD to the PMF. As reviewed in the introductory sections, ExbBD powers the unplugging of OM-embedded TonB-dependent transporters (TBDT) *via* the interaction of TonB with the "TonB-box" domain of TBDT. The TBDT thus acts as a gate that can be opened by the PMF, whose energy is harvested by ExbBD, through the action of TonB. TonB is a long protein that spans the periplasm. It has a short N-terminal domain in the cytoplasm, followed by a single transmembrane (TM) helix that interacts with ExbB (Higgs et al., 2002) and a periplasmic domain composed of a flexible linker and a folded C-terminal domain. Single-molecule studies of the unfolding of the plug domain of the TBDT by itself (Thoma et al., 2012) or mediated by TonB (Hickman et al., 2017) showed that forces of at least 50–60 pN were necessary to unfold the TonB boxes. This energy must be transmitted by TonB. TonB is energized by the IM-embedded ExbBD complex and must span the periplasm to interact with the OM-embedded TBDT. This raises two questions: how does TonB find the TBDT and how does it exert force on it?

Regarding the first question, one can formulate several hypotheses. TonB and ExbBD must be recruited to the vicinity of the TBTD and bind to the cell wall there. This process is similar to the dynamic recruitment of MotAB to the BFM (Leake et al., 2006). It is important to note, however, that the TonB-ExbBD complex cannot diffuse in the IM while TonB crosses the PG, as the PG is a solid structure with ~2 nm pores (Demchick and Koch, 1996). It is possible that ExbBD and TonB find the TBDT separately: either could take the lead and recruit the other. Alternatively, TonB might be able to retract to the IM side of the periplasm while bound to ExbBD, allowing IM diffusion of the whole complex. This is supported by NMR data showing that the central portion of TonB consists of two rods spanning 10 nm and joined by a short flexible sequence (Evans et al., 1986; Brewer et al., 1990). This short sequence could allow the extended TonB to fold back on itself in the IM-periplasmic space. The ExbBD-TonB complex could then diffuse, with TonB periodically extending to cross the cell wall to sample the OM until it finds a TBDT. It is interesting to note that ExbD has been shown to form a heterodimer with TonB *in vivo* (Ollis and Postle, 2011) through the same domain of ExbD (structurally similar to the PG-binding motif of LysM (Klebba, 2016), which can homo-dimerize). This suggests that the PG-binding of ExbBD could be induced by TonB and its interaction with the TBDT.

It then remains to explain how ExbBD-TonB can exert force on the TBDT. Klebba proposed that rotation of TonB might be involved in harnessing the PMF (Klebba, 2016). However, at that time there was no hint that ExbD might rotate relative to ExbB. Here, we propose a model in which rotation of ExbBD exerts a force on TBDT *via* displacement of the N-terminus of TonB (Figure 8). The free energy per proton depends on the PMF ($\Delta G = ev$), which in *E. coli* is about 25 pN.nm. The external radius of ExbBD is about 4 nm. In the rotary model ExbBD uses 10 ions per revolution. This allows a rough estimation of the tangential force (F) that ExbBD can apply at its external limit: $F = \frac{N_p \Delta G}{2\pi R} = 10\,\text{pN}$. Because TonB is anchored to the peptidoglycan and is not contained in the plane of the inner membrane, the maximum force applied on TonB is $F_{\max} \sim \frac{N_p \Delta G}{2\pi R \sin(\theta)}$, where θ is the angle between the direction of TonB and the normal to the plane of the inner membrane. One may note that in this model, the force will only be transmitted to the TonB-box: 1. if the space between the IM and OM is rigidly maintained; 2. if TonB is tensioned enough. Regarding the second point, TonB can always be tensioned by progressively wrapping around ExbBD until it reaches the right extension.

A general feature of this mechanical scheme is a high gear ratio: relatively small torques can exert very large forces if θ is small. Combined with the possibility of unlimited rotation, this allows the energy from many protons to be harnessed to pull hard and far on the linear element. In this case, a pulling force of 50 pN can be achieved as long as $\theta < \sim 10°$, suggesting that such a rotate-and-pull mechanism is plausible. The Ton system is reviewed elsewhere in this collection (Ratliff et al., 2022).

TolQR, Tol-Pal system

Although the structures of individual components are known, the structure of the overall TolQR complex, which shares sequence homology with other 5:2 rotary motors, is still missing (Abergel et al., 2001; Zhang et al., 2009; Szczepaniak et al., 2020a). TolR is predicted to contain a single TM helix with a conserved aspartate mid-way across the membrane. A structural model for the assembly of TolQR in a 5:2 stoichiometry, based on the structure of ExbBD, has been recently proposed (Szczepaniak et al., 2020b). TolQR is a MotAB-like complex that is essential for the function of the PMF-dependent Tol-Pal system (Germon et al., 2001; Witty

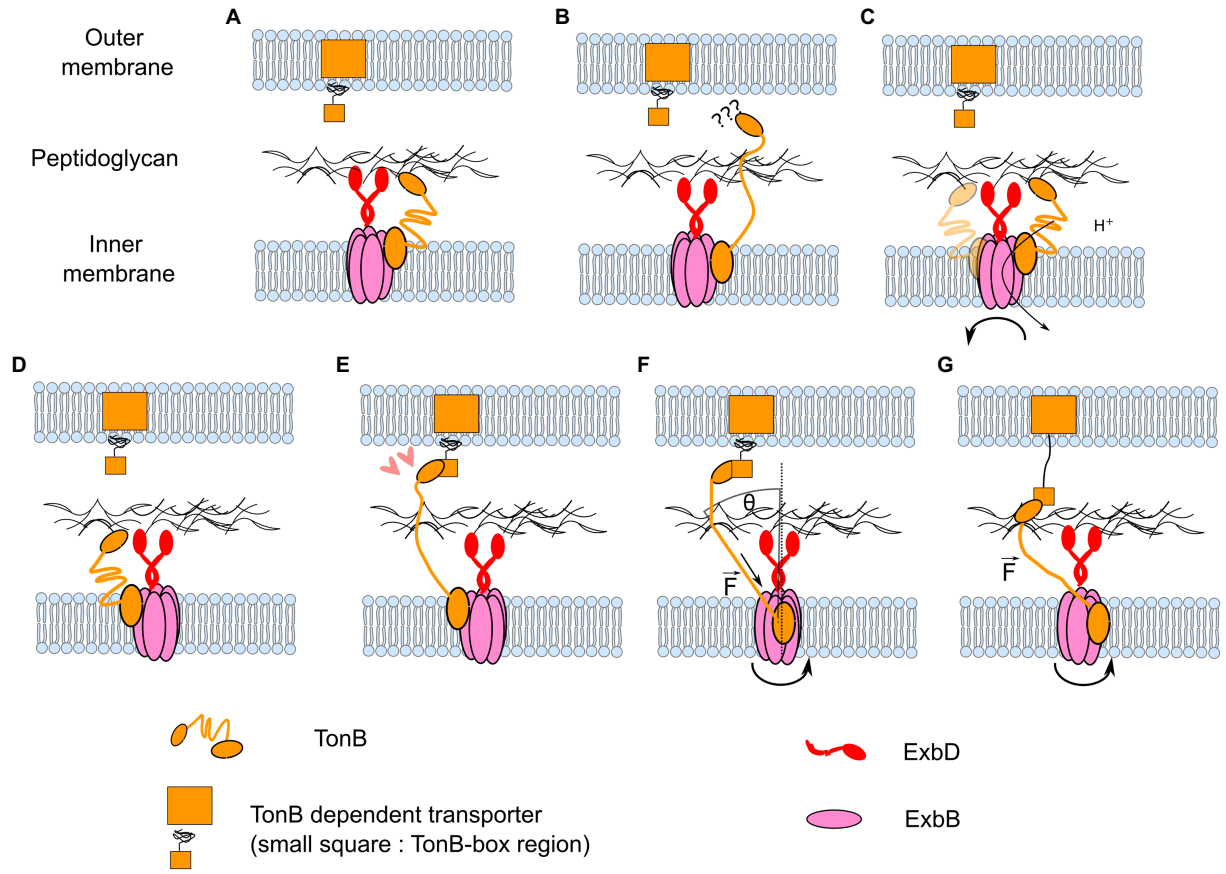


FIGURE 8
Model for how rotary motion of ExbBD could accomplish the functions of seeking TonB-dependent transporters and pulling on them. **(A–C)** Coupled with the flexibility of TonB, the rotation of ExbBD would allow the repositioning of TonB when it is retracted into the IM periplasmic space. **(D–E)** When it is properly positioned, TonB can bind to the TonB-dependent transporter. **(F)** Rotation of ExbBD pulls on the N-terminus of TonB. The maximum force applied to TonB depends on the angle θ and the number of ions per turn N_r. **(G)** A sufficiently high force partially unfolds the TBDT and allows the import of extracellular molecules.

et al., 2002; Goemaere et al., 2007). One of its many functions is to stabilize, through PG-binding of the OM lipoprotein Pal, the outer membrane at the septal site during bacterial cell division.

The stability of the outer membrane decreases and its porosity increases in Δ*pal* mutants. Much like TonB associates with ExbBD in the Ton system, the TolA protein can span the periplasmic space and interact at its N-terminus with the TolQR IM motor complex (Koebnik, 1993) and interact at its C-terminus with the outer membrane protein TolB. TolB inhibits the binding of Pal to the PG (Bonsor et al., 2009). Recent data (Petiti et al., 2019) show that, during cell division, TolQ proteins localize close to the septal site even in ΔTolA, ΔTolR, Δ*pal*, and ΔTolB mutants, and TolA proteins localize similarly even in ΔTolQR, ΔTolB, and Δ*pal* mutants. Pal also localizes at the division site, but only in cells expressing TolA and functional TolQR.

From these data, Petiti et al. propose that TolQR is first recruited to the septal site and then energizes and extends TolA through the periplasmic space to the OM. TolA then recruits TolB and Pal. The extension/retraction of TolA would be facilitated by the hairpin structure of its periplasmic domain. However, Szczepaniak et al. (2020a) showed that during cell division, when TolQR is recruited to the septal site, diffusion of Pal away from the division site increases compared to non-dividing cells. From this observation, combined with the knowledge that TolB inhibits PG-binding by Pal, they propose another model in which the energization of TolQR causes TolA to extend through the PG layer, bind to TolB, and pull on it to disassociate it from Pal (Szczepaniak et al., 2020b). Pal would then bind to the PG, explaining why it concentrates where TolQR is recruited. This model, with TolA pulling on TolB powered by PMF energization of TolQR, is similar to the opening of the TBTD by TonB, and thus also fits the seek-then-pull model described in Figure 8, including a rotary mechanism for TolQR. The Tol-Pal system is reviewed elsewhere in this collection (Webby et al., 2022).

AglRQ/S, adventurous (A) gliding system

The essential members AglRQ/S of the PMF-dependent adventurous (A) gliding machinery of *Myxococcus xanthus* also present sequence similarities with the stator units of the BFM: AglR is homologous to MotA, AglQ and S are homologous to

MotB and are predicted to contain a single TM helix with a conserved aspartate mid-way across the membrane, and both AglRQ and AglRS can theoretically form MotAB-like proton channels (Sun et al., 2011). AglR (Nan et al., 2013; Fu et al., 2018) and AglZ, a protein that co-localizes with AglQ, (Faure et al., 2016) were shown to follow helical trajectories. Furthermore, when the PMF is blocked, AglR stops moving (Nan et al., 2013). AglQ was shown to accumulate at focal adhesion points (Faure et al., 2016) with AglZ, where it stops moving relative to the extracellular matrix (ECM) and co-localize with the outer membrane components of the A-gliding machinery, GtlCD. The formation of such static clusters, which keep moving relative to a fixed marker on the cell wall, but are fixed relative to the ECM, is associated with the cell starting to move helically and gliding. From those data, a model was proposed in which AglRQ/S would power gliding by anchoring to the cell wall *via* the TolR-like PG-binding domains of AglQ/S (Wojdyla et al., 2015) and exerting a force between the cell wall and OM-bound proteins.

In this model, AglRQ/S would be able to anchor to the cell wall to exert a force on OM-bound proteins but also move relative to the cell. One can formulate two hypotheses to explain this observation. AglRQ/S could be anchored to a fixed patch of the PG, requiring dynamic re-polymerization of the PG to move relative to the cell. This seems to be excluded by data that show that antibiotics that block PG-polymerization do not affect the helical movement of MreB, the latter being dependent on AglQ/S and on the PMF (Fu et al., 2018). Alternatively, AglRQ/S could form complexes that move processively along the cell wall, in the same way that kinesin walks on microtubules but powered by PMF.

How could these results accommodate the hypothesis that AglRQ/S also forms 5:2 rotary motors? It is noteworthy that kinesins, although through completely different mechanisms, move by transforming a rotation between two anchoring points into translation (Asbury et al., 2003; Yildiz et al., 2004; Ramaiya et al., 2017). Figure 9 illustrates a model for AglRQ/S that works in the same way. In this model, however, it would be hard to account for the AglZ-dependent regulation of the direction of movement by the Frz pathway (Zhang et al., 2012; Nan et al., 2013). Other components would be necessary to bridge the gap between 36° random rotation and directed translation along helical paths. On the other hand, the similarity of GltG/GltJ to TonB (flexible linkers, TonBC-like motifs) and of GltF with the TonB-Box (Faure et al., 2016) is compatible with the same type of pulling model as for the Ton and Tol-Pal complexes. Rather than ExbBD opening the TBDT by pulling through the cell wall *via* TonB (Figure 8), AglRQ/S would pull on the OM adhesion point through the cell wall *via* GltGJ and move the cell wall towards the adhesion point to induce gliding. The *Myxococcus* gliding system is reviewed elsewhere in this collection (Chen and Nan, 2022).

ExbBD, TolQR, and AglRQ/S are thus possibly structurally and functionally similar 5:2 rotary motors that use PMF-driven rotation to pull on an OM-embedded component by using a flexible linker that spans the periplasmic space. All of these systems would benefit from the high gear ratio that results from pulling *via* rotation, as described above for ExbBD (Figure 8). This hypothesis suggests further experiments to understand the dynamics of their PG-binding. In particular, further measurements of the PG-binding efficiency of the various complexes could shed light on the difference between static complexes (e.g., MotAB) and those that can move along the cell wall. Single-molecule trajectories of MotAB, ExbBD, and TolQR are lacking and would be interesting to compare with AglRQ/S. Determining the stoichiometry of the AglRQ/S complex *in vivo* will also be a critical step in understanding their function: AglQ and S are both homologous to MotB, but it is not yet known whether they can form heterodimers or homodimers in their complex with AglR.

GldLM, bacteroidetes gliding system

In the case of the 5:2 GldLM complex, although there is no conclusive evidence of sequence homology with the other complexes, some biophysical results point towards a rotary mechanism. GldLM powers the gliding of *Flavobacterium johnsoniae* by inducing helical movement of the adhesin SprB relative to the cell (Shrivastava et al., 2016). Similar helical movements were seen in the 1980s in another gliding bacterium (Lapidus and Berg, 1982). However, cells sheared and attached to a slide coated with anti-SprB antibodies rotate (Shrivastava et al., 2015). Unlike AglRQ/S, GldLM is thought to be fixed relative to the cell wall while SprB moves (Shrivastava and Berg, 2020). This idea is consistent with the observation that dimeric GldM is longer than its equivalents in other 5:2 rotary motors (e.g., see Figure 5C), is less flexible, and may span the whole periplasmic space and cross the cell wall. These observations led to a rack-and-pinion model (Shrivastava and Berg, 2020), in which SprB is fixed to a helical track spanning the entire length of the cell that is set in motion along its length by rotating GldLM complexes that are anchored and distributed at various points over the cell surface. GldJ is a candidate for forming this track (Shrivastava and Berg, 2020), as it has been shown to decorate helical macrostructures (Braun and McBride, 2005). GldJ also was shown to interact with GldK (Johnston et al., 2018), which itself has been shown to form contacts with GldM (Vincent et al., 2022) and thus could serve to couple PMF-induced rotation of GldM to the movement of a GldJ track. GldM also forms contact with GldN, and GldK/N are suspected to form rings in the periplasmic space below the outer membrane (the formation of the ring has been shown for the homologous proteins PorK and PorN (Gorasia et al., 2016)). The fact that the periplasmic structure of GldM displays a strong bend led to the proposal that the tip of GldM describes a circle that could induce GldKN rotation (Hennell James et al., 2021). However, the measured diameter of the PorKN ring (50 nm) does not match the diameter of this circle (20 nm), suggesting that GldK/N would form smaller rings than PorK/N.

Overall, although a rotary mechanism for GldLM was proposed before the publication of the 5:2 structure, there is no direct evidence for rotation, and the proposed mechanism

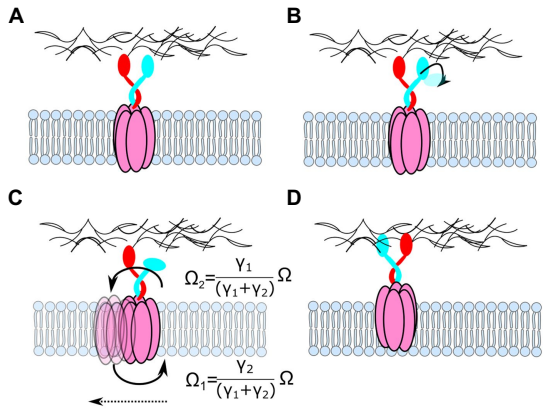


FIGURE 9
How rotation of a 5:2 AglRQ/S complex could accommodate the observed movement of AglR relative to the cell wall. **(A)** The two inner units are attached to the peptidoglycan. **(B)** One unit detaches from the cell wall. **(C)** Because both the dimer and the pentamer are free to rotate, PMF-driven rotation of one complex relative to the other would cause them to rotate in opposite directions, with angular velocities (Ω) depending on the ratio of the drag coefficients (γ). The detached domain binds again to the peptidoglycan, but it binds at a different location.

remains hypothetical. In particular, many proteins of the *spr* and *gld* operons, like GldA,B,D,F (Hunnicutt et al., 2002), GldI (McBride and Braun, 2004), and SprC,D (Rhodes et al., 2011) are necessary for the gliding-related spreading of colonies, but their role in the gliding machinery is not known. It is difficult to distinguish between proteins that are directly involved in the gliding mechanism and those that are involved in the associated T9SS export machinery. Indeed, in *F. johnsoniae*, gliding and the T9SS are intertwined because the adhesins necessary for gliding are themselves exported through the T9SS. Any defect in the export machinery would therefore cause a defect in gliding.

Gliding and export might be disentangled by adding the proteins necessary for gliding exogenously, but they would still need to cross the outer membrane, since many of them are located between the PG and the OM. In the case of the bacterial flagellar motor, rotation was observed by attaching beads to the hook or filament stubs (Ryu et al., 2000) that protrude outside the cell. However, in the case of the gliding machinery, the candidates for rotary motion, GldM, K, and N, lie inside the outer membrane, making them impossible to label with microparticles.

Another question is whether any protein complex of the gliding machinery might play the role of a drive shaft to transmit rotation of GldM through the PG, like the rod in the BFM. However, recent low-resolution cryo-ET images of a related Type-9 secretion system (Song et al., 2022) show no sign of such a shaft. If GldM rotates, the GldL pentamer must be anchored to the cell. This is another difference from the proposed mechanisms for MotAB, ExbBD, TolQR, and AglRQ/S, where the dimer is anchored to the cell wall and the pentamer rotates. The structure of GldLM does not leave space for GldL to anchor to the cell wall (Hennell James et al., 2021). Instead, the proposal is made that GldL is anchored to an as yet unidentified cytoskeletal protein through its long cytoplasmic tail.

All these questions will need to be addressed through advanced biochemical and biophysical measurements. In particular, *in vitro* reconstitution of single 5:2 complexes into artificial membranes and subsequent labeling with microspheres should confirm the rotary hypothesis and help understand the dynamics of these motors. *In vivo* orientation measurement through single-molecule polarization microscopy (Shroder et al., 2016) of fluorescently labeled proteins is another possible approach to circumvent the difficulty of labeling periplasmic proteins with microparticles. The Bacteroidetes gliding system is reviewed elsewhere in this collection (Trivedi et al., 2022).

General considerations of rotary motor symmetry

Is there any advantage to the 5:2 symmetry of the motors described in this review over other possible symmetries? 5 and 2 have no common divisor >1. This property was discussed for the case of the passive bearing in bacteriophage rotary injection systems (Hendrix, 1978). It prevents several proteins in the inner part of the phage from being in the same position relative to those of the outer part at the same time. This flattens the energy landscape of interaction, since neither the most energetically favorable nor unfavorable positions can be occupied simultaneously by many pairs of proteins, avoiding very stable "traps" and high energy barriers, respectively. The lowest possible motor symmetries with no common divisors are 2:1, then 3:1 and 3:2, then 5:1 and 5:2. The 5:2 rotary motor symmetry may be preferred to lower symmetries due to packing difficulties or structural constraints. However, another important factor is the relationship between symmetry and the number of ions that the rotary machine uses per revolution. In a motor with *a:b* symmetry, each of the *a* outer proteins will pass each of the *b* inner proteins exactly once per rev. If each ion transit corresponds to one instance of a pair of inner and outer protein subunits passing any given relative angular position, as in all current models of ion-driven rotary motors, an *a:b* motor will use *a x b* ions per rev.

Following this reasoning, both 5:2 rotary motors and the 1:10 F_O motor of *E. coli* F_OF_1-ATPase will use 10 ions per turn. The number of ions per turn has important biophysical implications: conservation of energy requires that it is proportional to the maximum torque and force that the motor can exert. Torque is an important parameter for the function of any motor – it determines what the motor can drive, and, in the case of dissipative loads, how fast it can be driven. For example, in the case of MotAB, the maximum torque that can be generated determines the ability of the BFM to rotate flagella in viscous media. The maximum average torque τ produced by a rotary motor depends on the number of quanta of "fuel" it uses per revolution N_r and on the free energy ΔG released per quantum (one ATP molecule hydrolyzed or one

ion transited), as $\tau = \frac{N_r \Delta G}{2\pi}$. The stoichiometry of F_OF_1 ATP synthase constitutes a good illustration of the importance of this relation. Each revolution is coupled to the transit of *n* protons through F_O (*n* = *10* in *E. coli* (Jiang et al., 2001), but *n* varies widely among species) and the synthesis or hydrolysis of 3 ATP molecules in F_1. For the complex to convert the free energy of protons to that of the synthesis of ATP with high efficiency, the energy $\tau_O \delta\theta$ released by the proton flux when F_O rotates through an angle $\delta\theta$ should be minimally larger than the energy $\tau_1 \delta\theta$ absorbed by ATP synthesis in F_1. Thus, $\tau_O \gtrsim \tau_1$, and therefore $\frac{\Delta G_{ATP}}{\Delta G_{H^+}} \lesssim \frac{n}{3}$.

ΔG_{ATP} depends on the pH and concentrations of ATP, magnesium, ADP, and phosphate. For typical metabolite concentrations in *E. coli* (Tran and Unden, 1998; Bennett et al., 2009), this corresponds to $\sim 20\, k_B T = 50\, kJ/mol$. On the other hand, the PMF across the inner membrane of *E. coli* is typically ~170 mV (Cheuk and Meier, 2021). Thus, the free energy per proton $\Delta G_{H^+} = e\Delta V \simeq 16$ kJ/mol, and $\frac{\Delta G_{ATP}}{\Delta G_{H^+}} \simeq 3.1$. This is slightly less than 10/3, exactly as expected. Increasing the stoichiometry of the c-ring from 11 to 12 allows the ATP synthase to work at a lower ion motive force (Pogoryelov et al., 2012), as predicted by the energetic argument presented here. A meta-study showed that species with a higher c-ring stoichiometry, like *Bacillus pseudofirmus* (*n* = 13), have a lower PMF (~150 mV), whereas ATP synthases with a lower c-ring stoichiometry, like those of *Bos taurus* mitochondria (*n* = 8), have a higher PMF (~210 mV). The lack of precise data regarding PMF and ΔG_{ATP} in all these species limits the rigor of this comparison. However, these considerations suggest that the stoichiometry of the F_OF_1 ATP synthase has evolved to favor efficient energetic coupling between PMF and ATP synthesis, demonstrating that torque and structural symmetry are intimately related.

Comparison of expected maximum torque and the thermodynamics of coiled coils

In *E. coli*, both 5:2 rotary motors and F_O use *n* = 10 protons per revolution and generate a maximum torque of ~40 pN.nm. Is this value special in any way, or is it just a coincidence? Both the BFM and ATP synthase require internal "anchoring" of components relative to each other, to prevent free rotation that would dissipate the proton energy as heat. In the BFM, the MotB dimers play this role by anchoring stator units into the peptidoglycan (Kojima et al., 2018). In *E. coli* F_OF_1 ATP synthase, the "second stalk" dimer of b-subunits prevents rotation of the a-subunit of F_O relative to the cap of F_1 (Dmitriev et al., 1999), ensuring that F_O rotation drives the conformational changes within F_1 that synthesize ATP. Both of these anchoring dimers are α-helical coiled coils (del Rizzo et al., 2006; Wise and Vogel, 2008; Andrews et al., 2017; Sobti et al., 2020). There is some disagreement on the handedness of the coiled coils in the *E. coli* F_OF_1 ATP synthase, and recent cryoEM studies of the F_OF_1 ATP synthase of *Saccharomyces cerevisiae* suggest that the handedness can change upon energization and under stress (Guo and Rubinstein, 2022). On the other hand, isothermal calorimetric thermodynamic measurements of coiled coiling (Jelesarov and Bosshard, 1996; Worrall and Mason, 2011) between two α-helices found consistent values for the standard free energy change $\Delta G^\circ_{coiling}$ between uncoiled and coiled states, which is about 9 kcal/mol for protein sequences that are four heptads long (a heptad corresponds to seven amino acids, two turns of an α-helix). Since one turn of a coiled-coil corresponds to 80–120 residues (Seo and Cohen, 1993; Lupas and Gruber, 2005; Sharp et al., 2012), four heptads correspond to a torsion angle φ of 1.45–2.2 rad. Thus, the characteristic uncoiling torque associated with the measured $\Delta G^\circ_{coiling}$ is $\tau = \frac{\Delta G^\circ_{coiling}}{\varphi} = 30 - 40$ pN.nm, close to the predicted maximum torque generated by MotAB and F_O. These thermodynamic considerations, and the observation that 10-fold periodicity is shared by F_O and presumably all 5:2 rotary motors, lead us to speculate that the maximum periodicity of these minimal motors could be limited by the maximum torque that can be withstood by the anchoring coiled coils. These quantities are rough estimates. The true dynamics and energetics of anchoring will be much more complex. In the case of F_OF_1 ATP synthases for example, the b-subunits are shifted from the axis of rotation and thus will be subject to a mixture of torque, tension, and bending stress. Single-molecule studies of those dimers and their ability to withstand and react to the applied torque, following the model of the experiments that have been performed on DNA (Strick et al., 1996), could test this hypothesis.

Finally, we note that in the case of the hypothetical TolQR and ExbBD *rotate-and-pull* mechanism discussed in this review, the most important parameter is not the torque but rather the force applied to TolA and TonB, respectively. The force transmitted to a protein attached to the outer side of the complex is directly proportional to the motor torque and inversely proportional to the outer radius of the complex. Exerting a high enough force on the TolB or TonB-box motifs thus requires that a rotary motor combines a large number of protons per turn (*n* = *a x b*) with a small outer radius. 5:2 may be the best symmetry to meet this requirement.

Author contributions

MR proposed models explaining how functions of known 5:2 motors could accommodate rotation, composed the corresponding parts of the section "Functions as components of larger systems," and composed the section "General considerations of rotary motor symmetry." RK composed the section "Phylogenetics." RK and NT composed the section "Structures of ion-driven 5:2 rotary motors." RB composed the Introduction, the "MotAB" part of the section

"Functions as components of larger systems," and the Section "A model for the rotary mechanism" and assembled and edited the manuscript. All authors contributed to the revision of the manuscript.

Funding

RB and MR are supported by UK Research and Innovation (UKRI, Engineering, and Physical Sciences Research Council) grant EP/S036660/1. The Novo Nordisk Foundation Center for Protein Research is supported financially by the Novo Nordisk Foundation (grant NNF14CC0001). This work was also supported by an NNF Hallas-Møller Emerging Investigator grant (NNF17OC0031006) to NT is a member of the Integrative Structural Biology Cluster (ISBUC) at the University of Copenhagen.

Acknowledgments

We thank Ben Berks, Colin Kleanthous, and Jean-Louis Sikorav for valuable discussions of Bacteroidetes gliding, Tol/Pal, and symmetry mismatches, respectively.

Conflict of interest

The authors declare that the research was conducted in the absence of any commercial or financial relationships that could be construed as a potential conflict of interest.

Publisher's note

All claims expressed in this article are solely those of the authors and do not necessarily represent those of their affiliated organizations, or those of the publisher, the editors and the reviewers. Any product that may be evaluated in this article, or claim that may be made by its manufacturer, is not guaranteed or endorsed by the publisher.

Supplementary material

The Supplementary material for this article can be found online at: https://www.frontiersin.org/articles/10.3389/fmicb.2022.948383/full#supplementary-material

References

Abergel, C., Walburger, A., Chenivesse, S., and Lazdunski, C. (2001). Crystallization and preliminary crystallographic study of the peptidoglycan-associated lipoprotein from *Escherichia coli*. *Acta Crystallogr. D Biol. Crystallogr.* 57, 317–319. doi: 10.1107/S0907444900019739

Abrahams, J. P., Leslie, A. G. W., Lutter, R., and Walker, J. E. (1994). Structure at 2.8 Â resolution of F1-ATPase from bovine heart mitochondria. *Nature* 370, 621–628. doi: 10.1038/370621a0

Andrews, D. A., Nesmelov, Y. E., Wilce, M. C., and Roujeinikova, A. (2017). Structural analysis of variant of *Helicobacter pylori* MotB in its activated form, engineered as chimera of MotB and leucine zipper. *Sci. Rep.* 7, 13435. doi: 10.1038/s41598-017-13421-0

Armitage, J. P., and Berry, R. M. (2020). Assembly and dynamics of the bacterial flagellum. *Annu. Rev. Microbiol.* 74, 181–200. doi: 10.1146/ANNUREV-MICRO-090816-093411

Asbury, C. L., Fehr, A. N., and Block, S. M. (2003). Kinesin moves by an asymmetric hand-over-hand mechanism. *Science* 302, 2130–2134. doi: 10.1126/science.1092985

Bennett, B. D., Kimball, E. H., Gao, M., Osterhout, R., van Dien, S. J., and Rabinowitz, J. D. (2009). Absolute metabolite concentrations and implied enzyme active site occupancy in *Escherichia coli*. *Nat. Chem. Biol.* 5, 593–599. doi: 10.1038/nchembio.186

Berg, H. C., and Anderson, R. A. (1973). Bacteria swim by rotating their flagellar filaments. *Nature* 245, 380–382. doi: 10.1038/245380a0

Berg, H. C., Manson, M. D., and Conley, M. P. (1982). Dynamics and energetics of flagellar rotation in bacteria. *Symp. Soc. Exp. Biol.* 35, 1–31. PMID: 6306855

Berry, R. M. (2000). Theories of rotary motors. *Philos. Trans. R. Soc. Lond. B Biol. Sci.* 355, 503–509. doi: 10.1098/RSTB.2000.0591

Berry, R. M., and Berg, H. C. (1999). Torque generated by the Flagellar Motor of *Escherichia coli* while driven backward. *Biophys. J.* 76, 580–587. doi: 10.1016/S0006-3495(99)77226-7

Biou, V., Adaixo, R. J. D., Chami, M., Coureux, P.-D., Laurent, B., Ntsogo, Y., et al. (2021). Functional and structural characterization of *Serratia marcescens* ExbB: determinants of the interaction with HasB/TonB. *BioRxiv* 2021:440815. doi: 10.1101/2021.04.21.440815

Bonsor, D. A., Hecht, O., Vankemmelbeke, M., Sharma, A., Krachler, A. M., Housden, N. G., et al. (2009). Allosteric β-propeller signalling in TolB and its manipulation by translocating colicins. *EMBO J.* 28, 2846–2857. doi: 10.1038/emboj.2009.224

Braun, T. F., Khubbar, M. K., Saffarini, D. A., and McBride, M. J. (2005). *Flavobacterium johnsoniae* gliding motility genes identified by mariner mutagenesis. *J. Bacteriol.* 187, 6943–6952. doi: 10.1128/JB.187.20.6943-6952.2005

Braun, T. F., and McBride, M. J. (2005). *Flavobacterium johnsoniae* GldJ is a lipoprotein that is required for gliding motility. *J. Bacteriol.* 187, 2628–2637. doi: 10.1128/JB.187.8.2628-2637.2005

Brewer, S., Tolley, M., Trayer, I. P., Barr, G. C., Dorman, C. J., Hannavy, K., et al. (1990). Structure and function of X-pro dipeptide repeats in the TonB proteins of Salmonella typhimurium and *Escherichia coli*. *J. Mol. Biol.* 216, 883–895. doi: 10.1016/S0022-2836(99)80008-4

Carroll, B. L., Nishikino, T., Guo, W., Zhu, S., Kojima, S., Homma, M., et al. (2020). The flagellar motor of *vibrio alginolyticus* undergoes major structural remodeling during rotational switching. *elife* 9, 1–19. doi: 10.7554/ELIFE.61446

Celia, H., Botos, I., Ni, X., Fox, T., de Val, N., Lloubes, R., et al. (2019). Cryo-EM structure of the bacterial ton motor subcomplex ExbB-ExbD provides information on structure and stoichiometry. *Commun. Biol.* 2, 358. doi: 10.1038/S42003-019-0604-2

Celia, H., Noinaj, N., and Buchanan, S. K. (2020). Structure and stoichiometry of the ton molecular motor. *Int. J. Mol. Sci.* 21, 375. doi: 10.3390/ijms21020375

Celia, H., Noinaj, N., Zakharov, S. D., Bordignon, E., Botos, I., Santamaria, M., et al. (2016). Structural insight into the role of the ton complex in energy transduction. *Nature* 538, 60–65. doi: 10.1038/NATURE19757

Chang, Y., Carroll, B. L., and Liu, J. (2021). Structural basis of bacterial flagellar motor rotation and switching. *Trends Microbiol.* 29, 1024–1033. doi: 10.1016/J.TIM.2021.03.009

Chang, Y., Zhang, K., Carroll, B. L., Zhao, X., Charon, N. W., Norris, S. J., et al. (2020). Molecular mechanism for rotational switching of the bacterial flagellar motor. *Nat. Struct. Mol. Biol.* 27, 1041–1047. doi: 10.1038/s41594-020-0497-2

Chen, S., Beeby, M., Murphy, G. E., Leadbetter, J. R., Hendrixson, D. R., Briegel, A., et al. (2011). Structural diversity of bacterial flagellar motors. *EMBO J.* 30, 2972–2981. doi: 10.1038/EMBOJ.2011.186

Chen, J., and Nan, B. (2022). Flagellar motor transformed: biophysical perspectives of the *Myxococcus xanthus* gliding mechanism. *Front. Microbiol.* 13, 1599. doi: 10.3389/FMICB.2022.891694

Cheuk, A., and Meier, T. (2021). Rotor subunits adaptations in ATP synthases from photosynthetic organisms. *Biochem. Soc. Trans.* 49, 541–550. doi: 10.1042/BST20190936

del Rizzo, P. A., Bi, Y., and Dunn, S. D. (2006). ATP synthase b subunit dimerization domain: a right-handed coiled coil with offset helices. *J. Mol. Biol.* 364, 735–746. doi: 10.1016/j.jmb.2006.09.028

Demchick, P., and Koch, A. L. (1996). The permeability of the wall fabric of Escherichia coli and *Bacillus subtilis*. *J. Bacteriol.* 178, 768–773. doi: 10.1128/jb.178.3.768-773.1996

Deme, J. C., Johnson, S., Vickery, O., Aron, A., Monkhouse, H., Griffiths, T., et al. (2020). Structures of the stator complex that drives rotation of the bacterial flagellum. *Nat. Microbiol.* 5, 1553–1564. doi: 10.1038/S41564-020-0788-8

Dmitriev, O., Jones, P. C., Jiang, W., and Fillingame, R. H. (1999). Structure of the membrane domain of subunit b of the *Escherichia coli* F0F1 ATP synthase. *J. Biol. Chem.* 274, 15598–15604. doi: 10.1074/jbc.274.22.15598

Du, D., Wang, Z., James, N. R., Voss, J. E., Klimont, E., Ohene-Agyei, T., et al. (2014). Structure of the AcrAB-TolC multidrug efflux pump. *Nature* 509, 512–515. doi: 10.1038/NATURE13205

Duncan, T. M., and Bulygin, V., Y. Zhou, M. L. Hutcheon and R. L. Cross (1995). Rotation of subunits during catalysis by *Escherichia coli* F1-ATPase. *Proc. Natl. Acad. Sci. U. S. A.*, 92, 10964–10968. doi: 10.1073/PNAS.92.24.10964

Evans, J. S., Levine, B. A., Trayer, I. P., Dorman, C. J., and Higgins, C. F. (1986). Sequence-imposed structural constraints in the TonB protein of *E. coli*. *FEBS Lett.* 208, 211–216. doi: 10.1016/0014-5793(86)81020-1

Faraldo-Gómez, J. D., and Sansom, M. S. P. (2003). Acquisition of siderophores in gram-negative bacteria. *Nat. Rev. Mol. Cell Biol.* 4, 105–116. doi: 10.1038/NRM1015

Faure, L. M., Fiche, J.-B., Espinosa, L., Ducret, A., Anantharaman, V., Luciano, J., et al. (2016). The mechanism of force transmission at bacterial focal adhesion complexes. *Nature* 539, 530–535. doi: 10.1038/nature20121

Fu, G., Bandaria, J. N., le Gall, A. V., Fan, X., Yildiz, A., Mignot, T., et al. (2018). MotAB-like machinery drives the movement of MreB filaments during bacterial gliding motility. *Proc. Natl. Acad. Sci.* 115, 2484–2489. doi: 10.1073/pnas.1716441115

Fung, D. C., and Berg, H. C. (1995). Powering the flagellar motor of *Escherichia coli* with an external voltage source. *Nature* 375, 809–812. doi: 10.1038/375809A0

Germon, P., Ray, M. C., Vianney, A., and Lazzaroni, J. C. (2001). Energy-dependent conformational change in the TolA protein of *Escherichia coli* involves its N-terminal domain, TolQ, and TolR. *J. Bacteriol.* 183, 4110–4114. doi: 10.1128/JB.183.14.4110-4114.2001

Goemaere, E. L., Cascales, E., and Lloubès, R. (2007). Mutational analyses define helix organization and key residues of a bacterial membrane energy-transducing complex. *J. Mol. Biol.* 366, 1424–1436. doi: 10.1016/J.JMB.2006.12.020

Gorasia, D. G., Veith, P. D., Hanssen, E. G., Glew, M. D., Sato, K., Yukitake, H., et al. (2016). Structural insights into the PorK and PorN components of the *Porphyromonas gingivalis* type IX secretion system. *PLoS Pathog.* 12:e1005820. doi: 10.1371/journal.ppat.1005820

Gorasia, D. G., Veith, P. D., and Reynolds, E. C. (2020). The type IX secretion system: advances in structure. *Funct. Organ. Microorganisms* 8, 1–9. doi: 10.3390/MICROORGANISMS8081173

Guo, H., and Rubinstein, J. L. (2018). Cryo-EM of ATP synthases. *Curr. Opin. Struct. Biol.* 52, 71–79. doi: 10.1016/J.SBI.2018.08.005

Guo, H., and Rubinstein, J. L. (2022). Structure of ATP synthase under strain during catalysis. *BioRxiv* 13, 477618. doi: 10.1101/2022.01.24.477618

Hendrix, R. W. (1978). Symmetry mismatch and DNA packaging in large bacteriophages. *Proc. Natl. Acad. Sci. U. S. A.* 75, 4779–4783. doi: 10.1073/PNAS.75.10.4779

Hennell James, R., Deme, J. C., Kjær, A., Alcock, F., Silale, A., Lauber, F., et al. (2021). Structure and mechanism of the proton-driven motor that powers type 9 secretion and gliding motility. *Nat. Microbiol.* 6, 221–233. doi: 10.1038/s41564-020-00823-6

Hickman, S. J., Cooper, R. E. M., Bellucci, L., Paci, E., and Brockwell, D. J. (2017). Gating of TonB-dependent transporters by substrate-specific forced remodelling. *Nat. Commun.* 8, 14804. doi: 10.1038/ncomms14804

Higgs, P. I., Larsen, R. A., and Postle, K. (2002). Quantification of known components of the *Escherichia coli* TonB energy transduction system: TonB, ExbB, ExbD and FepA. *Mol. Microbiol.* 44, 271–281. doi: 10.1046/j.1365-2958.2002.02880.x

Homma, M., Terashima, H., Koiwa, H., and Kojima, S. (2021). Putative spanner function of the vibrio PomB plug region in the stator rotation model for flagellar motor. *J. Bacteriol.* 203:e0015921. doi: 10.1128/JB.00159-21

Hosking, E. R., Vogt, C., Bakker, E. P., and Manson, M. D. (2006). The *Escherichia coli* MotAB proton channel unplugged. *J. Mol. Biol.* 364, 921–937. doi: 10.1016/j.jmb.2006.09.035

Hunnicutt, D. W., Kempf, M. J., and McBride, M. J. (2002). Mutations in *Flavobacterium johnsoniae gldF* and *gldG* disrupt gliding motility and interfere with membrane localization of GldA. *J. Bacteriol.* 184, 2370–2378. doi: 10.1128/JB.184.9.2370-2378.2002

Ito, K. I., Nakamura, S., and Toyabe, S. (2021). Cooperative stator assembly of bacterial flagellar motor mediated by rotation. *Nat. Commun.* 12, 3218–3217. doi: 10.1038/s41467-021-23516-y

Jelesarov, I., and Bosshard, H. R. (1996). Thermodynamic characterization of the coupled folding and association of heterodimeric coiled coils (leucine zippers). *J. Mol. Biol.* 263, 344–358. doi: 10.1006/jmbi.1996.0579

Jiang, W., Hermolin, J., and Fillingame, R. H. (2001). The preferred stoichiometry of c subunits in the rotary motor sector of *escherichia coli* ATP synthase is 10. *Proc. Natl. Acad. Sci. U. S. A.* 98, 4966–4971. doi: 10.1073/pnas.081424898

Johnson, S., Furlong, E. J., Deme, J. C., Nord, A. L., Caesar, J. J. E., Chevance, F. F. V., et al. (2021). Molecular structure of the intact bacterial flagellar basal body. *Nat. Microbiol.* 6, 712–721. doi: 10.1038/s41564-021-00895-y

Johnston, J. J., Shrivastava, A., and McBride, M. J. (2018). Untangling *Flavobacterium johnsoniae* gliding motility and protein secretion. *J. Bacteriol.* 200:e00362-17. doi: 10.1128/JB.00362-17

Jordan, L. D., Zhou, Y., Smallwood, C. R., Lill, Y., Ritchie, K., Yip, W. T., et al. (2013). Energy-dependent motion of TonB in the gram-negative bacterial inner membrane. *Proc. Natl. Acad. Sci.* 110, 11553–11558. doi: 10.1073/pnas.1304243110

Josts, I., Veith, K., and Tidow, H. (2019). Ternary structure of the outer membrane transporter FoxA with resolved signalling domain provides insights into TonB-mediated siderophore uptake. *elife* 8:e48528. doi: 10.7554/ELIFE.48528

Kawamoto, A., Miyata, T., Makino, F., Kinoshita, M., Minamino, T., Imada, K., et al. (2021). Native flagellar MS ring is formed by 34 subunits with 23-fold and 11-fold subsymmetries. *Nat. Commun.* 12, 4223–4210. doi: 10.1038/s41467-021-24507-9

Klebba, P. E. (2016). ROSET model of TonB action in gram-negative bacterial iron acquisition. *J. Bacteriol.* 198, 1013–1021. doi: 10.1128/JB.00823-15

Koebnik, R. (1993). The molecular interaction between components of the TonB-ExbBD-dependent and of the TolQRA-dependent bacterial uptake systems. *Mol. Microbiol.* 9, 219. doi: 10.1111/j.1365-2958.1993.tb01683.x

Kojima, S., and Blair, D. F. (2001). Conformational change in the stator of the bacterial flagellar motor. *Biochemistry* 40, 13041–13050. doi: 10.1021/BI011263O

Kojima, S., Imada, K., Sakuma, M., Sudo, Y., Kojima, C., Minamino, T., et al. (2009). Stator assembly and activation mechanism of the flagellar motor by the periplasmic region of MotB. *Mol. Microbiol.* 73, 710–718. doi: 10.1111/j.1365-2958.2009.06802.x

Kojima, S., Takao, M., Almira, G., Kawahara, I., Sakuma, M., Homma, M., et al. (2018). The Helix rearrangement in the periplasmic domain of the flagellar stator B subunit activates peptidoglycan binding and ion influx. *Structure* 26, 590.e5–598.e5. doi: 10.1016/j.str.2018.02.016

Krewulak, K. D., and Vogel, H. J. (2011). TonB or not TonB: is that the question? *Biochem. Cell Biol* 89, 87–97. doi: 10.1139/O10-141

Kühlbrandt, W., and Davies, K. M. (2016). Rotary ATPases: a new twist to an ancient machine. *Trends Biochem. Sci.* 41, 106–116. doi: 10.1016/J.TIBS.2015.10.006

Lapidus, I. R., and Berg, H. C. (1982). Gliding motility of Cytophaga sp. strain U67. *J. Bacteriol.* 151, 384–398. doi: 10.1128/JB.151.1.384-398.1982

Leake, M. C., Chandler, J. H., Wadhams, G. H., Bai, F., Berry, R. M., and Armitage, J. P. (2006). Stoichiometry and turnover in single, functioning membrane protein complexes. *Nature* 443, 355–358. doi: 10.1038/nature05135

Lele, P. P., Hosu, B. G., and Berg, H. C. (2013). Dynamics of mechanosensing in the bacterial flagellar motor. *Proc. Natl. Acad. Sci. U. S. A.* 110, 11839–11844. doi: 10.1073/PNAS.1305885110/SUPPL_FILE/SM02.AVI

Leone, P., Roche, J., Vincent, M. S., Tran, Q. H., Desmyter, A., Cascales, E., et al. (2018). Type IX secretion system PorM and gliding machinery GldM form arches spanning the periplasmic space. *Nat. Commun.* 9:429. doi: 10.1038/S41467-017-02784-7

Li, N., Kojima, S., and Homma, M. (2011). Characterization of the periplasmic region of PomB, a Na +−driven flagellar stator protein in *Vibrio alginolyticus*. *J. Bacteriol.* 193, 3773–3784. doi: 10.1128/JB.00113-11

Liu, R., and Ochman, H. (2007). Origins of flagellar gene operons and secondary flagellar systems. *J. Bacteriol.* 189, 7098–7104. doi: 10.1128/JB.00643-07

Lo, C. J., Sowa, Y., Pilizota, T., and Berry, R. M. (2013). Mechanism and kinetics of a sodium-driven bacterial flagellar motor. *Proc. Nat. Acad. Sci. U. S. A* 110:E2544-51. doi: 10.1073/PNAS.1301664110/SUPPL_FILE/SD01.XLS

Lupas, A. N., and Gruber, M. (2005). The structure of α-helical coiled coils. *Adv. Protein Chem.* 70, 37–38. doi: 10.1016/S0065-3233(05)70003-6

Maki-Yonekura, S., Matsuoka, R., Yamashita, Y., Shimizu, H., Tanaka, M., Iwabuki, F., et al. (2018). Hexameric and pentameric complexes of the ExbBD energizer in the ton system. *elife* 7:e37833. doi: 10.7554/ELIFE.35419

Manson, M. D. (2022). Rotary nanomotors in the rear view mirror. *Front. Microbiol.* 13, 906. doi: 10.3389/FMICB.2022.873573

Marmon, L. (2013). Elucidating the origin of the ExbBD components of the TonB system through Bayesian inference and maximum-likelihood phylogenies. *Mol. Phylogenet. Evol.* 69, 674–686. doi: 10.1016/J.YMPEV.2013.07.010

Martinez-Guerrero, C. E., Ciria, R., Abreu-Goodger, C., Moreno-Hagelsieb, G., and Merino, E. (2008). GeConT 2: gene context analysis for orthologous proteins, conserved domains and metabolic pathways. *Nucleic Acids Res.* 36, W176–W180. doi: 10.1093/NAR/GKN330

McBride, M. J. (2019). Bacteroidetes gliding motility and the type IX secretion system. *Microbiol. Spectr.* 7, 1–9. doi: 10.1128/MICROBIOLSPEC.PSIB-0002-2018

McBride, M. J., and Braun, T. F. (2004). GldI is a lipoprotein that is required for *Flavobacterium johnsoniae* gliding motility and chitin utilization. *J. Bacteriol.* 186, 2295–2302. doi: 10.1128/JB.186.8.2295-2302.2004

Merino, S., and Tomás, J. M. (2016). The FlgT protein is involved in *Aeromonas hydrophila* polar flagella stability and not affects anchorage of lateral flagella. *Front. Microbiol.* 7:1150. doi: 10.3389/FMICB.2016.01150

Mitchell, P. (1984). Bacterial flagellar motors and osmoelectric molecular rotation by an axially transmembrane well and turnstile mechanism. *FEBS Lett.* 176, 287–294. doi: 10.1016/0014-5793(84)81182-5

Morimoto, Y. V., Che, Y. S., Minamino, T., and Namba, K. (2010). Proton-conductivity assay of plugged and unplugged MotA/B proton channel by cytoplasmic pHluorin expressed in Salmonella. *FEBS Lett.* 584, 1268–1272. doi: 10.1016/J.FEBSLET.2010.02.051

Müller, V., and Grüber, G. (2003). ATP synthases: structure, function and evolution of unique energy converters. *Cell. Mol. Life Sci.* 60, 474–494. doi: 10.1007/S000180300040

Nan, B., Bandaria, J. N., Moghtaderi, A., Sun, I.-H., Yildiz, A., and Zusman, D. R. (2013). Flagella stator homologs function as motors for myxobacterial gliding motility by moving in helical trajectories. *Proc. Natl. Acad. Sci. U. S. A.* 110, E1508–E1513. doi: 10.1073/pnas.1219982110

Noinaj, N., Guillier, M., Barnard, T. J., and Buchanan, S. K. (2010). TonB-dependent transporters: regulation, structure, and function. *Annu. Rev. Microbiol.* 64, 43–60. doi: 10.1146/ANNUREV.MICRO.112408.134247

Noji, H., and Ueno, H. (2022). How does F1-ATPase generate torque?: analysis from cryo-electron microscopy and rotational catalysis of thermophilic F1. *Front. Microbiol.* 13:904084. doi: 10.3389/FMICB.2022.904084

Noji, H., Yasuda, R., Yoshida, M., and Kinosita, K. (1997). Direct observation of the rotation of F1-ATPase. *Nature* 386, 299–302. doi: 10.1038/386299a0

Nord, A. L., Gachon, E., Perez-Carrasco, R., Nirody, J. A., Barducci, A., Berry, R. M., et al. (2017a). Catch bond drives stator mechanosensitivity in the bacterial flagellar motor. *Proc. Natl. Acad. Sci. U. S. A.* 114, 12952–12957. doi: 10.1073/PNAS.1716002114/SUPPL_FILE/PNAS.201716002SI.PDF

Nord, A. L., Sowa, Y., Steel, B. C., Lo, C. J., and Berry, R. M. (2017b). Speed of the bacterial flagellar motor near zero load depends on the number of stator units. *Proc. Natl. Acad. Sci. U. S. A.* 114, 11603–11608. doi: 10.1073/PNAS.1708054114/SUPPL_FILE/PNAS.201708054SI.PDF

Ollis, A. A., and Postle, K. (2011). The same periplasmic ExbD residues mediate in vivo interactions between ExbD homodimers and ExbD-TonB heterodimers. *J. Bacteriol.* 193, 6852–6863. doi: 10.1128/JB.06190-11

Oneill, J., Xie, M., Hijnen, M., and Roujeinikova, A. (2011). Role of the MotB linker in the assembly and activation of the bacterial flagellar motor. *Acta Crystallogr. D Biol. Crystallogr.* 67, 1009–1016. doi: 10.1107/S0907444911041102

Pawelek, P. D., Croteau, N., Ng-Thow-Hing, C., Khursigara, C. M., Moiseeva, N., Allaire, M., et al. (2006). Structure of TonB in complex with FhuA, *E. coli* outer membrane receptor. *Science* 312, 1399–1402. doi: 10.1126/SCIENCE.1128057

Petiti, M., Serrano, B., Faure, L., Lloubes, R., Mignot, T., and Duché, D. (2019). Tol energy-driven localization of pal and anchoring to the peptidoglycan promote outer-membrane constriction. *J. Mol. Biol.* 431, 3275–3288. doi: 10.1016/j.jmb.2019.05.039

Pogoryelov, D., Klyszejko, A. L., Krasnoselska, G. O., Heller, E. M., Leone, V., Langer, J. D., et al. (2012). Engineering rotor ring stoichiometries in the ATP synthase. *Proc. Natl. Acad. Sci. U. S. A.* 109, E1599–E1608. doi: 10.1073/pnas.1120027109

Pogoryelov, D., Yildiz, Ö., Faraldo-Gómez, J. D., and Meier, T. (2009). High-resolution structure of the rotor ring of a proton-dependent ATP synthase. *Nat. Struct. Mol. Biol.* 16, 1068–1073. doi: 10.1038/NSMB.1678

Ramaiya, A., Roy, B., Bugiel, M., and Schäffer, E. (2017). Kinesin rotates unidirectionally and generates torque while walking on microtubules. *Proc. Natl. Acad. Sci.* 114, 10894–10899. doi: 10.1073/pnas.1706985114

Ratliff, A. C., Buchanan, S. K., and Celia, H. (2021). Ton motor complexes. *Curr. Opin. Struct. Biol.* 67, 95–100. doi: 10.1016/j.sbi.2020.09.014

Ratliff, A. C., Buchanan, S. K., and Celia, H. (2022). The ton motor. *Front. Microbiol.* 13:852955. doi: 10.3389/FMICB.2022.852955

Rhodes, R. G., Nelson, S. S., Pochiraju, S., and McBride, M. J. (2011). *Flavobacterium johnsoniae sprB* is part of an operon spanning the additional gliding motility genes *sprC*, *sprD*, and *sprF*. *J. Bacteriol.* 193, 599–610. doi: 10.1128/JB.01203-10

Ryu, W. S., Berry, R. M., and Berg, H. C. (2000). Torque-generating units of the flagellar motor of *Escherichia coli* have a high duty ratio. *Nature* 403, 444–447. doi: 10.1038/35000233

Sakai, T., Miyata, T., Terahara, N., Mori, K., Inoue, Y., Morimoto, Y., et al. (2019). Novel insights into conformational rearrangements of the bacterial flagellar switch complex. *mBio* 10, 1–14. doi: 10.1128/MBIO.00079-19

Santiveri, M., Roa-Eguiara, A., Kühne, C., Wadhwa, N., Hu, H., Berg, H. C., et al. (2020). Structure and function of stator units of the bacterial flagellar motor. *Cell* 183, 244–257.e16. doi: 10.1016/j.cell.2020.08.016

Seo, J., and Cohen, C. (1993). Pitch diversity in alpha-helical coiled coils. *Proteins* 15, 223–234. doi: 10.1002/PROT.340150302

Sharp, T. H., Bruning, M., Mantell, J., Sessions, R. B., Thomson, A. R., Zaccai, N. R., et al. (2012). Cryo-transmission electron microscopy structure of a gigadalton peptide fiber of de novo design. *Proc. Natl. Acad. Sci. U. S. A.* 109, 13266–13271. doi: 10.1073/PNAS.1118622109/SUPPL_FILE/SM01.GIF

Shrivastava, A., and Berg, H. C. (2020). A molecular rack and pinion actuates a cell-surface adhesin and enables bacterial gliding motility. Science. *Advances* 6:eaay6616. doi: 10.1126/sciadv.aay6616

Shrivastava, A., Lele, P. P., and Berg, H. C. (2015). A rotary motor drives Flavobacterium gliding. *Curr. Biol.* 25, 338–341. doi: 10.1016/j.cub.2014.11.045

Shrivastava, A., Roland, T., and Berg, H. C. (2016). The screw-like movement of a gliding bacterium is powered by spiral motion of cell-surface adhesins. *Biophys. J.* 111, 1008–1013. doi: 10.1016/j.bpj.2016.07.043

Shroder, D. Y., Lippert, L. G., and Goldman, Y. E. (2016). Single molecule optical measurements of orientation and rotations of biological macromolecules. *Methods Appl. Fluoresc.* 4:042004. doi: 10.1088/2050-6120/4/4/042004

Sobti, M., Ueno, H., Noji, H., and Stewart, A. G. (2021). The six steps of the complete F1-ATPase rotary catalytic cycle. *Nat. Commun.* 12, 4690–4610. doi: 10.1038/s41467-021-25029-0

Sobti, M., Walshe, J. L., Wu, D., Ishmukhametov, R., Zeng, Y. C., Robinson, C. V., et al. (2020). Cryo-EM structures provide insight into how *E. coli* F1Fo ATP synthase accommodates symmetry mismatch. *Nat. Commun.* 11, 2615. doi: 10.1038/s41467-020-16387-2

Song, L., Perpich, J. D., Wu, C., Doan, T., Nowakowska, Z., Potempa, J., et al. (2022). A unique bacterial secretion machinery with multiple secretion centers. *Proc. Nat. Acad. Sci.* 119, e2119907119. doi: 10.1073/PNAS.2119907119

Sowa, Y., Rowe, A. D., Leake, M. C., Yakushi, T., Homma, M., Ishijima, A., et al. (2005). Direct observation of steps in rotation of the bacterial flagellar motor. *Nature* 437, 916–919. doi: 10.1038/nature04003

Strick, T. R., Allemand, J.-F., Bensimon, D., Bensimon, A., and Croquette, V. (1996). The elasticity of a single supercoiled DNA molecule. *Science* 271, 1835–1837. doi: 10.1126/science.271.5257.1835

Sun, M., Wartel, M., Cascales, E., Shaevitz, J. W., and Mignot, T. (2011). Motor-driven intracellular transport powers bacterial gliding motility. *Proc. Natl. Acad. Sci.* 108, 7559–7564. doi: 10.1073/pnas.1101101108

Szczepaniak, J., Holmes, P., Rajasekar, K., Kaminska, R., Samsudin, F., Inns, P. G., et al. (2020a). The lipoprotein pal stabilises the bacterial outer membrane during constriction by a mobilisation-and-capture mechanism. *Nat. Commun.* 11, 1305. doi: 10.1038/s41467-020-15083-5

Szczepaniak, J., Press, C., and Kleanthous, C. (2020b). The multifarious roles of Tol-Pal in gram-negative bacteria. *FEMS Microbiol. Rev.* 44, 490–506. doi: 10.1093/femsre/fuaa018

Terahara, N., Kodera, N., Uchihashi, T., Ando, T., Namba, K., and Minamino, T. (2017). Na+−induced structural transition of MotPS for stator assembly of the Bacillus flagellar motor. *Sci. Adv.* 3, eaao4119. doi: 10.1126/sciadv.aao4119

Terashima, H., Kawamoto, A., Morimoto, Y. V., Imada, K., and Minamino, T. (2017). Structural differences in the bacterial flagellar motor among bacterial species. *Biophys. Physicobiol.* 14, 191–198. doi: 10.2142/BIOPHYSICO.14.0_191

Thoma, J., Bosshart, P., Pfreundschuh, M., and Müller, D. J. (2012). Out but not In: the large transmembrane β-barrel protein FhuA unfolds but cannot refold via β-hairpins. *Structure* 20, 2185–2190. doi: 10.1016/j.str.2012.10.006

Thomas, D. R., Francis, N. R., Xu, C., and DeRosier, D. J. (2006). The three-dimensional structure of the flagellar rotor from a clockwise-locked mutant of *Salmonella enterica* serovar typhimurium. *J. Bacteriol.* 188, 7039–7048. doi: 10.1128/JB.00552-06/ASSET/2D075046-9741-4392-A9CE-592152D0095C/ASSETS/GRAPHIC/ZJB0200661490011.JPEG

Tran, Q. H., and Unden, G. (1998). Changes in the proton potential and the cellular energetics of *Escherichia coli* during growth by aerobic and anaerobic respiration or by fermentation. *Eur. J. Biochem.* 251, 538–543. doi: 10.1046/j.1432-1327.1998.2510538.x

Trivedi, A., Gosai, J., Nakane, D., and Shrivastava, A. (2022). Design principles of the rotary type 9 secretion system. *Front. Microbiol.* 13:845563. doi: 10.3389/FMICB.2022.845563

Ueno, H., Suzuki, T., Kinosita, K., and Yoshida, M. (2005). ATP-driven stepwise rotation of FoF1-ATP synthase. *Proc. Natl. Acad. Sci. U. S. A.* 102, 1333–1338. doi: 10.1073/PNAS.0407857102

Vincent, M. S., Comas Hervada, C., Sebban-Kreuzer, C., Le Guenno, H., Chabalier, M., Kosta, A., et al. (2022). Dynamic proton-dependent motors power type IX secretion and gliding motility in *Flavobacterium*. *PLoS Biol.* 20:e3001443. doi: 10.1371/journal.pbio.3001443

Wadhwa, N., and Berg, H. C. (2021). Bacterial motility: machinery and mechanisms. *Nat. Rev. Microbiol.* 20, 161–173. doi: 10.1038/s41579-021-00626-4

Wadhwa, N., Tu, Y., and Berg, H. C. (2021). Mechanosensitive remodeling of the bacterial flagellar motor is independent of direction of rotation. *Proc. Nat. Acad. Sci. U. S. A.* 118:e2024608118. doi: 10.1073/pnas.2024608118

Webby, M. N., Williams-Jones, D. P., Press, C., and Kleanthous, C. (2022). Force-generation by the trans-envelope Tol-Pal system. *Front. Microbiol.* 13:852176. doi: 10.3389/FMICB.2022.852176

Wise, J. G., and Vogel, P. D. (2008). Subunit b-dimer of the *Escherichia coli* ATP synthase can form left-handed coiled-coils. *Biophys. J.* 94, 5040–5052. doi: 10.1529/biophysj.107.121012

Witty, M., Sanz, C., Shah, A., Grossmann, J. G., Mizuquchi, K., Perham, R. N., et al. (2002). Structure of the periplasmic domain of *Pseudomonas aeruginosa* TolA: evidence for an evolutionary relationship with the TonB transporter protein. *EMBO J.* 21, 4207–4218. doi: 10.1093/EMBOJ/CDF417

Wojdyla, J. A., Cutts, E., Kaminska, R., Papadakos, G., Hopper, J. T. S., Stansfeld, P. J., et al. (2015). Structure and function of the *Escherichia coli* Tol-Pal Stator protein TolR. *J. Biol. Chem.* 290, 26675–26687. doi: 10.1074/jbc.M115.671586

Worrall, J. A. R., and Mason, J. M. (2011). Thermodynamic analysis of Jun–Fos coiled coil peptide antagonists. *FEBS J.* 278, 663–672. doi: 10.1111/j.1742-4658.2010.07988.x

Yamaguchi, T., Makino, F., Miyata, T., Minamino, T., Kato, T., and Namba, K. (2021). Structure of the molecular bushing of the bacterial flagellar motor. *Nat. Commun.* 12, 4469. doi: 10.1038/s41467-021-24715-3

Yasuda, R., Noji, H., Yoshida, M., Kinosita, K., and Itoh, H. (2001). Resolution of distinct rotational substeps by submillisecond kinetic analysis of F1-ATPase. *Nature* 410, 898–904. doi: 10.1038/35073513

Yildiz, A., Tomishige, M., Vale, R. D., and Selvin, P. R. (2004). Kinesin Walks Hand-Over-Hand. *Science* 303, 676–678. doi: 10.1126/science.1093753

Zhang, Y., Ducret, A., Shaevitz, J., and Mignot, T. (2012). From individual cell motility to collective behaviors: insights from a prokaryote, *Myxococcus xanthus*. *FEMS Microbiol. Rev.* 36, 149–164. doi: 10.1111/j.1574-6976.2011.00307.x

Zhang, X. Y. Z., Goemaere, E. L., Thomé, R., Gavioli, M., Cascales, E., and Lloubès, R. (2009). Mapping the interactions between *escherichia coli* Tol subunits: rotation of the TolR transmembrane helix. *J. Biol. Chem.* 284, 4275–4282. doi: 10.1074/JBC.M805257200

Zhao, X., Zhang, K., Boquoi, T., Hu, B., Motaleb, M. A., Miller, K. A., et al. (2013). Cryoelectron tomography reveals the sequential assembly of bacterial flagella in *Borrelia burgdorferi*. *Proc. Natl. Acad. Sci. U. S. A.* 110, 14390–14395. doi: 10.1073/PNAS.1308306110

Zhou, J., Sharp, L. L., Tang, H. L., Lloyd, S. A., Billings, S., Braun, T. F., et al. (1998). Function of protonatable residues in the flagellar motor of *Escherichia coli*: a critical role for asp 32 of MotB. *J. Bacteriol.* 180, 2729–2735. doi: 10.1128/JB.180.10.2729-2735.1998

Zhu, S., Nishikino, T., Hu, B., Kojima, S., Homma, M., and Liu, J. (2017). Molecular architecture of the sheathed polar flagellum in *Vibrio alginolyticus*. *Proc. Natl. Acad. Sci. U. S. A.* 114, 10966–10971. doi: 10.1073/PNAS.1712489114

Zhu, S., Takao, M., Li, N., Sakuma, M., Nishino, Y., Homma, M., et al. (2014). Conformational change in the periplamic region of the flagellar stator coupled with the assembly around the rotor. *Proc. Natl. Acad. Sci. U. S. A.* 111, 13523–13528. doi: 10.1073/PNAS.1324201111

frontiers | Frontiers in Microbiology

PERSPECTIVE
published: 25 May 2022
doi: 10.3389/fmicb.2022.866141

Modeling Bacterial Flagellar Motor With New Structure Information: Rotational Dynamics of Two Interacting Protein Nano-Rings

Yuansheng Cao[1†], *Tairan Li*[2†] *and Yuhai Tu*[3*]

[1] Department of Physics, University of California, San Diego, San Diego, CA, United States, [2] Yuanpei College, Center for Quantitative Biology, Peking University, Beijing, China, [3] IBM T. J. Watson Research Center, New York, NY, United States

In this article, we develop a mathematical model for the rotary bacterial flagellar motor (BFM) based on the recently discovered structure of the stator complex ($MotA_5MotB_2$). The structure suggested that the stator also rotates. The BFM is modeled as two rotating nano-rings that interact with each other. Specifically, translocation of protons through the stator complex drives rotation of the MotA pentamer ring, which in turn drives rotation of the FliG ring in the rotor *via* interactions between the MotA ring of the stator and the FliG ring of the rotor. Preliminary results from the structure-informed model are consistent with the observed torque-speed relation. More importantly, the model predicts distinctive rotor and stator dynamics and their load dependence, which may be tested by future experiments. Possible approaches to verify and improve the model to further understand the molecular mechanism for torque generation in BFM are also discussed.

Keywords: bacterial flagellar motor, dynamics, stator structure, modeling, proton motive force, proton translocation, rotary motor

OPEN ACCESS

Edited by:
Pushkar Lele,
Texas A&M University, United States

Reviewed by:
Jasmine Nirody,
University of Oxford, United Kingdom
Laurence Wilson,
University of York, United Kingdom

***Correspondence:**
Yuhai Tu
yuhai@us.ibm.com

[†]*These authors have contributed equally to this work*

Specialty section:
This article was submitted to Microbiology, a section of the journal Frontiers in Microbiology

Received: *30 January 2022*
Accepted: *13 April 2022*
Published: *25 May 2022*

Citation:
Cao Y, Li T and Tu Y (2022) Modeling Bacterial Flagellar Motor With New Structure Information: Rotational Dynamics of Two Interacting Protein Nano-Rings. Front. Microbiol. 13:866141. doi: 10.3389/fmicb.2022.866141

1. INTRODUCTION

The swimming motion of many bacteria is powered by the rotary bacterial flagellar motor (BFM). As a canonical example, the motors in *E. coli* are fueled by electrochemical potential difference of protons (H^+) across the cytoplasmic membrane, i.e., the proton motive force (PMF) (Larsen et al., 1974; Hirota et al., 1981; Berg, 2003). The BFM can rotate bidirectionally. Without binding to the phosphorylated response regulator CheY protein (CheY-P), the BFM rotates in a counter-clockwise (CCW, viewed from the filament to the motor) direction. There are $\sim 4-6$ BFMs in an *E. coli* cell. The CCW rotation of the BFMs causes their flagellar filaments to form a coherent bundle and propels the swimming cells in a roughly straight line that is called a "run." However, the binding of CheY-P to BFM causes it to rotate in the clockwise (CW) direction, which disrupts the filament bundle. As a result, the rod-shaped *E. coli* cell changes its orientation randomly without translational movement in an event called a "tumble."

The bacterial flagellar motor consists of a rotor and a number of stators that can vary from 0 to 11 depending on gene expression and mechanical load (Blair and Berg, 1988; Lele et al., 2013; Tipping et al., 2013; Nord et al., 2017; Wadhwa et al., 2019, 2021). The rotor consists of FliF, FliG, FliM, and FliN. FliF forms the MS-ring embedded within the cytoplasmic membrane (Asai et al., 1997; Sato and Homma, 2000; Yorimitsu et al., 2004; Morimoto and Minamino, 2014; Baker et al., 2016). The

cytoplasmic face of the MS-ring is attached to the C-ring, which comprises the FliG, FliM, and FliN proteins. The diameter of the C-ring is $\sim$ 45*nm*. The C-ring is responsible for coupling the rotor to the stator units and for switching rotational directions. The membrane-bound stators, which consist of the MotA and MotB proteins, are powered by the PMF to drive the rotation of the rotor *via* direct interaction between MotA and FliG (Chun and Parkinson, 1988; Blair and Berg, 1990; Kojima and Blair, 2004; Roujeinikova, 2008).

The molecular mechanism of torque generation by the stator units has been suggested by two recent Cryo-EM studies of the stator structure (Deme et al., 2020; Santiveri et al., 2020). Both studies report that a stator unit consists of a MotB dimer surrounded by a MotA pentamer ring with a diameter of $\sim$ 5 − 7.5*nm*. The position of the MotB dimer, which is bound to the peptidoglycan layer in the rigid cell wall, remains fixed, while the MotA pentamer forms a ring that can rotate around the MotB dimer. Each MotB monomer progressively engages with each MotA monomer to form an ion channel through which one proton can pass to drive the rotation of the MotA pentamer ring.

Brownian ratchet models have attracted physicists' attention for modeling molecular motors since Richard Feynman popularized the idea more than half a century ago (Feynman et al., 1966; Parrondo et al., 1998; Astumian, 2010; Golubeva et al., 2012). Among all variants of the ratchet models, only isothermal chemical ratchets are relevant for biological motors (Jülicher et al., 1997; Parrondo and de Cisneros, 2002). A minimal model for the rotational ratchet model can be found in Xing et al. (2006), Meacci and Tu (2009), and Meacci et al. (2011). This model has two types of coordinates: the "physical" coordinate that describes the motion of the motor in physical space (angles for rotary motor); and the "chemical" coordinate that describes the different conformational states of the motor. For the BFM, the motor moves in a periodic potential in which torque, which is the gradient of the potential, is generated as the motor slide down from a position of high potential energy toward its equilibrium position, which has the lowest potential energy. The passage of an ion triggers a conformational change (stepping) of the motor. Because the landscape of potential energy is different for different conformational states of the motor, the conformational change driven by the PMF changes the potential energy landscape and can bring the motor to a position of high potential energy in the new potential energy landscape. The newly gained potential energy continues to drive the physical rotation of the motor. This continuous process drives the system toward a sequence of new equilibrium positions and gives rise to a directed stepwise rotation (Sowa et al., 2005).

One of the most important characteristics of a rotary motor is its torque-speed dependence (or force-speed dependence for linear motors). The measured torque-speed curve for the CCW BFM has a downward concave shape with a roughly constant high torque at low to medium speeds and a rapid and nearly linear decrease of torque at high speeds (Chen and Berg, 2000; Lo et al., 2013). This concave torque-speed curve has the advantage of generating high power output (or, equivalently, a high torque for a given speed) in a wide range of physiologically relevant loads. The minimal ratchet model can reproduce the observed torque-speed curve when certain general constraints for the rotor-stator interaction potential and the proton-assisted transition rate between different conformational states are applied (Tu and Cao, 2018).

Before the recent availability of an accurate picture of the structure of the stator (Deme et al., 2020; Santiveri et al., 2020), previous structure-based modeling studies assumed that the stator unit has a $MotA_4MotB_2$ composition (Braun et al., 2004; Kim et al., 2008). For example, it was proposed (Mandadapu et al., 2015; Nirody et al., 2016) that the power stroke for each rotational direction of the rotor (CCW or CW) is delivered by two of the four MotA subunits through a steric force generated by a "kink and swivel" conformational change of MotA induced by the binding of a proton to a corresponding MotB. The newly discovered structure of the stator complex has the different stoichiometry of $MotA_5MotB_2$ (Deme et al., 2020; Santiveri et al., 2020). The structure of the stator complex immediately led to an important new insight into the molecular mechanism by which the BFM operates: the MotA ring in the stator unit rotates. Consequently, all of the five MotA subunits are involved in torque generation independent of the rotational direction of the rotor, and the power stroke is generated directly by the rotational motion of the MotA subunits themselves instead of their internal conformational changes.

In terms of modeling, the new insight gained from the stator complex structure means that the stator unit must be described by its physical state in terms of the relative angle between the MotA pentamer ring and the MotB dimer in addition to its chemical (conformational) states. In the following section, we present an updated model for the BFM based on the general modeling framework described before (Tu and Cao, 2018), but now in the context of the new structure of the stator complex. Some preliminary results predicted by the model will also be described.

2. A STRUCTURE-INFORMED MODEL AND SOME PRELIMINARY RESULTS

Our new model describes the dynamics of the two coupled rotating nano-rings (the MotA ring and the FliG ring) as shown in **Figures 1A,B**. The stator unit is the active part of the motor. It can generate torque as a rotational ratchet powered by the PMF. Rotation of the MotA ring drives the rotation of the passive FliG ring through a coupling potential $V_R(\theta_S, \theta_R)$, where θ_S and θ_R are the rotational angles of the stator and the rotor, which have a periodicity of $\Delta\theta_S = 2\pi/5, \Delta\theta_R = 2\pi/26$, respectively. It is assumed that there are 26 FliG proteins in the C-ring (Thomas et al., 2006). The rotational motion of the rotor is described by a Langevin equation for the rotor angle θ_R:

$$\xi_R \frac{d\theta_R}{dt} = -\frac{\partial V_R(\theta_S, \theta_R)}{\partial \theta_R} + \eta_R(t), \tag{1}$$

where ξ_R is the load on the rotor, the first term on the right hand side of Equation 1 is the torque exerted on the rotor from the stator *via* the MotA-FliG interaction, and $\eta_R(t)$ is the rotor thermal noise: $< \eta_R(t)\eta_R(t') >= 2k_BT\xi_R\delta(t - t')$ with k_B

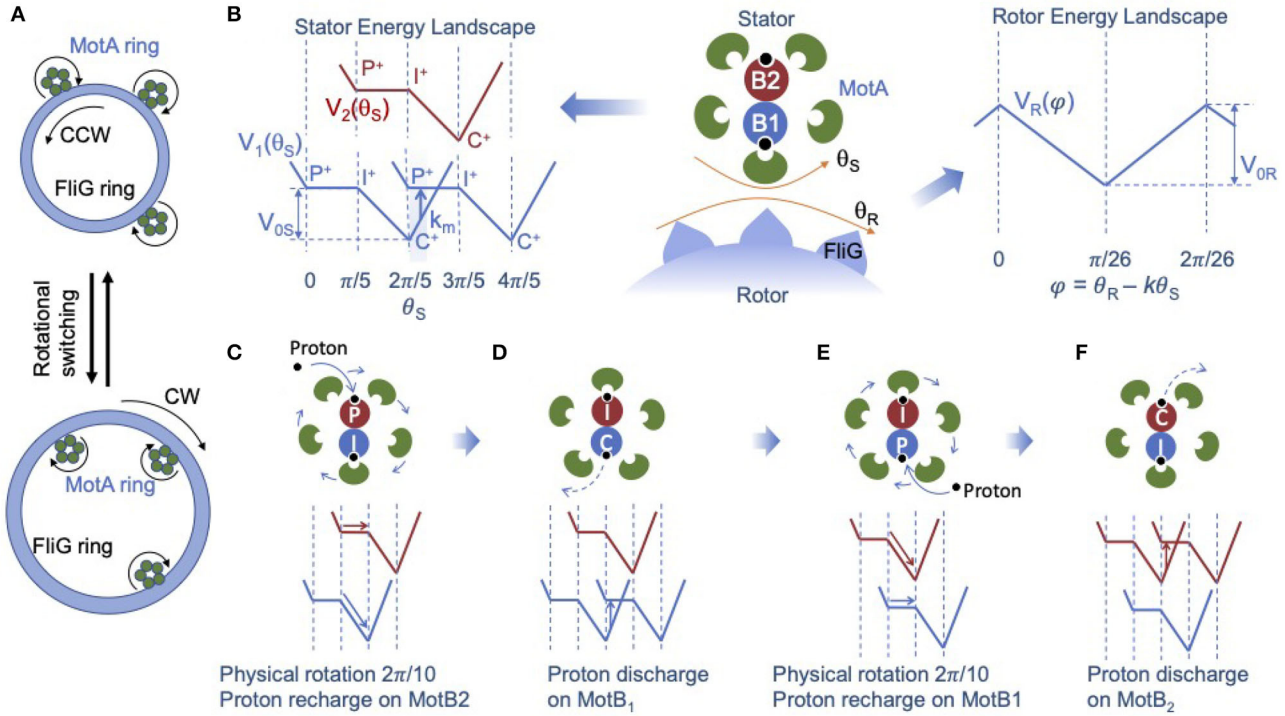


FIGURE 1 | A structure-informed model for the bacterial flagellar motor (BFM). **(A)** Illustration of the bidirectional rotation of the BFM. In counter-clovkwise (CCW) mode (top), the C- ring adapts a compact conformation, and the MotA ring on stator units contacts the FliG subunits on the outside of the C-ring. In the CW mode (bottom), the C-ring expands, and the MotA rings contact the FliG subunits on the inside of the C-ring. **(B)** Illustration of the two-rotating-ring model for the BFM (center panel). The stator energy landscape (left panel) shows the two interaction potentials between the MotA pentamer ring and the MotB dimer: $V_1(\theta_S)$ from $MotB_1$ (blue) and $V_2(\theta_S)$ from $MotB_2$ (red), which have the same shape but are shifted from each other by half a period $\Delta\theta_S/2 = 2\pi/10$. The blue and red energy landscapes are shifted vertically only for clarity. *P* and *C* stand for the two conformational states of MotB in which the proton acceptor residue faces the periplasm and the cytoplasm, respectively, and *I* stands for an intermediate state between P-state and C-state. The plus (or minus) superscript indicates the proton-bound (or proton-unbound) state. Transition (stepping) from one MotA-MotB interaction potential to another interaction potential occurs with a probability rate k_m near the potential minimum (shaded region in the left panel), which is driven by the proton discharge-recharge chain reaction $P^+ \rightarrow P^- \rightarrow C^- \rightarrow C^+$. For brevity, only the initial and final states (P^+ and C^+) are shown, and the intermediate discharged states C^- and P^- are omitted (see text for the full description). The rotor energy landscape (right panel) shows the interaction potential (V_R) between MotA and FliG, which depends only on the scaled angle difference $\varphi = \theta_R - k\theta_S$. For simplicity, we used a piece-wise linear form for $V_{1,2}$ and V_R. To the left of the $P \rightarrow I$ plateau in $V_{1,2}$, a barrier is added to prevent back flow. The four stages of stator dynamics during one full power stroke as described in Equation 2 are illustrated in C-F. **(C)** Physical rotation of the MotA pentamer ring, which is driven dominantly by $MotB_1$ and proton recharge (the black dot) on $MotB_2$. **(D)** Proton discharge on $MotB_1$, which causes the transition of the MotA-$MotB_1$ interaction potential and effectively shifts V_1 (blue line) by one period ($\Delta\theta_S$). **(E)** Physical rotation of the MotA pentamer ring, which is driven dominantly by $MotB_2$ and proton recharge on $MotB_1$. **(F)** Proton discharge on $MotB_2$, which shifts the MotA-$MotB_2$ potential V_2 (red line) by one period.

the Boltzmann constant and T the temperature. The coupling potential $V_R(\theta_S, \theta_R)$ should be periodic in both θ_S and θ_R. To satisfy this dual periodicity, we write $V_R(\theta_S, \theta_R) = V_R(\varphi)$ where $\varphi = \theta_R - k\theta_S$ is the scaled relative angle, with $k = \Delta\theta_R/\Delta\theta_S = \frac{5}{26}$, which is the gear ratio between the two rotating rings in *E. coli*.

We model the stator unit as a rotational ratchet driven by the PMF. Based on the new structural information, the MotA pentamer ring rotates around the fixed MotB dimer. Given the incommensurate stoichiometry (5 : 2) within the stator unit, the two MotB monomers engage with MotA monomers alternately – when one MotB is engaged directly with one MotA monomer the other MotB is positioned between two MotA monomers. Consequently, the two MotB monomers generate two different energy potentials shifted by half a period ($\Delta\theta_S/2$). To account for this effect, the overall stator potential can be written as the sum of two identical periodic potentials shifted by an angle difference of $\Delta\theta_S/2$: $V_S(\theta_S) = V_1(\theta_S) + V_2(\theta_S)$ with $V_2(\theta_S) = V_1(\theta_S + \Delta\theta_S/2)$ as shown in **Figure 1B**.

During one power stroke, the MotA pentamer ring rotates one period ($2\pi/5$). Each full power stroke consists of two half strokes, each of which is powered by a proton passing through one of the two ion channels alternately. During each half stroke, the proton acceptor residue (D32 for *E. coli*) on the corresponding MotB monomer becomes protonated, which drives rotation of the MotA ring. At the same time, the protonated MotB undergoes a conformational change in which the proton acceptor residue changes from a periplasm-facing position to a cytoplasm-facing position, from which the proton can be released to the cytoplasm. To describe this process, we define three conformational states for each MotB: a periplasm-facing state called the P-state, a cytoplasm-facing state called the C-state, and an intermediate state between the P-state and C-state, which we call the I-state.

Each MotB can be either protonated or unprotonated (indicated by a plus or minus sign). A proton can bind with MotB when it is in the P-state; and a bound proton can enter the cytoplasm when the MotB is in the C-state.

As suggested by the recent Cryo-EM study (Santiveri et al., 2020), different conformational states occur at different relative positions between MotB and the closest MotA monomer, or, equivalently, at different locations within the MotA-MotB landscape of interaction energy potential, as shown in **Figure 1B** (left). In particular, the P-state occurs near the peak potential and the C-state occurs near the minimum. For simplicity, we used a simple piece-wise linear potential ($V_{1,2}$) that is flat over half of the period and linear in the other half, as shown in **Figure 1B** (left). Using this simple representation of the internal chemical states of the stator, evolution of the internal states of the two MotB monomers in a stator unit during one full rotational period ($2\pi/5$) can be described by the reaction cycle:

$$P_2^+ \underbrace{I_1^+ \rightarrow I_2^+}_{\text{Rotation}} \underbrace{C_1^+ \rightarrow I_2^+ C_1^- \rightarrow I_2^+ P_1^- \rightarrow I_2^+}_{\text{Proton discharge and recharge on MotB}_1} \underbrace{P_1^+ \rightarrow C_2^+}_{\text{Rotation}} \underbrace{I_1^+ \rightarrow C_2^- I_1^+ \rightarrow P_2^- I_1^+ \rightarrow P_2^+}_{\text{Proton discharge and recharge on MotB}_2} I_1^+, \quad (2)$$

where the subscripts (1,2) indicate the two MotB monomers. For each MotB, torque is generated during the transitions $P^+ \rightarrow I^+ \rightarrow C^+$, which drives the physical rotation of the MotA ring. After reaching the C^+-state near the potential energy minimum, MotB is rejuvenated by the release of the proton to the cytoplasm followed by a conformational change from the C-state to the P-state and subsequent addition of a new proton to the P-state: $C^+ \rightarrow C^- \rightarrow P^- \rightarrow P^+$. This chain reaction returns MotB to its high-energy protonated P-state (P^+) to continue driving the rotation of the stator. It is clear from the reaction cycle (Equation 2) that one full power stroke is powered by translocation of two protons (or 2PMF), each "consumed" by one MotB. The four stages of the alternating physical rotations and proton discharge-charge reactions during one full power stroke as described in Equation 2 are illustrated in **Figures 1C–F**, respectively.

In our model, the rotation dynamics of the MotA ring can also be described by a Langevin equation for the stator angle θ_S:

$$\xi_S \frac{d\theta_S}{dt} = -\frac{\partial V_R(\theta_S, \theta_R)}{\partial \theta_S} - \frac{\partial V_S(\theta_S)}{\partial \theta_S} + \eta_S(t), \quad (3)$$

where ξ_S is the load (viscosity) of the stator, the first and the second terms on the right hand side of Equation 4 are the torque exerted on the stator from the rotor *via* the MotA-FliG interaction and the torque generated by the MotA-MotB interaction, respectively, and $\eta_S(t)$ is the stator thermal noise with $< \eta_S(t)\eta_S(t') >= 2k_BT\xi_S\delta(t-t')$. The shape of $V_S(\theta_S)$ is given in **Figure 1B**. To prevent back flow at the maximum potential energy, we introduce an additional energy barrier which extends to the left of the $P \rightarrow I$ plateau.

The key chemical reaction that powers rotation of the stator is the proton discharge-recharge chain reaction ($C^+ \rightarrow C^- \rightarrow P^- \rightarrow P^+$), which leads to the transition (stepping) from one potential landscape, in which the system has a low (near minimum) potential energy, to another potential landscape where the system has a high (near maximum) potential energy. For simplicity, this chain reaction is modeled here by an overall transition rate $k_m(\theta_S)$ that depends on the MotA-MotB relative angle θ_S (see **Figure 1B** for an illustration of k_m, the blue arrow in the left panel). Specifically,

$$\text{Prob (transition from low to high potential energy during } t \rightarrow t+dt) = k_m(\theta_S)dt. \quad (4)$$

In summary, our model considers the coupled rotations of both the active stator and the passive rotor as well as the key chemical reactions that power the rotation of the stator. The dynamics of the BFM are fully described by Equations 1, 3 and 4, which depend on three biologically meaningful functions: two interaction energy (potential) functions - $V_R(\theta_S - k\theta_R)$ between the FliG-ring of the rotor and the MotA ring, $V_S(\theta_S)$ between the MotB dimer and the MotA ring, and the chemical transition rate function $k_m(\theta_S)$. Next, we present some preliminary results based on simulations of the model with simple choices for these functions to demonstrate the general utility of the model.

In our simulations, we set the stator load ξ_S to be a small constant and change the rotor load ξ_R to obtain the torque and speed for different values of ξ_R. The motor dynamics depend on the relative strength between the MotA-FliG coupling interaction potential V_R and the torque-generating potential V_S. In **Figure 2**, we present the results for a case in which these two potentials are comparable. As shown in **Figure 2A**, the torque-speed curve shows a downward concave shape consistent with experiments. In addition to the torque-speed relationship, our model allows us to investigate the rotational dynamics of both the rotor and the stator. In **Figure 2B**, we plot the time trajectories of the stator (dashed lines) and rotor (solid lines) angles for different loads. At a low load, the two trajectories are close to each other, whereas, at a high load, the trajectory of the rotor is almost flat, even though the stator still rotates at a finite speed. As shown in **Figure 2C**, as load increases, the rotor's speed quickly decreases to zero, while the stator's speed approaches a constant speed (reduced but still finite). Our results indicate that the rotations of the stator and the rotor are in-sync at low load: when the stator rotates at an angle of $\Delta\theta$, the rotor rotates at approximately $k\Delta\theta$, i.e., there is no slippage between the two rotating rings. However, slippage between the two rings increases with the load. Near stall, the rotor speed vanishes while the stator still rotates at a finite speed. The existence of the stator-rotor slippage depends on the strength of the stator-rotor (MotA-FliG) coupling (V_R) relative to that of the MotA-MotB coupling (V_S). When we used a V_R that is much stronger than V_S, slippage disappears. Here, we choose to show a case in which V_R and V_S are comparable to highlight the possibility of slippage between the two rotating protein nano-rings.

To investigate the relative motion (rotation) of the stator and rotor in details, we plot the trajectories of $\theta_R(t)$ vs. $\theta_S(t)$ for different loads in **Figure 2D**, where the dashed black line

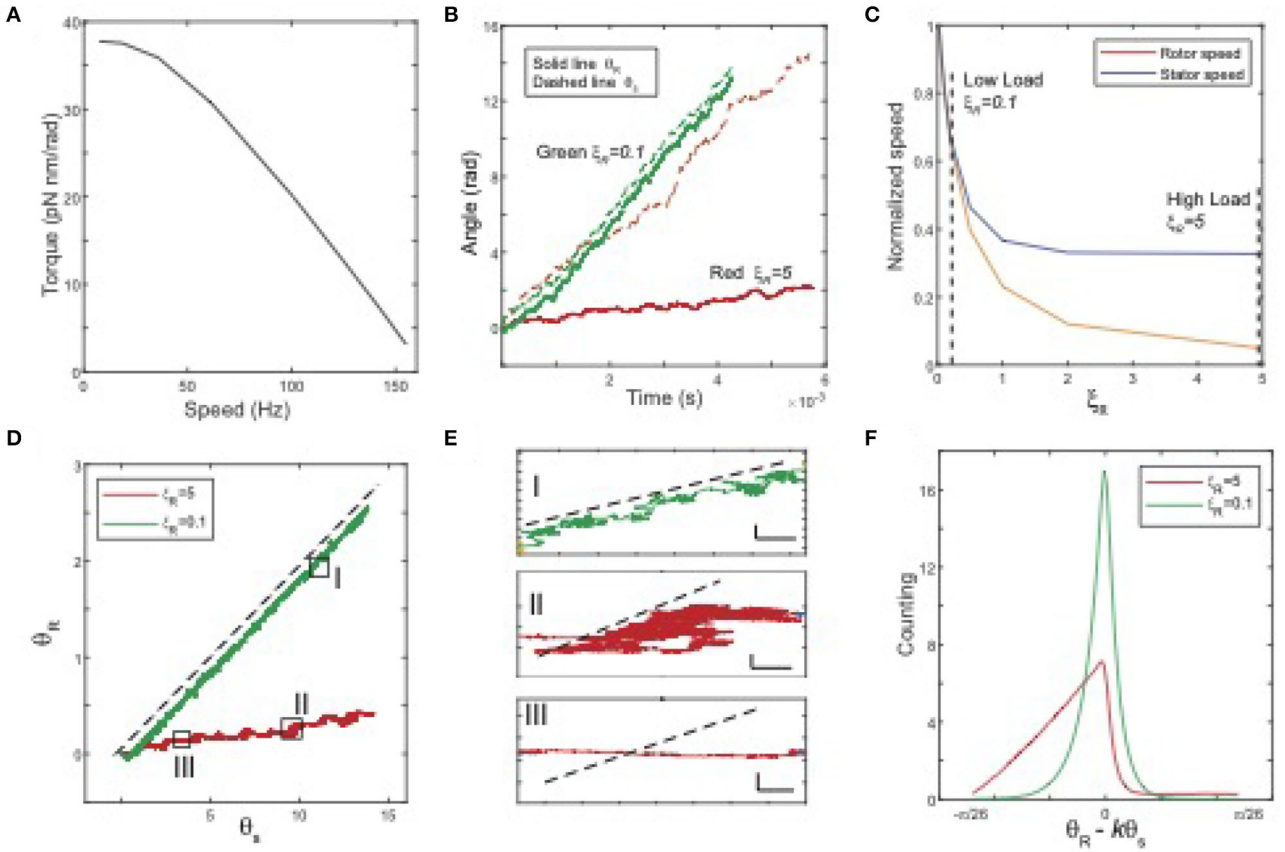


FIGURE 2 | Model results. **(A)** The torque-speed curve from the model with simple choices of the interaction potentials (V_R and V_S) and the transition (stepping) rate k_m (parameters are given at the end of the caption). **(B)** Time series of θ_R (solid line) and θ_S (dashed line) for different rotor loads. Red: high load $\xi_R = 5$, green: low load $\xi_R = 0.1$. **(C)** The normalized average speeds of the rotor (yellow) and stator (blue) vs. the rotor load ξ_R. **(D)** Trajectories in (θ_R, θ_S) space for different loads. Dashed black line: $\theta_R = k\theta_S$, with $k = \Delta\theta_R/\Delta\theta_S = 5/26$. The three boxes highlight the three different types of motions. **(E)** Three typical movements with zoom-in trajectories [highlighted in **(D)**]. I: rotor moves along with stator without slipping; II: reduced net speed for both rotor and stator; III: stator rotates while rotor speed is near zero. The black dashed lines indicate the no-slip motion $\theta_R = k\theta_S$. Horizontal scale bar: 0.3 rad; vertical scale bar: 0.1 rad. **(F)** The distributions (histogram) of $\varphi = \theta_R - k\theta_S$ for a high load and a low load. Parameters and simulation methods are given in the **Supplementary Materials**.

indicates the tight coupling (no slippage) limit when $\theta_R = k\theta_S$ (dotted black line). At low load (the green line), the trajectory is almost a straight line parallel to the tight coupling limit, while at high load (the red line), the trajectory wiggles closer to the horizontal direction. We can categorize the relative stator-rotor motion by coarse-graining the trajectories in the $\theta_S - \theta_R$ space. We found three types of relative motion, which are shown in the zoom-in plots in **Figure 2E**. In type I movement, the rotor moves with the stator without slippage; in type II movement, the rotor-stator system follows a biased random walk in the (θ_S, θ_R) space with net motion lower for both the stator and the rotor; in type III movement, the stator rotates at a finite speed but the rotor has almost no net motion, which indicates a high degree of slippage between the rotor and the stator. Type III movement can be considered as the extreme case of type II movement. From the results of our simulation, we find that as load increases, the motor spends more time in the type II&III movements, i.e., slipping. This observation is further confirmed by the distributions of the scaled angle difference between the rotor and stator, i.e., $\varphi = \theta_R - k\theta_S$, as shown in **Figure 2F**. At low load, the distribution is concentrated around $\varphi = 0$, indicating the absence of slippage. As load increases, the distribution of φ becomes more populated in the region with $\varphi < 0$, which shows that the stator leaves the rotor behind more often, i.e., the motor spends more time slipping.

The most unique feature of our model is its ability to investigate the rotational motion of the stator in addition to the rotational motion of the rotor, which was the main focus of previous modeling studies. The model predictions, such as the dependence of the stator speed on the rotor load (**Figure 2C**) and the distributions of the relative rotor-stator angle (**Figure 2F**), can be tested by future experiments that directly measure the rotational motion of the stator in addition to the existing measurements of the rotor motion. These experiments together with our model can also be used to infer the interaction potentials (V_S and V_R) as well as the proton-assisted transition rate (k_m).

3. DISCUSSION

In this article, we propose a new model for BFM based on a general modeling framework and the recently discovered molecular structure of the stator complex. The most important update in our model is that the stator is now modeled as an active rotating nano-machine that consumes PMF and drives the rotation of the rotor. The model can generate the characteristic torque-speed curve observed in experiments. More importantly, our model can be used to investigate and predict the dynamics of both the rotor and the stator, which can be tested in experiments.

It is generally believed that proton flux and motor rotation are "tightly coupled" in the BFM, which implies that there is no proton flux at stall and the efficiency of the BFM is close to 1 near stall (Berg, 2003). Here, we find that if the MotA-FliG interaction is comparable to (or weaker than) the MotA-MotB interaction, there is slippage between the rotor and the stator. The probability of slippage increases as the load increases, which leads to a motor efficiency that is less than 1 near stall. On the other hand, we also find that slippage can be suppressed by increasing the rotor-stator interaction strength. Thus, our study poses a simple but important question. Does the BFM slip? Ultimately, this question needs to be answered experimentally by measuring the rotation of the stator (MotA-ring) at different loads, especially at the high load where the probability of slippage is expected to be the highest if it exists. Alternatively, one may be able to look for signatures of slipping by measuring fluctuations of the rotor's instantaneous speed at a high load. In the absence of slipping, the rotor should run smoothly at a high load with the dominant fluctuations coming from thermal fluctuations (Meacci and Tu, 2009). However, if there is slipping, then fluctuations in the rotor speed can be much larger with additional contributions coming from the slipping events.

Our model can be extended to cases with multiple stators. At low load, the stators and rotor rotate in sync without slippage, so the rotor's maximum speed is determined by the maximum speed of the individual stator units independent of the number of stators. However, at high load (e.g., near stall), the effective duty ratio of the stator can be far below 1 due to the higher probability of slippage and/or the relatively long time spent at the energy potential minima waiting for the conformational change (Meacci and Tu, 2009). Note that the effective duty ratio during slipping is zero although the stator is not disengaged with the rotor. Assuming no direct coordination among stators, there should be little overlap among the duty cycles of each stator. Thus, the maximum torque at stall is simply the sum of torques generated by all the stators. The dependence of maximum speed and maximum torque on the number of stators has been reported before (Blair and Berg, 1988; Yuan and Berg, 2008), and our model may provide a natural explanation for these experimental observations.

The rotation of the stator units is also essential for understanding switching between CW and CCW rotation of the rotor. As pointed out in Santiveri et al. (2020) and illustrated in **Figure 1A** here, the MotA ring always rotates clockwise around the MotB dimer, and the switch between the CW and CCW rotation of the rotor ring is determined by conformational changes of the C-ring. In the CCW mode, the C-ring adopts a compact conformation, and the stator units contact FliG subunits on the outside of the C-ring; thus, the C-ring rotates CCW. Upon binding of CheY-P to FliM in the C-ring, the C-ring expands, and the stator units are now in contact with FliG subunits on the inside of the C-ring, so the C-ring rotates clockwise. In this manner, the unidirectional rotation of the stator drives the bidirectional rotation of the motor. In our modeling framework, the coupling between rotor and stator is modeled by $V_R(\theta_R, \theta_S)$. We hypothesize that the CW and CCW rotation modes correspond to different forms of the interaction potential V_R, which can lead to the different torque-speed curves for the BFM in CCW and CW rotation observed experimentally (Yuan et al., 2010).

The BFM, like all other biological motors, converts chemical energy (e.g. from ATP hydrolysis or ion translocations) into mechanical work. A fundamental question is whether there are thermodynamic bounds to the power generation and energy efficiency for these highly non-equilibrium molecular engines (Parmeggiani et al., 1999; Parrondo and de Cisneros, 2002; Astumian, 2010). A related question is what microscopic design principles allow a molecular motor to approach these bounds under realistic constraints. In our model, the motor design space is spanned by three functions: $V_S(\theta_S)$, $V_R(\varphi)$, and $k_m(\theta_S)$, which determine the motor dynamics. For example, as we showed in this paper, depending on the relative strength of V_R and V_S, there could be slippage between the stator and the rotor, which strongly affects the efficiency of the motor. Each of these functions contains information about the molecular details of the motor, which, in principle, can be estimated from or constrained by the structural data. A systematical exploration of the motor design space will lead to a better understanding of the fundamental limits and possible design principles for optimal motor performance.

DATA AVAILABILITY STATEMENT

The original contributions presented in the study are included in the article/**Supplementary Material**, further inquiries can be directed to the corresponding author.

AUTHOR CONTRIBUTIONS

YT originated the study. YC and TL performed all simulations. YC and YT prepared the manuscript. All authors read and approved the final manuscript.

FUNDING

The work by YT is supported by a NIH grant (R35GM131734).

ACKNOWLEDGMENTS

YT would like to express deepest thanks to Howard Berg for introducing the bacterial flagellar motor—a biotechnological marvel (Berg, 2003) to him more than a decade ago and for

Howard's constant enlightenment and encouragement on the topic till his untimely passing at the end of 2021. We dedicate this work in the memory of Howard—it was Howard and members of the Berg lab who first told us about the new stator structure (Deme et al., 2020; Santiveri et al., 2020), who launched this study. YT would also like to thank Nicholas Taylor for an insightful discussion on details of the stator structure and proton translocation process.

REFERENCES

Asai, Y., Kojima, S., Kato, H., Nishioka, N., Kawagishi, I., and Homma, M. (1997). Putative channel components for the fast-rotating sodium-driven flagellar motor of a marine bacterium. *J. Bacteriol.* 179, 5104–5110. doi: 10.1128/jb.179.16.5104-5110.1997

Astumian, R. (2010). Thermodynamics and kinetics of molecular motors. *Biophys. J.* 98, 2401–2409. doi: 10.1016/j.bpj.2010.02.040

Baker, M. A. B., Hynson, R. M. G., Ganuelas, L. A., Mohammadi, N. S., Liew, C. W., Rey, A. A., et al. (2016). Domain-swap polymerization drives the self-assembly of the bacterial flagellar motor. *Nat. Struct. Mol. Biol.* 23, 197–203. doi: 10.1038/nsmb.3172

Berg, H. C. (2003). The rotatory motor of bacterial flagella. *Annu. Rev. Biochem.* 72, 19–54. doi: 10.1146/annurev.biochem.72.121801.161737

Blair, D. F., and Berg, H. C. (1988). Restoration of torque in defective flagellar motors. *Science* 242, 1678–1681. doi: 10.1126/science.2849208

Blair, D. F., and Berg, H. C. (1990). The mota protein of *E. coli* is a proton-conducting component of the flagellar motor. *Cell* 60, 439–449. doi: 10.1016/0092-8674(90)90595-6

Braun, T. F., Al-Mawsawi, L. Q., Kojima, S., and Blair, D. F. (2004). Arrangement of core membrane segments in the mota/motb proton-channel complex of escherichia coli. *Biochemistry* 43, 35–45. doi: 10.1021/bi035406d

Chen, X., and Berg, H. C. (2000). Torque-speed relationship of the flagellar rotary motor of escherichia coli. *Biophys. J.* 78, 1036–1041. doi: 10.1016/S0006-3495(00)76662-8

Chun, S. Y., and Parkinson, J. S. (1988). Bacterial motility: membrane topology of the escherichia coli motb protein. *Science* 239, 276–278. doi: 10.1126/science.2447650

Deme, J. C., Johnson, S., Vickery, O., Aron, A., Monkhouse, H., Griffiths, T., et al. (2020). Structures of the stator complex that drives rotation of the bacterial flagellum. *Nat. Microbiol.* 5, 1553–1564. doi: 10.1038/s41564-020-0788-8

Feynman, R. P., Leighton, R. B., and Sands, M. (1966). *The Feynman Lectures on Physics, Vol. I*. Reading, MA: Addison-Wesley.

Golubeva, N., Imparato, A., and Peliti, L. (2012). Efficiency of molecular machines with continuous phase space. *EPL* 97, 60005. doi: 10.1209/0295-5075/97/60005

Hirota, N., Kitada, M., and Imae, Y. (1981). Flagellar motors of alkalophilic bacillus are powered by an electrochemical potential gradient of na+. *FEBS Lett.* 132, 278–280. doi: 10.1016/0014-5793(81)81178-7

Jülicher, F., Ajdari, A., and Prost, J. (1997). Modeling molecular motors. *Rev. Mod. Phys.* 69, 1269–1282. doi: 10.1103/RevModPhys.69.1269

Kim, E. A., Price-Carter, M., Carlquist, W. C., and Blair, D. F. (2008). Membrane segment organization in the stator complex of the flagellar motor: Implications for proton flow and proton-induced conformational change? *Biochemistry* 47, 11332–11339. doi: 10.1021/bi801347a

Kojima, S., and Blair, D. F. (2004). Solubilization and purification of the mota/motb complex of escherichia coli. *Biochemistry* 43, 26–34. doi: 10.1021/bi035405l

Larsen, S. H., Adler, J., Gargus, J. J., and Hogg, R. W. (1974). Chemomechanical coupling without atp: the source of energy for motility and chemotaxis in bacteria. *Proc. Natl. Acad. Sci. U.S.A.* 71, 1239–1243. doi: 10.1073/pnas.71.4.1239

Lele, P. P., Hosu, B. G., and Berg, H. C. (2013). Dynamics of mechanosensing in the bacterial flagellar motor. *Proc. Natl. Acad. Sci. U.S.A.* 110, 11839–11844. doi: 10.1073/pnas.1305885110

Lo, C.-J., Sowa, Y., Pilizota, T., and Berry, R. M. (2013). Mechanism and kinetics of a sodium-driven bacterial flagellar motor. *Proc. Natl. Acad. Sci. U.S.A.* 110, E2544–2551. doi: 10.1073/pnas.1301664110

Mandadapu, K. K., Nirody, J. A., Berry, R. M., and Oster, G. (2015). Mechanics of torque generation in the bacterial flagellar motor. *Proc. Natl. Acad. Sci. U.S.A.* 112, E4381–4389. doi: 10.1073/pnas.1501734112

Meacci, G., Lan, G., and Tu, Y. (2011). Dynamics of the bacterial flagellar motor: the effects of stator compliance, back steps, temperature, and rotational asymmetry. *Biophys. J.* 100, 1986–1995. doi: 10.1016/j.bpj.2011.02.045

Meacci, G., and Tu, Y. (2009). Dynamics of the bacterial flagellar motor with multiple stators. *Proc. Natl. Acad. Sci. U.S.A.* 106, 3746–3751. doi: 10.1073/pnas.0809929106

Morimoto, Y. V., and Minamino, T. (2014). Structure and function of the bi-directional bacterial flagellar motor. *Biomolecules* 4, 217–234. doi: 10.3390/biom4010217

Nirody, J. A., Berry, R. M., and Oster, G. (2016). The limiting speed of the bacterial flagellar motor. *Biophys. J.* 111, 557–564. doi: 10.1016/j.bpj.2016.07.003

Nord, A. L., Gachon, E., Perez-Carrasco, R., Nirody, J. A., Barducci, A., Berry, R. M., et al. (2017). Catch bond drives stator mechanosensitivity in the bacterial flagellar motor. *Proc. Natl. Acad. Sci. U.S.A.* 114, 12952–12957. doi: 10.1073/pnas.1716002114

Parmeggiani, A., Julicher, F., Ajdari, A., and Prost, J. (1999). Energy transduction of isothermal ratchets: generic aspects and specific examples close to and far from equilibrium. *Phys. Rev. E* 60, 2127. doi: 10.1103/PhysRevE.60.2127

Parrondo, J., and de Cisneros, B. (2002). Energetics of brownian motors: a review. *Appl. Phys. A* 75, 179–191. doi: 10.1007/s003390201332

Parrondo, J. M., Blanco, J., Cao, F., and Brito, R. (1998). Efficiency of brownian motors. *Europhys. Lett.* 43, 248–254. doi: 10.1209/epl/i1998-00348-5

Roujeinikova, A. (2008). Crystal structure of the cell wall anchor domain of motb, a stator component of the bacterial flagellar motor: implications for peptidoglycan recognition. *Proc. Natl. Acad. Sci. U.S.A.* 105, 10348–10353. doi: 10.1073/pnas.0803039105

Santiveri, M., Roa-Eguiara, A., Kühne, C., Wadhwa, N., Hu, H., Berg, H. C., et al. (2020). Structure and function of stator units of the bacterial flagellar motor. *Cell* 183, 244–257. doi: 10.1016/j.cell.2020.08.016

Sato, K., and Homma, M. (2000). Functional reconstitution of the Na+-driven polar flagellar motor component of vibrio alginolyticus. *J. Biol. Chem.* 275, 5718–5722. doi: 10.1074/jbc.275.8.5718

Sowa, Y., Rowe, A. D., Leake, M. C., Yakushi, T., Homma, M., Ishijima, A., et al. (2005). Direct observation of steps in rotation of the bacterial flagellar motor. *Nature* 437, 916–919. doi: 10.1038/nature04003

Thomas, D. R., Francis, N. R., Xu, C., and DeRosier, D. J. (2006). The three-dimensional structure of the flagellar rotor from a clockwise-locked mutant of salmonella enterica serovar typhimurium. *J. bacteriol.* 188, 7039–7048. doi: 10.1128/JB.00552-06

Tipping, M. J., Delalez, N. J., Lim, R., Berry, R. M., and Armitage, J. P. (2013). Load-dependent assembly of the bacterial flagellar motor. *mBio.* 4, e00551-13. doi: 10.1128/mBio.00551-13

Tu, Y., and Cao, Y. (2018). Design principles and optimal performance for molecular motors under realistic constraints. *Phys. Rev. E* 97, 022403. doi: 10.1103/PhysRevE.97.022403

Wadhwa, N., Phillips, R., and Berg, H. C. (2019). Torque-dependent remodeling of the bacterial flagellar motor. *Proc. Natl. Acad. Sci. U.S.A.* 116, 11764–11769. doi: 10.1073/pnas.1904577116

Wadhwa, N., Tu, Y., and Berg, H. C. (2021). Mechanosensitive remodeling of the bacterial flagellar motor is independent of direction of rotation. *Proc. Natl. Acad. Sci. U.S.A.* 118, e2024608118. doi: 10.1073/pnas.2024608118

Xing, J., Bai, F., Berry, R., and Oster, G. (2006). Torque-speed relationship of the bacterial flagellar motor. *Proc. Natl. Acad. Sci. U.S.A.* 103, 1260–1265. doi: 10.1073/pnas.0507959103

Yorimitsu, T., Kojima, M., Yakushi, T., and Homma, M. (2004). Multimeric structure of the poma/pomb channel complex in the Na+-driven flagellar motor of vibrio alginolyticus. *J. Biochem.* 135, 43–51. doi: 10.1093/jb/mvh005

Yuan, J., and Berg, H. C. (2008). Resurrection of the flagellar rotary motor near zero load. *Proc. Natl. Acad. Sci. U.S.A.* 105, 1182–1185. doi: 10.1073/pnas.0711539105

Yuan, J., Fahrner, K. A., Turner, L., and Berg, H. C. (2010). Asymmetry in the clockwise and counterclockwise rotation of the bacterial flagellar motor. *Proc. Natl. Acad. Sci. U.S.A.* 107, 12846–12849. doi: 10.1073/pnas.1007333107

Conflict of Interest: YT is employed by IBM T. J. Watson Research Center.

The remaining authors declare that the research was conducted in the absence of any commercial or financial relationships that could be construed as a potential conflict of interest.

Publisher's Note: All claims expressed in this article are solely those of the authors and do not necessarily represent those of their affiliated organizations, or those of the publisher, the editors and the reviewers. Any product that may be evaluated in this article, or claim that may be made by its manufacturer, is not guaranteed or endorsed by the publisher.

Copyright © 2022 Cao, Li and Tu. This is an open-access article distributed under the terms of the Creative Commons Attribution License (CC BY). The use, distribution or reproduction in other forums is permitted, provided the original author(s) and the copyright owner(s) are credited and that the original publication in this journal is cited, in accordance with accepted academic practice. No use, distribution or reproduction is permitted which does not comply with these terms.

SUPPLEMENTARY MATERIAL

Piece-wise linear forms for V_R and $V_{1,2}$ are used. $V_{1,2}$: $k_BT = 4.11pN \times nm$, $V_{0S} = 10k_BT$, $\tau_S^+ = 2V_{0S}/\Delta\theta_S$, $\tau_S^- = 4V_{0S}/\Delta\theta_S$, where $\tau_S^{\pm}$ is the positive and negative torque on stator potential $V_{1,2}$, respectively, and the extended potential to the left of $P \rightarrow I$ has the same slope as τ_S^+. V_R: a symmetric form is used with $V_{0R} = 10k_BT$. Load on the stator $\xi_S = 0.01$(pN nm rad^{-1} s). The transition rate is $k_m = 10^5 s^{-1}$ for $\theta_S \geq 2\pi/5$ and 0 otherwise.

Equations 1 and 3 are solved with discrete time step $dt = 5 \times 10^{-6}$, and in the format of $\theta_{R,S}^{i+1} = \theta_{R,S}^{i} + dt(\cdots)/\xi_{R,S} + \sqrt{2k_BTdt/\xi_{R,S}}N(0,1)$, where $(\cdots)$ is the drift term, and $N(0,1)$ is a random number with standard normal distribution. During each step, the transition from low to high energy potential happens when $k_m(\theta)dt > U(0,1)$, where $U(0,1)$ is a random number with uniform distribution on (0,1).

frontiers | Frontiers in Microbiology

REVIEW
published: 30 May 2022
doi: 10.3389/fmicb.2022.911114

The Bacterial Flagellar Motor: Insights Into Torque Generation, Rotational Switching, and Mechanosensing

Shuaiqi Guo[1,2] *and Jun Liu*[1,2]*

[1]*Microbial Sciences Institute, Yale University, West Haven, CT, United States,* [2]*Department of Microbial Pathogenesis, Yale School of Medicine, New Haven, CT, United States*

The flagellar motor is a bidirectional rotary nanomachine used by many bacteria to sense and move through environments of varying complexity. The bidirectional rotation of the motor is governed by interactions between the inner membrane-associated stator units and the C-ring in the cytoplasm. In this review, we take a structural biology perspective to discuss the distinct conformations of the stator complex and the C-ring that regulate bacterial motility by switching rotational direction between the clockwise (CW) and counterclockwise (CCW) senses. We further contextualize recent *in situ* structural insights into the modulation of the stator units by accessory proteins, such as FliL, to generate full torque. The dynamic structural remodeling of the C-ring and stator complexes as well as their association with signaling and accessory molecules provide a mechanistic basis for how bacteria adjust motility to sense, move through, and survive in specific niches both outside and within host cells and tissues.

Keywords: rotary motor, molecular machine, rotational switching, torque generation, electron tomography

OPEN ACCESS

Edited by:
Zhaomin Yang,
Virginia Tech, United States

Reviewed by:
Navish Wadhwa,
Harvard University, United States
Daisuke Nakane,
The University of Electro-Communications, Japan

***Correspondence:**
Jun Liu
jliu@yale.edu

Specialty section:
This article was submitted to Microbial Physiology and Metabolism, a section of the journal Frontiers in Microbiology

Received: *02 April 2022*
Accepted: *06 May 2022*
Published: *30 May 2022*

Citation:
Guo S and Liu J (2022) The Bacterial Flagellar Motor: Insights Into Torque Generation, Rotational Switching, and Mechanosensing. Front. Microbiol. 13:911114. doi: 10.3389/fmicb.2022.911114

THE FLAGELLAR MOTOR PROPELS BACTERIAL MOTILITY IN VARIOUS ENVIRONMENTS

More than 300 years after Antonie van Leeuwenhoek discovered minuscule moving creatures using his homemade single-lensed microscope, we are now beginning to unravel the molecular details that govern bacterial motility. Bacteria have evolved distinct mechanisms to adapt to and navigate through environments of varying complexity (Wadhwa and Berg, 2021). The flagellum is a molecular nanomachine used by many bacteria for swimming motility (Berg and Anderson, 1973; Berg, 2003; Nakamura and Minamino, 2019) and for responding to environmental cues, such as chemotaxis to move to favorable locations, sense mechanical stimuli (i.e., surfaces), and initiate colonization of a niche by forming surface-attached communities known as biofilms (Lele et al., 2013; Belas, 2014; Hug et al., 2017; Nord et al., 2017; Gordon and Wang, 2019). In this review, we summarize recent findings that address longstanding fundamental questions about torque generation and rotational switching by the flagellar motor. In addition, we discuss new findings that demonstrate how periplasmic accessory proteins, such as the transmembrane protein FliL with previously unclear functions, enhance flagellar motor performance. Overall, this review aims to provide mechanistic insights into how diverse

bacteria sense environments and adjust motility *via* their rotary flagellar motors.

THE FLAGELLAR MOTOR IS A DYNAMIC SUPRAMOLECULAR NANOMACHINE

A canonical flagellum, such as that produced by *Escherichia coli*, is composed of an extracellular filament, a cell envelope-spanning rotary motor, and a flexible hook that joins the filament with the motor (Berg, 2003; Nakamura and Minamino, 2019; **Figure 1** middle panel). The flagellar motor, which powers the rotation of the filament, is composed of approximately 25 different proteins that include a central rotor surrounded by multiple inner membrane-associated stator complexes (**Figure 1** left panel). Within the rotor, the shaft-like rod engages with the MS-ring embedded in the inner membrane. The C-ring, also known as the switch complex, is a larger structure attached to the MS-ring from the cytoplasm (**Figure 1** middle and right panels), and its interaction with the stator complexes is critical for the rotation and directional switching of the flagellar motor. The L- and P-rings are fixed to the outer membrane and peptidoglycan, respectively, which act as bushings to support the rotor to transmit torque to the filament *via* the flexible hook in the extracellular environment (Yamaguchi et al., 2021).

Despite intensive research over the past several decades, there has been a lack of mechanistic understanding of how the stator complexes activate the rotation of the rotor. In the past few years, technical breakthroughs in imaging tools, particularly cryo-electron microscopy (cryo-EM) and cryo-electron tomography (cryo-ET), have revealed unprecedented structural details of the individual motor components that make up the torque generation device as well as insights into how they cohesively work together as a dynamic nanomachine.

STATOR COMPLEXES ARE THE TORQUE GENERATORS THAT DRIVE C-RING ROTATION

The rotation of the rotor requires the presence of one or more torque-generating stator units (Wadhwa and Berg, 2021). Each stator complex is composed of two proteins: MotA and

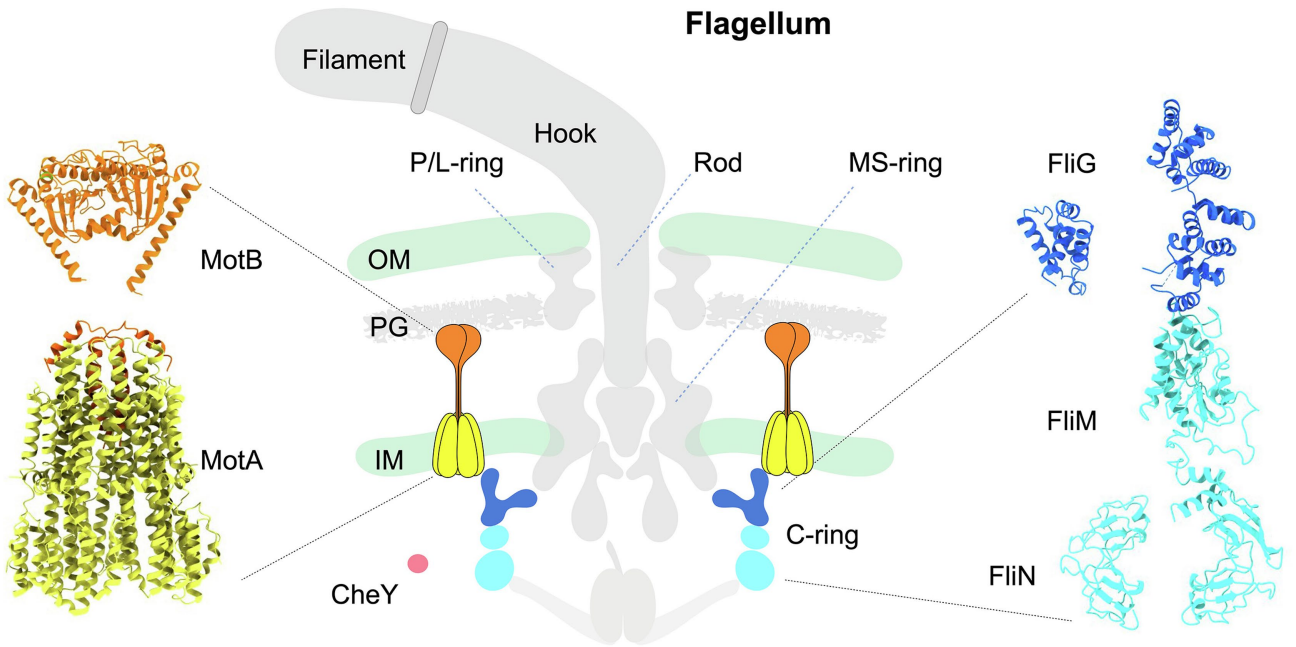


FIGURE 1 | Schematic diagram illustrating the architecture of the canonical flagellum from *Escherichia coli*. Middle panel: The flagellum is composed of the extracellular filament, a flexible hook, and a motor spanning the cell envelope. The motor is further composed of a central rotor surrounded by multiple stator units. The MS-ring is anchored in the inner membrane. Above the MS-ring are the P- and L-rings associated with the PG and outer membrane. Beneath the MS-ring is the C-ring (blue and cyan) in the cytoplasm. Each stator complex has two subunits: the pentameric cone-shaped MotA (yellow) is embedded in the inner membrane, and the extended MotB (orange) is anchored to the PG on one end, while its other end is inserted into MotA. CheY-like chemotactic signaling proteins are illustrated as a red sphere. OM: outer membrane. IM: inner membrane. PG: peptidoglycan. Left panel: Structure of a stator complex in its compact, inactive conformation. The structure of MotA (yellow) in complex with partial MotB (N-terminal helix, orange) from *Campylobacter jejuni* was resolved by cryo-EM single-particle analysis (PDB: 6ykm). The $MotB_{PGB}$ structure (C-terminal domain of MotB; orange) from *Salmonella enterica* was determined by X-ray crystallography (PDB: 2zvz). Right panel: Pseudoatomic structure of a C-ring subunit rotating in the CCW direction. The FliG subunit is colored blue, and the FliM/N subunits are colored cyan. The molecular models of individual C-ring proteins FliG, FliM, and FliN were generated with ITASSER using respective X-ray crystal structures as templates (PDBs of FliG domains: 4FHR, 3HJL; PDBs of FliM: 4FHR, 4YXB; PDB for FliN: 1YAB). Assembly of these proteins was guided by the C-ring architecture resolved by cryo-ET and subtomogram averaging.

MotB (Tang et al., 1996). MotA is an inner membrane-associated protein with a large cytoplasmic domain that directly interacts with the rotor (Dean et al., 1984; Blair and Berg, 1991; Zhou et al., 1995). MotB is primarily situated in the periplasmic space, except for its N-terminal domain, which acts as a plug inserted into the interior of MotA in the inner membrane (Kojima and Blair, 2001; Hosking et al., 2006; Roujeinikova, 2008; Kojima et al., 2009, 2018; Yonekura et al., 2011; Chang et al., 2021; Homma et al., 2021; Terashima et al., 2021; **Figure 1** left panel). At its C terminus, MotB contains a peptidoglycan-binding domain ($MotB_{PGB}$) critical for activation of the stator ion channel (**Figure 2A**). While the diffusive stator unit engages with the C-ring, MotB undergoes a large conformational change, whereby $MotB_{PGB}$ moves upward to anchor the peptidoglycan, thus unplugging the MotA ion channel (**Figures 2A,B**). As H^+ or Na^+ ions flow through the stator channel, electrochemical potential across the membrane powers rotation of the C-ring (Sharp et al., 1995a,b; Tang et al., 1996; Sato and Homma, 2000; Braun and Blair, 2001; Hosking et al., 2006; Takekawa et al., 2020). Because all components of the rotor rotate as a single unit, torque is transmitted from the C-ring to propel the rotation of the flagellar filament on the outside of the cell, thus achieving flagella-based motility.

Several high-resolution crystal structures of $MotB_{PGB}$ (called $PomB_{PGB}$ in *Vibrio alginolyticus*) are available, revealing that $MotB_{PGB}$ forms a dimer critical for binding peptidoglycan and activating the stator unit (Roujeinikova, 2008; Kojima et al., 2009; Zhu et al., 2014). Until recently, structural details of MotA as well as the N-terminal region of MotB were unknown. For almost a decade, functional mutagenesis and molecular dynamics studies of the stator complex relied on a low-resolution map (~20 Å) determined by single-particle analysis with negative staining (Yonekura et al., 2011). Although the structure revealed an overall compact shape of the stator complex in its inactive conformation, the ambiguity of the low-resolution map as well as biochemical results led to the interpretation that the stator complex is comprised of two MotB subunits in complex with four MotA subunits (Kojima and Blair, 2004; Yonekura et al., 2011; Takekawa et al., 2016). This lack of well-resolved structural details of the stator complex hampered efforts to elucidate the mechanism of torque generation.

In 2020, several near-atomic resolution structures of partial stator complexes were resolved independently by two groups using cryo-EM single-particle analysis (Deme et al., 2020; Santiveri et al., 2020; Hu et al., 2021; **Figures 1** left panel, **2A**). These structures revealed, unexpectedly, that MotA forms a pentameric (not tetrameric), hollow cone-shaped structure that peripherally surrounds a MotB dimer. With high-resolution

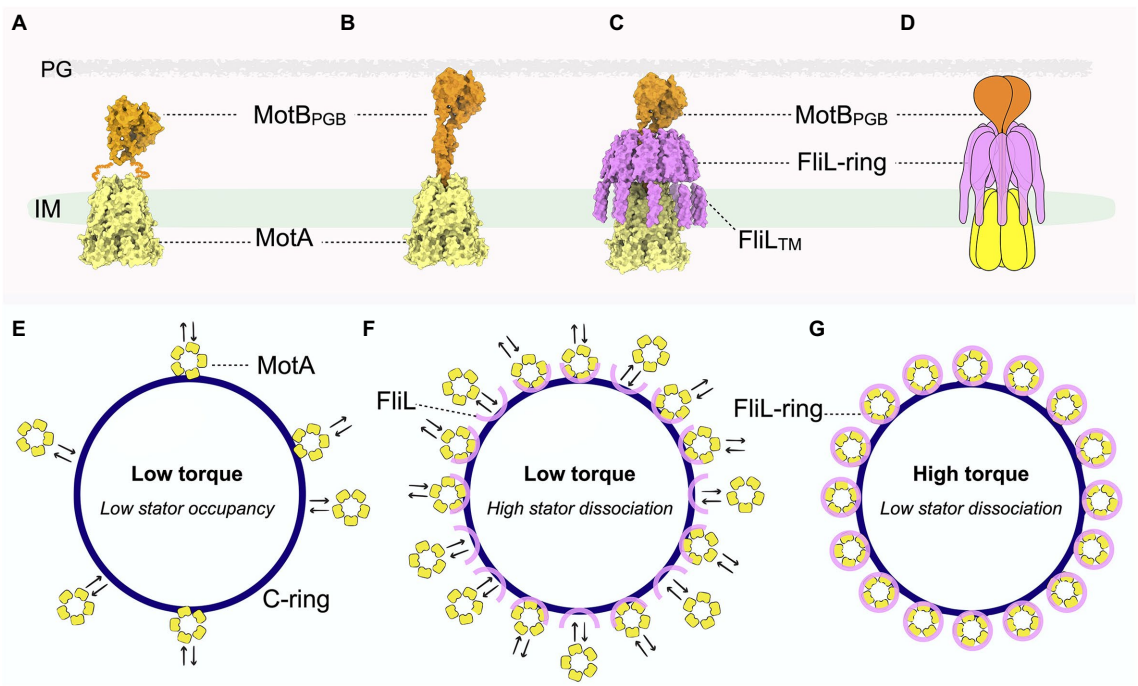


FIGURE 2 | Pseudoatomic structure of the stator-FliL-supramolecular complex and proposed model for modulating torque generation. **(A)** Side view of the stator structure in its compact, inactive conformation. MotA is colored yellow and MotB orange. The squiggly orange lines indicate the flexible MotB linkers with unknown structure. The cryo-ET map for the inner membrane is colored green. **(B)** Side view of the pseudoatomic model of the stator complex in its extended, active conformation. **(C)** Side view of the pseudoatomic model of the stator-FliL supramolecular complex. The FliL-ring is colored magenta. **(D)** Cartoon representation of the stator-FliL supramolecular complex. **(E)** In the absence of FliL, the stator units rapidly bind and unbind the rotor. Low stator occupancy results in low torque production by the motor. **(F)** Under low-load conditions, stator units bind and unbind the rotor rapidly before FliL can properly assemble into full rings to enclose the stator. **(G)** Under high-load conditions, FliL forms a full ring to surround and stabilize the stator complex in its active, extended conformation to maximize PMF to generate high torque.

structural features clearly resolved, these remarkable studies indicate that protons in the periplasm are shuttled throughout key charged residues between MotA and MotB to the cytoplasm. It was proposed that the flux of ions across the inner membrane triggers 36° stepwise rotations of the MotA pentamer relative to the immobile MotB dimer (Santiveri et al., 2020), providing a mechanistic model in which torque generation requires the gyration of the stator complexes.

Also in 2020, two cryo-ET studies revealed that the stator complexes and the C-ring interact intimately with each other *in situ* (Carroll et al., 2020; Chang et al., 2020, 2021). Viewed from the top, the multiple stator complexes that surround and interact with the C-ring resemble how cogwheels engage and drive the rotation of a conveyor belt (**Figures 2E–G**). Consistent with the described model based on near-atomic stator structures, it was further proposed that ion motive force triggers the stator units to rotate, which then drives rotation of the C-ring in a cogwheel-like manner. This elegant model, based on a combination of *in vitro* cryo-EM and *in situ* cryo-ET data, provides critical mechanistic insights that significantly shift how the field views the longstanding question: how do the stator complexes couple ion motive force to generate torque? The model suggests that the stator complexes act as an array of rotary motors themselves to drive rotation of the rotor.

THE ENIGMATIC FLAGELLAR PROTEIN FLIL LIKELY MODULATES STATOR FUNCTION IN MANY BACTERIA

With the prevailing view now shifted to regard stator complexes as rotary motors themselves, it is essential to understand how these dynamic structures are stabilized around the rotor. Though the cryo-EM single-particle studies described above aimed at solving high-resolution structures of the entire stator complex (Deme et al., 2020; Santiveri et al., 2020), MotB was only partially visible in these structures (**Figure 2A**). In the inactive stator complex, the N-terminal MotB dimeric domains are in *trans* conformation, wedged above MotA to plug the ion channel (**Figures 1** left panel, **2A**). By contrast, mutations that lock MotB in an active conformation revealed that the plug lifts to help open the MotA channel. However, the C-terminal $MotB_{PGB}$ as well as the flexible linker region that connects $MotB_{PGB}$ to the MotB N-terminal region were not visible in these cryo-EM structures of the stator complex (**Figure 2A**). Although this is likely due to a high degree of flexibility of MotB, it is also possible that the flexible linkers of MotB were proteolyzed during the purification steps. These observations raise key questions about the mechanism by which the stator complexes stabilize in their active and extend conformations *in situ*. How is the dynamic MotA stabilized and how do the flexible MotB linkers withstand the large torsional force during rapid rotation of MotA without compromising stator function and thus negatively impacting motility?

FliL is a 20-kDa inner membrane-associated protein produced by all flagellated bacteria (Jenal et al., 1994; Raha et al., 1994; Belas and Suvanasuthi, 2005; Attmannspacher et al., 2008). The *fliL* gene is often in the first position of the operon that also transcribes the C-ring genes *fliM* and *fliN*, or it is adjacent to stator genes *motA* and *motB* within the same operon (Partridge et al., 2015), suggesting that FliL interacts with the key components of the torque-generating complexes. However, since the discovery of FliL over 30 years ago, its role in torque generation has remained under debate. In fact, FliL has until now been described as a protein with "enigmatic" or "mysterious" functions, given its apparently different roles in diverse bacteria (Cusick et al., 2012).

An early study by Jenal et al. demonstrated in 1994 that FliL in *Caulobacter crescentus* is essential for flagellar rotation and bacterial motility (Jenal et al., 1994). By contrast, another study in the same year indicated that loss of FliL appeared to have a minimal effect on the swimming motility of *E. coli*, suggesting that it is not part of the flagellar nanomachinery (Raha et al., 1994). Consistent with the earlier results in *E. coli*, more recent studies have demonstrated that loss of FliL causes only small defects in swimming motility in *E. coli* and *Salmonella* (Attmannspacher et al., 2008; Partridge et al., 2015). Intriguingly, it has emerged that FliL is required for the swarming motility of *E. coli* and *Salmonella* when they encounter environments with higher external load, such as semi-solid agar media. Closer examination of Δ*fliL* mutants revealed that flagellar filaments more easily break off from bacteria under swarming conditions, suggesting a role for FliL in stabilizing the filament to the flagellar basal body. In addition, *E. coli* and *Salmonella* flagella without FliL appear to switch rotational direction less frequently. Although FliL had been implicated in the surface(mechano)-sensing pathway of the urinary tract pathogen *Proteus mirabilis* (Belas and Suvanasuthi, 2005), more recently, Chawla et al. (2017) demonstrated that FliL is not involved in mechanosensing by *E. coli*.

In the Lyme disease-causing spirochete *Borrelia burgdorferi*, loss of FliL causes noticeable defects in motility (Motaleb et al., 2011). Cryo-ET studies indicated that periplasmic flagellar filaments of Δ*fliL* mutant *B. burgdorferi* have abnormal orientations compared to those of wild type, with stator occupancy reduced to approximately 40% (Chang et al., 2019). As a mechanism to counter resistive forces in high-load environments, more stator complexes are typically recruited to the flagellar motor to produce higher torque (**Figures 2E–G**). A significantly lower stator occupancy in the absence of FliL again implicated this protein in torque generation *via* mediation of stator assembly to the rotor. Although cryo-ET and subtomogram averaging further indicated that FliL is localized between the rotor and stator complex in the periplasmic space, the resolution attained at the time of the study was insufficient to determine the exact location and structure of the protein (Motaleb et al., 2011).

Despite conflicting results for the functions of FliL in diverse species, it appears to help optimize motor performance to produce full torque in bacteria, especially in complex, viscous environments that require higher torque. This is reminiscent of the recently discovered gene *swrd*, which enhances the power of the flagellar motor under swarming conditions

(Hall et al., 2018). FliL may therefore play a dual role in stabilizing the structure of the flagella and in optimizing stator function, thus enhancing bacterial motility.

FLIL FORMS A RING STRUCTURE AROUND THE STATOR COMPLEX *IN SITU*

Like its function in flagellum-based motility, the structure of FliL had remained enigmatic until very recently. Takekawa et al. demonstrated in 2019 that the crystal structure of the C-terminal periplasmic region of FliL forms a 10-membered ring assembly within the crystal unit cell (Takekawa et al., 2019). Bioinformatic analyses showed that the FliL-ring is structurally homologous to proteins in the stomatin family, which form oligomeric complexes, including rings (Brand et al., 2012), to regulate ion channels. The size of the FliL-ring is compatible with that of the stator complex. In addition, mutational analyses suggest that FliL interacts directly with the stator units and rotor components, such as the MS-ring subunit FliF and C-ring protein FliG (Partridge et al., 2015; Zhu et al., 2015; Lin et al., 2018; Takekawa et al., 2019). Combining experimental evidence from diverse species, the authors proposed an intriguing model, whereby FliL forms a ring that surrounds the stator complex to regulate its ion channel activity, thus modulating torque (Takekawa et al., 2019; Zhou and Roujeinikova, 2021).

In two recent parallel studies (Guo et al., 2022; Tachiyama et al., 2022), cryo-ET and subtomogram averaging with focused refinement demonstrated that FliL indeed forms a ring-like structure around the stator units *in situ* in the flagellar motors of *B. burgdorferi* (**Figures 2B–D,F,G**) and of the stomach ulcer-causing human pathogen *Helicobacter pylori* (Tachiyama et al., 2022). Strikingly, in the absence of the stator complexes, FliL remains on the *B. burgdorferi* flagellar collar (a unique flagellar protein complex in spirochete motors) as a "half ring"-like structure (**Figure 2F**; Guo et al., 2022), indicating that the stator complex is required for proper assembly of FliL into a ring. This work further proposed that the FliL-half-ring "waits" for the stator complex to be recruited, then further multimerizes to encircle the stator complex and help stabilize its extended, active conformation, allowing ions to continuously flow through to generate torque.

To clarify the molecular basis for interactions between the FliL-ring and stator complex, structure prediction tools, such as the recently developed deep learning-based algorithm Alphafold2, were used to model the individual stator unit and FliL units within the *B. burgdorferi* motor (Jumper et al., 2021). These high-confidence molecular models are in excellent agreement with the ~20-Å cryo-ET map, revealing a pseudoatomic structure of the stator-FliL supramolecular complex (**Figures 2C,D**; Guo et al., 2022). The C-terminal periplasmic domain of FliL in *B. burgdorferi* (*Bb*FliL-ring) was modeled to oligomerize into a decameric ring in the same manner as that of the FliL-ring of *V. alginolyticus* resolved by X-ray crystallography. The *Bb*FliL-ring is situated above pentameric MotA embedded in the inner membrane (**Figure 2C**). While the flexible linker of MotB threads through the FliL-ring interior, $MotB_{PGB}$ binds peptidoglycan above the ring (**Figure 2C**). The *Bb*FliL-ring would thus stabilize the stator complex in an extended, active conformation, whereby individual stator ion channels stay open for continuous ion flux. As 16 stator-FliL-supramolecular complexes can assemble around the *B. burgdorferi* motor, the *Bb*FliL-rings would influence the collective ion flow through the motor to help maximize torque.

Furthermore, the *Bb*FliL-ring provides MotB with a second anchoring point below $MotB_{PGB}$ immobilized on the peptidoglycan (**Figure 2C**) and thus would help mitigate the torsional strain exerted on the MotB linker while MotA rotates rapidly beneath it. As the *Bb*FliL-ring in the periplasmic space encircles the MotA transmembrane ion channel, 10 N-terminal transmembrane domains of *Bb*FliL would form a fence-like structure to properly position the dynamic MotA within the inner membrane.

The *Bb*FliL-ring appears to act as a hub for extensive protein–protein interactions among motor components. Its ring exterior is embraced by various proteins that make up the spirochete-specific collar complex, while it interacts *via* multiple contact sites with the stator complex (Guo et al., 2022), providing an explanation for the low stator occupancy in the absence of FliL in *B. burgdorferi* (**Figure 2E**). FliL has relatively low shared sequence identity across species (Jenal et al., 1994; Takekawa et al., 2019). Though the oligomerization state and structure of FliL in other species are unknown, it is conceivable that FliL mediates an extensive network of protein-protein interactions that help stabilize the rotor and stator complexes. Further investigations are needed to test this hypothesis and to clarify the molecular basis for the observed phenotypes of bacteria, such as *E. coli* and *Salmonella*, which, in the absence of FliL, lose their flagellar filament under high-load conditions.

THE C-RING EXHIBITS REMARKABLE STRUCTURAL PLASTICITY DURING ROTATIONAL SWITCHING

All flagellated bacteria must be able to control their swimming direction *via* the bidirectional rotary motor to survive in various environments. The directional switch of the motor is regulated by the C-ring, which forms a cylindrical, wall-like structure at the base of the rotor in the cytoplasm (Liu et al., 2009; Wadhwa and Berg, 2021). Although protein components of each C-ring subunit are well conserved (Carroll and Liu, 2020), the oligomerization state and symmetry vary across species, resulting in significant differences in the size of C-rings and their capacity to generate torque. For instance, the canonical motor of *E. coli* has a relatively small C-ring with a ~34-fold symmetry. By contrast, the Lyme disease-causing spirochete bacterium *B. burgdorferi* has a significantly larger motor that powers the rotation of internal, periplasmic flagellar filaments (Tilly et al., 2008; Liu et al., 2009; Motaleb et al., 2011; Moon et al., 2016, 2018; Zhu et al., 2017; Chang et al., 2021), with

a C-ring that has a 46-fold symmetry (**Figures 3D–F**). Due to this larger C-ring, 16 stator units can assemble around the motor of *B. burgdorferi*, whereas only ~12 stator complexes fit around that of *E. coli*. The higher number of power-generating stator units enables *B. burgdorferi* to produce higher torque and may be a key mechanism evolved by spirochetes to "drill" through viscous, mucus-like host environments that have high resistive forces.

Each C-ring subunit has a "Y-shaped" structure comprising three proteins: FliG, FliM, and FliN (Brown et al., 2005, 2007; Paul et al., 2011; McDowell et al., 2016; **Figure 1** right panel). FliG comprises the upper arms of the "Y," which interacts with the stator complex at one end while contacting the MS-ring subunit *via* the opposite arm (**Figures 3A–C**; Lee et al., 2010; Vartanian et al., 2012). FliM and FliN (Brown et al., 2005; Ahn et al., 2013; Notti et al., 2015), localized below FliG, interact with various effectors to help bacteria adjust motility in response to changing environments (**Figures 1**, **3A–C**). These effectors include CheY and its analogs, which are well-characterized chemotactic signaling proteins that directly interact with the C-ring (Rossmann et al., 2020). One example discussed extensively in this review is the phosphorylated form of CheY, named CheY-P, which binds the C-ring to regulate flagellar rotational direction, thereby helping bacteria change swimming patterns in response to environmental signals. In the default state, the flagellar motor rotates in the counterclockwise (CCW) direction (**Figures 3B,E**). By contrast, the binding of CheY-P to FliM induces a conformational change in the C-ring subunit that causes the motor to switch and rotate in the clockwise (CW) direction (Dyer et al., 2009; Sarkar et al., 2010; **Figures 3C,F**). In addition, a recent study demonstrated that in *C. crescentus*, binding of the small molecule second messenger cyclic-di-GMP (c-di-GMP) induces conformational changes in a family of CheY-like proteins (Nesper et al., 2017). These CheY-like proteins in their c-di-GMP-bound states can then interact with the C-ring to regulate a range of motor activity, such as promoting the rapid attachment of motile bacteria to surfaces as seed for biofilm formation.

Although high-resolution structures of the individual C-ring subunits and CheY had been available, how multiple stator complexes interact with the intact C-ring *in situ* was unknown. The detailed mechanisms for motor rotation as well as directional switching had therefore remained unclear until recently. High-resolution structural biology tools, such as X-ray crystallography, nuclear magnetic resonance (NMR), and cryo-EM single-particle analysis, typically require proteins of interest to be isolated from their native environments within the organisms, an approach that often disrupts key protein–protein interactions necessary for the proper folding and assembly of complexes.

In recent years, cryo-ET, in conjunction with subtomogram averaging, has emerged as a leading technique to resolve the *in situ* structures of protein complexes within their native cellular context. In 2020, two parallel cryo-ET studies investigated the *in situ* structures of flagellar motors during rotation in both the CCW and CW directions in *V. alginolyticus* and *B. burgdorferi* (Carroll et al., 2020; Chang et al., 2020).

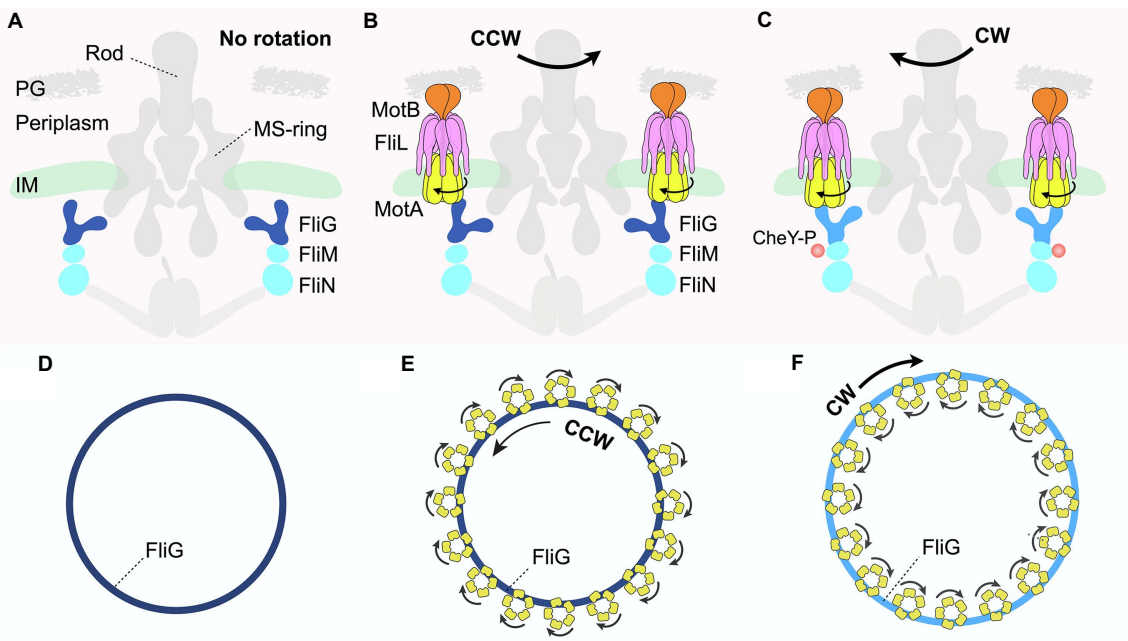


FIGURE 3 | Distinct interactions between the C-ring and stator complexes in response to environmental signals regulate rotational switching of the flagellum. **(A,D)** Schematic diagrams depicting side and top views, respectively, of the *Borrelia burgdorferi* periplasmic motor in the absence of the stator complex. **(B,E)** Schematic diagrams illustrating the side and top views of the *B. burgdorferi* motor rotating in the CCW direction. The transmembrane FliL is colored pink in **(B)**. **(C,F)** Schematic diagrams illustrating the side and top views of the *B. burgdorferi* motor rotating in the CW direction when bound to a chemotactic protein, CheY-P. The FliG subunit is colored light blue in contrast to dark blue when rotating in the CCW direction.

Subtomogram averaging with focused refinement revealed that the C-rings in the flagellar motors of both bacteria undergo major remodeling upon CheY-P binding to switch the rotational direction. In the absence of the stator complexes, the intact C-ring of *B. burgdorferi* has a diameter of ~60 nm (**Figures 3A,D**). Upon stator association, the C-ring contracts slightly, rotating in the CCW direction (**Figures 3B,E**). Strikingly, binding of CheY-P to the base of the cylindrical, wall-like C-ring exterior causes it to expand into a larger structure that switches to rotate in the CW direction (**Figures 3C,F**). Critically, these large conformational changes of the C-ring alter how it interacts with the multiple stator units assembled around it (**Figures 3B,C,E,F**), providing a key to understanding the molecular mechanisms of both rotation and directional switching of the motor.

When the C-rings rotate in a CCW direction, the FliG subunits interact with the inner rims of the cone-shaped stator MotA subunit in the cytoplasm (**Figures 3B,E**). By contrast, upon binding of CheY-P to the C-ring subunits FliMN, FliG tilts outward to interact with the outer rims of MotA, resulting in the expansion of the C-ring (**Figures 3C,F**). Viewed from the top, 16 stator units surround and use their inner rims to contact the C-ring in the wild-type flagellar motor of *B. burgdorferi* (**Figure 3E**). As proton motive force (PMF) drives the rotation of the stator complexes in a CW direction, the C-ring would rotate in the CCW direction (**Figure 3E**). By contrast, CheY-P binding causes the C-ring to expand and interact with the outer rims of the stator complexes (**Figures 3C,F**). As the stator complexes rotate in the CW direction, they would then drive the C-ring to switch and rotate in the CW direction.

NEW INSIGHTS INTO FLAGELLAR MOTORS AS SENSORS FOR VARIOUS ENVIRONMENTS

In addition to propelling motility, the flagellar motor is a key component in sensing mechanical and chemical stimuli, thus helping bacteria adapt to various environments (Hug et al., 2017; Hughes and Berg, 2017). As described above, the C-ring undergoes large structural remodeling upon receiving chemotactic signals from the environment to regulate motor activity, such as switching rotational direction. Mechanosensing by flagellar motors is intimately associated with the change in total ion flux through the stator units (Lele et al., 2013; Belas, 2014; Chawla et al., 2017; Nord et al., 2017; Laganenka et al., 2020; Antani et al., 2021; Wadhwa et al., 2021), which interact with the rotor in a dynamic fashion in response to external load changes (**Figures 2E–G**; Nirody et al., 2016; Nord et al., 2017; Sato et al., 2019; Nakamura et al., 2020). The stators units dissociate from the motor more quickly in low-load conditions than in high-load environments (Wadhwa et al., 2019). Given the observed intimate interactions between the FliL-ring and the active stator units, this raises the question: does FliL play a role in the regulation of mechanosensing by the flagellar motor?

The assembly of the FliL-half-ring into a full ring may provide insight into this key question. Cryo-ET studies with *B. burgdorferi* reveal that even before the diffusive stator complexes are recruited, FliL has oligomerized into a half ring (**Figure 2F**). Once a stator complex contacts the rotor, its interaction with the C-ring and the PMF would induce remodeling of the stator complex from an inactive, compact form to an extended, active conformation to enable passage of ions through the transmembrane channel. As loss of FliL does not abolish motor rotation in many bacteria, including *B. burgdorferi* (Raha et al., 1994; Attmannspacher et al., 2008; Motaleb et al., 2011; Partridge et al., 2015; Takekawa et al., 2019), activation of the stator complex is independent of the presence of FliL. Nevertheless, once the stator complex is activated near the FliL-half-ring, FliL would continue to oligomerize into a full ring to help stabilize the stator complex in the extended conformation (**Figures 2C,G**). Under low-load conditions, as the stator units have high dissociation rates, many of them might detach from the FliL-half-rings before the full rings can form. We speculate that it is possible that some of these stator units are in their inactive conformation to limit ion flux, and their compact shape cannot fit within the narrow constricting interior of the FliL-rings to help better stabilize them around the rotor. Indeed, we observed that the PMF-blocking D24N mutation of MotB not only causes the reduction of *B. burgdorferi* stator occupancy by over 50% (Chang et al., 2019) but also significantly disrupts the FliL-ring formation. By contrast, the stator complex dissociates more slowly in high-load conditions. The longer retention time of the stator complex should allow adequate time for the FliL-half-ring to oligomerize and further stabilize the unplugged, active stator complex within a full ring to help maximize ion flux and generate high torque (**Figures 2F,G**). We speculate that the FliL-ring-stator association is not permanent, given that excessive ion leakage is harmful to bacteria. However, the kinetics for stator dissociation would be slower as the FliL-ring needs to disassemble first before clearing a path for the stator complex to diffuse away from the motor (**Figures 2F,G**). In particular, the dissociation rate of the stator units might be even smaller for spirochete motors, whose collar structures further envelop the stator-FliL-supramolecular complexes (Chang et al., 2021; Guo et al., 2022). The presence of accessory scaffold proteins around the stator units may be an adaptation mechanism evolved by spirochetes to sustain motility in order to survive and cause disease in various complex host environments (Zhou and Roujeinikova, 2021).

Unique aspects of the stator-FliL-supramolecular complex may very well have enabled its discovery and structural elucidation because spirochetes have evolved an intricate, intrinsically high-duty-ratio motor stabilized by the collar. Similarly, although the *H. pylori* motor lacks a collar, it contains a different periplasmic scaffold, referred to as the "cage" (Qin et al., 2017; Zhou and Roujeinikova, 2021), which is also necessary for stabilizing stator-FliL-supramolecular complexes to generate full torque. This may be why the stator-FliL-supramolecular complex in *H. pylori* can be observed by cryo-ET, as in *B. burgdorferi*. For bacteria, such as *E. coli*, which naturally reside in less

complex liquid environments with lower external load, the stator units are likely too dynamic to be captured in association with the rotor. It would thus be intriguing to test whether stator-FliL-supramolecular complexes are sufficiently stable to be seen by cryo-ET and subtomogram averaging *in situ* when bacteria with these dynamic motors are subjected to higher external loads.

CONCLUSION AND FUTURE PERSPECTIVES

Remarkable technical breakthroughs in cryo-EM over the past few years have laid a solid foundation for answering fundamental questions: how do flagellar motors generate torque mediated by ion motive force, and what is the structural basis for switching rotational direction? Combining a wealth of knowledge of the biophysics, biochemistry, and genetics of rotary motors with an integrative structural biology approach that includes increasingly powerful machine learning-based structure prediction methods (e.g., Alphafold2) will elucidate the mechanisms of the flagellar motor in response to various environments. One exciting challenge is to directly visualize stator units in association with the rotor in diverse bacteria *via in situ* methods, such as cryo-ET. This approach stands not only to validate the proposed model to unravel the structure and function of FliL in various species but also to open opportunities to delve into species-specific flagellar features (e.g., the collar in spirochetes) required by bacteria to generate full torque across different environments. In addition, revealing the structural basis for how the C-ring and stator units remodel in response to binding by a range of chemotactic molecules, such as CheY analogs, will yield mechanistic explanations for the fascinating question of how bacteria use the flagellar motor to accelerate, brake, and initiate colonization in distinct niches in response to environmental cues. Such future studies hold great promise for researchers to design inhibitors of motility in pathogens and to engineer more powerful motors in synthetic microorganisms for wide-ranging clinical and biomedical applications.

AUTHOR CONTRIBUTIONS

SG and JL wrote the manuscript and approved it for publication.

FUNDING

SG and JL are supported by grants R01AI087946 and R01AI132818 from National Institute of Allergy and Infectious Diseases (NIAID) and National Institutes of Health (NIH). SG is also supported by a CIHR fellowship from the Canadian Institutes of Health Research.

ACKNOWLEDGMENTS

We thank Yunjie Chang for fruitful discussions and Jennifer Aronson for critical reading of the manuscript.

REFERENCES

Ahn, D. R., Song, H., Kim, J., Lee, S., and Park, S. (2013). The crystal structure of an activated *Thermotoga maritima* CheY with N-terminal region of FliM. *Int. J. Biol. Macromol.* 54, 76–83. doi: 10.1016/j.ijbiomac.2012.12.003

Antani, J. D., Gupta, R., Lee, A. H., Rhee, K. Y., Manson, M. D., and Lele, P. P. (2021). Mechanosensitive recruitment of stator units promotes binding of the response regulator CheY-P to the flagellar motor. *Nat. Commun.* 12:5442. doi: 10.1038/s41467-021-25774-2

Attmannspacher, U., Scharf, B. E., and Harshey, R. M. (2008). FliL is essential for swarming: motor rotation in absence of FliL fractures the flagellar rod in swarmer cells of *Salmonella enterica*. *Mol. Microbiol.* 68, 328–341. doi: 10.1111/j.1365-2958.2008.06170.x

Belas, R. (2014). Biofilms, flagella, and mechanosensing of surfaces by bacteria. *Trends Microbiol.* 22, 517–527. doi: 10.1016/j.tim.2014.05.002

Belas, R., and Suvanasuthi, R. (2005). The ability of *Proteus mirabilis* to sense surfaces and regulate virulence gene expression involves FliL, a flagellar basal body protein. *J. Bacteriol.* 187, 6789–6803. doi: 10.1128/JB.187.19.6789-6803.2005

Berg, H. C. (2003). The rotary motor of bacterial flagella. *Annu. Rev. Biochem.* 72, 19–54. doi: 10.1146/annurev.biochem.72.121801.161737

Berg, H. C., and Anderson, R. A. (1973). Bacteria swim by rotating their flagellar filaments. *Nature* 245, 380–382. doi: 10.1038/245380a0

Blair, D. F., and Berg, H. C. (1991). Mutations in the MotA protein of *Escherichia coli* reveal domains critical for proton conduction. *J. Mol. Biol.* 221, 1433–1442. doi: 10.1016/0022-2836(91)90943-Z

Brand, J., Smith, E. S., Schwefel, D., Lapatsina, L., Poole, K., Omerbasic, D., et al. (2012). A stomatin dimer modulates the activity of acid-sensing ion channels. *EMBO J.* 31, 3635–3646. doi: 10.1038/emboj.2012.203

Braun, T. F., and Blair, D. F. (2001). Targeted disulfide cross-linking of the MotB protein of *Escherichia coli*: evidence for two H(+) channels in the stator complex. *Biochemistry* 40, 13051–13059. doi: 10.1021/bi011264g

Brown, P. N., Mathews, M. A., Joss, L. A., Hill, C. P., and Blair, D. F. (2005). Crystal structure of the flagellar rotor protein FliN from *Thermotoga maritima*. *J. Bacteriol.* 187, 2890–2902. doi: 10.1128/JB.187.8.2890-2902.2005

Brown, P. N., Terrazas, M., Paul, K., and Blair, D. F. (2007). Mutational analysis of the flagellar protein FliG: sites of interaction with FliM and implications for organization of the switch complex. *J. Bacteriol.* 189, 305–312. doi: 10.1128/JB.01281-06

Carroll, B. L., and Liu, J. (2020). Structural conservation and adaptation of the bacterial flagella motor. *Biomol. Ther.* 10, 1–24. doi: 10.3390/biom10111492

Carroll, B. L., Nishikino, T., Guo, W., Zhu, S., Kojima, S., Homma, M., et al. (2020). The flagellar motor of *Vibrio alginolyticus* undergoes major structural remodeling during rotational switching. *eLife* 9:e61446. doi: 10.7554/eLife.61446

Chang, Y., Carroll, B. L., and Liu, J. (2021). Structural basis of bacterial flagellar motor rotation and switching. *Trends Microbiol.* 29, 1024–1033. doi: 10.1016/j.tim.2021.03.009

Chang, Y., Moon, K. H., Zhao, X., Norris, S. J., Motaleb, M. A., and Liu, J. (2019). Structural insights into flagellar stator-rotor interactions. *eLife* 8:e48979. doi: 10.7554/eLife.48979

Chang, Y., Xu, H., Motaleb, M. A., and Liu, J. (2021). Characterization of the flagellar collar reveals structural plasticity essential for spirochete motility. *mBio* 12:e02494-21. doi: 10.1128/mBio.02494-21

Chang, Y., Zhang, K., Carroll, B. L., Zhao, X., Charon, N. W., Norris, S. J., et al. (2020). Molecular mechanism for rotational switching of the bacterial flagellar motor. *Nat. Struct. Mol. Biol.* 27, 1041–1047. doi: 10.1038/s41594-020-0497-2

Chawla, R., Ford, K. M., and Lele, P. P. (2017). Torque, but not FliL, regulates mechanosensitive flagellar motor-function. *Sci. Rep.* 7:5565. doi: 10.1038/s41598-017-05521-8

Cusick, K., Lee, Y. Y., Youchak, B., and Belas, R. (2012). Perturbation of FliL interferes with *Proteus mirabilis* swarmer cell gene expression and differentiation. *J. Bacteriol.* 194, 437–447. doi: 10.1128/JB.05998-11

Dean, G. E., Macnab, R. M., Stader, J., Matsumura, P., and Burks, C. (1984). Gene sequence and predicted amino acid sequence of the motA protein, a membrane-associated protein required for flagellar rotation in *Escherichia coli*. *J. Bacteriol.* 159, 991–999. doi: 10.1128/jb.159.3.991-999.1984

Deme, J. C., Johnson, S., Vickery, O., Aron, A., Monkhouse, H., Griffiths, T., et al. (2020). Structures of the stator complex that drives rotation of the bacterial flagellum. *Nat. Microbiol.* 5, 1553–1564. doi: 10.1038/s41564-020-0788-8

Dyer, C. M., Vartanian, A. S., Zhou, H., and Dahlquist, F. W. (2009). A molecular mechanism of bacterial flagellar motor switching. *J. Mol. Biol.* 388, 71–84. doi: 10.1016/j.jmb.2009.02.004

Gordon, V. D., and Wang, L. (2019). Bacterial mechanosensing: the force will be with you, always. *J. Cell Sci.* 132, 1–9. doi: 10.1242/jcs.227694

Guo, S., Xu, H., Chang, Y., Motaleb, M. A., and Liu, J. (2022). FliL ring enhances the function of periplasmic flagella. *Proc. Natl. Acad. Sci. U. S. A.* 119:e2117245119. doi: 10.1073/pnas.2117245119

Hall, A. N., Subramanian, S., Oshiro, R. T., Canzoneri, A. K., and Kearns, D. B. (2018). SwrD (YlzI) promotes swarming in *Bacillus subtilis* by increasing power to flagellar motors. *J. Bacteriol.* 200, 1–16. doi: 10.1128/JB.00529-17

Homma, M., Terashima, H., Koiwa, H., and Kojima, S. (2021). Putative spanner function of the vibrio PomB plug region in the stator rotation model for flagellar motor. *J. Bacteriol.* 203:e0015921. doi: 10.1128/JB.00159-21

Hosking, E. R., Vogt, C., Bakker, E. P., and Manson, M. D. (2006). The *Escherichia coli* MotAB proton channel unplugged. *J. Mol. Biol.* 364, 921–937. doi: 10.1016/j.jmb.2006.09.035

Hu, H., Santiveri, M., Wadhwa, N., Berg, H. C., Erhardt, M., and Taylor, N. M. I. (2021). Structural basis of torque generation in the bi-directional bacterial flagellar motor. *Trends Biochem. Sci.* 47, 160–172. doi: 10.1016/j.tibs.2021.06.005

Hug, I., Deshpande, S., Sprecher, K. S., Pfohl, T., and Jenal, U. (2017). Second messenger-mediated tactile response by a bacterial rotary motor. *Science* 358, 531–534. doi: 10.1126/science.aan5353

Hughes, K. T., and Berg, H. C. (2017). The bacterium has landed. *Science* 358, 446–447. doi: 10.1126/science.aaq0143

Jenal, U., White, J., and Shapiro, L. (1994). Caulobacter flagellar function, but not assembly, requires FliL, a non-polarly localized membrane protein present in all cell types. *J. Mol. Biol.* 243, 227–244. doi: 10.1006/jmbi.1994.1650

Jumper, J., Evans, R., Pritzel, A., Green, T., Figurnov, M., Ronneberger, O., et al. (2021). Highly accurate protein structure prediction with AlphaFold. *Nature* 596, 583–589. doi: 10.1038/s41586-021-03819-2

Kojima, S., and Blair, D. F. (2001). Conformational change in the stator of the bacterial flagellar motor. *Biochemistry* 40, 13041–13050. doi: 10.1021/bi011263o

Kojima, S., and Blair, D. F. (2004). Solubilization and purification of the MotA/MotB complex of *Escherichia coli*. *Biochemistry* 43, 26–34. doi: 10.1021/bi035405l

Kojima, S., Imada, K., Sakuma, M., Sudo, Y., Kojima, C., Minamino, T., et al. (2009). Stator assembly and activation mechanism of the flagellar motor by the periplasmic region of MotB. *Mol. Microbiol.* 73, 710–718. doi: 10.1111/j.1365-2958.2009.06802.x

Kojima, S., Takao, M., Almira, G., Kawahara, I., Sakuma, M., Homma, M., et al. (2018). The helix rearrangement in the periplasmic domain of the flagellar stator B subunit activates peptidoglycan binding and ion influx. *Structure* 26, 590.e5–598.e5. doi: 10.1016/j.str.2018.02.016

Laganenka, L., Lopez, M. E., Colin, R., and Sourjik, V. (2020). Flagellum-mediated Mechanosensing and RflP control motility state of pathogenic *Escherichia coli*. *mBio* 11:e02269-19. doi: 10.1128/mBio.02269-19

Lee, L. K., Ginsburg, M. A., Crovace, C., Donohoe, M., and Stock, D. (2010). Structure of the torque ring of the flagellar motor and the molecular basis for rotational switching. *Nature* 466, 996–1000. doi: 10.1038/nature09300

Lele, P. P., Hosu, B. G., and Berg, H. C. (2013). Dynamics of mechanosensing in the bacterial flagellar motor. *Proc. Natl. Acad. Sci. U. S. A.* 110, 11839–11844. doi: 10.1073/pnas.1305885110

Lin, T. S., Zhu, S., Kojima, S., Homma, M., and Lo, C. J. (2018). FliL association with flagellar stator in the sodium-driven vibrio motor characterized by the fluorescent microscopy. *Sci. Rep.* 8:11172. doi: 10.1038/s41598-018-29447-x

Liu, J., Lin, T., Botkin, D. J., McCrum, E., Winkler, H., and Norris, S. J. (2009). Intact flagellar motor of *Borrelia burgdorferi* revealed by cryo-electron tomography: evidence for stator ring curvature and rotor/C-ring assembly flexion. *J. Bacteriol.* 191, 5026–5036. doi: 10.1128/JB.00340-09

McDowell, M. A., Marcoux, J., McVicker, G., Johnson, S., Fong, Y. H., Stevens, R., et al. (2016). Characterisation of shigella Spa33 and thermotoga FliM/N reveals a new model for C-ring assembly in T3SS. *Mol. Microbiol.* 99, 749–766. doi: 10.1111/mmi.13267

Moon, K. H., Zhao, X., Manne, A., Wang, J., Yu, Z., Liu, J., et al. (2016). Spirochetes flagellar collar protein FlbB has astounding effects in orientation of periplasmic flagella, bacterial shape, motility, and assembly of motors in *Borrelia burgdorferi*. *Mol. Microbiol.* 102, 336–348. doi: 10.1111/mmi.13463

Moon, K. H., Zhao, X., Xu, H., Liu, J., and Motaleb, M. A. (2018). A tetratricopeptide repeat domain protein has profound effects on assembly of periplasmic flagella, morphology and motility of the Lyme disease spirochete *Borrelia burgdorferi*. *Mol. Microbiol.* 110, 634–647. doi: 10.1111/mmi.14121

Motaleb, M. A., Pitzer, J. E., Sultan, S. Z., and Liu, J. (2011). A novel gene inactivation system reveals altered periplasmic flagellar orientation in a *Borrelia burgdorferi* fliL mutant. *J. Bacteriol.* 193, 3324–3331. doi: 10.1128/JB.00202-11

Nakamura, S., Hanaizumi, Y., Morimoto, Y. V., Inoue, Y., Erhardt, M., Minamino, T., et al. (2020). Direct observation of speed fluctuations of flagellar motor rotation at extremely low load close to zero. *Mol. Microbiol.* 113, 755–765. doi: 10.1111/mmi.14440

Nakamura, S., and Minamino, T. (2019). Flagella-driven motility of bacteria. *Biomolecules* 9:279. doi: 10.3390/biom9070279

Nesper, J., Hug, I., Kato, S., Hee, C. S., Habazettl, J. M., Manfredi, P., et al. (2017). Cyclic di-GMP differentially tunes a bacterial flagellar motor through a novel class of CheY-like regulators. *eLife* 6:e28842. doi: 10.7554/eLife.28842

Nirody, J. A., Berry, R. M., and Oster, G. (2016). The limiting speed of the bacterial flagellar motor. *Biophys. J.* 111, 557–564. doi: 10.1016/j.bpj.2016.07.003

Nord, A. L., Gachon, E., Perez-Carrasco, R., Nirody, J. A., Barducci, A., Berry, R. M., et al. (2017). Catch bond drives stator mechanosensitivity in the bacterial flagellar motor. *Proc. Natl. Acad. Sci. U. S. A.* 114, 12952–12957. doi: 10.1073/pnas.1716002114

Nord, A. L., Sowa, Y., Steel, B. C., Lo, C. J., and Berry, R. M. (2017). Speed of the bacterial flagellar motor near zero load depends on the number of stator units. *Proc. Natl. Acad. Sci. U. S. A.* 114, 11603–11608. doi: 10.1073/pnas.1708054114

Notti, R. Q., Bhattacharya, S., Lilic, M., and Stebbins, C. E. (2015). A common assembly module in injectisome and flagellar type III secretion sorting platforms. *Nat. Commun.* 6:7125. doi: 10.1038/ncomms8125

Partridge, J. D., Nieto, V., and Harshey, R. M. (2015). A new player at the flagellar motor: FliL controls both motor output and bias. *mBio* 6:e02367-14. doi: 10.1128/mBio.02367-14

Paul, K., Gonzalez-Bonet, G., Bilwes, A. M., Crane, B. R., and Blair, D. (2011). Architecture of the flagellar rotor. *EMBO J.* 30, 2962–2971. doi: 10.1038/emboj.2011.188

Qin, Z., Lin, W. T., Zhu, S., Franco, A. T., and Liu, J. (2017). Imaging the motility and chemotaxis machineries in helicobacter pylori by cryo-electron tomography. *J. Bacteriol.* 199:e00695-16. doi: 10.1128/JB.00695-16

Raha, M., Sockett, H., and Macnab, R. M. (1994). Characterization of the fliL gene in the flagellar regulon of *Escherichia coli* and *Salmonella typhimurium*. *J. Bacteriol.* 176, 2308–2311. doi: 10.1128/jb.176.8.2308-2311.1994

Rossmann, F. M., Hug, I., Sangermani, M., Jenal, U., and Beeby, M. (2020). In situ structure of the *Caulobacter crescentus* flagellar motor and visualization of binding of a CheY-homolog. *Mol. Microbiol.* 114, 443–453. doi: 10.1111/mmi.14525

Roujeinikova, A. (2008). Crystal structure of the cell wall anchor domain of MotB, a stator component of the bacterial flagellar motor: implications for peptidoglycan recognition. *Proc. Natl. Acad. Sci. U. S. A.* 105, 10348–10353. doi: 10.1073/pnas.0803039105

Santiveri, M., Roa-Eguiara, A., Kuhne, C., Wadhwa, N., Hu, H., Berg, H. C., et al. (2020). Structure and function of stator units of the bacterial flagellar motor. *Cell* 183, 244.e16–257.e16. doi: 10.1016/j.cell.2020.08.016

Sarkar, M. K., Paul, K., and Blair, D. (2010). Chemotaxis signaling protein CheY binds to the rotor protein FliN to control the direction of flagellar rotation in *Escherichia coli*. *Proc. Natl. Acad. Sci. U. S. A.* 107, 9370–9375. doi: 10.1073/pnas.1000935107

Sato, K., and Homma, M. (2000). Multimeric structure of PomA, a component of the Na+−driven polar flagellar motor of *Vibrio alginolyticus*. *J. Biol. Chem.* 275, 20223–20228. doi: 10.1074/jbc.M002236200

Sato, K., Nakamura, S., Kudo, S., and Toyabe, S. (2019). Evaluation of the duty ratio of the bacterial flagellar motor by dynamic load control. *Biophys. J.* 116, 1952–1959. doi: 10.1016/j.bpj.2019.04.004

Sharp, L. L., Zhou, J., and Blair, D. F. (1995a). Features of MotA proton channel structure revealed by tryptophan-scanning mutagenesis. *Proc. Natl. Acad. Sci. U. S. A.* 92, 7946–7950. doi: 10.1073/pnas.92.17.7946

Sharp, L. L., Zhou, J., and Blair, D. F. (1995b). Tryptophan-scanning mutagenesis of MotB, an integral membrane protein essential for flagellar rotation in *Escherichia coli*. *Biochemistry* 34, 9166–9171. doi: 10.1021/bi00028a028

Tachiyama, S., Chan, K. L., Liu, X., Hathroubi, S., Peterson, B., Khan, M. F., et al. (2022). The flagellar motor protein FliL forms a scaffold of circumferentially positioned rings required for stator activation. *Proc. Natl. Acad. Sci. U. S. A.* 119, 1–9. doi: 10.1073/pnas.2118401119

Takekawa, N., Imada, K., and Homma, M. (2020). Structure and energy-conversion mechanism of the bacterial Na(+)-driven flagellar motor. *Trends Microbiol.* 28, 719–731. doi: 10.1016/j.tim.2020.03.010

Takekawa, N., Isumi, M., Terashima, H., Zhu, S., Nishino, Y., Sakuma, M., et al. (2019). Structure of vibrio FliL, a new stomatin-like protein that assists the bacterial flagellar motor function. *mBio* 10, 1–13. doi: 10.1128/mBio.00292-19

Takekawa, N., Terahara, N., Kato, T., Gohara, M., Mayanagi, K., Hijikata, A., et al. (2016). The tetrameric MotA complex as the core of the flagellar motor stator from hyperthermophilic bacterium. *Sci. Rep.* 6:31526. doi: 10.1038/srep31526

Tang, H., Braun, T. F., and Blair, D. F. (1996). Motility protein complexes in the bacterial flagellar motor. *J. Mol. Biol.* 261, 209–221. doi: 10.1006/jmbi.1996.0453

Terashima, H., Kojima, S., and Homma, M. (2021). Site-directed crosslinking identifies the stator-rotor interaction surfaces in a hybrid bacterial flagellar motor. *J. Bacteriol.* 203, 1–11. doi: 10.1128/JB.00016-21

Tilly, K., Rosa, P. A., and Stewart, P. E. (2008). Biology of infection with *Borrelia burgdorferi*. *Infect. Dis. Clin. N. Am.* 22, 217–234. doi: 10.1016/j.idc.2007.12.013

Vartanian, A. S., Paz, A., Fortgang, E. A., Abramson, J., and Dahlquist, F. W. (2012). Structure of flagellar motor proteins in complex allows for insights into motor structure and switching. *J. Biol. Chem.* 287, 35779–35783. doi: 10.1074/jbc.C112.378380

Wadhwa, N., and Berg, H. C. (2021). Bacterial motility: machinery and mechanisms. *Nat. Rev. Microbiol.* 20, 1–6. doi: 10.1074/jbc.C112.378380

Wadhwa, N., Phillips, R., and Berg, H. C. (2019). Torque-dependent remodeling of the bacterial flagellar motor. *Proc. Natl. Acad. Sci. U. S. A.* 116, 11764–11769. doi: 10.1073/pnas.1904577116

Wadhwa, N., Tu, Y., and Berg, H. C. (2021). Mechanosensitive remodeling of the bacterial flagellar motor is independent of direction of rotation. *Proc. Natl. Acad. Sci. U. S. A.* 118. doi: 10.1073/pnas.2024608118

Yamaguchi, T., Makino, F., Miyata, T., Minamino, T., Kato, T., and Namba, K. (2021). Structure of the molecular bushing of the bacterial flagellar motor. *Nat. Commun.* 12:4469. doi: 10.1038/s41467-021-24715-3

Yonekura, K., Maki-Yonekura, S., and Homma, M. (2011). Structure of the flagellar motor protein complex PomAB: implications for the torque-generating conformation. *J. Bacteriol.* 193, 3863–3870. doi: 10.1128/JB.05021-11

Zhou, J., Fazzio, R. T., and Blair, D. F. (1995). Membrane topology of the MotA protein of *Escherichia coli*. *J. Mol. Biol.* 251, 237–242. doi: 10.1006/jmbi.1995.0431

Zhou, X., and Roujeinikova, A. (2021). The structure, composition, and role of periplasmic stator scaffolds in polar bacterial flagellar motors. *Front. Microbiol.* 12:639490. doi: 10.3389/fmicb.2021.639490

Zhu, S., Kumar, A., Kojima, S., and Homma, M. (2015). FliL associates with the stator to support torque generation of the sodium-driven polar flagellar motor of *Vibrio*. *Mol. Microbiol.* 98, 101–110. doi: 10.1111/mmi.13103

Zhu, S., Qin, Z., Wang, J., Morado, D. R., and Liu, J. (2017). In situ structural analysis of the spirochetal flagellar motor by cryo-electron tomography. *Methods Mol. Biol.* 1593, 229–242. doi: 10.1007/978-1-4939-6927-2_18

Zhu, S., Takao, M., Li, N., Sakuma, M., Nishino, Y., Homma, M., et al. (2014). Conformational change in the periplamic region of the flagellar stator coupled with the assembly around the rotor. *Proc. Natl. Acad. Sci. U. S. A.* 111, 13523–13528. doi: 10.1073/pnas.1324201111

Conflict of Interest: The authors declare that the research was conducted in the absence of any commercial or financial relationships that could be construed as a potential conflict of interest.

Publisher's Note: All claims expressed in this article are solely those of the authors and do not necessarily represent those of their affiliated organizations, or those of the publisher, the editors and the reviewers. Any product that may be evaluated in this article, or claim that may be made by its manufacturer, is not guaranteed or endorsed by the publisher.

Copyright © 2022 Guo and Liu. This is an open-access article distributed under the terms of the Creative Commons Attribution License (CC BY). The use, distribution or reproduction in other forums is permitted, provided the original author(s) and the copyright owner(s) are credited and that the original publication in this journal is cited, in accordance with accepted academic practice. No use, distribution or reproduction is permitted which does not comply with these terms.

frontiers | Frontiers in Microbiology

REVIEW
published: 01 June 2022
doi: 10.3389/fmicb.2022.893524

Swimming Using a Unidirectionally Rotating, Single Stopping Flagellum in the Alpha Proteobacterium *Rhodobacter sphaeroides*

*Judith P. Armitage**

Department of Biochemistry, University of Oxford, Oxford, United Kingdom

Rhodobacter sphaeroides has 2 flagellar operons, one, Fla2, encoding a polar tuft that is not expressed under laboratory conditions and a second, Fla1, encoding a single randomly positioned flagellum. This single flagellum, unlike the flagella of other species studied, only rotates in a counterclockwise direction. Long periods of smooth swimming are punctuated by short stops, caused by the binding of one of 3 competing CheY homologs to the motor. During a stop, the motor is locked, not freely rotating, and the flagellar filament changes conformation to a short wavelength, large amplitude structure, reforming into a driving helix when the motor restarts. The cell has been reoriented during the brief stop and the next period of smooth swimming is a new direction.

Keywords: *Rhodobacter*, motor, swimming, chemotaxis, model

OPEN ACCESS

Edited by:
Jun Liu,
Yale University, United States

Reviewed by:
Michio Homma,
Nagoya University, Japan
Timothy Randall Hoover,
University of Georgia, United States

***Correspondence:**
Judith P. Armitage
Judith.armitage@bioch.ox.ac.uk

Specialty section:
This article was submitted to Microbial Physiology and Metabolism, a section of the journal Frontiers in Microbiology

Received: *10 March 2022*
Accepted: *27 April 2022*
Published: *01 June 2022*

Citation:
Armitage JP (2022) Swimming Using a Unidirectionally Rotating, Single Stopping Flagellum in the Alpha Proteobacterium Rhodobacter sphaeroides. Front. Microbiol. 13:893524. doi: 10.3389/fmicb.2022.893524

INTRODUCTION

One of the distinguishing features used to identify bacterial species in the days before genomics was the number and position of their flagella and pattern of swimming. When we first started investigating the behavior of the small coccobacillus-shaped purple non-sulfur alphaproteobacterium *Rhodobacter sphaeroides* (*R. sphaeroides*), it was clear that it only had one flagellum, but unlike the better studied monoflagellate species, it did not change direction by briefly reversing its swimming direction, but rather it occasionally just stopped swimming. The stopped cell is buffeted about by the local environment, so that when the cell starts to swim again it is usually pointing in a new direction.

It had been shown that bacterial motility is driven by the electrochemical ion gradient across the bacterial membrane, with either the proton (pmf) or the sodium motive force driving rotation of the flagellar motor depending on the species (Manson et al., 1977). Howard Berg had also shown that under high external load, the speed of the motor is linearly related to the size of the pmf, while at low loads, the motor reaches maximum speed at low pmf values (Meister and Berg, 1987). The pmf in most bacterial species tends to be maintained at a high level, even under adverse metabolic conditions to ensure bacterial survival. These experiments suggest that under adverse conditions,

motility is one of the last physiological activities to stop, indeed probably running even after the ATP synthase has stopped or reversed activity to keep a residual pmf across the membrane. The *R. sphaeroides* flagellar motor is driven by the pmf. In early experiments, we reduced the pmf of photosynthetically growing cells using ionophores and found the bacteria stopped swimming in the dark, but regained motility when illuminated by actinic light. Intriguingly, it could take minutes for the cells to start swimming after the light was switched back on, leading us to speculate that the motor structure might disassemble when the pmf driving force was removed, something we only discovered to be true 20 years later (Armitage et al., 1985). The loss of the pmf led to a loss of swimming, so we needed to be sure that the motor really stops when the pmf is high. Two experiments confirmed that the motor really stops while maintaining a pmf, while another experiment suggested that loss of the pmf might alter the motor stability.

Back in the early 1980s, it was not possible to see a bacterial flagellum on a living, swimming bacterium because the diameter of the filament is below the resolution of a standard light microscope. However, Bob Macnab at Yale, building on some early experiments carried out by Pijper in South Africa (Pijper, 1955), had built a dark-field light microscope that uses extremely bright light. Light scattering allowed the filament to be seen on living, swimming cells, although only at a distance from the cell body as scattering of very high-intensity light made the cell body appears as a superbright ball. Using a modified version of this microscope, we saw the *R. sphaeroides* single flagellar filament rotate and push the bacterium forward and occasionally abruptly stop (Armitage and Macnab, 1987). When the bacterium stopped the functional helical filament collapsed from the distal end of the filament, coiling into a short wavelength, large amplitude form against the cell body (**Figure 1B**). After a brief stopped period, the smaller amplitude, longer wavelength conformation of the filament reformed from the cell body outward to the filament tip when the cell started to swim again, usually in a new direction. This suggested that motor rotation is needed to force the flagellar filament flagellin subunits into a conformation that forms a waveform that allows swimming. Early study examining the structure of the flagellin subunits in a filament suggests that they can form 12 filament waveforms dependent on the forces on the filament, with only a limited number able to push a cell through it environment. The experiments visualizing the *R. sphaeroides* flagellum suggested a waveform allowing swimming only occurs when the motor rotates (Kamiya et al., 1982). Interestingly, in both the negative-stained electron micrographs and in the high light dark-field experiments, there were large numbers of free circular structures, which we now realize were detached filaments collapsed into the relaxed waveform (**Figure 1A**). Again, this suggests that only the torque force caused by motor rotation can alter the interaction of the flagellin monomers to drive formation of a functional waveform.

The second experiment confirming the *R. sphaeroides* stop-start motor used antiflagellin antibody to tether cells to a glass slide by their flagella (Poole et al., 1988). Experiments with *Escherichia coli* (*E. coli*) had used such experiments to confirm that bacteria use a rotary motor to drive flagellar rotation (Silverman and Simon, 1974). Tethering *E. coli* by short filaments or hooks resulted in cell bodies rotating smoothly in one direction and occasionally switching the direction of rotation, reflecting the smooth swimming that occurs with counterclockwise rotation and a direction changing tumble that occurs with a brief period of clockwise rotation. The *R. sphaeroides* single motor, however, only rotates in one direction, counterclockwise, stopping occasionally, and then resuming counterclockwise rotation. Occasional cells have been seen to rotate clockwise, but no cell has ever been seen to switch its direction of rotation (Packer and Armitage, 1993).

GENOMICS AND STRUCTURE

It now seems that *R. sphaeroides* flagella have a complex evolutionary history. In the laboratory, *R. sphaeroides* has only been seen to swim using a single, unidirectionally rotating flagellum; genome sequencing has revealed that it has 2 complete flagellar regulons, Fla1 and Fla2 (Mackenzie et al., 2001; Poggio et al., 2007; Porter et al., 2011b). The laboratory of George Dreyfus has been able to express the second set of flagella genes in mutants unable to express the Fla1 unidirectional flagellum (**Figure 2A**). These mutants express a polar tuft of filaments, similar to polar tufts seem on other alpha proteobacteria (**Figure 2B**). The expression of the Fla2 regulon is dependent on the Ctr regulatory system known to control lifestyle switching and motility in many alpha proteobacteria (de la Mora et al., 2015; Vega-Baray et al., 2015; Poncin et al., 2018). Genome sequencing also revealed that *R. sphaeroides* encodes 3 chemotaxis pathway operons. Two of these operons are expressed under laboratory conditions and regulate the activity of the Fla1 unidirectional motor (Porter et al., 2002). The third operon, resembling in organization of the chemosensory operons found in related alpha proteobacteria, is not normally expressed, but appears to be able to interact with the motor of the Fla2 polar tuft of flagella (Martinez-del Campo et al., 2011). These operons encoding the normally unexpressed flagella and chemotaxis system does not appear to be degenerate and are, therefore, probably expressed under specific environmental conditions; however, these have yet to be identified. It has been suggested that the Fla2 flagellar system and controlling CheOp1 are probably the ancestral system and Fla1 and *CheOp2* and *CheOp3* genes were acquired by horizontal gene transfer (Hernandez-Valle et al., 2020).

The Fla1 single, unidirectional flagellum driving bacterial swimming in the laboratory is encoded by a completely separate regulon whose expression is controlled by a sigma 54 transcription factor (Pena-Sanchez et al., 2009). The stopping frequency of the motor is controlled by two different chemosensory operons (Porter et al., 2008b). The genes of the different operons cannot complement mutations in the other flagella or chemosensory systems (Scott et al., 2010). Interestingly, most polar flagella are precisely positioned by sets of targeting proteins, e.g., TipN/TipF, HupP, or FhlF (Schuhmacher et al., 2015). There are no obviously polar targeting genes associated with the expressed Fla1 unidirectional

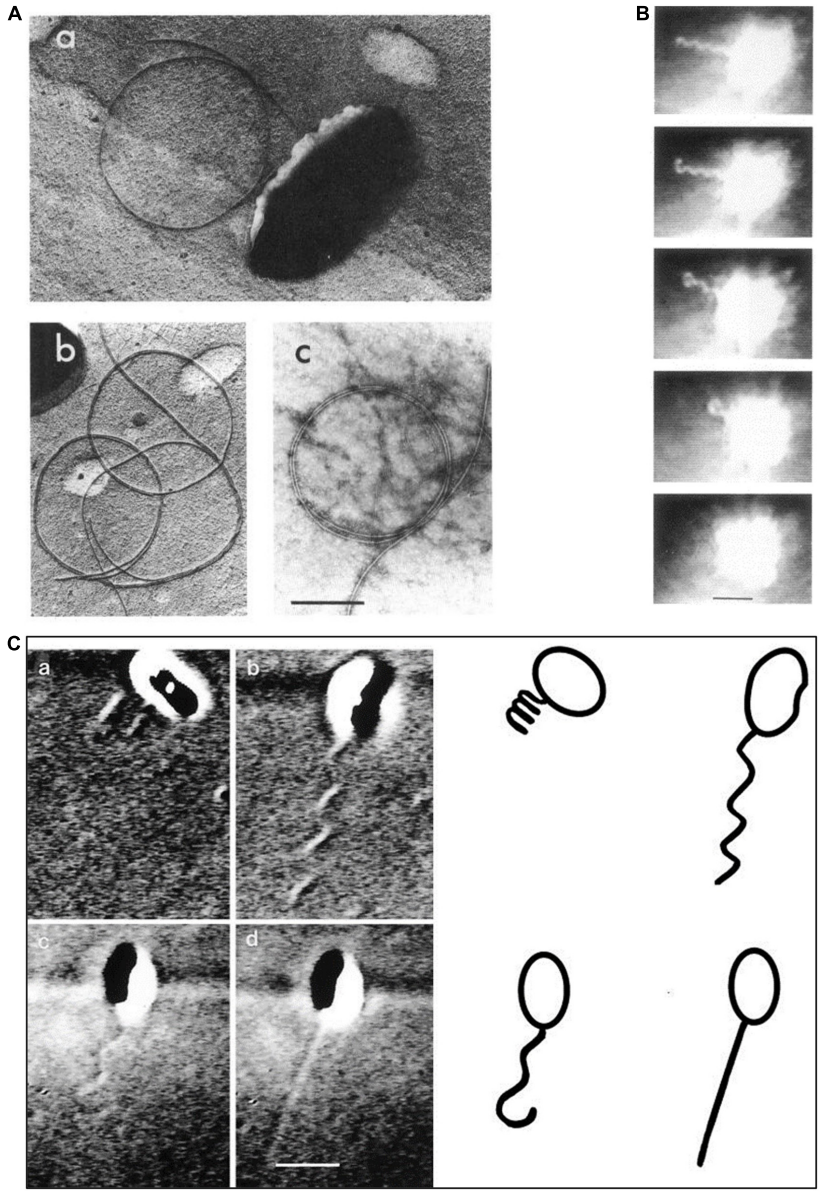


FIGURE 1 | Images of the Rhodobacter *sphaeroides* (*R. sphaeroides*) flagellum. **(A)** Various electron micrographs showing relaxed non-functioning filament. **(B)** Still images from dark-field light microscopy of swimming cell showing filament coiling against cell body after a stop. **(C)** Differential interference contrast (DIC) light microscopy images of swimming cells showing different conformations (a) coiled, (b) swimming, (c) starting to relax during a stop, and (d) fast rotating probably small amplitude filament. From Armitage and Macnab (1987) and Armitage et al. (1999) with permission.

filament. In our early observations, we described the filament as subpolar, as we never saw it at the poles. Later, painstaking analysis by Chi Aizawa of large number of electron micrographs suggested that these single flagella are in fact randomly positioned (personal communication), rather like the peritrichous filaments of *E. coli*, but with the regulon expressed only once per cell cycle. When following dividing cells, a new filament is only seen on the new daughter cell and it is very rare to see two filaments within a single body length. The new filament starts to rotate just before cells separation and results in doublets of cells spinning on their axes, until the cells separate and swim off in different directions.

Adding to the idea that the active *R. sphaeroides* flagellum evolved from a different bacterial group is the unusual structure of the hook. Images of most peritrichously flagellate bacteria show a curved hook linking the rod to the flagellar filament. The hook monomers ordered to interface through hook-associated proteins with the flagellin subunits and enabled the torque to be transmitted from the rotating motor to the filament, driving the helical conformation of the flagellum. Driving the interactions between the flagellin molecules in the 11 protofilaments that make up the hollow filament causes it to form a helix rather than straight tube and drives the switch between different wavelengths

and handedness upon a switch in direction of motor rotation. The hook shape is thought to allow the 6 or more filaments to come together as a bundle to push the cell forward (Samatey et al., 2004; Brown et al., 2012). The periodic switch in motor rotational direction drives a change in hook waveform and, thus, filament waveform and this forces the bundle apart and causes the bacterium to tumble transiently. *R. sphaeroides* has a straight rather than bent hook and a diameter smaller rather than larger than the filament (**Figure 2C**). Although there does not seem to have been an extensive survey, the hook of polar flagellate species such as *Caulobacter crescentus* and *Campylobacter jejuni* also appears to be straight (Wagenknecht et al., 1981; Matsunami et al., 2016). This may suggest that the Fla1 flagellum thought to be acquired by horizontal gene transfer may have been polar, but because the associated polar positioning protein was lost, it is now positioned randomly. The unidirectional motor means that on a stop, the torque normally forcing the hook and then the flagellin subunits into interactions resulting in helical conformations is lost and the structure returns to a minimal energy state. Measuring rotation rates of tethered cells suggests that the motor can change periodically speed, something seen in some other related species such as *Sinorhizobium* (Poole and Armitage, 1988; Packer and Armitage, 1994; Attmannspacher et al., 2005). The reason for speed change is unclear, particularly as the driving pmf is expected to be stable. Using early differential interference contrast (DIC) microscopy to visualize the flagella of free swimming cells, we saw some cells transiently swimming very fast that appeared to be have short wavelength and small amplitude helical filaments. This suggests that *R. sphaeroides* has at least 3 patterns of movement, long periods of medium speed, smooth swimming punctuated by short periods of fast swimming and stops (**Figure 1C**; Armitage et al., 1999). How this complex pattern of behavior impacts movement in the natural environment is unclear.

Swimming *R. sphaeroides* cells have usually been studied in buffer and, therefore, with a low load on their motors; it is known that in the environment, they can form extensive biofilms. While electron micrographs of the isolated motors look similar to the basic motors of enteric species, the Dreyfus laboratory has identified additional motor proteins, an H-ring plus FliL and MotF. These appear to sit in the periplasmic region of the motor close to the outer membrane L/P ring, but unlike related FliL proteins, they appears to interact with the stator and be essential for motility (**Figure 2C**; Suaste-Olmos et al., 2010; Ramirez-Cabrera et al., 2012; Camarena and Dreyfus, 2020). The basic flagellar motors of species such as *E. coli* have a series of rings in the cytoplasmic and outer membrane. On the cytoplasmic face of the FliG rotor, ring sits on the FliM/FliN switch complex. FliG is associated with the MS ring, embedded in the cytoplasmic membrane. FliG rotation is driven by the ring of peptidoglycan anchored MotA/MotB stator proteins. These are the site of proton or sodium transport. Ion flow changes the structure of the Mot stators and, thus, the electrostatic interaction with the FliG ring and drives rotation. A rod protein is attached

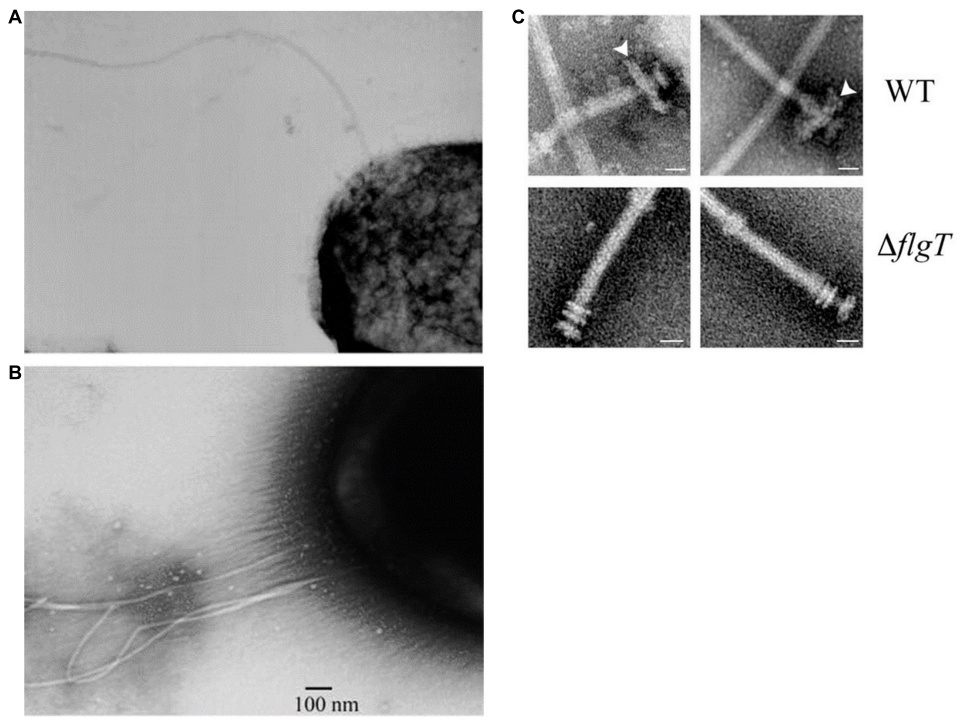


FIGURE 2 | Electron micrographs showing **(A)** single unidirectional flagellum expressed under laboratory conditions, Fla1. **(B)** Polar tuft of flagella, Fla2 expressed from CtrA controlled regulon when Fla1 is repressed. **(C)** Additional ring associated with L/P ring of Fla1, lost in FlgT mutants. Taken from Poggio et al. (2007) and Fabela et al. (2013) with permission.

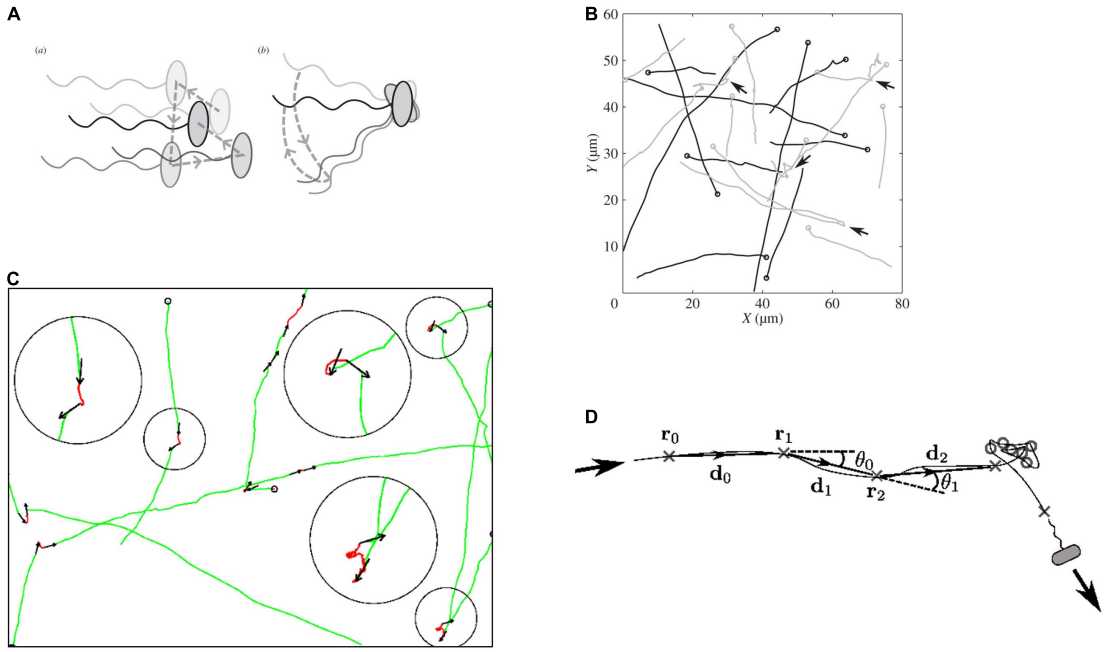


FIGURE 3 | Measurement of *R. sphaeroides* free swimming tracks. **(A)** Difference between rotational Brownian diffusion during a stop (a) vs. active reorientation (b). **(B)** Tracks with arrows marking stops, **(C)** details of movement during stops, and **(D)** analysis of angles changed while free swimming and stops (details in Rosser et al., 2013, 2014).

to the rotor and spans the periplasm, passing through the outer membrane L and P rings. A type 3 secretion system ATPase sits inside the FliM/FliN ring, a switch ring, and exports the unfolded proteins of the hook and then filament through the rod to polymerize at the distal end of the filament (Armitage and Berry, 2020). Cryoelectron tomography has revealed that while this is the basic motor architecture, species that need to produce a higher torque, for example, species that move through very viscous environments often have extra rings or rings with a larger diameter to produce increased torque (Beeby et al., 2016). The motors of species driven by sodium motive forces also have additional rings. Why *R. sphaeroides* has an extra ring is unclear. While it is clear that the *R. sphaeroides* Fla1 motor rotation is driven by the pmf, *R. sphaeroides* can be isolated from brackish water and is tolerant of high sodium concentrations as well as being able to form extensive biofilms. While loss of the pmf does cause swimming to stop, supporting the hypothesis that Fla1 is a proton driven motor; further investigation is required to understand the possible role of these additional motor rings in different environments.

ANALYSIS OF SWIMMING PATTERNS PERSISTENCE AND ACTIVE DIRECTION CHANGING

Detailed analysis of the swimming patterns of bacterial populations in 3 dimensions, with each bacterium following a random swimming pattern was, and still is, challenging. Over the years, both the microscopy and tracking software able to follow multiple cells simultaneously have been steadily improved. The simultaneous tracking and analysis of trajectories in greater detail have provided increased understanding of *R. sphaeroides* swimming patterns (**Figure 3**). Tethering and free swimming data both show that the *R.* sphaeroides motor has an unstimulated motor bias of 0.85, i.e., it spends most of the time rotating, driving, swimming, with only very occasional stops. This is similar to the free swimming bias of *E.* coli swimming with a bundle of flagella where the cells swim for more time than they tumble; however, a single tethered *E.* coli motor has a bias closer to 0.5 making behavioral responses easier to measure (Berry and Armitage, 2000; **Figure 4A**). The high motor bias makes it hard to measure a response to a positive stimulus and much easier to identify a stimulus-related stop. Detailed analysis of swimming tracks suggests that while there is directional persistence during stops, there needs to be more than just Brownian rotational motion for reorientation, suggesting that either the hook might change angle or, more likely, as the motor starts to rotate at the end of a stop, the reforming functional waveform being pushed down the length of the filament by the increasing torque reorients the cell body (**Figure 3**; Rosser et al., 2013, 2014).

BRAKE VS. CLUTCH

How does the motor stop and when it stops does it brake or declutch? Do the stators disengage from the rotor allowing free spinning without proton flow or do they lock to the rotor, possible allowing continued proton flow without rotor movement.

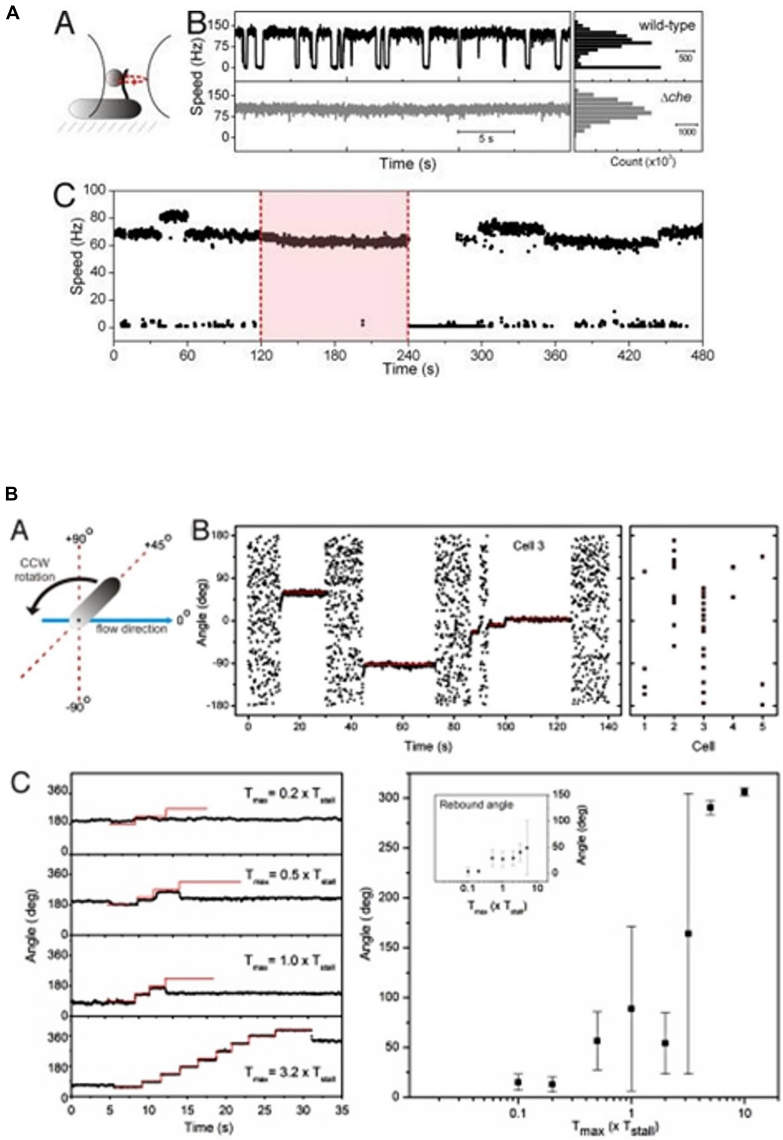


FIGURE 4 | Tethered cell analysis of *R. sphaeroides* motor behavior. **(A)** Behavior of bead attached to a truncated filament of a wt and a non-chemotactic mutant. Wt motors show long periods of smooth swimming with occasional stops, while non-chemotactic mutants show constant smooth swimming. (C) Longer timescale shows a tethered wt cell rotating smoothly with occasional increases in speed. Pink box shows addition of attractant and loss of stops, removal results in stopped cell and adaptation. **(B)** Shows cell tethered by its flagellum and stopped by large chemosensory stimulus and the force required to rotate the cell (details in Pilizota et al., 2009).

In *E. coli* and indeed most bacterial species, direction changing is caused by the binding of the phosphorylated chemosensory protein CheY to the FliM component of the flagellar motor switch (Wadhams and Armitage, 2004). As mentioned above, the structure of the motor resembles that of the simple *E. coli* motor, but with the addition of an extra periplasmic ring. Recent structural studies have revealed details of the complete structure of the *E.* coli and *Salmonella* flagellar motors and suggested mechanisms for switching mechanisms (Johnson et al., 2021; Tan et al., 2021). Unfortunately, there are no detailed molecular structures of the *R. sphaeroides* motor proteins to allow comparisons between a switching and stopping motor. Unlike the simple chemosensory system of *E. coli* with one signaling CheY protein, *R. sphaeroides* expresses 3 CheY proteins under normal laboratory conditions. Two of these CheYs, CheY3 and CheY4, are regulated by a large membrane spanning cluster of chemotaxis proteins, assumed to sense the extracellular concentration of chemoeffectors, while the 3rd protein, CheY6, is regulated by a large complex of chemosensory proteins in a single cytoplasmic cluster, localized to the surface of the nucleoid (Porter et al., 2011a; Jones and Armitage, 2015, 2017). The phosphorylation state of CheY6 is regulated by an unusual CheA

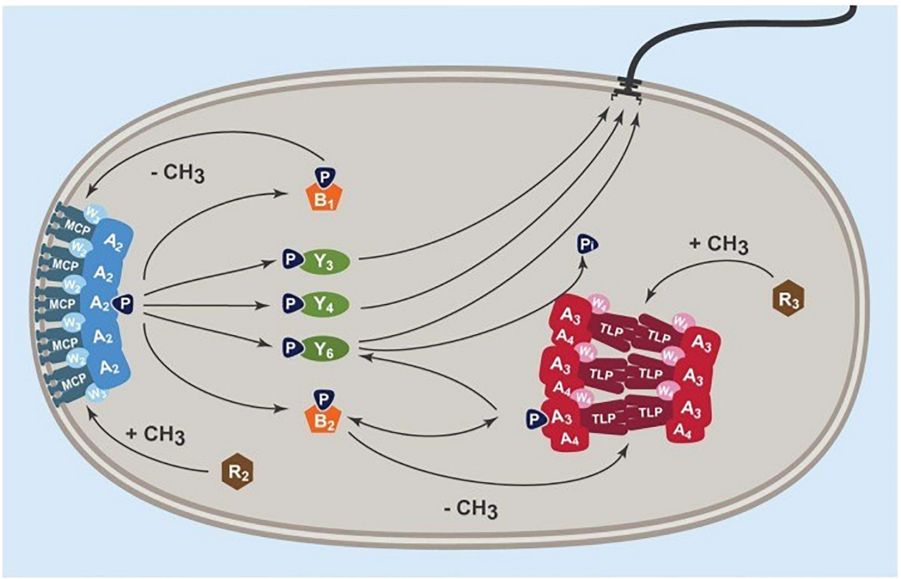


FIGURE 5 | Current model of chemosensory control of *R. sphaeroides* Fla1 motor stopping. Signals from the transmembrane chemosensory cluster, MCP, W3, and A2 control the phosphorylation state of CheY3 and CheY4. These compete with CheY6 whose phosphorylation state is controlled by the kinase CheA4 and the phosphatase CheA3 through the cytoplasmic chemoreceptor TlpT. Each cluster has an independent adaptation system consisting of a constitutive methyltransferase (CheR) and a constitutive methylesterase (CheB) regulated by the associated histidine kinase, CheA (from Beyer et al., 2019).

kinase divided into 2 separate proteins, CheA4 acts as the kinase and when active phosphotransfers to a His residue on CheA3, which phosphotransfers only to CheY6 and an adaptation protein CheB2 (Porter et al., 2008a). CheA3 also has a dephosphorylation domain, exclusively removing phosphoryl residues from CheY6-P. The activity of CheA3 and CheA4 is regulated by two cytoplasmic receptors, assumed to sense the metabolic state of the cell and balance the kinase to dephosphorylation rate and, thus, control the level of CheY6-P in the cytoplasm (Beyer et al., 2019).

CheY6-P is the only CheY able to stop the motor, although all the CheYs can bind the motor and CheY6 and either CheY3 or CheY4 is required for chemotaxis (Porter et al., 2006). Deletion of CheY6 results in smooth swimming, while deletion of CheY3 and CheY4 results in wild-type swimming patterns, but no chemotaxis. Models suggest that there is steady-state phosphorylation of the phosphotransfer site of CheA3 by CheA4, but signals through the cytoplasmic receptor TlpT regulate CheA3 and specifically the activity of the dephosphorylation domain, which dephosphorylated CheY6-P. TlpT is the only cytoplasmic chemoreceptor showing adaptation (Beyer et al., 2019). A steady state level of CheY6-P controls the unstimulated stopping frequency of the *R. sphaeroides* motor. A study by Dreyfus suggested that *in vitro,* both the phosphorylated and unphosphorylated CheYs can bind the motor (del Campo et al., 2007). As only CheY6-P stops the motor, it suggests that during a fall in chemoeffector concentration, there must be an increase in CheY6-P concentration causing motor stopping. It is likely that steady state levels of CheY3 and CheY4 compete with CheY6-P for binding to the motor allowing periods of swimming and stopping as concentrations fluctuate. A fall in a metabolic chemoeffector causes an increase in CheY6-P levels, probably by a reduction in dephosphorylation activity and it outcompetes the other CheYs for FliM, stopping the motor. Adaptation of TlpT, controlling CheA3 activity, then resets the dephosphorylation state and the level of CheY6-P returns to normal and CheY3 and CheY4 can again compete and allow periods of free swimming (current model shown in **Figure 5**; Beyer et al., 2019). Unfortunately, while there has been detailed structural analysis of FliM and changes that occur to CheY∼P binding in enteric bacterial species, we have no detailed knowledge of the structure of FliM in *R. sphaeroides* or how 3 CheY homologs can bind FliM, but only one stop motor rotation.

To identify whether a stop caused by CheY6-P binding locks the motor or released the stator proteins, *R. sphaeroides* was tethered by their flagella to microscope slides and the motors stopped using a large chemotactic stimulus. Using either viscous flow or attaching a bead to the flagellum and holding that bead in an optical trap, we measured the force needed to make a stopped motor rotate. The force needed to rotate the cells was compared to the stall torque of the motor under swimming conditions, i.e., the force needed to stop a smoothly rotating motor. Using either method, the force required was 2–3 times the stall torque of the motor, showing that the motor is locked (**Figure 4B**; Pilizota et al., 2009). This is supported by the fixed angles measured during stops, suggesting that there is no drift in the stopped motor. Interestingly, measurement of the stiffness of the tether, the hook, in these experiments, shows it is an order of magnitude stiffer than that of *E. coli*, consistent with the straight rather than curved hook.

As mentioned above, the FliG ring rotates against a ring of MotA/MotB stator proteins. However, we showed that in *E. coli*, the stators are in constant exchange with

stators diffusing in the cytoplasmic membrane. Individual stators only staying associated for about 30 s and the number associated linked to the external force on the motor. Each stator engages individually, with the numbers engaged increases as the external viscosity increases. This suggests that the off-rate changes as the force on the motor changes, presumably transmitted through the filament, and hook from the external environment. When the *R. sphaeroides* motor locks during a stop, the stators were found to still be exchanging, suggesting that the release of stators from the peptidoglycan required to exchange is independent from their engagement to the rotor.

SUMMARY

While the basic structure of bacterial flagellar motors appears to be conserved through evolution, there are obvious variations on a theme. Species such as *R. sphaeroides* are extremely metabolically and structurally diverse, with some activities mutually exclusive. It can grow anaerobically, using either anaerobic respiration or photosynthesis; under these conditions, its cytoplasm is filled with vesicles and it can fix nitrogen, if complex nitrogen becomes limiting. It can also grow aerobically, with organic acids, as its favored carbon source. However, although components of the electron transport chain are shared between aerobic respiration and photosynthesis, the two systems are, as with most photosynthetic bacteria, mutually exclusive. Has this metabolic complexity led to the unusual swimming behavior seen in this species? It seems probably that the ancestral species swam using a tuft of polar filaments controlled by a classical chemosensory system, as these look similar to those of several other related species. However, during evolution, *R. sphaeroides* appears to have acquired not only a second flagellar system, but 2 chemosensory pathways. The chemosensory pathways now interplay to allow *R. sphaeroides* to make a "decision" about whether to respond to a specific metabolite by controlling the activity of very unusual single, stopping flagellar motor. We can only speculate about why this is the flagellum and control system we see expressed in the laboratory and why it is unable to switch direction of rotation. It works, *R. sphaeroides* swims rapidly through liquid environments, at speeds of over 50 μms^{-1}, responding to changes in light, oxygen, and a wide range of organic acids by modulating the stopping frequency of the motor. Despite years of trying, we have not been able to get both the systems to express together. We need to work out when this Fla1 system is repressed and the second Fla2 system expressed to really understand how this bacterium exploits it environment to the full.

AUTHOR CONTRIBUTIONS

JA wrote the manuscript.

FUNDING

The research from my laboratory outlined here has been continuously supported by funding from the BBSRC with additional funding from the Leverhulme Trust and the EPA Cephalosporin Trust.

REFERENCES

Armitage, J. P., and Berry, R. M. (2020). Assembly and dynamics of the bacterial flagellum. *Annu. Rev. Microbiol.* 74, 181–200. doi: 10.1146/annurev-micro-090816-093411

Armitage, J. P., and Macnab, R. M. (1987). Unidirectional, intermittent rotation of the flagellum of *Rhodobacter sphaeroides*. *J. Bacteriol.* 169, 514–518. doi: 10.1128/jb.169.2.514-518.1987

Armitage, J. P., Ingham, C., and Evans, M. C. (1985). Role of proton motive force in phototactic and aerotactic responses of *Rhodopseudomonas sphaeroides*. *J. Bacteriol.* 161, 967–972. doi: 10.1128/jb.161.3.967-972.1985

Armitage, J. P., Pitta, T. P., Vigeant, M. A., Packer, H. L., and Ford, R. M. (1999). Transformations in flagellar structure of *Rhodobacter sphaeroides* and possible relationship to changes in swimming speed. *J. Bacteriol.* 181, 4825–4833. doi: 10.1128/JB.181.16.4825-4833.1999

Attmannspacher, U., Scharf, B., and Schmitt, R. (2005). Control of speed modulation (chemokinesis) in the unidirectional rotary motor of *Sinorhizobium meliloti*. *Mol. Microbiol.* 56, 708–718. doi: 10.1111/j.1365-2958.2005.04565.x

Beeby, M., Ribardo, D. A., Brennan, C. A., Ruby, E. G., Jensen, G. J., and Hendrixson, D. R. (2016). Diverse high-torque bacterial flagellar motors assemble wider stator rings using a conserved protein scaffold. *Proc. Natl. Acad. Sci. U S A.* 113, E1917–E1926.

Berry, R. M., and Armitage, J. P. (2000). Response kinetics of tethered *Rhodobacter sphaeroides* to changes in light intensity. *Biophys. J.* 78, 1207–1215. doi: 10.1016/S0006-3495(00)76678-1

Beyer, J. A., Szollossi, A., Byles, E., Fischer, R., and Armitage, J. P. (2019). Mechanism of signalling and adaptation through the *Rhodobacter sphaeroides* cytoplasmic chemoreceptor cluster. *Int. J. Mol. Sci.* 20:5095. doi: 10.3390/ijms20205095

Brown, M. T., Steel, B. C., Silvestrin, C., Wilkinson, D. A., Delalez, N. J., Lumb, C. N., et al. (2012). Flagellar hook flexibility is essential for bundle formation in swimming *Escherichia coli* cells. *J. Bacteriol.* 194, 3495–3501. doi: 10.1128/JB.00209-12

Camarena, L., and Dreyfus, G. (2020). Living in a foster home: the single subpolar flagellum fla1 of *Rhodobacter sphaeroides*. *Biomolecules* 10:774. doi: 10.3390/biom10050774

de la Mora, J., Uchida, K., Del Campo, A. M., Camarena, L., Aizawa, S., and Dreyfus, G. (2015). Structural characterization of the fla2 flagellum of *Rhodobacter sphaeroides*. *J. Bacteriol.* 197, 2859–2866. doi: 10.1128/JB.00170-15

del Campo, A. M., Ballado, T., De La Mora, J., Poggio, S., Camarena, L., and Dreyfus, G. (2007). Chemotactic control of the two flagellar systems of *Rhodobacter sphaeroides* is mediated by different sets of CheY and FliM proteins. *J. Bacteriol.* 189, 8397–8401. doi: 10.1128/JB.00730-07

Fabela, S., Domenzaine, C., De la More, J., Osorio, A., Ramirez-Cabera, V., Poggio, S., et al. (2013). A distant homologue of the FlgT protein interacts with MotB and FliL and is essential for flagellar rotation in *Rhodobacter sphaeroides*. *J. Bacteriol.* 195, 5285–5296. doi: 10.1128/JB.00760-13

Hernandez-Valle, J., Sanchez-Flores, A., Poggio, S., Dreyfus, G., and Camarena, L. (2020). The CtrA regulon of *Rhodobacter sphaeroides* favors adaptation to a particular lifestyle. *J. Bacteriol.* 202:e00678-19. doi: 10.1128/JB.00678-19

Johnson, S., Furlong, E. J., Deme, J. C., Nord, A. L., Caesar, J. J. E., Chevance, F. F. V., et al. (2021). Molecular structure of the intact bacterial flagellar basal body. *Nat. Microbiol.* 6, 712–721. doi: 10.1038/s41564-021-00895-y

Jones, C. W., and Armitage, J. P. (2015). Positioning of bacterial chemoreceptors. *Trends Microbiol.* 23, 247–256. doi: 10.1016/j.tim.2015.03.004

Jones, C. W., and Armitage, J. P. (2017). Essential role of the cytoplasmic chemoreceptor TlpT in the de novo formation of chemosensory complexes in *Rhodobacter sphaeroides*. *J. Bacteriol.* 199:e00366-17. doi: 10.1128/JB.00366-17

Kamiya, R., Hotani, H., and Asakura, S. (1982). Polymorphic transition in bacterial flagella. *Symp. Soc. Exp. Biol.* 35, 53–76.

Mackenzie, C., Choudhary, M., Larimer, F. W., Predki, P. F., Stilwagen, S., Armitage, J. P., et al. (2001). The home stretch, a first analysis of the nearly completed genome of *Rhodobacter sphaeroides* 2.4.1. *Photosynth Res.* 70, 19–41. doi: 10.1023/A:1013831823701

Manson, M. D., Tedesco, P., Berg, H. C., Harold, F. M., and Van Der Drift, C. (1977). A protonmotive force drives bacterial flagella. *Proc. Natl. Acad. Sci. U S A.* 74, 3060–3064. doi: 10.1073/pnas.74.7.3060

Martinez-del Campo, A., Ballado, T., Camarena, L., and Dreyfus, G. (2011). In *Rhodobacter sphaeroides*, chemotactic operon 1 regulates rotation of the flagellar system 2. *J. Bacteriol.* 193, 6781–6786. doi: 10.1128/JB.05933-11

Matsunami, H., Barker, C. S., Yoon, Y. H., Wolf, M., and Samatey, F. A. (2016). Complete structure of the bacterial flagellar hook reveals extensive set of stabilizing interactions. *Nat. Commun.* 7:13425. doi: 10.1038/ncomms13425

Meister, M., and Berg, H. C. (1987). The stall torque of the bacterial flagellar motor. *Biophys. J.* 52, 413–419.

Packer, H. L., and Armitage, J. P. (1993). The unidirectional flagellar motor of *Rhodobacter sphaeroides* Ws8 can rotate either clockwise or counterclockwise: characterization of the flagellum under both conditions by antibody decoration. *J. Bacteriol.* 175, 6041–6045. doi: 10.1128/jb.175.18.6041-6045.1993

Packer, H. L., and Armitage, J. P. (1994). The chemokinetic and chemotactic behavior of *Rhodobacter sphaeroides*: two independent responses. *J. Bacteriol.* 176, 206–212. doi: 10.1128/jb.176.1.206-212.1994

Pena-Sanchez, J., Poggio, S., Flores-Perez, U., Osorio, A., Domenzain, C., Dreyfus, G., et al. (2009). Identification of the binding site of the {sigma}54 hetero-oligomeric FleQ/FleT activator in the flagellar promoters of *Rhodobacter sphaeroides*. *Microbiology (Reading)* 155, 1669–1679. doi: 10.1099/mic.0.024455-0

Pijper, A. (1955). Shape of bacterial flagella. *Nature* 175, 214–215.

Pilizota, T., Brown, M. T., Leake, M. C., Branch, R. W., Berry, R. M., and Armitage, J. P. (2009). A molecular brake, not a clutch, stops the *Rhodobacter sphaeroides* flagellar motor. *Proc. Natl. Acad. Sci. U S A.* 106, 11582–11587.

Poggio, S., Abreu-Goodger, C., Fabela, S., Osorio, A., Dreyfus, G., Vinuesa, P., et al. (2007). A complete set of flagellar genes acquired by horizontal transfer coexists with the endogenous flagellar system in *Rhodobacter sphaeroides*. *J. Bacteriol.* 189, 3208–3216. doi: 10.1128/JB.01681-06

Poncin, K., Gillet, S., and De Bolle, X. (2018). Learning from the master: targets and functions of the CtrA response regulator in *Brucella abortus* and other alpha-proteobacteria. *FEMS Microbiol. Rev.* 42, 500–513. doi: 10.1093/femsre/fuy019

Poole, P. S., and Armitage, J. P. (1988). Motility response of Rhodobacter sphaeroides to chemotactic stimulation. *J. Bacteriol.* 170, 5673–5679. doi: 10.1128/jb.170.12.5673-5679.1988

Poole, P. S., Sinclair, D. R., and Armitage, J. P. (1988). Real time computer tracking of free-swimming and tethered rotating cells. *Anal. Biochem.* 175, 52–58. doi: 10.1016/0003-2697(88)90359-4

Porter, S. L., Roberts, M. A., Manning, C. S., and Armitage, J. P. (2008a). A bifunctional kinase-phosphatase in bacterial chemotaxis. *Proc. Natl. Acad. Sci. U S A.* 105, 18531–18536. doi: 10.1073/pnas.0808010105

Porter, S. L., Wadhams, G. H., and Armitage, J. P. (2008b). *Rhodobacter sphaeroides*: complexity in chemotactic signalling. *Trends Microbiol.* 16, 251–260. doi: 10.1016/j.tim.2008.02.006

Porter, S. L., Wadhams, G. H., Martin, A. C., Byles, E. D., Lancaster, D. E., and Armitage, J. P. (2006). The CheYs of *Rhodobacter sphaeroides*. *J. Biol. Chem.* 281, 32694–32704.

Porter, S. L., Warren, A. V., Martin, A. C., and Armitage, J. P. (2002). The third chemotaxis locus of *Rhodobacter sphaeroides* is essential for chemotaxis. *Mol. Microbiol.* 46, 1081–1094. doi: 10.1046/j.1365-2958.2002.03218.x

Porter, S. L., Wadhams, G. H., and Armitage, J. P. (2011a). Signal processing in complex chemotaxis pathways. *Nat. Rev. Microbiol.* 9, 153–165. doi: 10.1038/nrmicro2505

Porter, S. L., Wilkinson, D. A., Byles, E. D., Wadhams, G. H., Taylor, S., Saunders, N. J., et al. (2011b). Genome sequence of *Rhodobacter sphaeroides* strain Ws8N. *J. Bacteriol.* 193, 4027–4028. doi: 10.1128/JB.05257-11

Ramirez-Cabrera, V., Poggio, S., Domenzain, C., Osorio, A., Dreyfus, G., and Camarena, L. (2012). A novel component of the *Rhodobacter sphaeroides* Fla1 flagellum is essential for motor rotation. *J. Bacteriol.* 194, 6174–6183. doi: 10.1128/JB.00850-12

Rosser, G., Baker, R. E., Armitage, J. P., and Fletcher, A. G. (2014). Modelling and analysis of bacterial tracks suggest an active reorientation mechanism in *Rhodobacter sphaeroides*. *J. R. Soc. Interface* 11:20140320. doi: 10.1098/rsif.2014.0320

Rosser, G., Fletcher, A. G., Wilkinson, D. A., De Beyer, J. A., Yates, C. A., Armitage, J. P., et al. (2013). Novel methods for analysing bacterial tracks reveal persistence in *Rhodobacter sphaeroides*. *PLoS Comput. Biol.* 9:e1003276. doi: 10.1371/journal.pcbi.1003276

Samatey, F. A., Matsunami, H., Imada, K., Nagashima, S., Shaikh, T. R., Thomas, D. R., et al. (2004). Structure of the bacterial flagellar hook and implication for the molecular universal joint mechanism. *Nature* 431, 1062–1068. doi: 10.1038/nature02997

Schuhmacher, J. S., Thormann, K. M., and Bange, G. (2015). How bacteria maintain location and number of flagella? *FEMS Microbiol. Rev.* 39, 812–822. doi: 10.1093/femsre/fuv034

Scott, K. A., Porter, S. L., Bagg, E. A., Hamer, R., Hill, J. L., Wilkinson, D. A., et al. (2010). Specificity of localization and phosphotransfer in the CheA proteins of *Rhodobacter sphaeroides*. *Mol. Microbiol.* 76, 318–330. doi: 10.1111/j.1365-2958.2010.07095.x

Silverman, M., and Simon, M. (1974). Flagellar rotation and the mechanism of bacterial motility. *Nature* 249, 73–74.

Suaste-Olmos, F., Domenzain, C., Mireles-Rodriguez, J. C., Poggio, S., Osorio, A., Dreyfus, G., et al. (2010). The flagellar protein FliL is essential for swimming in *Rhodobacter sphaeroides*. *J. Bacteriol.* 192, 6230–6239. doi: 10.1128/JB.00655-10

Tan, J., Zhang, X., Wang, X., Xu, C., Chang, S., Wu, H., et al. (2021). Structural basis of assembly and torque transmission of the bacterial flagellar motor. *Cell* 184, 2665–2679.e19 doi: 10.1016/j.cell.2021.03.057

Vega-Baray, B., Domenzain, C., Rivera, A., Alfaro-Lopez, R., Gomez-Cesar, E., Poggio, S., et al. (2015). The flagellar set Fla2 in *Rhodobacter sphaeroides* is controlled by the CckA pathway and is repressed by organic acids and the expression of Fla1. *J. Bacteriol.* 197, 833–847. doi: 10.1128/JB.02429-14

Wadhams, G. H., and Armitage, J. P. (2004). Making sense of it all: bacterial chemotaxis. *Nat. Rev. Mol. Cell Biol.* 5, 1024–1037. doi: 10.1038/nrm1524

Wagenknecht, T., Derosier, D., Shapiro, L., and Weissborn, A. (1981). Three-dimensional reconstruction of the flagellar hook from Caulobacter crescentus. *J. Mol. Biol.* 151, 439–465. doi: 10.1016/0022-2836(81)90005-x

Conflict of Interest: The author declares that the research was conducted in the absence of any commercial or financial relationships that could be construed as a potential conflict of interest.

Publisher's Note: All claims expressed in this article are solely those of the authors and do not necessarily represent those of their affiliated organizations, or those of the publisher, the editors and the reviewers. Any product that may be evaluated in this article, or claim that may be made by its manufacturer, is not guaranteed or endorsed by the publisher.

Copyright © 2022 Armitage. This is an open-access article distributed under the terms of the Creative Commons Attribution License (CC BY). The use, distribution or reproduction in other forums is permitted, provided the original author(s) and the copyright owner(s) are credited and that the original publication in this journal is cited, in accordance with accepted academic practice. No use, distribution or reproduction is permitted which does not comply with these terms.

frontiers | Frontiers in Microbiology

REVIEW
published: 12 April 2022
doi: 10.3389/fmicb.2022.863804

Dynamic Hybrid Flagellar Motors—Fuel Switch and More

*Kai M. Thormann**

Fachbereich für Chemie und Biologie, Institut für Mikrobiologie und Molekularbiologie, Justus-Liebig-Universität Gießen, Gießen, Germany

Flagellar motors are intricate rotating nanomachines that are powered by transmembrane ion gradients. The stator complexes are the powerhouses of the flagellar motor: They convert a transmembrane ion gradient, mainly of H^+ or Na^+, into rotation of the helical flagellar filament. They are thus essential for motor function. The number of stators synchronously engaged in the motor is surprisingly dynamic and depends on the load and the environmental concentration of the corresponding coupling ion. Thus, the rotor–stator interactions determine an important part of the properties of the motor. Numerous bacteria have been identified as possessing more than one set of stators, and some species have been demonstrated to use these different stators in various configurations to modify motor functions by dynamic in-flight swapping. Here, we review knowledge of the properties, the functions, and the evolution of these hybrid motors and discuss questions that remain unsolved.

Keywords: flagellum, swimming, swarming, regulation, bacteria, stator swapping

OPEN ACCESS

Edited by:
Pushkar Lele,
Texas A&M University, United States

Reviewed by:
Daniel B. Kearns,
Indiana University Bloomington, United States
Michael Manson,
Texas A&M University, United States

***Correspondence:**
Kai M. Thormann
kai.thormann@mikro.bio.uni-giessen.de

Specialty section:
This article was submitted to Microbial Physiology and Metabolism, a section of the journal Frontiers in Microbiology

Received: *27 January 2022*
Accepted: *25 February 2022*
Published: *12 April 2022*

Citation:
Thormann KM (2022) Dynamic Hybrid Flagellar Motors—Fuel Switch and More. Front. Microbiol. 13:863804. doi: 10.3389/fmicb.2022.863804

INTRODUCTION: FLAGELLA-MEDIATED MOTILITY

During the billions of years of their existence, bacteria have evolved a range of different systems that allow them to move actively toward environments that are more favorable and to conquer new habitats (Jarrell and McBride, 2008; Wadhwa and Berg, 2021). Among the different means of locomotion, flagella are highly common. Flagella are long, rotating helical protein fibers (Berg and Anderson, 1973; Silverman and Simon, 1974) that extend from the cell surface and act as propellers to drive the cell efficiently through aqueous habitats and through more-structured environments or across surfaces (Kearns, 2010; Kühn et al., 2017).

Rotation of the flagellar filament is conferred by a rotating nanomachine, the flagellar motor, to which the filament is connected by a structure that serves as a universal joint structure, the flagellar hook (**Figure 1A**). Along with the flagellar protein export system, the motor is embedded into the cell envelope to form the flagellar basal body. Motor rotation is powered by transmembrane gradients, most commonly of protons (H^+) or sodium ions (Na^+) (Manson et al., 1977; Matsura et al., 1977; Hirota et al., 1981; Li et al., 2011). The majority of flagellar motors are bi-directional and can rotate in both the clockwise and counterclockwise directions, which allows the cells to navigate within environmental signal gradients *via* chemotaxis systems coupled to the flagella. Decades of work by many research groups in concert with constantly advancing techniques, e.g., in fluorescence microscopy and cryo-tomography, have provided deep insights into the structure of the flagellum, the composition of its motor, and the mechanism of rotation (Berg, 2003; Sowa and Berry, 2008; Johnson et al., 2021; Tan et al., 2021; Wadhwa and Berg, 2021).

Active motility provides a huge advantage for many organisms in nature (Fenchel, 2002; Reichenbach et al., 2007; Gude et al., 2020). This benefit, however, always comes with the cost of a substantial investment of energy and resources. For bacteria, not only the assembly but also the operation up to many flagella is a significant metabolic burden, as the cells have to constantly maintain the appropriate ion gradient to power the rotation. In addition, most bacteria thrive in rapidly changing environments and thus have to adjust the performance of their flagella accordingly. To this end, a range of mechanisms has evolved, which include direct binding of effector proteins that act as brakes, accelerators, clutches, or mediators of directional switching, sometimes even including the shedding the flagellar filament and part of the basal body (Minamino et al., 2019; Subramanian and Kearns, 2019; Zhu and Gao, 2020). These mechanisms will not be considered in detail here. Instead, we will review and discuss the inherent properties of the structure of the flagellar motor and its components that allow specific control and adaptation of the performance of the motor.

A ROTARY MACHINE DRIVEN BY ROTARY MACHINES—ROTOR–STATOR INTERACTION IN THE FLAGELLAR MOTOR

In general, rotational motors require two parts to generate torque between them: a part that rotates, the rotor, and a part that remains static, the stator. In all bacterial flagellar motors, the rotor comprises the cytoplasmic C-ring, which consists of dozens of copies of the proteins FliG, FliM, and FliN (or FliY in some bacterial motors) (Johnson et al., 2021; Tan et al., 2021; Wadhwa and Berg, 2021). The C-ring is shaped like a shallow, inverted cup with a diameter of about 45 nm (in *Salmonella* or *Vibrio*), where FliG is located close to the membrane and FliN is at the distal position within the cytoplasm (Francis et al., 1994; **Figures 1A,B**). FliG associates with FliF, the protein that forms the MS ring in the stator, which transduces rotation to the flagellar rod.

The stator is formed by distinct, ion-specific stator units. Each stator unit is an independent ion-conducting complex (Braun and Blair, 2001) built from seven copies of two transmembrane proteins, commonly referred to as MotA and MotB (as in the H^+-dependent motors of *E. coli* or *S. enterica*) (Silverman et al., 1976; Dean et al., 1984; Stader et al., 1986) or PomA and PomB (as in their Na^+-dependent counterparts in species of *Vibrio* or *Shewanella*) (Asai et al., 1997). MotA (or PomA) is embedded in the cytoplasmic membrane by four transmembrane regions and has a large cytoplasmic loop connecting transmembrane helices two and three and another cytoplasmic extension at the C-terminal end (Zhou et al., 1995). MotB possesses a short N-terminal cytoplasmic segment followed by a single transmembrane helix and a large periplasmic region (Chun and Parkinson, 1988), which harbors a peptidoglycan-binding domain (PBD) at its C-terminal end (De Mot and Vanderleyden, 1994). Each stator unit consists of five MotA/PomA subunits that are arranged in a ring around two MotB/PomB proteins (Deme et al., 2020; Santiveri et al., 2020; Hu et al., 2021). In a fully assembled motor of *E. coli* or *Vibrio* sp., about a dozen stators surround the MS-ring in the membrane, where they are positioned above FliG in the cytoplasmic C-ring and are bound to the cell wall by the MotB/PomB PBD domain (Khan et al., 1988; Reid et al., 2006; Thomas et al., 2006; Beeby et al., 2016; **Figures 1B,C**). The most recent model predicts that, driven by ion flow through each stator unit, the MotA proteins rotate around the two center MotB proteins and thus are themselves rotary nanomachines. The MotA cytoplasmic sections interact electrostatically with the C-terminal domains of the FliG proteins in the C-ring below the stators (Zhou and Blair, 1997; Zhou et al., 1998; Terashima et al., 2021; **Figure 1B**). Conformational changes in the C-ring, e.g., by binding of the phosphorylated form of the chemotaxis response regulator CheY, alter the interaction of MotA/PomA with FliG and switch the C-ring's rotational direction (Paul et al., 2011; Stock et al., 2012; Santiveri et al., 2020; Hu et al., 2021).

DYNAMICS OF ROTOR–STATOR INTERACTION AND MOTOR REMODELING

As described above, the stator units are the powerhouses of the flagellar motor and determine the nature of the coupling ion and the torque that can be produced. Despite this designation and their role in torque production, the rotor–stator configuration has been demonstrated to be surprisingly dynamic (Armitage and Berry, 2020).

The coupling of stator units to, and uncoupling from, the motors was observed by an incremental increase (or decrease) in torque (Block and Berg, 1984; Blair and Berg, 1988; Muramoto et al., 1994; Sowa et al., 2005) and, later, more directly by microscopic observation of fluorescently labeled stator units (Leake et al., 2006). When they are first assembled, the stator units diffuse as a pool of inactive precomplexes [about 300 in *E. coli* (Leake et al., 2006)] within the cytoplasmic membrane (**Figure 1D**). At that stage, the periplasmic section of the B-subunit is not bound to the cell wall; it assumes a conformation that prevents premature ion flow through the membrane. Only when they engage with the flagellar motor are the stators activated through conformational changes that allow binding to the peptidoglycan and release of ion flow (Van Way et al., 2000; Hosking et al., 2006; Kojima et al., 2009, 2018; Morimoto et al., 2010; Zhu et al., 2014). Each stator unit can also disengage from the flagellar motor and join the pool of membrane-diffusing inactive precomplexes. Thus, the stators in the flagellar motor are constantly turned over. Notably, stator exchange occurs while the motor continues to function.

The stability of rotor–stator interactions depends on at least two major factors: the ion motive force and the load acting on the filament (**Figure 1D**). Collapsing the ion motive force results in physical uncoupling and diffusion of the stator units from the motor, e.g., in *E. coli* (**Figure 1E**), whereas restoring the proton motive force leads to re-incorporation of stators

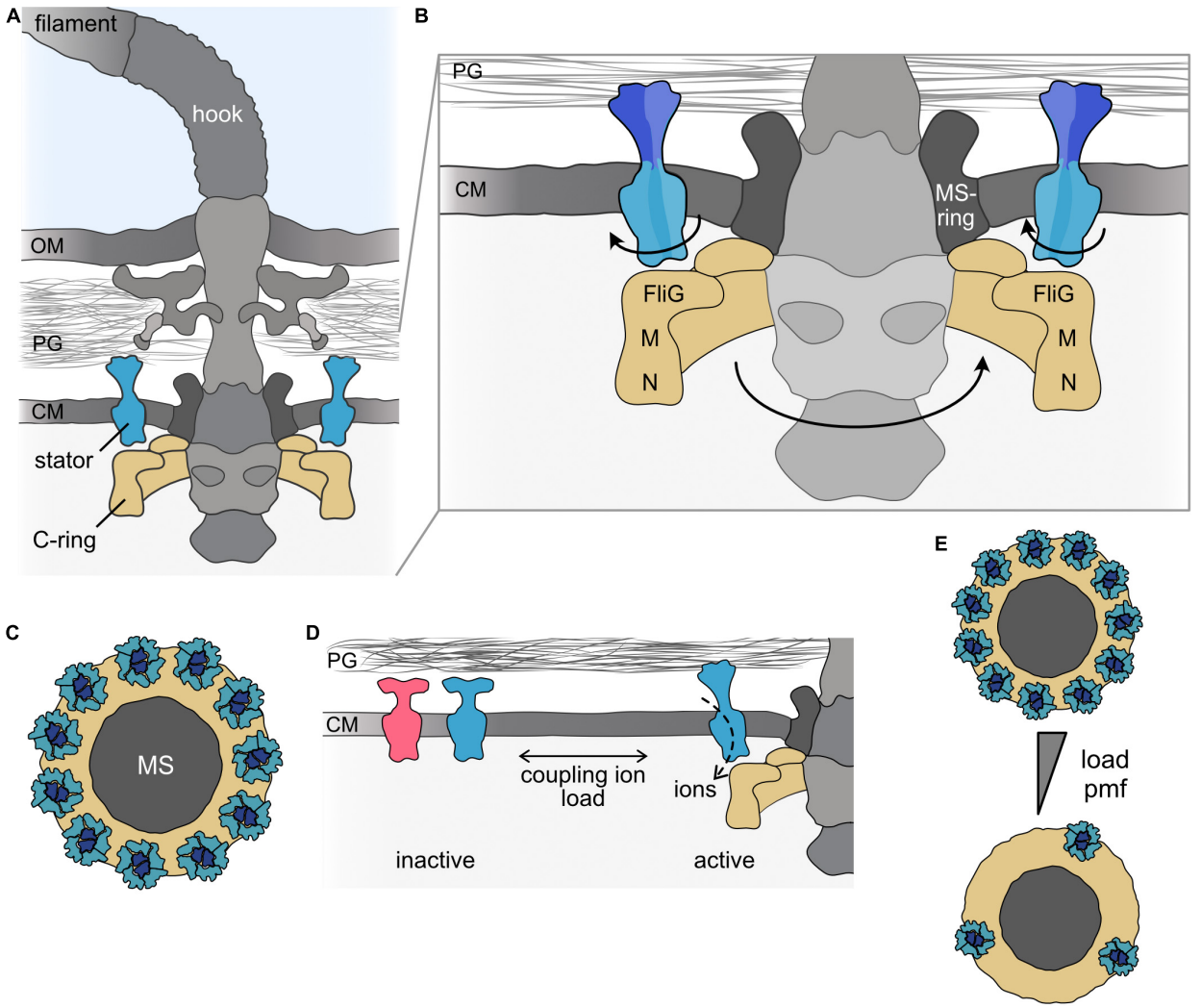


FIGURE 1 | The bacterial flagellar motor. **(A)** Cartoon of the bacterial flagellum of a Gram-negative bacterial cell. The flagellum consists of the long helical filament and the universal joint, the hook, which connects the filament and the flagellar motor. The motor is part of the basal body, which firmly anchors the flagellar apparatus in the cell envelope and, in addition, houses a type III–like protein export system. The main flagellar components involved in torque generation, the rotary C-ring and the stators, are shown in the same colors (here and throughout all figures). **(B)** Magnification of the flagellar motor. In the rotating motor, the ion-conducting stators (here blue) are anchored to the cell wall by a peptidoglycan-binding domain at the C-terminus of the B subunit of the stator. The ion flow leads to rotation of the A-subunits of the stator around the centered B-subunits. The rotation is transferred to the flagellar rotor, the C-ring (depicted in yellow), which consists of multiple copies of the proteins FliG, FliM, and FliN. Rotation of the C-ring is induced by electrostatic interaction of the A-subunits of the stator with FliG. **(C)** Top view on the transmembrane MS-ring (dark gray) to which the C-ring (yellow) is mounted. The stator units are positioned around the MS-ring above the C-ring. In a fully assembled motor of *E. coli*, about 11 stators are engaged with the rotor. **(D)** Stator units are produced as inactive precomplexes, which diffuse in the membrane. Upon engaging with the motor, the stators bind to the peptidoglycan and the ion channel opens. Stator units can also leave the motor to re-join the pool of inactive stator units in the cytoplasmic membrane. The equilibrium is affected by environmental signals, e.g., the concentration of the coupling ion and/or the load acting on the flagellar filament. Stator coupling and uncoupling occurs while the flagellum continues to rotate. Notably, more than one stator type can be present (indicated by the blue and red colors). **(E)** Under conditions of low load or at a low concentration of the coupling ion, only a few stators are engaged with the motor. A single stator is generally sufficient to drive flagellar rotation under conditions of low load. Under conditions of increasing load and/or increasing concentration of the coupling ion (indicated by the gray triangle), the maximal number of stators can be engaged. OM, outer membrane; PG, peptidoglycan; CM, cytoplasmic membrane; M, FliM; N, FliN; MS, MS-ring.

into the motor (Fung and Berg, 1995; Tipping et al., 2013b). A similar behavior occurs in the Na^+-dependent motor of *Vibrio alginolyticus*: The stators disengage from the motor when Na^+ in the environment is depleted or when Na^+ transport through the stator unit is blocked (Fukuoka et al., 2009; Kojima, 2015). The stability of rotor interactions with the stator may be regulated by conformational changes induced by binding of the coupling ion to the stator complex, (Kojima, 2015; Terahara et al., 2017a).

In addition to the concentration of the coupling ion, the load on the flagellum affects the stability of rotor–stator interactions and, by this, the number of stators engaged in the motor. Several studies provide evidence that the number of stators

synchronously engaged in the motor increases with progressively rising load on the flagellum and, *vice versa*, decreases when the torque 141 is lowered (Lele et al., 2013; Tipping et al., 2013a; Nord et al., 2017a,b; Wadhwa et al., 2019). The observations support a catch-bond model, where the interaction between the stator and the cell wall is strengthened with increasing force and is lowered with decreasing force (Nord et al., 2017a; Nirody et al., 2019). Thus, at very low load, only one or a few stators drive motor rotation, and engagement of the maximum number of stators occurs only at maximal load or when the rotation is stalled.

The dynamic assembly of the stator ring may save energy by restricting the ion flow through the flagellar motor when the load on the filament is low so that little advantage in propulsion would be gained by using more stators (Armitage and Berry, 2020). The mechanosensing property of the flagellar motor could also allow the cell to determine the viscosity of the environments or attachment to a solid substratum and to elicit an appropriate response (Chawla et al., 2020; Laventie and Jenal, 2020). However, as stator dynamics have been properly determined for only few species, it should be noted that not all bacteria may exhibit stator exchange, e.g., the stator ring of Spirochetes appears to be rather stable (Chang et al., 2019). On the other hand, a number of species have taken this mode of motor regulation one step further, as they can remodel the configuration and performance of the motor using different types of stators.

THE DYNAMIC HYBRID-FUELED MOTORS OF *Shewanella oneidensis* AND *Bacillus subtilis*

The majority of the bacteria that swim by flagellar motility encode a single specific stator unit to drive the corresponding flagellar motor. In contrast, there are a number of species that harbor genes encoding more than one distinct stator unit, among them species of the genus *Pseudomonas*, *Bacillus*, and *Shewanella* (Doyle et al., 2004; Ito et al., 2004, 2005; Toutain et al., 2005; Paulick et al., 2009; Thormann and Paulick, 2010). Some bacteria may use only one of the stators at a time by producing each of the stator units only under certain conditions. Alternatively, the bacteria could be able to use both stators synchronously. In two species, *Shewanella oneidensis* and *Bacillus subtilis*, it has been shown that the flagellar motor allows mixed stator configurations.

Shewanella oneidensis has two types of stators to power rotation of its single polar flagellum. One of them, PomAB, is powered by Na^+. The function of the second stator, MotAB, depends on H^+ gradients. PomAB is the dominant stator under all conditions tested, but full swimming speed, as a measure of motor performance, at low Na^+ concentrations requires the presence of MotAB (Paulick et al., 2009). In the absence of MotAB, about eight stator units are present in the flagellar motor, each of which is exchanged after some 30 s on average (**Figure 2**, upper panel). In contrast to the *Vibrio alginolyticus* motor, the PomAB stators do not uncouple from the motor, nor does the exchange half-time increase even at very low Na^+ concentrations. This suggests that the load on the motor affects PomAB binding

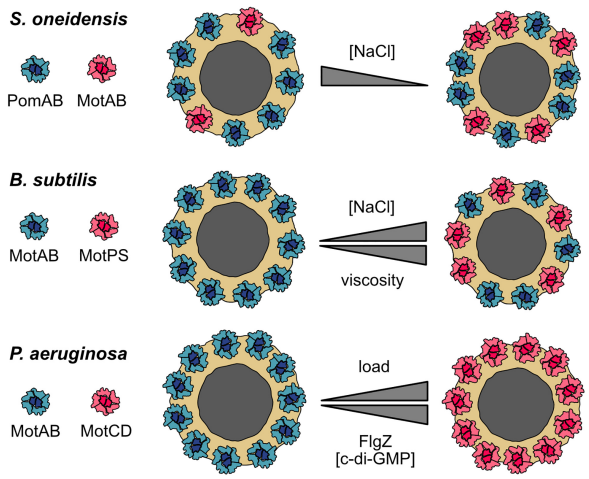


FIGURE 2 | Stator dynamics and dual stator systems. Cartoons of top views of the MS-ring and C-ring (gray and yellow, respectively) with the surrounding stator units. Upper panel: *S. oneidensis* possesses two types of stator units: Na^+-dependent PomAB (blue) and H^+-dependent MotAB (red). A low environmental concentration of Na^+ favors disengagement of PomAB from the motor and engagement of MotAB. At low Na^+ concentrations, the motor runs as a hybrid, synchronously using Na^+ and H^+ to drive rotation. The gray triangle indicates an increasing or decreasing concentration of the coupling ion Na^+. Middle panel: a similar motor–stator arrangement is present in *B. subtilis*, which also has H^+-dependent MotAB (blue) and Na^+-dependent MotPS (red) stators. The MotAB stator is dominant under most conditions, but increasing concentrations of Na^+ and higher loads favor the incorporation of MotPS into the active stator ring. The upper triangle represents differences in the environmental Na^+ concentration, the lower triangle increase or decrease in environmental viscosity. Lower panel: *P. aeruginosa* has two H^+-dependent individual stator units, MotAB (blue) and MotCD (red). MotAB powers rotation during planktonic free swimming, whereas MotCD is used under conditions of high load, e.g., during swarming across surfaces (indicated by the upper gray triangle). It should be noted that it is not clear if all MotAB stators are replaced. Notably, the regulator of the flagellar motor, FlgZ, when it is binds the secondary messenger c-di-GMP, uncouples MotCD (but not MotAB) from the motor (indicated by the lower gray triangle). MotCD then interacts with the membrane-localized diguanylate cyclase SadC to stimulate production of more c-di-GMP. Thus, at high c-di-GMP concentrations, cells of *P. aeruginosa* are unlikely to induce swarming but rather remain associated tightly with the surface (see the main text for explanations).

(Paulick et al., 2015). When MotAB was the only stator present, up to 11 stators were observed to be engaged with the motor. The rate of exchange of MotAB was similar to that of PomAB at low Na^+ concentrations, but the rate almost doubled at high levels of Na^+. When both stators were present, the motor exhibited a mixed configuration: In the presence of Na^+, the ratio of PomAB to MotAB was about 7:2 with a slow turnover of PomAB. In the absence of Na^+, the PomAB/MotAB ratio switched to 6:5, and there was a high rate of PomAB turnover (Paulick et al., 2015).

In agreement with cryo–electron tomography studies, the data indicate that, in the *S. oneidensis* motor, eleven stators can be synchronously engaged (Kaplan et al., 2019; Blagotinsek et al., 2020). In the presence of Na^+, eight of the 11 positions are occupied by the Na^+-dependent PomAB stator. The remaining vacant slots are taken up by MotAB stators, although these have only a meager effect on flagellar rotation. However, when the

concentration of Na^+ is low, the rate of MotAB incorporation increases and contributes significantly to motor performance (Paulick et al., 2009, 2015).

A similar motor–stator arrangement is present in *B. subtilis*, which possesses H^+-dependent stators (MotAB) and Na^+-conducting stators (MotPS) to power one type of flagellar motor (Ito et al., 2004, 2005). MotAB is the dominant stator for normal swimming, whereas MotPS-mediated swimming required appropriate conditions with respect to increased pH, adequate Na^+ levels, and high viscosity as well as elevated levels of stator proteins (Ito et al., 2004, 2005; Terahara et al., 2006; Chan et al., 2014). The *B. subtilis* motor is also highly dynamic (**Figure 2**, middle panel): At low environmental Na^+ concentrations, only MotAB is associated with the flagellar motor, but a mixed MotAB/MotPS motor–stator configuration occurs at elevated Na^+ levels (Terahara et al., 2017a). In addition, increased viscosity results in a decrease in MotAB stators interacting with the flagellar motor and favors engagement of the Na^+-dependent MotPS stators (Terahara et al., 2020). A high concentration of polysaccharides may also increase incorporation of MotPS into the motor (Terahara et al., 2017b, 2020). It should, however, be noted that, in the wild-type *B. subtilis* strain, a significant contributing role of MotPS to swimming or swarming motility under natural conditions has yet to be demonstrated.

Both studies cited above nicely demonstrate that both *S. oneidensis* and *B. subtilis* can adjust flagellar motor function by using more than one stator type. Notably, in both cases, hybrid motors can run synchronously on two fuels, H^+ and Na^+, and thus function over a wide range of Na^+ concentrations. The motor–stator configuration can be adjusted by "in-flight" stator swapping while the motor continues to operate. The general mechanism appears to be rather simple: two distinct populations of stator precomplexes compete with each other for incorporation into the stator ring. The actual configuration is dynamically determined by the stability of the interaction of the corresponding stator with the motor, which depends on the local environmental conditions as elaborated above. In *S. oneidensis,* the motor composition is certainly governed by the Na^+ concentration. In *B. subtilis*, the choice of stator type also depends upon the polysaccharide concentration and viscosity.

THE TWO-STATOR SYSTEM OF *Pseudomonas aeruginosa*

In the last paragraph, it was shown how bacteria may use a dynamic hybrid motor to run on two different fuels at the same time. However, there are also different examples of how different sets of stators can be used to upgrade the flagellar machinery. As the before-mentioned *S. oneidensis* and *B. subtilis*, *Pseudomonas aeruginosa* also possesses two different stator types to power rotation of the single polar flagellum (Doyle et al., 2004; Toutain et al., 2005). However, the *P. aeruginosa* system is different in that both stator units, MotAB and MotCD, are powered by H^+ gradients. MotAB is used primarily for planktonic swimming at normal viscosity, whereas MotCD powers flagella rotation during swarming across surfaces when the load on the flagellum is high (Doyle et al., 2004; Toutain et al., 2005; Kuchma et al., 2015). Similar to *B. subtilis*, stator selection may be regulated by environmental viscosity because MotCD-motor interactions are more stable at high load (**Figure 2**, lower panel). Thus, the dual stator setup of *P. aeruginosa* allows a configuration better suited to motility at high load. It will be highly interesting to further study the stator exchange dynamics of this system in dependence of increasing and decreasing load. In addition, as both depend on the same coupling ion, the dual stators of *P. aeruginosa* provide an excellent model to investigate, which structural properties of the stator units allow the generation of higher torque.

Intriguingly, the *P. aeruginosa* dual stator system was additionally demonstrated to regulate and be regulated at another level: MotCD (but not MotAB) can additionally be bound by the c-di-GMP–responsive regulator FlgZ, which prevents functional rotor–stator interaction (Baker et al., 2016). Thus, a high c-di-GMP level inhibits MotCD engagement and swarming motility, and the cell rather commits to surface adhesion and biofilm formation. Notably, disengaged MotCD in the cytoplasmic membrane can make direct contact with the membrane-localized diguanylate cyclase SadC (Baker et al., 2019). This interaction stimulates c-di-GMP synthesis by SadC, which further promotes a surface-associated lifestyle. Thus, MotCD of *P. aeruginosa* not only functions as a high-duty stator for motility at elevated load but also as structural component of a feed-forward regulator that influences the decision to adopt a planktonic or surface-associated lifestyle.

IMPLICATIONS AND FURTHER QUESTIONS

The studies so far have demonstrated that the dynamics underlying the interactions between the stator and the flagellar motor are used by bacteria to optimize performance of the motor according to the environmental conditions. There are, however, still numerous unsolved questions and fascinating new flagellar motor systems to be discovered.

What is the full range of motor configurations that exist? To date, there are three systems with multiple stators that have been characterized in detail, as elaborated above. There are, however, many more species that are likely to expand the range of possibilities for ways to regulate motor functions by stator swapping. *Aeromonas hydrophila* is among the species with multiple stators. It possesses two Na^+-dependent stators (PomA1B1 and PomA2B2) to power its single polar flagellum (Wilhelms et al., 2009). Each stator is able to power swimming at normal and elevated viscosity. However, PomA1B1 appears to function better at lower Na^+ concentrations. It is conceivable that *A. hydrophila* also dynamically adjusts the rotor–stator configuration in response to changes in the external Na^+ concentration, but this remains to be shown.

An analysis of the available genome sequences indicates that some bacterial species, e.g., *Desulfovibrio* sp., not only possess two stator isoforms but also have three or even four stator units that may contribute to motor function (Thormann and Paulick, 2010). Thus, it may be hypothesized that motor systems

synchronously powered by three or four types of stator units exist in nature to extend further the range over which the function of a flagellar motor may be regulated by stator switching. However, as these motor–stator systems have not yet been characterized, this possibility remains speculative for the time being.

How is stator selection regulated? As elaborated above, the thorough studies demonstrate that the motor–stator configuration can be passively adjusted by the stability of the interaction of one or more stator types with the motor. This regulation may depend on the concentration of the corresponding coupling ion or the load on the motor. However, it has been demonstrated that additional mechanisms to regulate stator selection exist, and we expect additional mechanisms to be identified in the future.

As the abundance of a stator unit has been shown to affect incorporation into the motor (Terahara et al., 2006), stator selection may additionally be mediated by specific upregulation or downregulation of the corresponding stator, as suggested for *A. hydrophila* (Wilhelms et al., 2009). This may be a way of affecting stator selection in other bacteria as well.

In addition, as demonstrated for *P. aeruginosa*, stators can be specifically uncoupled from the motor by binding of regulatory proteins, such as FlgZ in the presence of elevated levels of the secondary messenger c-di-GMP (Baker et al., 2016). Several such c-di-GMP–responsive regulators that may interfere with rotor–stator interaction have been described, such as MotI in *B. subtilis* or YcgR in *E. coli* (Boehm et al., 2010; Fang and Gomelsky, 2010; Paul et al., 2010; Gao et al., 2013; Subramanian et al., 2017; Subramanian and Kearns, 2019). Therefore, stator selection by regulator binding to the stators could occur in species with multiple stator sets. Potential regulators do not necessarily have to be c-di-GMP–binding proteins and may also be involved in other cellular processes. An example for such a protein is *B. subtilis* EpsE, a glycosyltransferase involved in synthesis of an extracellular polysaccharide. It moonlights as a clutch for the flagellar motor by binding to the flagellar C-ring (Blair et al., 2008).

How did hybrid flagellar motors evolve? Generally, flagellar systems with two or more stator units may have evolved either by gene duplication followed by development of functional divergence through mutations or by the genes encoding another stator system having been acquired by lateral gene transfer. Previous studies in which stators were swapped between *E. coli* and *Vibrio* sp. showed that "foreign" stators using different coupling ions can interact with the flagellar C-ring to enable motility, albeit at a significant cost in motor performance. However, in many cases, gain-of-function mutants readily emerged, indicating that even a few mutations are sufficient to improve motor–stator interaction significantly (Gosink and Häse, 2000; Asai et al., 2003; Sowa et al., 2005). In all species discussed in detail above—*S. oneidensis*, *B. subtilis*, *P. aeruginosa*, and *A. hydrophila*—the two stator systems share little identity at the level of amino acid sequence. This fact, and a significant similarity of one the stators to those from other species, suggests that, in all four cases, a second "foreign" stator has been acquired and evolved to become a helpful functional upgrade of the flagellar machinery. Notably, secondary stator systems are present in many species of *Pseudomonas*, *Bacillus*, and *Aeromonas* (Thormann and Paulick, 2010), suggesting that acquisition of the second stator occurred before phylogenetic divergence. In contrast, the MotAB stator system of *S. oneidensis* appears to be a rather recent acquisition that is present only in this particular species within the genus *Shewanella*. It may have been selected to facilitate adaptation from a marine to a fresh-water environment (Paulick et al., 2009, 2015; Brenzinger et al., 2016).

Together, the conservation of rotor–stator interactions enables functional upgrades of the flagellar motor by a later acquisition of additional stator types. The dynamics involved in stator coupling to the motor allow mixed stator configurations, even enabling the motor to use two different fuels synchronously. Motor performance can be constantly adjusted by in-flight stator swapping. So far, we have characterized a mere handful of systems, and many discoveries on flagellar systems with multiple stators remain to be discovered. The acquisition and functional adaptation of novel stators is an outstanding model system to study the mechanism of rotor–stator interaction, in particular, and the functional evolution of bacterial nanomachines, in general.

AUTHOR CONTRIBUTIONS

KT conceptualized and wrote the manuscript.

FUNDING

This study was funded by the Deutsche Forschungsgemeinschaft DFG (TH 831/4-1) and the Max Planck Society.

ACKNOWLEDGMENTS

KT gratefully acknowledges the Deutsche Forschungsgemeinschaft DFG (TH 831/4-1) and the Max Planck Society for providing funding of the author's lab contributions and highly appreciates the assistance of Meike Schwan in figure preparation and the input of Matthew McIntosh who critically read and commented on the manuscript.

REFERENCES

Armitage, J. P., and Berry, R. M. (2020). Assembly and Dynamics of the Bacterial Flagellum. *Annu. Rev. Microbiol.* 74, 181–200. doi: 10.1146/annurev-micro-090816-093411

Asai, Y., Kojima, S., Kato, H., Nishioka, N., Kawagishi, I., and Homma, M. (1997). Putative channel components for the fast-rotating sodium-driven flagellar motor of a marine bacterium. *J. Bacteriol.* 179, 5104–5110. doi: 10.1128/jb.179.16.5104-5110.1997

Asai, Y., Yakushi, T., Kawagishi, I., and Homma, M. (2003). Ion-coupling determinants of Na^+-driven and H^+-driven flagellar motors. *J. Mol. Biol.* 327, 453–463. doi: 10.1016/s0022-2836(03)00096-2

Baker, A. E., Diepold, A., Kuchma, S. L., Scott, J. E., Ha, D. G., Orazi, G., et al. (2016). PilZ domain protein FlgZ mediates cyclic di-GMP-dependent swarming motility control in *Pseudomonas aeruginosa*. *J. Bacteriol.* 198, 1837–1846. doi: 10.1128/JB.00196-16

Baker, A. E., Webster, S. S., Diepold, A., Kuchma, S. L., Bordeleau, E., Armitage, J. P., et al. (2019). Flagellar stators stimulate c-di-GMP production by *Pseudomonas aeruginosa*. *J. Bacteriol.* 201, e741–e718. doi: 10.1128/JB.00741-18

Beeby, M., Ribardo, D. A., Brennan, C. A., Ruby, E. G., Jensen, G. J., and Hendrixson, D. R. (2016). Diverse high-torque bacterial flagellar motors assemble wider stator rings using a conserved protein scaffold. *Proc. Natl. Acad. Sci.U.S.A.* 113, 1917–1926. doi: 10.1073/pnas.1518952113

Berg, H. C. (2003). The rotary motor of bacterial flagella. *Annu. Rev. Biochem.* 72, 19–54. doi: 10.1146/annurev.biochem.72.121801.161737

Berg, H. C., and Anderson, R. A. (1973). Bacteria swim by rotating their flagellar filaments. *Nature* 245, 380–382. doi: 10.1038/245380a0

Blagotinsek, V., Schwan, M., Steinchen, W., Mrusek, D., Hook, J. C., Rossmann, F., et al. (2020). An ATP-dependent partner switch links flagellar C-ring assembly with gene expression. *Proc. Natl. Acad. Sci.U.S.A.* 117, 20826–20835. doi: 10.1073/pnas.2006470117

Blair, D. F., and Berg, H. C. (1988). Restoration of torque in defective flagellar motors. *Science* 242, 1678–1681. doi: 10.1126/science.2849208

Blair, K. M., Turner, L., Winkelman, J. T., Berg, H. C., and Kearns, D. B. (2008). A molecular clutch disables flagella in the *Bacillus subtilis* biofilm. *Science* 320, 1636–1638. doi: 10.1126/science.1157877

Block, S. M., and Berg, H. C. (1984). Successive incorporation of force-generating units in the bacterial rotary motor. *Nature* 309, 470–472. doi: 10.1038/309470a0

Boehm, A., Kaiser, M., Li, H., Spangler, C., Kasper, C. A., Ackermann, M., et al. (2010). Second messenger-mediated adjustment of bacterial swimming velocity. *Cell* 141, 107–116. doi: 10.1016/j.cell.2010.01.018

Braun, T. F., and Blair, D. F. (2001). Targeted disulfide cross-linking of the MotB protein of *Escherichia coli*: evidence for two H(+) channels in the stator Complex. *Biochemistry* 40, 13051–13059. doi: 10.1021/bi011264g

Brenzinger, S., Dewenter, L., Delalez, N. J., Leicht, O., Berndt, V., Paulick, A., et al. (2016). Mutations targeting the plug-domain of the *Shewanella oneidensis* proton-driven stator allow swimming at increased viscosity and under anaerobic conditions. *Mol. Microbiol.* 102, 925–938. doi: 10.1111/mmi.13499

Chan, J. M., Guttenplan, S. B., and Kearns, D. B. (2014). Defects in the flagellar motor increasesynthesis of poly-γ-glutamate in *Bacillus subtilis*. *J. Bacteriol.* 196, 740–753. doi: 10.1128/JB.01217-13

Chang, Y., Moon, K. H., Zhao, X., Norris, S. J., Motaleb, M. A., and Liu, J. (2019). Structural insightsinto flagellar stator-rotor interactions. *Elife* 17:e48979. doi: 10.7554/eLife.48979

Chawla, R., Gupta, R., Lele, T. P., and Lele, P. P. (2020). A skeptic's guide to bacterial mechanosensing. *J. Mol. Biol.* 432, 523–533. doi: 10.1016/j.jmb.2019.09.004

Chun, S. Y., and Parkinson, J. S. (1988). Bacterial motility: membrane topology of the *Escherichia coli* MotB protein. *Science* 239, 276–278. doi: 10.1126/science.2447650

De Mot, R., and Vanderleyden, J. (1994). The C-terminal sequence conservation between OmpA-related outer membrane proteins and MotB suggests a common function in both gram-positive and gram-negative bacteria, possibly in the interaction of these domains with peptidoglycan. *Mol. Microbiol.* 12, 333–334. doi: 10.1111/j.1365-2958.1994.tb01021.x

Dean, G. E., Macnab, R. M., Stader, J., Matsumura, P., and Burks, C. (1984). Gene sequence and predicted amino acid sequence of the MotA protein, a membrane-associated protein required for flagellar rotation in *Escherichia coli*. *J. Bacteriol.* 159, 991–999. doi: 10.1128/jb.159.3.991-999.1984

Deme, J. C., Johnson, S., Vickery, O., Aron, A., Monkhouse, H., Griffiths, T., et al. (2020). Structures of the stator complex that drives rotation of the bacterial flagellum. *Nat. Microbiol.* 5, 1553–1564. doi: 10.1038/s41564-020-0788-8

Doyle, T. B., Hawkins, A. C., and McCarter, L. L. (2004). The complex flagellar torque generator of *Pseudomonas aeruginosa*. *J. Bacteriol.* 186, 6341–6350. doi: 10.1128/JB.186.19.6341-6350.2004

Fang, X., and Gomelsky, M. (2010). A post-translational, c-di-GMP-dependent mechanism regulating flagellar motility. *Mol. Microbiol.* 76, 1295–1305. doi: 10.1111/j.1365-2958.2010.07179.x

Fenchel, T. (2002). Microbial behavior in a heterogeneous world. *Science* 296, 1068–1071. doi: 10.1126/science.1070118

Francis, N. R., Sosinsky, G. E., Thomas, D., and DeRosier, D. J. (1994). Isolation, characterization and structure of bacterial flagellar motors containing the switch complex. *J. Mol. Biol.* 235, 1261–1270. doi: 10.1006/jmbi.1994.1079

Fukuoka, H., Wada, T., Kojima, S., Ishijima, A., and Homma, M. (2009). Sodium-dependent dynamic assembly of membrane complexes in sodium-driven flagellar motors. *Mol. Microbiol.* 71, 825–835. doi: 10.1111/j.1365-2958.2008.06569.x

Fung, D. C., and Berg, H. C. (1995). Powering the flagellar motor of *Escherichia coli* with an external voltage source. *Nature* 375, 809–812. doi: 10.1038/375809a0

Gao, X., Mukherjee, S., Matthews, P. M., Hammad, L. A., Kearns, D. B., and Dann, C. E. (2013). Functional characterization of core components of the *Bacillus subtilis* cyclic-di-GMP signaling pathway. *J. Bacteriol.* 195, 4782–4792. doi: 10.1128/JB.00373-13

Gosink, K. K., and Häse, C. C. (2000). Requirements for conversion of the Na(+)-driven flagellar motor of *Vibrio cholerae* to the H(+)-driven motor of *Escherichia coli*. *J. Bacteriol.* 182, 4234–4240. doi: 10.1128/JB.182.15.4234-4240.2000

Gude, S., Pinçe, E., Taute, K. M., Seinen, A.-B., Shimizu, T. S., and Tans, S. J. (2020). Bacterial coexistence driven by motility and spatial competition. *Nature* 578, 588–592. doi: 10.1038/s41586-020-2033-2

Hirota, N., Kitada, M., and Imae, Y. (1981). Flagellar motors of alkalophilic bacillus are powered by an electrochemical potential gradient of Na^+. *FEBS Lett.* 132, 278–280. doi: 10.1016/0014-5793(81)81178-7

Hosking, E. R., Vogt, C., Bakker, E. P., and Manson, M. D. (2006). The *Escherichia coli* MotAB proton channel unplugged. *J. Mol. Biol.* 364, 921–937. doi: 10.1016/j.jmb.2006.09.035

Hu, H., Santiveri, M., Wadhwa, N., Berg, H. C., Erhardt, M., and Taylor, N. M. I. (2021). Structural basis of torque generation in the bi-directional bacterial flagellar motor. *Trends Biochem. Sci.* 47, 160–172 doi: 10.1016/j.tibs.2021.06.005

Ito, M., Hicks, D. B., Henkin, T. M., Guffanti, A. A., Powers, B. D., Zvi, L., et al. (2004). MotPS is the stator-force generator for motility of alkaliphilic Bacillus, and its homologue is a second functional Mot in *Bacillus subtilis*. *Mol. Microbiol.* 53, 1035–1049. doi: 10.1111/j.1365-2958.2004.04173.x

Ito, M., Terahara, N., Fujinami, S., and Krulwich, T. A. (2005). Properties of motility in *Bacillus subtilis* powered by the H^+-coupled MotAB flagellar stator. Na^+-coupled MotPS or hybrid stators MotAS or MotPB. *J. Mol. Biol.* 352, 396–408. doi: 10.1016/j.jmb.2005.07.030

Jarrell, K. F., and McBride, M. J. (2008). The surprisingly diverse ways that prokaryotes move. *Nat Rev. Microbiol.* 6, 466–476. doi: 10.1038/nrmicro1900

Johnson, S., Furlong, E. J., Deme, J. C., Nord, A. L., Caesar, J. J. E., Chevance, F. F. V., et al. (2021). Molecular structure of the intact bacterial flagellar basal body. *Nat. Microbiol.* 6, 712–721. doi: 10.1038/s41564-021-00895-y

Kaplan, M., Subramanian, P., Ghosal, D., Oikonomou, C. M., Pirbadian, S., Starwalt-Lee, R., et al. (2019). In situ imaging of the bacterial flagellar motor disassembly and assembly processes. *EMBO J.* 38:e100957. doi: 10.15252/embj.2018100957

Kearns, D. B. (2010). A field guide to bacterial swarming motility. *Nat. Rev. Microbiol.* 8, 634–644. doi: 10.1038/nrmicro2405

Khan, S., Dapice, M., and Reese, T. S. (1988). Effects of *mot* gene expression on the structure of the flagellar motor. *J. Mol. Biol.* 202, 575–584. doi: 10.1016/0022-2836(88)90287-2

Kojima, S. (2015). Dynamism and regulation of the stator, the energy conversion complex of the bacterial flagellar motor. *Curr. Opin. Microbiol.* 28, 66–71. doi: 10.1016/j.mib.2015.07.015

Kojima, S., Imada, K., Sakuma, M., Sudo, Y., Kojima, C., Minamino, T., et al. (2009). Stator assembly and activation mechanism of the flagellar motor by the periplasmic region of MotB. *Mol. Microbiol.* 73, 710–718. doi: 10.1111/j.1365-2958.2009.06802.x

Kojima, S., Takao, M., Almira, G., Kawahara, I., Sakuma, M., Homma, M., et al. (2018). The helix rearrangement in the periplasmic domain of the flagellar stator B subunit activates peptidoglycan binding and ion Influx. *Structure* 26, 590.e–598.e. doi: 10.1016/j.str.2018.02.016

Kuchma, S. L., Delalez, N. J., Filkins, L. M., Snavely, E. A., Armitage, J. P., and O'Toole, G. A. (2015). Cyclic di-GMP-mediated repression of swarming

motility by *Pseudomonas aeruginosa* PA14 requires the MotAB stator. *J. Bacteriol.* 197, 420–430. doi: 10.1128/JB.02130-14

Kühn, M. J., Schmidt, F. K., Eckhardt, B., and Thormann, K. M. (2017). Bacteria exploit a polymorphic instability of the flagellar filament to escape from traps. *Proc. Natl. Acad. Sci.U.S.A.* 114, 6340–6345. doi: 10.1073/pnas.1701644114

Laventie, B.-J., and Jenal, U. (2020). Surface sensing and adaptation in bacteria. *Annu. Rev. Microbiol.* 74, 735–760. doi: 10.1146/annurev-micro-012120-063427

Leake, M. C., Chandler, J. H., Wadhams, G. H., Bai, F., Berry, R. M., and Armitage, J. P. (2006). Stoichiometry and turnover in single, functioning membrane protein complexes. *Nature* 443, 355–358. doi: 10.1038/nature05135

Lele, P. P., Hosu, B. G., and Berg, H. C. (2013). Dynamics of mechanosensing in the bacterial flagellar motor. *Proc. Natl. Acad. Sci.* 110, 11839–11844. doi: 10.1073/pnas.1305885110

Li, N., Kojima, S., and Homma, M. (2011). Sodium-driven motor of the polar flagellum in marine bacteria *Vibrio*. *Genes Cells* 16, 985–999. doi: 10.1111/j.1365-2443.2011.01545.x

Manson, M. D., Tedesco, P., Berg, H. C., Harold, F. M., and Van der Drift, C. (1977). A protonmotive force drives bacterial flagella. *Proc. Natl. Acad. Sci.U.S.A.* 74, 3060–3064. doi: 10.1073/pnas.74.7.3060

Matsura, S., Shioi, J., and Imae, Y. (1977). Motility in *Bacillus subtilis* driven by an artificial protonmotive force. *FEBS Lett.* 82, 187–190. doi: 10.1016/0014-5793(77)80581-4

Minamino, T., Kinoshita, M., and Namba, K. (2019). Directional switching mechanism of the bacterial flagellar motor. *Comput. Struct. Biotechnol. J.* 17, 1075–1081. doi: 10.1016/j.csbj.2019.07.020

Morimoto, Y. V., Nakamura, S., Kami-ike, N., Namba, K., and Minamino, T. (2010). Charged residues in the cytoplasmic loop of MotA are required for stator assembly into the bacterial flagellar motor. *Mol. Microbiol.* 78, 1117–1129. doi: 10.1111/j.1365-2958.2010.07391.x

Muramoto, K., Sugiyama, S., Cragoe, E. J., and Imae, Y. (1994). Successive inactivation of the force-generating units of sodium-driven bacterial flagellar motors by a photoreactive amiloride analog. *J. Biol. Chem.* 269, 3374–3380. doi: 10.1016/S0021-9258(17)41872-2

Nirody, J. A., Nord, A. L., and Berry, R. M. (2019). Load-dependent adaptation near zero load in the bacterial flagellar motor. *J. R. Soc. Interface* 16:20190300. doi: 10.1098/rsif.2019.0300

Nord, A. L., Gachon, E., Perez-Carrasco, R., Nirody, J. A., Barducci, A., Berry, R. M., et al. (2017a). Catch bond drives stator mechanosensitivity in the bacterial flagellar motor. *Proc. Natl. Acad. Sci.* 114, 12952–12957. doi: 10.1073/pnas.1716002114

Nord, A. L., Sowa, Y., Steel, B. C., Lo, C.-J., and Berry, R. M. (2017b). Speed of the bacterial flagellar motor near zero load depends on the number of stator units. *Proc. Natl. Acad. Sci.U.S.A.* 114, 11603–11608. doi: 10.1073/pnas.1708054114

Paul, K., Brunstetter, D., Titen, S., and Blair, D. F. (2011). A molecular mechanism of direction switching in the flagellar motor of *Escherichia coli*. *Proc. Natl. Acad. Sci.U.S.A.* 108, 17171–17176. doi: 10.1073/pnas.1110111108

Paul, K., Nieto, V., Carlquist, W. C., Blair, D. F., and Harshey, R. M. (2010). The c-di-GMP binding protein YcgR controls flagellar motor direction and speed to affect chemotaxis by a "backstop brake" mechanism. *Mol. Cell* 38, 128–139. doi: 10.1016/j.molcel.2010.03.001

Paulick, A., Delalez, N. J., Brenzinger, S., Steel, B. C., Berry, R. M., Armitage, J. P., et al. (2015). Dual stator dynamics in the *Shewanella oneidensis* MR-1 flagellar motor. *Mol. Microbiol.* 96, 993–1001. doi: 10.1111/mmi.12984

Paulick, A., Koerdt, A., Lassak, J., Huntley, S., Wilms, I., Narberhaus, F., et al. (2009). Two different stator systems drive a single polar flagellum in *Shewanella oneidensis* MR-1. *Mol. Microbiol.* 71, 836–850. doi: 10.1111/j.1365-2958.2008.06570.x

Reichenbach, T., Mobilia, M., and Frey, E. (2007). Mobility promotes and jeopardizes biodiversity in rock–paper–scissors games. *Nature* 448, 1046–1049. doi: 10.1038/nature06095

Reid, S. W., Leake, M. C., Chandler, J. H., Lo, C.-J., Armitage, J. P., and Berry, R. M. (2006). The maximum number of torque-generating units in the flagellar motor of *Escherichia coli* is at least 11. *Proc. Natl. Acad. Sci.U.S.A.* 103, 8066–8071. doi: 10.1073/pnas.0509932103

Santiveri, M., Roa-Eguiara, A., Kühne, C., Wadhwa, N., Hu, H., Berg, H. C., et al. (2020). Structure and function of stator units of the bacterial flagellar motor. *Cell* 183, 244.e–257.e. doi: 10.1016/j.cell.2020.08.016

Silverman, M., Matsumura, P., and Simon, M. (1976). The identification of the *mot* gene product with *Escherichia coli*-lambda hybrids. *Proc. Natl. Acad. Sci.U.S.A.* 73, 3126–3130. doi: 10.1073/pnas.73.9.3126

Silverman, M., and Simon, M. (1974). Flagellar rotation and the mechanism of bacterial motility. *Nature* 249, 73–74. doi: 10.1038/249073a0

Sowa, Y., and Berry, R. M. (2008). Bacterial flagellar motor. *Q. Rev. Biophys.* 41, 103–132. doi: 10.1017/S0033583508004691

Sowa, Y., Rowe, A. D., Leake, M. C., Yakushi, T., Homma, M., Ishijima, A., et al. (2005). Direct observation of steps in rotation of the bacterial flagellar motor. *Nature* 437, 916–919. doi: 10.1038/nature04003

Stader, J., Matsumura, P., Vacante, D., Dean, G. E., and Macnab, R. M. (1986). Nucleotide sequence of the *Escherichia coli motB* gene and site-limited incorporation of its product into the cytoplasmic membrane. *J. Bacteriol.* 166, 244–252. doi: 10.1128/jb.166.1.244-252.1986

Stock, D., Namba, K., and Lee, L. K. (2012). Nanorotors and self-assembling macromolecular machines: The torque ring of the bacterial flagellar motor. *Curr. Opin. Biotechnol.* 23, 545–554. doi: 10.1016/j.copbio.2012.01.008

Subramanian, S., Gao, X., Dann, C. E., and Kearns, D. B. (2017). MotI (DgrA) acts as a molecular clutch on the flagellar stator protein MotA in *Bacillus subtilis*. *Proc. Natl. Acad. Sci.* 114, 13537–13542. doi: 10.1073/pnas.1716231114

Subramanian, S., and Kearns, D. B. (2019). Functional regulators of bacterial flagella. *Annu. Rev. Microbiol.* 73, 225–246. doi: 10.1146/annurev-micro-020518-115725

Tan, J., Zhang, X., Wang, X., Xu, C., Chang, S., Wu, H., et al. (2021). Structural basis of assembly and torque transmission of the bacterial flagellar motor. *Cell* 184, 2665–2679. doi: 10.1016/j.cell.2021.03.057

Terahara, N., Fujisawa, M., Powers, B., Henkin, T. M., Krulwich, T. A., and Ito, M. (2006). An intergenic stem-loop mutation in the *Bacillus subtilis ccpA-motPS* operon increases *motPS* transcription and the MotPS contribution to motility. *J. Bacteriol.* 188, 2701–2705. doi: 10.1128/JB.188.7.2701-2705.2006

Terahara, N., Kodera, N., Uchihashi, T., Ando, T., Namba, K., and Minamino, T. (2017a). Na^+-induced structural transition of MotPS for stator assembly of the *Bacillus* flagellar motor. *Sci. Adv.* 3:eaao4119. doi: 10.1126/sciadv.aao4119

Terahara, N., Noguchi, Y., Nakamura, S., Kami-ike, N., Ito, M., Namba, K., et al. (2017b). Load- and polysaccharide-dependent activation of the Na^+-type MotPS stator in the *Bacillus subtilis* flagellar motor. *Sci. Rep.* 7:46081. doi: 10.1038/srep46081

Terahara, N., Namba, K., and Minamino, T. (2020). Dynamic exchange of two types of stator units in *Bacillus subtilis* flagellar motor in response to environmental changes. *Comput. Struct. Biotechnol. J.* 18, 2897–2907. doi: 10.1016/j.csbj.2020.10.009

Terashima, H., Kojima, S., and Homma, M. (2021). Site-directed crosslinking identifies the stator-rotor interaction surfaces in a hybrid bacterial flagellar motor. *J. Bacteriol.* 203, e00016–21. doi: 10.1128/JB.00016-21

Thomas, D. R., Francis, N. R., Xu, C., and DeRosier, D. J. (2006). The three-dimensional structure of the flagellar rotor from a clockwise-locked mutant of *Salmonella enterica* serovar Typhimurium. *J. Bacteriol.* 188, 7039–7048. doi: 10.1128/JB.00552-06

Thormann, K. M., and Paulick, A. (2010). Tuning the flagellar motor. *Microbiology* 156, 1275–1283. doi: 10.1099/mic.0.029595-0

Tipping, M. J., Delalez, N. J., Lim, R., Berry, R. M., and Armitage, J. P. (2013a). Load-dependent assembly of the bacterial flagellar motor. *mBio* 4, e551–e513. doi: 10.1128/mBio.00551-13

Tipping, M. J., Steel, B. C., Delalez, N. J., Berry, R. M., and Armitage, J. P. (2013b). Quantification of flagellar motor stator dynamics through in vivo proton-motive force control. *Mol. Microbiol.* 87, 338–347. doi: 10.1111/mmi.12098

Toutain, C. M., Zegans, M. E., and O'Toole, G. A. (2005). Evidence for two flagellar stators and their role in the motility of *Pseudomonas aeruginosa*. *J. Bacteriol.* 187, 771–777. doi: 10.1128/JB.187.2.771-777.2005

Van Way, S. M., Hosking, E. R., Braun, T. F., and Manson, M. D. (2000). Mot protein assembly into the bacterial flagellum: a model based on mutational analysis of the *motB* gene. *J. Mol. Biol.* 297, 7–24. doi: 10.1006/jmbi.2000.3548

Wadhwa, N., and Berg, H. C. (2021). Bacterial motility: machinery and mechanisms. *Nat. Rev. Microbiol.* 20, 161–173. doi: 10.1038/s41579-021-00626-4

Wadhwa, N., Phillips, R., and Berg, H. C. (2019). Torque-dependent remodeling of the bacterial flagellar motor. *Proc. Natl. Acad. Sci.U.S.A.* 116, 11764–11769. doi: 10.1073/pnas.1904577116

Wilhelms, M., Vilches, S., Molero, R., Shaw, J. G., Tomás, J. M., and Merino, S. (2009). Two redundant sodium-driven stator motor proteins are involved in *Aeromonas hydrophila* polar flagellum rotation. *J. Bacteriol.* 191, 2206–2217. doi: 10.1128/JB.01526-08

Zhou, J., and Blair, D. F. (1997). Residues of the cytoplasmic domain of MotA essential for torque generation in the bacterial flagellar motor. *J. Mol. Biol.* 273, 428–439. doi: 10.1006/jmbi.1997.1316

Zhou, J., Fazzio, R. T., and Blair, D. F. (1995). Membrane topology of the MotA protein of *Escherichia coli*. *J. Mol. Biol.* 251, 237–242. doi: 10.1006/jmbi.1995.0431

Zhou, J., Lloyd, S. A., and Blair, D. F. (1998). Electrostatic interactions between rotor and stator in the bacterial flagellar motor. *Proc. Natl. Acad. Sci.U.S.A.* 95, 6436–6441. doi: 10.1073/pnas.95.11.6436

Zhu, S., and Gao, B. (2020). Bacterial flagella loss under starvation. *Trends Microbiol.* 28, 785–788. doi: 10.1016/j.tim.2020.05.002

Zhu, S., Takao, M., Li, N., Sakuma, M., Nishino, Y., Homma, M., et al. (2014). Conformational change in the periplamic region of the flagellar stator coupled with the assembly around the rotor. *Proc. Natl. Acad. Sci.U.S.A.* 111, 13523–13528. doi: 10.1073/pnas.1324201111

Conflict of Interest: The author declares that the research was conducted in the absence of any commercial or financial relationships that could be construed as a potential conflict of interest.

Publisher's Note: All claims expressed in this article are solely those of the authors and do not necessarily represent those of their affiliated organizations, or those of the publisher, the editors and the reviewers. Any product that may be evaluated in this article, or claim that may be made by its manufacturer, is not guaranteed or endorsed by the publisher.

Copyright © 2022 Thormann. This is an open-access article distributed under the terms of the Creative Commons Attribution License (CC BY). The use, distribution or reproduction in other forums is permitted, provided the original author(s) and the copyright owner(s) are credited and that the original publication in this journal is cited, in accordance with accepted academic practice. No use, distribution or reproduction is permitted which does not comply with these terms.

frontiers | Frontiers in Microbiology

REVIEW
published: 27 April 2022
doi: 10.3389/fmicb.2022.869187

The Periplasmic Domain of the Ion-Conducting Stator of Bacterial Flagella Regulates Force Generation

Michio Homma and Seiji Kojima**

Division of Biological Science, Graduate School of Science, Nagoya University, Nagoya, Japan

The bacterial flagellar stator is a unique ion-conducting membrane protein complex composed of two kinds of proteins, the A subunit and the B subunit. The stator couples the ion-motive force across the membrane into rotational force. The stator becomes active only when it is incorporated into the flagellar motor. The periplasmic region of the B subunit positions the stator by using the peptidoglycan-binding (PGB) motif in its periplasmic C-terminal domain to attach to the cell wall. Functional studies based on the crystal structures of the C-terminal domain of the B subunit ($MotB_C$ or $PomB_C$) reveal that a dramatic conformational change in a characteristic α-helix allows the stator to conduct ions efficiently and bind to the PG layer. The plug and the following linker region between the transmembrane (TM) and PG-binding domains of the B subunit function in regulating the ion conductance. In *Vibrio* spp., the transmembrane protein FliL and the periplasmic MotX and MotY proteins also contribute to the motor function. In this review, we describe the functional and structural changes which the stator units undergo to regulate the activity of the stator to drive flagellar rotation.

Keywords: FliL, MotX, MotY, peptidoglycan, flagellar motor

OPEN ACCESS

Edited by:
Pushkar Lele,
Texas A&M University, United States

Reviewed by:
Michael Manson,
Texas A&M University, United States
Matt Arthur Baker,
University of New South Wales, Australia

****Correspondence:***
Michio Homma
g44416a@cc.nagoya-u.ac.jp
Seiji Kojima
z47616a@cc.nagoya-u.ac.jp

Specialty section:
This article was submitted to Microbial Physiology and Metabolism, a section of the journal Frontiers in Microbiology

Received: *04 February 2022*
Accepted: *24 March 2022*
Published: *27 April 2022*

Citation:
Homma M and Kojima S (2022) The Periplasmic Domain of the Ion-Conducting Stator of Bacterial Flagella Regulates Force Generation. Front. Microbiol. 13:869187. doi: 10.3389/fmicb.2022.869187

INTRODUCTION

Many motile bacteria can swim in liquid or swarm on surfaces by rotating a structure called the flagellum (Beeby et al., 2020; Miyata et al., 2020). The flagellum consists of three parts: the long helical filament provides thrusts for the cell body, a rotary motor embedded in the cell surface, and a hook that connects the filament and the motor and serves as a universal joint. The flagellar motor rotates reversibly either clockwise (CW) or counterclockwise (CCW). Its energy source is an ion-motive force across the inner membrane: most of the bacteria, including *E. coli* and *Salmonella* spp., utilize H^+, while *Vibrio* and some other species utilize Na^+ (**Figure 1A**). The motor consists of a rotary part, the rotor (also called the flagellar basal body), which is composed of several rings and an axial rod that is connected to the hook; and the stator units, which are an energy-converting membrane protein complex (Terashima et al., 2008; Biquet-Bisquert et al., 2021; Hu et al., 2021). About a dozen stator units surround a single rotor. They are anchored at the peptidoglycan layer of the cell wall, and movement of the stator that is coupled to ion influx through the ion channel of the stator generates the rotational force (torque) (**Figures 1B,C**). Since the discovery of bacterial flagellar rotation in the 1970s (Berg and Anderson, 1973; Silverman and Simon, 1974), many researchers have been attracted to this rotary machine and studied the mechanism of its rotation, but still many details remain unknown.

To understand how the flagellar motor operates, the characterization of proteins in both the stator and the rotor is essential. Already in the 1990s, intensive genetic and biochemical analyses had identified most components of the motor. The locations of these proteins in the motor have been demonstrated by electron microscopic analyses of the isolated motor (Silverman and Simon, 1977; Macnab, 1992). In the 2000s, crystal structures of the rotor components were solved, and those structures were superimposed into the electron density maps of purified basal bodies obtained by cryo-electron microscopy (cryo-EM) (Kojima and Blair, 2004a; Minamino et al., 2008). Such analyses allow us to visualize the rotor structure in detail, and functional analyses to understand rotation from the rotor side, especially focused on rotational switching, have been conducted. In contrast, structural analysis of the stator has made little progress until recently. This is because the stator units dissociate from the flagellar basal body during isolation from the cell due to the weak interaction at the rotor–stator interface. However, in 2020, two groups reported high-resolution stator structures obtained by cryo-EM single-particle analyses (Deme et al., 2020; Santiveri et al., 2020). For details of the structural information, please see the review article in this issue of special topics on Biological Rotary Nanomotors.

Although the structural analysis of the stator units has lagged behind studies of the rotor, many genetic, functional, and biophysical characterizations of the stator units have been conducted (Minamino and Imada, 2015; Takekawa et al., 2020). Those efforts revealed unique features of the stator as an energy converter of the ion-motive force across the membrane. One of the notable properties is that the stator has two components: it has a static core, the B subunit, that is necessary to produce stable and constant torque, but it also has a dynamic periphery that allows it to deliver torque. The activity of the stator is regulated in response to environmental stimuli or load changes (Lele et al., 2013; Tipping et al., 2013; Antani et al., 2021). Here, we review the current state of knowledge about stator structure and function, focusing especially on its assembly-coupled mechanism of activation.

THE STATOR COMPONENTS

The stator is composed of two membrane proteins: MotA and MotB for the proton-driven motor in *E. coli* and *Salmonella* (Silverman et al., 1976), PomA and PomB for the sodium-driven motor in *Vibrio* and *Shewanella* (Asai et al., 1997). MotA and PomA are orthologs, as are MotB and PomB, and both pairs share functionally critical residues and motifs at similar positions (**Figure 2A**). MotA/PomA have four transmembrane (TM) segments with a relatively large cytoplasmic loop between the second (TM2) and third (TM3) TM segments. This loop contains conserved charged residues that are important for electrostatic interactions with charged residues in the C-terminal domain of the rotor protein FliG. These electrostatic interactions are critically important for motor rotation (Yakushi et al., 2006; Takekawa et al., 2014). MotB/PomB have a single TM segment at their N-termini and a large periplasmic C-terminal region that is anchored to the peptidoglycan (PG) layer. The single TM of MotB/PomB contains a functionally critical aspartate residue (Asp32 in *E. coli* MotB, Asp24 of *Vibrio* PomB). This residue functions as a proton/sodium-ion-binding site in the stator and is essential for the stator function. Na^+ binding at Asp24 of PomB was demonstrated using the Fourier Transform Infrared Spectroscopy (FTIR) (Sudo et al., 2009; Onoue et al., 2019). The periplasmic region of MotB/PomB contains a structurally conserved OmpA-like domain that is known to bind to the PG layer (Hizukuri et al., 2009). Mutations at a conserved PG-binding motif in this domain abolish motor rotation (Blair et al., 1991). Immediately C-terminal to the single TM of MotB/PomB is a characteristic amphipathic helix found in MotB family proteins (Hosking et al., 2006). Overproduction of the mutant stators with a deletion of this helix causes impairment of cell growth because of a massive proton- or sodium-ion flux through the stator ion channel. This segment is proposed to function as a "plug" of the stator channel to prevent premature ion flow when the stator is not incorporated into the motor (Hosking et al., 2006; Takekawa et al., 2013). In the 2000s, biochemical analyses and comprehensive disulfide crosslinking between the TM segments revealed the multimeric structure of a stator complex in which two MotB molecules were proposed to be surrounded by four MotA molecules (Braun and Blair, 2001; Blair, 2003; Braun et al., 2004; Kojima and Blair, 2004b). This model was updated by the high-resolution cryo-EM structure of the MotA/MotB stators reported in 2020: five, not four, MotA molecules form a ring that surrounds a central MotB dimer (Deme et al., 2020; Santiveri et al., 2020; **Figure 2B**). The structure inspired a novel model for torque generation in which a pentameric MotA ring rotates around the MotB dimer in response to ion influx; this rotation drives the rotor (Hu et al., 2021). In this structure, the C-terminal periplasmic region following the plug segment of the MotB was not visible.

DYNAMIC PROPERTIES OF THE STATOR UNITS

Although the details of the stator structure have only recently been elucidated, biophysical studies provided many insights into the properties of a single stator unit. Berg and coworkers developed the "resurrection" experiments in which the plasmid-borne stator restores rotation to the motor of a tethered stator-defective strain (Block and Berg, 1984). They found the stepwise recovery of rotation speed with the same increment in speed for each step. Similarly, a stepwise decrease in the rotational speed of alkalophilic *Bacillus* sodium-driven motor was seen after UV-induced irreversible inhibition of the stator (Muramoto et al., 1994). These results indicate that each stator unit is incorporated into the motor and functions independently. Later, resurrection experiments were conducted with a low viscous load on the flagellum using a bead attached to the flagellar stub (Ryu et al., 2000; Sowa et al., 2005). It was found that around eleven stator units can be incorporated into the fully functional motor (Reid et al., 2006) and that a single motor rotates with 26 steps per revolution, a number consistent with the periodicity of the ring of the FliG protein in the rotor (Sowa et al., 2005).

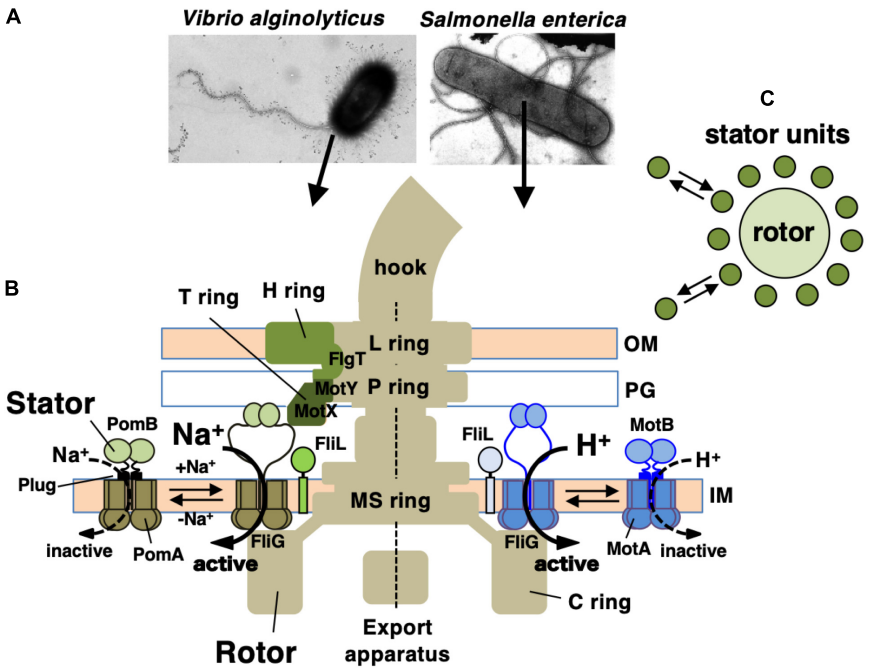


FIGURE 1 | (A) Negatively stained bacteria were observed by electron microscopy in *Vibrio alginolyticus* (left side) and *Salmonella enterica* (right side). **(B)** Schematic drawing of the flagellum, which is a motility organelle that has a motor associated with the cell membrane. On the left is the sodium-driven polar flagellar motor of *V. alginolyticus*, and to the right shown the proton-driven flagellar motor of *S. enterica*. The *Vibrio* motor contains additional ring structures, the T ring and H ring, in addition to the L ring and P ring. The stator complex is composed of two integral membrane proteins, PomA and PomB, for the sodium-driven motor and MotA and MotB for the proton-driven motor. The stator is anchored to the PG layer around the rotor *via* the periplasmic domain of the B subunit. OM, outer membrane; IM, inner membrane; PG, peptidoglycan layer. FliL is located at the flagellar base close to the stator. **(C)** Schematic drawing of the dynamic assembly and disassembly of the stator units in the flagellar motor.

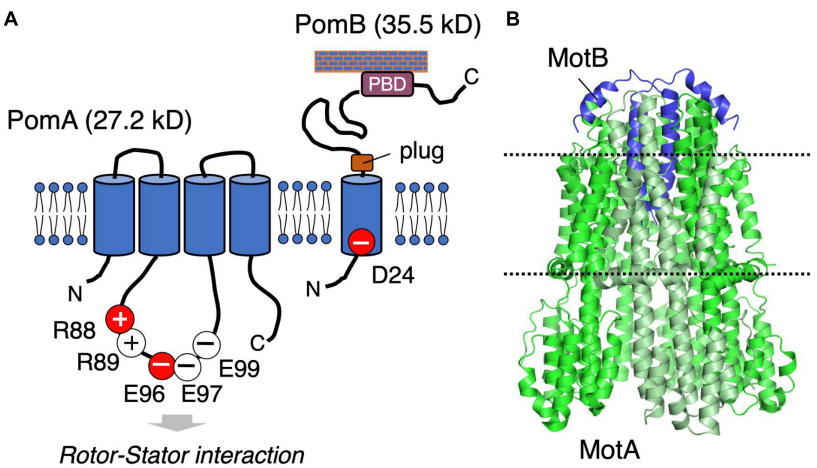


FIGURE 2 | (A) Schematic of the stator structure. The stator of the sodium-driven motor is composed of the PomA and PomB proteins. PomA has important charged residues (R88, R89, E96, E97, and E99) in the cytoplasmic loop region. PomB has the essential charged residue (D24), which is the ion-binding site. **(B)** The structure of the flagellar stator (PDB: 6YKM) obtained by cryo-electron microscopy is shown in a ribbon diagram with MotA green and MotB purple. The dotted lines represent the predicted boundaries of the lipid bilayer.

Motor rotation, observed at a high-load condition using tethered cells or at low-load using laser-dark field microscopy or a bead-flagellar stub system, appears to be quite stable (Kudo et al., 1990; Ryu et al., 2000). This stability suggests that stator units are static and, once incorporated into the motor, are stably anchored. However, another property of the stator was revealed by the observation of a single stator unit *in vivo*, using green fluorescent protein (GFP, fusion to MotB) (Leake et al., 2006).

This study showed that the stator units in a functional motor can be exchanged rapidly with a turnover rate of only ∼0.5 min. Similar dynamic properties were observed in the Na^+-driven PomA/PomB stator in *Vibrio* and *Shewanella* motors (Fukuoka et al., 2009; Paulick et al., 2009). The stator dissociates from and associates with the rotor in response to a changing Na^+ concentration. These findings have changed the image of the stator as being static: the stator has dynamic properties that respond to the environmental conditions. Indeed, evidence has accumulated to show that the stator works as a mechanosensor: the stator number changes in response to the load on the motor (Armitage and Berry, 2020). As the environmental load increases, the number of stator units around the rotor increases. Under a high-load condition, the tension applied on the binding interface between the PG layer and MotB promotes conformational changes that further expose additional binding residues in MotB to tighten the non-covalent binding between MotB and the PG layer to increase the lifetime of the stator around the rotor. Such a "catch-bond" mechanism equipped in MotB/PomB leads to an increase in the number of stators that enables the cells to rotate the motor in high viscous load (Nord et al., 2017). New insights were reported recently showing the involvement of the rotor side for mechanosensing in the flagellar motor (Antani et al., 2021).

The overproduction of the full-length stator complex does not affect cell growth, suggesting that the channels of unincorporated stator units are closed (Wilson and Macnab, 1988; Stolz and Berg, 1991). Rapidly diffusing intact stator units have been observed in the membrane, indicating that unincorporated stators are not anchored to the PG layer (Fukuoka et al., 2007, 2009). Considering the dynamic properties described above, a stator should have at least two distinct states: (i) an unincorporated inactive state with the ion channel closed and no attachment to the PG layer; (ii) an incorporated active state with the ion channel open and MotB anchored to the PG layer (**Figure 3**).

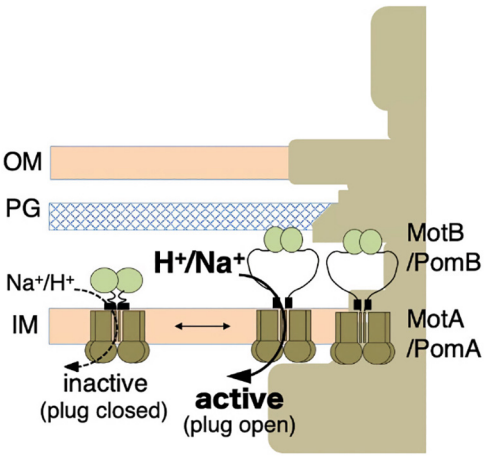


FIGURE 3 | Stator activation by the two-state model. The stator, composed of MotA or PomA and MotB or PomB, is activated by the coupling ions. The plug region is open in the active state. OM, outer membrane; IM, inner membrane; PG, peptidoglycan layer.

ASSEMBLY-COUPLED ACTIVATION MECHANISM OF THE MOTA/MOTB STATOR

The inactive, unincorporated, and active incorporated forms of the stator may have evolved to prevent wasting the energy by unincorporated stators. It requires that there must be a regulatory mechanism by which the stator is activated only when it is incorporated into the motor. How does such activation occur? It is plausible that the key conformational change is induced in the periplasmic region of MotB/PomB, where the binding to the PG layer must occur. To test this idea, the crystal structure of the periplasmic region of *Salmonella* MotB was determined (Kojima et al., 2009). Deletion studies of MotB identified the periplasmic region of MotB as essential for motility, which we call PEM (residues 111–270) (Muramoto and Macnab, 1998; **Figure 4A**).

Various fragments containing the entire PEM were constructed, and the crystal structure was determined for one of those fragments, $MotB_{C2}$ (residues 99–276), which was crystallized (**Figure 4B**). $MotB_{C2}$ forms a homodimer and appears in an unexpectedly compact conformation (Kojima et al., 2009). It has a single domain with considerable similarity to known OmpA-like domain structures. This domain is connected to a long N-terminal long α-helix (α1), which is followed by a short helix (α2) and a β-strand (β1). MotB/PomB proteins from various bacterial species do not show sequence similarity at the N-terminus of the PEM, but secondary structural predictions suggest that α1, α2, and β1 are common structural features. A MotB protein deleted for residues 51–100 (named MotBΔL), in which the TM segment is directly connected to the crystallized region of $MotB_{C2}$, is known to function (Muramoto and Macnab, 1998), so the MotBΔL stator must be anchored at the PG layer. However, the $MotB_{C2}$ dimer is only 50 Å tall and is, therefore, too short to reach the PG layer: the distance between the PG layer and the surface of the hydrophobic core layer of the cytoplasmic membrane is about 100 Å (**Figure 4C**). Therefore, a large conformational change must be induced in the PEM when the stator is incorporated into the motor. Since the OmpA-like domain is structurally well conserved, such structural change must occur in the N-terminal PEM (α1, α2, β1).

What kind of conformational changes are likely to occur? If the β1 detaches from the OmpA-like domain and extends collinearly with the α1 and α2 helices, the entire PEM of MotBΔL is now long enough to reach the PG layer. This model is supported by structure-guided mutagenesis in the N-terminal PEM, which shows that a Pro or Glu replacement at Leu119 in α1 of MotBΔL affects cell growth when co-overproduced with MotA (Kojima et al., 2009). The measurement of cytoplasmic pH revealed that this growth inhibition was caused by high proton conduction by this mutant stator (Morimoto et al., 2010a). These results suggest that the L119P (or L119E) substitution alters the stator structure in a way that mimics the active state. Inconsistent with this idea that low-level expression of this mutant still allows motility although the MotA/MotBΔL stator requires overexpression for function. The MotA/MotBΔL

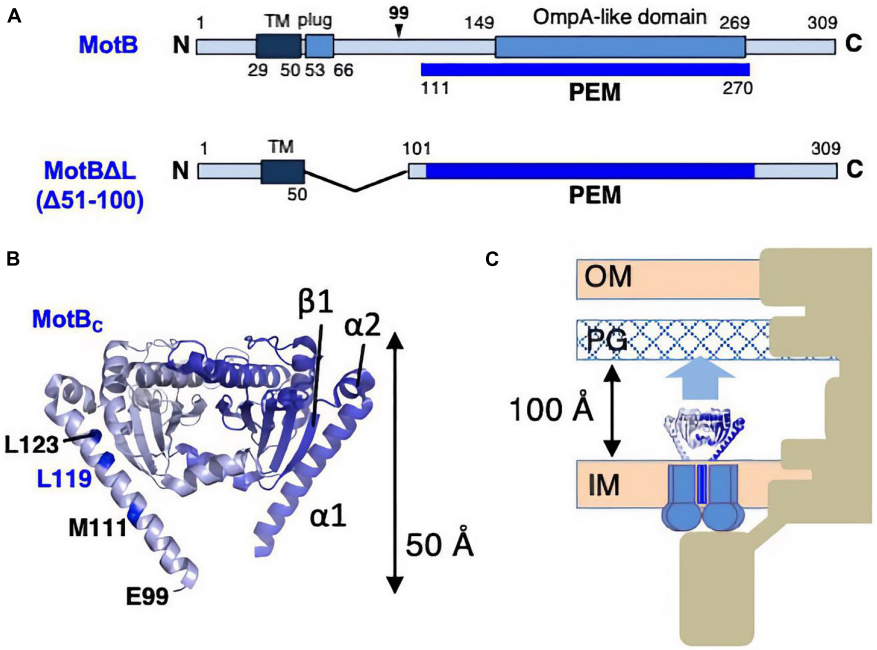


FIGURE 4 | (A) Primary structures of *Salmonella enterica* MotB; the PEMs for MotB are shown by the blue lines below each primary structure. **(B)** Dimer structures of the periplasmic fragments (MotB$_C$) of *Salmonella* MotB (PDB: 2ZVY). **(C)** Schematic drawing of the compact conformation of the stator complex composed of MotA and MotBΔL. OM, outer membrane; IM, inner membrane; PG, peptidoglycan layer.

(L119P/E) stator exhibits more favorable conformation than MotA/MotBΔL stator for efficient incorporation into the motor.

MotB is believed to bind to the PG layer *via* the conserved PG-binding motif in the structurally conserved OmpA-like domain; mutations targeting the PG-binding motif abolish cell motility (Blair et al., 1991) and localization of the stator around the rotor (Fukuoka et al., 2009). However, little direct evidence for this interaction has been reported. Only a very weak interaction between the isolated PG layer and the periplasmic fragment of *Helicobacter* MotB was observed (Roujeinikova, 2008; Andrews et al., 2017). If the L119P mutation alters the conformation of PEM so that it mimics the conformation in the active state of the stator, then this mutant should bind to the PG layer. To test this idea, the PG-binding activity of the MotB$_{C2}$-L119P fragment was investigated by the co-sedimentation assay (Kojima et al., 2018). Although wild-type MotB$_{C2}$ did not co-precipitate with the isolated PG and remained in the supernatant, most of the MotB$_{C2}$-L119P co-precipitated with PG. Therefore, the L119P replacement in MotB$_{C2}$ changes its conformation such that it can bind to the PG layer.

What kind of conformational change is induced by the L119P substitution? First, solution NMR analysis of selectively labeled MotB$_{C2}$ with (α-)^{15}N-lysine was conducted to investigate the structure in the solution (Kojima et al., 2018). The NMR data revealed that structural changes caused by the L119P mutation were localized in helix α1, not in the OmpA-like domain. Next, the crystal structure of MotB$_{C2}$-L119P protein was solved (Kojima et al., 2018). Consistent with the NMR results, the crystal structure of the MotB$_{C2}$-L119P dimer was almost identical to that of MotB$_{C2}$ except the helix α1 was disordered and not visible in the structure. No significant structural changes were found in the putative PG-binding residues in the OmpA-like domain. Since the MotB$_{C2}$-L119P fragment showed the PG-binding property, the conformational change that occurs in helix α1 unmasks/exposes additional residues in the OmpA-like domain required for PG-binding. The L119P substitution seems to induce a structural change that converts helix α1 into an extended open conformation. We propose that this rearrangement is responsible for stator activation both for PG-binding and proton conductivity.

To test whether similar conformational changes occur *in vivo*, crosslinking assays were conducted in intact cells. The MotA/MotBΔL stator with double-cysteine replacements in the PEM region, one in helix α1 (I127C) and the other in the PG-binding core (L140C), was constructed (Kojima et al., 2018). Cells expressing this mutant stator were only slightly motile both in semisolid agar and in the liquid, but the addition of the reducing agent dithiothreitol (DTT) dramatically improved motility, suggesting that the disulfide bridge formation between I127C and L140C residues reversibly inhibits motility. This *in vivo* assay provided evidence for a conformational change in the entirety of helix α1 during stator incorporation into the motor.

Based on these results, a model for the assembly-coupled MotA/MotB stator activation was proposed: (i) Stator units diffuse in the cell membrane in an inactive state. (ii) When they contact the rotor, helix α1 of MotB changes from a compact form into an extended open conformation. (iii) This conformational change pulls the plug to allow efficient proton translocation

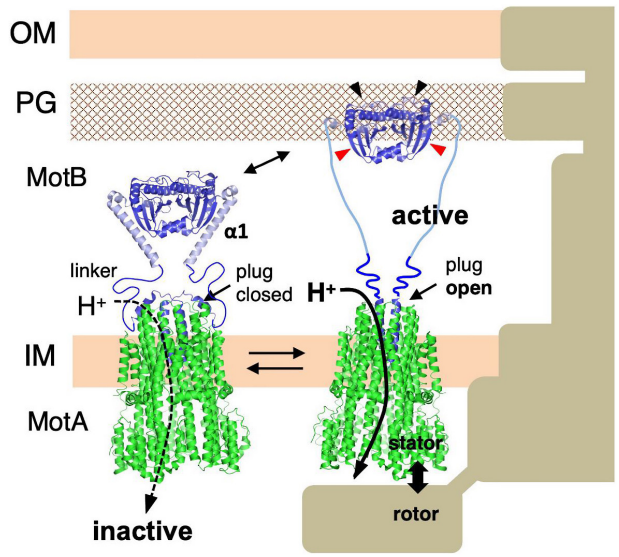


FIGURE 5 | Molecular model of stator activation. In the MotB protein, the crystallized MotB$_C$ region (PDB: 2ZVY) was directly connected to the transmembrane segment by way of the linker region and plug regions. A conformational change must be induced in MotB to enable it to reach the PG layer (black arrows). The structures of the flagellar stator (PDB: 6YKM) and the periplasmic fragments (MotB$_C$) of *Salmonella* MotB (PDB: 2ZVY) shown by a ribbon diagram are connected with a linker (left image). The structures of the unplugged stator (PDB: 6YKP) and the periplasmic fragments (MotB$_C$) of *Salmonella* MotB L119P mutant (PDB: 5Y40) are shown by a ribbon diagram are connected by the linker and the disordered helix α1 region (right image). OM, outer membrane; IM, inner membrane; PG, peptidoglycan layer.

through the ion channel in the stator. (iv) At the same time, the conformational change extends the PG-binding domain of MotB to the PG layer and exposes/unmasks the region essential for PG-binding. The stator can now bind to the cell wall and generate/transmit the torque to the motor (**Figure 5**).

ACTIVATION MECHANISM OF THE NA$^+$-DRIVEN *VIBRIO* STATOR

All the stators, regardless of the bacterial species of coupling ions they use (H^+ or Na^+), could use the same mechanism for their assembly-coupled activation. To address this point, the conformational change in the sodium-driven stator protein PomB of *Vibrio alginolyticus* was investigated. Deletion studies identified the PEM region of PomB as consisting of residues 121–315 (Li et al., 2011), and crystal structures of PomB fragments encoding PEM (PomB$_{C4}$, residues 121–315; PomB$_{C5}$, residues 135–315) were solved (Zhu et al., 2014; **Figure 6A**). The structures of PomB$_{C4}$ and PomB$_{C5}$ are identical, as the residues before 154 and after 305 are disordered in both structures. The solved structure we describe here as PomB$_C$, is quite similar to that of MotB$_{C2}$, forming a homodimer consisting of a single OmpA-like domain with a characteristic N-terminal helix (α1) (**Figure 6B**). The major difference between MotB$_C$ and PomB$_C$ is in the N-terminal PEM, including helix α1. In PomB$_C$, residues 121–154 are disordered in the crystal and α1 is 10 residues shorter than in MotB$_C$. It should be noted that in the *Vibrio* motor, stator units must interact not only with the PG layer but also with the T ring in the basal body (Terashima et al., 2006). Even though PomB$_C$ has a more flexible region in the PEM (the smallest functional PomB mutant named PomBΔL, is deleted for residues 41–120), the compact PomB$_C$ dimer still appears to be too small to reach the PG layer and T ring. Therefore, it is likely that PomB changes the conformation of its N-terminal PEM upon incorporation into a motor, as proposed in MotB.

To test this possibility, an *in vivo* disulfide crosslinking approach, similarly conducted for MotB, was employed (Zhu et al., 2014). It was expected that an intramolecular disulfide crosslink between helix α1 and the PG-binding core would impair any major conformational change and abolish motility. Indeed, the crosslink between M157C (in α1) and I186C (in the PG-binding core) abolished motility and the reduction of this crosslink by DTT restored motility. However, the slightly more C-terminal I164C-V179C crosslink still allows motility. This result is inconsistent with the previous model that strand β1 in PomB$_C$ (or MotB$_C$) extends to release the PG-binding core for anchoring the stator, but it is consistent with the updated model that the N-terminal PEM, including helix α1, is responsible for the conformational change upon stator activation. In the case of *Vibrio* PomB, only the N-terminal two-thirds of α1 changes its conformation. This partial rearrangement of the α1 helix, along with a conformational change in the adjacent N-terminal disordered region (residues 121–154), would allow PomBΔL to reach the PG layer.

We conclude that at least some H^+ and Na^+ stator units share the common mechanism for assembly-coupled activation. It should be noted that in the original paper that reported the PomA/PomB activation, a two-step conformational change was proposed, in which the first conformational change occurs in the disordered region in the N-terminal PEM to interact with the T ring, and the second conformational change occurs in the N-terminal two-thirds of α1 to reach the PG layer (Zhu et al., 2014). This model was based on the observation that the M157C-I186C crosslink in full-length PomB abolished motility but still allowed localization of PomAB to the motor. Subsequent cryo-electron tomography revealed a globular density at the periphery of the T ring (Zhu et al., 2020). Because the crystal structure of PomB$_C$ dimer fits well to this density, which is not observed in the motor of Δ*pomAB* strain, it was suggested that the *Vibrio* PomA/PomB stator is anchored to the T ring, instead of the PG layer. Therefore, the N-terminal PEM seems not to be the binding site for the T ring. The two-step conformational change model (**Figure 3**) in PomB for stator activation must be tested in the light of the PomB$_C$ interaction with the PG layer or with MotX, the component located at the tip of the T ring.

PULLING THE PLUG TO ALLOW ION FLOW THROUGH THE STATOR

It has been proposed that the interaction of the stator with the rotor induces the opening of the ion channel (Kojima et al., 2011).

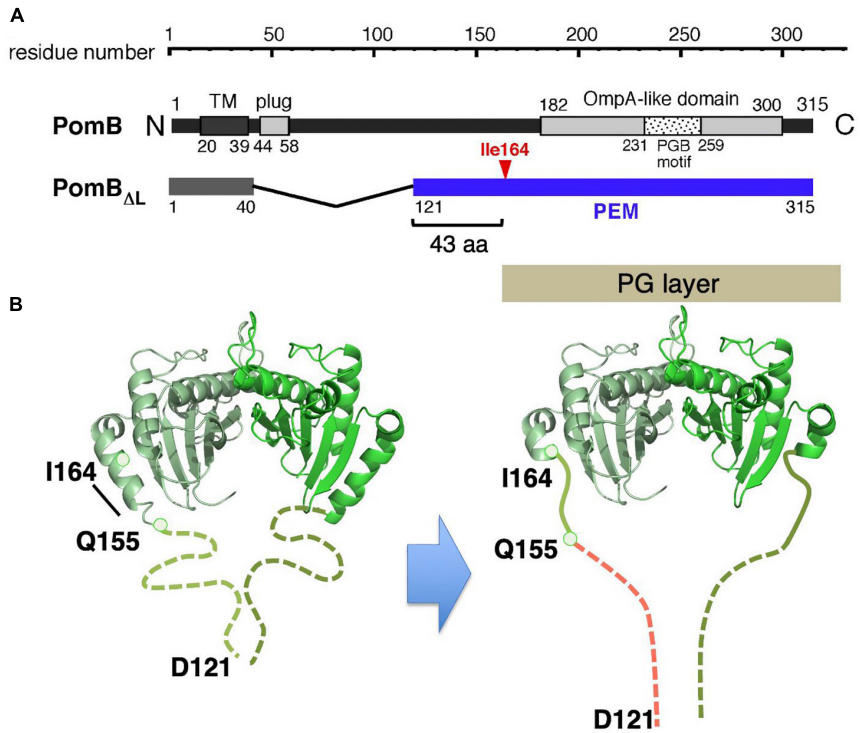


FIGURE 6 | (A) Primary structure of *Vibrio alginolyticus* PomB. The PEM for MotB is shown by the blue line in the in-frame deletion mutant (PomB$_{\Delta L}$). **(B)** A model of the conformational change in PomB coupled to the stator assembly. The periplasmic fragments (PomB$_C$) of *Vibrio* PomB (PDB: 3WPW) shown by the ribbon diagram are connected with a linker (dotted lines) (left). The N-terminal two-thirds of helix α1 change conformation to an extended form that is able to anchor to the PG layer (right).

The plug segment, a characteristic amphipathic helix located immediately at the C-terminal of a single TM segment of the B subunit, is proposed to regulate the ion-conducting activity of the stator, by "plugging" the channel (Hosking et al., 2006; Takekawa et al., 2013). How unplugging occurs during stator activation is not yet known. However, the high-resolution structures of the MotA/MotB stators included the plug helix and combined with a functional analysis revealed its novel role. The structure shows that the plug helix lies between the MotA subunits in the pentameric MotA ring, with three MotA subunits on one side and two on the other (Deme et al., 2020; Santiveri et al., 2020). The interaction of the plug with the MotA ring interferes with the ion flux, presumably by affecting the structure of the ion pathway, and the disruption of this interaction allows efficient ion flux through the stator channel. As discussed above, stator activation would induce movement of, or a conformational change in, the plug helix to open the channel.

Recently, the site-specific photograph-crosslinking between the PomA periplasmic loop and the plug helix of PomB was conducted. The results are consistent with the MotA/MotB structure (Homma et al., 2021). A disulfide crosslink between PomA (M169C in the large periplasmic loop) and PomB (I50C in the plug) reversibly inhibits motility. The structure of the stator complex implies that the MotA ring rotates around the MotB dimer in response to ion flux. The inhibition of motility suggests that the crosslink between the plug and MotA ring interferes with ion influx through the stator by physically blocking the rotation of the stator ring like a spanner or a stopper (**Figure 7**). This model is supported by the observation that a plug deletion in PomB weakens the PomA–PomB interaction and results in their dissociation from each other during the purification (Nishikino et al., 2020). It should be noted that the plug deletion of the plug in MotB of *Campylobacter jejuni* did not weaken the MotA–MotB interaction, and the plug-deleted stator complex could be purified and used for the structural analysis (Santiveri et al., 2020).

COMPONENTS THAT STABILIZE ACTIVE STATOR

As described above, stator units exhibit dynamic properties. They undergo rapid turnover, which involves frequent association and dissociation with the motor. However, the motor rotates quite stably, indicating that incorporated stators can be stabilized in the motor. The sodium-driven *Vibrio* polar flagellar motor, as discussed in the previous section, rotates remarkably fast, up to ca. 1,700 Hz, as compared to the proton-driven motors of *E. coli* and *Salmonella* which rotate up to ca. 300 Hz (Kudo et al., 1990; Gabel and Berg, 2003). The basal body of the *Vibrio* polar flagellum has unique ring structures, the T ring and H ring (Terashima et al., 2006, 2013). These extra rings are thought to allow the motor to perform high-speed rotation. The T ring is

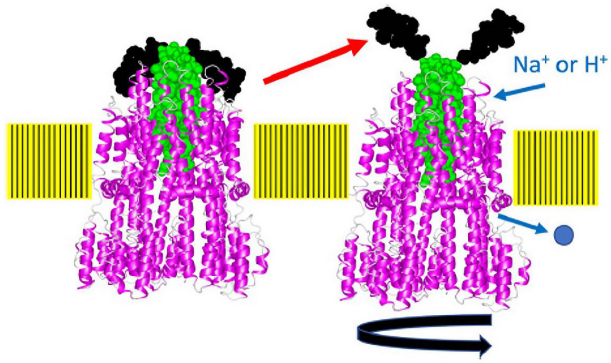


FIGURE 7 | A model of how the plug may block stator rotation and stator activation. When the cytoplasmic region of MotA or PomA interacts with FliG, the plug region of PomB or MotB, which seems to function as a spanner or stopper, is released from the periplasmic loop regions (the putative right structure). The pentamer of the A subunit rotates around the B subunit driven by ion flow. The structure of the flagellar stator (PDB: 6YKM) which is stopped state (the left structure), is shown by a ribbon diagram, with MotA in magenta and MotB in green. The spanner region is shown in black in a space-filling model. This figure is taken from our previous paper (Homma et al., 2021).

located beneath the H ring and is required for the assembly of PomA/PomB around the rotor. It is presumably also important for the stabilization of the active stator in the motor. The T ring is composed of MotX and MotY, and the loss of either abolishes motor rotation (Terashima et al., 2006). MotY has a two-domain structure, with a unique N-terminal fold that is responsible for interaction with MotX and the basal body, and with a C-terminal OmpA-like domain that stabilizes stator association by binding to the PG layer. The structure of MotX has not yet been solved because its precipitation hampers its purification. MotX has a characteristic SEL1 motif, a repeat of α helices that is involved in protein-protein interaction, and an *in silico* structure has been predicted (Zhu et al., 2020). Cryo-electron tomographic analysis of *Vibrio* polar flagellar motor shows that this predicted structure of MotX fits well into the T ring density if MotX and MotY form a 1:1 heterodimer, with MotX positioned at the tip of the T ring (**Figures 8A,B**). Whatever the actual structure may be, the interaction between MotX in the T ring and PomB in the stator stabilizes the active stator units incorporated around the rotor.

FliL is another component that stabilizes the active stator. When FliL is not present, motility is impaired when the cells swim or swarm in a highly viscous environment. Under such conditions, the motor must turn against the large friction imposed by a high load, and the stator units must associate tightly with the rotor to generate maximal torque. A catch-bond mechanism in the stator B subunit would contribute to this mechano-sensing reaction. However, an additional factor is required under high-load conditions, presumably to stabilize the active stator units around the rotor. FliL is a small protein with a single transmembrane segment. Most of it is located in the periplasm (**Figure 8C**). It is essential for the swimming motility of some species, including *Caulobacter crescentus* (Jenal et al., 1994), *Rhodobacter sphaeroides* (Suaste-Olmos et al., 2010), and for the surface swarming of *E coli* and *Salmonella* (Attmannspacher et al., 2008). It should be noted that the torque generated by the *E. coli* strain lacking FliL is reported to be similar to that in the wild-type strain at high-load conditions (Chawla et al., 2017), raising a question about FliL involvement in mechanosensing by the motor. FliL is encoded in an operon containing other flagellar genes, and it associates with the flagellar basal body (Partridge et al., 2015). Because it is not essential for swimming motility in *Salmonella* and *E. coli*, its function has not been intensively studied although it was identified a while ago (Raha et al., 1994). Recent work has revealed the diverse functions of FliL. Cryo-electron tomography revealed that, in *Borrelia burgdorferi* motor, FliL is located close to the rotor and stator (Motaleb et al., 2011). FliL interacts with basal body proteins such as FliF of the MS-ring protein and the FlgT protein associated with the H ring. Most importantly for this discussion, it also interacts with the periplasmic region of the B subunit in the stator. FliL-stator interaction is important for the localization of FliL at the motor (Lin et al., 2018). It has been shown that *Vibrio alginolyticus* polar FliL forms an oligomer (ca. 150 kDa) in a detergent (Kumar et al., 2017). The crystal structure of the periplasmic region of FliL ($FliL_P$) shows remarkable structural similarity to the mammalian stomatin/prohibitin/flotillin/HflK/C (SPFH) domain of stomatin (**Figure 8D**). The SPFH domain is conserved in membrane-associated proteins of eukaryotes, where it is known to interact with various ion channels and transporters to modulate their activities (Takekawa et al., 2019). Furthermore, proteins with the SPFH domain are often involved in the mechanosensing of sensory neurons, raising the possibility that FliL is also involved in mechanosensing by the flagellum.

The structure of $FliL_P$ and functional studies suggest that FliL forms a multimer in the periplasm, possibly a decameric ring, which surrounds a single stator unit. One model proposes that 10 molecules of FliL surround a single PomA/PomB stator unit. The FliL–PomB interaction in the periplasm stabilizes the active conformation of a stator whose ion channel is open and is anchored to the PG layer or T ring (Takekawa et al., 2019; Guo et al., 2022; Tachiyama et al., 2022; **Figure 8E**). FliL may also assist in the catch-bond function of the PG-binding core of PomB. Although the high-resolution structure provided insight, it is still not clear how FliL senses the environmental load and modulates stator function. Further studies will be needed to test how prevalent it is to have a FliL ring around a stator unit and to determine the molecular details of the stator–FliL interaction.

REMAINING QUESTION: WHAT IS THE TRIGGER?

Structure-based functional analyses revealed the conformational change in the PEM region of the stator B subunit that alters the stator structure to the active conformation. What triggers this conformational change? The short answer is, we do not know. Because the stator unit is activated only when it is incorporated into the motor. It is most likely that rotor–stator contacts provide the signal for stator activation (Fukuoka et al., 2009). Genetic studies have provided information about the rotor–stator

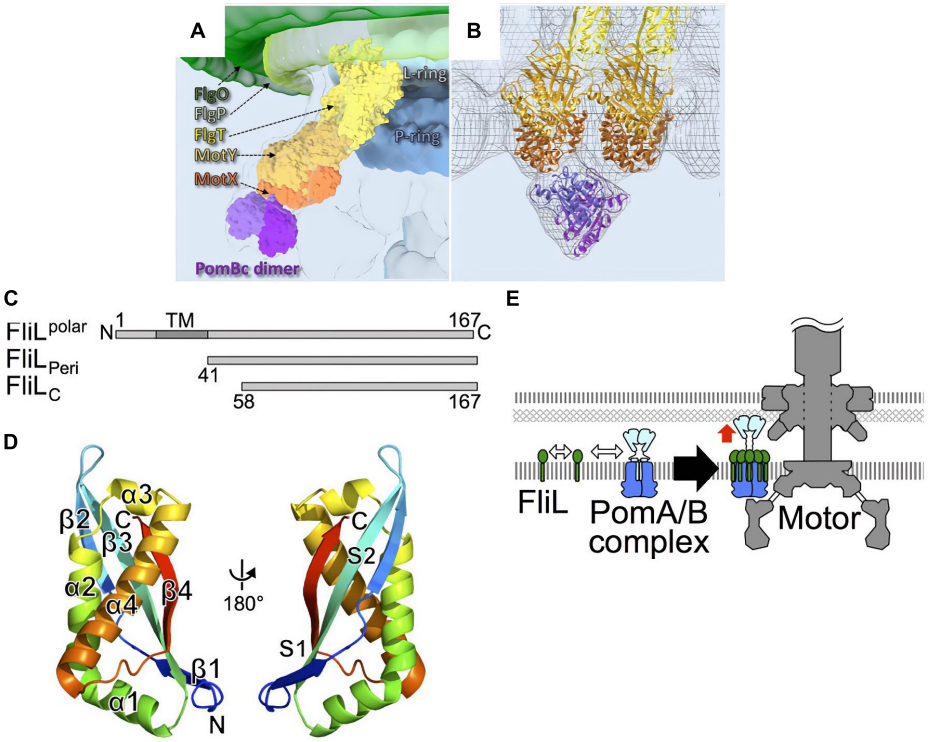


FIGURE 8 | (A) A 3D surface rendering of the part of the *Vibrio* flagellar basal body including the L ring and the P ring in addition to the O ring, the H ring, and the T ring. The location of the H ring is inferred based on our previous results. FlgO is labeled in deep green and located at the distal area of the H ring, and FlgP is labeled in light green and located in the middle of the H ring. FlgT might be located outside of the P/L rings and on the top of the T ring. **(B)** Superposition of the cryo-ET density map (mesh) and the atomic models of FlgT, MotY, MotX, and PomB, as previously shown (Zhu et al., 2020). The models are shown as ribbon diagrams and colored as in **(A)**. **(C)** Primary structure of *Vibrio alginolyticus* FliL and the truncations, $FliL_{Peri}$, and $FliL_C$. **(D)** The structure of $FliL_C$ (PDB: 6AHP) is shown as a ribbon diagram colored like a rainbow from the N-terminus (blue) to the C-terminus (red). **(E)** A model for the role of FliL in stator assembly. The white two-way arrows indicate the protein-protein interactions of the stator with FliL, and the red arrow indicates the activation of the stator. Figures are taken from our previous papers: Zhu et al. (2020) for **(A,B)**, Takekawa et al. (2019) for **(C–E)**.

interaction in the cytoplasm, which occurs between conserved charged residues in the loop between TM2 and TM3 of the A subunit of the stator, and the C-terminal domain of the rotor protein FliG ($FliG_C$) (Kojima et al., 2011). Genetic suppression and synergistic effects between these charged residues indicate that electrostatic interactions at the rotor–stator interface are critical for motor rotation (Zhou et al., 1998; Takekawa et al., 2014). Therefore, a plausible scenario is that once a diffusing stator unit in the membrane encounters a rotor, electrostatic interactions at the rotor–stator interface trigger a signal that is transmitted to the periplasmic side of the stator to induce the conformational change of PEM in the B subunit.

Although this hypothesis is attractive, more experimental evidence is needed to prove the model. Some evidence has been reported to show that the proper interactions between rotor and stator are required for stator incorporation/assembly into the motor. In the *Salmonella* motor, the investigation of stator localization using a C-terminally GFP-tagged MotA revealed that electrostatic interaction between MotA (Arg90)-FliG (Asp289) was critical for proper positioning of the stators around the rotor, whereas that of MotA (Glu98)-FliG (Arg281) is more important for torque generation (Morimoto et al., 2010b, 2013). In the *Vibrio* motor, mutations targeting the cytoplasmic region of the A subunit or $FliG_C$ abolish the stator localization around the rotor (Kojima et al., 2011; Takekawa et al., 2012). These results support the idea that the rotor–stator contact acts as a trigger. A possible intermediate state in the association process was detected in the *Vibrio* PomA/PomB stator in the presence of coupling ion Na^+, by site-specific labeling experiments (Mino et al., 2019). This state presumably represents the conformation before the activation, as it was observed in a mutant stator missing a critical Na^+ binding site in TM of PomB. In the MotA/MotB stator, such an intermediate state has not been reported yet.

Recently, the direct physical interaction between the rotor and stator was demonstrated in the *E. coli* hybrid motor by using the Na^+-driven PomA/PotB chimeric stator and the site-specific photograph- and disulfide crosslinking *in vivo* (Terashima et al., 2021). PotB is the chimera consisting of an N-terminal PomB fusing to the periplasmic C-terminal MotB (Asai et al., 2003). In this study, a photograph-reactive amino acid derivative (*p*-benzoyl-$_L$-phenylalanine, pBPA) was used to replace a series of residues at the rotor–stator interface. UV-irradiation induces a covalent photograph-crosslink with nearby residues. This approach allowed the detection of weak or transient interactions

at the rotor–stator interface. The results show that the region of PomA containing conserved charged residues indeed interacts with the region containing charged residues in $FliG_C$, and some specific interaction pairs were discovered. Because the positively or negatively charged residues are located next to each other in the recently solved high-resolution structure of MotA, the rotation gear model was proposed, in which the stator A subunit ring rotates against the rotor ring by alternate electrostatic repulsion and attraction in coupling with ion flux through the rotor.

A cryo-electron tomography analysis of the *Borrelia* motor *in situ* revealed the structural remodeling that accompanies rotational switching (Chang et al., 2020). It was proposed that a stator ring changes its contact sites to the rotor depending on the rotational directions (counterclockwise or clockwise). Because the crosslinking studies described above used a strain whose motor rotates in both directions, the contact residues at the rotor–stator interface may be the same regardless of the rotational direction. Therefore, stator activation may be induced when the motor is in either direction of rotation *via* electrostatic interactions of the same charged residues. However, further analyses are required to clarify the activation mechanism.

This still leaves an open question of how the signal from the rotor–stator contact is transmitted to the PEM region of the B subunit, which is distant from the contact interface. In the current model, we propose that conformational changes in helix α1 of the N-terminal PEM of MotB simultaneously open the plug and expose PG-binding determinants (Kojima et al., 2018). The cytoplasmic signal may induce unplugging. This movement of the plug segment could induce the rearrangement of helix α1. To understand the series of conformational rearrangements in the stator that occur during assembly-coupled activation, we need the whole structure of the part of the periplasmic domain of the B subunit that is currently invisible. However, having most of the structure of the stator allows us to conduct structure-based functional analysis. We also have a variety of methods to analyze the behavior of each stator unit. We can observe and visualize the single stator unit *in vivo* by using state-of-art light or electron microscopy. High-speed atomic force microscopy would be suitable to characterize *in vitro* physicochemical properties of the stator *in vitro*. We should soon be able to understand the assembly, activation, and function of the stator units, which are unique energy-converting complex in the bacterial cell membrane.

AUTHOR CONTRIBUTIONS

Both authors listed have made a substantial, direct, and intellectual contribution to the work, and approved it for publication.

FUNDING

This work was supported in part by the JSPS KAKENHI (Grant No. 20H03220) to MH.

REFERENCES

Andrews, D. A., Nesmelov, Y. E., Wilce, M. C., and Roujeinikova, A. (2017). Structural analysis of variant of *Helicobacter* pylori MotB in its activated form, engineered as chimera of MotB and leucine zipper. *Sci. Rep.* 7:13435. doi: 10.1038/s41598-017-13421-0

Antani, J. D., Gupta, R., Lee, A. H., Rhee, K. Y., Manson, M. D., and Lele, P. P. (2021). Mechanosensitive recruitment of stator units promotes binding of the response regulator CheY-P to the flagellar motor. *Nat. Commun.* 12:5442. doi: 10.1038/s41467-021-25774-2

Armitage, J. P., and Berry, R. M. (2020). Assembly and dynamics of the bacterial flagellum. *Annu. Rev. Microbiol.* 74, 181–200. doi: 10.1146/annurev-micro-090816-093411

Asai, Y., Kojima, S., Kato, H., Nishioka, N., Kawagishi, I., and Homma, M. (1997). Putative channel components for the fast-rotating sodium-driven flagellar motor of a marine bacterium. *J. Bacteriol.* 179, 5104–5110. doi: 10.1128/jb.179.16.5104-5110.1997

Asai, Y., Yakushi, T., Kawagishi, I., and Homma, M. (2003). Ion-coupling determinants of Na^+-driven and H^+-driven flagellar motors. *J. Mol. Biol.* 327, 453–463. doi: 10.1016/s0022-2836(03)00096-2

Attmannspacher, U., Scharf, B. E., and Harshey, R. M. (2008). FliL is essential for swarming: motor rotation in absence of flil fractures the flagellar rod in swarmer cells of *Salmonella enterica*. *Mol. Microbiol.* 68, 328–341. doi: 10.1111/j.1365-2958.2008.06170.x

Beeby, M., Ferreira, J. L., Tripp, P., Albers, S. V., and Mitchell, D. R. (2020). Propulsive nanomachines: the convergent evolution of archaella, flagella and cilia. *FEMS Microbiol. Rev.* 44, 253–304. doi: 10.1093/femsre/fuaa006

Berg, H. C., and Anderson, R. A. (1973). Bacteria swim by rotating their flagellar filaments. *Nature* 245, 380–382. doi: 10.1038/245380a0

Biquet-Bisquert, A., Labesse, G., Pedaci, F., and Nord, A. L. (2021). The dynamic ion motive force powering the bacterial flagellar motor. *Front. Microbiol.* 12:659464. doi: 10.3389/fmicb.2021.659464

Blair, D. F. (2003). Flagellar movement driven by proton translocation. *FEBS Lett.* 545, 86–95. doi: 10.1016/s0014-5793(03)00397-1

Blair, D. F., Kim, D. Y., and Berg, H. C. (1991). Mutant Motb proteins in *Escherichia coli*. *J. Bacteriol.* 173, 4049–4055. doi: 10.1128/jb.173.13.4049-4055.1991

Block, S. M., and Berg, H. C. (1984). Successive incorporation of force-generating units in the bacterial rotary motor. *Nature* 309, 470–472. doi: 10.1038/309470a0

Braun, T. F., Al-Mawsawi, L. Q., Kojima, S., and Blair, D. F. (2004). Arrangement of core membrane segments in the MotA/MotB proton-channel complex of *Escherichia coli*. *Biochemistry* 43, 35–45. doi: 10.1021/bi035406d

Braun, T. F., and Blair, D. F. (2001). Targeted disulfide cross-linking of the MotB protein of *Escherichia coli*: evidence for two H^+ channels in the stator complex. *Biochemistry* 40, 13051–13059. doi: 10.1021/bi011264g

Chang, Y., Zhang, K., Carroll, B. L., Zhao, X., Charon, N. W., Norris, S. J., et al. (2020). Molecular mechanism for rotational switching of the bacterial flagellar motor. *Nat. Struct. Mol. Biol.* 27, 1041–1047. doi: 10.1038/s41594-020-0497-2

Chawla, R., Ford, K. M., and Lele, P. P. (2017). Torque, but not flil, regulates mechanosensitive flagellar motor-function. *Sci. Rep.* 7:5565. doi: 10.1038/s41598-017-05521-8

Deme, J. C., Johnson, S., Vickery, O., Aron, A., Monkhouse, H., Griffiths, T., et al. (2020). Structures of the stator complex that drives rotation of the bacterial flagellum. *Nat. Microbiol.* 5, 1553–1564. doi: 10.1038/s41564-020-0788-8

Fukuoka, H., Sowa, Y., Kojima, S., Ishijima, A., and Homma, M. (2007). Visualization of functional rotor proteins of the bacterial flagellar motor in the cell membrane. *J. Mol. Biol.* 367, 692–701. doi: 10.1016/j.jmb.2007.01.015

Fukuoka, H., Wada, T., Kojima, S., Ishijima, A., and Homma, M. (2009). Sodium-dependent dynamic assembly of membrane complexes in sodium-driven flagellar motors. *Mol. Microbiol.* 71, 825–835. doi: 10.1111/j.1365-2958.2008.06569.x

Gabel, C. V., and Berg, H. C. (2003). The speed of the flagellar rotary motor of *Escherichia coli* varies linearly with protonmotive force. *Proc. Natl. Acad. Sci. U.S.A.* 100, 8748–8751. doi: 10.1073/pnas.1533395100

Guo, S., Xu, H., Chang, Y., Motaleb, M. A., and Liu, J. (2022). FliL ring enhances the function of periplasmic flagella. *Proc. Natl. Acad. Sci. U.S.A.* 119:e2117245119. doi: 10.1073/pnas.2117245119

Hizukuri, Y., Morton, J. F., Yakushi, T., Kojima, S., and Homma, M. (2009). The peptidoglycan-binding (PGB) domain of the *Escherichia coli* pal protein can also function as the PGB domain in E. coli flagellar motor protein MotB. *J. Biochem.* 146, 219–229. doi: 10.1093/jb/mvp061

Homma, M., Terashima, H., Koiwa, H., and Kojima, S. (2021). Putative spanner function of the vibrio pomb plug region in the stator rotation model for flagellar motor. *J. Bacteriol.* 203:e0015921. doi: 10.1128/JB.00159-21

Hosking, E. R., Vogt, C., Bakker, E. P., and Manson, M. D. (2006). The *Escherichia coli* Motab proton channel unplugged. *J. Mol. Biol.* 364, 921–937. doi: 10.1016/j.jmb.2006.09.035

Hu, H., Santiveri, M., Wadhwa, N., Berg, H. C., Erhardt, M., and Taylor, N. M. I. (2021). Structural basis of torque generation in the bi-directional bacterial flagellar motor. *Trends Biochem. Sci.* 47, 160–172. doi: 10.1016/j.tibs.2021.06.005

Jenal, U., White, J., and Shapiro, L. (1994). Caulobacter flagellar function, but not assembly, requires Flil, a non-polarly localized membrane protein present in all cell types. *J. Mol. Biol.* 243, 227–244. doi: 10.1006/jmbi.1994.1650

Kojima, S., and Blair, D. F. (2004a). The bacterial flagellar motor: structure and function of a complex molecular machine. *Int. Rev. Cytol.* 233, 93–134. doi: 10.1016/S0074-7696(04)33003-2

Kojima, S., and Blair, D. F. (2004b). Solubilization and purification of the MotA/MotB complex of *Escherichia coli*. *Biochemistry* 43, 26–34. doi: 10.1021/bi035405l

Kojima, S., Imada, K., Sakuma, M., Sudo, Y., Kojima, C., Minamino, T., et al. (2009). Stator assembly and activation mechanism of the flagellar motor by the periplasmic region of MotB. *Mol. Microbiol.* 73, 710–718. doi: 10.1111/j.1365-2958.2009.06802.x

Kojima, S., Nonoyama, N., Takekawa, N., Fukuoka, H., and Homma, M. (2011). Mutations targeting the C-terminal domain of FliG can disrupt motor assembly in the Na^+-driven flagella of vibrio alginolyticus. *J. Mol. Biol.* 414, 62–74. doi: 10.1016/j.jmb.2011.09.019

Kojima, S., Takao, M., Almira, G., Kawahara, I., Sakuma, M., Homma, M., et al. (2018). The helix rearrangement in the periplasmic domain of the flagellar stator b subunit activates peptidoglycan binding and ion influx. *Structure* 26, 590–598. doi: 10.1016/j.str.2018.02.016

Kudo, S., Magariyama, Y., and Aizawa, S.-I. (1990). Abrupt changes in flagellar rotation observed by laser dark-field microscopy. *Nature* 346, 677–680. doi: 10.1038/346677a0

Kumar, A., Isumi, M., Sakuma, M., Zhu, S., Nishino, Y., Onoue, Y., et al. (2017). Biochemical characterization of the flagellar stator-associated inner membrane protein Flil from *Vibrio alginolyticus*. *J. Biochem.* 161, 331–337. doi: 10.1093/jb/mvw076

Leake, M. C., Chandler, J. H., Wadhams, G. H., Bai, F., Berry, R. M., and Armitage, J. P. (2006). Stoichiometry and turnover in single, functioning membrane protein complexes. *Nature* 443, 355–358. doi: 10.1038/nature05135

Lele, P. P., Hosu, B. G., and Berg, H. C. (2013). Dynamics of mechanosensing in the bacterial flagellar motor. *Proc. Natl. Acad. Sci. U.S.A.* 110, 11839–11844. doi: 10.1073/pnas.1305885110

Li, N., Kojima, S., and Homma, M. (2011). Characterization of the periplasmic region of Pomb, a Na^+-driven flagellar stator protein in vibrio alginolyticus. *J. Bacteriol.* 193, 3773–3784. doi: 10.1128/JB.00113-11

Lin, T. S., Zhu, S., Kojima, S., Homma, M., and Lo, C. J. (2018). FliL association with flagellar stator in the sodium-driven Vibrio motor characterized by the fluorescent microscopy. *Sci. Rep.* 8:11172. doi: 10.1038/s41598-018-29447-x

Macnab, R. M. (1992). Genetics and biogenesis of bacterial flagella. *Annu. Rev. Genet.* 26, 131–158. doi: 10.1146/annurev.ge.26.120192.001023

Minamino, T., and Imada, K. (2015). The bacterial flagellar motor and its structural diversity. *Trends Microbiol.* 23, 267–274. doi: 10.1016/j.tim.2014.12.011

Minamino, T., Imada, K., and Namba, K. (2008). Molecular motors of the bacterial flagella. *Curr. Opin. Struct. Biol.* 18, 693–701. doi: 10.1016/j.sbi.2008.09.006

Mino, T., Nishikino, T., Iwatsuki, H., Kojima, S., and Homma, M. (2019). Effect of sodium ions on conformations of the cytoplasmic loop of the Poma stator protein of vibrio alginolyticus. *J. Biochem.* 166, 331–341. doi: 10.1093/jb/mvz040

Miyata, M., Robinson, R. C., Uyeda, T. Q. P., Fukumori, Y., Fukushima, S. I., Haruta, S., et al. (2020). Tree of motility –a proposed history of motility systems in the tree of life. *Genes Cells* 25, 6–21. doi: 10.1111/gtc.12737

Morimoto, Y. V., Che, Y. S., Minamino, T., and Namba, K. (2010a). Proton-conductivity assay of plugged and unplugged MotA/B proton channel by cytoplasmic pHluorin expressed in *Salmonella*. *FEBS Lett.* 584, 1268–1272. doi: 10.1016/j.febslet.2010.02.051

Morimoto, Y. V., Nakamura, S., Kami-Ike, N., Namba, K., and Minamino, T. (2010b). Charged residues in the cytoplasmic loop of MotA are required for stator assembly into the bacterial flagellar motor. *Mol. Microbiol.* 78, 1117–1129. doi: 10.1111/j.1365-2958.2010.07391.x

Morimoto, Y. V., Nakamura, S., Hiraoka, K. D., Namba, K., and Minamino, T. (2013). Distinct roles of highly conserved charged residues at the MotA-FliG interface in bacterial flagellar motor rotation. *J. Bacteriol.* 195, 474–481. doi: 10.1128/JB.01971-12

Motaleb, M. A., Pitzer, J. E., Sultan, S. Z., and Liu, J. (2011). A novel gene inactivation system reveals an altered periplasmic flagellar orientation in a *Borrelia burgdorferi* flil mutant. *J. Bacteriol.* 193, 3324–3331. doi: 10.1128/JB.00202-11

Muramoto, K., and Macnab, R. M. (1998). Deletion analysis of MotA and MotB, components of the force-generating unit in the flagellar motor of *Salmonella*. *Mol. Microbiol.* 29, 1191–1202. doi: 10.1046/j.1365-2958.1998.00998.x

Muramoto, K., Sugiyama, S., Cragoe, E. J., and Imae, Y. (1994). Successive inactivation of the force-generating units of sodium-driven bacterial flagellar motors by a photoreactive amiloride analog. *J. Biol. Chem.* 269, 3374–3380. doi: 10.1016/s0021-9258(17)41872-2

Nishikino, T., Iwatsuki, H., Mino, T., Kojima, S., and Homma, M. (2020). Characterization of Poma periplasmic loop and sodium ion entering in stator complex of sodium-driven flagellar motor. *J. Biochem.* 167, 389–398. doi: 10.1093/jb/mvz102

Nord, A. L., Gachon, E., Perez-Carrasco, R., Nirody, J. A., Barducci, A., Berry, R. M., et al. (2017). Catch bond drives stator mechanosensitivity in the bacterial flagellar motor. *Proc. Natl. Acad. Sci. U.S.A.* 114, 12952–12957. doi: 10.1073/pnas.1716002114

Onoue, Y., Iwaki, M., Shinobu, A., Nishihara, Y., Iwatsuki, H., Terashima, H., et al. (2019). Essential ion binding residues for Na^+ flow in stator complex of the vibrio flagellar motor. *Sci. Rep.* 9:11216. doi: 10.1038/s41598-019-46038-6

Partridge, J. D., Nieto, V., and Harshey, R. M. (2015). A new player at the flagellar motor: Flil controls both motor output and bias. *mBio* 6:e02367. doi: 10.1128/mBio.02367-14

Paulick, A., Koerdt, A., Lassak, J., Huntley, S., Wilms, I., Narberhaus, F., et al. (2009). Two different stator systems drive a single polar flagellum in Shewanella oneidensis MR-1. *Mol. Microbiol.* 71, 836–850. doi: 10.1111/j.1365-2958.2008.06570.x

Raha, M., Sockett, H., and Macnab, R. M. (1994). Characterization of the flil gene in the flagellar regulon of *Escherichia coli* and *Salmonella* typhimurium. *J. Bacteriol.* 176, 2308–2311. doi: 10.1128/jb.176.8.2308-2311.1994

Reid, S. W., Leake, M. C., Chandler, J. H., Lo, C. J., Armitage, J. P., and Berry, R. M. (2006). The maximum number of torque-generating units in the flagellar motor of *Escherichia coli* is at least 11. *Proc. Natl. Acad. Sci. U.S.A.* 103, 8066–8071. doi: 10.1073/pnas.0509932103

Roujeinikova, A. (2008). Crystal structure of the cell wall anchor domain of MotB, a stator component of the bacterial flagellar motor: implications for peptidoglycan recognition. *Proc. Natl. Acad. Sci. U.S.A.* 105, 10348–10353. doi: 10.1073/pnas.0803039105

Ryu, W. S., Berry, R. M., and Berg, H. C. (2000). Torque-generating units of the flagellar motor of *Escherichia coli* have a high duty ratio. *Nature* 403, 444–447. doi: 10.1038/35000233

Santiveri, M., Roa-Eguiara, A., Kühne, C., Wadhwa, N., Hu, H., Berg, H. C., et al. (2020). Structure and function of stator units of the bacterial flagellar motor. *Cell* 183, 244–257. doi: 10.1016/j.cell.2020.08.016

Silverman, M., Matsumura, P., and Simon, M. (1976). The identification of the mot gene product with *Escherichia coli*-lambda hybrids. *Proc. Natl. Acad. Sci. U.S.A.* 73, 3126–3130. doi: 10.1073/pnas.73.9.3126

Silverman, M., and Simon, M. I. (1974). Flagellar rotation and the mechanism of bacterial motility. *Nature* 249, 73–74. doi: 10.1038/249073a0

Silverman, M., and Simon, M. I. (1977). Bacterial flagella. *Annu. Rev. Microbiol.* 31, 397–419.

Sowa, Y., Rowe, A. D., Leake, M. C., Yakushi, T., Homma, M., Ishijima, A., et al. (2005). Direct observation of steps in rotation of the bacterial flagellar motor. *Nature* 437, 916–919. doi: 10.1038/nature04003

Stolz, B., and Berg, H. C. (1991). Evidence for interactions between MotA and MotB, torque-generating elements of the flagellar motor of *Escherichia coli*. *J. Bacteriol.* 173, 7033–7037. doi: 10.1128/jb.173.21.7033-7037.1991

Suaste-Olmos, F., Domenzain, C., Mireles-Rodriguez, J. C., Poggio, S., Osorio, A., Dreyfus, G., et al. (2010). The flagellar protein FliI is essential for swimming in *Rhodobacter* sphaeroides. *J. Bacteriol.* 192, 6230–6239. doi: 10.1128/JB.00655-10

Sudo, Y., Kitade, Y., Furutani, Y., Kojima, M., Kojima, S., Homma, M., et al. (2009). Interaction between Na+ ion and carboxylates of the PomA-PomB stator unit studied by ATR-FTIR spectroscopy. *Biochemistry* 48, 11699–11705. doi: 10.1021/bi901517n

Tachiyama, S., Chan, K. L., Liu, X., Hathroubi, S., Peterson, B., Khan, M. F., et al. (2022). The flagellar motor protein FliI forms a scaffold of circumferentially positioned rings required for stator activation. *Proc. Natl. Acad. Sci. U.S.A.* 119:e2118401119.

Takekawa, N., Imada, K., and Homma, M. (2020). Structure and energy-conversion mechanism of the bacterial Na^+-driven flagellar motor. *Trends Microbiol.* 28, 719–731. doi: 10.1016/j.tim.2020.03.010

Takekawa, N., Isumi, M., Terashima, H., Zhu, S., Nishino, Y., Sakuma, M., et al. (2019). Structure of vibrio flil, a new stomatin-like protein that assists the bacterial flagellar motor function. *MBio* 10, e292–e219. doi: 10.1128/mBio.00292-19

Takekawa, N., Kojima, S., and Homma, M. (2014). Contribution of many charged residues at the stator-rotor interface of the Na^+-driven flagellar motor to torque generation in *Vibrio alginolyticus*. *J. Bacteriol.* 196, 1377–1385. doi: 10.1128/JB.01392-13

Takekawa, N., Li, N., Kojima, S., and Homma, M. (2012). Characterization of PomA mutants defective in the functional assembly of the Na^+-driven flagellar motor in *Vibrio alginolyticus*. *J. Bacteriol.* 194, 1934–1939. doi: 10.1128/JB.06552-11

Takekawa, N., Terauchi, T., Morimoto, Y. V., Minamino, T., Lo, C. J., Kojima, S., et al. (2013). Na^+ conductivity of the Na^+-driven flagellar motor complex composed of unplugged wild-type or mutant Pomb with Poma. *J. Biochem.* 153, 441–451. doi: 10.1093/jb/mvt011

Terashima, H., Fukuoka, H., Yakushi, T., Kojima, S., and Homma, M. (2006). The vibrio motor proteins, MotX and MotY, are associated with the basal body of Na+-driven flagella and required for stator formation. *Mol. Microbiol.* 62, 1170–1180. doi: 10.1111/j.1365-2958.2006.05435.x

Terashima, H., Kojima, S., and Homma, M. (2008). Flagellar motility in bacteria structure and function of flagellar motor. *Int. Rev. Cell Mol. Biol.* 270, 39–85. doi: 10.1016/S1937-6448(08)01402-0

Terashima, H., Kojima, S., and Homma, M. (2021). Site-directed crosslinking identifies the stator-rotor interaction surfaces in a hybrid bacterial flagellar motor. *J. Bacteriol.* 9:e00016–e21. doi: 10.1128/JB.00016-21

Terashima, H., Li, N., Sakuma, M., Koike, M., Kojima, S., Homma, M., et al. (2013). Insight into the assembly mechanism in the supramolecular rings of the sodium-driven Vibrio flagellar motor from the structure of FlgT. *Proc. Natl. Acad. Sci. U.S.A* 110, 6133–6138. doi: 10.1073/pnas.1222655110

Tipping, M. J., Delalez, N. J., Lim, R., Berry, R. M., and Armitage, J. P. (2013). Load-dependent assembly of the bacterial flagellar motor. *MBio* 4, e551–e513.

Wilson, M. L., and Macnab, R. M. (1988). Overproduction of the MotA protein of *Escherichia coli* and estimation of its wild-type level. *J. Bacteriol.* 170, 588–597. doi: 10.1128/jb.170.2.588-597.1988

Yakushi, T., Yang, J., Fukuoka, H., Homma, M., and Blair, D. F. (2006). Roles of charged residues of rotor and stator in flagellar rotation: comparative study using H^+-driven and Na^+-driven motors in *Escherichia coli*. *J. Bacteriol.* 188, 1466–1472. doi: 10.1128/JB.188.4.1466-1472.2006

Zhou, J. D., Lloyd, S. A., and Blair, D. F. (1998). Electrostatic interactions between rotor and stator in the bacterial flagellar motor. *Proc. Natl. Acad. Sci. U.S A.* 95, 6436–6441. doi: 10.1073/pnas.95.11.6436

Zhu, S., Nishikino, T., Takekawa, N., Terashima, H., Kojima, S., Imada, K., et al. (2020). *In situ* structure of the *Vibrio* polar flagellum reveals a distinct outer membrane complex and its specific interaction with the stator. *J. Bacteriol.* 202, e592–e519. doi: 10.1128/JB.00592-19

Zhu, S., Takao, M., Li, N., Sakuma, M., Nishino, Y., Homma, M., et al. (2014). Conformational change in the periplamic region of the flagellar stator coupled with the assembly around the rotor. *Proc. Natl. Acad. Sci. U.S.A.* 111, 13523–13528. doi: 10.1073/pnas.1324201111

Conflict of Interest: The authors declare that the research was conducted in the absence of any commercial or financial relationships that could be construed as a potential conflict of interest.

Publisher's Note: All claims expressed in this article are solely those of the authors and do not necessarily represent those of their affiliated organizations, or those of the publisher, the editors and the reviewers. Any product that may be evaluated in this article, or claim that may be made by its manufacturer, is not guaranteed or endorsed by the publisher.

Copyright © 2022 Homma and Kojima. This is an open-access article distributed under the terms of the Creative Commons Attribution License (CC BY). The use, distribution or reproduction in other forums is permitted, provided the original author(s) and the copyright owner(s) are credited and that the original publication in this journal is cited, in accordance with accepted academic practice. No use, distribution or reproduction is permitted which does not comply with these terms.

frontiers | Frontiers in Microbiology

REVIEW
published: 07 July 2022
doi: 10.3389/fmicb.2022.928408

Bacterial Proprioception: Can a Bacterium Sense Its Movement?

*Rachit Gupta[1], Junhua Yuan[2] and Pushkar P. Lele[1]**

[1] Artie McFerrin Department of Chemical Engineering, Texas A&M University, College Station, TX, United States,
[2] Department of Physics, University of Science and Technology of China, Hefei, China

The evolution of the bacterial flagellum gave rise to motility and repurposing of a signaling network, now termed the chemotaxis network, enabled biasing of cell movements. This made it possible for the bacterium to seek out favorable chemical environments. To enable chemotaxis, the chemotaxis network sensitively detects extracellular chemical stimuli and appropriately modulates flagellar functions. Additionally, the flagellar motor itself is capable of detecting mechanical stimuli and adapts its structure and function in response, likely triggering a transition from planktonic to surface-associated lifestyles. Recent work has shown a link between the flagellar motor's response to mechanical stimuli and the chemotactic output. Here, we elaborate on this link and discuss how it likely helps the cell sense and adapt to changes in its swimming speeds in different environments. We discuss the mechanism whereby the motor precisely tunes its chemotaxis output under different mechanical loads, analogous to proprioception in higher order organisms. We speculate on the roles bacterial proprioception might play in a variety of phenomena including the transition to surface-associated lifestyles such as swarming and biofilms.

Keywords: mechanosensing, proton-motive force, CheY, chemotaxis, motility

OPEN ACCESS

Edited by:
Jiqiang Ling,
University of Maryland, College Park, United States

Reviewed by:
Daniel B. Kearns,
Indiana University Bloomington, United States
Jonathan David Partridge,
University of Texas at Austin, United States

****Correspondence:***
Pushkar P. Lele
plele@tamu.edu

Specialty section:
This article was submitted to Microbial Physiology and Metabolism, a section of the journal Frontiers in Microbiology

Received: *25 April 2022*
Accepted: *16 June 2022*
Published: *07 July 2022*

Citation:
Gupta R, Yuan J and Lele PP (2022) Bacterial Proprioception: Can a Bacterium Sense Its Movement? Front. Microbiol. 13:928408. doi: 10.3389/fmicb.2022.928408

INTRODUCTION

Propulsion by rotating flagella is among the dominant forms of motility in the bacterial kingdom. Rotation of the flagellum is enabled by a rotary device called the flagellar motor. Modulation of the direction or the speed of flagellar rotation can bias the cell's migration in three-dimensional space (Dickinson and Tranquillo, 1993; Armitage, 1999; Attmannspacher et al., 2005; Wadhwa and Berg, 2022). Unsurprisingly therefore, many bacterial species modulate flagellar functions to swim toward favorable habitats (Silversmith and Bourret, 1999; Eisenbach, 2004). Migration up or down a gradient of extracellular ligands, known as chemotaxis, powerfully influences the likelihood of successful host invasion, colonization, and survival (Kollmann et al., 2005; Lertsethtakarn et al., 2011).

Chemotaxis is enabled by the coupling of a two-component signaling pathway and the flagella (Falke et al., 1997). Chemoreceptors detect changes in the concentration of extracellular ligands and respond by controlling the activity levels of a histidine kinase, CheA. In turn, CheA modulates the phosphorylation of CheY. CheY-P is a freely diffusible cytoplasmic molecule that interacts with the flagellar motor to modulate its function (Welch et al., 1993; Sarkar et al., 2010). In *Escherichia coli*, the dephosphorylation of CheY-P is accelerated by a phosphatase CheZ that localizes mostly at the receptors (Hess et al., 1988; Cantwell et al., 2003), while in some

bacteria such as *Bacillus subtilis*, a structural component (FliY) within the motor itself contributes to CheY-P dephosphorylation (Szurmant et al., 2003). In many chemotactic species, multiple CheY homologues exist that exhibit complex interactions with the motor (Porter et al., 2006). In *E. coli*, a single CheY modulates flagellar switching: the binding of CheY-P to the base of the flagellar motor promotes clockwise (CW) rotation in an otherwise counterclockwise (CCW) rotating motor (Pan et al., 2017). Modulation of the directional switching gives rise to the run-tumble pattern of movement that forms the basis of chemotaxis in *E. coli*. Additionally, certain metabolites can interact directly with the motor to modulate directional switching independent of CheY (Yang et al., 2020; Gupta et al., 2022).

As the bacterium swims up or down a ligand gradient, the varying ligand concentration offsets the CheA activity from its basal value. This response could saturate the response unless CheA activity resets. The resetting, called adaptation, is mediated by two enzymes—a methyltransferase (CheR) and a methylesterase (CheB). CheR and CheB methylate and demethylate the receptors to *precisely* adapt the activity of CheA and thus of CheY-P levels (Parkinson and Kofoid, 1992; Armitage, 1999). Precise adaptation in CheY-P levels helps maintain a constant switching activity in the motor at a basal value despite fluctuations in the chemical environment. Continually adapting and maintaining a basal switching activity, measured as the fraction of time the motor rotates CW, helps the cell retain the ability to respond to novel stimuli. Thus, adaptation is crucial for chemotaxis.

In addition to motility and chemotaxis, the flagellar motor has another function, termed mechanosensing (see **Table 1** for glossary). Flagellar mechanosensing enables the cell to detect changes in its mechanical environment by sensing changes in the viscous resistance (viscous load) to the rotation of the flagellar motor (Lele et al., 2013). Mechanosensing appears to be crucial for the bacterium to sense its adhesion to solid surfaces (Hughes and Berg, 2017). In turn, the flagellum and other appendages such as the pili likely trigger gene regulatory changes or post-translational modifications that help the cell adopt surface-associated lifestyles such as swarming or biofilms (Kearns, 2010; Jones et al., 2015; Chawla et al., 2020; Webster et al., 2022). These regulatory changes and surface-related phenotypes have been reviewed elsewhere (Belas, 2014; Laventie and Jenal, 2020; Wong et al., 2021). Recent work has identified an intimate link between flagellar mechanosensing, adaptation, and chemotaxis (Antani et al., 2021a). Here, we discuss possible mechanisms for this coupling and how it likely gives rise to proprioception—which refers to the ability of an organism to sense its position and velocity in space—in bacteria. We will conclude with a brief note on the implications of bacterial proprioception for bacterial colonization of surfaces.

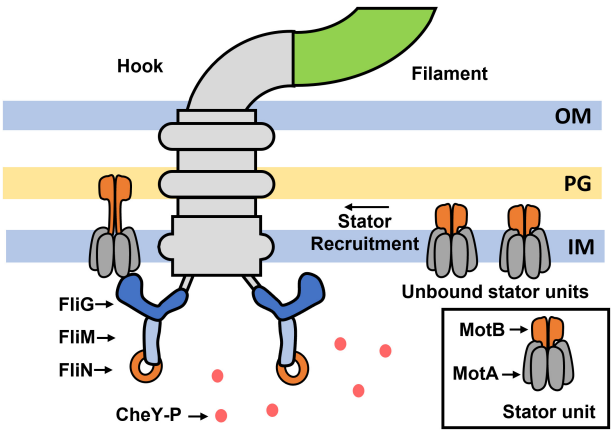


FIGURE 1 | The flagellar motor. Major parts of the flagellar motor are indicated. Unbound stator units diffuse in the membrane and reversibly bind to the motor to induce rotation. The motor recruits additional stator units when the resistance to its rotation is increased (Lele et al., 2013). The FliG ring within the rotor interacts with the stator units, and its conformation determines the direction of rotation. Freely diffusing CheY-P binds to the FliM and FliN complexes located beneath the FliG ring to promote conformational changes in FliG.

TABLE 1 | Glossary.

Term	Definition
Viscous load	Fluid resistance to the rotation of the flagellum or physical obstruction of rotation due to the adhesion of the filament to a surface. A motor lacking the flagellar hook and the filament is under negligible viscous load irrespective of any changes in the extracellular environment of the cell (Chawla et al., 2020).
Mechanical stimulus	Change in the viscous load on the flagellar motor
Mechanosensing	Adaptation/changes in protein function induced by mechanical stimulus
CW_{bias}	Fraction of time the motor rotates CW
Torque	Force applied by a stator unit on the FliG ring, which induces the latter to rotate.
Reversal frequency	Number of switches between CW and CCW directions of rotation per unit time (usually per second)
Stalled motor	A motor that is unable to rotate because the resistance to its rotation exceeds the maximal torque it can generate.
Ultra-sensitivity curve	Sigmoidal relationship between CW_{bias} and CheY-P, characterized by a Hill coefficient $\sim$ 10–20.
Precise adaptation	Restoration of a function after a stimulus to its exact pre-stimulus value.

Flagellar Switching and Torque

The flagellum consists of an extracellular filament connected to a transmembrane rotary motor by a hook that serves as a universal joint (**Figure 1**). The flagellar motor consists of a rotor and a stator; the latter delivers torque to the former to induce rotation (Berg, 2004). Torque is generated by multiple stator units that may associate and dissociate from the motor as a function of several factors (Muramoto et al., 1994; Fung and Berg, 1995; Berg, 2003; Leake et al., 2006; Blair et al., 2008; Paulick et al., 2009; Lin et al., 2021). To generate torque, the stator units typically utilize the proton-motive force, although alternate sources of ion-motive force also may be used (Manson et al., 1977; Yorimitsu and Homma, 2001; Wilhelms et al., 2009; Terahara et al., 2012; Minamino and Imada, 2015; Imazawa et al., 2016). The stator

complex functions as a mechanosensor by sensing changes in the viscous resistance to the rotation of the motor—also known as the viscous load—and adapts structurally and functionally in response to increased load (Lele et al., 2013; Chawla et al., 2017). The direction of motor rotation is determined by the conformations of the ring of FliG proteins within the flagellar rotor, which forms the track along which the stator units operate (**Figure 1**). The FliG ring consists of multiple subunits (34 in *E. coli*) (Lee et al., 2010). When every FliG subunit adopts the same conformation, the motor rotates at the maximum possible speed in a given direction for a particular viscous load (Bray and Duke, 2004). The FliG ring switches stochastically between two conformations, one favoring CCW rotation and the other favoring CW rotation. CheY-P binds to FliMN to stabilize the CW conformation of the FliG ring (Sarkar et al., 2010; Minamino et al., 2011, 2019).

Switching activity is quantified by the CW_{bias}, which refers to the fraction of time the motor rotates CW. The CW_{bias} depends ultra-sensitively on CheY-P levels: the motor exhibits the entire range of CW_{bias} from 0 to 1 with an $\sim$1 μM change in intracellular CheY-P levels (Cluzel et al., 2000; Korobkova et al., 2006; Tu, 2008). The cell must maintain a steady, intermediate value of the basal bias ($0 < CW_{bias} < 1$), otherwise it cannot respond to chemical signals (Antani et al., 2021b). As motor reversals are inherently stochastic, the direction of rotation may change multiple times unpredictably in a second. The reversal frequency vs. CheY-P relationship is unimodal or bell-shaped (Cluzel et al., 2000), which means that there is no unique value of the reversal frequency with respect to the CheA activity. Hence, it is easier to interpret the response of the chemotaxis network to chemical stimuli from changes in CW_{bias} (Antani et al., 2021b).

Biophysical characterization of the flagellar motor typically involves monitoring the rotational direction and speeds of a latex bead attached to it. The viscous load on the motor is varied by using beads of different sizes. In *E. coli*, such experiments showed that variations in the viscous load alter the reversal frequency even when no chemical stimulus is present (Fahrner et al., 2003; Yuan et al., 2009a). The viscous resistance to rotation (load) only exists in the presence of torque—a large and a small latex bead do not represent significantly different loads in the absence of torque. The torque delivered by each stator unit increases with the viscous load (Ryu et al., 2000), which indicates that the reason the reversal frequency is load-sensitive is because torque influences the conformations of the FliG subunits.

How might torque influence FliG conformations? One possibility is that torque influences the activation barriers for FliG to switch between the CW and CCW conformations (Yuan et al., 2009a). This can cause each FliG subunit that comes in contact with a stator unit, as the rotor turns, to flip between CW and CCW conformations more or less frequently as a function of the torque experienced and of the duration of contact between the stator units and FliG subunits (Bai et al., 2012). But, these and other models offer limited quantitative insights as they assume that a constant number of stator units engage with the rotor irrespective of the load. In other words, the number of FliG subunits simultaneously experiencing torque under low and high loads are assumed to be the same (Bai et al., 2012).

This assumption was invalidated when it was observed that the number of stator units associated with the motor increases with the viscous load: the motor recruits $\sim$1 stator unit under very low viscous loads and as many as 8–11 stator units under very high viscous loads (**Figure 1**; Lele et al., 2013; Tipping et al., 2013). When the viscous load on a motor that was rotated by a single stator unit was suddenly increased, torque increased in response and switching was inhibited. As the motor rotated predominantly CCW, this suggests that increased torque inhibits changes in the conformation of FliG from CCW to CW. Recent observations are consistent with this idea – in cells in which stator proteins are under-expressed, motors stably rotated by 1–2 stator units under high loads rotated mostly CCW (low CW_{bias}) even when the CheY-P pool was above the native levels (Antani et al., 2021a). A key feature of flagellar mechanosensing is that additional stator units are gradually recruited to the motor under high loads, increasing the overall torque on FliG (**Figure 2A**). Interestingly, the CW_{bias} also increases as new stator units are recruited, suggesting that the switching activity adapts to variations in torque (**Figure 2B**; Lele et al., 2013). If increased torque applied by each stator unit inhibits changes in conformations of FliG subunits from CCW to CW, how do motors increase their CW_{bias} under high loads?

Models are evaluated based on their ability to accurately predict load-dependent variations in several characteristic features of flagellar switching: the reversal frequencies, the ultrasensitive dependence of CW_{bias} on CheY-P levels, and the wait-time distributions for CW and CCW rotation. Models invoking non-equilibrium mechanisms have explained the non-exponential distributions that have been observed for the time-intervals for CW or CCW rotation. Subsequent measurements of the interval distributions under near zero to high loads at various values of the proton motive force (PMF), and for different number of stator units bound to the motor, are all consistent with non-equilibrium mechanisms that involve some effect of torque on the probability of conformational changes in FliG (Wang et al., 2017). Recent measurements of switching under very high viscous loads, which almost prevent motor rotation, are also consistent with a model that attributes differential effects of load on switching to the asymmetry in torque experienced by FliG in the CW and CCW conformations (Yuan et al., 2009b; Wang et al., 2021).

To determine the mechanism by which constant CW_{bias} is maintained at high loads, Antani and co-workers imaged the binding of fluorescently labeled CheY-P to motors in tethered cells using total internal reflection fluorescence microscopy (Antani et al., 2021a). The tethered cell assay involves adhering a single flagellar filament to a glass substrate, which causes the cell body to rotate around the motor of interest (Silverman and Simon, 1974). In such motors, the authors observed that CheY-P binding was maximal when motors rotated with a full complement of stator units. In the absence of stator units, CheY-P binding was weaker (Antani et al., 2021a). This suggested that there is a proton flux-dependent mechanism of CheY-P binding as there is no significant flux of protons in motors lacking stator units. However, when optical traps were used to block the

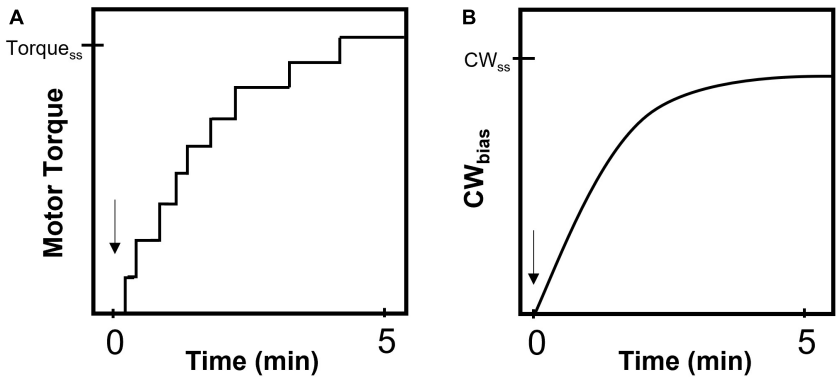


FIGURE 2 | Mechano-response in a flagellar motor. Cartoon representations of the response of a single motor that is mechanically stimulated by suddenly increasing the viscous load (Lele et al., 2013). The arrow indicates the instant of stimulus. **(A)** The motor responds by recruiting additional stator units resulting in a stepwise increase in torque (and speed). Torque$_{SS}$ indicates the final, steady-state value of torque following the completion of stator recruitment and can range from 2,000 to 4,000 pN.nm under high loads (Berg, 2004). **(B)** The probability of CW rotation (CW$_{bias}$) increases from a very low value to a steady-state or basal value (CW$_{SS}$) over a similar timescale as that for stator recruitment. The CW$_{SS}$ value remains constant irrespective of the magnitude of the load-change (Antani et al., 2021a).

rotation of a tethered cell to inhibit proton flux, no inhibition in CheY-P binding was observed. In such stalled motors, the stator units remain engaged and continue to deliver torque (Tipping et al., 2013). Thus, it is not the change in proton flux but changes in torque that induced differential CheY-P binding (Antani et al., 2021a). Based on these findings, we proposed a model in which increased torque interferes with the conformational change in FliG from CCW to CW. However, increased torque also promotes CheY-P binding. This mechanosensitive binding of CheY-P appears to compensate for the inhibitory effects of torque on switching to CW rotation.

Torque-Dependent Mechanisms of Stator Recruitment and CheY-P Binding

Experiments in *E. coli* suggest that there is a pool of ∼100 stator units within the cell membrane (Leake et al., 2006). Each stator unit consists of a pentamer of MotA and a dimer of MotB, forming proton channels that remain blocked by two plugs that prevent the leakage of protons into the cytoplasm from the periplasm (Hosking et al., 2006). When MotA interacts with FliG, the plugs open and interact with one another to allow the flow of protons (Hosking et al., 2006). This may enable relative motion between the MotB and the MotA interfaces; as per latest models, the relative motion involves the rotation of the MotA pentamer around the MotB dimer (Deme et al., 2020; Santiveri et al., 2020). This relative motion can transmit force to contacting FliG subunits resulting in a torque that rotates the motor. However, for proper transmission of the force to FliG and for the plugs to persist in the open position, the stator unit must be anchored in the cell wall (Zhu et al., 2014). Anchoring is achieved by extending the peptidoglycan binding domain (PGB) in MotB such that it associates with the cell wall (Van Way et al., 2000; Kojima et al., 2009, 2018).

There are numerous C-ring assemblies in the cell membrane that are not necessarily parts of functional motors (Delalez et al., 2010; Li and Sourjik, 2011). Co-isolation assays showed weak interactions between MotA and FliG (Tang et al., 1996), so the latter does not need to be a part of a fully functioning motor to interact with a stator unit. If stator-FliG interactions occur frequently in the membrane, what prevents stator units from conducting non-productive transmembrane proton flow? Probably, the PGB fail to anchor stably during such interactions. Hence, the opening of the plugs would be short-lived. Consequently, the stator units may simply diffuse away rather than continuously interacting with the pre-assembled C-rings. We propose that the reason the PGB does not anchor stably is because the FliG rings in pre-assemblies offer negligible viscous resistance for the stator units to work against – without the flagellar hook and a filament, the pre-assembled structure is always under negligible load irrespective of the viscosity of the extracellular environment (Chawla et al., 2020).

There is support for the idea that the strength of the association between the PGB and the cell wall increases with load. First, high loads induce higher torque from the stator units (Ryu et al., 2000), which indicates that there is a correlation between high loads and stable association between the PGB and the cell wall. Second, paralyzed or defective stator units with mutant MotA subunits exhibit weak association with motors, as seen in tethered cells, likely because the PGB fails to anchor properly in these mutants (Chawla et al., 2017). Finally, experimental observations are consistent with a model in which the dissociation rate of a stator unit from the motor decreases with an increase in the torque it delivers (Chawla et al., 2017). Thus, application of torque to FliG requires stator anchoring within the cell wall and increases the strength of that attachment, which potentially explains how mechanosensitive recruitment of stator units to the motor occurs (Lele et al., 2013; Nord et al., 2017; Terahara et al., 2017). Interested readers are referred elsewhere for a detailed theoretical exposition of the torque-dependent stator binding (Wadhwa et al., 2019).

Once MotB anchors and the stator unit begins delivering torque, Newton's third law dictates that an equal and opposite (reactive) torque must simultaneously act on the interface

between the PGB and the peptidoglycan (Antani et al., 2021a). The notion of a reactive torque acting on the PGB is consistent with the notion that the stator unit itself is a rotary motor (Chang et al., 2020; Deme et al., 2020; Santiveri et al., 2020). The reactive torque could strengthen the association of the PGB with the cell wall by creating a torsional twist within the stator unit, thereby uncovering additional peptidoglycan-binding sites within PGB (Chawla et al., 2017) or by activating a mechanosensitive component within MotB that stabilizes the extended conformation of the PGB (Chawla et al., 2017; Nord et al., 2017). We propose an alternate basis for the mechanosensitive association of the stator units with the cell wall. The torsional twist could embed the PGB within the peptidoglycan, like a fork spinning in spaghetti, strengthening the association between the PGB and peptidoglycan. The entanglement of the PGB in the peptidoglycan is likely stronger when the stator unit delivers higher torque, causing a decrease in the dissociation rate and an increase in the dwell time of the stator unit at the motor. There is only partial cross-linking within the peptidoglycan (Glauner, 1988; Glauner et al., 1988; Meroueh et al., 2006) and the pore-size of the cell wall is similar to the dimensions of the PGB (Meroueh et al., 2006; Roujeinikova, 2008), suggesting that the cell wall is flexible locally and could support torque-dependent entanglement of the PGB.

The proposed mechanism does not require the presence of a mechanosensitive domain within the stator unit, and it is consistent with a strong chemical affinity between the PGB and the peptidoglycan (Roujeinikova, 2008). In some bacterial species, such as *Pseudomonas aeruginosa*, which carries more than one type of stator, the viscous load modulates competitive docking of stator units at the motor (Wu et al., 2021). The outcome of the competition between different stator types will be determined by differences in the torsional rigidity of stator components, the rigidity of the peptidoglycan network, the amount of torque each stator type can generate against a particular load, the ionic strength, and the relative affinities of the different PGB domains for the cell wall. Several types of regulators also interact with the stator and/or the rotor to modulate torque (Subramanian and Kearns, 2019). These regulators may affect the load-dependence of the association of the PGB with the cell wall to influence mechanosensitive stator recruitment.

Although the predicted effects of the reactive torque on the interactions of the PGB with the cell wall are yet to be tested, in *E. coli* the torque on FliG has recently been shown to affect CheY-P interactions with the motor. The force delivered to FliG strengthens the binding of CheY-P to FliM and FliN complexes at the base of the motor although the binding sites are almost 15 nm away from the site of torque delivery (**Figure 1**). An allosteric mechanism is likely involved, but details are lacking (Antani et al., 2021a). It is possible that small conformational shifts induced in FliG because of increasing torque might cause downstream conformational changes in FliM or FliN to increase their affinity for CheY-P. The exact mechanism is unknown; a complication is that the affinity of FliM/FliN for CheY-P is lower when FliG is in its CCW conformation (Fukuoka et al., 2014). As the increased torque increases the probability that FliG adopts the CCW conformation, CheY-P binding is predicted to decrease as more stator units are recruited following a load increase, contrary to observations. Nevertheless, the mechanosensitive nature of CheY-P binding suggests that chemotaxis and flagellar mechanosensing are coupled.

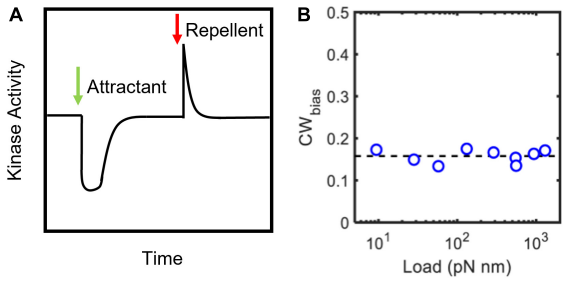


FIGURE 3 | Precise adaptation in chemotactic activity. **(A)** Cartoon representation of CheA responses to step changes in ligand levels (Sourjik and Berg, 2002). CheA activity was calculated from measurements of Förster resonance energy transfer (FRET) between CheY-eYFP and CheZ-CFP in live cells (Sourjik and Berg, 2002). The addition of an attractant (green arrow) or repellent (red arrow) decreases or increases the kinase activity, respectively. CheR and CheB help adapt the activity precisely to its basal value. Consequently, CheY-P levels and CW_{bias} (not shown) also precisely adapt. **(B)** The steady-state CW_{bias} is independent of the load (Yuan et al., 2009a; Antani et al., 2021a). This observation suggests that the adaptation of the CW_{bias} to mechanical stimuli (shown in **Figure 2B**) is precise. The adaptation is network independent.

Mechanosensitive CheY-P Binding and Precise Adaptation

The chemotaxis network is highly sensitive to extracellular ligands over a wide range of concentrations (Berg, 2004). Chemical signals sensed by the chemoreceptors are greatly amplified to modulate the flagellar switch response. To avoid saturating a system with such high gain, CheR and CheB help adapt the kinase activity to keep CheY-P levels at the basal value (**Figure 3A**; Sourjik and Berg, 2002). This adaptation at the input of the chemotaxis network is rapid, typically occurring over a few seconds (Segall et al., 1982). Such short-time adaptation maintains a basal level of flagellar switch activity (CW_{bias}) that ensures that the cell can respond to novel chemical stimuli and continue swimming along a gradient of ligands (Berg and Purcell, 1977). There is no evidence that chemoreceptors respond to mechanical feedback from the motor (Shimizu et al., 2006). As mechanical stimuli can inhibit switching (**Figure 2B**), the flagellar motor must find a way to adapt to changes in viscous load, failing which the cell will lose its ability to perform chemotaxis in environments with widely different viscosities.

Yuan et al. (2012) discovered that the motor adapts to changes in CW_{bias} induced by chemical stimuli. The FliM and FliN complexes in *E. coli* can remodel to offset long-term fluctuations in CheA activity. FliM/FliN remodeling probably occurs because FliG subunits bind to FliM and FliN subunits with a higher affinity when the motor is in the CCW conformation compared to the CW conformation (Lele et al., 2012). For example, a long-lived decrease in the CheA activity, leading to lower CheY-P levels, induces FliG subunits to adopt the CCW conformation,

thereby decreasing the CW_{bias}. This causes the number of FliM/FliN subunits bound to the motor to increase, presumably helping the motor bind more CheY-P. What follows is a partial adaptation in the CW_{bias}. Later work indicated that FliM/FliN remodel each time the motor stochastically switches between the CCW and CCW directions irrespective of the CheA activity, with the number of FliM/FliN subunits added or removed increasing with the duration of the CCW or CW interval, respectively (Lele et al., 2015; Liu et al., 2020). FliM/FliN remodeling does not promote precise adaptation in CW_{bias} but does appear to complement and accelerate chemoreceptor-mediated adaptation for optimizing chemotaxis (Dufour et al., 2014; Zhang et al., 2018).

The basal value of CW_{bias} is independent of load (**Figure 3B**), despite the inhibitory effects of load on switching (**Figure 2B**). This suggests that the CW_{bias} adapts precisely any time there is a change in the load. Do FliM and FliN remodel to enable precise adaptation in switching in response to such mechanical stimuli? Experiments have ruled out this possibility (Antani et al., 2021a). Instead, the motor precisely adapts by modulating the affinity of FliM/FliN for CheY-P following the mechanical stimulus. These changes in affinity fine-tune the dependence of the CW_{bias} on CheY-P, a relationship characterized by a steep sigmoidal curve (Cluzel et al., 2000). Experiments indicate that the tuning mechanism involves shifts in the CW_{bias}–CheY-P curve with varying torque, as shown in **Figure 4**, increasing or decreasing the sensitivity of the motor for CheY-P (Antani et al., 2021a). An undescribed feedback mechanism must be required for such precision. In addition to torque-dependent affinity for CheY-P, the duration of the contact between each FliG subunit and the stator likely plays a key role in the feedback as it may affect the duration of mechanosensitive CheY-P binding to the FliM/FliN subunits in contact with that FliG subunit. The time each stator unit and FliG are in contact depends on the rotation rate (Bai et al., 2012), and the rotation rate determines the swimming speed. Hence, the swimming speed is indirectly expected to influence the feedback. It is possible, therefore, that this mechanism enables adaptation to changes in the swimming speed, as when the bacterium enters an environment of a different viscosity.

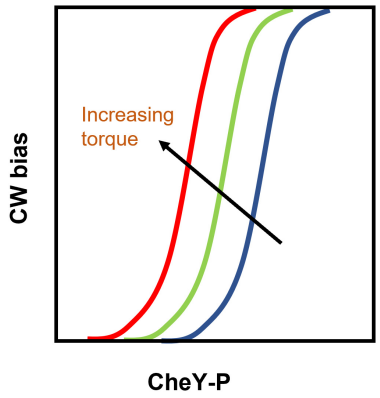


FIGURE 4 | Tuning of the CW_{bias} –CheY-P relationship by torque: Cartoon representation of the analysis of experimental results (Antani et al., 2021a). Increasing torque shifts the CW_{bias} versus [CheY-P] curve leftward (from the position indicated by the blue curve to the one indicated by the red curve) by modulating the affinity of FliM/FliN for CheY-P. As a result, the CW_{bias} increases with increasing torque even though CheY-P levels remain constant. Thus, the shifting curves compensate for the inhibitory effects of increased viscous load on the motor and help maintain a load-independent CW_{bias} (shown in **Figure 3B**).

Bacterial Proprioception

The tendency of the flagellum to maintain a constant switching activity under varying viscous loads is likely to be critical for allowing peritrichous bacterial species such as *E. coli* to run and tumble even as new flagella are being assembled. As a new flagellum is being formed, the filament length initially is very short, and the new motor experiences a low load. As the filament grows, the motor experiences an increasing viscous load. Without the tuning of the sensitivity curves (**Figure 4**), the growing filaments will cease to switch once the filament reaches a certain length. The same principle will apply to polarly flagellated species; as the filaments grow, the polar motors must adapt to the increasing load to continue performing runs and reversals. Therefore, mechanosensitive binding of CheY-P is likely a widespread phenomenon.

The tuning of sensitivity to stimuli in response to mechanical stress, such as the one seen in **Figure 4**, is common in higher organisms. For example, proprioceptive feedback in the motor neurons that enervate the leg muscles in insects helps maintain maximal sensitivity to different mechanical loads. This allows the organism to maintain posture and grip when walking on the floor or the ceiling. More broadly, proprioception refers to an organism's ability to sense its movements and/or position in space (Tuthill and Azim, 2018; Harris et al., 2020). A familiar example would be a soccer player judging how fast a ball is traveling to intercept it precisely in three dimensions. Bacteria lack sophisticated sensory systems and a central nervous system. Nonetheless, the coupling between the mechanosensitive stators, CheY-P, and the output of the chemotaxis system provides bacteria with what are essentially proprioceptive abilities.

Bacterial proprioception probably helps the cell sense its own position relative to a surface and its adhesion to the surface. It also enables chemotaxis when cells encounter highly viscous environments such as the mucous layers coating the intestine or gel-like media. Thus, the cell can adapt its flagellar functions to continue chemotaxis, which is important for surface colonization (Tamar et al., 2016).

However, the limits of mechanosensitive adaptation may be exceeded in certain scenarios. For example, in swarming colonies, CheY-P levels are so low that the probability of switching is significantly diminished despite any adaptations (Ford et al., 2018; Partridge et al., 2019). We speculate that such a loss in switching may trigger downstream signaling events to sustain the swarming state of the colony. Although stator mechanosensing and mechanosensitive CheY-P binding were the focus in this review, it is possible that a similar proprioceptive coupling

exists between stators and other functional regulators of the motor. In that case, proprioception might regulate numerous other developmental effects, including biofilm formation, possibly by modulating secondary messenger levels (Boyd and O'toole, 2012; Webster et al., 2022).

AUTHOR CONTRIBUTIONS

RG and PL wrote the manuscript with inputs from JY. All authors approved it for publication.

FUNDING

PL acknowledged funding from the National Institute of General Medical Sciences United States (R01-GM123085 and R01GM132436). JY acknowledged funding from National Natural Science Foundation of China (11925406 and 12090053).

ACKNOWLEDGMENTS

We thank Michael D. Manson for his inputs and careful reading of the manuscript.

REFERENCES

Antani, J. D., Gupta, R., Lee, A. H., Rhee, K. Y., Manson, M. D., and Lele, P. P. (2021a). Mechanosensitive recruitment of stator units promotes binding of the response regulator CheY-P to the flagellar motor. *Nat. Commun.* 12:5442. doi: 10.1038/s41467-021-25774-2

Antani, J. D., Sumali, A. X., Lele, T. P., and Lele, P. P. (2021b). Asymmetric random walks reveal that the chemotaxis network modulates flagellar rotational bias in *Helicobacter pylori*. *eLife* 10:e63936. doi: 10.7554/eLife.63936

Armitage, J. P. (1999). Bacterial tactic responses. *Adv. Microb. Physiol.* 41, 229–289.

Attmannspacher, U., Scharf, B., and Schmitt, R. (2005). Control of speed modulation (chemokinesis) in the unidirectional rotary motor of *Sinorhizobium meliloti*. *Mol. Microbiol.* 56, 708–718. doi: 10.1111/j.1365-2958.2005.04565.x

Bai, F., Minamino, T., Wu, Z., Namba, K., and Xing, J. (2012). Coupling between Switching Regulation and Torque Generation in Bacterial Flagellar Motor. *Phys. Rev. Lett.* 108:178105.

Belas, R. (2014). Biofilms, flagella, and mechanosensing of surfaces by bacteria. *Trends Microbiol.* 22, 517–527.

Berg, H. C. (2003). The Rotary Motor of Bacterial Flagella. *Annu. Rev. Biochem.* 72, 19–54.

Berg, H. C. (2004). *E. Coli in Motion*. New York: Springer.

Berg, H. C., and Purcell, E. M. (1977). Physics of Chemoreception. *Biophys. J.* 20, 193–219.

Blair, K. M., Turner, L., Winkelman, J. T., Berg, H. C., and Kearns, D. B. (2008). A molecular clutch disables flagella in the *Bacillus subtilis* biofilm. *Science* 320, 1636–1638. doi: 10.1126/science.1157877

Boyd, C. D., and O'toole, G. A. (2012). Second messenger regulation of biofilm formation: breakthroughs in understanding c-di-GMP effector systems. *Annu. Rev. Cell Dev. Biol.* 28, 439–462. doi: 10.1146/annurev-cellbio-101011-155705

Bray, D., and Duke, T. (2004). Conformational Spread: the Propagation of Allosteric States in Large Multiprotein Complexes. *Annu. Rev. Biophys. Biomol. Struct.* 33, 53–73.

Cantwell, B. J., Draheim, R. R., Weart, R. B., Nguyen, C., Stewart, R. C., and Manson, M. D. (2003). CheZ phosphatase localizes to chemoreceptor patches via CheA-short. *J. Bacteriol.* 185, 2354–2361. doi: 10.1128/JB.185.7.2354-2361.2003

Chang, Y., Zhang, K., Carroll, B. L., Zhao, X., Charon, N. W., Norris, S. J., et al. (2020). Molecular mechanism for rotational switching of the bacterial flagellar motor. *Nat. Struct. Mol. Biol.* 27, 1041–1047.

Chawla, R., Ford, K. M., and Lele, P. P. (2017). Torque, but not FliL, regulates mechanosensitive flagellar motor-function. *Sci. Rep.* 7:5565.

Chawla, R., Gupta, R., Lele, T. P., and Lele, P. P. (2020). A Skeptic's Guide to Bacterial Mechanosensing. *J. Mol. Biol.* 432, 523–533. doi: 10.1016/j.jmb.2019.09.004

Cluzel, P., Surette, M., and Leibler, S. (2000). An ultrasensitive bacterial motor revealed by monitoring signaling proteins in single cells. *Science* 287, 1652–1655. doi: 10.1126/science.287.5458.1652

Delalez, N. J., Wadhams George, H., Rosser, G., Xue, Q., Brown Mostyn, T., Dobbie Ian, M., et al. (2010). Signal-dependent turnover of the bacterial flagellar switch protein FliM. *Proc. Natl. Acad. Sci. U. S. A.* 107, 11347–11351. doi: 10.1073/pnas.1000284107

Deme, J. C., Johnson, S., Vickery, O., Aron, A., Monkhouse, H., Griffiths, T., et al. (2020). Structures of the stator complex that drives rotation of the bacterial flagellum. *Nat. Microbiol.* 5, 1553–1564.

Dickinson, R. B., and Tranquillo, R. T. (1993). A stochastic model for adhesion-mediated cell random motility and haptotaxis. *J. Math. Biol.* 31, 563–600. doi: 10.1007/BF00161199

Dufour, Y. S., Fu, X., Hernandez-Nunez, L., and Emonet, T. (2014). Limits of Feedback Control in Bacterial Chemotaxis. *PLoS Comput. Biol.* 10:e1003694. doi: 10.1371/journal.pcbi.1003694

Eisenbach, M. (2004). *Chemotaxis*. London: Imperial College Press.

Fahrner, K. A., Ryu, W. S., and Berg, H. C. (2003). Bacterial flagellar switching under load. *Nature* 423, 938–938.

Falke, J. J., Bass, R. B., Butler, S. L., Chervitz, S. A., and Danielson, M. A. (1997). The two-component signaling pathway of bacterial chemotaxis: a molecular view of signal transduction by receptors, kinases, and adaptation enzymes. *Annu. Rev. Cell Dev. Biol.* 13, 457–512. doi: 10.1146/annurev.cellbio.13.1.457

Ford, K. M., Antani, J. D., Nagarajan, A., Johnson, M. M., and Lele, P. P. (2018). Switching and Torque Generation in Swarming E. coli. *Front. Microbiol.* 9:2197. doi: 10.3389/fmicb.2018.02197

Fukuoka, H., Sagawa, T., Inoue, Y., Takahashi, H., and Ishijima, A. (2014). Direct Imaging of Intracellular Signaling Components That Regulate Bacterial Chemotaxis. *Sci. Signal.* 7:ra32. doi: 10.1126/scisignal.2004963

Fung, D. C., and Berg, H. C. (1995). Powering the flagellar motor of *Escherichia coli* with an external voltage source. *Nature* 375, 809–812. doi: 10.1038/375809a0

Glauner, B. (1988). Separation and quantification of muropeptides with high-performance liquid chromatography. *Anal. Biochem.* 172, 451–464.

Glauner, B., Holtje, J. V., and Schwarz, U. (1988). The composition of the murein of *Escherichia coli*. *J. Biol. Chem.* 263, 10088–10095.

Gupta, R., Rhee, K. Y., Beagle, S. D., Chawla, R., Perdomo, N., Lockless, S. W., et al. (2022). Indole modulates cooperative protein–protein interactions in the flagellar motor. *PNAS Nexus* 1:pgac035. doi: 10.1093/pnasnexus/pgac035

Harris, C. M., Dinges, G. F., Haberkorn, A., Gebehart, C., Buschges, A., and Zill, S. N. (2020). Gradients in mechanotransduction of force and body weight in insects. *Arthropod Struct. Dev.* 58:100970. doi: 10.1016/j.asd.2020.100970

Hess, J. F., Oosawa, K., Kaplan, N., and Simon, M. I. (1988). Phosphorylation of three proteins in the signaling pathway of bacterial chemotaxis. *Cell* 53, 79–87.

Hosking, E. R., Vogt, C., Bakker, E. P., and Manson, M. D. (2006). The *Escherichia coli* MotAB proton channel unplugged. *J. Mol. Biol.* 364, 921–937. doi: 10.1016/j.jmb.2006.09.035

Hughes, K. T., and Berg, H. C. (2017). The bacterium has landed. *Science* 358, 446–447.

Imazawa, R., Takahashi, Y., Aoki, W., Sano, M., and Ito, M. (2016). A novel type bacterial flagellar motor that can use divalent cations as a coupling ion. *Sci. Rep.* 6:19773. doi: 10.1038/srep19773

Jones, C. J., Utada, A., Davis, K. R., Thongsomboon, W., Zamorano Sanchez, D., Banakar, V., et al. (2015). C-di-GMP Regulates Motile to Sessile Transition by Modulating MshA Pili Biogenesis and Near-Surface Motility Behavior in *Vibrio cholerae*. *PLoS Pathog.* 11:e1005068. doi: 10.1371/journal.ppat.1005068

Kearns, D. B. (2010). A field guide to bacterial swarming motility. *Nat. Rev. Microbiol.* 8, 634–644.

Kojima, S., Imada, K., Sakuma, M., Sudo, Y., Kojima, C., Minamino, T., et al. (2009). Stator assembly and activation mechanism of the flagellar motor by the periplasmic region of MotB. *Mol. Microbiol.* 73, 710–718.

Kojima, S., Takao, M., Almira, G., Kawahara, I., Sakuma, M., Homma, M., et al. (2018). The Helix Rearrangement in the Periplasmic Domain of the Flagellar Stator B Subunit Activates Peptidoglycan Binding and Ion Influx. *Structure* 26:e595. doi: 10.1016/j.str.2018.02.016

Kollmann, M., Løvdok, L., Bartholomé, K., Timmer, J., and Sourjik, V. (2005). Design principles of a bacterial signalling network. *Nature* 438, 504–507.

Korobkova, E. A., Emonet, T., Park, H., and Cluzel, P. (2006). Hidden stochastic nature of a single bacterial motor. *Phys. Rev. Lett.* 96:058105. doi: 10.1103/PhysRevLett.96.058105

Laventie, B.-J., and Jenal, U. (2020). Surface Sensing and Adaptation in Bacteria. *Annu. Rev. Microbiol.* 74, 735–760.

Leake, M. C., Chandler, J. H., Wadhams, G. H., Bai, F., Berry, R. M., and Armitage, J. P. (2006). Stoichiometry and turnover in single, functioning membrane protein complexes. *Nature* 443, 355–358.

Lee, L. K., Ginsburg, M. A., Crovace, C., Donohoe, M., and Stock, D. (2010). Structure of the torque ring of the flagellar motor and the molecular basis for rotational switching. *Nature* 466, 996–1000.

Lele, P. P., Branch, R. W., Nathan, V. S. J., and Berg, H. C. (2012). Mechanism for adaptive remodeling of the bacterial flagellar switch. *Proc. Natl. Acad. Sci. U. S. A.* 109:20018.

Lele, P. P., Hosu, B. G., and Berg, H. C. (2013). Dynamics of mechanosensing in the bacterial flagellar motor. *Proc. Natl. Acad. Sci. U. S. A.* 110:11839.

Lele, P. P., Shrivastava, A., Roland, T., and Berg, H. C. (2015). Response thresholds in bacterial chemotaxis. *Sci. Adv.* 1:e1500299.

Lertsethtakarn, P., Ottemann, K. M., and Hendrixson, D. R. (2011). Motility and chemotaxis in Campylobacter and Helicobacter. *Annu. Rev. Microbiol.* 65, 389–410.

Li, H., and Sourjik, V. (2011). Assembly and stability of flagellar motor in *Escherichia coli*. *Mol. Microbiol.* 80, 886–899. doi: 10.1111/j.1365-2958.2011.07557.x

Lin, T.-S., Kojima, S., Fukuoka, H., Ishijima, A., Homma, M., and Lo, C.-J. (2021). Stator Dynamics Depending on Sodium Concentration in Sodium-Driven Bacterial Flagellar Motors. *Front. Microbiol.* 12:765739. doi: 10.3389/fmicb.2021.765739

Liu, G., Tao, A., Zhang, R., and Yuan, J. (2020). Robustness in an Ultrasensitive Motor. *mBio* 11, e03050–19. doi: 10.1128/mBio.03050-19

Manson, M. D., Tedesco, P., Berg, H. C., Harold, F. M., and Van Der Drift, C. (1977). A protonmotive force drives bacterial flagella. *Proc. Natl. Acad. Sci. U. S. A.* 74, 3060–3064.

Meroueh, S. O., Bencze, K. Z., Hesek, D., Lee, M., Fisher, J. F., Stemmler, T. L., et al. (2006). Three-dimensional structure of the bacterial cell wall peptidoglycan. *Proc. Natl. Acad. Sci. U. S. A.* 103, 4404–4409.

Minamino, T., and Imada, K. (2015). The bacterial flagellar motor and its structural diversity. *Trends Microbiol.* 23, 267–274.

Minamino, T., Imada, K., Kinoshita, M., Nakamura, S., Morimoto, Y. V., and Namba, K. (2011). Structural Insight into the Rotational Switching Mechanism of the Bacterial Flagellar Motor. *PLoS Biol.* 9:e1000616. doi: 10.1371/journal.pbio.1000616

Minamino, T., Kinoshita, M., and Namba, K. (2019). Directional Switching Mechanism of the Bacterial Flagellar Motor. *Comput. Struct. Biotechnol. J.* 17, 1075–1081.

Muramoto, K., Sugiyama, S., Cragoe, E. J. Jr., and Imae, Y. (1994). Successive inactivation of the force-generating units of sodium-driven bacterial flagellar motors by a photoreactive amiloride analog. *J. Biol. Chem.* 269, 3374–3380.

Nord, A. L., Gachon, E., Perez-Carrasco, R., Nirody Jasmine, A., Barducci, A., Berry Richard, M., et al. (2017). Catch bond drives stator mechanosensitivity in the bacterial flagellar motor. *Proc. Natl. Acad. Sci. U. S. A.* 114, 12952–12957. doi: 10.1073/pnas.1716002114

Pan, W., Dahlquist, F. W., and Hazelbauer, G. L. (2017). Signaling complexes control the chemotaxis kinase by altering its apparent rate constant of autophosphorylation. *Protein Sci.* 26, 1535–1546. doi: 10.1002/pro.3179

Parkinson, J. S., and Kofoid, E. C. (1992). Communication modules in bacterial signaling proteins. *Annu. Rev. Genet.* 26, 71–112.

Partridge, J. D., Nhu, N. T. Q., Dufour, Y. S., and Harshey, R. M. (2019). *Escherichia coli* Remodels the Chemotaxis Pathway for Swarming. *mBio* 10, e316–e319. doi: 10.1128/mBio.00316-19

Paulick, A., Koerdt, A., Lassak, J., Huntley, S., Wilms, I., Narberhaus, F., et al. (2009). Two different stator systems drive a single polar flagellum in Shewanella oneidensis MR-1. *Mol. Microbiol.* 71, 836–850. doi: 10.1111/j.1365-2958.2008.06570.x

Porter, S. L., Wadhams, G. H., Martin, A. C., Byles, E. D., Lancaster, D. E., and Armitage, J. P. (2006). The CheYs of Rhodobacter sphaeroides. *J. Biol. Chem.* 281, 32694–32704.

Roujeinikova, A. (2008). Crystal structure of the cell wall anchor domain of MotB, a stator component of the bacterial flagellar motor: implications for peptidoglycan recognition. *Proc. Natl. Acad. Sci. U. S. A.* 105, 10348–10353.

Ryu, W. S., Berry, R. M., and Berg, H. C. (2000). Torque-generating units of the flagellar motor of *Escherichia coli* have a high duty ratio. *Nature* 403, 444–447. doi: 10.1038/35000233

Santiveri, M., Roa-Eguiara, A., Kühne, C., Wadhwa, N., Hu, H., Berg, H. C., et al. (2020). Structure and Function of Stator Units of the Bacterial Flagellar Motor. *Cell* 183, 244–257.e16.

Sarkar, M. K., Paul, K., and Blair, D. (2010). Chemotaxis signaling protein CheY binds to the rotor protein FliN to control the direction of flagellar rotation in *Escherichia coli*. *Proc. Natl. Acad. Sci. U. S. A.* 107, 9370–9375. doi: 10.1073/pnas.1000935107

Segall, J. E., Manson, M. D., and Berg, H. C. (1982). Signal processing times in bacterial chemotaxis. *Nature* 296, 855–857.

Shimizu, T. S., Delalez, N., Pichler, K., and Berg Howard, C. (2006). Monitoring bacterial chemotaxis by using bioluminescence resonance energy transfer: absence of feedback from the flagellar motors. *Proc. Natl. Acad. Sci. U. S. A.* 103, 2093–2097. doi: 10.1073/pnas.0510958103

Silverman, M., and Simon, M. (1974). Flagellar rotation and the mechanism of bacterial motility. *Nature* 249, 73–74.

Silversmith, R. E., and Bourret, R. B. (1999). Throwing the switch in bacterial chemotaxis. *Trends Microbiol.* 7, 16–22.

Sourjik, V., and Berg, H. C. (2002). Receptor sensitivity in bacterial chemotaxis. *Proc. Natl. Acad. Sci. U. S. A.* 99, 123–127.

Subramanian, S., and Kearns, D. B. (2019). Functional Regulators of Bacterial Flagella. *Annu. Rev. Microbiol.* 73, 225–246.

Szurmant, H., Bunn, M. W., Cannistraro, V. J., and Ordal, G. W. (2003). *Bacillus subtilis* hydrolyzes CheY-P at the location of its action, the flagellar switch. *J. Biol. Chem.* 278, 48611–48616. doi: 10.1074/jbc.M306180200

Tamar, E., Koler, M., and Vaknin, A. (2016). The role of motility and chemotaxis in the bacterial colonization of protected surfaces. *Sci. Rep.* 6:19616.

Tang, H., Braun, T. F., and Blair, D. F. (1996). Motility protein complexes in the bacterial flagellar motor. *J. Mol. Biol.* 261, 209–221.

Terahara, N., Noguchi, Y., Nakamura, S., Kami-Ike, N., Ito, M., Namba, K., et al. (2017). Load- and polysaccharide-dependent activation of the Na(+)-type MotPS stator in the *Bacillus subtilis* flagellar motor. *Sci. Rep.* 7:46081. doi: 10.1038/srep46081

Terahara, N., Sano, M., and Ito, M. (2012). A Bacillus flagellar motor that can use both Na+ and K+ as a coupling ion is converted by a single mutation to use only Na+. *PLoS One* 7:e46248. doi: 10.1371/journal.pone.0046248

Tipping, M. J., Delalez, N. J., Lim, R., Berry, R. M., and Armitage, J. P. (2013). Load-dependent assembly of the bacterial flagellar motor. *mBio* 4, e00551–13.

Tu, Y. (2008). The nonequilibrium mechanism for ultrasensitivity in a biological switch: sensing by Maxwell's demons. *Proc. Natl. Acad. Sci. U. S. A.* 105, 11737–11741. doi: 10.1073/pnas.0804641105

Tuthill, J. C., and Azim, E. (2018). Proprioception. *Curr. Biol.* 28, R194–R203.

Van Way, S. M., Hosking, E. R., Braun, T. F., and Manson, M. D. (2000). Mot protein assembly into the bacterial flagellum: a model based on mutational analysis of the motB gene. *J. Mol. Biol.* 297, 7–24. doi: 10.1006/jmbi.2000.3548

Wadhwa, N., and Berg, H. C. (2022). Bacterial motility: machinery and mechanisms. *Nat. Rev. Microbiol.* 20, 161–173.

Wadhwa, N., Phillips, R., and Berg Howard, C. (2019). Torque-dependent remodeling of the bacterial flagellar motor. *Proc. Natl. Acad. Sci. U. S. A.*116, 11764–11769.

Wang, B., Niu, Y., Zhang, R., and Yuan, J. (2021). Dynamics of Switching at Stall Reveals Nonequilibrium Mechanism in the Allosteric Regulation

of the Bacterial Flagellar Switch. *Phys. Rev. Lett.* 127:268101. doi: 10.1103/PhysRevLett.127.268101

Wang, F., Shi, H., He, R., Wang, R., Zhang, R., and Yuan, J. (2017). Non-equilibrium effect in the allosteric regulation of the bacterial flagellar switch. *Nat. Phys.* 13, 710–714.

Webster, S. S., Wong, G. C. L., and O'toole, G. A. (2022). The Power of Touch: type 4 Pili, the von Willebrand A Domain, and Surface Sensing by *Pseudomonas aeruginosa*. *J. Bacteriol.* e0008422. doi: 10.1128/jb.00084-22 [Epub ahead of print].

Welch, M., Oosawa, K., Aizawa, S., and Eisenbach, M. (1993). Phosphorylation-dependent binding of a signal molecule to the flagellar switch of bacteria. *Proc. Natl. Acad. Sci. U. S. A.* 90, 8787. doi: 10.1073/pnas.90.19.8787

Wilhelms, M., Vilches, S., Molero, R., Shaw, J. G., Tomas, J. M., and Merino, S. (2009). Two redundant sodium-driven stator motor proteins are involved in *Aeromonas hydrophila* polar flagellum rotation. *J. Bacteriol.* 191, 2206–2217. doi: 10.1128/JB.01526-08

Wong, G. C. L., Antani, J. D., Lele, P. P., Chen, J., Nan, B., and Kühn, M. J. (2021). Roadmap on emerging concepts in the physical biology of bacterial biofilms: from surface sensing to community formation. *Phys. Biol.* 18:051501. doi: 10.1088/1478-3975/abdc0e

Wu, Z., Tian, M., Zhang, R., and Yuan, J. (2021). Dynamics of the Two Stator Systems in the Flagellar Motor of *Pseudomonas aeruginosa* Studied by a Bead Assay. *Appl. Environ. Microbiol.* 87:e0167421. doi: 10.1128/AEM.01674-21

Yang, J., Chawla, R., Rhee Kathy, Y., Gupta, R., Manson Michael, D., Jayaraman, A., et al. (2020). Biphasic chemotaxis of *Escherichia coli* to the microbiota metabolite indole. *Proc. Natl. Acad. Sci. U. S. A.* 117, 6114–6120. doi: 10.1073/pnas.1916974117

Yorimitsu, T., and Homma, M. (2001). Na+-driven flagellar motor of Vibrio. *Biochim. Biophys. Acta Bioenerg.* 1505, 82–93.

Yuan, J., Branch, R. W., Hosu, B. G., and Berg, H. C. (2012). Adaptation at the output of the chemotaxis signalling pathway. *Nature* 484, 233–236.

Yuan, J., Fahrner, K. A., and Berg, H. C. (2009a). Switching of the Bacterial Flagellar Motor Near Zero Load. *J. Mol. Biol.* 390, 394–400.

Yuan, J., Fahrner, K. A., Turner, L., and Berg, H. C. (2009b). Asymmetry in the clockwise and counterclockwise rotation of the bacterial flagellar motor. *Proc. Natl. Acad. Sci. U. S. A.* 107, 12846–12849.

Zhang, C., He, R., Zhang, R., and Yuan, J. (2018). Motor Adaptive Remodeling Speeds Up Bacterial Chemotactic Adaptation. *Biophys. J.* 114, 1225–1231. doi: 10.1016/j.bpj.2018.01.018

Zhu, S., Takao, M., Li, N., Sakuma, M., Nishino, Y., Homma, M., et al. (2014). Conformational change in the periplamic region of the flagellar stator coupled with the assembly around the rotor. *Proc. Natl. Acad. Sci. U. S. A.*111, 13523–13528. doi: 10.1073/pnas.1324201111

Conflict of Interest: The authors declare that the research was conducted in the absence of any commercial or financial relationships that could be construed as a potential conflict of interest.

Publisher's Note: All claims expressed in this article are solely those of the authors and do not necessarily represent those of their affiliated organizations, or those of the publisher, the editors and the reviewers. Any product that may be evaluated in this article, or claim that may be made by its manufacturer, is not guaranteed or endorsed by the publisher.

Copyright © 2022 Gupta, Yuan and Lele. This is an open-access article distributed under the terms of the Creative Commons Attribution License (CC BY). The use, distribution or reproduction in other forums is permitted, provided the original author(s) and the copyright owner(s) are credited and that the original publication in this journal is cited, in accordance with accepted academic practice. No use, distribution or reproduction is permitted which does not comply with these terms.

frontiers | Frontiers in Microbiology

REVIEW
published: 04 May 2022
doi: 10.3389/fmicb.2022.864178

Insight Into Distinct Functional Roles of the Flagellar ATPase Complex for Flagellar Assembly in *Salmonella*

Tohru Minamino[1], Miki Kinoshita[1] and Keiichi Namba[1,2,3]*

[1] *Graduate School of Frontier Biosciences, Osaka University, Osaka, Japan,* [2] *RIKEN SPring-8 Center and Center for Biosystems Dynamics Research, Osaka, Japan,* [3] *JEOL YOKOGUSHI Research Alliance Laboratories, Osaka University, Osaka, Japan*

Most motile bacteria utilize the flagellar type III secretion system (fT3SS) to construct the flagellum, which is a supramolecular motility machine consisting of basal body rings and an axial structure. Each axial protein is translocated via the fT3SS across the cytoplasmic membrane, diffuses down the central channel of the growing flagellar structure and assembles at the distal end. The fT3SS consists of a transmembrane export complex and a cytoplasmic ATPase ring complex with a stoichiometry of 12 FliH, 6 FliI and 1 FliJ. This complex is structurally similar to the cytoplasmic part of the F_OF_1 ATP synthase. The export complex requires the $FliH_{12}$-$FliI_6$-$FliJ_1$ ring complex to serve as an active protein transporter. The $FliI_6$ ring has six catalytic sites and hydrolyzes ATP at an interface between FliI subunits. FliJ binds to the center of the $FliI_6$ ring and acts as the central stalk to activate the export complex. The FliH dimer binds to the N-terminal domain of each of the six FliI subunits and anchors the $FliI_6$-$FliJ_1$ ring to the base of the flagellum. In addition, FliI exists as a hetero-trimer with the FliH dimer in the cytoplasm. The rapid association-dissociation cycle of this hetero-trimer with the docking platform of the export complex promotes sequential transfer of export substrates from the cytoplasm to the export gate for high-speed protein transport. In this article, we review our current understanding of multiple roles played by the flagellar cytoplasmic ATPase complex during efficient flagellar assembly.

Keywords: ATPase, bacterial flagella, F_0F_1 ATP synthase, flagellar assembly, proton motive force (pmf), protein translocation, type III secretion system (T3SS)

OPEN ACCESS

Edited by:
Michael Manson,
Texas A&M University, United States

Reviewed by:
Tom Duncan,
Upstate Medical University, United States
Phillip Aldridge,
Newcastle University, United Kingdom

****Correspondence:***
Tohru Minamino
tohru@fbs.osaka-u.ac.jp

Specialty section:
This article was submitted to Microbial Physiology and Metabolism, a section of the journal Frontiers in Microbiology

Received: *28 January 2022*
Accepted: *13 April 2022*
Published: *04 May 2022*

Citation:
Minamino T, Kinoshita M and Namba K (2022) Insight Into Distinct Functional Roles of the Flagellar ATPase Complex for Flagellar Assembly in Salmonella. Front. Microbiol. 13:864178. doi: 10.3389/fmicb.2022.864178

INTRODUCTION

Pathogenic bacteria use virulence-associated type III secretion systems (vT3SS), also known as the injectisomes, to inject virulence effector proteins directly into eukaryotic host cells as part of their infection process. Motile bacteria employ the flagellar type III secretion system (fT3SS) to construct a supramolecular motility machine, the flagellum, on the cell surface (Wagner and Diepold, 2020). A remarkable feature of both the vT3SS and fT3SS is that the protein export apparatus is capable of translocating export substrates across the cytoplasmic membrane at a rate of tens of thousands of amino acids per second (Iino, 1974; Chen et al., 2017; Renault et al., 2017). The protein export apparatus of the T3SS is composed of a transmembrane export complex powered by the proton

motive force (PMF) across the cytoplasmic membrane and a cytoplasmic ATPase ring complex (**Figure 1**). The transmembrane export complex is composed of five conserved membrane proteins: FlhA, FlhB, FliP, FliQ, and FliR in the fT3SS; SctV, SctU, SctR, SctS, and SctT in the vT3SS. The cytoplasmic ATPase ring complex is composed of three cytoplasmic proteins, FliH, FliI, and FliJ in the fT3SS and SctL, SctN, and SctO in the vT3SS. The ATPase ring complex is structurally similar to the cytoplasmic part of the F_OF_1 ATP synthase, which is a rotary motor that couples proton (H^+) flow through F_O with ATP synthesis by F_1 (Minamino, 2014; Minamino et al., 2020b).

The flagellum of *Salmonella enterica* serovar Typhimurium (hereafter referred to as *Salmonella*) is composed of about 30 different proteins whose copy numbers range from a few to tens of thousands. The *Salmonella* flagellum is divided into three main structural parts: the basal body, the hook, and the filament (**Figure 2**). The basal body is located within the cell envelop and serves as a bi-directional rotary motor fueled by the PMF across the cytoplasmic membrane. The hook and filament extend into the cell exterior. The filament functions as a helical propeller to produce the thrust that pushes the cell body forward. The hook between the basal body and filament acts as a universal joint to transmit torque produced by the motor to the filament (Nakamura and Minamino, 2019).

The axial structure of the *Salmonella* flagellum is composed of the rod (FliE, FlgB, FlgC, FlgF, FlgG), the hook (FlgE), the hook-filament junction (FlgK, FlgL), the filament (flagellin, FliC or FljB) and the filament cap (FliD) (**Figure 2**). The assembly of the axial structure begins with the rod, followed by the hook with the help of the hook cap (FlgD). Upon completion of hook assembly, the hook cap is replaced by FlgK, and then FlgK and FlgL self-assemble into the hook-filament junction structure at the hook tip. FliD forms the filament cap at the tip of the junction structure and promotes the assembly of newly transported flagellin molecules into the long helical filament (Macnab, 2003).

To construct the axial structure beyond the cellular membranes, fourteen different proteins are translocated across the cytoplasmic membrane via the fT3SS, diffuse down the narrow central channel, and assemble at the tip of the growing structure (**Figure 2**). They can be classified into two export classes: one is the rod-type (FliE, FlgB, FlgC, FlgF, FlgG, FlgJ) and hook-type (FlgD, FlgE, FliK) class needed for assembly of the rod and hook. The other is the filament-type class (FlgK, FlgL, FlgM, FliC, FliD) responsible for filament assembly. The fT3SS secrets a molecular ruler protein, FliK, to measure the length of the hook during hook assembly and switches its substrate specificity from rod/hook-type proteins to filament-type proteins when the hook reaches its mature length of about 55 nm. At that point hook assembly terminates and filament assembly initiates (Minamino, 2018).

The fT3SS and vT3SS utilize the PMF across the cytoplasmic membrane and ATP hydrolysis to drive protein translocation across the cytoplasmic membrane (Minamino and Namba, 2008; Paul et al., 2008; Lee et al., 2014). The *Salmonella* fT3SS has a backup engine powered by a sodium (Na^+) motive force (SMF) across the cytoplasmic membrane to continue flagellar assembly when the cytoplasmic ATPase ring complex does not work properly, as during biofilm development (Minamino et al., 2016b, 2021a).

Once the transmembrane export complex of the *Salmonella* fT3SS is activated by ATP hydrolysis in the cytoplasmic ATPase ring complex, it becomes an active H^+/protein antiporter that couples inward-directed H^+ flow with outward-directed protein export (Minamino et al., 2011). Furthermore, the cytoplasmic ATPase complex allows the export complex to coordinate flagellar protein export with assembly in *Salmonella* (Minamino et al., 2016a; Inoue et al., 2018). Thus, the cytoplasmic ATPase ring complex acts as an activator of the H^+-driven export engine and also contributes to efficient and robust protein export by the export complex. This review describes our current understanding of the structure and function of the flagellar cytoplasmic ATPase complex in *Salmonella*.

Structure and Function of the Transmembrane Export Complex

The transmembrane export complex of the fT3SS is located inside the MS-ring formed by the transmembrane protein FliF (**Figure 1**; Johnson et al., 2021; Kawamoto et al., 2021; Takekawa et al., 2021; Tan et al., 2021). It consists of nine copies of FlhA, a single copy of FlhB, five copies of FliP, four copies of FliQ, and a single copy of FliR (Abrusci et al., 2013; Kuhlen et al., 2018, 2020; Johnson et al., 2019).

FliP and FliR assemble into the $FliP_5$-$FliR_1$ complex with the help of the FliO scaffolding protein and form the polypeptide channel for the translocation of export substrates across the cytoplasmic membrane (**Figure 3**, left panel) (Fabiani et al., 2017; Fukumura et al., 2017). Four FliQ subunits bind to the outside of the $FliP_5$-$FliR_1$ complex to form the $FliP_5$-$FliQ_4$-$FliR_1$ complex (**Figure 3**, middle panel). A flexible loop formed by the highly conserved Met-209, Met-210, and Met-211 residues of FliP (the M-loop) on the cytoplasmic side of the polypeptide channel and a plug loop composed of residues 106–122 of FliR (the R-plug) seem to prevent the leakage of small molecules during high-speed protein translocation (**Figure 3**, right panel) (Ward et al., 2018; Hüsing et al., 2021). The $FliP_5$-$FliQ_4$-$FliR_1$ complex has a helical arrangement of subunits similar to the rod (**Figure 3**), so FliE, which is the first export substrate transported by the fT3SS (Minamino and Macnab, 1999; Minamino et al., 2000), can directly assemble at the distal end of the $FliP_5$-$FliQ_4$-$FliR_1$ complex to form the most proximal part of the rod. Interactions between FliE and FliF not only firmly connect the rod with the MS ring but also open the exit gate of the polypeptide channel through conformational changes of FliP and FliR (Hendriksen et al., 2021).

Salmonella FlhB consists of an N-terminal transmembrane domain ($FlhB_{TM}$) with four transmembrane helices (TMHs) (residues 1–211) and a large C-terminal cytoplasmic domain ($FlhB_C$) (residues 212–383) (Minamino et al., 1994; Kinoshita et al., 2021). $FlhB_{TM}$ associates with the $FliP_5$-$FliQ_4$-$FliR_1$ complex to form the $FliP_5$-$FliQ_4$-$FliR_1$-$FlhB_1$ complex (**Figure 3**, middle panel), and the cytoplasmic loop connecting TMH-2 and TMH-3 ($FlhB_{Loop}$) wraps around

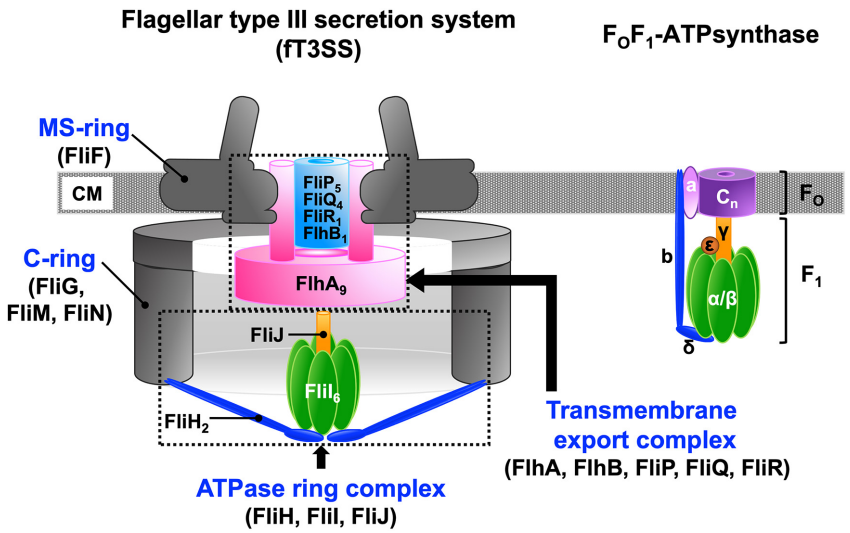


FIGURE 1 | Schematic diagrams of the flagellar type III export apparatus and F_OF ATP synthase. The flagellar type III secretion system (fT3SS) is composed of five membrane proteins, FlhA, FlhB, FliP, FliQ, and FliR and three cytoplasmic proteins, FliH, FliI, and FliJ. FlhA, FlhB, FliP, FliQ and FliR assembles into a transmembrane export complex within the MS-ring of the basal body of the flagellum. FliH, FliI, and FliJ form a cytoplasmic ATPase ring. The $FliI_6$-$FliJ_1$ ring complex is structurally similar to the $\alpha_3\beta_3\gamma_1$ ring complex of the F_OF_1 ATP synthase. The N-terminal and C-terminal domains of FliH structurally are similar in structure to the b and δ subunits, respectively, of the F_OF_1 ATP synthase. The FliH dimer acts as a peripheral stalk that anchors the $FliI_6$-FliJ ring complex to the base of the flagellum in a similar manner as the b and δ subunits of the F_OF1 ATP synthase connect the $\alpha_3\beta_3\gamma$ ring complex to membrane-embedded F_O. The stoichiometry of the c-ring varies dramatically from c_8 up to at least c_{15}. CM, cytoplasmic membrane.

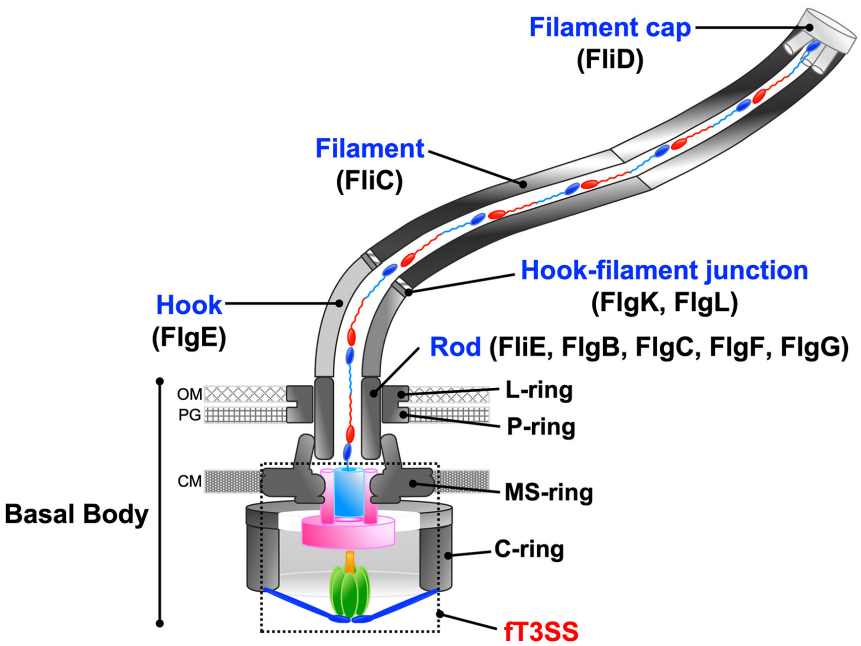


FIGURE 2 | Schematic diagram of the bacterial flagellum. The bacterial flagellum is composed of basal body rings, namely the C-ring, MS-ring, L-ring, and P-ring, and an axial structure consisting of the rod, the hook, the hook-filament junction, the filament, and the filament cap. To construct the axial structure beyond the cytoplasmic membrane, flagellar axial proteins are translocated through the fT3SS, diffuse down a narrow central channel, and assemble at the tip of the growing structure. OM, outer membrane; PG, peptidoglycan layer; CM, cytoplasmic membrane.

the entrance gate of the $FliP_5$-$FliQ_4$-$FliR_1$ complex through interactions of the loop with each FliQ subunit (**Figure 3**, right panel). It is thus plausible that FlhB may coordinate gate opening for substrate entry into the polypeptide channel. Recent genetic analysis has suggested that the N-terminal cytoplasmic tail of FlhB and $FlhB_C$ are involved, along with the

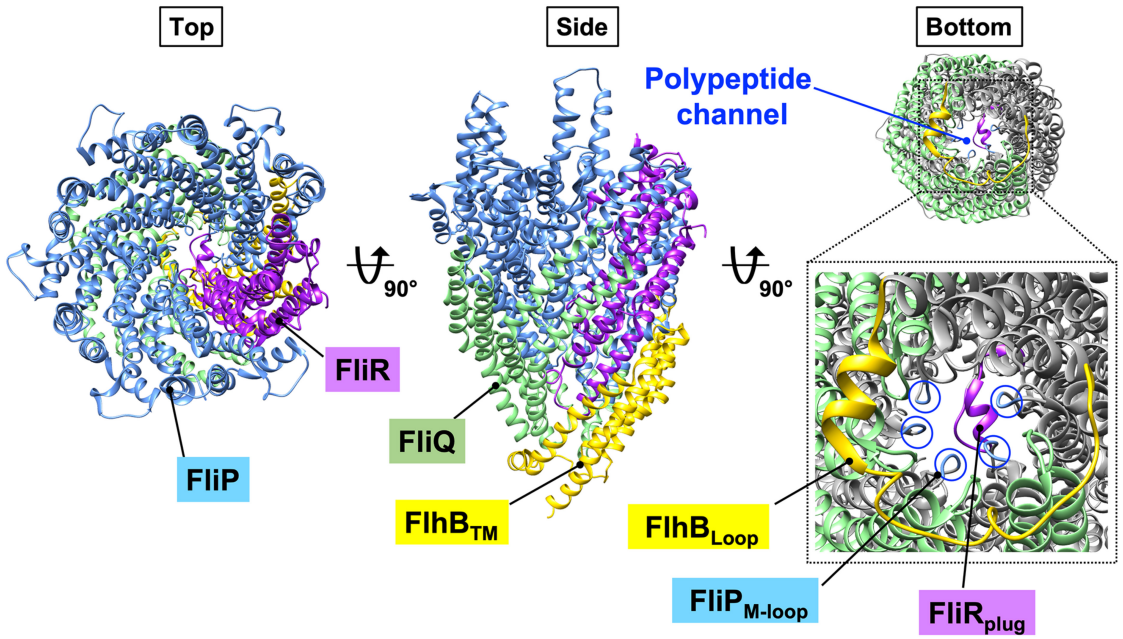


FIGURE 3 | CryoEM structure of the FlhB$_1$-FliP$_5$-FliQ$_4$-FliR$_1$ complex (PDB ID: 6S3L). FliP and FliR assemble into the FliP$_5$-FliR$_1$ complex with the help of the flagellum-specific transmembrane protein, FliO. Four copies of FliQ associates with the outside of the FliP$_5$-FliR$_1$ complex. The central pore of the FliP$_5$-FliR$_1$ complex is thought to be a polypeptide channel. The FliP$_5$-FliQ$_4$-FliR$_1$ complex adopts a right-handed helix similar to that of the flagellar axial structure. The transmembrane domain of FlhB (FlhB$_{TM}$) associates with the FliP$_5$-FliQ$_4$-FliR$_1$ complex. The highly conserved M-loop formed by Met-209, Met-210, and Met-211 of FliP (FliP$_{M-loop}$) and the plug loop composed of residues 106–122 of FliR (FliR$_{plug}$) block leakage of any small molecules during protein translocation. The cytoplasmic loop of FlhB FlhB$_{Loop}$) interacts with all four FliQ subunits. Because the entrance gate of the FlhB$_1$-FliP$_5$-FliQ$_4$-FliR$_1$ complex is closed, FlhB is proposed to regulate opening of the gate to the polypeptide channel. Cyan, FliP; green, FliQ; magenta, FliR; yellow, FlhB$_{TM}$.

cytoplasmic ATPase complex, in the gating function of FlhB (Kinoshita et al., 2021).

Salmonella FlhA is divided into two distinct regions: an N-terminal transmembrane region (FlhA$_{TM}$) with eight TMHs (residues 1–327) and a large C-terminal cytoplasmic region (residues 328–692) (**Figure 4A**; Minamino et al., 1994; Kinoshita et al., 2021). The crystal structure of the C-terminal cytoplasmic region is composed of a compactly folded domain (FlhA$_C$, residues 362–692) and a flexible linker (FlhA$_L$, residues 328–361) connecting FlhA$_C$ with FlhA$_{TM}$ (**Figure 4A**; Saijo-Hamano et al., 2010). FlhA assembles into a homo-nonamer through intermolecular interactions between FlhA$_C$ subunits, and the interactions of FlhA$_L$ with its neighboring FlhA$_C$ subunit stabilize the FlhA$_C$-ring structure (**Figure 4B**; Terahara et al., 2018; Kuhlen et al., 2021). FlhA$_{TM}$ associates not only with the FliP$_5$-FliQ$_4$-FliR$_1$ complex but also with the MS-ring (Kihara et al., 2001).

If either MS-ring or the FliP$_5$FliQ$_4$FliR$_1$ complex is missing in *Salmonella* cells, FlhA cannot efficiently form the oligomer at the flagellar base as monitored with FlhA labeled with yellow fluorescent protein (YFP), suggesting that FlhA assembles into the export complex along with other export-gate proteins during MS-ring formation (Morimoto et al., 2014). The highly conserved Arg-94, Lys-203, Asp-208, and Asp-249 residues of FlhA$_{TM}$ are critical for H^+-coupled protein export (Hara et al., 2011; Erhardt et al., 2017). Over-expression of FlhA in *Escherichia coli* decreases the intracellular pH. Furthermore, over-expression of FlhA increases intracellular Na^+ concentration in the presence of 100 mM NaCl. These observations suggest that FlhA forms a pathway for the transit of both H^+ and Na^+ across the cytoplasmic membrane. The *flhA(D208A)* mutation facilitates the H^+-channel activity of FlhA, suggesting that Asp-208 of FlhA may coordinate H^+ flow though the FlhA channel with protein export. However, this mutation does not affect the Na^+-channel activity of FlhA at all, suggesting that the Na^+ pathway is different from the H^+ pathway (Minamino et al., 2016b).

FlhA$_C$ and FlhB$_C$ project into the cytoplasmic cavity of the basal body C-ring and form a docking platform for the cytoplasmic ATPase complex, flagellar export chaperones, and export substrates (Minamino and Macnab, 2000c; Minamino et al., 2003, 2010, 2012a; Bange et al., 2010). The FlhA$_C$-FlhB$_C$ docking platform determines the order of substrate export to facilitate efficient flagellar assembly and also regulates gate opening of the FlhA ion channel and the FliP$_5$-FliQ$_4$-FliR polypeptide channel (Minamino and Macnab, 2000a; Kinoshita et al., 2013; Inoue et al., 2019; Minamino et al., 2020a, 2021b).

A highly conserved hydrophobic dimple including Phe-459, Asp-456, and Thr-490 of FlhA is critical for substrate recognition by the fT3SS during flagellar assembly (**Figure 4A**; Xing et al., 2018). The C-terminal part of FlhA$_L$ binds to its neighboring FlhA$_C$ subunit to stabilize the open conformation of FlhA$_C$ in the nonameric ring, allowing flagellar export

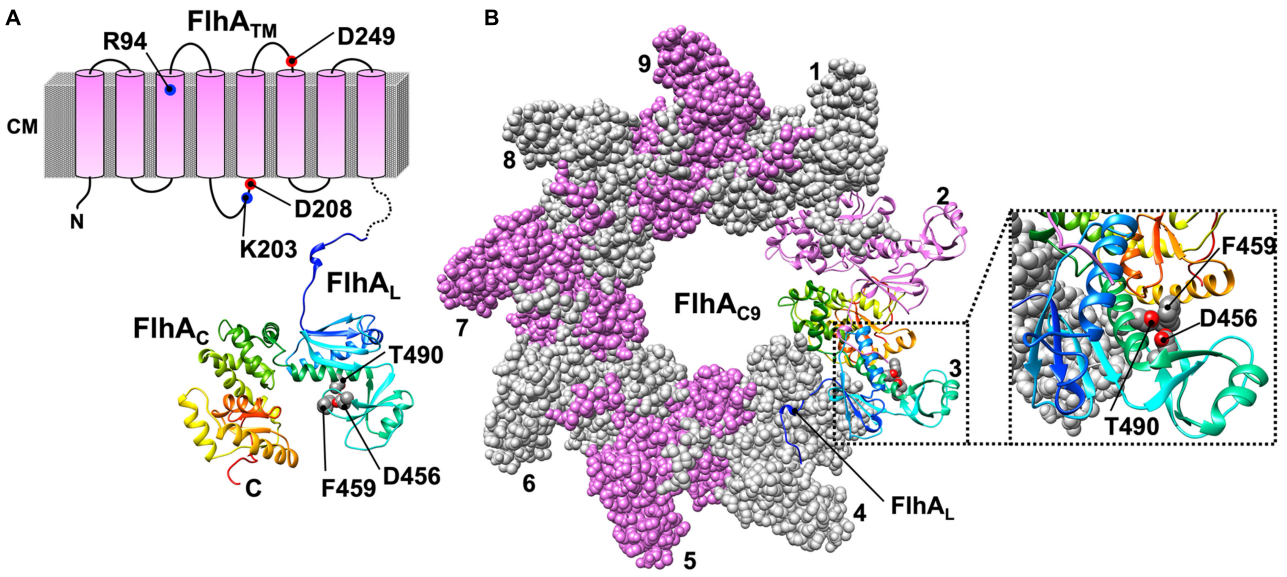


FIGURE 4 | Atomic model of the cytoplasmic domain of FlhA (PDB ID: 3A5I). **(A)** Topological model of FlhA. FlhA is composed of an N-terminal transmembrane region with eight transmembrane helices ($FlhA_{TM}$) and a large C-terminal cytoplasmic domain ($FlhA_C$). $FlhA_{TM}$ acts as a dual-ion channel that can conduct both H^+ and Na^+. The highly conserved charged residues R94, K203, D208 and D249 are involved in H^+-coupled protein export. The highly conserved residues D456, F459 and T490 of $FlhA_C$ are critical for substrate recognition. A flexible linker region of FlhA ($FlhA_L$), which connects $FlhA_C$ with $FlhA_{TM}$, is involved in the interaction with FliJ. The interaction between $FlhA_L$ and FliJ activates the FlhA ion channel. **(B)** Model of the $FlhA_C$-ring. $FlhA_C$ forms a homo-nonameric ring structure. The C-terminal part of $FlhA_L$ binds to the neighboring $FlhA_C$ subunit to stabilize the open conformation of $FlhA_C$, allowing flagellar export chaperones in complex with their cognate substrates to bind to a chaperone-binding site of $FlhA_C$, which includes the D456, F459, and T490 residues.

chaperones associated with their cognate substrates to bind to the conserved hydrophobic dimple with a nanomolar affinity (Inoue et al., 2021).

Catalytic Mechanism of the $FliI_6$-$FliJ_1$ Ring Complex

The F_1 ATPase is composed of three copies of the α subunit, three copies of the β subunit, a single copy of the γ subunit and a single copy of the ε subunit (**Figure 1**). The α and β subunits form a hetero-hexameric $\alpha_3\beta_3$ ring, and the γ subunit binds within the central pore of the $\alpha_3\beta_3$ ring (Abrahams et al., 1994). The ε subunit binds to the γ subunit to control the ATP hydrolysis activity of the F_1 ATPase in an ATP-dependent manner (Kato-Yamada et al., 2000). The $\alpha_3\beta_3\gamma_1$ subcomplex is the minimum unit that can function as an ATP-driven rotary motor to couple ATP hydrolysis with the rotation of the γ subunit within the $\alpha_3\beta_3$ ring. ATP binds to three catalytic sites in the $\alpha_3\beta_3$ ring, each of which is located at an interface between the α and β subunits. Three catalytic β subunits in the $\alpha_3\beta_3$ ring undergo highly cooperative and sequential conformational changes in their C-terminal domains during ATP hydrolysis. These conformational changes drive the γ subunit to rotate within the $\alpha_3\beta_3$ ring (Watanabe and Noji, 2013). The $FliI_6$-$FliJ_1$ subcomplex of the fT3SS, which looks similar to the $\alpha_3\beta_3\gamma_1$ subcomplex, can act as the ATPase at the base of the flagellum (**Figure 1**; Ibuki et al., 2011).

FliI is the flagellum-specific ATPase. It has highly conserved Walker A and B motifs (Vogler et al., 1991; Fan and Macnab, 1996). *Salmonella* FliI consists of three domains: N-terminal (residues 2–97, $FliI_N$), ATPase (residues 109–380, $FliI_{CAT}$) and C-terminal (residues 381–456, $FliI_C$) (**Figure 5A**; Imada et al., 2007). Residues 98–105, most of which are invisible in the electron density map, form a flexible hinge connecting $FliI_N$ and $FliI_{CAT}$, and this flexible hinge loop undergoes conformational changes during ATP binding and hydrolysis (Minamino et al., 2001).

The structures of FliI and its fT3SS homolog SctN are remarkably similar to the α and β subunits of the F_1 ATPase (Zarivach et al., 2007). However, in contrast to the F_1 ATPase, FliI and SctN form homo-hexamers in an ATP-dependent manner (**Figure 5B, C**), and both hexamers themselves can hydrolyze ATP at the interface between FliI/SctN subunits (Claret et al., 2003; Kazetani et al., 2009). Thus, the ATPase ring complex of the T3SS has six catalytic sites. The $FliI_6$ and $SctN_6$ ring structures have been identified at the base of the flagellum and injectisome, respectively, by electron cryotomography and sub-tomogram averaging (Chen et al., 2011; Kawamoto et al., 2013).

Intermolecular interactions between $FliI_N$ domains are required for FliI ring formation (**Figure 5C**; Okabe et al., 2009). The core structure of $FliI_N$ can be superimposed onto the N-terminal domains of the α and β subunits of the F_1 ATPase within $\alpha_3\beta_3$ hetero-hexamer. In the $FliI_6$-ring model, which was generated by fitting the crystal structure of FliI into the structures of the α and β subunits, $FliI_N$ shows steric hindrance at the subunit interfaces, suggesting that a conformational change in $FliI_N$ is required for FliI ring formation. Deletion of residues 2–7 of $FliI_N$ suppresses FliI hexamerization and decreases the

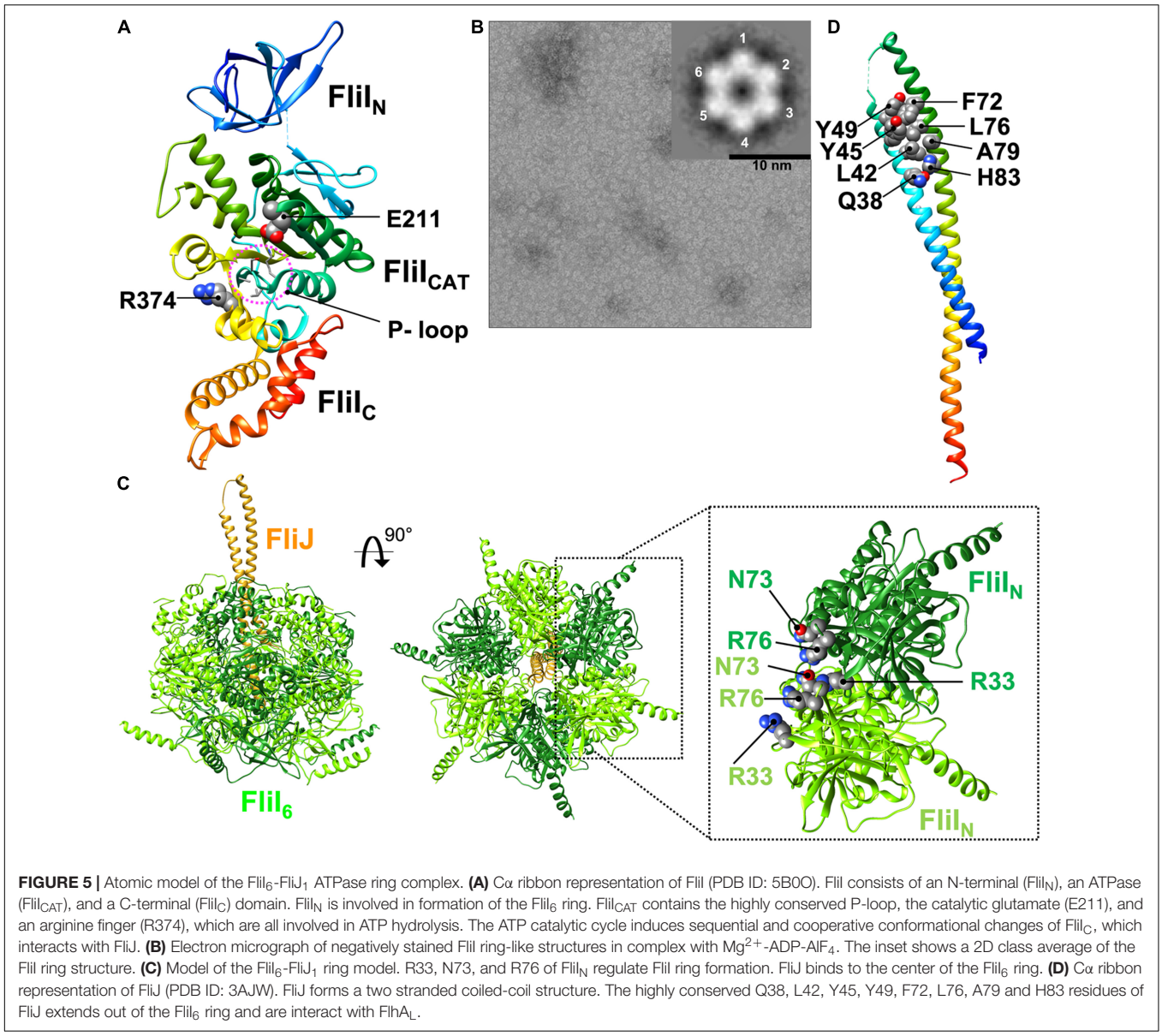


FIGURE 5 | Atomic model of the FliI$_6$-FliJ$_1$ ATPase ring complex. **(A)** Cα ribbon representation of FliI (PDB ID: 5B0O). FliI consists of an N-terminal (FliI$_N$), an ATPase (FliI$_{CAT}$), and a C-terminal (FliI$_C$) domain. FliI$_N$ is involved in formation of the FliI$_6$ ring. FliI$_{CAT}$ contains the highly conserved P-loop, the catalytic glutamate (E211), and an arginine finger (R374), which are all involved in ATP hydrolysis. The ATP catalytic cycle induces sequential and cooperative conformational changes of FliI$_C$, which interacts with FliJ. **(B)** Electron micrograph of negatively stained FliI ring-like structures in complex with Mg^{2+}-ADP-AlF_4. The inset shows a 2D class average of the FliI ring structure. **(C)** Model of the FliI$_6$-FliJ$_1$ ring model. R33, N73, and R76 of FliI$_N$ regulate FliI ring formation. FliJ binds to the center of the FliI$_6$ ring. **(D)** Cα ribbon representation of FliJ (PDB ID: 3AJW). FliJ forms a two stranded coiled-coil structure. The highly conserved Q38, L42, Y45, Y49, F72, L76, A79 and H83 residues of FliJ extends out of the FliI$_6$ ring and are interact with FlhA$_L$.

ATPase activity of FliI (Minamino et al., 2006), suggesting that the extreme N-terminal region of FliI regulates FliI oligomerization. Recently, it has been reported that Arg-33, Asn-73, and Arg-76 are also responsible for well-regulated FliI ring formation (**Figure 5C**; Kinoshita et al., 2021).

Amino acid residues in the F_1 ATPase that are known to be involved in ATP hydrolysis are highly conserved in the FliI/SctN family. FliI$_{CAT}$ contains the highly conserved P-loop (residues 182–188), the catalytic glutamate (Glu-211), and the arginine finger (Arg-374) (**Figure 5A**; Walker, 2013). ADP binds to the P-loop of FliI, as it does in the F_1 ATPase. The carboxyl group of Glu-190 in the β subunit of the thermophilic *Bacillus* F_1 ATPase, which corresponds to Glu-211 of FliI, polarizes a water molecule for the nucleophilic attack on the γ-phosphate of ATP, and the G190Q substitution results in a complete loss of ATPase activity (Shimabukuro et al., 2003). The *fliI(E211Q)* mutation completely abolishes ATPase activity but does not affect the binding of ATP to the P-loop, and FliI with the E211Q substitution can form the hexamer ring in the presence of Mg^{2+}-ATP. Thus, Glu-211 of FliI$_{CAT}$ acts as the catalytic glutamate.

Arg-373 in the α subunit of the F_1 ATPase, which corresponds to Arg-374 of FliI, functions as the arginine finger that protrudes into the nucleotide-binding site of the adjacent β-subunit. The side chain of this arginine residue forms a positively charged binding pocket for the negative charge of the γ-phosphate of ATP (Rees et al., 2012). The *fliI(R374A)* mutation inhibits FliI ring formation significantly and decreases ATPase activity. This effect indicates that Arg-374 of FliI stabilizes the binding of ATP to the P-loop in a way similar to Arg-373 of the α subunit. These observations suggest that FliI and the F_1 ATPase share a similar catalytic pathway for ATP hydrolysis.

The binding of ADP to the P-loop induces a conformational change in $FliI_C$ relative to $FliI_{CAT}$, suggesting that the FliI hexamer may undergo conformational changes in its C-terminal domains that are coupled with the catalytic reaction cycle in the same way as in the F_1 ATPase. This idea is supported by the asymmetric cryoEM structure of the $SctN_6$-$SctO_1$ ring complex with a non-hydrolyzable ATP analog (Majewski et al., 2019).

FliJ and its vT3SS homolog SctO adopt an antiparallel coiled-coil structure that is similar to the two-stranded α-helical coiled-coil part of the γ subunit of the F_1 ATPase (**Figure 5D**; Ibuki et al., 2011). FliJ binds to the C-terminal region of the first α-helix of $FliI_C$ (residues 382–406 of *Salmonella* FliI), which corresponds to the region of the β subunit that is responsible for interaction with the γ subunit. This interaction facilitates FliI ring formation and increases the ATPase activity of FliI. FliJ penetrates the central cavity of the $FliI_6$ ring like the γ subunit in the F_1 ATPase (**Figure 5C**). These observations have been confirmed by the cryoEM structure of the $SctN_6$-$SctO_1$ ring complex. FliJ has been shown to exert a rotor-like function in both rotary F_1 and V_1 ATPases (Kishikawa et al., 2013; Baba et al., 2016). Thus, the $FliI_6$-$FliJ_1$ ring complex may function as an ATP-driven rotary motor that couples ATP hydrolysis with the rotation of FliJ within the FliI hexamer.

Peripheral Stalk of Flagellar ATPase Ring Complex

The b and δ subunits of the F_OF_1 ATP synthase form the peripheral stalk that connects the $\alpha_3\beta_3\gamma_1\varepsilon_1$ ring complex to the membrane-embedded F_O unit (**Figure 1**). The extreme N-terminal region of the b subunit binds to F_O, whereas the δ subunit interacts with the extreme N-terminal region of the α subunit of F_1 (Walker and Dickson, 2006). The N-terminal and C-terminal regions of FliH and its vT3SS homolog SctL are homologous to the b and δ subunits of the ATP synthase (Pallen et al., 2006). This is confirmed by the crystal structure of an N-terminally truncated variant of *Salmonella* FliH consisting of residues 99–235 in complex with FliI (**Figure 6**; Imada et al., 2016).

Salmonella FliH consists of 235 amino-acid residues and forms a homo-dimer through residues 101–140, which form a coiled-coil structure (Minamino and Macnab, 2000b; González-Pedrajo et al., 2002). The FliH dimer binds to each $FliI_N$ domain of the $FliI_6$ ring (**Figure 6**, left panel) and also to the FliN protein in the C-ring (González-Pedrajo et al., 2006; McMurry et al., 2006; Paul et al., 2006). The interactions of FliH with FliN and $FliI_N$ are required for efficient and robust association of the $FliI_6$-FliJ ring complex with the flagellar basal body (**Figure 1**; Minamino et al., 2009). The N-terminal domain of FliH (residues 1–140, $FliH_N$) adopts a quite elongated α-helical coiled coil structure similar to that of the b subunit of the ATP synthase, and the extreme N-terminal region of FliH is involved in the interaction with FliN (Hara et al., 2012). Both C-terminal domains (residues 141–235, $FliH_C$) in the FliH dimer are involved in the interaction with FliI (Minamino et al., 2002). These two $FliH_C$ domains have completely different conformations; one binds to the extreme N-terminal α-helix of FliI consisting of residues 2–21, and the other binds to a positively charged cluster consisting of Arg-26, Arg-27, Arg-30, Arg-33, Arg-76, and Arg-93 of $FliI_N$ (**Figure 6**, middle and right panels). Because FliI cannot localize to the flagellar base in the absence of FliH, FliH seems to act as a peripheral stalk to firmly anchor the $FliI_6$-$FliJ_1$ ring complex to the C-ring.

Mechanism of Gate Activation

The PMF consists of the electric potential difference ($\Delta\psi$) and the proton concentration difference (ΔpH) across the cytoplasmic membrane. When the cytoplasmic ATPase ring complex works properly for flagellar assembly, the transmembrane export gate complex uses the $\Delta\psi$ component to drive H^+-coupled protein export under a variety of environmental conditions (Paul et al., 2008; Minamino et al., 2011, 2021b). However, when the ATPase ring complex becomes

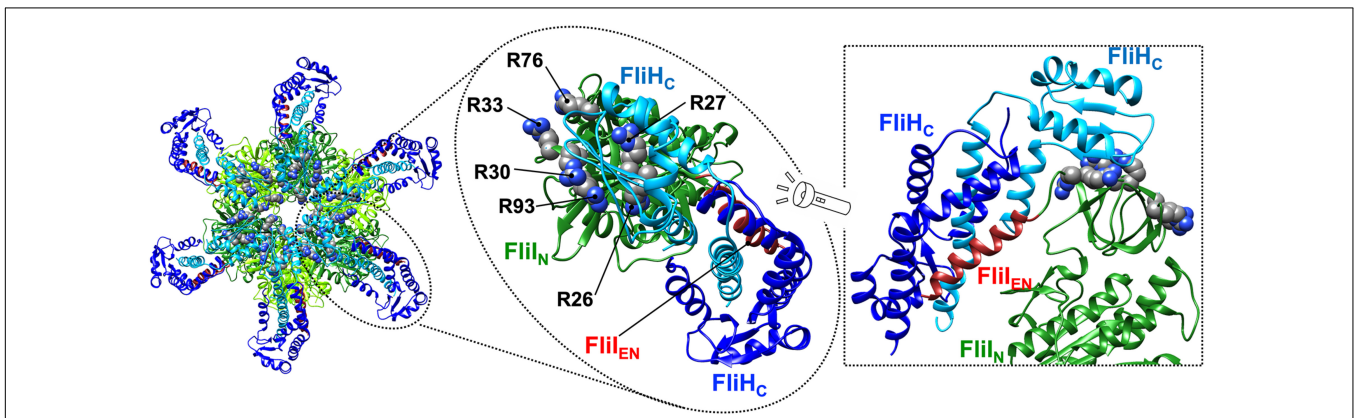


FIGURE 6 | Atomic model of the $FliH_{C12}$-$FliI_6$ ring complex. Cα ribbon representation of the $FliH_{C2}$-$FliI_1$ complex (PDB ID: 5B0O) is shown. The C-terminal domain of FliH (residues 141–235, $FliH_C$) forms a dimer via an interaction of residues 101–140, which adopt a coiled-coil structure. The $FliH_C$ dimer binds to each N-terminal domain ($FliI_N$) of the $FliI_6$ ring. Interestingly, one $FliH_C$ domain (blue) binds to the N-terminal α-helix consisting of residues 2–21 of FliI (brown, $FliI_{EN}$), and the other (cyan) binds to a positively charged region formed by R26, R27, R30, R33, R76, and R93 of FliI. These two domains adopt conformations that are completely different from each other.

non-functional under certain physiological conditions, the export gate complex prefers to use the SMF over a wide range of external pH, indicating that the transmembrane export complex is intrinsically a dual-fuel export engine that can use either H^+ or Na^+ as the coupling ion (Minamino et al., 2016b, 2021a). This in turn suggests that the cytoplasmic ATPase ring complex switches the export gate complex from the dual-fuel engine mode to a highly efficient $\Delta\psi$-driven one.

FliJ binds to $FlhA_L$ with high affinity to activate the H^+ channel of $FlhA_{TM}$ and to unlock the entrance gate of the polypeptide channel. As a result, the export gate complex becomes an active H^+/protein antiporter that couples inward-directed H^+ flow through the FlhA ion channel with outward-directed protein translocation across the polypeptide channel (Minamino et al., 2011). An inactive export gate complex can also be activated by an increase in $\Delta\psi$ above a certain threshold through an interaction between FliJ and $FlhA_L$, suggesting that $\Delta\psi$ is required for efficient and stable interaction between FliJ and $FlhA_L$ (Minamino et al., 2021b).

A helix-loop-helix formed by Gln-38, Leu-42, Tyr-45, Tyr-49, Phe-72, Leu-76, Ala-79, and His-83 of FliJ, which are highly conserved residues in FliJ homologs, extends out of the $FliI_6$-ring

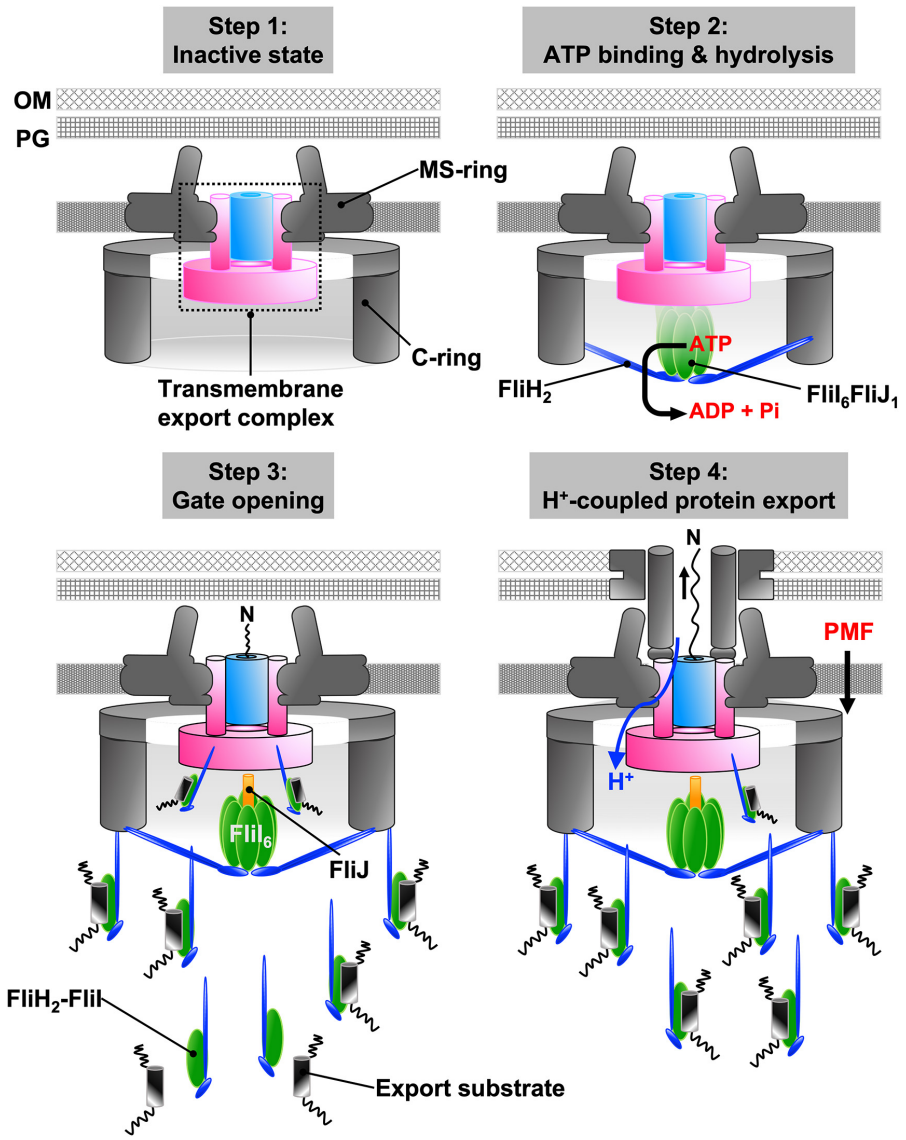


FIGURE 7 | Energy coupling mechanism of the fT3SS. The transmembrane export complex remains inactive until the cytoplasmic ATPase ring complex is formed at the base of the flagellum; the polypeptide and proton channels of the export complex remain closed (step 1). When ATP hydrolysis by FliI induces the rotation of FliJ in the $FliI_6$ ring, interactions between FliJ and $FlhA_L$ induces conformational rearrangements of the export complex. As a result, the complex becomes an active protein transporter (step 2). The cytoplasmic $FliH_2$-$FliI_1$ complex acts as a dynamic carrier to deliver export substrates from the cytoplasm to the export complex (step 3). Upon docking of an export substrate to the entrance gate of the polypeptide channel, the gates of both polypeptide and proton channels are opened. The export complex can now act as a H^+/protein antiporter that couples H^+ flow through the ion channel with protein translocation into the polypeptide channel (step 4).

(**Figure 5D**; Ibuki et al., 2013). This is confirmed by the cryoEM structure of the $SctN_6$-$SctO_1$ ring. Tyr-45, Tyr-49, and Phe-72 of FliJ are also conserved between FliJ and the γ subunit of the F_1 ATPase. Among these conserved, surface-exposed residues of FliJ, Phe-72 and Leu-76 are critical for the interaction with $FlhA_L$. Residues in the γ subunit corresponding to Phe-72 and Leu-76 are involved in the interaction with an α-helix of the δ subunit of the bovine mitochondrial F_1 ATPase, which is a homolog of the conserved ε subunit in the F_1 ATPase family (PDB ID: 1E79) (Gibbons et al., 2000). The *flhA(E351A/W354A/D356A)* triple mutation significantly reduces the binding affinity of $FlhA_L$ for FliJ (Inoue et al., 2021). Because the residues from Val-349 to Val-357 of FlhA form an α-helix, FliJ may bind to this α-helix in $FlhA_L$ as is seen in the γ-δ interaction in the bovine mitochondrial F_1 ATPase.

Mechanistic Role of ATP Hydrolysis for Flagellar Protein Export

ATP hydrolysis by the FliI ATPase and rapid protein translocation by the export complex are both linked to efficient H^+ translocation through the FlhA ion channel (Morimoto et al., 2016). Recently, it has been reported that ATP hydrolysis by the FliI ATPase also unlocks the entrance gate of the polypeptide channel formed by FliP, FliQ, and FliR for efficient entry of export substrates into the channel (Kinoshita et al., 2021). Furthermore, the *Salmonella* Δ*fliHIJ flhB(P28T) flhA(T490M)* mutant has been isolated as a revertant of the Δ*fliHIJ* mutant that has increased motility (Minamino et al., 2021a). The protein-export activity of the transmembrane export complex in cells with both the *flhA(T490M)* and *flhB(P28T)* mutations is almost at the wild-type level under a variety of experimental conditions even in the absence of the $FliH_{12}$-$FliI_6$-$FliJ_1$ ring complex (Minamino et al., 2021b). This finding suggests that the export complex normally requires the $FliH_{12}$-$FliI_6$-$FliJ_1$ complex to serve as a H^+-coupled protein transporter. Because FliJ requires FliH and FliI to bind efficiently to $FlhA_L$ (Minamino et al., 2011), this observation raises the question of how this ATPase ring complex activates the export complex.

The conserved Glu-211 residue of FliI catalyzes ATP hydrolysis. The E211D substitution decreases FliI ATPase activity by about 100-fold (Minamino et al., 2014). *Salmonella* wild-type cells produce an average of 4.4 ± 1.6 flagellar filaments per cell. In contrast, more than 90% of *Salmonella fliI(E211D)* cells have an average of 2.3 ± 1.5 flagellar filaments, and the average length of those filament is only half that of the wild type. Because the fT3SS transports 20,000–30,000 flagellin molecules per flagellum to form a 10–15 μm long helical filament (Minamino and Namba, 2004), the rate of ATP hydrolysis by the FliI ATPase cannot determine the rate of filament assembly, as ATP consumption by the fT3SS during flagellar assembly must be relatively small. Because the export complex still transports flagellar axial proteins even with the infrequent ATP hydrolysis provided by FliI(E211D), ATP hydrolysis appears to be required only for activation of the H^+-driven export engine.

The six $FliI_C$ domains undergo cooperative and sequential conformational changes triggered by ATP hydrolysis. Deletion of residues 401–410 in the first α-helix of $FliI_C$, which is responsible for the interaction with FliJ, significantly decreases the protein transport activity of the fT3SS although the ATPase activity is still at about 40% of the wild-type level. Because this deletion does not inhibit the interaction between FliI and FliJ, it may affect conformational changes in the $FliI_C$ domains that rotate FliJ within the FliI hexamer. Rotation of FliJ may induce conformational changes in the $FlhA_{TM}$ domain through an interaction between FliJ and $FlhA_L$, thereby activating the FlhA ion channel and unlocking the entrance gate of the polypeptide channel (**Figure 7**).

The elementary step size of γ rotation within the $\alpha_3\beta_3$ ring is 120°, which is composed of 80° and 40° sub-steps driven by ATP binding–ADP release and ATP hydrolysis–Pi release, respectively (Watanabe and Noji, 2013). The cryoEM structure of the $SctN_6$-$SctO_1$ ring complex has suggested a possible rotational mechanism for catalysis. In this model, the SctO stalk rotates in the $SctN_6$ ring through an interaction between each $SctN_C$ domain and SctO. Because the $SctN_6$-$SctO_1$ ring complex has six catalytic sites, the elementary step size of SctO rotation within the $SctN_6$ ring is probably 60° (Majewski et al., 2019). The FliI(E211Q) substitution in *Salmonella*, which completely eliminates ATPase activity but not ATP binding to the P-loop of $FliI_{CAT}$, results in only 17% of cells having one or two flagellar filaments about 25% the length of those of the wild type (Minamino et al., 2014). Thus, ATP binding to the P-loop is sufficient to activate the H^+-driven export engine of the fT3SS to some degree. So, the 60° rotation of FliJ may be divided into two sub-steps, and ATP binding may induce the first sub-step, which may be sufficient to activate the H^+-driven export engine weakly.

The Heterotrimeric $FliH_2$-$FliI_1$ Complex Acts as Dynamic Carrier

The FliI monomer interacts with the FliH dimer to form a heterotrimer in the cytoplasm (Minamino and Macnab, 2000b; Auvray et al., 2002). High-resolution imaging of fluorescently labeled FliI *in vivo* has revealed that $FliH_2$-$FliI_1$ complexes are associated with the basal body through interactions of FliH with FlhA and FliN. FliI-YFP shows a rapid exchange between the basal body and a freely diffusing cytoplasmic pool. The FliI(K188I) substitution, which inhibits ATP binding to the P-loop in $FliI_{CAT}$, does not affect the exchange rate of FliI-YFP, suggesting that ATP hydrolysis does not drive the association-dissociation cycle (Bai et al., 2014). FliH also suppresses the ATPase activity of the $FliH_2$-$FliI_1$ complex (Minamino and Macnab, 2000b). Deletion of *flhA* decreases the number of FliI-YFP molecules associated with the basal body but does not affect the exchange rate. The highly conserved Trp-7 and Trp-10 residues of $FliH_N$ are directly involved in the interactions of FliH with FliN and $FlhA_{TM}$ (Hara et al., 2012; Notti et al., 2015). Because the interaction between FliH and FliN is required for efficient localization of the $FliH_2$-$FliI_1$ complex to the flagellar base, the FliH-FliN interaction must be highly dynamic to achieve rapid and efficient flagellar protein export by the fT3SS. Flagellar chaperones in complex with their cognate substrates both bind to $FliI_C$, suggesting that $FliI_C$ is also involved in substrate recognition (Thomas et al., 2004;

Imada et al., 2010; Minamino et al., 2012b). Pull-down assays have demonstrated that chaperone-associated export substrates bind to $FlhA_C$ and $FlhB_C$ even in the absence of FliHI (Evans et al., 2013; Kinoshita et al., 2013; Inoue et al., 2019). However, they require the $FliH_2$-$FliI_1$ complex to efficiently interact with $FlhA_C$ and $FlhB_C$ *in vivo* (Minamino et al., 2016b; Inoue et al., 2018; Kinoshita et al., 2021).

In vitro protein transport assays using inverted membrane vesicles have shown that addition of the purified $FliH_2$-$FliI_1$ complex considerably increases the transport of flagellar axial protein into the lumen of the membrane vesicles (Terashima et al., 2018, 2020). Thus, the $FliH_2$-$FliI_1$ complex acts as a dynamic carrier to deliver chaperone-associated export substrates from the cytoplasm to the flagellar base and to facilitate their docking to $FlhA_C$ and $FlhB_C$, thereby allowing the activated export complex to unfold and transport export substrates into the central channel of the flagellum.

The $FliH_2FliI$ Complex Is Required for Efficient Flagellar Assembly

Salmonella cells lacking the FliH and FliI proteins display a very weak motile phenotype. This defect is considerably alleviated by either an increase in the expression level of export substrates and chaperones or an increase in the PMF (Erhardt et al., 2014). Expression of *Vibrio alginolyticus* FlhA, which has 73.2% similarity and 52.9% identity in amino acid sequence with *Salmonella* FlhA, restores motility in the *Salmonella* Δ*flhA* mutant but does not increase motility in the *Salmonella* Δ*fliHI flhB(P28T)*Δ*flhA* mutant (Minamino et al., 2016a). Thus, *Vibrio* FlhA requires FliH and FliI to perform protein export in the *Salmonella* fT3SS. Deletion of *flgM*, which encodes the negative regulator of the flagellar regulon, increases the expression levels of FliJ, export substrates and flagellar export chaperones and allows *Vibrio* FlhA to perform protein transport even in the absence of FliH and FliI. These results suggest that FlhA needs FliH and FliI to buffer protein export against internal perturbations (Minamino et al., 2016a).

The fT3SS utilizes the secreted molecular ruler protein FliK to stop growth of the hook at about 55 nm (Minamino et al., 1999; Erhardt et al., 2011; Kinoshita et al., 2017). The Δ*fliHI flhB(P28T)* bypass mutant cannot properly control the length of the hook, although it secrets the hook capping protein FlgD and the FliK ruler into the culture media almost at the wild-type level (Inoue et al., 2018). However, secretion level of the hook protein FlgE is about 10-fold lower than the wild-type level. The *flhA(F459A)* mutation, which targets a residue within $FlhA_C$ (**Figure 4**), significantly increases the secretion of FlgE, so the secreted FliK ruler can measure the length of the hook more precisely. Neither the secretion levels nor control of hook length is affected by the FlhB(P28T) and FlhA(F459A) substitutions when FliH and FliI are present. Because FlgD, FlgE, and FliK bind to FliH and FliI as well as $FlhA_C$ and $FlhB_C$ (Minamino and Macnab, 2000c), the $FliH_2$-FliI complex may coordinate targeting of FlgD, FlgE, and FliK to the $FlhA_C$-$FlhB_C$ docking platform to make control of the hook length more robust.

FlgN, FliS, and FliT act as export chaperones for FlgK/FlgL, FliC, and FliD, respectively (Fraser et al., 1999; Auvray et al., 2001). The chaperone-substrate complexes bind $FlhA_C$ with nanomolar affinity (**Figure 4**; Kinoshita et al., 2013). This strong interaction of the chaperone with $FlhA_C$ facilitates protein unfolding and transport by the H^+-driven export complex (Furukawa et al., 2016; Minamino et al., 2021c). In wild-type cells, more than 90% of flagellin molecules transported by the fT3SS assemble into the filament. The Δ*fliHI flhB(P28T) flhA(F459A)* cannot efficiently produce the hook-filament junction and filament cap structures at the hook tip, and hence more than 90% of the flagellin molecules are secreted as monomer into the culture supernatant. Because FlgN and FliT bind to the $FliH_2$-$FliI_1$ complex whereas FliS does not (Thomas et al., 2004; Minamino et al., 2012b; Sajó et al., 2014), the $FliH_2$-$FliI_1$ complex may contribute to hierarchical targeting of the flagellar chaperones to $FlhA_C$, thereby allowing the junction and filament cap structures to be efficiently formed at the hook tip prior to filament formation. Thus, the $FliH_2$-$FliI_1$ complex works with the $FlhA_C$-$FlhB_C$ docking platform to ensure the correct order of protein export.

Energy Coupling Mechanism

The information thus far summarized allows us to propose a model for the energetics of protein export by the fT3SS (**Figure 7**). The transmembrane export complex remains inactive until the cytoplasmic ATPase ring complex localizes to the flagellar base through an interaction between $FliH_N$ and FlN (Step 1). ATP hydrolysis by the FliI ATPase induces the rotation of FliJ within the $FliI_6$-ring at the $FlhA_C$-$FlhB_C$ docking platform. The interactions of FliJ and $FlhA_L$ induce conformational changes in the export complex that activate the FlhA ion channel and unlock the entrance gate of the polypeptide channel (Step 2). Then, cytoplasmic $FliH_2$-$FliI_1$ complexes escort export substrates and chaperone-substrate complexes from the cytoplasm to the $FlhA_C$-$FlhB_C$ docking platform through the interactions of FliH with FliN and FlhA (Step 3). The binding of the export substrate to the docking platform induces opening of the gate to the polypeptide channel, and the activated export complex acts as an H^+/protein antiporter that couples proton flow through the FlhA ion channel with the translocation of export substrates into the polypeptide channel (Step 4). The association-dissociation cycle of the $FliH_2$-FliI complex with the docking platform allows the transport of flagellar axial proteins in a highly controlled manner.

CONCLUSION AND PERSPECTIVES

The transmembrane export complex of the fT3SS is a dual-fuel export engine that uses either H^+ or Na^+ as the coupling ion to drive export of flagellar proteins. Interestingly, when the cytoplasmic ATPase ring complex works properly, the export gate preferentially utilizes the PMF to drive H^+-coupled protein export. $FlhA_{TM}$ acts as a dual ion channel to conduct both H^+ and Na^+. Because there is not yet structural information about the $FlhA_{TM}$, it remains unknown how the cytoplasmic ATPase ring complex switches the ion channel mode of $FlhA_{TM}$ from an inefficient dual-ion channel to a highly efficient H^+ channel.

The export complex couples inward-directed ion flow through FlhA with outward-directed protein translocation through the polypeptide channel. Recently, the cryoEM structure of the $FliP_5$-$FliQ_4$-$FliR_1$ complex associated with the basal body has been obtained with near atomic level (Johnson et al., 2021; Tan et al., 2021). Unfortunately, both FlhA and FlhB are lacking in the structure. To clarify the energy coupling mechanism, high-resolution structures of the entire export complex in different states of substrate export will be required.

The entire structure of the $FliI_6$-$FliJ_1$ ring complex looks similar those of rotary F_1 and V_1 ATPases. The $FliI_6$-$FliJ_1$ ring complex hydrolyzes ATP at the interfaces between FliI subunits and may induce sequential and cooperative conformational changes in $FliI_C$, which is involved in the interaction with FliJ. These observations lead to the hypothesis that ATP hydrolysis by the FliI ATPase presumably allows FliJ to rotate within the $FliI_6$ ring. This idea is supported by the cryoEM structure of the $SctN_6$-$SctO_1$ ring complex. To demonstrate the rotational catalytic mechanism of the $FliI_6$-$FliJ_1$ ring complex directly will require a biophysical approach.

The fT3SS transports fourteen different flagellar proteins in their copy numbers ranging from a few to tens of thousands in a sequential manner so that the flagellum can be built efficiently. The fT3SS must ensure the correct order of export of flagellar proteins for this to be an efficient process. The $FliH_2$-$FliI_1$ complex is required for efficient and robust flagellar assembly. Although an *in vitro* protein transport assay using inverted membrane vesicles has been established for the fT3SS, a quantitative measurement of ordered flagellar protein export will be needed to understand how the $FliH_2$-$FliI_1$ complex contributes to hierarchical protein targeting to the export complex.

AUTHOR CONTRIBUTIONS

TM, MK, and KN researched and wrote the review article. All authors contributed to the article and approved the submitted version.

FUNDING

This work was supported in part by JSPS KAKENHI Grant Numbers JP19H03182 (to TM) and JP20K15749 (to MK) and MEXT KAKENHI Grant No. JP20H05532 (to TM). This work has also been supported by Platform Project for Supporting Drug Discovery and Life Science Research (BINDS) from AMED under Grant No. JP19am0101117 to KN, by the Cyclic Innovation for Clinical Empowerment (CiCLE) from AMED under Grant No. JP17pc0101020 to KN, and by JEOL YOKOGUSHI Research Alliance Laboratories of Osaka University to KN.

ACKNOWLEDGMENTS

We acknowledge Katsumi Imada for his kind gift of a structural model of the $FliH_{C12}FliI_6FliJ_1$ ring complex and Akihiro Kawamoto for his kind gift of an electron micrograph of negatively stained FliI ring structures.

REFERENCES

Abrahams, J. P., Leslie, A. G., Lutter, R., and Walker, J. E. (1994). Structure at 2.8 Å resolution of F_1-ATPase from bovine heart mitochondria. *Nature* 370, 621–628. doi: 10.1038/370621a0

Abrusci, P., Vergara-Irigaray, M., Johnson, S., Beeby, M. D., Hendrixson, D. R., Roversi, P., et al. (2013). Architecture of the major component of the type III secretion system export apparatus. *Nat. Struct. Mol. Biol.* 20, 99–104. doi: 10.1038/nsmb.2452

Auvray, F., Ozin, A. J., Claret, L., and Hughes, C. (2002). Intrinsic membrane targeting of the flagellar export ATPase FliI: interaction with acidic phospholipids and FliH. *J. Mol. Biol.* 318, 941–950. doi: 10.1016/S0022-2836(02)00172-9

Auvray, F., Thomas, J., Fraser, G. M., and Hughes, C. (2001). Flagellin polymerisation control by a cytosolic export chaperone. *J. Mol. Biol.* 308, 221–229. doi: 10.1006/jmbi.2001.4597

Baba, M., Iwamoto, K., Iino, R., Ueno, H., Hara, M., Nakanishi, A., et al. (2016). Rotation of artificial rotor axles in rotary molecular motors. *Proc. Natl. Acad. Sci. U. S. A.* 113, 11214–11219. doi: 10.1073/pnas.1605640113

Bai, F., Morimoto, Y. V., Yoshimura, S. D. J., Hara, N., Kami-Ike, N., Namba, K., et al. (2014). Assembly dynamics and the roles of FliI ATPase of the bacterial flagellar export apparatus. *Sci. Rep.* 4:6528. doi: 10.1038/srep06528

Bange, G., Kümmerer, N., Engel, C., Bozkurt, G., Wild, K., and Sinning, I. (2010). FlhA provides the adaptor for coordinated delivery of late flagella building blocks to the type III secretion system. *Proc. Natl. Acad. Sci. U. S. A.* 107, 11295–11300. doi: 10.1073/pnas.1001383107

Chen, M., Zhao, Z., Yang, J., Peng, K., Baker, M. A., Bai, F., et al. (2017). Length-dependent flagellar growth of *Vibrio alginolyticus* revealed by real time fluorescent imaging. *Elife* 6:e22140. doi: 10.7554/eLife.22140

Chen, S., Beeby, M., Murphy, G. E., Leadbetter, J. R., Hendrixson, D. R., Briegel, A., et al. (2011). Structural diversity of bacterial flagellar motors. *EMBO J.* 30, 2972–2981. doi: 10.1038/emboj.2011.186

Claret, L., Calder, S. R., Higgins, M., and Hughes, C. (2003). Oligomerization and activation of the FliI ATPase central to bacterial flagellum assembly. *Mol. Microbiol.* 48, 1349–1355. doi: 10.1046/j.1365-2958.2003.03506.x

Erhardt, M., Mertens, M. E., Fabiani, F. D., and Hughes, K. T. (2014). ATPase-independent type-III protein secretion in *Salmonella enterica*. *PLoS Genet.* 10:e1004800. doi: 10.1371/journal.pgen.1004800

Erhardt, M., Singer, H. M., Wee, D. H., Keener, J. P., and Hughes, K. T. (2011). An infrequent molecular ruler controls flagellar hook length in *Salmonella enterica*. *EMBO J.* 30, 2948–2961. doi: 10.1038/emboj.2011.185

Erhardt, M., Wheatley, P., Kim, E. A., Hirano, T., Zhang, Y., Sarkar, M. K., et al. (2017). Mechanism of type-III protein secretion: regulation of FlhA conformation by a functionally critical charged-residue cluster. *Mol. Microbiol.* 104, 234–249. doi: 10.1111/mmi.13623

Evans, L. D., Poulter, S., Terentjev, E. M., Hughes, C., and Fraser, G. M. (2013). A chain mechanism for flagellum growth. *Nature* 504, 287–290. doi: 10.1038/nature12682

Fabiani, F. D., Renault, T. T., Peters, B., Dietsche, T., Gálvez, E. J. C., Guse, A., et al. (2017). A flagellum-specific chaperone facilitates assembly of the core type III export apparatus of the bacterial flagellum. *PLoS Biol.* 15:e2002267. doi: 10.1371/journal.pbio.2002267

Fan, F., and Macnab, R. M. (1996). Enzymatic characterization of FliI. An ATPase involved in flagellar assembly in *Salmonella typhimurium*. *J. Biol. Chem.* 271, 31981–31988. doi: 10.1074/jbc.271.50.31981

Fraser, G. M., Bennett, J. C. Q., and Hughes, C. (1999). Substrate-specific binding of hook-associated proteins by FlgN and FliT, putative chaperones for flagellum assembly. *Mol. Microbiol.* 32, 569–580. doi: 10.1046/j.1365-2958.1999.01372.x

Fukumura, T., Makino, F., Dietsche, T., Kinoshita, M., Kato, T., Wagner, S., et al. (2017). Assembly and stoichiometry of the core structure of the bacterial flagellar type III export gate complex. *PLoS Biol.* 15:e2002281. doi: 10.1371/journal.pbio.2002281

Furukawa, Y., Inoue, Y., Sakaguchi, A., Mori, Y., Fukumura, T., Miyata, T., et al. (2016). Structural stability of flagellin subunit affects the rate of flagellin export in the absence of FliS chaperone. *Mol. Microbiol.* 102, 405–416. doi: 10.1111/mmi.13469

Gibbons, C., Montgomery, M. G., Leslle, A. G., and Walker, J. E. (2000). The structure of the central stalk in bovine F_1-ATPase at 2.4 Å resolution. *Nat. Struct. Biol.* 7, 1055–1061. doi: 10.1038/80981

González-Pedrajo, B., Fraser, G. M., Minamino, T., and Macnab, R. M. (2002). Molecular dissection of *Salmonella* FliH, a regulator of the ATPase FliI and the type III flagellar protein export pathway. *Mol. Microbiol.* 45, 967–982. doi: 10.1046/j.1365-2958.2002.03047.x

González-Pedrajo, B., Minamino, T., Kihara, M., and Namba, K. (2006). Interactions between C ring proteins and export apparatus components: a possible mechanism for facilitating type III protein export. *Mol. Microbiol.* 60, 984–998. doi: 10.1111/j.1365-2958.2006.05149.x

Hara, N., Morimoto, Y. V., Kawamoto, A., Namba, K., and Minamino, T. (2012). Interaction of the extreme N-terminal region of FliH with FlhA is required for efficient bacterial flagellar protein export. *J. Bacteriol.* 194, 5353–5360. doi: 10.1128/JB.01028-12

Hara, N., Namba, K., and Minamino, T. (2011). Genetic characterization of conserved charged residues in the bacterial flagellar type III export protein FlhA. *PLoS One* 6:e22417. doi: 10.1371/journal.pone.0022417

Hendriksen, J. J., Lee, H. J., Bradshaw, A. J., Namba, K., Chevance, F. F. V., Minamino, T., et al. (2021). Genetic analysis of the *Salmonella* FliE protein that forms the base of the flagellar axial structure. *mBio* 12:e0239221. doi: 10.1128/mBio.02392-21

Hüsing, S., Halte, M., van Look, U., Guse, A., Gálvez, E. J. C., Charpentier, E., et al. (2021). Control of membrane barrier during bacterial type-III protein secretion. *Nat. Commun.* 12:3999. doi: 10.1038/s41467-021-24226-1

Ibuki, T., Imada, K., Minamino, T., Kato, T., Miyata, T., and Namba, K. (2011). Common architecture of the flagellar type III protein export apparatus and F- and V-type ATPases. *Nat. Struct. Mol. Biol.* 18, 277–282. doi: 10.1038/nsmb.1977

Ibuki, T., Uchida, Y., Hironaka, Y., Namba, K., Imada, K., and Minamino, T. (2013). Interaction between FliJ and FlhA, components of the bacterial flagellar type III export apparatus. *J. Bacteriol.* 195, 466–473. doi: 10.1128/JB.01711-12

Iino, T. (1974). Assembly of *Salmonella* flagellin *in vitro* and *in vivo*. *J. Supramol. Struct.* 2, 372–384. doi: 10.1002/jss.400020226

Imada, K., Minamino, T., Kinoshita, M., Furukawa, Y., and Namba, K. (2010). Structural insight into the regulatory mechanisms of interactions of the flagellar type III chaperone FliT with its binding partners. *Proc. Natl. Acad. Sci. U. S. A.* 107, 8812–8817. doi: 10.1073/pnas.1001866107

Imada, K., Minamino, T., Tahara, A., and Namba, K. (2007). Structural similarity between the flagellar type III ATPase FliI and F1-ATPase subunits. *Proc. Natl. Acad. Sci. U. S. A.* 104, 485–490. doi: 10.1073/pnas.0608090104

Imada, K., Minamino, T., Uchida, Y., Kinoshita, M., and Namba, K. (2016). Insight into the flagella type III export revealed by the complex structure of the type III ATPase and its regulator. *Proc. Natl. Acad. Sci. U. S. A.* 113, 3633–3638. doi: 10.1073/pnas.1524025113

Inoue, Y., Kinoshita, M., Kida, M., Takekawa, N., Namba, K., Imada, K., et al. (2021). The FlhA linker mediates flagellar protein export switching during flagellar assembly. *Commun. Biol.* 4:646. doi: 10.1038/s42003-021-02177-z

Inoue, Y., Morimoto, Y. V., Namba, K., and Minamino, T. (2018). Novel insights into the mechanism of well-ordered assembly of bacterial flagellar proteins in *Salmonella*. *Sci. Rep.* 8:1787. doi: 10.1038/s41598-018-20209-3

Inoue, Y., Ogawa, Y., Kinoshita, M., Terahara, N., Shimada, M., Kodera, N., et al. (2019). Structural insight into the substrate specificity switching mechanism of the type III protein export apparatus. *Structure* 27, 965–976. doi: 10.1016/j.str.2019.03.017

Johnson, S., Furlong, E. J., Deme, J. C., Nord, A. L., Caesar, J. J. E., Chevance, F. F. V., et al. (2021). Molecular structure of the intact bacterial flagellar basal body. *Nat. Microbiol.* 6, 712–721. doi: 10.1038/s41564-021-00895-y

Johnson, S., Kuhlen, L., Deme, J. C., Abrusci, P., and Lea, S. M. (2019). The structure of an injectisome export gate demonstrates conservation of architecture in the core export gate between flagellar and virulence type III secretion systems. *mBio* 10, e00818–19. doi: 10.1128/mBio.00818-19

Kato-Yamada, Y., Yoshida, M., and Hisabori, T. (2000). Movement of the helical domain of the epsilon subunit is required for the activation of thermophilic F1-ATPase. *J. Biol. Chem.* 275, 35746–35750. doi: 10.1074/jbc.M006575200

Kawamoto, A., Miyata, T., Makino, F., Kinoshita, M., Minamino, T., Imada, K., et al. (2021). Native flagellar MS ring is formed by 34 subunits with 23-fold and 11-fold subsymmetries. *Nat. Commun.* 12:4223. doi: 10.1038/s41467-021-24507-9

Kawamoto, A., Morimoto, Y. V., Miyata, T., Minamino, T., Hughes, K. T., Kato, T., et al. (2013). Common and distinct structural features of *Salmonella* injectisome and flagellar basal body. *Sci. Rep.* 3:3369. doi: 10.1038/srep03369

Kazetani, K., Minamino, T., Miyata, T., Kato, T., and Namba, K. (2009). ATP-induced FliI hexamerization facilitates bacterial flagellar protein export. *Biochem. Biophys. Res. Commun.* 388, 323–327. doi: 10.1016/j.bbrc.2009.08.004

Kihara, M., Minamino, T., Yamaguchi, S., and Macnab, R. M. (2001). Intergenic suppression between the flagellar MS ring protein FliF of *Salmonella* and FlhA, a membrane component of its export apparatus. *J. Bacteriol.* 183, 1655–1662. doi: 10.1128/JB.183.5.1655-1662.2001

Kinoshita, M., Aizawa, S.-I., Inoue, Y., Namba, K., and Minamino, T. (2017). The role of intrinsically disordered C-terminal region of FliK in substrate specificity switching of the bacterial flagellar type III export apparatus. *Mol. Microbiol.* 105, 572–588. doi: 10.1111/mmi.13718

Kinoshita, M., Hara, N., Imada, K., Namba, K., and Minamino, T. (2013). Interactions of bacterial chaperone-substrate complexes with FlhA contribute to coordinating assembly of the flagellar filament. *Mol. Microbiol.* 90, 1249–1261. doi: 10.1111/mmi.12430

Kinoshita, M., Namba, K., and Minamino, T. (2021). A positive charge region of *Salmonella* FliI is required for ATPase formation and efficient flagellar protein export. *Commun. Biol.* 4:464. doi: 10.1038/s42003-021-01980-y

Kishikawa, J., Ibuki, T., Nakamura, S., Nakanishi, A., Minamino, T., Miyata, T., et al. (2013). Common evolutionary origin for the rotor domain of rotary ATPases and flagellar protein export apparatus. *PLoS One* 8:e64695. doi: 10.1371/journal.pone.0064695

Kuhlen, L., Abrusci, P., Johnson, S., Gault, J., Deme, J., Caesar, J., et al. (2018). Structure of the core of the type III secretion system export apparatus. *Nat. Struct. Mol. Biol.* 25, 583–590. doi: 10.1038/s41594-018-0086-9

Kuhlen, L., Johnson, S., Cao, J., Deme, J. C., and Lea, S. M. (2021). Nonameric structures of the cytoplasmic domain of FlhA and SctV in the context of the full-length protein. *PLoS One* 16:e0252800. doi: 10.1371/journal.pone.0252800

Kuhlen, L., Johnson, S., Zeitler, A., Bäurle, S., Deme, J. C., Caesar, J. J. E., et al. (2020). The substrate specificity switch FlhB assembles onto the export gate to regulate type three secretion. *Nat. Commun.* 11:1296. doi: 10.1038/s41467-020-15071-9

Lee, P. C., Zmina, S. E., Stopford, C. M., Toska, J., and Rietsch, A. (2014). Control of type III secretion activity and substrate specificity by the cytoplasmic regulator PcrG. *Proc. Natl. Acad. Sci. U. S. A.* 111, E2027–E2036. doi: 10.1073/pnas.1402658111

Macnab, R. M. (2003). How bacteria assemble flagella. *Annu. Rev. Microbiol.* 57, 77–100. doi: 10.1146/annurev.micro.57.030502.090832

Majewski, D. D., Worrall, L. J., Hong, C., Atkinson, C. E., Vuckovic, M., Watanabe, N., et al. (2019). Cryo-EM structure of the homohexameric T3SS ATPase-central stalk complex reveals rotary ATPase-like asymmetry. *Nat. Commun.* 10:626. doi: 10.1038/s41467-019-08477-7

McMurry, J. L., Murphy, J. W., and González-Pedrajo, B. (2006). The FliN-FliH interaction mediates localization of flagellar export ATPase FliI to the C ring complex. *Biochemistry* 45, 11790–11798. doi: 10.1021/bi0605890

Minamino, T. (2014). Protein export through the bacterial flagellar type III export pathway. *Biochim. Biophys. Acta* 1843, 1642–1648. doi: 10.1016/j.bbamcr.2013.09.005

Minamino, T. (2018). Hierarchical protein export mechanism of the bacterial flagellar type III protein export apparatus. *FEMS Microbiol. Lett.* 365:fny117. doi: 10.1093/femsle/fny117

Minamino, T., and Macnab, R. M. (1999). Components of the *Salmonella* flagellar export apparatus and classification of export substrates. *J. Bacteriol.* 181, 1388–1394. doi: 10.1128/JB.181.5.1388-1394.1999

Minamino, T., and Macnab, R. M. (2000c). Interactions among components of the *Salmonella* flagellar export apparatus and its substrates.

Mol. Microbiol. 35, 1052–1064. doi: 10.1046/j.1365-2958.2000.01771.x

Minamino, T., and Macnab, R. M. (2000a). Domain structure of *Salmonella* FlhB, a flagellar export component responsible for substrate specificity switching. *J. Bacteriol.* 182, 4906–4914. doi: 10.1128/JB.182.17.4906-4914.2000

Minamino, T., and Macnab, R. M. (2000b). FliH, a soluble component of the type III flagellar export apparatus of *Salmonella*, forms a complex with FliI and inhibits its ATPase activity. *Mol. Microbiol.* 37, 1494–1503. doi: 10.1046/j.1365-2958.2000.02106.x

Minamino, T., and Namba, K. (2004). Self-assembly and type III protein export of the bacterial flagellum. *J. Mol. Microbiol. Biotechnol.* 7, 5–17. doi: 10.1159/000077865

Minamino, T., and Namba, K. (2008). Distinct roles of the FliI ATPase and proton motive force in bacterial flagellar protein export. *Nature* 451, 485–488. doi: 10.1038/nature06449

Minamino, T., González-Pedrajo, B., Kihara, M., Namba, K., and Macnab, R. M. (2003). The ATPase FliI can interact with the type III flagellar protein export apparatus in the absence of its regulator, FliH. *J. Bacteriol.* 185, 3983–3988. doi: 10.1128/JB.185.13.3983-3988.2003

Minamino, T., González-Pedrajo, B., Oosawa, K., Namba, K., and Macnab, R. M. (2002). Structural properties of FliH, an ATPase regulatory component of the *Salmonella* type III flagellar export apparatus. *J. Mol. Biol.* 322, 281–290. doi: 10.1016/s0022-2836(02)00754-4

Minamino, T., González-Pedrajo, B., Yamaguchi, K., Aizawa, S.-I., and Macnab, R. M. (1999). FliK, the protein responsible for flagellar hook length control in *Salmonella*, is exported during hook assembly. *Mol. Microbiol.* 34, 295–304. doi: 10.1046/j.1365-2958.1999.01597.x

Minamino, T., Iino, T., and Kutsukake, K. (1994). Molecular characterization of the *Salmonella typhimurium flhB* operon and its protein products. *J. Bacteriol.* 176, 7630–7637. doi: 10.1128/jb.176.24.7630-7637.1994

Minamino, T., Kawamoto, A., Kinoshita, M., and Namba, K. (2020b). Molecular organization and assembly of the export apparatus of flagellar type III secretion systems. *Curr. Top. Microbiol. Immunol.* 427, 91–107. doi: 10.1007/82_2019_170

Minamino, T., Inoue, Y., Kinoshita, M., and Namba, K. (2020a). FliK-driven conformational rearrangements of FlhA and FlhB are required for export switching of the flagellar protein export apparatus. *J. Bacteriol.* 202, e00637–19. doi: 10.1128/JB.00637-19

Minamino, T., Kazetani, K., Tahara, A., Suzuki, H., Furukawa, Y., Kihara, M., et al. (2006). Oligomerization of the bacterial flagellar ATPase FliI is controlled by its extreme N-terminal region. *J. Mol. Biol.* 360, 510–519. doi: 10.1016/j.jmb.2006.05.010

Minamino, T., Kinoshita, M., Hara, N., Takeuchi, S., Hida, A., Koya, S., et al. (2012a). Interaction of a bacterial flagellar chaperone FlgN with FlhA is required for efficient export of its cognate substrates. *Mol. Microbiol.* 83, 1775–1788. doi: 10.1111/j.1365-2958.2011.07964.x

Minamino, T., Kinoshira, M., Imada, K., and Namba, K. (2012b). Interaction between FliI ATPase and a flagellar chaperone FliT during bacterial flagellar export. *Mol. Microbiol.* 83, 168–178. doi: 10.1111/j.1365-2958.2011.07924.x

Minamino, T., Morimoto, Y. V., Hara, N., Aldridge, P. D., and Namba, K. (2016b). The bacterial flagellar type III export gate complex is a dual fuel engine that can use both H^+ and Na^+ for flagellar protein export. *PLoS Pathog.* 12:e1005495. doi: 10.1371/journal.ppat.1005495

Minamino, T., Kinoshita, M., Inoue, Y., Morimoto, Y. V., Ihara, K., Koya, S., et al. (2016a). FliH and FliI ensure efficient energy coupling of flagellar type III protein export in *Salmonella*. *Microbiologyopen* 5, 424–435. doi: 10.1002/mbo3.340

Minamino, T., Morimoto, Y. V., Hara, N., and Namba, K. (2011). An energy transduction mechanism used in bacterial flagellar type III protein export. *Nat. Commun.* 2:475. doi: 10.1038/ncomms1488

Minamino, T., Morimoto, Y. V., Kinoshita, M., Aldridge, P. D., and Namba, K. (2014). The bacterial flagellar protein export apparatus processively transports flagellar proteins even with extremely infrequent ATP hydrolysis. *Sci. Rep.* 4:7579. doi: 10.1038/srep07579

Minamino, T., Kinoshita, M., Morimoto, Y. V., and Namba, K. (2021a). The FlgN chaperone activates the Na^+-driven engine of the *Salmonella* flagellar protein export apparatus. *Commun. Biol.* 4:335. doi: 10.1038/s42003-021-01865-0

Minamino, T., Morimoto, Y. V., Kinoshita, M., and Namba, K. (2021b). Membrane voltage-dependent activation mechanism of the bacterial flagellar protein export apparatus. *Proc. Natl. Acad. Sci. U. S. A.* 118:e2026587118. doi: 10.1073/pnas.2026587118

Minamino, T., Morimoto, Y. V., Kinoshita, M., and Namba, K. (2021c). Multiple roles of flagellar export chaperones for efficient and robust flagellar filament formation in *Salmonella*. *Front. Microbiol.* 12:756044. doi: 10.3389/fmicb.2021.756044

Minamino, T., Shimada, M., Okabe, M., Saijo-Hamano, Y., Imada, K., Kihara, M., et al. (2010). Role of the C-terminal cytoplasmic domain of FlhA in bacterial flagellar type III protein export. *J. Bacteriol.* 192, 1929–1936. doi: 10.1128/JB.01328-09

Minamino, T., Tame, J. R., Namba, K., and Macnab, R. M. (2001). Proteolytic analysis of the FliH/FliI complex, the ATPase component of the type III flagellar export apparatus of *Salmonella*. *J. Mol. Biol.* 312, 1027–1036. doi: 10.1006/jmbi.2001.5000

Minamino, T., Yamaguchi, S., and Macnab, R. M. (2000). Interaction between FliE and FlgB, a proximal rod component of the flagellar basal body of *Salmonella*. *J. Bacteriol.* 182, 3029–3036. doi: 10.1128/JB.182.11.3029-3036.2000

Minamino, T., Yoshimura, S. D., Morimoto, Y. V., González-Pedrajo, B., Kami-Ike, N., and Namba, K. (2009). Roles of the extreme N-terminal region of FliH for efficient localization of the FliH-FliI complex to the bacterial flagellar type III export apparatus. *Mol. Microbiol.* 74, 1471–1483. doi: 10.1111/j.1365-2958.2009.06946.x

Morimoto, Y. V., Ito, M., Hiraoka, K. D., Che, Y.-S., Bai, F., Kami-Ike, N., et al. (2014). Assembly and stoichiometry of FliF and FlhA in *Salmonella* flagellar basal body. *Mol. Microbiol.* 91, 1214–1226. doi: 10.1111/mmi.12529

Morimoto, Y. V., Kami-Ike, N., Miyata, T., Kawamoto, A., Kato, T., Namba, K., et al. (2016). High-resolution pH imaging of living bacterial cells to detect local pH differences. *mBio* 7, e01911–16. doi: 10.1128/mBio.01911-16

Nakamura, S., and Minamino, T. (2019). Flagella-driven motility of bacteria. *Biomolecules* 9:279. doi: 10.3390/biom9070279

Notti, R. Q., Bhattacharya, S., Lilic, M., and Stebbins, C. E. (2015). A common assembly module in injectisome and flagellar type III secretion sorting platforms. *Nat. Commun.* 6:7125. doi: 10.1038/ncomms8125

Okabe, M., Minamino, T., Imada, K., Namba, K., and Kihara, M. (2009). Role of the N-terminal domain of FliI ATPase in bacterial flagellar protein export. *FEBS Lett.* 583, 743–748. doi: 10.1016/j.febslet.2009.01.026

Pallen, M. J., Bailey, C. M., and Beatson, S. A. (2006). Evolutionary links between FliH/YscL-like proteins from bacterial type III secretion systems and second-stalk components of the F_OF_1 and vacuolar ATPases. *Protein Sci.* 15, 935–941. doi: 10.1110/ps.051958806

Paul, K., Erhardt, M., Hirano, T., Blair, D. F., and Hughes, K. T. (2008). Energy source of flagellar type III secretion. *Nature* 451, 489–492. doi: 10.1038/nature06497

Paul, K., Harmon, J. G., and Blair, D. F. (2006). Mutational analysis of the flagellar rotor protein FliN: identification of surfaces important for flagellar assembly and switching. *J. Bacteriol.* 188, 5240–5248. doi: 10.1128/JB.00110-06

Rees, D. M., Montgomery, M. G., Leslie, A. G., and Walker, J. E. (2012). Structural evidence of a new catalytic intermediate in the pathway of ATP hydrolysis by F_1-ATPase from bovine heart mitochondria. *Proc. Natl. Acad. Sci. U. S. A.* 109, 11139–11143. doi: 10.1073/pnas.1207587109

Renault, T. T., Abraham, A. O., Bergmiller, T., Paradis, G., Rainville, S., Charpentier, E., et al. (2017). Bacterial flagella grow through an injection-diffusion mechanism. *Elife* 6:e23136. doi: 10.7554/eLife.23236

Saijo-Hamano, Y., Imada, K., Minamino, T., Kihara, M., Shimada, M., Kitao, A., et al. (2010). Structure of the cytoplasmic domain of FlhA and implication for flagellar type III protein export. *Mol. Microbiol.* 76, 260–268. doi: 10.1111/j.1365-2958.2010.07097.x

Sajó, R., Liliom, K., Muskotál, A., Klein, A., Závodszky, P., Vonderviszt, F., et al. (2014). Soluble components of the flagellar export apparatus, FliI, FliJ, and FliH, do not deliver flagellin, the major filament protein, from the cytosol to the export gate. *Biochim. Biophys. Acta* 1843, 2414–2423. doi: 10.1016/j.bbamcr.2014.07.004

Shimabukuro, K., Yasuda, R., Muneyuki, E., Hara, K. Y., Kinosita, K. Jr., and Yoshida, M. (2003). Catalysis and rotation of F_1 motor: cleavage of ATP at the catalytic site occurs in 1 ms before 40° substep rotation. *Proc. Natl. Acad. Sci. U. S. A.* 100, 14731–14736. doi: 10.1073/pnas.2434983100

Takekawa, N., Kawamoto, A., Sakuma, M., Kato, T., Kojima, S., Kinoshita, M., et al. (2021). Two distinct conformations in 34 FliF subunits generate three different symmetries within the flagellar MS-ring. *mBio* 12, e03199–20. doi: 10.1128/mBio.03199-20

Tan, J., Zhang, X., Wang, X., Xu, C., Chang, S., Wu, H., et al. (2021). Structural basis of assembly and torque transmission of the bacterial flagellar motor. *Cell* 184, 2665–2679.e19. doi: 10.1016/j.cell.2021.03.057

Terahara, N., Inoue, Y., Kodera, N., Morimoto, Y. V., Uchihashi, T., Imada, K., et al. (2018). Insight into structural remodeling of the FlhA ring responsible for bacterial flagellar type III protein export. *Sci. Adv.* 4:eaao7054. doi: 10.1126/sciadv.aao7054

Terashima, H., Kawamoto, A., Tastumi, C., Namba, K., Minamino, T., and Imada, K. (2018). In vitro reconstitution of functional type III protein export and insights into flagellar assembly. *mBio* 9, e00988–18. doi: 10.1128/mBio.00988-18

Terashima, H., Tastumi, C., Kawamoto, A., Namba, K., Minamino, T., and Imada, K. (2020). In vitro autonomous construction of the flagellar axial structure in inverted membrane vesicles. *Biomolecules* 10:126. doi: 10.3390/biom10010126

Thomas, J., Stafford, G. P., and Hughes, C. (2004). Docking of cytosolic chaperone-substrate complexes at the membrane ATPase during flagellar type III protein export. *Proc. Natl. Acad. Sci. U. S. A.* 101, 3945–3950. doi: 10.1073/pnas.0307223101

Vogler, A. P., Homma, M., Irikura, V. M., and Macnab, R. M. (1991). *Salmonella typhimurium* mutants defective in flagellar filament regrowth and sequence similarity of FliI to F_0F_1, vacuolar, and archaebacterial ATPase subunits. *J. Bacteriol.* 173, 3564–3572. doi: 10.1128/jb.173.11.3564-3572.1991

Wagner, S., and Diepold, A. (2020). A unified nomenclature for injectisome-type type III secretion systems. *Curr. Top. Microbiol. Immunol.* 427, 91–107. doi: 10.1007/82_2020_210

Walker, J. E. (2013). The ATP synthase: the understood, the uncertain and the unknown. *Biochem. Soc. Trans.* 41, 1–16. doi: 10.1042/BST20110773

Walker, J. E., and Dickson, V. K. (2006). The peripheral stalk of the mitochondrial ATP synthase. *Biochim. Biophys. Acta* 1757, 286–296. doi: 10.1016/j.bbabio.2006.01.001

Ward, E., Renault, T. T., Kim, E. A., Erhardt, M., Hughes, K. T., and Blair, D. F. (2018). Type-III secretion pore formed by flagellar protein FliP. *Mol. Microbiol.* 107, 94–103. doi: 10.1111/mmi.13870

Watanabe, R., and Noji, H. (2013). Chemomechanical coupling mechanism of F_1-ATPase: catalysis and torque generation. *FEBS Lett.* 587, 1030–1035. doi: 10.1016/j.febslet.2013.01.063

Xing, Q., Shi, K., Portaliou, A., Rossi, P., Economou, A., and Kalodimos, C. G. (2018). Structure of chaperone-substrate complexes docked onto the export gate in a type III secretion system. *Nat. Commun.* 9:1773. doi: 10.1038/s41467-018-04137-4

Zarivach, R., Vuckovic, M., Deng, W., Finlay, B. B., and Strynadka, N. C. (2007). Structural analysis of a prototypical ATPase from the type III secretion system. *Nat. Struct. Mol. Biol.* 14, 131–137. doi: 10.1038/nsmb1196

Conflict of Interest: The authors declare that the research was conducted in the absence of any commercial or financial relationships that could be construed as a potential conflict of interest.

Publisher's Note: All claims expressed in this article are solely those of the authors and do not necessarily represent those of their affiliated organizations, or those of the publisher, the editors and the reviewers. Any product that may be evaluated in this article, or claim that may be made by its manufacturer, is not guaranteed or endorsed by the publisher.

Copyright © 2022 Minamino, Kinoshita and Namba. This is an open-access article distributed under the terms of the Creative Commons Attribution License (CC BY). The use, distribution or reproduction in other forums is permitted, provided the original author(s) and the copyright owner(s) are credited and that the original publication in this journal is cited, in accordance with accepted academic practice. No use, distribution or reproduction is permitted which does not comply with these terms.

frontiers | Frontiers in Microbiology

HYPOTHESIS AND THEORY
published: 06 May 2022
doi: 10.3389/fmicb.2022.891694

Flagellar Motor Transformed: Biophysical Perspectives of the *Myxococcus xanthus* Gliding Mechanism

Jing Chen[1*†] *and Beiyan Nan*[2*†]

[1] *Department of Biological Sciences, Virginia Polytechnic Institute and State University, Blacksburg, VA, United States,*
[2] *Department of Biology, Texas A&M University, College Station, TX, United States*

Many bacteria move on solid surfaces using gliding motility, without involvement of flagella or pili. Gliding of *Myxococcus xanthus* is powered by a proton channel homologous to the stators in the bacterial flagellar motor. Instead of being fixed in place and driving the rotation of a circular protein track like the flagellar basal body, the gliding machinery of *M. xanthus* travels the length of the cell along helical trajectories, while mechanically engaging with the substrate. Such movement entails a different molecular mechanism to generate propulsion on the cell. In this perspective, we will discuss the similarities and differences between the *M. xanthus* gliding machinery and bacterial flagellar motor, and use biophysical principles to generate hypotheses about the operating mechanism, efficiency, sensitivity to control, and mechanosensing of *M. xanthus* gliding.

Keywords: myxobacteria, bacterial motility, bacterial gliding, proton channel, cell polarity, mechanosensing, force transmission

OPEN ACCESS

Edited by:
Ronald Mark Wooten, University of Toledo, United States

Reviewed by:
Abhishek Shrivastava, Arizona State University, United States
Daisuke Nakane, The University of Electro-Communications, Japan

***Correspondence:**
Jing Chen
chenjing@vt.edu
Beiyan Nan
bnan@tamu.edu

[†] These authors have contributed equally to this work

Specialty section:
This article was submitted to Microbial Physiology and Metabolism, a section of the journal Frontiers in Microbiology

Received: *08 March 2022*
Accepted: *13 April 2022*
Published: *06 May 2022*

Citation:
Chen J and Nan B (2022) Flagellar Motor Transformed: Biophysical Perspectives of the Myxococcus xanthus Gliding Mechanism. Front. Microbiol. 13:891694. doi: 10.3389/fmicb.2022.891694

INTRODUCTION

Bacteria navigate their environments using diverse motility systems, yet many distinct mechanisms can find homology between each other, possibly as a result of divergent evolution. Such systems could use analogous energy sources and be subject to similar physical and chemical constraints. For example, rotary bacterial flagella, regardless of their localization (inside or outside of the cell wall) and energy sources (proton motive force or other ion gradient across the membrane), are all subject to comparable mechanochemical and hydrodynamic limits. In this perspective, we will focus on the gliding machinery of *Myxococcus xanthus*, which mediates linear cellular translocation on solid surfaces, yet uses a proton channel that is homologous to the energy-harvesting unit in rotary flagella (Nan et al., 2011; Sun et al., 2011).

Myxococcus xanthus is a rod-shaped gram-negative bacterium that cannot swim due to the lack of flagella. Instead, it moves on surfaces using two motility systems, a social (S)-motility system that works more effectively in cells within groups, and an adventurous (A)-motility system that predominates in isolated cells. S-motility, also termed twitching motility, depends on extension and retraction of the Type IV pili (Wu and Kaiser, 1995; Chang et al., 2016), while A-motility, also termed gliding motility, is driven by a rather unique system. The entire gliding machinery consists of about 20 proteins and spans across the cytoplasm, inner membrane, peptidoglycan (PG) wall and outer membrane to interact with the substrate (**Figure 1**). The energy-harvesting unit in the inner

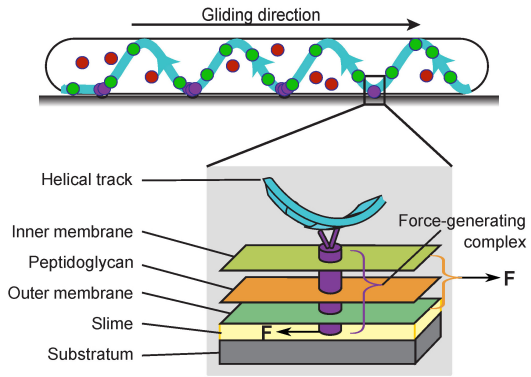


FIGURE 1 | The gliding machinery of *Myxococcus xanthus*. The AglR/Q/S motors can be categorized into three subpopulations: those in the stationary force-generating complexes (purple), those undergoing directed motion along helical trajectories (green), and those that are diffusive (red). The fully assembled force-generating complexes span the entire cell envelop (gray box). To propel the cell forward, the force-generating complexes must exert opposite forces on the cell and substrate.

membrane consists of AglR, AglQ, and AglS, which show significant homology with the MotA/B proteins in the flagellar stator of *Escherichia coli* (AglR is homologous to MotA, whereas AglQ and AglS are homologous to MotB; Nan et al., 2011; Sun et al., 2011). As a conserved proton-binding site on AglQ is essential for gliding, AglR/Q/S, similar to MotA/B, are predicted to form proton channels that convert the proton motive force into mechanical forces (Sun et al., 2011). For brevity, hereafter we will refer to the energy-harvesting proton channel as the "motor", to be distinguished from the fully assembled gliding machinery. In contrast to the flagellar MotA/B stator, however, the AglR/Q/S motors are not fixed in the cell envelop, but rather travel the length of the cell along helical trajectories (Nan et al., 2011; Fu et al., 2018). When the motors travel to the sites where the cell contacts the substrate, they interact with the substrate through a group of Glt proteins that span the periplasm (**Figure 1**; Nan et al., 2010; Faure et al., 2016). In order to propel the cell forward, the motors must exert opposite mechanical forces on the substrate and the cell to cause relative motion between the two.

Single molecules of the motor and motor-associated proteins typically exhibit three subcellular dynamic patterns, stationary, directed motion, and diffusion. Current data suggest that the force-generating units are stationary, in which the motors assemble with other gliding proteins into fully functional gliding machineries (Nan et al., 2013; Faure et al., 2016; Nan, 2017). Most prominently, the stationary subpopulation aggregate in regularly spaced "focal adhesion" sites where the substrate interfaces with a helical intracellular track (**Figure 1**, purple circles; Nan et al., 2013). As the cell moves forward, these motor aggregations remain static with respect to the substrate; relative to the cell, they move toward the trailing pole at the speed of the cell (Mignot et al., 2007; Nan et al., 2010, 2013; Faure et al., 2016). Another subpopulation of motors travel along the helical track. The helical pattern of the motors (**Figure 1**, green circles) colocalizes with that of MreB, a bacterial cytoskeletal protein and homolog of eukaryotic actin. Disruption of MreB abolishes the helical motion of the motors and blocks gliding motility (Mauriello et al., 2010; Nan et al., 2011; Fu et al., 2018). However, it is yet unclear whether MreB directly provides the intracellular track for the motors, or rather, guides the helical motion of the motors indirectly. Although the helical motion of motors depends on the proton motive force and can reach ∼2 μm/s (Nan et al., 2013, 2015), the motors in directed motion could be in an intermediate state before the complete assembly of the force-generating units at the "focal adhesion" sites. Such incomplete machineries probably lack mechanical engagement with the substrate, and are thus not likely to provide propulsion for gliding (Nan et al., 2013; Faure et al., 2016; Nan, 2017). The third subpopulation of motor proteins are diffusive (**Figure 1**, red circles). As this subpopulation increases when either the proton motive force or MreB is disrupted[1], it may be composed of incomplete motors, which are unable to harvest the proton motive force (Nan et al., 2013). Individual gliding proteins switch among the three states dynamically, out of which the switch into the stationary state likely reflects the assembly of the force-generating machineries and their engagement with the substrate. Notably, this assembly responds to substrate stiffness: the aggregation of stationary motors and motor-associated proteins intensifies on harder substrates and nearly all motors become stationary when the whole cell is embedded in the substrate (Nan et al., 2010, 2013). This phenomenon suggests that external mechanical cues can influence the gliding of *M. xanthus*, which is a hallmark of cellular mechanosensing.

Although the proteins constituting the *M. xanthus* gliding machinery are largely known, it remains unclear how the gliding machinery generates propulsion and drives linear motion of the cell. Based on prominent biophysical characteristics, such as the velocities of the motors and the intracellular helical track, a number of studies have proposed physical models for various aspects of gliding (Wolgemuth et al., 2002; Nan et al., 2011; Balagam et al., 2014; Tchoufag et al., 2019). As increasing amount of experimental data become available, we will review the similarities and differences between the gliding machinery in *M. xanthus* and the well-studied bacterial flagellar system in *E. coli*. Based on these comparisons, we will leverage biophysical principles to make hypotheses about the elusive mechanistic aspects of the *M. xanthus* gliding machinery, such as its assembly, force transmission, and sensitivity to control.

OPEN QUESTIONS ON THE MECHANISM OF *M. XANTHUS* GLIDING

How Does the Gliding Machinery Move Without Tearing the Cell Wall?

The envelop-spanning force-generating units at the "focal adhesion" sites are stationary relative to the substrate, while

[1]In Nan et al., 2013, the authors simplified the data analysis, in which particles are only categorized as stationary or in directed motion. The increase of the "slow-moving" particles actually corresponds to an increase in the diffusive population in a three-population analysis.

the cell wall moves forward at the cell velocity. Intuitively, the relative motion between the force-generating units and the cell wall would tear the wall and compromise its mechanical integrity. Yet, the cell wall is not broken in moving *M. xanthus* cells. How does the gliding machinery move without tearing the cell wall? This is a challenge that the statically positioned flagellar motor does not face.

The answer to the above question depends on how the gliding machineries interact with the substrate. An early theory proposes a viscous coupling between the gliding machinery and the substrate, which entirely avoids penetrating the PG cell wall (Nan et al., 2011; Nan and Zusman, 2011; Tchoufag et al., 2019; **Figure 2A**). Particularly, some motor-associated proteins are of extraordinary sizes. For instance, AgmK, a transmembrane protein, contains 3,812 amino acids. Such proteins could form a bulky complex beneath the PG layer and deform the cell envelop locally. As the gliding machinery moves, the resulting bump at the surface of the cell would push against the extracellular slime, a putative layer of polysaccharides between the cell surface and the substrate (**Figure 2A**). The viscous drag from the slime thereby imposes thrust on the cell. This theory readily explains the correlation between the aggregation of motors at the "focal adhesion" sites and the stiffness of substrate: harder substrates presumably exert higher viscous drag on the gliding machineries and slow them down to create stronger aggregations (Nan et al., 2010, 2011, 2013). However, this viscous coupling cannot explain the cell's resistance to sideway collisions (Balagam et al., 2014), unless the viscous drag between the cell and the substrate is highly anisotropic, with a much stronger drag perpendicular to the cell body. Currently, there is no evidence for such a strong anisotropy.

Recently, an updated theory proposes that the gliding machinery may consists of two subcomplexes inside and outside the PG wall, respectively (Faure et al., 2016; **Figure 2B**). The inner subcomplex contains the proton channel motor and the outer subcomplex directly binds the substrate. Transient association between the two subcomplexes across the mesh-like structure of PG (Hughes et al., 1975; Demchick and Koch, 1996; Vollmer et al., 2008) forms a fully assembled gliding machinery at the "focal adhesion" site. The fully assembly machinery is mechanically engaged with the substrate and generates propulsion (**Figure 2B**). Meanwhile, constant disassociation between the inner and outer subcomplexes allows the inner subcomplex to move relative to PG. Whereas this attractive hypothesis successfully circumvents the breach of PG, it also incurs a new problem: once the inner subcomplex disassociates from the outer subcomplex, without resistance from the substrate it may quickly escape from the "focal adhesion" site, causing a low duty ratio of the motor (i.e., the fraction of time a motor actually contributes to force generation). This also conflicts with the observation that most motors become stationary and stay engaged with the substrate under certain conditions, e.g., on very hard substrates (Nan et al., 2013). How do the inner and outer subcomplexes re-associate sufficiently fast across the PG so that the motors remain at the "focal adhesion" sites?

To address the above question, here we hypothesize that individual inner subcomplexes are coupled with each other: they bind with the outer subcomplexes alternately and hence help each other stay on the track (**Figure 2C**). Similar processive mechanisms are widely observed in well studied molecular motors, with the best example found in the hand-over-hand mechanism in dimeric kinesins (Yildiz et al., 2004; Gennerich and Vale, 2009). In *M. xanthus*, aggregation of motor proteins at the "focal adhesion" sites could reflect such coupling among multiple motors. Alternatively, the two MotB homologs, AglQ and AglS, may each constitute one of two coupled subunits, giving rise to a hand-over-hand mechanism within a single motor.

How Do Motors Propel the Cell Body?

As motors reside in the fluid membrane, they require a certain structure to transmit the force onto the cell body. Part of this structure must be localized inside the cytoplasm, such that the

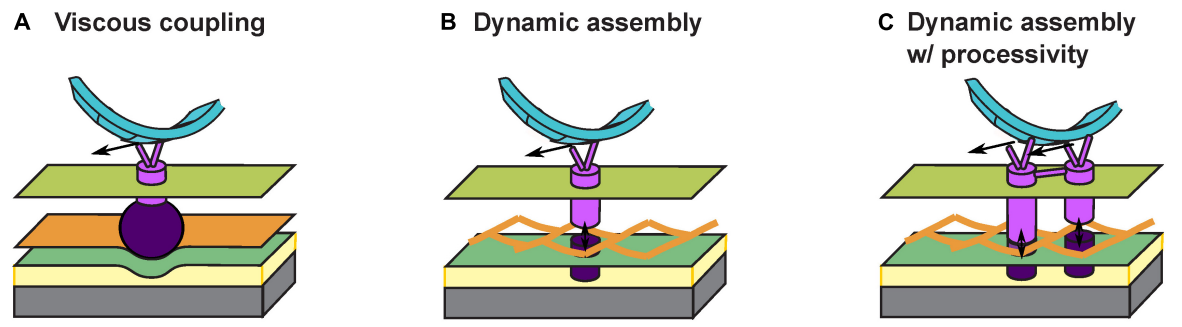


FIGURE 2 | Models for interaction between the gliding machinery and substrate. **(A)** Viscous coupling between the gliding machinery and substrate. Large motor-associated proteins (dark purple) may deform the PG and the resulting bump exerts a viscous force on the substrate as the proton channel motor (bright purple) moves. **(B)** Dynamic assembly of the force-generating gliding machinery. An inner subcomplex (bright purple) that includes the motor and an outer subcomplex (dark purple) that binds with the substrate bind with each other dynamically across the PG mesh to allow force generation without tearing the PG. **(C)** Dynamic assembly of coupled gliding machineries confers processivity. The dynamic binding between the inner (bright purple) and outer (dark purple) subcomplexes is similar to **(B)**. Coordinated activities of coupled motors keep the motors on the helical track and/or at the "focal adhesion" sites for an extended period of time.

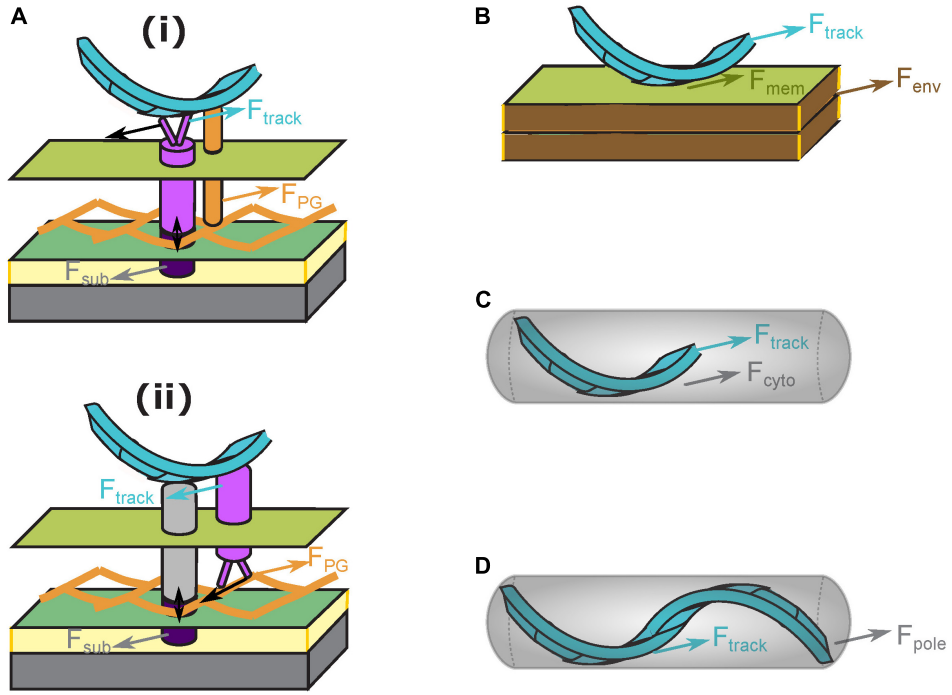


FIGURE 3 | Hypotheses about transmission of motor force to the cell body. **(A)** Mechanical tethering between the intracellular track and cell envelop. The mechanical tethering can be mediated either through non-motor components of the gliding machinery **(i)** or directly through the motor components **(ii)**. In case **(ii)**, the "feet" of the motor are on the periplasmic side because the motor must travel with respect to the PG to stay static to the substrate. Bright purple: proton channel motor. Dark purple: outer subcomplex. Orange cylinder in case **(i)** mechanical tethering between the intracellular track and PG. Gray cylinder in case **(ii)** molecules connecting the intracellular track to the outer subcomplex (through dynamic binding/unbinding to avoid tearing the PG). Black arrows illustrate the moving direction of the motor. **(B)** Interaction between the intracellular track and cell membrane/envelop. **(C)** Viscous drag between the intracellular track and cytoplasm. **(D)** Direct push on the cell pole by the intracellular track.

motors in the inner membrane can exert opposite forces on the cell and the substrate. The helical track along which the motors travel is a candidate for such a mechanical structure (**Figure 1**). But how exactly is the force transmitted? Generally speaking, the intracellular track may transmit force to the cell body in four ways (**Figure 3**): (i) through mechanical tethering with the cell envelop, (ii) through interaction with the membrane and cell envelop, (iii) through viscous drag against the cytoplasm, and (iv) by direct pushing against the cell pole. Note that the four mechanisms are not exclusive to each other, and may co-contribute to cell propulsion.

The first mechanism, tethering between the intracellular track and cell envelop, may effectively transmit the force from the former to the latter, thereby pushing the cell forward. Note that the intracellular track can tether to the cell envelop either indirectly through non-motor components of the gliding machinery, such as through the Rod PG synthesis complex associated with MreB (Garner, 2021; Rohs and Bernhardt, 2021; **Figure 3A(i)**) or directly through AglQ and AglS, if these proteins interact with PG mechanically (**Figure 3A(ii)**). In the former case, the motors push the intracellular track toward the leading pole, and the track in turn, pushes the PG forward. Whereas in the latter case, the intracellular track acts as a mechanical extension of the substrate and is pushed by the motors toward the trailing pole. These two mechanisms predict opposite directions of motion in the track relative to the cell, and can be tested by future experiments. In both cases, PG strands, if oriented helically, can guide the helical motion of the motors without MreB forming a continuous cytoplasmic track, as a recent report speculates (Faure et al., 2016); in the latter case, the PG even provides the direct track for the motors to move on.

The second mechanism, interaction between the intracellular track and cell membrane/envelop (**Figure 3B**), can effectively transmit the force from the intracellular track to the cell body, only if the interaction is sufficiently strong and the cell membrane exhibits glass-like properties in terms of its mechanical resistance against the motion of the track. The latter is possible if the membrane is crowded (Munguira et al., 2016). If the cell membrane behaves like fluid, as in *in vitro* membrane systems like the giant unilamellar vesicle (GUV), or the track interacts with the membrane too weakly, the mechanism would be insufficient for transmitting the motor force onto the cell. Verification of this hypothesis requires data on the physical properties and molecular components of the membranes in *M. xanthus*.

The third mechanism, viscous drag between the intracellular track and cytoplasm (**Figure 3C**), is unlikely to transmit significant force, because such a viscous drag is typically orders

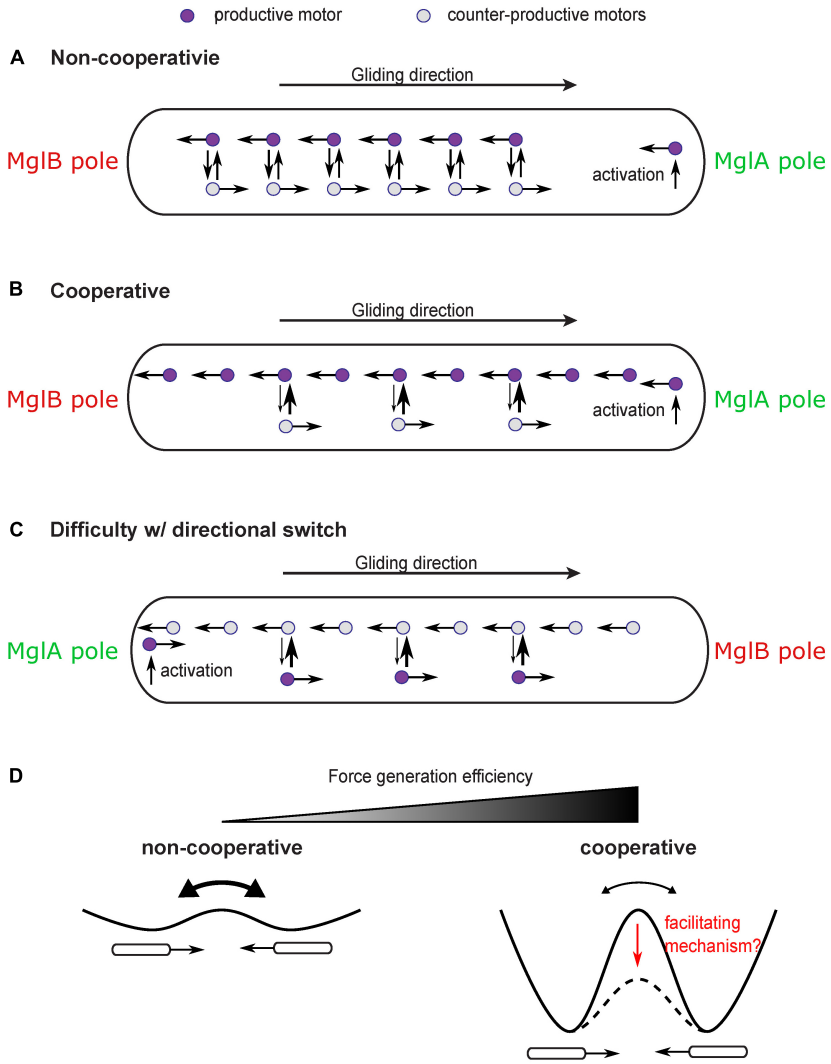


FIGURE 4 | Cooperativity of gliding motors and issue with directional switch. **(A)** Constant reversal of gliding motors diminishes efficiency and stability of force generation. A large number of motors would travel in the counter-productive direction and produce forces in the counter-productive direction. **(B)** A cooperativity mechanism makes motors more likely to convert to the direction in which more motors are traveling, which enhances the bias toward productive motors and significantly increases the efficiency and stability of force generation. **(C)** The cooperativity mechanism may inhibit the reversal of the moving direction of the cell after the switch of cell polarity. The motors which are activated at the new MglA pole and travel in the new productive direction may be forced by the cooperativity mechanism to join the majority that remains traveling in the old productive direction. **(D)** Cooperativity among motors increases efficiency and stability of force generation at the price of inhibiting reversals. Reversals can be regarded as transitions between two symmetric states with equal energy. Cooperativity increases the energy barrier between the two states. A facilitating mechanism may be needed to reduce the energy barrier and promote state transition despite cooperativity.

of magnitude lower than the force required to move a cell on a substrate surface ($\sim 10^2$ pN (Wolgemuth, 2005; Sabass et al., 2017; Tchoufag et al., 2019). For example, a 10-μm microtubule traveling at ∼1 μm/s (observed speed of fluorescent MreB particles in *M. xanthus* (Fu et al., 2018) in the cytoplasm would encounter a sub-piconewton (pN) viscous drag force.

The fourth mechanism, the intracellular track directly pushing on the cell pole (**Figure 3D**), can only transmit the force effectively if the track is a continuous and relatively rigid structure, like the rotor ring in the bacterial flagellar motor. However, such a track may not exist, as MreB, the most likely constituent of the track, only forms patchy filaments (Fu et al., 2018), which probably lack the continuity and mechanical rigidity to generate a push on the cell pole.

How Does the Gliding Machinery Switch Its Direction?

M. xanthus is known for periodic reversal of its direction of gliding, which is crucial for its "social" behaviors (Wu et al., 2007; Berleman and Kirby, 2009; Patra et al., 2016). Many previous models have investigated how intercellular coordination of gliding and reversals mediates formation of complex patterns and structures in the *M. xanthus* populations, e.g., rippling waves

and fruiting bodies (Igoshin et al., 2001; Borner et al., 2002; Alber et al., 2004; Igoshin et al., 2004; Borner et al., 2006; Sliusarenko et al., 2007; Wu et al., 2009; Holmes et al., 2010; Harvey et al., 2012; Zhang et al., 2012a; Janulevicius et al., 2015; Patra et al., 2016). At the single-cell level, reversals are achieved by switching the cell's polarity, which in turn, is determined by a group of polarity-setting molecules localized at the cell poles. Particularly, MglA is concentrated at the leading pole, and MglB, its antagonist, at the trailing pole (Leonardy et al., 2010; Zhang et al., 2010). MglA and MglB periodically switch between the two poles, causing cell polarity to switch (Leonardy et al., 2010; Zhang et al., 2010, 2012b; Keilberg and Sogaard-Andersen, 2014; Rashkov et al., 2014; Guzzo et al., 2018; Carreira et al., 2020). Moreover, the frequency of polarity switching is modulated by the Frz chemosensory pathway (Guzzo et al., 2018). This is reminiscent of the clockwise-counterclockwise switches in the bacterial flagellar motor, which is also controlled by the chemosensory pathway. We do not intend to discuss here the chemosensory pathway or polarity switching itself. Rather, we would like to raise the question of how the gliding machineries change the direction of force in response to the switched cell polarity.

This question may seem trivial at first sight, because MglA directly binds the gliding motor and likely mediates its activation (Nan et al., 2015; Treuner-Lange et al., 2015). One may envision that the gliding motor is activated at the MglA-concentrated pole and deactivated at the MglB-concentrated pole; traveling from the MglA pole to the MglB pole would generate a propulsion on the cell in the direction of the MglA pole. Hence, as the polar localization of MglA and MglB switches, the direction of propulsion also switches. This straightforward model, however, is challenged by the observation of constant reversals of single gliding motors as they travel along the intracellular track (**Figure 4A**; Nan et al., 2013, 2015). Due to the constant reversals, the gliding machinery cannot generate force consistently in one direction. Even though polarized activation and deactivation can bias the motion of gliding machineries in the productive direction (i.e., bound for the MglB pole), a large fraction of gliding machineries still generate counter-productive forces on the cell, with a 2∼20% estimated relative difference between motors in the two directions (the relative difference is roughly the ratio between the average time for motor reversal, ∼1 s (Nan et al., 2013, 2015) and the time for a motor to traverse the cell length without reversing, 5 s∼1 min (Sun et al., 2011; Nan et al., 2013, 2015). This makes the motility mechanism highly inefficient. With significant noise, this could also incur random switches of the cell's direction of motion, which further reduces the efficiency of directional gliding.

In order to increase efficiency and stability of the gliding mechanism, a cooperativity mechanism is required to magnify the bias of motors in the productive direction (**Figure 4B**). For example, those gliding machineries traveling in the same direction as the cell may have a disadvantage in engaging with the substrate because they move at a higher speed relative to the substrate (relative speed to the cell + speed of cell). Therefore, the gliding machinery is more likely to stay in the productive direction. Cooperativity can also be boosted by intermolecular interactions among aggregated motors. In any case, the cooperativity can bring an asymmetry between motors traveling in opposite directions, which can magnify the directional bias induced by the established cell polarity and increase the fraction of productive gliding machineries over the counter-productive ones.

While significantly improving the efficiency and stability of force generation, such cooperativity has a down side: it may inhibit reversal of the cell's moving direction even after cell polarity switches (**Figure 4C**). This is because the gliding machineries which are activated at the new MglA pole and travel in the new productive direction can be forced by the cooperativity mechanism to rejoin the majority that are still traveling in the old productive direction. The rate at which the new MglA pole generates productive motors is physically limited by the active motion and diffusion of motors. Therefore, it may not be strong enough to overcome the cooperativity mechanism and tip the balance in the new direction. Similar conflict between cooperativity and sensitivity of the directional switch was studied in the bacterial flagellar motor (Duke et al., 2001; Bai et al., 2010). Reversing the direction of rotation entails a switch of the C-ring—the rotor part of the flagellar motor (Chang et al., 2020). The switch requires cooperative conformational changes in all the rotor subunits that constitute the C-ring. Strong cooperativity among these subunits can suppress random switch of their conformation, promote structural homogeneity of the C-ring, and hence gauge the motor forces toward one direction. However, the cooperativity also imposes a challenge in switching the entire ring from one conformation to another in response to chemotactic signals (Duke et al., 2001; Bai et al., 2010). To circumvent this problem, Bai et al. (2010) proposed a mechanism: as a stator exerts force on a rotor subunit, it also promotes conformational changes in the latter and hence facilitate the switch of the rotor ring. It remains to be investigated if the force generated by the gliding machinery of *M. xanthus* plays a similar role in facilitating directional switch and overcoming the efficiency-boosting cooperativity (**Figure 4D**).

How Does the Gliding Machinery Respond to Mechanical Load?

The observation that aggregations of gliding proteins at the "focal adhesion" sites intensify on harder substrates (Nan et al., 2010, 2013) implies that external mechanical cues can influence assembly and/or activity of the gliding machinery. This phenomenon is reminiscent of the observation that external load on the bacterial flagellar motor boosts the recruitment of stators into the motor complex (Lele et al., 2013; Tipping et al., 2013). The underlying molecular mechanism for the mechanosensing in the bacterial flagellar motor is known: the stators are dynamically recruited to and released from the motor and a "catch bond" mechanism retains the stators in the motor for longer time in response to a higher load (Nord et al., 2017; Wadhwa et al., 2019). Sharing homologous energy-harvesting proteins with the bacterial flagellar motor, the *M. xanthus* gliding machinery may exploit a similar force-sensitive mechanism that strengthens the engagement with the substrate upon higher load.

Interestingly, substrate stiffness also affects the reversal frequency of the *M. xanthus* cell (Zhou and Nan, 2017). It is possible that the gliding machinery further transduces the external mechanical cues into a signal that controls polarity switching. Currently, the most promising candidate that mediates the transduction from mechanical cues to regulatory signals for polarity switching is probably MglA, as it is not only a key molecule of the polarity-switching mechanism but also an essential component of the gliding machinery (Nan et al., 2015; Treuner-Lange et al., 2015). As the gliding machineries travel from the leading pole to the trailing pole, they carry the MglA along. The directed transport of MglA toward the trailing pole could affect the dynamics of polarity switching. Hence, the external mechanical cues could affect the reversal frequency through modulating the activity of the gliding machineries. Future investigations are needed to test this hypothesis.

CONCLUSION

The *M. xanthus* gliding machinery exploits similar energy-harvesting units as the rotary flagellar motor, yet operates on a helical intracellular track. This is yet another testimony on the versatility of flagellar motors in biological systems. In this article, we brought up a few unresolved questions on the mechanism of *M. xanthus* gliding. As rotary motors are ubiquitous in nature and helical-tracking motors are also found in a number of bacteria (Nan et al., 2014), we predict that the answers to these questions will make wide impacts, much beyond the gliding motility in *M. xanthus*.

DATA AVAILABILITY STATEMENT

The original contributions presented in the study are included in the article/supplementary material, further inquiries can be directed to the corresponding authors.

AUTHOR CONTRIBUTIONS

JC and BN conceptualized and designed the work, curated and interpreted the relevant literature, and drafted the article. Both authors contributed to the article and approved the submitted version.

FUNDING

National Institutes of Health R35GM138370 to JC and R01GM129000 to BN.

REFERENCES

Alber, M. S., Kiskowski, M. A., and Jiang, Y. (2004). Two-stage aggregate formation via streams in myxobacteria. *Phys. Rev. Lett.* 93, 068102. doi: 10.1103/PhysRevLett.93.068102

Bai, F., Branch, R. W., Nicolau, D. V. Jr., Pilizota, T., Steel, B. C., Maini, P. K., et al. (2010). Conformational spread as a mechanism for cooperativity in the bacterial flagellar switch. *Science* 327, 685–689. doi: 10.1126/science.1182105

Balagam, R., Litwin, D. B., Czerwinski, F., Sun, M., Kaplan, H. B., Shaevitz, J. W., et al. (2014). *Myxococcus xanthus* gliding motors are elastically coupled to the substrate as predicted by the focal adhesion model of gliding motility. *PLoS Comput. Biol.* 10:e1003619. doi: 10.1371/journal.pcbi.1003619

Berleman, J. E., and Kirby, J. R. (2009). Deciphering the hunting strategy of a bacterial wolfpack. *FEMS Microbiol. Rev.* 33, 942–957. doi: 10.1111/j.1574-6976.2009.00185.x

Borner, U., Deutsch, A., and Bar, M. (2006). . A generalized discrete model linking rippling pattern formation and individual cell reversal statistics in colonies of myxobacteria. *Phys. Biol.* 3, 138–146. doi: 10.1088/1478-3975/3/2/006

Borner, U., Deutsch, A., Reichenbach, H., and Bar, M. (2002). Rippling patterns in aggregates of myxobacteria arise from cell-cell collisions. *Phys. Rev. Lett.* 89:078101. doi: 10.1103/PhysRevLett.89.078101

Carreira, L. A. M., Tostevin, F., Gerland, U., and Sogaard-Andersen, L. (2020). Protein-protein interaction network controlling establishment and maintenance of switchable cell polarity. *PLoS Genet.* 16:e1008877. doi: 10.1371/journal.pgen.1008877

Chang, Y., Zhang, K., Carroll, B. L., Zhao, X., Charon, N. W., Norris, S. J., et al. (2020). Molecular mechanism for rotational switching of the bacterial flagellar motor. *Nat. Struct. Mol. Biol.* 27, 1041–1047. doi: 10.1038/s41594-020-0497-2

Chang, Y. W., Rettberg, L. A., Treuner-Lange, A., Iwasa, J., Sogaard-Andersen, L., and Jensen, G. J. (2016). Architecture of the type IVa pilus machine. *Science.* 351:aad2001.

Demchick, P., and Koch, A. L. (1996). The permeability of the wall fabric of *Escherichia coli* and *Bacillus subtilis*. *J. Bacteriol.* 178, 768–773. doi: 10.1128/jb.178.3.768-773.1996

Duke, T. A., Le Novere, N., and Bray, D. (2001). Conformational spread in a ring of proteins: a stochastic approach to allostery. *J. Mol. Biol.* 308, 541–553. doi: 10.1006/jmbi.2001.4610

Faure, L. M., Fiche, J. B., Espinosa, L., Ducret, A., Anantharaman, V., Luciano, J., et al. (2016). The mechanism of force transmission at bacterial focal adhesion complexes. *Nature* 539:530. doi: 10.1038/nature20121

Fu, G., Bandaria, J. N., Le Gall, A. V., Fan, X., Yildiz, A., Mignot, T., et al. (2018). MotAB-like machinery drives the movement of MreB filaments during bacterial gliding motility. *Proc. Natl. Acad. Sci. U.S.A.* 115, 2484–2489. doi: 10.1073/pnas.1716441115

Garner, E. C. (2021). Toward a mechanistic understanding of bacterial rod shape formation and regulation. *Annu. Rev. Cell Dev. Biol.* 37, 1–21. doi: 10.1146/annurev-cellbio-010521-010834

Gennerich, A., and Vale, R. D. (2009). Walking the walk: how kinesin and dynein coordinate their steps. *Curr. Opin. Cell Biol.* 21, 59–67. doi: 10.1016/j.ceb.2008.12.002

Guzzo, M., Murray, S. M., Martineau, E., Lhospice, S., Baronian, G., My, L., et al. (2018). A gated relaxation oscillator mediated by FrzX controls morphogenetic movements in *Myxococcus xanthus*. *Nat. Microbiol.* 3, 948–959. doi: 10.1038/s41564-018-0203-x

Harvey, C. W., Du, H., Xu, Z., Kaiser, D., Aranson, I., and Alber, M. (2012). Interconnected cavernous structure of bacterial fruiting bodies. *PLoS Comput. Biol.* 8:e1002850. doi: 10.1371/journal.pcbi.1002850

Holmes, A. B., Kalvala, S., and Whitworth, D. E. (2010). Spatial simulations of myxobacterial development. *PLoS Comput. Biol.* 6:e1000686. doi: 10.1371/journal.pcbi.1000686

Hughes, R. C., Thurman, P. F., and Stokes, E. (1975). Estimates of the porosity of *Bacillus licheniformis* and *Bacillus subtilis* cell walls. *Z. Immunitatsforsch. Exp. Klin. Immunol.* 149, 126–135.

Igoshin, O. A., Mogilner, A., Welch, R. D., Kaiser, D., and Oster, G. (2001). Pattern formation and traveling waves in myxobacteria: theory and modeling. *Proc. Natl. Acad. Sci. U.S.A.* 98, 14913–14918. doi: 10.1073/pnas.221579598

Igoshin, O. A., Welch, R., Kaiser, D., and Oster, G. (2004). Waves and aggregation patterns in myxobacteria. *Proc. Natl. Acad. Sci. U.S.A.* 101, 4256–4261. doi: 10.1073/pnas.0400704101

Janulevicius, A., van Loosdrecht, M., and Picioreanu, C. (2015). Short-range guiding can result in the formation of circular aggregates in myxobacteria populations. *PLoS Comput. Biol.* 11:e1004213. doi: 10.1371/journal.pcbi.1004213

Keilberg, D., and Sogaard-Andersen, L. (2014). Regulation of bacterial cell polarity by small GTPases. *Biochemistry* 53, 1899–1907. doi: 10.1021/bi500141f

Lele, P. P., Hosu, B. G., and Berg, H. C. (2013). Dynamics of mechanosensing in the bacterial flagellar motor. *Proc. Natl. Acad. Sci. U.S.A.* 110, 11839–11844. doi: 10.1073/pnas.1305885110

Leonardy, S., Miertzschke, M., Bulyha, I., Sperling, E., Wittinghofer, A., and Sogaard-Andersen, L. (2010). Regulation of dynamic polarity switching in bacteria by a Ras-like G-protein and its cognate GAP. *EMBO J.* 29, 2276–2289. doi: 10.1038/emboj.2010.114

Mauriello, E. M., Mouhamar, F., Nan, B., Ducret, A., Dai, D., Zusman, D. R., et al. (2010). Bacterial motility complexes require the actin-like protein, MreB and the Ras homologue, MglA. *EMBO J.* 29, 315–326. doi: 10.1038/emboj.2009.356

Mignot, T., Shaevitz, J. W., Hartzell, P. L., and Zusman, D. R. (2007). Evidence that focal adhesion complexes power bacterial gliding motility. *Science* 315, 853–856. doi: 10.1126/science.1137223

Munguira, I., Casuso, I., Takahashi, H., Rico, F., Miyagi, A., Chami, M., et al. (2016). Glasslike membrane protein diffusion in a crowded membrane. *ACS Nano* 10, 2584–2590. doi: 10.1021/acsnano.5b07595

Nan, B. (2017). Bacterial gliding motility: rolling out a consensus model. *Curr. Biol.* 27, R154–R156. doi: 10.1016/j.cub.2016.12.035

Nan, B., Chen, J., Neu, J. C., Berry, R. M., Oster, G., and Zusman, D. R. (2011). Myxobacteria gliding motility requires cytoskeleton rotation powered by proton motive force. *Proc. Natl. Acad. Sci. U.S.A.* 108, 2498–2503. doi: 10.1073/pnas.1018556108

Nan, B., Mauriello, E. M., Sun, I. H., Wong, A., and Zusman, D. R. (2010). A multi-protein complex from *Myxococcus xanthus* required for bacterial gliding motility. *Mol. Microbiol.* 76, 1539–1554. doi: 10.1111/j.1365-2958.2010.07184.x

Nan, B., McBride, M. J., Chen, J., Zusman, D. R., and Oster, G. (2014). Bacteria that glide with helical tracks. *Curr. Biol.* 24, R169–R173. doi: 10.1016/j.cub.2013.12.034

Nan, B., and Zusman, D. R. (2011). Uncovering the mystery of gliding motility in the myxobacteria. *Annu. Rev. Genet.* 45, 21–39. doi: 10.1146/annurev-genet-110410-132547

Nan, B. Y., Bandaria, J. N., Guo, K. Y., Fan, X., Moghtaderi, A., Yildiz, A., et al. (2015). The polarity of myxobacterial gliding is regulated by direct interactions between the gliding motors and the Ras homolog MglA. *Proc. Natl. Acad. Sci. U.S.A.* 112, E186–E193. doi: 10.1073/pnas.1421073112

Nan, B. Y., Bandaria, J. N., Moghtaderi, A., Sun, I. H., Yildiz, A., and Zusman, D. R. (2013). Flagella stator homologs function as motors for myxobacterial gliding motility by moving in helical trajectories. *Proc. Natl. Acad. Sci. U.S.A.* 110, E1508–E1513. doi: 10.1073/pnas.1219982110

Nord, A. L., Gachon, E., Perez-Carrasco, R., Nirody, J. A., Barducci, A., Berry, R. M., et al. (2017). Catch bond drives stator mechanosensitivity in the bacterial flagellar motor. *Proc. Natl. Acad. Sci. U.S.A.* 114, 12952–12957. doi: 10.1073/pnas.1716002114

Patra, P., Kissoon, K., Cornejo, I., Kaplan, H. B., and Igoshin, O. A. (2016). Colony expansion of socially motile *Myxococcus xanthus* cells is driven by growth, motility, and exopolysaccharide production. *PLoS Comput. Biol.* 12:e1005010. doi: 10.1371/journal.pcbi.1005010

Rashkov, P., Schmitt, B. A., Keilberg, D., Beck, K., Sogaard-Andersen, L., and Dahlke, S. (2014). A model for spatio-temporal dynamics in a regulatory network for cell polarity. *Math. Biosci.* 258, 189–200. doi: 10.1016/j.mbs.2014.10.005

Rohs, P. D. A., and Bernhardt, T. G. (2021). Growth and division of the peptidoglycan matrix. *Annu. Rev. Microbiol.* 75, 315–336. doi: 10.1146/annurev-micro-020518-120056

Sabass, B., Koch, M. D., Liu, G. N., Stone, H. A., and Shaevitz, J. W. (2017). Force generation by groups of migrating bacteria. *Proc. Natl. Acad. Sci. U.S.A.* 114, 7266–7271. doi: 10.1073/pnas.1621469114

Sliusarenko, O., Zusman, D. R., and Oster, G. (2007). Aggregation during fruiting body formation in *Myxococcus xanthus* is driven by reducing cell movement. *J. Bacteriol.* 189, 611–619. doi: 10.1128/JB.01206-06

Sun, M., Wartel, M., Cascales, E., Shaevitz, J. W., and Mignot, T. (2011). Motor-driven intracellular transport powers bacterial gliding motility. *Proc. Natl. Acad. Sci. U.S.A.* 108, 7559–7564. doi: 10.1073/pnas.1101101108

Tchoufag, J., Ghosh, P., Pogue, C. B., Nan, B., and Mandadapu, K. K. (2019). Mechanisms for bacterial gliding motility on soft substrates. *Proc. Natl. Acad. Sci. U.S.A.* 116, 25087–25096. doi: 10.1073/pnas.1914678116

Tipping, M. J., Delalez, N. J., Lim, R., Berry, R. M., and Armitage, J. P. (2013). Load-dependent assembly of the bacterial flagellar motor. *mBio* 4, e00551–13.

Treuner-Lange, A., Macia, E., Guzzo, M., Hot, E., Faure, L. M., Jakobczak, B., et al. (2015). The small G-protein MglA connects to the MreB actin cytoskeleton at bacterial focal adhesions. *J. Cell Biol.* 210, 243–256. doi: 10.1083/jcb.201412047

Vollmer, W., Blanot, D., and de Pedro, M. A. (2008). Peptidoglycan structure and architecture. *FEMS Microbiol Rev.* 32, 149–167. doi: 10.1111/j.1574-6976.2007.00094.x

Wadhwa, N., Phillips, R., and Berg, H. C. (2019). Torque-dependent remodeling of the bacterial flagellar motor. *Proc. Natl. Acad. Sci. U.S.A.* 116, 11764–11769. doi: 10.1073/pnas.1904577116

Wolgemuth, C., Hoiczyk, E., Kaiser, D., and Oster, G. (2002). How myxobacteria glide. *Curr. Biol.* 12, 369–377. doi: 10.1016/s0960-9822(02)00716-9

Wolgemuth, C. W. (2005). Force and flexibility of flailing myxobacteria. *Biophys. J.* 89, 945–950. doi: 10.1529/biophysj.105.062513

Wu, S. S., and Kaiser, D. (1995). Genetic and functional evidence that type IV pili are required for social gliding motility in *Myxococcus xanthus*. *Mol. Microbiol.* 18, 547–558. doi: 10.1111/j.1365-2958.1995.mmi_18030547.x

Wu, Y., Jiang, Y., Kaiser, D., and Alber, M. (2007). Social interactions in myxobacterial swarming. *PLoS Comput. Biol.* 3:e253. doi: 10.1371/journal.pcbi.0030253

Wu, Y., Kaiser, A. D., Jiang, Y., and Alber, M. S. (2009). Periodic reversal of direction allows Myxobacteria to swarm. *Proc. Natl. Acad. Sci. U.S.A.* 106, 1222–1227. doi: 10.1073/pnas.0811662106

Yildiz, A., Tomishige, M., Vale, R. D., and Selvin, P. R. (2004). Kinesin walks hand-over-hand. *Science* 303, 676–678. doi: 10.1126/science.1093753

Zhang, H., Vaksman, Z., Litwin, D. B., Shi, P., Kaplan, H. B., and Igoshin, O. A. (2012a). The mechanistic basis of *Myxococcus xanthus* rippling behavior and its physiological role during predation. *PLoS Comput. Biol.* 8:e1002715. doi: 10.1371/journal.pcbi.1002715

Zhang, Y., Franco, M., Ducret, A., and Mignot, T. (2010). A bacterial Ras-like small GTP-binding protein and its cognate GAP establish a dynamic spatial polarity axis to control directed motility. *PLoS Biol.* 8:e1000430. doi: 10.1371/journal.pbio.1000430

Zhang, Y., Guzzo, M., Ducret, A., Li, Y. Z., and Mignot, T. (2012b). A dynamic response regulator protein modulates G-protein-dependent polarity in the bacterium *Myxococcus xanthus*. *PLoS Genet.* 8:e1002872. doi: 10.1371/journal.pgen.1002872

Zhou, T., and Nan, B. (2017). Exopolysaccharides promote *Myxococcus xanthus* social motility by inhibiting cellular reversals. *Mol. Microbiol.* 103, 729–743. doi: 10.1111/mmi.13585

Conflict of Interest: The authors declare that the research was conducted in the absence of any commercial or financial relationships that could be construed as a potential conflict of interest.

Publisher's Note: All claims expressed in this article are solely those of the authors and do not necessarily represent those of their affiliated organizations, or those of the publisher, the editors and the reviewers. Any product that may be evaluated in this article, or claim that may be made by its manufacturer, is not guaranteed or endorsed by the publisher.

Copyright © 2022 Chen and Nan. This is an open-access article distributed under the terms of the Creative Commons Attribution License (CC BY). The use, distribution or reproduction in other forums is permitted, provided the original author(s) and the copyright owner(s) are credited and that the original publication in this journal is cited, in accordance with accepted academic practice. No use, distribution or reproduction is permitted which does not comply with these terms.

frontiers | Frontiers in Microbiology

REVIEW
published: 10 May 2022
doi: 10.3389/fmicb.2022.845563

Design Principles of the Rotary Type 9 Secretion System

Abhishek Trivedi[1,2,3], *Jitendrapuri Gosai*[1,2,3], *Daisuke Nakane*[4] and *Abhishek Shrivastava*[1,2,3]*

[1] School of Life Sciences, Arizona State University, Tempe, AZ, United States, [2] Biodesign Center for Fundamental and Applied Microbiomics, Arizona State University, Tempe, AZ, United States, [3] Center for Biological Physics, Arizona State University, Tempe, AZ, United States, [4] Department of Engineering Science, The University of Electro-Communications, Tokyo, Japan

The F_O ATP synthase, the bacterial flagellar motor, and the bacterial type 9 secretion system (T9SS) are the three known proton motive force driven biological rotary motors. In this review, we summarize the current information on the nuts and bolts of T9SS. Torque generation by T9SS, its role in gliding motility of bacteria, and the mechanism *via* which a T9SS-driven swarm shapes the microbiota are discussed. The knowledge gaps in our current understanding of the T9SS machinery are outlined.

Keywords: bacterial motility, T9SS, gliding motility, bacterial swarming, Flavobacteria

OPEN ACCESS

Edited by:
Beiyan Nan,
Texas A&M University, United States

Reviewed by:
Mark J. McBride,
University of Wisconsin–Milwaukee, United States
Ben Berks,
University of Oxford, United Kingdom

***Correspondence:**
Abhishek Shrivastava
ashrivastava@asu.edu

Specialty section:
This article was submitted to Microbial Physiology and Metabolism, a section of the journal Frontiers in Microbiology

Received: *29 December 2021*
Accepted: *17 January 2022*
Published: *10 May 2022*

Citation:
Trivedi A, Gosai J, Nakane D and Shrivastava A (2022) Design Principles of the Rotary Type 9 Secretion System. Front. Microbiol. 13:845563. doi: 10.3389/fmicb.2022.845563

THE DIVERSITY OF BACTERIAL PROTEIN SECRETION SYSTEMS

The hydrophobic lipid bilayer of the bacterial cell membrane stops proteins from diffusing outside the cell. However, physiological processes such as the degradation and uptake of complex extracellular nutrition sources, adhesion to biotic and abiotic surfaces, colonization, motility, virulence, and interbacterial antagonism require transport of proteins across membranes. Protein secretion systems serve this purpose and form a pore that provides a gateway to a select group of proteins. Thus far, eleven bacterial protein secretion systems have been discovered (**Figure 1**). Additionally, the Sec and Tat transporters (Kudva et al., 2013), Chaperon-usher pathway (Waksman and Hultgren, 2009), the YidC insertase (Hennon et al., 2015), Sortases (Spirig et al., 2011), and a TonB-dependent machinery (Gómez-Santos et al., 2019) are also involved in bacterial protein export. Majority of this review is focused on the bacterial Type 9 Secretion System (T9SS), its mechanism of rotation, gliding motility, and collective behavior. However, without an appreciation of the diversity of bacterial secretion machineries, the beauty of T9SS can be lost on the reader. Hence, we initiate this review with a brief and up-to date overview of bacterial protein secretion machineries.

Type 1 to Type 11 bacterial secretion systems are known to facilitate extracellular transport of proteins. Some bacterial secretion systems work in conjunction with either the Sec or the Tat transporters, whereas others work independently. The bacterial Sec protein export pathway allows transport of unfolded proteins through the cytoplasmic membrane (Papanikou et al., 2007; Kusters and Driessen, 2011; Denks et al., 2014) while the Twin Arginine translocation (Tat) system

allows transport of folded proteins across the cytoplasmic membrane (Palmer and Berks, 2012). Interestingly, some protein secretion systems are associated with machineries that power bacterial motility. Examples include the Type 2 Secretion System (T2SS) associated type IV pilus (Craig et al., 2019), the Type 3 Secretion System (T3SS) associated with the flagellar motor (Abrusci et al., 2013), and the T9SS that is integral to gliding motility of Bacteroidetes (Sato et al., 2010; Shrivastava et al., 2013; Zhu and McBride, 2014; Kita et al., 2016; Lauber et al., 2018; Shrivastava and Berg, 2020; Hennell James et al., 2021).

The Type 1 Secretion System (T1SS) is comprised of an ABC transporter-like protein complex spanning the cytoplasmic membrane. It is coupled with a viral fusion protein and a β-barrel channel that spans the outer membrane. T1SS enables secretion of unfolded protein substrates from the cytoplasm to the extracellular milieu (Spitz et al., 2019). The T2SS secretes proteins that are already exported to the periplasm *via* Sec or Tat pathway. The multiprotein piston-like pseudopilus component of the T2SS pushes its folded protein substrates out of the outer membrane secretin in a process powered by ATP hydrolysis (Korotkov and Sandkvist, 2019; Naskar et al., 2021). The T3SS forms an injectisome and transports proteins from the cytosol either to the extracellular milieu or across the plasma membrane of a eukaryotic host cell (Portaliou et al., 2016). The core of both the bacterial flagellar apparatus and the injectisome have a T3SS. While there is some debate on the evolution of injectisome and the flagellum, it has been proposed that the flagellum is the ancestor of the injectisome-T3SS complex (Diepold and Armitage, 2015). The Type 4 Secretion System (T4SS) is found in both eubacteria and archaea. It exports both proteins and DNA from the cytosol of T4SS containing bacteria to either a prokaryotic or a eukaryotic host cell (Li et al., 2019). Additionally, a class of T4SS is also employed by bacteria to take up extracellular DNA (Hofreuter et al., 2001; Li et al., 2019). The Type 5 Secretion System (T5SS), also known as autotransporter, contains a single protein that spans the Gram negative bacterial outer membrane. The translocator domain of the T5SS protein is a β-barrel. In most cases, its secretory substrate (passenger domain) is a polypeptide chain contiguous to the translocator domain (Fan et al., 2016; Meuskens et al., 2019). The Type 6 Secretion System (T6SS) is formed by the association of homologs of T4SS components and bacteriophage contractile tails. It is widely employed to inject effector proteins from the cytoplasm directly across other bacterial or eukaryotic host membranes (Cianfanelli et al., 2016; Coulthurst, 2019). The Type 7 Secretion System (T7SS) is found in Gram positive bacteria of the genus *Mycobacterium* and other members of the phylum Actinobacteria. Five paralogous *esx* loci are found in Mycobacteria and a recent high resolution Cryo-EM structure of an Esx-5 paralog revealed the formation of an inner membrane pore (Bunduc et al., 2020; Beckham et al., 2021; Rivera-Calzada et al., 2021). The Type 8 Secretion System (T8SS), widely known as the curli biogenesis pathway spans the outer membrane of Gram-negative bacteria. It secretes monomeric curli particles and enables their extracellular assembly and nucleation (Van Gerven et al., 2015; Bhoite et al., 2019). The Type 9 Secretion System (T9SS) spans both membranes and is found in the Gram negative Fibrobacteres-Chlorobi-Bacteroidetes superphylum. The substrates are delivered to the periplasm by Sec transport pathway and T9SS secretes them across the outer membrane. The T9SS contains a motor that drives secretion. This is one of the only three known biological rotary motors driven by a proton motive force (pmf) and is the focus of this review. The components of Type 10 Secretion System (T10SS) comprise of holins and peptidoglycan modifying enzymes. T10SS secretes hydrolytic enzymes and toxins (Palmer et al., 2021). Recently, the presence of a Type 11 Secretion System (T11SS) was proposed. It comprises of DUF560 family proteins and it transports periplasmic cargo across the outer membrane (Grossman et al., 2021).

A BRIEF HISTORY OF TYPE 9 SECRETION SYSTEM

Proteins that are now known to form the core of the bacterial type 9 secretion system (T9SS) were discovered around similar timelines in two model organisms *Flavobacterium johnsoniae* and *Porphyromonas gingivalis*. Transposon mutagenesis led to the discovery that *F. johnsoniae* GldK, GldL, GldM, and GldN are required for motility and chitin utilization (Braun et al., 2005). Similarly, it was identified that *P. gingivalis* PorT (Sato et al., 2005) and SprA/Sov are required for the transport of gingipain proteases (Saiki and Konishi, 2010). Later, it was shown that PorT of *F. johnsoniae* is also required for the secretion of chitinase and that GldK, GldL, GldM, and GldN form a multi-protein complex. Hence, it was inferred that these set of proteins form a secretion system that was initially named as the Por secretion system (PorSS) (Sato et al., 2010). It was later found that these proteins are prevalent in the Bacteroidetes phylum (McBride and Zhu, 2013; Shrivastava, 2013) and they are required for secretion of multiple classes of proteins. Because the components of the T9SS are not similar to those of other secretion systems, it was renamed as T9SS (Shrivastava et al., 2013). In recent years, the T9SS field has moved forward by leaps and bounds. We now know that T9SS forms a rotary machinery that enables gliding motility (Shrivastava et al., 2015) and we know the identity and structure of the ion channel that powers rotation (Shrivastava et al., 2015; Hennell James et al., 2021). Additionally, structures of several T9SS proteins have recently been resolved (Gorasia et al., 2016; Lauber et al., 2018; Leone et al., 2018; Trinh et al., 2020; Hennell James et al., 2021). T9SS secretes many enzymes, adhesins, and virulence factors. The signatures of T9SS secreted proteins have recently been characterized (Sato et al., 2013; de Diego et al., 2016; Kulkarni et al., 2017, 2019).

DIVERSITY OF SUBSTRATES SECRETED BY TYPE 9 SECRETION SYSTEM

Type 9 secretion system driven protein export occurs in conjunction with the Sec transport machinery. T9SS substrates

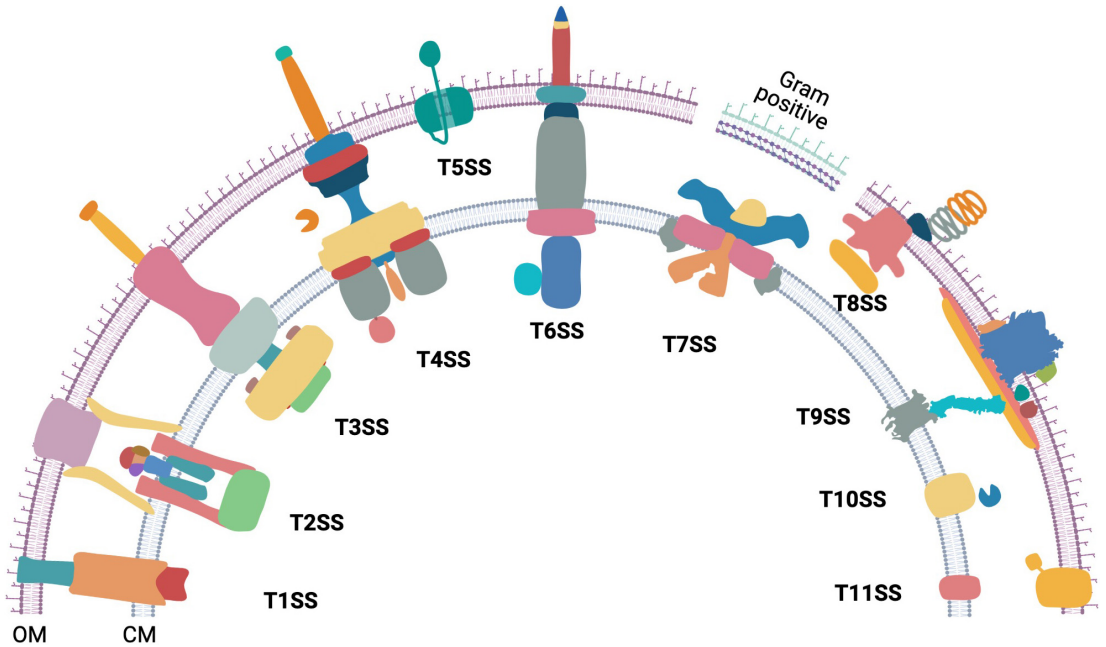


FIGURE 1 | The diversity of bacterial protein secretion systems. Graphical representation of the currently known bacterial protein secretion systems ranging from Type 1 to Type 11 and their localization in the outer (OM) and cytoplasmic membrane (CM). Except T7SS (Gram positive), all the above shown secretion systems are found in Gram negative bacteria. Occurrence of T7SS mediated protein secretion is found within some Gram positive members of the phylum Actinobacteria that have an outer lipid layer.

have a N-terminal Sec signal peptide and a C-terminal T9SS signal sequence (CTD). *Via* the Sec system, T9SS substrates reach the periplasm and the N-terminal Sec signal peptide is cleaved. T9SS CTD containing periplasmic proteins are exported either to the extracellular milieu or they attach to the outer membrane (OM) (Slakeski et al., 2011; Kulkarni et al., 2017, 2019). T9SS secreted extracellular proteins lose their CTD (Sato et al., 2013) and it is unclear whether CTD cleavage occurs during or after transport. The T9SS CTD is divided into two protein domain families namely TIGR04183 (Type A CTD) and TIGR04131 (Type B CTD). Type A CTD have seven β strands and lg-like folds which are thought to interact with the structural components of T9SS (de Diego et al., 2016; Lasica et al., 2016). Super folder GFP (sfGFP) fused with T9SS CTD and N-terminal Sec signal peptide is secreted by T9SS (Kulkarni et al., 2017, 2019) which further confirms that substrate recognition by T9SS only occurs due to the CTD. Additionally, a T9SS secreted chitinase possesses a CTD different from both Type A and Type B CTD (Kharade and McBride, 2014). We found that on InterPro (Blum et al., 2021) 179,000 different bacterial proteins are annotated to have TIGR04183 domain and 28,000 different proteins are annotated to have TIGR04131 domain. Many of T9SS encoding proteomes belong to bacteria of the phylum Bacteroidetes. The environmental microbe *F. johnsoniae* UW101 encodes 40 Type A and 12 Type B CTD containing proteins. These include the motility adhesins SprB (Nelson et al., 2008) and RemA (Shrivastava et al., 2012). Additionally, multiple enzymes including a chitinase are secreted by the T9SS of *F. johnsoniae* (Kharade and McBride, 2014, 2015). SprB is one of the largest known adhesin protein (669 kDa) and cells lacking SprB are severely deficient for gliding motility (Nelson et al., 2008). SprB moves spirally on the bacterial cell-surface (Nakane et al., 2013; Shrivastava et al., 2016) and is driven by pmf (Nakane et al., 2013). Adhesion of SprB to an external substratum enables screw-like motion of the rod-shaped *F. johnsoniae* (Shrivastava et al., 2016). The human oral microbe *P. gingivalis* W83 encodes 17 Type A CTD-containing proteins (including the virulent gingipain proteases) and one Type B CTD-containing protein. In contrast, another prominent human oral microbe *Capnocytophaga ochracea* ATCC 27872 encodes 2 Type A CTD containing proteins and 8 Type B CTD containing proteins.

Many of the shared T9SS components identified in *F. johnsoniae* and *P. gingivalis* were given different names (e.g., Gld vs. Por). These nuts and bolts of T9SS enable both gliding motility and protein secretion (**Figure 2A**). Below, we compile information on T9SS proteins from both model organisms *F. johnsoniae* and *P. gingivalis*.

THE NUTS AND BOLTS THAT FORM THE CORE OF ROTARY TYPE 9 SECRETION SYSTEM

GldK/PorK (Fjoh_1853/PGN_1676) is attached to the outer membrane *via* a lipid anchor and is localized in the periplasmic space (Shrivastava et al., 2013; Vincent et al., 2017). GldK/PorK of *P. gingivalis* forms a ring that has an outer diameter of 50 nm

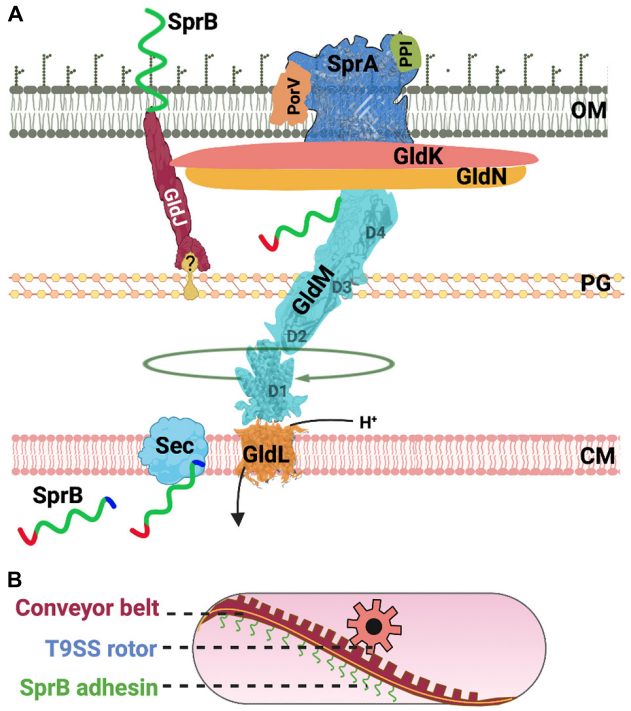


FIGURE 2 | Structure and function of the T9SS. **(A)** A cartoon of the nuts and bolts of the T9SS motor that drives protein secretion and gliding motility. T9SS substrates (SprB shown as an example) are transported to the periplasm *via* the Sec transport pathway. The CTD of T9SS substrates is cleaved during transport. A recent model suggests that the proton channel GldL powers the rotation of T9SS. **(B)** A cartoon of the molecular rack and pinion machinery that drives gliding motility. A model based on recent data suggests that the rotary T9SS pinion drives a cell-surface conveyor belt (rack). Cell-surface adhesins such as SprB are secreted by T9SS and are loaded onto the conveyor belt. Interaction of SprB with an external substratum results in screw-like gliding motility of the bacterial cell.

and a pore of 35 nm. This ring comprises 32–36 GldK/PorK monomers (Gorasia et al., 2016, Gorasia D. et al., 2020).

GldN/PorN (Fjoh_1856/PGN_1673) forms a ring and is associated with GldK/PorK in a 1:1 stoichiometry (Gorasia et al., 2016, Gorasia D. et al., 2020). GldN/PorN is localized in the periplasm. *Flavobacterium johnsoniae* has a paralog of GldN/PorN called as GldO. The two proteins are partially redundant. In the genomic context, *gldO* of *F. johnsoniae* is located next to *gldN* (Rhodes et al., 2010).

GldL/PorL (Fjoh_1854/PGN_1675) is a cytoplasmic membrane protein (Shrivastava, 2013) and is found near the axis of rotation of a tethered cell (Shrivastava and Berg, 2020). *Flavobacterium johnsoniae* cells containing amino acid substitution of protonatable residues of GldL/PorL (E49Q and E49D) are completely deficient for secretion (Hennell James et al., 2021). Additionally, secretion is reduced for strains that contain GldL/PorL Y13A and K27A substitutions. This suggests that GldL/PorL is an ion channel that generates pmf driven power stroke for the rotation of T9SS (Hennell James et al., 2021). Aspartate and glutamate residues of ion channels are known to play important roles in the generation of pmf (Zhou et al., 1998; Vorburger et al., 2009). GldL/PorL has two glutamates, one is in the transmembrane helix 2 (TMH2) (E49) and the other (E59) is located between TMH2 and cytoplasmic domain. Cells with GldL/PorL E49A substitution are unable to secrete SprB and fail to attach to a glass surface. Cells with GldL/PorL E59A substitution secrete SprB to the surface yet they are non-motile (Vincent et al., 2021).

GldM/PorM (Fjoh_1855/PGN_1674) interacts with GldL/PorL to form an asymmetric complex with two subunits of GldL/PorL surrounded by five subunits of GldM/PorM. It has one transmembrane domain that contains a protonable residue. Y17A substitution in the transmembrane domain of GldM/PorM resulted in reduced secretion. GldM/PorM has four periplasmic domains D1–D4. X-ray crystallography of GldM/PorM showed a hinge between D2 and D3 (Leone et al., 2018) whereas cryo-EM structural determination of truncated GldM/PorM in complex with GldL/PorL showed a bend between D1 and D2 (Hennell James et al., 2021).

THE MECHANISM OF ROTATION AND COMPARISON OF TYPE 9 SECRETION SYSTEM WITH THE BACTERIAL FLAGELLAR MOTOR

Similar to the flagellar FlgH-FlgI LP ring that forms a molecular bushing, GldK/PorK-N rings of T9SS localize in the outer membrane and periplasmic region. Like GldK/PorK, FlgH is a lipoprotein and like GldN/PorN, FlgI is a periplasmic protein. The LP ring of the flagellar motor interacts with the distal end of the driveshaft (rod), supports stable rotation of the rod, and reduces friction (Yamaguchi et al., 2021). The GldK/PorK-N ring may play a similar role in T9SS rotation. If it does, this implies that T9SS might have a currently undiscovered driveshaft. Alternatively, the mechanism of torque generation could be unique and the rotary component (Gld/PorK-N ring) could be placed on the periplasmic face of the outer membrane of T9SS containing bacteria.

Based on structural data, a model was recently presented where due to asymmetry, GldL/PorL enables rotation of GldM/PorM (Hennell James et al., 2021). The only experimental evidence for rotation of T9SS is from tethered cell analysis (Shrivastava et al., 2015) and it depicts rotation of an outer membrane protein. How does rotary GldM/PorM cross the peptidoglycan barrier and transmit rotation to an outer membrane protein? In one scenario, it might be possible that GldM/PorM might pass through a pore in the peptidoglycan. This pore could be formed by a protein that has a structure like the P ring bushing of the flagellar motor. Given the current structural data, the ring shaped GldN/PorN appears to be a candidate for the bushing. GldM/PorM might be the driveshaft that passes the peptidoglycan *via* the GldN/PorN bushing, and it can induce rotation of the outer membrane associated GldK/PorK ring. However, one caveat to this model is that GldN/PorN ring is shown to directly interact with the GldK/PorK

ring (Gorasia et al., 2016). It is possible that the linkage between GldK/PorK and GldN/PorN is weak and transient. Hence, GldM/PorM driven GldK/PorK might rotate relative to the static GldN/PorN bushing. There is also a possibility that GldN/PorN might not form the bushing and it rotates along with GldK/PorK ring. This scenario implies that another protein might from the pore that allows passage of GldM/PorM through the peptidoglycan. Future structural and biochemical data will help fill the current knowledge gaps regarding the mechanism of rotation of T9SS.

PorE (Multiple homologs in *F. johnsoniae*/PGN_1296) is a periplasmic protein that is anchored to inner leaflet of outer membrane (Heath et al., 2016). Sequence analysis and modeling suggest that PGN_1296 has four domains (i) a tetratricopeptide repeat domain (TPR, residues 25–149); (ii) a β–propeller domain (WD40, residues 167–435); (iii) a carboxypeptidase regulatory domain-like fold (CRD, residues 441–527) and (iv) an OmpA_C-like putative peptidoglycan-binding domain (PBD) (residues 534–668). The OmpA_C (PBD) structure of PorE consists of a three-stranded β-sheet (β1–3) and five α-helices (α1–5) (Trinh et al., 2020).

The MotA–MotB stator units of the flagellar motor are attached to the cell wall by a peptidoglycan binding domain of MotA. Neither GldL/PorL nor GldM/PorM contain a detectable peptidoglycan binding domain. For the Gld/PorLM complex to function as a stator unit, attachment to a rigid part of the cell is necessary. This might be achieved by the PBD of PorE. However, there is no direct evidence for interaction between PorE and Gld/PorLM and whether PorE enables T9SS anchoring remains to be seen. *P. gingivalis* cells lacking PorE have reduced T9SS activity (Heath et al., 2016). The Role of PorE homolog of *F. johnsoniae* is unknown. There are multiple homologs of PorE in *F. johnsoniae*. Future experimental evidence might clear our understanding of anchoring of GldL/PorL. In an alternate scenario, it is possible that PorE might not interact with core T9SS proteins and GldL/PorL might be anchored *via* a cytoskeleton protein.

SprF/PorP (Multiple homologs in *F. johnsoniae*/PGN_1677) of *P. gingivalis* has been reported to interact individually with PorE, Gld/PorK and GldM/PorM (Gorasia D. et al., 2020) and could be the connection between T9SS and the peptidoglycan bound PorE. However, if this scenario is correct, neither GldK/PorK ring or GldM/PorM can rotate. It might imply that like LP rings of the flagellar motor, both GldK/PorK and GldN/PorN act as bushings. Alternatively, as discussed below, the interaction of SprF/PorP with PorE might not have any role in motility and it might only occur during the process of protein secretion.

SprF/PorP is required for secretion of TIGR04131 domain containing proteins. In the genomic context, a cell often has multiple copies of SprF/PorP and genes encoding SprF/PorP are often localized next to genes encoding TIGR04131 domain containing proteins (Kulkarni et al., 2019). As an example, one *F. johnsoniae* SprF encoding gene (Fjoh_0978) is localized downstream of the mobile cell-surface adhesin SprB encoding gene (Fjoh_0979). SprF/PorP is required for secretion of SprB, and it might be possible that SprF interacts with SprB during transport. If correct, this might imply that the interaction of SprF/PorP with GldK/PorK and GldM/PorM happens solely during transport and that it might help the T9SS pore recognize TIGR04131 containing substrates.

SprA/Sov (Fjoh_1653/PGN_0832) is required for secretion SprB, RemA, chitinase, and gingipains (Saiki and Konishi, 2007; Shrivastava et al., 2013). It forms the largest single polypeptide outer membrane ß-barrel (36 strand) known and acts as the protein translocon of the T9SS. SprA is found in two states one with PorV and the other with a plug protein. In both the states, SprA is bound to a lipoprotein Peptidyl-prolyl cis-trans isomerase (PPI). SprA forms a transmembrane β-barrel structure which rises about 20 Å above the membrane on the cell-surface. Two folded inserts are present between β-barrel strand 7–8 and 11–12. They form a 50 Å high cap structure that seals the extracellular end of the barrel. The cap insert consist of two domains with a β-sheet structure and the first domain surrounding the second domain from both the sides (Lauber et al., 2018).

PorV (Fjoh_1555/PGN_0023) is bound to the outer membrane pore of SprA and acts as a gate. There are highly conserved packing interactions between PorV and the lateral opening of SprA. When in complex with SprA, the PorV barrel is tilted by 25°. While in a free state, it is proposed that PorV adopts a more vertical position in the membrane bilayer (Lauber et al., 2018). *F. johnsoniae* cells lacking PorV are deficient in secretion of the motility adhesin RemA, the chitinase ChiA, and many other proteins. However, cells lacking PorV have the ability to secrete SprB hence they form spreading colonies on agar (Kharade and McBride, 2015).

Peptidyl-prolyl *cis-trans* isomerase (PPI: Fjoh_4997/PGN_0742/PGN_0744) binds to the lateral face of SprA opposite to PorV. PPIases are chaperones which catalyze the cis/trans isomerization of proline and act as a regulatory switch during protein folding (Dunyak and Gestwicki, 2016). Deletion of this PPI has no notable effect on T9SS function or gliding motility (Lauber et al., 2018). However, another predicted PPI, GldI (discussed later), is essential for motility.

Plug (Fjoh_1759/putative PGN_0144) can be bound to SprA ß-barrel when SprA is not in a complex with PorV. The plug protein mutant neither has gliding defect nor is defective in T9SS secretion. When PorV is not bound to SprA, the plug prevents leakage of small molecules through the SprA pore (Lauber et al., 2018).

SprT/PorT (Fjoh_1466/PGN_0778) is an outer membrane protein (Nguyen et al., 2009). Weak activity of gingipains Kgp and RgpA are observed in lysates and culture supernatants of *P. gingivalis* cells that lack PorT (Sato et al., 2005). *F. johnsoniae* cells lacking SprT form non-spreading colonies on agar. They fail to secrete SprB to the cell surface, and are deficient in chitin utilization (Sato et al., 2010).

SprE/PorW (Fjoh_1051/PGN_1877) is required for the secretion of an array of T9SS proteins (Gorasia D. G. et al., 2020). *F. johnsoniae* cells lacking SprE exhibit very little motility and are deficient in chitin utilization (Rhodes et al., 2011). It is reported

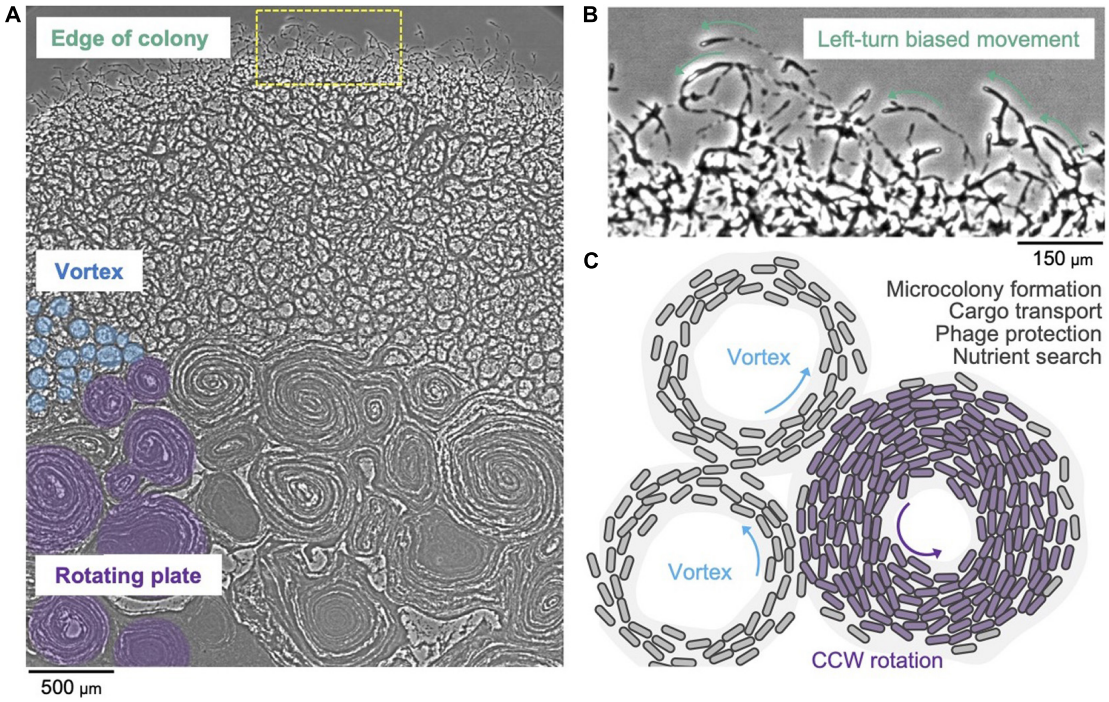


FIGURE 3 | Collective motion of gliding *F. johnsoniae*. **(A)** Colony spreading pattern in a starved environment. **(B)** Left-turn biased cell movement at the edge of the colony. **(C)** Schematic of the vortex pattern formation and its possible roles.

that PorW of *P. gingivalis* acts as a bridge between Sov/SprA translocon and PorK/N rings (Gorasia et al., 2022).

ADDITIONAL PROTEINS REQUIRED FOR GLIDING MOTILITY

It is proposed that a molecular rack and pinion assembly enables gliding motility of Bacteroidetes (Shrivastava and Berg, 2020). Here, T9SS rotary motor is the pinion that pushes a conveyor belt on the cell-surface (**Figure 2B**). As described above, the identity of proteins that form T9SS is now well-known, however, the nature of proteins that form the rack or the conveyor belt are mysterious. Comparative genomic analysis has shown that non-motile Bacteroidetes lack several accessory Gld proteins. It is possible that the additional Gld proteins help in the formation of the rack or the conveyor belt (rack) which is only found in motile Bacteroidetes. The localization and function of the additional Gld proteins are described below.

GldJ (Fjoh_1557) is a lipoprotein that appears to form helical tracks on the cell-surface (Braun and McBride, 2005) and it might be one of the central components of the gliding machinery. GldJ is required for the stability of GldK (Johnston et al., 2018). However, *F. johnsoniae* cells lacking GldK/PorK, GldL/PorL, GldM/PorM, and GldN/PorN have wild-type like levels of GldJ (Braun et al., 2005). Cells lacking either 8 or 13 C-terminal amino acids (AA) of GldJ have functional T9SS, however, cells lacking C-terminal 13 AA of GldJ are completely non-motile and cells lacking C-terminal 8 AA of GldJ exhibit very little motility. This is the first instance where the motility phenotype is completely separated from T9SS secretion (Johnston et al., 2018). GldJ has 30% sequence similarity with *F. johnsoniae* GldK/PorK. It is a homolog of a sulfatase activating enzyme (SUMF1) but it lacks the active site of SUMF1 (Braun and McBride, 2005).

GldA (Fjoh_1516) belongs to the ATP binding cassette family of transport proteins (ABC transporter proteins) essential for gliding motility. GldA has Walker "A" and "B" motifs, which are characteristics of an ATP hydrolyzing domain of an ABC transporter (Agarwal et al., 1997). Furthermore, GldA point mutations in ABC transporter putative active site G40R result in reduction of cellular levels of GldJ and GldK/PorK. Similarly, a point mutation in ABC transporter signature sequence LSKGYRQR (site of point mutation underlined) shows that a functional GldA is required for the stability of both GldJ and GldK/PorK (Braun et al., 2005; Johnston et al., 2018).

GldB (Fjoh_1793) is a lipoprotein essential for gliding motility and cells lacking GldB have a defective T9SS (Hunnicutt and McBride, 2000). GldB is required for the stability of both GldJ and GldK/PorK (Braun and McBride, 2005; Johnston et al., 2018).

GldD (Fjoh_1540) is a lipoprotein essential for gliding motility (Hunnicutt and McBride, 2001; McBride et al., 2003). Furthermore, *F. johnsoniae* cells lacking GldD do not propel latex beads. GldD is required for the stability of both GldJ and GldK/PorK (Braun and McBride, 2005; Johnston et al., 2018).

GldF (Fjoh_2722) is essential for gliding motility (Hunnicutt et al., 2002). Both GldF and GldG are required for membrane

localization of GldA (Agarwal et al., 1997; Hunnicutt et al., 2002). GldF is required for the stability of GldK/PorK (Johnston et al., 2018).

GldG (Fjoh_2721). Cells lacking GldG are non-motile (Hunnicutt et al., 2002). GldG is predicted to be a transmembrane protein that interacts with GldA to form an ABC transporter (Agarwal et al., 1997; Hunnicutt et al., 2002).

GldH (Fjoh_0890) is a lipoprotein essential for gliding motility. Cell lacking GldH do not propel latex beads and are unable to utilize chitin (McBride et al., 2003). GldH is required for the stability of GldJ and GldK/PorK (Braun and McBride, 2005; Johnston et al., 2018).

GldI (Fjoh_2369) mutants form non-spreading colonies on agar. GldI has a PPI domain (McBride and Braun, 2004). Cells lacking GldI do not propel latex beads and are unable to utilize chitin. GldI is required for the stability of GldJ and GldK/PorK (Braun and McBride, 2005; Johnston et al., 2018).

ACCESSORY PROTEINS NOT REQUIRED FOR GLIDING MOTILITY

Evolutionary forces can drive modifications in components of biological machineries from different model organisms. As examples, the shape of bacterial flagellar motor varies amongst organisms (Chen et al., 2011; Beeby et al., 2016) and the F_o ATP synthase varies across taxa (Nirody et al., 2020). The F_o rotor c-ring stoichiometry ranges from eight subunits in mammalian mitochondrion (Zhou et al., 2015) to 17 in the bacterium *Burkholderia pseudomallei* (Schulz et al., 2017). Following this trend of organism-based modifications of molecular machines, three proteins described below interact with the T9SS of *P. gingivalis* but they are not essential for the functioning of the *F. johnsoniae* T9SS.

PorU (Fjoh_1556/PGN_0022) PorU of *P. gingivalis* is a part of the attachment complex that also involves PorZ, PorV, and PorQ. This complex modifies the T9SS substrates with an anionic lipopolysaccharide (A-LPS) and attaches them to the cell surface (Gorasia et al., 2015; Glew et al., 2017). PorU is a sortase which cleaves the CTD signal of the T9SS substrate and attaches the newly generated CTD of T9SS substrate to the cell surface *via* A-LPS (Glew et al., 2012, 2017). *P. gingivalis* cells lacking PorU have a partial T9SS defect and gingipain secretion is reduced (Glew et al., 2012). However, the *F. johnsoniae* PorU is not required for secretion of ChiA, RemA, or SprB, indicating that it does not play an essential role in the secretion of proteins by T9SS of *F. johnsoniae* (Kharade and McBride, 2015).

PorZ (Fjoh_0707/PGN_0509) and PorQ (Fjoh_2755/PGN_0645) PorZ of *P. gingivalis* interacts with A-LPS and PorU. Hence, it may play a role in providing A-LPS substrate to PorU (Madej et al., 2021). *P. gingivalis* cells lacking PorZ are defective in gingipain secretion (Lasica et al., 2016). PorQ is required for the association of PorZ with the outer membrane (Lasica et al., 2016). *F. johnsoniae* does not need PorQ (Fjoh_2755) for either gliding motility or chitin utilization (Shrivastava, 2013). No *porZ* mutant of *F. johnsoniae* has been reported thus far.

Type 9 Secretion System Driven Swarm Behavior of Flavobacteria

It has long been known that *F. johnsoniae* forms spreading colonies on agar plates (Wolkin and Pate, 1984; Gorski et al., 1993). A recent study showed that the cells at high density are connected with one another and that in a starved environment they move in counterclockwise trajectories (Nakane et al., 2021). A *F. johnsoniae* swarm exhibits a vortex pattern that spontaneously appears as a lattice that is integrated into a large-scale circular plate (**Figure 3A**). Notably, the rotational direction of the circular plate is counterclockwise (**Figure 3B**). This two-dimensional pattern possibly appears due to the collision of cells and it further induces a nematic alignment of dense cells (Sumino et al., 2012). It is hypothesized that swarm behavior of T9SS driven Bacteroidetes may be involved in survival strategies and the efficient search of nutrients (**Figure 3C**; Nakane et al., 2021). A three-dimensional spherical microcolony was recently studied in a microfluidic device and it was reported that this biofilm-like microcolony self-assembles by the gliding motility (Li et al., 2021). It has also been reported that gliding motility contributes to the robustness of a *F. johnsoniae* biofilm (Eckroat et al., 2021). The colony of *Flavobacterium* strain Iridescent 1 (IR1) displays a bright brilliant green structural coloration, which is caused by the 2D close-packed cell arrangement aided by gliding motility (Johansen et al., 2018; Hamidjaja et al., 2020). This may provide photoprotection to either bacteria or host. Additionally, this structure might lead to the optimum cellular organization for the degradation of biological polymers (Johansen et al., 2018). The role of the structural coloration of the colony in the natural environment needs to be studied further. It is evident that our understanding of biofilm formation of *F. johnsoniae* and its dependence on swarm behavior is currently in its nascent stage. Future investigations in this area might reveal details about bacterial cooperation and behavior.

Benefits of Swarm Behavior to the Microbiota

Type 9 secretion systems are found in bacterial genera that are abundant in the human oral and gut microbiota. Examples include the genera *Prevotella*, *Bacteroides*, *Parabacteroides*, *Capnocytophaga*, *Tanerella*, and *Porphyromonas*. *Capnocytophaga* sp. exhibit robust gliding motility (Holt et al., 1979; Leadbetter et al., 1979; Shrivastava et al., 2018) and are found in abundance in the oral microbiota. They are prominent members of human supra-gingival and sub-gingival biofilms (Mark Welch et al., 2016). In contrast with the wild-type strains isolated from the human oral microbiota, cells of *C. ochracea* that lack T9SS are non-motile and are deficient for biofilm formation (Kita et al., 2016).

Capnocytophaga gingivalis swarm in a multilayered counter clockwise vortex pattern (Shrivastava et al., 2018). *C. gingivalis* cells transport non-motile bacteria as cargo and shape the spatial organization of a polymicrobial community (Shrivastava et al., 2018). A *C. gingivalis* swarm can also transport bacteriophages as cargo (Ratheesh et al., 2021) and can increase the kinetics of death of a colony of prey bacteria. *Via* a combination of vortexing, layering, transportation of other

bacteria, and phage transportation, T9SS-driven microbes play a crucial role in shaping a polymicrobial community. This amazing molecular machinery holds many secrets, which once unraveled, can significantly enrich our understanding of microbiology.

AUTHOR CONTRIBUTIONS

AT and AS contributed all sections besides the ones described below and created **Figure 2**. JG and AS contributed the section on diversity of protein secretion systems and created **Figure 1**. DN contributed the section on swarm behavior of Flavobacteria and created **Figure 3**. All authors contributed to the article and approved the submitted version.

FUNDING

AS was supported by NIH grant DE026826.

REFERENCES

Abrusci, P., Vergara-Irigaray, M., Johnson, S., Beeby, M. D., Hendrixson, D. R., Roversi, P., et al. (2013). Architecture of the major component of the type III secretion system export apparatus. *Nat. Struct. Mol. Biol.* 20, 99–104. doi: 10.1038/nsmb.2452

Agarwal, S., Hunnicutt, D. W., and McBride, M. J. (1997). Cloning and characterization of the *Flavobacterium johnsoniae* (*Cytophaga* johnsonae) gliding motility gene, gldA. *Proc. Natl. Acad. Sci. U.S.A.* 94, 12139–12144. doi: 10.1073/pnas.94.22.12139

Beckham, K. S. H., Ritter, C., Chojnowski, G., Ziemianowicz, D. S., Mullapudi, E., Rettel, M., et al. (2021). Structure of the mycobacterial ESX-5 type VII secretion system pore complex. *Sci. Adv.* 7:eabg9923. doi: 10.1126/sciadv.abg9923

Beeby, M., Ribardo, D. A., Brennan, C. A., Ruby, E. G., Jensen, G. J., and Hendrixson, D. R. (2016). Diverse high-torque bacterial flagellar motors assemble wider stator rings using a conserved protein scaffold. *Proc. Natl. Acad. Sci. U.S.A.* 113, E1917–E1926. doi: 10.1073/pnas.1518952113

Bhoite, S., van Gerven, N., Chapman, M. R., and Remaut, H. (2019). Curli biogenesis: bacterial amyloid assembly by the type VIII secretion pathway. *Ecosal Plus* 8, ecosalplus.ESP-0037-2018. doi: 10.1128/ecosalplus.ESP-0037-2018

Blum, M., Chang, H.-Y., Chuguransky, S., Grego, T., Kandasaamy, S., Mitchell, A., et al. (2021). The InterPro protein families and domains database: 20 years on. *Nucleic Acids Res.* 49, D344–D354. doi: 10.1093/nar/gkaa977

Braun, T. F., and McBride, M. J. (2005). Flavobacterium johnsoniae GldJ is a lipoprotein that is required for gliding motility. *J. Bacteriol.* 187, 2628–2637. doi: 10.1128/JB.187.8.2628-2637.2005

Braun, T. F., Khubbar, M. K., Saffarini, D. A., and McBride, M. J. (2005). Flavobacterium johnsoniae gliding motility genes identified by mariner mutagenesis. *J. Bacteriol.* 187, 6943–6952. doi: 10.1128/JB.187.20.6943-6952.2005

Bunduc, C. M., Bitter, W., and Houben, E. N. G. (2020). Structure and function of the mycobacterial type VII secretion systems. *Annu. Rev. Microbiol.* 74, 315–335. doi: 10.1146/annurev-micro-012420-081657

Chen, S., Beeby, M., Murphy, G. E., Leadbetter, J. R., Hendrixson, D. R., Briegel, A., et al. (2011). Structural diversity of bacterial flagellar motors: structural diversity of bacterial flagellar motors. *EMBO J.* 30, 2972–2981. doi: 10.1038/emboj.2011.186

Cianfanelli, F. R., Monlezun, L., and Coulthurst, S. J. (2016). Aim, load, fire: the type vi secretion system, a bacterial nanoweapon. *Trends Microbiol.* 24, 51–62. doi: 10.1016/j.tim.2015.10.005

Coulthurst, S. (2019). The type VI secretion system: a versatile bacterial weapon. *Microbiology* 165, 503–515. doi: 10.1099/mic.0.000789

Craig, L., Forest, K. T., and Maier, B. (2019). Type IV pili: dynamics, biophysics and functional consequences. *Nat. Rev. Microbiol.* 17, 429–440. doi: 10.1038/s41579-019-0195-4

de Diego, I., Ksiazek, M., Mizgalska, D., Koneru, L., Golik, P., Szmigielski, B., et al. (2016). The outer-membrane export signal of *Porphyromonas gingivalis* type IX secretion system (T9SS) is a conserved C-terminal β-sandwich domain. *Sci. Rep.* 6:23123. doi: 10.1038/srep23123

Denks, K., Vogt, A., Sachelaru, I., Petriman, N.-A., Kudva, R., and Koch, H.-G. (2014). The Sec translocon mediated protein transport in prokaryotes and eukaryotes. *Mol. Membr. Biol.* 31, 58–84. doi: 10.3109/09687688.2014.907455

Diepold, A., and Armitage, J. P. (2015). Type III secretion systems: the bacterial flagellum and the injectisome. *Philos. Trans. R. Soc. Lond. B. Biol. Sci.* 370:20150020. doi: 10.1098/rstb.2015.0020

Dunyak, B. M., and Gestwicki, J. E. (2016). Peptidyl-Proline Isomerases (PPIases): targets for natural products and natural product-inspired compounds. *J. Med. Chem.* 59, 9622–9644. doi: 10.1021/acs.jmedchem.6b00411

Eckroat, T. J., Greguske, C., and Hunnicutt, D. W. (2021). The type 9 secretion system is required for *Flavobacterium johnsoniae* biofilm formation. *Front. Microbiol.* 12:660887. doi: 10.3389/fmicb.2021.660887

Fan, E., Chauhan, N., Udatha, D. B. R. K. G., Leo, J. C., and Linke, D. (2016). Type V secretion systems in bacteria. *Microbiol. Spectr.* 4. doi: 10.1128/microbiolspec.VMBF-0009-2015

Glew, M. D., Veith, P. D., Chen, D., Gorasia, D. G., Peng, B., and Reynolds, E. C. (2017). PorV is an outer membrane shuttle protein for the type IX secretion system. *Sci. Rep.* 7:8790. doi: 10.1038/s41598-017-09412-w

Glew, M. D., Veith, P. D., Peng, B., Chen, Y.-Y., Gorasia, D. G., Yang, Q., et al. (2012). PG0026 is the C-terminal signal peptidase of a novel secretion system of *Porphyromonas gingivalis*. *J. Biol. Chem.* 287, 24605–24617. doi: 10.1074/jbc.M112.369223

Gómez-Santos, N., Glatter, T., Koebnik, R., Świątek-Połatyńska, M. A., and Søgaard-Andersen, L. (2019). A TonB-dependent transporter is required for secretion of protease PopC across the bacterial outer membrane. *Nat. Commun.* 10:1360. doi: 10.1038/s41467-019-09366-9

Gorasia, D. G., Glew, M. D., Veith, P. D., and Reynolds, E. C. (2020). Quantitative proteomic analysis of the type IX secretion system mutants in *Porphyromonas gingivalis*. *Mol. Oral Microbiol.* 35, 78–84. doi: 10.1111/omi.12283

Gorasia, D. G., Lunar Silva, I., Butler, C. A., Chabalier, M., Doan, T., Cascales, E., et al. (2022). Protein interactome analysis of the type IX secretion system identifies PorW as the missing link between the PorK/N ring complex and the Sov Translocon. *Microbiol. Spectr.* 10:e0160221. doi: 10.1128/spectrum.01602-21

Gorasia, D. G., Veith, P. D., Chen, D., Seers, C. A., Mitchell, H. A., Chen, Y.-Y., et al. (2015). *Porphyromonas gingivalis* type IX secretion substrates are cleaved and modified by a sortase-like mechanism. *PLoS Pathog.* 11:e1005152. doi: 10.1371/journal.ppat.1005152

Gorasia, D. G., Veith, P. D., Hanssen, E. G., Glew, M. D., Sato, K., Yukitake, H., et al. (2016). Structural insights into the PorK and PorN components of the *Porphyromonas gingivalis* type IX secretion system. *PLoS Pathog.* 12:e1005820. doi: 10.1371/journal.ppat.1005820

Gorasia, D., Chreifi, G., Seers, C., Butler, C., Heath, J., Glew, M., et al. (2020). *In situ* structure and organisation of the type IX secretion system. *bioRxiv* [Preprint]. doi: 10.1101/2020.05.13.094771

Gorski, L., Godchaux, W., and Leadbetter, E. R. (1993). Structural specificity of sugars that inhibit gliding motility of *Cytophaga* johnsonae. *Arch. Microbiol.* 160, 121–125. doi: 10.1007/BF00288713

Grossman, A. S., Mauer, T. J., Forest, K. T., and Goodrich-Blair, H. (2021). A widespread bacterial secretion system with diverse substrates. *mBio* 12:e0195621. doi: 10.1128/mBio.01956-21

Hamidjaja, R., Capoulade, J., Catón, L., and Ingham, C. J. (2020). The cell organization underlying structural colour is involved in Flavobacterium IR1 predation. *ISME J.* 14, 2890–2900. doi: 10.1038/s41396-020-00760-6

Heath, J. E., Seers, C. A., Veith, P. D., Butler, C. A., Nor Muhammad, N. A., Chen, Y.-Y., et al. (2016). PG1058 is a novel multidomain protein component of the bacterial type IX secretion system. *PLoS One* 11:e0164313. doi: 10.1371/journal.pone.0164313

Hennell James, R., Deme, J. C., Kjær, A., Alcock, F., Silale, A., Lauber, F., et al. (2021). Structure and mechanism of the proton-driven motor that powers type 9 secretion and gliding motility. *Nat. Microbiol.* 6, 221–233. doi: 10.1038/s41564-020-00823-6

Hennon, S. W., Soman, R., Zhu, L., and Dalbey, R. E. (2015). YidC/Alb3/Oxa1 family of insertases. *J. Biol. Chem.* 290, 14866–14874. doi: 10.1074/jbc.R115.638171

Hofreuter, D., Odenbreit, S., and Haas, R. (2001). Natural transformation competence in *Helicobacter pylori* is mediated by the basic components of a type IV secretion system: H. pylori natural transformation competence. *Mol. Microbiol.* 41, 379–391. doi: 10.1046/j.1365-2958.2001.02502.x

Holt, S. C., Leadbetter, E. R., and Socransky, S. S. (1979). Capno*cytophaga*: new genus of gram-negative gliding bacteria. II. Morphology and ultrastructure. *Arch. Microbiol.* 122, 17–27. doi: 10.1007/BF00408041

Hunnicutt, D. W., and McBride, M. J. (2000). Cloning and characterization of the *Flavobacterium johnsoniae* gliding-motility genes gldB and gldC. *J. Bacteriol.* 182, 911–918. doi: 10.1128/JB.182.4.911-918.2000

Hunnicutt, D. W., and McBride, M. J. (2001). Cloning and characterization of the *Flavobacterium johnsoniae* gliding motility genes gldD and gldE. *J. Bacteriol.* 183, 4167–4175. doi: 10.1128/JB.183.14.4167-4175.2001

Hunnicutt, D. W., Kempf, M. J., and McBride, M. J. (2002). Mutations in *Flavobacterium johnsoniae* gldF and gldG disrupt gliding motility and interfere with membrane localization of GldA. *J. Bacteriol.* 184, 2370–2378. doi: 10.1128/JB.184.9.2370-2378.2002

Johansen, V. E., Catón, L., Hamidjaja, R., Oosterink, E., Wilts, B. D., Rasmussen, T. S., et al. (2018). Genetic manipulation of structural color in bacterial colonies. *Proc. Natl. Acad. Sci. U.S.A.* 115, 2652–2657. doi: 10.1073/pnas.1716214115

Johnston, J. J., Shrivastava, A., and McBride, M. J. (2018). Untangling *Flavobacterium johnsoniae* gliding motility and protein secretion. *J. Bacteriol.* 200, e00362-17. doi: 10.1128/JB.00362-17

Kharade, S. S., and McBride, M. J. (2014). *Flavobacterium johnsoniae* chitinase ChiA is required for chitin utilization and is secreted by the type IX secretion system. *J. Bacteriol.* 196, 961–970. doi: 10.1128/JB.01170-13

Kharade, S. S., and McBride, M. J. (2015). *Flavobacterium johnsoniae* PorV is required for secretion of a subset of proteins targeted to the type IX secretion system. *J. Bacteriol.* 197, 147–158. doi: 10.1128/JB.02085-14

Kita, D., Shibata, S., Kikuchi, Y., Kokubu, E., Nakayama, K., Saito, A., et al. (2016). Involvement of the Type IX secretion system in *Capnocytophaga ochracea* gliding motility and biofilm formation. *Appl. Environ. Microbiol.* 82, 1756–1766. doi: 10.1128/AEM.03452-15

Korotkov, K. V., and Sandkvist, M. (2019). Architecture, function, and substrates of the Type II secretion system. *EcoSal Plus* 8, ecosallus.ES–0034–2018. doi: 10.1128/ecosalplus.ESP-0034-2018

Kudva, R., Denks, K., Kuhn, P., Vogt, A., Müller, M., and Koch, H.-G. (2013). Protein translocation across the inner membrane of Gram-negative bacteria: the Sec and Tat dependent protein transport pathways. *Res. Microbiol.* 164, 505–534. doi: 10.1016/j.resmic.2013.03.016

Kulkarni, S. S., Johnston, J. J., Zhu, Y., Hying, Z. T., and McBride, M. J. (2019). The carboxy-terminal region of *Flavobacterium johnsoniae* SprB facilitates its secretion by the type IX secretion system and propulsion by the gliding motility machinery. *J. Bacteriol.* 201, e218–e219. doi: 10.1128/JB.00218-19

Kulkarni, S. S., Zhu, Y., Brendel, C. J., and McBride, M. J. (2017). Diverse C-terminal sequences involved in *Flavobacterium johnsoniae* protein secretion. *J. Bacteriol.* 199, e00884–16. doi: 10.1128/JB.00884-16

Kusters, I., and Driessen, A. J. M. (2011). SecA, a remarkable nanomachine. *Cell. Mol. Life Sci.* 68, 2053–2066. doi: 10.1007/s00018-011-0681-y

Lasica, A. M., Goulas, T., Mizgalska, D., Zhou, X., de Diego, I., Ksiazek, M., et al. (2016). Structural and functional probing of PorZ, an essential bacterial surface component of the type-IX secretion system of human oral-microbiomic Porphyromonas gingivalis. *Sci. Rep.* 6:37708. doi: 10.1038/srep37708

Lauber, F., Deme, J. C., Lea, S. M., and Berks, B. C. (2018). Type 9 secretion system structures reveal a new protein transport mechanism. *Nature* 564, 77–82. doi: 10.1038/s41586-018-0693-y

Leadbetter, E. R., Holt, S. C., and Socransky, S. S. (1979). Capno*cytophaga*: new genus of gram-negative gliding bacteria. I. General characteristics, taxonomic considerations and significance. *Arch. Microbiol.* 122, 9–16. doi: 10.1007/BF00408040

Leone, P., Roche, J., Vincent, M. S., Tran, Q. H., Desmyter, A., Cascales, E., et al. (2018). Type IX secretion system PorM and gliding machinery GldM form arches spanning the periplasmic space. *Nat. Commun.* 9:429. doi: 10.1038/s41467-017-02784-7

Li, C., Hurley, A., Hu, W., Warrick, J. W., Lozano, G. L., Ayuso, J. M., et al. (2021). Social motility of biofilm-like microcolonies in a gliding bacterium. *Nat. Commun.* 12:5700. doi: 10.1038/s41467-021-25408-7

Li, Y. G., Hu, B., and Christie, P. J. (2019). Biological and structural diversity of type IV secretion systems. *Microbiol. Spectr.* 7. doi: 10.1128/microbiolspec.PSIB-0012-2018

Madej, M., Nowakowska, Z., Ksiazek, M., Lasica, A. M., Mizgalska, D., Nowak, M., et al. (2021). PorZ, an essential component of the type IX secretion system of *Porphyromonas gingivalis*, delivers anionic lipopolysaccharide to the PorU sortase for transpeptidase processing of T9SS cargo proteins. *mBio* 12, e02262–20. doi: 10.1128/mBio.02262-20

Mark Welch, J. L., Rossetti, B. J., Rieken, C. W., Dewhirst, F. E., and Borisy, G. G. (2016). Biogeography of a human oral microbiome at the micron scale. *Proc. Natl. Acad. Sci. U.S.A.* 113, E791–E800. doi: 10.1073/pnas.1522149113

McBride, M. J., and Braun, T. F. (2004). GldI is a lipoprotein that is required for *Flavobacterium johnsoniae* gliding motility and chitin utilization. *J. Bacteriol.* 186, 2295–2302. doi: 10.1128/JB.186.8.2295-2302.2004

McBride, M. J., and Zhu, Y. (2013). Gliding motility and Por secretion system genes are widespread among members of the phylum bacteroidetes. *J. Bacteriol.* 195, 270–278. doi: 10.1128/JB.01962-12

McBride, M. J., Braun, T. F., and Brust, J. L. (2003). *Flavobacterium johnsoniae* GldH is a lipoprotein that is required for gliding motility and chitin utilization. *J. Bacteriol.* 185, 6648–6657. doi: 10.1128/JB.185.22.6648-6657.2003

Meuskens, I., Saragliadis, A., Leo, J. C., and Linke, D. (2019). Type V secretion systems: an overview of passenger domain functions. *Front. Microbiol.* 10:1163. doi: 10.3389/fmicb.2019.01163

Nakane, D., Odaka, S., Suzuki, K., and Nishizaka, T. (2021). Large-Scale vortices with dynamic rotation emerged from monolayer collective motion of gliding Flavobacteria. *J. Bacteriol.* 203:e0007321. doi: 10.1128/JB.00073-21

Nakane, D., Sato, K., Wada, H., McBride, M. J., and Nakayama, K. (2013). Helical flow of surface protein required for bacterial gliding motility. *Proc. Natl. Acad. Sci. U.S.A.* 110, 11145–11150. doi: 10.1073/pnas.1219753110

Naskar, S., Hohl, M., Tassinari, M., and Low, H. H. (2021). The structure and mechanism of the bacterial type II secretion system. *Mol. Microbiol.* 115, 412–424. doi: 10.1111/mmi.14664

Nelson, S. S., Bollampalli, S., and McBride, M. J. (2008). SprB is a cell surface component of the *Flavobacterium johnsoniae* gliding motility machinery. *J. Bacteriol.* 190, 2851–2857. doi: 10.1128/JB.01904-07

Nguyen, K.-A., Żylicz, J., Szczesny, P., Sroka, A., Hunter, N., and Potempa, J. (2009). Verification of a topology model of PorT as an integral outer-membrane protein in *Porphyromonas gingivalis*. *Microbiol. Read. Engl.* 155, 328–337. doi: 10.1099/mic.0.024323-0

Nirody, J. A., Budin, I., and Rangamani, P. (2020). ATP synthase: evolution, energetics, and membrane interactions. *J. Gen. Physiol.* 152:e201912475. doi: 10.1085/jgp.201912475

Palmer, T., and Berks, B. C. (2012). The twin-arginine translocation (Tat) protein export pathway. *Nat. Rev. Microbiol.* 10, 483–496. doi: 10.1038/nrmicro2814

Palmer, T., Finney, A. J., Saha, C. K., Atkinson, G. C., and Sargent, F. (2021). A holin/peptidoglycan hydrolase-dependent protein secretion system. *Mol. Microbiol.* 115, 345–355. doi: 10.1111/mmi.14599

Papanikou, E., Karamanou, S., and Economou, A. (2007). Bacterial protein secretion through the translocase nanomachine. *Nat. Rev. Microbiol.* 5, 839–851. doi: 10.1038/nrmicro1771

Portaliou, A. G., Tsolis, K. C., Loos, M. S., Zorzini, V., and Economou, A. (2016). Type III secretion: building and operating a remarkable nanomachine. *Trends Biochem. Sci.* 41, 175–189. doi: 10.1016/j.tibs.2015.09.005

Ratheesh, N. K., Calderon, C. A., Zdimal, A. M., and Shrivastava, A. (2021). Bacterial swarm-mediated phage transportation disrupts a biofilm inherently protected from phage penetration. *bioRxiv* [Preprint]. doi: 10.1101/2021.06.25.449910

Rhodes, R. G., Samarasam, M. N., Shrivastava, A., van Baaren, J. M., Pochiraju, S., Bollampalli, S., et al. (2010). *Flavobacterium johnsoniae* gldN and gldO are partially redundant genes required for gliding motility and surface localization of SprB. *J. Bacteriol.* 192, 1201–1211. doi: 10.1128/JB.01495-09

Rhodes, R. G., Samarasam, M. N., Van Groll, E. J., and McBride, M. J. (2011). Mutations in *Flavobacterium johnsoniae* sprE result in defects in gliding motility and protein secretion. *J. Bacteriol.* 193, 5322–5327. doi: 10.1128/JB.05480-11

Rivera-Calzada, A., Famelis, N., Llorca, O., and Geibel, S. (2021). Type VII secretion systems: structure, functions and transport models. *Nat. Rev. Microbiol.* 19, 567–584. doi: 10.1038/s41579-021-00560-5

Saiki, K., and Konishi, K. (2007). Identification of a *Porphyromonas gingivalis* novel protein sov required for the secretion of gingipains. *Microbiol. Immunol.* 51, 483–491. doi: 10.1111/j.1348-0421.2007.tb03936.x

Saiki, K., and Konishi, K. (2010). The role of Sov protein in the secretion of gingipain protease virulence factors of *Porphyromonas gingivalis*. *FEMS Microbiol. Lett.* 302, 166–174. doi: 10.1111/j.1574-6968.2009.01848.x

Sato, K., Naito, M., Yukitake, H., Hirakawa, H., Shoji, M., McBride, M. J., et al. (2010). A protein secretion system linked to bacteroidete gliding motility and pathogenesis. *Proc. Natl. Acad. Sci. U.S.A.* 107, 276–281. doi: 10.1073/pnas.0912010107

Sato, K., Sakai, E., Veith, P. D., Shoji, M., Kikuchi, Y., Yukitake, H., et al. (2005). Identification of a new membrane-associated protein that influences transport/maturation of gingipains and adhesins of *Porphyromonas gingivalis*. *J. Biol. Chem.* 280, 8668–8677. doi: 10.1074/jbc.M413544200

Sato, K., Yukitake, H., Narita, Y., Shoji, M., Naito, M., and Nakayama, K. (2013). Identification of *Porphyromonas gingivalis* proteins secreted by the Por secretion system. *FEMS Microbiol. Lett.* 338, 68–76. doi: 10.1111/1574-6968.12028

Schulz, S., Wilkes, M., Mills, D. J., Kühlbrandt, W., and Meier, T. (2017). Molecular architecture of the N-type ATPase rotor ring from Burkholderia pseudomallei. *EMBO Rep.* 18, 526–535. doi: 10.15252/embr.201643374

Shrivastava, A. K. (2013). *Cell Surface Adhesins, Exopolysaccharides and the Por (Type IX) Secretion System of Flavobacterium johnsoniae. Theses and Dissertations*. Milwaukee, WI: University of Wisconsin-Milwaukee.

Shrivastava, A., and Berg, H. C. (2020). A molecular rack and pinion actuates a cell-surface adhesin and enables bacterial gliding motility. *Sci. Adv.* 6:eaay6616. doi: 10.1126/sciadv.aay6616

Shrivastava, A., Johnston, J. J., van Baaren, J. M., and McBride, M. J. (2013). Flavobacterium johnsoniae GldK, GldL, GldM, and SprA are required for secretion of the cell surface gliding motility adhesins SprB and RemA. *J. Bacteriol.* 195, 3201–3212. doi: 10.1128/JB.00333-13

Shrivastava, A., Lele, P. P., and Berg, H. C. (2015). A rotary motor drives Flavobacterium gliding. *Curr. Biol.* 25, 338–341. doi: 10.1016/j.cub.2014.11.045

Shrivastava, A., Patel, V. K., Tang, Y., Yost, S. C., Dewhirst, F. E., and Berg, H. C. (2018). Cargo transport shapes the spatial organization of a microbial community. *Proc. Natl. Acad. Sci. U.S.A.* 115, 8633–8638. doi: 10.1073/pnas.1808966115

Shrivastava, A., Rhodes, R. G., Pochiraju, S., Nakane, D., and McBride, M. J. (2012). *Flavobacterium johnsoniae* RemA is a mobile cell surface lectin involved in gliding. *J. Bacteriol.* 194, 3678–3688. doi: 10.1128/JB.00588-12

Shrivastava, A., Roland, T., and Berg, H. C. (2016). The screw-like movement of a gliding bacterium is powered by spiral motion of cell-surface adhesins. *Biophys. J.* 111, 1008–1013. doi: 10.1016/j.bpj.2016.07.043

Slakeski, N., Seers, C. A., Ng, K., Moore, C., Cleal, S. M., Veith, P. D., et al. (2011). C-Terminal domain residues important for secretion and attachment of RgpB in *Porphyromonas gingivalis*. *J. Bacteriol.* 193, 132–142. doi: 10.1128/JB.00773-10

Spirig, T., Weiner, E. M., and Clubb, R. T. (2011). Sortase enzymes in Gram-positive bacteria: sortase enzymes in Gram-positive bacteria. *Mol. Microbiol.* 82, 1044–1059. doi: 10.1111/j.1365-2958.2011.07887.x

Spitz, O., Erenburg, I. N., Beer, T., Kanonenberg, K., Holland, I. B., and Schmitt, L. (2019). Type I secretion systems—one mechanism for all? *Microbiol. Spectr.* 7. doi: 10.1128/microbiolspec.PSIB-0003-2018

Sumino, Y., Nagai, K. H., Shitaka, Y., Tanaka, D., Yoshikawa, K., Chaté, H., et al. (2012). Large-scale vortex lattice emerging from collectively moving microtubules. *Nature* 483, 448–452. doi: 10.1038/nature10874

Trinh, N. T. T., Tran, H. Q., Van Dong, Q., Cambillau, C., Roussel, A., and Leone, P. (2020). Crystal structure of Type IX secretion system PorE C-terminal domain from *Porphyromonas gingivalis* in complex with a peptidoglycan fragment. *Sci. Rep.* 10:7384. doi: 10.1038/s41598-020-64115-z

Van Gerven, N., Klein, R. D., Hultgren, S. J., and Remaut, H. (2015). Bacterial amyloid formation: structural insights into curli biogensis. *Trends Microbiol.* 23, 693–706. doi: 10.1016/j.tim.2015.07.010

Vincent, M. S., Canestrari, M. J., Leone, P., Stathopulos, J., Ize, B., Zoued, A., et al. (2017). Characterization of the *Porphyromonas gingivalis* type IX secretion trans-envelope PorKLMNP core complex. *J. Biol. Chem.* 292, 3252–3261. doi: 10.1074/jbc.M116.765081

Vincent, M. S., Hervada, C. C., Sebban-Kreuzer, C., Guenno, H. L., Chabalier, M., Kosta, A., et al. (2021). Dynamic proton-dependent motors power type IX secretion and gliding adhesin movement in Flavobacterium. *bioRxiv* [Preprint]. doi: 10.1101/2021.10.19.464928

Vorburger, T., Stein, A., Ziegler, U., Kaim, G., and Steuber, J. (2009). Functional role of a conserved aspartic acid residue in the motor of the Na(+)-driven flagellum from *Vibrio cholerae*. *Biochim. Biophys. Acta* 1787, 1198–1204. doi: 10.1016/j.bbabio.2009.05.015

Waksman, G., and Hultgren, S. J. (2009). Structural biology of the chaperone–usher pathway of pilus biogenesis. *Nat. Rev. Microbiol.* 7, 765–774. doi: 10.1038/nrmicro2220

Wolkin, R. H., and Pate, J. L. (1984). Translocation of motile cells of the gliding bacterium *Cytophaga johnsonae* depends on a surface component that may be modified by sugars. *Microbiology* 130, 2651–2669. doi: 10.1099/00221287-130-10-2651

Yamaguchi, T., Makino, F., Miyata, T., Minamino, T., Kato, T., and Namba, K. (2021). Structure of the molecular bushing of the bacterial flagellar motor. *Nat. Commun.* 12:4469. doi: 10.1038/s41467-021-24715-3

Zhou, A., Rohou, A., Schep, D. G., Bason, J. V., Montgomery, M. G., Walker, J. E., et al. (2015). Structure and conformational states of the bovine mitochondrial ATP synthase by cryo-EM. *eLife* 4:e10180. doi: 10.7554/eLife.10180

Zhou, J., Sharp, L. L., Tang, H. L., Lloyd, S. A., Billings, S., Braun, T. F., et al. (1998). Function of protonatable residues in the flagellar motor of *Escherichia coli*: a critical role for Asp 32 of MotB. *J. Bacteriol.* 180, 2729–2735. doi: 10.1128/JB.180.10.2729-2735.1998

Zhu, Y., and McBride, M. J. (2014). Deletion of the *Cytophaga hutchinsonii* type IX secretion system gene sprP results in defects in gliding motility and cellulose utilization. *Appl. Microbiol. Biotechnol.* 98, 763–775. doi: 10.1007/s00253-013-5355-2

Conflict of Interest: The authors declare that the research was conducted in the absence of any commercial or financial relationships that could be construed as a potential conflict of interest.

Publisher's Note: All claims expressed in this article are solely those of the authors and do not necessarily represent those of their affiliated organizations, or those of the publisher, the editors and the reviewers. Any product that may be evaluated in this article, or claim that may be made by its manufacturer, is not guaranteed or endorsed by the publisher.

Copyright © 2022 Trivedi, Gosai, Nakane and Shrivastava. This is an open-access article distributed under the terms of the Creative Commons Attribution License (CC BY). The use, distribution or reproduction in other forums is permitted, provided the original author(s) and the copyright owner(s) are credited and that the original publication in this journal is cited, in accordance with accepted academic practice. No use, distribution or reproduction is permitted which does not comply with these terms.

frontiers | Frontiers in Microbiology

REVIEW
published: 07 April 2022
doi: 10.3389/fmicb.2022.852955

The Ton Motor

Anna C. Ratliff, Susan K. Buchanan and Herve Celia*

Laboratory of Molecular Biology, National Institute of Diabetes and Digestive and Kidney Diseases, National Institutes of Health, Bethesda, MD, United States

The Ton complex is a molecular motor at the inner membrane of Gram-negative bacteria that uses a proton gradient to apply forces on outer membrane (OM) proteins to permit active transport of nutrients into the periplasmic space. Recently, the structure of the ExbB–ExbD subcomplex was determined in several bacterial species, but the complete structure and stoichiometry of TonB have yet to be determined. The C-terminal end of TonB is known to cross the periplasm and interact with TonB-dependent outer membrane transport proteins with high affinity. Yet despite having significant knowledge of these transport proteins, it is not clear how the Ton motor opens a pathway across the outer membrane for nutrient import. Additionally, the mechanism by which energy is harnessed from the inner membrane subcomplex and transduced to the outer membrane *via* TonB is not well understood. In this review, we will discuss the gaps in the knowledge about the complete structure of the Ton motor complex and the relationship between ion flow used to generate mechanical work at the outer membrane and the nutrient transport process.

Keywords: TonB, ExbB, ExbD, TonB-dependent transport, proton motive force (pmf), Gram-negative bacteria, membrane proteins, molecular motors

OPEN ACCESS

Edited by:
Jun Liu,
Yale University, United States

Reviewed by:
Martin Picard,
UMR7099 Laboratoire de biologie physico chimique des protéines membranaires (LBPCPM), France
Vassiliy Bavro,
University of Essex, United Kingdom

****Correspondence:***
Susan K. Buchanan
susan.buchanan2@nih.gov

Specialty section:
This article was submitted to Microbial Physiology and Metabolism, a section of the journal Frontiers in Microbiology

Received: *11 January 2022*
Accepted: *21 March 2022*
Published: *07 April 2022*

Citation:
Ratliff AC, Buchanan SK and Celia H (2022) The Ton Motor. Front. Microbiol. 13:852955. doi: 10.3389/fmicb.2022.852955

INTRODUCTION

The bacterial outer membrane (OM) is the first line of defense for Gram-negative bacteria against its environment. The outer membrane forms a resistant barrier against toxins and environmental threats yet must allow a variety of substances to cross without compromising the membrane. The OM can be permeated through outer membrane proteins that facilitate the diffusion of small molecules and nutrients into the periplasm (Nikaido, 2003; Vergalli et al., 2019). The OM lacks a hydrolysable energy source or an electrochemical gradient; thus, some nutrients are large or at low concentrations are actively transported across the OM with the aid of the Ton complex. Ton is a multi-subunit membrane protein complex (TonB–ExbB–ExbD) that uses the proton gradient across the inner membrane as its energy source (**Figure 1**). At the inner membrane, ExbB and ExbD harness the proton motive force (pmf) and transfer it to the TonB subunit. TonB is anchored to the inner membrane by a single N-terminal transmembrane helix and has an ordered C-terminal domain linked by a central proline-rich periplasmic domain (Kohler et al., 2010). This linker is long enough to span the whole periplasmic space, allowing the TonB C-terminal domain to reach the OM and interact with TonB-dependent transporters (TBDTs), providing energy for nutrient import. In this review, we will discuss the gaps in the knowledge about the structure of the complete Ton motor complex (TonB–ExbB–ExbD, or TBD), as well as the molecular interactions and mechanism by which the complex uses the pmf at the inner membrane to generate mechanical work at the outer membrane for the transport of nutrients.

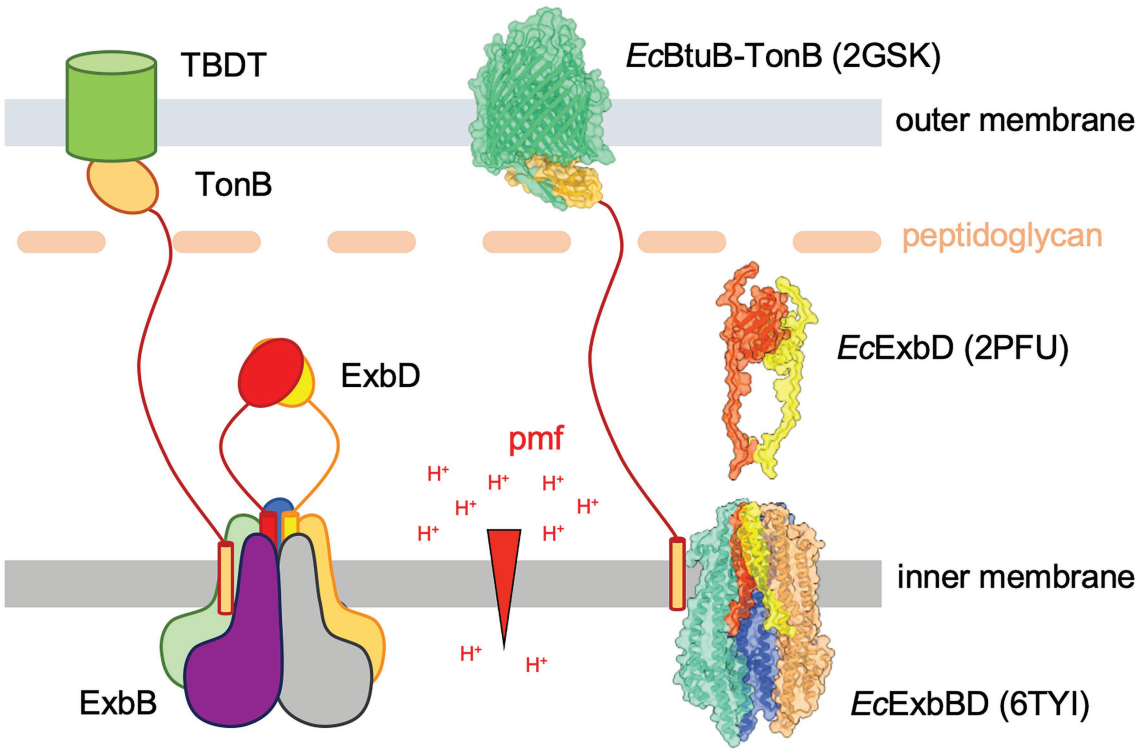


FIGURE 1 | A schematic representation of the Ton uptake system (left) and molecular models of the different components (right). Left panel: the TonB-dependent transporter (TBDT, green cylinder) is anchored in the outer membrane (OM). The ligand binds on the extracellular face of the TBDT and exposes a conserved domain called the TonB box to the periplasmic side. The TonB–ExbB–ExbD (TBD) complex is anchored in the inner membrane (IM) and uses the proton motive force (pmf, proton gradient across the IM, symbolized with the red arrowhead) to generate force and movement. The TBD complex is made of a pentamer of the ExbB subunit (blue, orange, grey, purple, and green) that defines a central pore in which a dimer of ExbD subunits (red and yellow) resides. The TonB subunit (gold) binds at the periphery of the ExbBD subcomplex. The elongated periplasmic domain of TonB allows its C-terminal globular domain to reach the OM and form a stable interaction with the TBDT TonB box. It is hypothesized that the ExbBD subcomplex forms the proton channel and that the energy derived from proton translocation is propagated through the TonB subunit to the TBDT, eventually opening a channel into the TBDT and allowing the bound ligand to diffuse into the periplasm. Right panel: molecular representations of known components of the *Escherichia coli* Ton system. The structural models are shown with ribbons and molecular surfaces. The color coding is the same than for the schematic view on the left. The TM and flexible periplasmic domain on the *Ec*TonB subunit are not known and shown as in the schematic representation. The crystallographic structure of *Ec*BtuB (green) in complex with the *Ec*TonB periplasmic domain (gold) is represented in the OM (pdb 2GSK; Shultis et al., 2006). Two models of the NMR structure of the *Ec*ExbD periplasmic domains are shown in red and yellow (pdb 2PFU; Garcia-Herrero et al., 2007). The cryo-EM structure of the *Ec*ExbBD complex is shown in the IM (pdb 6TYI; Celia et al., 2019). The grey and purple ExbB subunits are not represented in order to show the ExbD TM domains. Molecular graphics have been performed with UCSF ChimeraX (Pettersen et al., 2021).

OVERVIEW OF THE TON UPTAKE SYSTEM

TonB-dependent transporters are comprised of a 22-stranded ß-barrel C-terminal domain with a N-terminal plug domain inserted into the interior of the barrel (Noinaj et al., 2010). TBDTs import a range of small molecules and nutrients based on the specificity of the transporter, which include iron-siderophores, divalent metals, carbohydrates, cobalamin, and peptides (Schauer et al., 2008; Noinaj et al., 2010; Calmettes et al., 2015; Madej et al., 2020). Upon ligand binding on the extracellular face of the TBDT, conformational changes are induced, exposing the TonB box, a short, conserved N-terminal sequence, to the periplasm. The C-terminal periplasmic domain of the TonB subunit then interacts with the TBDT TonB box, forming a stable complex that physically connects the TBDT to the inner membrane with measured affinity up to tens of nanomolar (Freed et al., 2013; Sarver et al., 2018; Josts et al., 2019). What happens after the formation of the TBDT and TonB complex is widely unknown, but it is hypothesized that the energy from the pmf is transmitted to TonB and used to alter the conformation of the TBDT, eventually opening a channel in the TBDT.

STRUCTURES OF THE TON COMPLEX

Over the past decade the stoichiometry of ExbB and ExbD has been highly disputed, but recent reports strongly support that the ExbBD subcomplex has a 5:2 ratio with ExbB forming a pentameric hydrophobic central pore encircling a dimer of ExbD single helices (**Figure 1**; Celia et al., 2020). The first high-resolution structure of the *Ec*ExbBD subcomplex showed *Ec*ExbB as a pentameric structure (Celia et al., 2016). Mass

spectrometry experiments performed on *Escherichia coli*-native membranes further supported the pentameric nature of *Ec*ExbB (Chorev et al., 2018). Cryo-EM single-particle analysis (SPA) was also used to determine high-resolution structures of the ExbBD complexes from *E. coli*, *Pseudomonas savastanoi*, and *Serratia marcescens*, all revealing a 5:2 ratio (Celia et al., 2019; Deme et al., 2020; Biou et al., 2021).

MotAB and PomAB are the motor complexes that power the rotation of the flagellum, using the proton or sodium gradient, respectively. Both share extensive homology with ExbBD and are believed to derive from a common ancestor (Marmon, 2013; Lai et al., 2020).

MotAB, PomAB, and ExbBD share a high level of conservation in the transmembrane helices that form the central hydrophobic pore of ExbB/MotA/PomA. Recently published cryo-EM structures of MotAB and PomAB also confirmed 5:2 ratio of these motor complexes (Deme et al., 2020; Santiveri et al., 2020). For all these structures of ExbBD and MotAB determined by cryo-EM, the periplasmic domains of ExbD and MotB were not visible because of their high flexibility.

TonB appears to cycle through binding and release from TBDTs, sometimes referred to as the TonB energization cycle (Larsen et al., 1999; Kaserer et al., 2008; Gresock et al., 2015). While the structure of the *Ec*ExbBD subcomplex is now established, a detailed molecular description of a full TBD complex is not yet available. A cryo-EM map of the full *P. savastanoi PS*ExbB complex has been reported (EMD-10897; Deme et al., 2020). The 3.8 Å resolution structure clearly shows the *Ps*ExbB and *Ps*ExbD subunits, with an additional rod-like structure that likely corresponds to a single TMH of a TonB subunit. The density traverses the micelle on the exterior of the *Ps*ExbB complex and packs against a region of TM1 of one *Ps*ExbB, in a location predicted by analysis of covariance and close to the cytoplasmic leaflet of the membrane (Deme et al., 2020). The lower density and resolution of the TonB TMH in the cryo-EM map were attributed to a partial dissociation of TonB from ExbBD upon freezing. Cryo-EM SPA of the *E. coli Ec*TBD complex brought similar observations, showing the TonB TMH in a similar orientation compared to *Ec*ExbBD, and interacting with part of TM1 of *Ec*ExbB (H.C. unpublished results). The precise oligomeric state of TonB in the TBD complex is still not clearly known and needs to be further investigated.

Numerous studies have focused on the molecular interactions between the periplasmic domains of ExbD and TonB. The C-terminal domain of TonB can form a dimer *in vivo* (Sauter et al., 2003). The physiological importance of this dimer is not well-established, but it might be involved in the binding to the peptidoglycan (PG) layer, therefore localizing the TonB C-terminal domain close to the OM (Ghosh and Postle, 2004, 2005; Kaserer et al., 2008; Postle et al., 2010). The C-terminal folded domain of *Ec*ExbD is a dimer in the *Ec*ExbBD complex (**Figure 1**; Gresock et al., 2015; Celia et al., 2016). The *Ec*ExbD dimerization interface might be altered during the energization cycle as some *Ec*ExbD monomers were found to be interacting with the TonB C-terminal domain in a pmf-dependent fashion (Ollis and Postle, 2011, 2012). This network of interactions likely reflects a dynamic interplay between ExbD and TonB during the energization process.

Both TonB and ExbD have a flexible periplasmic linker between their TM and C-terminal folded domains (**Figure 1**). Recent studies have highlighted the importance of the disordered, periplasmic linker domain of *Ec*ExbD. A conserved motif just upstream of the TM domain of *Ec*ExbD, V45, V47, L49, and P50 was found to be required for Ton function (Kopp and Postle, 2020). The TonB periplasmic linker is long enough to allow the C-terminal folded domain of TonB to reach the TBDTs in the OM. Most TonB sequences exhibit a conserved proline-rich domain in the linker region that is suspected to adopt a poly-proline type II helical rod conformation, conferring rigidity to the linker (Chu et al., 2007; Kohler et al., 2010). However the presence of this poly-proline-rich domain was found nonessential for energy transduction (Larsen et al., 1994).

ExbBD AND MotAB SHARE A SIMILAR PROTON CHANNEL

The Ton, Tol, and Mot complexes use the pmf to generate movement and share extensive homology (Cascales et al., 2001; Marmon, 2013; Ratliff et al., 2021). Tol is involved in the regulation of the OM integrity and cell division through interaction with the OM-associated Pal-TolB protein complex. Mot is powering the flagellum rotation. The Ton and Tol complexes are the most closely related: the TonB–ExbB–ExbD and TolA–TolQ–TolR subunits have the same topology, are highly homologous, and cross-complementation between TolA and ExbBD, and TonB and TolQR, has been observed (Braun and Herrmann, 1993; Lloubes et al., 2012). While there is no reported structure of TolQR, it is expected to be very similar to ExbBD (for more information on the Tol system, see Szczepaniak et al., 2020; and the dedicated review in this issue of *Frontiers in Microbiology*).

The MotAB complex is homologous to ExbBD/TolQR but lacks a TonB/TolA-like subunit. It associates with the motility apparatus and uses the pmf to generate torque, driving the rotation of the flagellum (Minamino and Imada, 2015; Lai et al., 2020). Like ExbD and TolR, MotB has a single TM domain, followed by a flexible periplasmic linker and a folded C-terminal domain. Between the TM and the periplasmic linker, MotB has a conserved sequence that associates with MotA and acts as a plug that prevents the flux of protons through the complex (Hosking et al., 2006). It is believed that upon association of the MotAB complex to the flagellar apparatus, the C-terminal domains of MotB bind the PG and the plug domains dissociate from MotA, allowing the flux of proton and torque generation (Kojima et al., 2009, 2018; O'Neill et al., 2011).

Several high-resolution cryo-EM structures of MotAB have been reported, and all show the same 5:2 architecture as ExbBD (Celia et al., 2019; Deme et al., 2020; Santiveri et al., 2020; Biou et al., 2021). The transmembrane region that forms the pore encircling the ExbD/MotB TM helices is particularly conserved between MotAB and ExbBD (Deme et al., 2020;

Ratliff et al., 2021). The Taylor lab reported three distinct structures of the *Campylobacter jejuni Cj*MotAB complex: *Cj*MotAB in the plugged state, a construct lacking the *Cj*MotB plug domain, and a construct lacking the *Cj*MotB plug domain plus a substitution of the conserved essential Asp22 residue in the *Cj*MotB TM domain into Asn, so as to mimic the protonated state of Asp22 (Santiveri et al., 2020). Using Mole 2.5, a software that detects tunnels and cavities in macromolecules, a potential proton channel that connects the conserved Asp22 on *Cj*MotB to the periplasm was revealed (Pravda et al., 2018; Santiveri et al., 2020). Close to the opening on the periplasmic side, the side chain of residue Phe186 on *Cj*MotA TM4 was found in two different conformations, eventually acting as a gate that would open and close the proton channel to the periplasm. Sequence alignments show that the Phe186 is a conserved residue with a bulky side chain, mostly appearing as Leu in the consensus conserved sequence of MotA, ExbB, and TolQ (see **Figure 2E**; Cascales et al., 2001).

We used a similar approach to probe the structure of *Ec*ExbBD (PDB 6TYI) for potential channels. Using the same parameters for Mole 2.5 and omitting in the calculation the side chain of Leu178 in TM3 of *Ec*ExbB (equivalent of Phe186 in TM4 of *Cj*MotA), a channel was found that connects the periplasmic side of *Ec*ExbBD and the essential Asp25 on *Ec*ExbD TM that opens to the cytoplasmic cavity (**Figures 2A–D**). The channel opens between two *Ec*ExbB subunits (blue and green represented chains) on the periplasmic side, close to Phe156 (**Figures 2C,D**). In the configuration shown in **Figure 2C**, the channel is occluded by Leu178 side chain. As for Phe186 of *Cj*MotA, Leu178 could act as a gate that would modulate the opening of the proton channel. **Figure 2E** shows the consensus sequence resulting from multiple alignments of ExbB/TolQ/MotA and ExbD/TolR/MotB (Cascales et al., 2001). Highlighted in blue and green (*Ec*ExbB TM2-3) and red (*Ec*ExbD TM) are the residues that are lining up the channel found in the *Ec*ExbBD structure.

It is noteworthy that most of these conserved residues apparently involved in the channel formation are highly conserved among ExbB, TolQ, and MotA as shown in the consensus sequence **Figure 2E**. The channels for *Ec*ExbBD and *Cj*MotAB are remarkably similar, reflecting the high homology of the two systems, and likely a similar usage of proton translocation to generate movement.

Rotary models have been proposed for the MotAB complex to harness the pmf, which are discussed elsewhere in this issue of *Frontiers in Microbiology*. These models suggest that the MotA pentamer rotates around the MotB dimer at 36° increments for each proton translocated (Deme et al., 2020; Santiveri et al., 2020). While it is not yet clear what prompts the movement of MotA following the protonation/deprotonation of the conserved Asp on MotB, it is likely that a rotation mechanism is responsible for torque generation. Since the MotAB and ExbBD complexes are highly homologous, it is expected that the use of the pmf is the same and that the ExbB pentamer rotates around the ExbD dimer as well during proton translocation.

Based on these models, we propose a rotary model in which the ExbD TMs rotate by increments of 36° for each proton translocated (**Figure 2F**). It is hypothesized that the proton travels through the open channel from the periplasm to the highly conserved Asp on ExbD TM, inducing a change of conformation of protonated Asp that would drive the power stroke, resulting in the rotation of the two ExbD TMs by 36°. The change of conformation would close the channel on the side of the protonated Asp, while a new channel would open on the opposite ExbD TM, allowing a new cycle to take place. The rotation would then continue as long as the channels are in the open state. Is it not known how the proton channel opens, and how the open state is regulated, but it likely depends on the TonB subunit.

WRAP AND PULL MODEL MECHANISM

Several models for the mechanism of action of Ton have been proposed. They all rely on the association of the TonB C-terminal domain with the TBDT TonB box, and the application of force to displace or alter the conformation of the TBDT plug domain, either through rotation or pulling of TonB (Chimento et al., 2005; Klebba, 2016).

In the *pulling model*, the TonB C-terminal domain bound to the TBDT is pulled into the periplasm by the ExbBD complex and gradually unfolds the TBDT plug domain, eventually opening a channel large enough to allow the bound nutrient to diffuse toward the periplasm (Chimento et al., 2005). Molecular simulations using the BtuB TBDT in complex with TonB show that the interaction between BtuB and TonB is strong enough to sustain a pulling force perpendicular to the OM plane and would partially unfold the BtuB plug domain (Gumbart et al., 2007). This mechanism is supported by *in vitro* single-molecule force spectroscopy experiments on the BtuB/TonB and FhuA/TonB complexes, providing direct evidence that the interaction between TonB and the TonB box is strong and can withstand the amount of force needed to unfold half of the TBDT plug domain before dissociation occurs (Hickman et al., 2017).

Some bacteriocins bind TBDTs and hijack the Ton system to gain access and kill bacteria with high efficiency (Atanaskovic and Kleanthous, 2019). The bacteriocin pyocin S2 has its own TonB box motif and has been shown to translocate through the *P. aeruginosa* iron transporter FpvAI (White et al., 2017). Pyocin S2 binds FpvAI at the same binding site than the natural pyoverdin-iron siderophore and initiates the partial unfolding of the plug domain through interaction of the FpvA TonB box with TonB. The TonB box motif of pyocin S2 is then presented to TonB through the channel created, and the force exerted by the Ton system eventually unfolds the pyocin and drags it into the periplasm (White et al., 2017). This work represents the first time the translocation of a bacteriocin through a TBDT was shown, and the mechanism is in good agreement with the pulling model.

To reconciliate the pulling model with an eventual rotation of ExbBD, we propose a model in which the rotation of the ExbD dimer leads to the wrapping of the TonB linker around

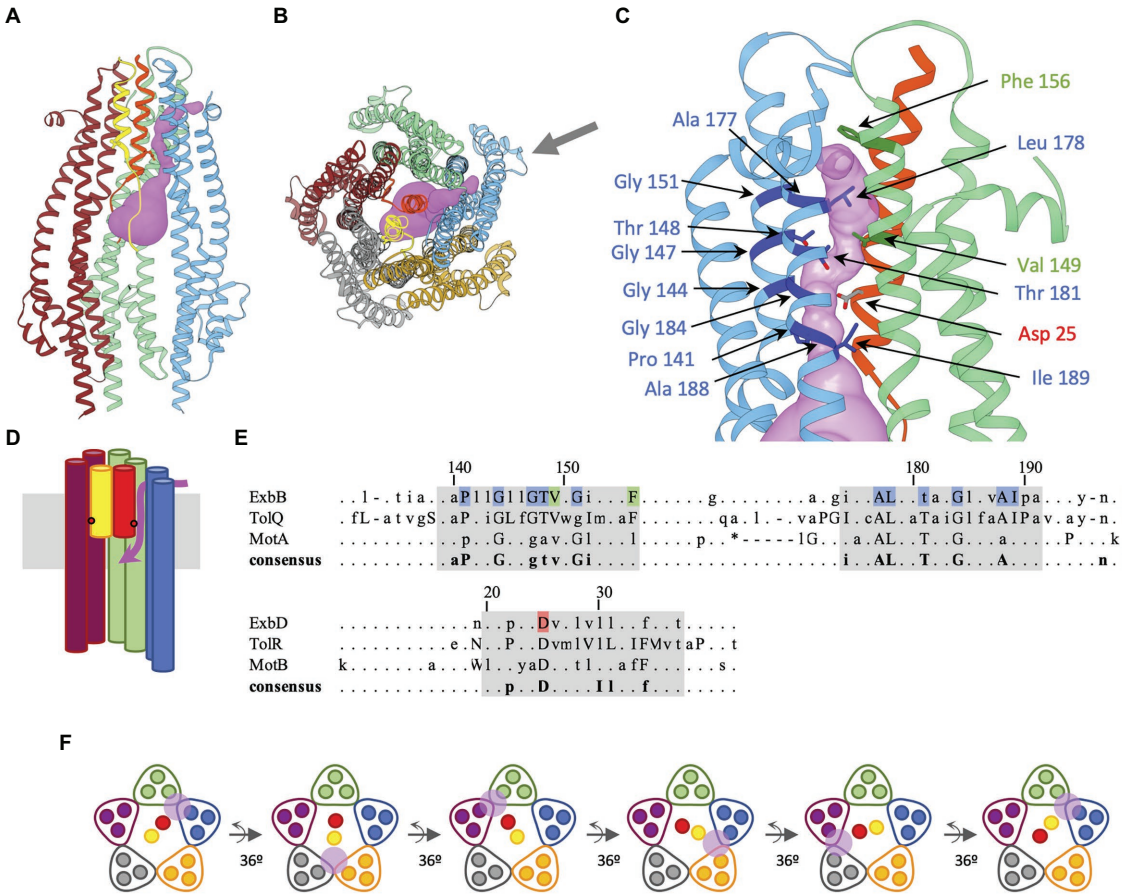


FIGURE 2 | Predicted proton channel in *Ec*ExbBD, sequence conservation of residues lining the channel, and rotary model of the ExbD TMs in the ExbB pentamer. The color coding of the different subunits is the same as in **Figure 1**. **(A)** Ribbon representation of the *Ec*ExbBD complex (pdb 6TYI), with the predicted proton channel represented as pink isosurface. For clarity, two ExbB subunits (grey and orange) have been omitted to reveal the interior of the complex. The blue and green *Ec*ExbB subunits are involved in the channel formation. The TM helices of *Ec*ExbD are colored yellow and red, with the side chains of the essential Asp25 represented as ball and sticks. The red helix is involved in the formation of the channel. **(B)** Same ribbon representation as **(A)**, but viewed from the periplasm, all the *Ec*ExbBD subunits are shown. The online version of Mole 2.5 (https://mole.upol.cz/; Pravda et al., 2018) was used to probe for cavities and channels in the *Ec*ExbBD structure. The same parameters reported for the *Cj*MotAB channel (Santiveri et al., 2020) were used: 1 Å radius bottleneck, and omission of Leu178 side chain for the calculation. The black arrow shows the direction of viewing for **(C)**. **(C)** Enlarged view of the channel. Only the *Ec*ExbB and *Ec*ExbD subunits involved in the channel formation are shown (blue, green, and red). The most conserved residues in the consensus sequence shown in **(E)** are highlighted in darker colors and side chains are shown as ball and stick. **(D)** Schematic representation of **(A)**, showing the path of the channel. Only the TMs 2 and 3 of the blue, green, and purple *Ec*ExbB subunits are shown. The approximate location of the conserved Asp on *Ec*ExbD TM is shown with red dots. The membrane is shown in grey. The channel is symbolized in pink. It opens between the blue and green *Ec*ExbB subunits on the periplasmic side, connects to the Asp25 of the red *Ec*ExbD TM, and opens on the cytoplasmic cavity of the *Ec*ExbB pentamer. **(E)** Consensus from the multiple sequence alignment of ExbB/TolQ/MotA last two TM domains and ExbD/TolR/MotB TM domain, adapted from Figure 4 from Cascales et al. (2001). Lowercase letters represent residues present in the 60% consensus and uppercase letters for residues in the 90% consensus. Gaps are marked "–" and "*" when present in the 90 and 60% consensus, respectively (Cascales et al., 2001). The numbering corresponds to the *E. coli* sequences of ExbB and ExbD. The highlighted residues in blue, green, and red are the ones shown with arrows on **(C)**. They all are in the 90% consensus range, except for Thr181. The regions highlighted in grey correspond to the last two TMs of ExbB, TolQ, and MotA, and the single TM of ExbD, TolR, and MotB. **(F)** Rotary model of ExbBD. The view is the same as in **(B)** and shows a schematic slice of the TM domains of ExbB and ExbD. The positions of the proton channel are shown with the pink circle. The cycle starts with the channel opening between the green and blue ExbB subunits. The proton travels to the conserved Asp on the red ExbD TM, inducing a conformational change resulting in the rotation of the two ExbD TMs by 36°. The conformational changes lead to the closure of the channel between the green and blue ExbB subunits, while a new channel opens between the grey and orange ExbB subunits. A second proton now travels to the Asp on the yellow ExbD TM, resulting in a new rotation of 36°. The channel between the grey and orange ExbB subunits closes, while a new channel opens between the purple and green subunits, allowing a third proton to travel to the Asp on the red ExbD TM. The rotation can proceed as long as the channels are in the open state. Molecular graphics have been performed with UCSF Chimera (Pettersen et al., 2004).

ExbD, leading to the pulling of the TonB C-terminal domain bound to the TBDT TonB box (**Figure 3**). In this model, the tethering of TonB to the OM, through the interaction between the TonB C-terminal domain and the TBDT TonB box, induces a conformational change in ExbBD that opens the proton channel. The translocation of protons through ExbBD leads to the rotation of the ExbD dimer within the ExbB pentamer (**Figure 2F**) and the associated TonB. The periplasmic domain

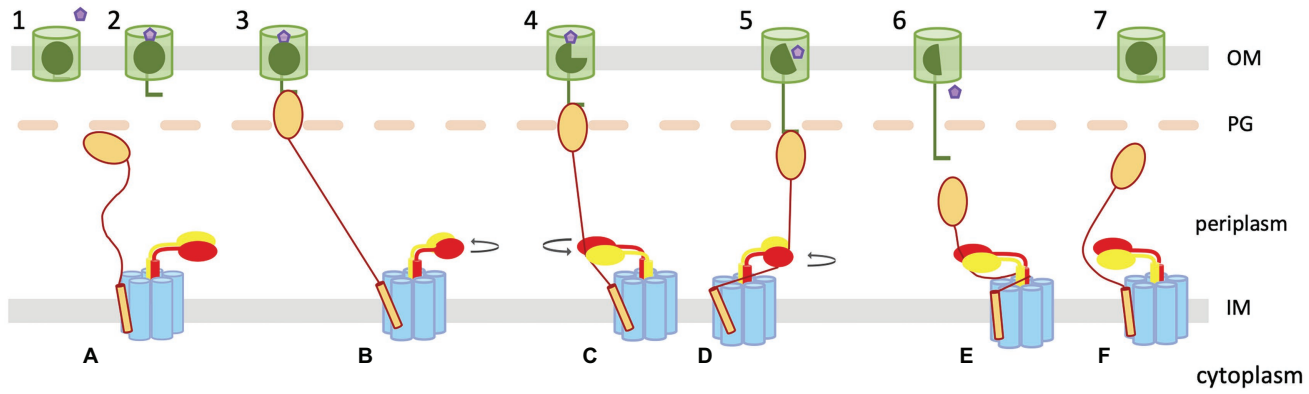


FIGURE 3 | Wrap and pull mechanistic model. The TBDT in the OM is represented with a green cylinder, with the plug domain and TonB box in dark green. The ligand to be transported is represented as a pink pentagon. TonB–ExbB–ExbD in the inner membrane are shown in gold (TonB), blue (ExbB), and red and yellow (ExbD), respectively. (1) The TBDT binds to its ligand inducing the exposure of the TonB box (2). **(A)** The TBD complex is in its resting state. The TonB C-terminal domain binds to the exposed TonB box of the loaded TBDT (3; **B**) tethering TonB to the OM, and somehow inducing a conformational change in ExbBD that opens the proton channel, triggering the rotation of the ExbD dimer **(B)**. (4; **C**) The rotation of ExbD leads to direct contact of ExbD with the TonB periplasmic linker and starts to pull on the C-terminal domain of TonB bound to the TBDT. **(D)** While the rotation of ExbD continues, the TonB linker wraps around ExbD, pulling further on the TonB–TBDT complex, partially unfolding the TBDT plug domain (5). (6) The unfolding of the plug domain reaches a point where the opening of the channel allows the ligand to diffuse to the periplasm, and the force necessary to unfold the rest of the plug is greater than the force necessary to maintain the interaction between TonB and the TonB box. TonB then dissociates from the TBDT **(E)**, releasing the tension on the TonB periplasmic linker and reverting the ExbBD complex to the closed state. (7) The plug domain folds back into the TBDT barrel; and **(F)** the TBD complex goes back to its resting state.

of ExbD comes into contact with the TonB periplasmic linker, which starts to wrap around ExbD while the rotation proceeds. The wrapping of the two proteins leads to a pulling motion on the C-terminal domain of TonB, which gradually unfolds the plug domain of the TBDT. With the unfolding of the plug domain proceeding, a channel through the TBDT gradually opens, allowing the ligand to move into the periplasm. At some point, the force necessary to further unfold the plug domain is greater than the interaction between the TonB box and TonB, causing TonB to dissociate from the TBDT. TonB is no longer tethered to the OM, causing the proton channel to close. The TonB box and plug domains fold back into the TBDT barrel, and the TonB linker unwraps, reverting both the TBDT and TBD complex to their resting states.

Further work is needed to better understand how the Ton system functions. The high-resolution structures of ExbBD and MotAB have provided insights on how the pmf is used by these protein complexes. The high structural and sequence homologies between the two systems suggest that they share the same mechanism, and any new information gathered on one system will likely translate to the other. Some of the important unanswered questions for the Ton system are: how is the signal of the binding of TonB to the TBDT TonB box at the OM transmitted to TBD at the IM? what are the molecular events that open the proton channel in ExbBD?; and how is the potential rotation of ExbB and ExbD transferred to TonB? A combination of *in vivo* and *in vitro* approaches is needed to further understand this multicompartment system.

AUTHOR CONTRIBUTIONS

AR, SB, and HC contributed to writing the manuscript and editing. HC prepared figures. All authors contributed to the article and approved the submitted version.

FUNDING

AR, HC, and SB are supported by the Intramural Research Program of the NIH, National Institute of Diabetes and Digestive and Kidney Diseases (NIDDK).

REFERENCES

Atanaskovic, I., and Kleanthous, C. (2019). Tools and approaches for dissecting protein Bacteriocin import in gram-negative bacteria. *Front. Microbiol.* 10:646. doi: 10.3389/fmicb.2019.00646

Biou, V., Diogo Adaixo, R.J., Chami, M., Coureux, P.-D., Laurent, B., Ntsogo, Y., et al. (2021). Functional and structural characterization of *Serratia marcescens* ExbB: determinants of the interaction with HasB/TonB. bioRxiv [Preprint]. doi: 10.1101/2021.04.21.440815

Braun, V., and Herrmann, C. (1993). Evolutionary relationship of uptake systems for biopolymers in *Escherichia coli*: cross-complementation between the TonB-ExbB-ExbD and the TolA-TolQ-TolR proteins. *Mol. Microbiol.* 8, 261–268. doi: 10.1111/j.1365-2958.1993.tb01570.x

Calmettes, C., Ing, C., Buckwalter, C. M., El Bakkouri, M., Chieh-Lin Lai, C., Pogoutse, A., et al. (2015). The molecular mechanism of zinc acquisition by the neisserial outer-membrane transporter ZnuD. *Nat. Commun.* 6:7996. doi: 10.1038/ncomms8996

Cascales, E., Lloubes, R., and Sturgis, J. N. (2001). The TolQ-TolR proteins energize TolA and share homologies with the flagellar motor proteins MotA-MotB. *Mol. Microbiol.* 42, 795–807. doi: 10.1046/j.1365-2958.2001.02673.x

Celia, H., Botos, I., Ni, X., Fox, T., De Val, N., Lloubes, R., et al. (2019). Cryo-EM structure of the bacterial ton motor subcomplex ExbB-ExbD

provides information on structure and stoichiometry. *Commun. Biol.* 2:358. doi: 10.1038/s42003-019-0604-2

Celia, H., Noinaj, N., and Buchanan, S. K. (2020). Structure and stoichiometry of the ton molecular motor. *Int. J. Mol. Sci.* 21:375. doi: 10.3390/ijms21020375

Celia, H., Noinaj, N., Zakharov, S. D., Bordignon, E., Botos, I., Santamaria, M., et al. (2016). Structural insight into the role of the ton complex in energy transduction. *Nature* 538, 60–65. doi: 10.1038/nature19757

Chimento, D. P., Kadner, R. J., and Wiener, M. C. (2005). Comparative structural analysis of TonB-dependent outer membrane transporters: implications for the transport cycle. *Proteins* 59, 240–251. doi: 10.1002/prot.20416

Chorev, D. S., Baker, L. A., Wu, D., Beilsten-Edmands, V., Rouse, S. L., Zeev-Ben-Mordehai, T., et al. (2018). Protein assemblies ejected directly from native membranes yield complexes for mass spectrometry. *Science* 362, 829–834. doi: 10.1126/science.aau0976

Chu, B. C., Peacock, R. S., and Vogel, H. J. (2007). Bioinformatic analysis of the TonB protein family. *Biometals* 20, 467–483. doi: 10.1007/s10534-006-9049-4

Deme, J. C., Johnson, S., Vickery, O., Aron, A., Monkhouse, H., Griffiths, T., et al. (2020). Structures of the stator complex that drives rotation of the bacterial flagellum. *Nat. Microbiol.* 5, 1553–1564. doi: 10.1038/s41564-020-0788-8

Freed, D. M., Lukasik, S. M., Sikora, A., Mokdad, A., and Cafiso, D. S. (2013). Monomeric TonB and the Ton box are required for the formation of a high-affinity transporter-TonB complex. *Biochemistry* 52, 2638–2648. doi: 10.1021/bi3016108

Garcia-Herrero, A., Peacock, R. S., Howard, S. P., and Vogel, H. J. (2007). The solution structure of the periplasmic domain of the TonB system ExbD protein reveals an unexpected structural homology with siderophore-binding proteins. *Mol. Microbiol.* 66, 872–889. doi: 10.1111/j.1365-2958.2007.05957.x

Ghosh, J., and Postle, K. (2004). Evidence for dynamic clustering of carboxy-terminal aromatic amino acids in TonB-dependent energy transduction. *Mol. Microbiol.* 51, 203–213. doi: 10.1046/j.1365-2958.2003.03816.x

Ghosh, J., and Postle, K. (2005). Disulphide trapping of an in vivo energy-dependent conformation of *Escherichia coli* TonB protein. *Mol. Microbiol.* 55, 276–288. doi: 10.1111/j.1365-2958.2004.04384.x

Gresock, M. G., Kastead, K. A., and Postle, K. (2015). From Homodimer to heterodimer and Back: elucidating the TonB energy transduction cycle. *J. Bacteriol.* 197, 3433–3445. doi: 10.1128/JB.00484-15

Gumbart, J., Wiener, M. C., and Tajkhorshid, E. (2007). Mechanics of force propagation in TonB-dependent outer membrane transport. *Biophys. J.* 93, 496–504. doi: 10.1529/biophysj.107.104158

Hickman, S. J., Cooper, R. E. M., Bellucci, L., Paci, E., and Brockwell, D. J. (2017). Gating of TonB-dependent transporters by substrate-specific forced remodelling. *Nat. Commun.* 8:14804. doi: 10.1038/ncomms14804

Hosking, E. R., Vogt, C., Bakker, E. P., and Manson, M. D. (2006). The *Escherichia coli* MotAB proton channel unplugged. *J. Mol. Biol.* 364, 921–937. doi: 10.1016/j.jmb.2006.09.035

Josts, I., Veith, K., and Tidow, H. (2019). Ternary structure of the outer membrane transporter FoxA with resolved signalling domain provides insights into TonB-mediated siderophore uptake. *elife* 8:e48528. doi: 10.7554/eLife.48528

Kaserer, W. A., Jiang, X., Xiao, Q., Scott, D. C., Bauler, M., Copeland, D., et al. (2008). Insight from TonB hybrid proteins into the mechanism of iron transport through the outer membrane. *J. Bacteriol.* 190, 4001–4016. doi: 10.1128/JB.00135-08

Klebba, P. E. (2016). ROSET model of TonB action in gram-negative bacterial iron acquisition. *J. Bacteriol.* 198, 1013–1021. doi: 10.1128/JB.00823-15

Kohler, S. D., Weber, A., Howard, S. P., Welte, W., and Drescher, M. (2010). The proline-rich domain of TonB possesses an extended polyproline II-like conformation of sufficient length to span the periplasm of gram-negative bacteria. *Protein Sci.* 19, 625–630. doi: 10.1002/pro.345

Kojima, S., Imada, K., Sakuma, M., Sudo, Y., Kojima, C., Minamino, T., et al. (2009). Stator assembly and activation mechanism of the flagellar motor by the periplasmic region of MotB. *Mol. Microbiol.* 73, 710–718. doi: 10.1111/j.1365-2958.2009.06802.x

Kojima, S., Takao, M., Almira, G., Kawahara, I., Sakuma, M., Homma, M., et al. (2018). The helix rearrangement in the Periplasmic domain of the Flagellar stator B subunit activates peptidoglycan binding and ion influx. *Structure* 26, 590–598.e5. doi: 10.1016/j.str.2018.02.016

Kopp, D. R., and Postle, K. (2020). The intrinsically disordered region of ExbD is required for signal transduction. *J. Bacteriol.* 202, e00687–e00719. doi: 10.1128/JB.00687-19

Lai, Y. W., Ridone, P., Peralta, G., Tanaka, M. M., and Baker, M. A. B. (2020). Evolution of the stator elements of rotary prokaryote motors. *J. Bacteriol.* 202, e00557–e00619. doi: 10.1128/JB.00557-19

Larsen, R. A., Thomas, M. G., and Postle, K. (1999). Protonmotive force, ExbB and ligand-bound FepA drive conformational changes in TonB. *Mol. Microbiol.* 31, 1809–1824. doi: 10.1046/j.1365-2958.1999.01317.x

Larsen, R. A., Wood, G. E., and Postle, K. (1994). The conserved proline-rich motif is not essential for energy transduction by *Escherichia coli* TonB protein. *Mol. Microbiol.* 12:857. doi: 10.1111/j.1365-2958.1994.tb01072.x

Lloubes, R., Goemaere, E., Zhang, X., Cascales, E., and Duche, D. (2012). Energetics of colicin import revealed by genetic cross-complementation between the Tol and Ton systems. *Biochem. Soc. Trans.* 40, 1480–1485. doi: 10.1042/BST20120181

Madej, M., White, J. B. R., Nowakowska, Z., Rawson, S., Scavenius, C., Enghild, J. J., et al. (2020). Structural and functional insights into oligopeptide acquisition by the RagAB transporter from Porphyromonas gingivalis. *Nat. Microbiol.* 5, 1016–1025. doi: 10.1038/s41564-020-0716-y

Marmon, L. (2013). Elucidating the origin of the ExbBD components of the TonB system through Bayesian inference and maximum-likelihood phylogenies. *Mol. Phylogenet. Evol.* 69, 674–686. doi: 10.1016/j.ympev.2013.07.010

Minamino, T., and Imada, K. (2015). The bacterial flagellar motor and its structural diversity. *Trends Microbiol.* 23, 267–274. doi: 10.1016/j.tim.2014.12.011

Nikaido, H. (2003). Molecular basis of bacterial outer membrane permeability revisited. *Microbiol. Mol. Biol. Rev.* 67, 593–656. doi: 10.1128/mmbr.67.4.593-656.2003

Noinaj, N., Guillier, M., Barnard, T. J., and Buchanan, S. K. (2010). TonB-dependent transporters: regulation, structure, and function. *Annu. Rev. Microbiol.* 64, 43–60. doi: 10.1146/annurev.micro.112408.134247

O'Neill, J., Xie, M., Hijnen, M., and Roujeinikova, A. (2011). Role of the MotB linker in the assembly and activation of the bacterial flagellar motor. *Acta Crystallogr. D Biol. Crystallogr.* 67, 1009–1016. doi: 10.1107/S0907444911041102

Ollis, A. A., and Postle, K. (2011). The same periplasmic ExbD residues mediate in vivo interactions between ExbD homodimers and ExbD-TonB heterodimers. *J. Bacteriol.* 193, 6852–6863. doi: 10.1128/JB.06190-11

Ollis, A. A., and Postle, K. (2012). Identification of functionally important TonB-ExbD periplasmic domain interactions in vivo. *J. Bacteriol.* 194, 3078–3087. doi: 10.1128/JB.00018-12

Pettersen, E. F., Goddard, T. D., Huang, C. C., Couch, G. S., Greenblatt, D. M., Meng, E. C., et al. (2004). UCSF Chimera—a visualization system for exploratory research and analysis. *J. Comput. Chem.* 25, 1605–1612. doi: 10.1002/jcc.20084

Pettersen, E. F., Goddard, T. D., Huang, C. C., Meng, E. C., Couch, G. S., Croll, T. I., et al. (2021). UCSF ChimeraX: structure visualization for researchers, educators, and developers. *Protein Sci.* 30, 70–82. doi: 10.1002/pro.3943

Postle, K., Kastead, K. A., Gresock, M. G., Ghosh, J., and Swayne, C. D. (2010). The TonB dimeric crystal structures do not exist in vivo. *MBio* 1, e00307–e00310. doi: 10.1128/mBio.00307-10

Pravda, L., Sehnal, D., Tousek, D., Navratilova, V., Bazgier, V., Berka, K., et al. (2018). MOLEonline: a web-based tool for analyzing channels, tunnels and pores (2018 update). *Nucleic Acids Res.* 46, W368–W373. doi: 10.1093/nar/gky309

Ratliff, A. C., Buchanan, S. K., and Celia, H. (2021). Ton motor complexes. *Curr. Opin. Struct. Biol.* 67, 95–100. doi: 10.1016/j.sbi.2020.09.014

Santiveri, M., Roa-Eguiara, A., Kuhne, C., Wadhwa, N., Hu, H., Berg, H. C., et al. (2020). Structure and function of stator units of the bacterial Flagellar motor. *Cell* 183, 244–257.e16. doi: 10.1016/j.cell.2020.08.016

Sarver, J. L., Zhang, M., Liu, L., Nyenhuis, D., and Cafiso, D. S. (2018). A dynamic protein-protein coupling between the TonB-dependent transporter FhuA and TonB. *Biochemistry* 57, 1045–1053. doi: 10.1021/acs.biochem.7b01223

Sauter, A., Howard, S. P., and Braun, V. (2003). In vivo evidence for TonB dimerization. *J. Bacteriol.* 185, 5747–5754. doi: 10.1128/jb.185.19.5747-5754.2003

Schauer, K., Rodionov, D. A., and de Reuse, H. (2008). New substrates for TonB-dependent transport: do we only see the 'tip of the iceberg'? *Trends Biochem. Sci.* 33, 330–338. doi: 10.1016/j.tibs.2008.04.012

Shultis, D. D., Purdy, M. D., Banchs, C. N., and Wiener, M. C. (2006). Outer membrane active transport: structure of the BtuB:TonB complex. *Science* 312, 1396–1399. doi: 10.1126/science.1127694

Szczepaniak, J., Press, C., and Kleanthous, C. (2020). The multifarious roles of Tol-pal in gram-negative bacteria. *FEMS Microbiol. Rev.* 44, 490–506. doi: 10.1093/femsre/fuaa018

Vergalli, J., Bodrenko, I. V., Masi, M., Moynie, L., Acosta-Gutierrez, S., Naismith, J. H., et al. (2019). Porins and small-molecule translocation across the outer membrane of gram-negative bacteria. *Nat. Rev. Microbiol.* 18, 164–176. doi: 10.1038/s41579-019-0294-2

White, P., Joshi, A., Rassam, P., Housden, N. G., Kaminska, R., Goult, J. D., et al. (2017). Exploitation of an iron transporter for bacterial protein antibiotic import. *Proc. Natl. Acad. Sci. U. S. A.* 114, 12051–12056. doi: 10.1073/pnas.1713741114

Conflict of Interest: The authors declare that the research was conducted in the absence of any commercial or financial relationships that could be construed as a potential conflict of interest.

Publisher's Note: All claims expressed in this article are solely those of the authors and do not necessarily represent those of their affiliated organizations, or those of the publisher, the editors and the reviewers. Any product that may be evaluated in this article, or claim that may be made by its manufacturer, is not guaranteed or endorsed by the publisher.

Copyright © 2022 Ratliff, Buchanan and Celia. This is an open-access article distributed under the terms of the Creative Commons Attribution License (CC BY). The use, distribution or reproduction in other forums is permitted, provided the original author(s) and the copyright owner(s) are credited and that the original publication in this journal is cited, in accordance with accepted academic practice. No use, distribution or reproduction is permitted which does not comply with these terms.

frontiers in Microbiology

REVIEW
published: 03 March 2022
doi: 10.3389/fmicb.2022.852176

Force-Generation by the Trans-Envelope Tol-Pal System

*Melissa N. Webby†, Daniel P. Williams-Jones†, Cara Press and Colin Kleanthous**

Department of Biochemistry, University of Oxford, Oxford, United Kingdom

The Tol-Pal system spans the cell envelope of Gram-negative bacteria, transducing the potential energy of the proton motive force (PMF) into dissociation of the TolB-Pal complex at the outer membrane (OM), freeing the lipoprotein Pal to bind the cell wall. The primary physiological role of Tol-Pal is to maintain OM integrity during cell division through accumulation of Pal molecules at division septa. How the protein complex couples the PMF at the inner membrane into work at the OM is unknown. The effectiveness of this trans-envelope energy transduction system is underscored by the fact that bacteriocins and bacteriophages co-opt Tol-Pal as part of their import/infection mechanisms. Mechanistic understanding of this process has been hindered by a lack of structural data for the inner membrane TolQ-TolR stator, of its complexes with peptidoglycan (PG) and TolA, and of how these elements combined power events at the OM. Recent studies on the homologous stators of Ton and Mot provide a starting point for understanding how Tol-Pal works. Here, we combine *ab initio* protein modeling with previous structural data on sub-complexes of Tol-Pal as well as mutagenesis, crosslinking, co-conservation analysis and functional data. Through this composite pooling of *in silico*, *in vitro*, and *in vivo* data, we propose a mechanism for force generation in which PMF-driven rotary motion within the stator drives conformational transitions within a long TolA helical hairpin domain, enabling it to reach the TolB-Pal complex at the OM.

Keywords: Tol-Pal, proton motive force, cell envelope, Gram-negative bacteria, force transduction, outer membrane

OPEN ACCESS

Edited by:
Michael Manson,
Texas A&M University, United States

Reviewed by:
Thomas Bernhardt,
Harvard Medical School,
United States
Ariane Briegel,
Leiden University, Netherlands

***Correspondence:**
Colin Kleanthous
colin.kleanthous@bioch.ox.ac.uk

†These authors have contributed equally to this work

Specialty section:
This article was submitted to Microbial Physiology and Metabolism, a section of the journal Frontiers in Microbiology

Received: *10 January 2022*
Accepted: *26 January 2022*
Published: *03 March 2022*

Citation:
Webby MN, Williams-Jones DP, Press C and Kleanthous C (2022) Force-Generation by the Trans-Envelope Tol-Pal System. Front. Microbiol. 13:852176. doi: 10.3389/fmicb.2022.852176

INTRODUCTION

The cell envelope of Gram-negative bacteria is a three-layered structure that protects the cell and enables survival in changing, often hostile environments. The asymmetric outer membrane (OM) has an outer leaflet of lipopolysaccharide (LPS) and an inner leaflet of phospholipids that exclude both hydrophilic and hydrophobic molecules (Nikaido, 2003). The OM is not an energized membrane, thus active processes at the OM require energy input from either ATP hydrolysis in the cytoplasm or coupling to the proton motive force (PMF). One such active process is constriction of the OM during cell division. As bacterial cells divide, the cell envelope must be remodeled, a process that involves the Tol-Pal system (Gerding et al., 2007). Tol-Pal spans the cell envelope exploiting the PMF to coordinate separation of daughter cells and facilitate accumulation of the peptidoglycan (PG)-binding lipoprotein Pal at division sites, which provides stabilization of the OM during division (Lazzaroni et al., 1999; Cascales et al., 2000; Gerding et al., 2007; Egan, 2018; Petiti et al., 2019; Szczepaniak et al., 2020a; Yakhnina and Bernhardt, 2020). In addition to its normal

physiological roles, Tol-Pal is exploited by group A bacteriocins and filamentous bacteriophages to promote their entry into Gram-negative bacteria (Nagel de Zwaig and Luria, 1967; Sun and Webster, 1986; Cascales et al., 2007; Kleanthous, 2010).

Seven genes are encoded within the *E. coli* Tol-Pal operon, including, *ybgC, tolQ, tolR, tolA, tolB, pal,* and *ybgF/cpoB* (Sturgis, 2001). However, the core components required for function comprise TolQ, TolR, TolA, TolB, and Pal. Perturbing this system by mutation and modulation of the expression of core genes confers a deleterious *tol* phenotype characterized by OM blebbing, cell-chaining, increased detergent/bile salt sensitivity, alteration of OM lipid ratios, and loss of pathogenicity (Bernadac et al., 1998; Szczepaniak et al., 2020b). Although the effects of *tol-pal* mutations are well-documented [reviewed in Szczepaniak et al. (2020b)], how force is transduced across the cell envelope is largely unknown despite a multitude of functional and biochemical studies on the individual proteins.

Recent data have suggested that a mobilization-and-capture mechanism underpins Tol-Pal function. The basis of the mechanism relies on force-dependent accumulation of Pal at division sites, where PG binding maintains cell wall interactions. Concentration of Pal at division sites prevents OM blebbing, a phenotype that is often observed in *tol-pal* mutants (Weigand et al., 1976; Weigand and Rothfield, 1976; Fung et al., 1978, 1980). This mechanism was first proposed by Szczepaniak et al. (2020b) who analyzed Pal-diffusion rates, showing that, in non-dividing cells, Pal diffuses slowly while in dividing cells Pal diffusion is accelerated (Connolley et al., 2021). Both the PMF and all components of the Tol-Pal system are required for these effects. In the proposed mechanism, TolB in the outer-periplasm (i.e., near the outer membrane) binds Pal to interrupt binding to PG (Bonsor et al., 2009), thereby increasing Pal diffusion in the OM. Following mobilization of Pal by TolB, the complex is recruited to the division site, where TolQ-TolR-TolA complexes accumulate (Gerding et al., 2007; Petiti et al., 2019). At the divisome, diffusing TolB-Pal complexes are captured by the TolQ-TolR-TolA complex and, in a force-dependent manner, Pal is released from TolB by TolA. Establishment of the TolA-TolB complex results in spatial segregation of TolB from Pal through translocation to the inner periplasm, where it is then released and free to diffuse and recycle. The force that drives this capture-release mechanism is hypothesized to rely on proton flux through the TolQ-TolR stator, which drives conformational changes in TolR and TolA in the periplasm.

To transmit force across the cell envelope, the TolQ-TolR-TolA complex likely transitions through a series of conformational states. This conformational plasticity hinders structural studies and is compounded by a lack of direct functional assays for TolQ-TolR-TolA activity *in vitro*. Nonetheless, structures for isolated domains of TolR (Parsons et al., 2008; Wojdyla et al., 2015) and TolA (Witty et al., 2002; Deprez et al., 2005; Lorenz et al., 2011; Ford et al., 2012; Li et al., 2012) from different species, in conjunction with structures of stator complexes from homologous systems, principally ExbB-ExbD (Celia et al., 2016, 2019; Hu et al., 2021) and MotA-MotB (Deme et al., 2020), provide insights into how the TolQ-TolR-TolA complex assembles. ExbB-ExbD is the inner membrane component of the Ton system, whilst MotA-MotB is the analogous complex in the Mot system. Like the Tol-Pal system, the Ton system and Mot system are protein complexes that span the cell envelope, transducing energy from the PMF across the inner membrane to facilitate nutrient import across the OM, and flagellum rotation, respectively. A multitude of structures for the Mot system components make this the best characterized of the three systems that are likely to function through a conserved mechanism. Unlike the Ton and Tol-Pal systems where a single copy of the stator complex is hypothesized to interact with periplasmic components TonB and TolA, respectively, multiple copies of the MotA-MotB stator complex interact in series with a large multimeric ring (the C-ring). Rotation of MotA about the stationary, PG-bound MotB, drives rotation of the flagellum via synchronized rotation of the C-ring (Deme et al., 2020; Johnson et al., 2021). Here, we review current structural and mutational data for TolQ-TolR-TolA and apply molecular modeling and co-conservation analysis to evaluate Tol-Pal function in the context of structural models. We propose a speculative mechanism to describe how the Tol-Pal system may utilize the PMF to transduce force to the OM during mobilization-and-capture of Pal.

TolQ FORMS A PENTAMERIC PORE IN THE INNER MEMBRANE

To understand mechanisms of force generation through the Tol-Pal system, we first reviewed current data for the IM stator complex formed by TolQ and TolR. Structural, biophysical, and native mass spectrometry data are consistent with stator complexes, including TolQ-TolR and homologs ExbB-ExbD and MotA-MotB, adopting a 5:2 stoichiometry (Celia et al., 2016, 2019; Deme et al., 2020; Santiveri et al., 2020). Recent structures of ExbB-ExbD and MotA-MotB solved by single-particle cryo-electron microscopy (EM) show that both ExbB and MotA form a conserved pentameric pore structure, suggesting that TolQ forms an analogous assembly. The monomeric structures of ExbB (244 amino acids in *E. coli*) and MotA (295 amino acids in *E. coli*) show that these proteins are predominantly helical. The first 100 amino acids at the N-terminus of these proteins form a variable number of short helices (**Figures 1A,B**). The remaining residues extend toward the C-terminus and assemble into two longer helices that span the membrane (**Figures 1A,B**). These transmembrane helices pack together to assemble the pentameric pore. The AlphaFold (Jumper et al., 2021) model of TolQ (230 amino acids in *E. coli*; **Figure 1C**) adopts an identical structural arrangement to that of ExbB (RSMD = 2.5 Å in Pymol), suggesting that the pentamers assemble in similar manner. We generated a TolQ pentamer through symmetry expansion of the AlphaFold monomer and energy minimization of the model using RosettaRelax (Khatib et al., 2011; Maguire et al., 2021; **Figure 1D**). The global assembly of the TolQ pore resembled the previously reported homology model (Szczepaniak et al., 2020b), although the *ab initio* model generated with Rosetta shows a distortion of helices that results in a wider pore relative to the homology model.

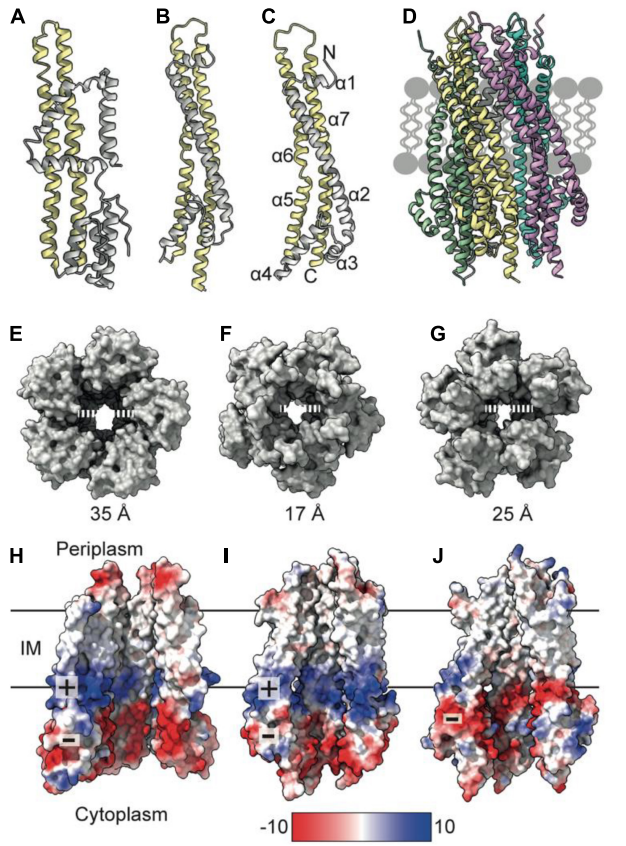


FIGURE 1 | TolQ forms a pentameric pore. **(A)** MotA monomer transmembrane helices pack together to form a pentameric pore (*yellow*) and accessory helices are located on the exterior of the pore (*gray*). **(B)** ExbB monomer colored as in panel **(A)**. **(C)** The TolQ monomer (*E. coli* AlphaFold model) colored as in panel **(A)**, adopts a structure like that observed for ExbB. **(D)** Pentameric TolQ complex was generated following symmetry expansion of the AlphaFold monomer and energy minimization using RosettaRelax. Each monomer is colored separately. **(E–G)** The MotA, ExbB, and TolQ pentamers viewed from the cytoplasm to show the outward movement of helices that generate an expanded pore. By contrast, the structures can be overlaid almost perfectly at the periplasmic side. **(H–J)** A cut through the electrostatic surface of the MotA, ExbB, and TolQ pentamers, respectively, showing that the cytoplasmic side of the pore has a region of negative charge that is conserved across all three systems. A band of positive charge that spans the center of the pore is only observed in MotA and ExbB.

Comparison of the pentameric structures for MotA, ExbB, and TolQ (**Figures 1E–G**) shows that the pore sizes on the periplasmic side of the pentamers are almost identical (∼25 Å). However, the diameter of the cytoplasmic pore is much wider in MotA (35 Å) relative to those of TolQ and ExbB, which are 25 and 17 Å, respectively (**Figures 1E–G**). Whether these differences have any physiological impact is unknown. The electrostatic profile of the interior of the MotA and ExbB pores comprises a region of positive charge spanning the middle section of the lumen, which sits directly above a band of negative charge (**Figures 1H–I**). In contrast, TolQ has only a single electronegative region spanning the lower section of the pore (**Figure 1J**). Across all structures, the location of the electronegative band within the pore is conserved, suggesting that electrostatics likely play a role in stator function.

TolR FORMS A DIMER THAT INSERTS WITHIN THE TolQ PORE

The periplasmic side of the stator pore in both MotA and ExbB is blocked by two helices (Celia et al., 2019; Deme et al., 2020) contributed by the dimer of MotB and ExbD, respectively. Assuming that the TolQR complex adopts an analogous 5:2 structure, it is likely to assemble in a similar manner, with the TolR dimer inserting within the pentameric pore of TolQ (**Figure 2A**). These transpore helices (TPHs) that bind TolQ are connected through a disordered linker sequence to the periplasmic domain of TolR, which binds to PG (Wojdyla et al., 2015). It is thought that the periplasmic domain of TolR extends and contracts via this disordered sequence to allow TolR to bind both TolQ and PG simultaneously. Structures of the periplasmic domain of the TolR dimer from both *E. coli* ($TolR^E$) and *H. influenzae* ($TolR^H$), respectively, have been solved to reveal that two distinct dimer conformations are adopted (**Figures 2B–E**). Because of the high degree of sequence conservation (60%) and identical secondary structure predictions, it is unlikely that the unique dimer conformations are species specific. Rather, it has been proposed that these two conformations represent different functional states, one capable of binding PG and one in which PG binding is occluded (Wojdyla et al., 2015).

The concept of transitioning between binding-competent and binding-incompetent conformations has also been proposed for MotB, where truncations of the N-terminal domain are thought to be associated with rearrangement of the C-terminal helix to occlude the PG-binding site (Roujeinikova, 2008). Later studies showed that it is the unfolding of the N-terminal helix that results in extension of the disordered linker sequence (Kojima et al., 2009; O'Neill et al., 2011). This extension allows MotB to reach and bind PG, stabilizing the complex and allowing protons to access the exposed MotA channel. This model suggests that rearrangement of the dimer to modulate PG binding might be a mechanism that is conserved across these molecular motors.

Analysis of the dimer structures for $TolR^E$ and $TolR^H$ reveals that, in the $TolR^E$ structure solved by X-ray crystallography (**Figure 2D**), TolR monomers are rotated ∼180° relative to each other, thereby obliterating the proposed PG binding cleft due to strand swapping (**Figures 2B,D**). In contrast, the $TolR^H$ dimer solved by NMR (Parsons et al., 2008) adopts an open conformation (**Figure 2D**), with a cleft appearing between the two monomers in which PG is proposed to bind (**Figure 2E**). Like MotB, the $TolR^H$ structure was obtained by truncating N- and C-terminal sequences that are otherwise present in the $TolR^E$ structure; 22 residues at the N-terminus form a short helix (residues 51–58) and β-strand (residues 81–86), while at the C-terminus 10 residues form another β-stand (residues 135–139). It is β-strand 1 of $TolR^E$ that is involved in generation of the strand-swapped dimer. To acquire more information regarding state transitions, we used Rosetta to generate a model of the

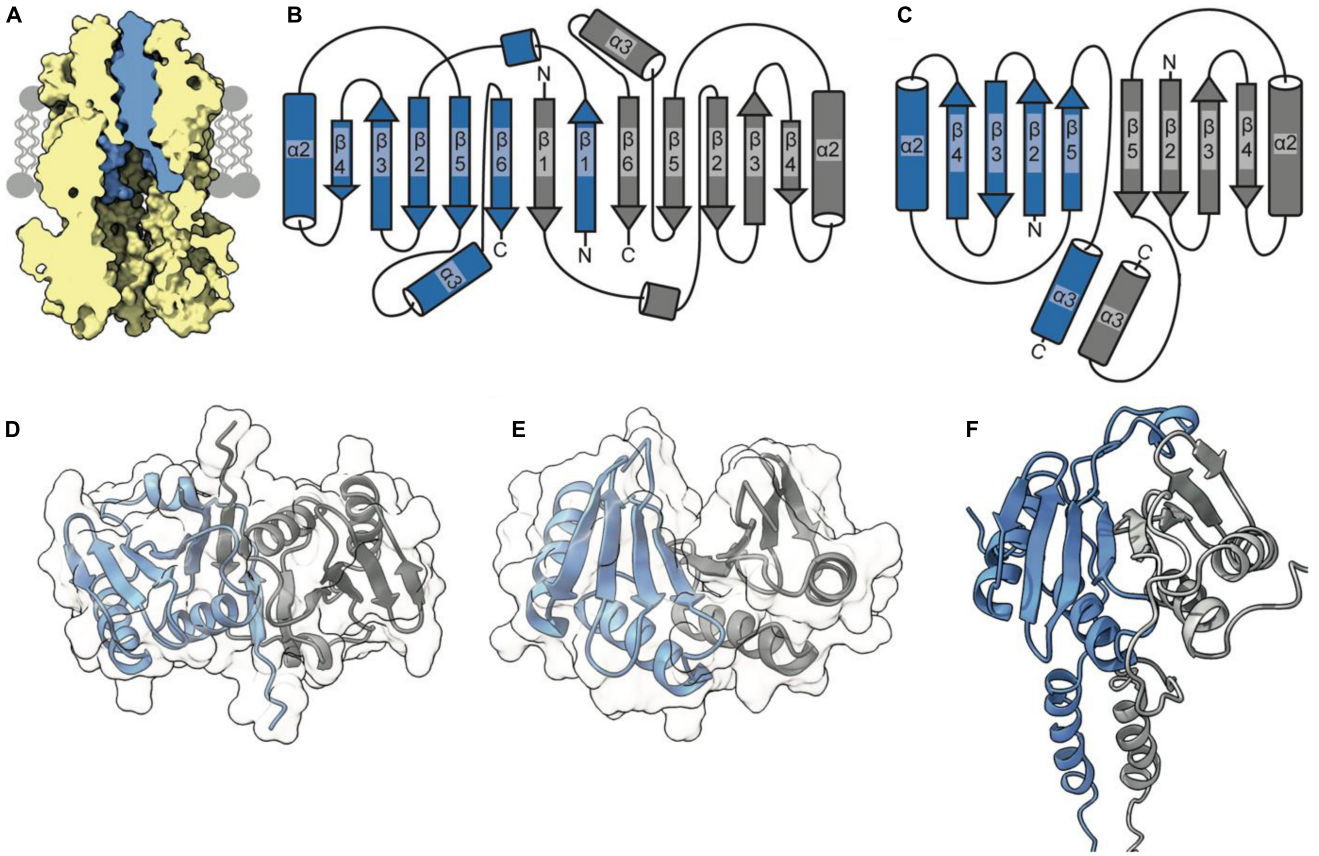


FIGURE 2 | The TolR dimer has two distinct conformations. **(A)** The periplasmic entrance to the TolQ (*yellow*) pore is blocked by the transpore helices of the TolR dimer (*blue*). The TolQ-TolR model shown was assembled following alignment of the AlphaFold TolR monomer with the truncated TolR dimer from *H. influenzae* ($TolR^H$). The full-length TolR dimer was then docked into the TolQ pentamer previously generated (**Figure 1**) based on position of ExbD in the ExbBD complex structure (Celia et al., 2019). The final TolQ-TolR complex shown was determined following energy minimization using RosettaRelax. **(B)** A depiction of the secondary structure of TolR from *E. coli* ($TolR^E$) highlighting the strand-swapped dimer formed by β1 and β6 of each monomer. **(C)** A depiction of the secondary structure of $TolR^H$ has a dimer interface formed through interactions of β5-β5. **(D)** The $TolR^E$ strand-swapped dimer (PDB ID 5BY4) solved by X-ray crystallography shows the 180° rotation of one monomer (*gray*) relative to the other (*blue*). **(E)** The $TolR^H$ structure solved by NMR (PDB ID 2JWK) is in an open PG-binding conformation. Each monomer is represented in *blue* and *gray*, respectively. **(F)** The *E. coli* TolR dimer, generated in Rosetta, models the entirety of the protein, which adopts an open conformation like that of $TolR^H$.

full-length *E. coli* TolR dimer (**Figure 2F**), starting from the monomer predicted by AlphaFold (Jumper et al., 2021). During model building the movement of the N-terminal TPH of TolR, which is involved in binding TolQ (**Figure 2A**), was more restricted than that of the periplasmic domain. The dimer model produced from Rosetta adopted a PG-binding conformation similar to that of $TolR^H$ (**Figure 2F**).

To generate the $TolR^E$ strand-swapped conformation from our TolR model, the dimer interface formed by β5-β5 interactions must be broken, and the β-sheet spanning residues 81–86 (β1) must form. In addition, one monomer must rotate ∼180° relative to the other (**Figure 2D**), which can only be achieved through breaking the dimer interface and moving the TPH upward (∼10–15 Å) out of the TolQ pore. Secondary structure predictions of *E. coli* TolR predict that the sequence corresponding to β6 has a high propensity to form a β-strand. However, residues 81–86 surrounding β1 are predicted to be disordered. Based on these secondary structure predictions and structural data, β1 and β6 are likely transient structures. We suggest that a strand-swapped dimer could form if β1 and β6 were present and if the TPHs were not fixed within the TolQ pore. Further experimental evidence is required to determine if TolR transitions between PG-binding competent and occluded states, or if these states are artifacts induced by sequence truncation and crystallization.

MUTAGENESIS AND CO-CONSERVATION ANALYSIS CORROBORATE INSERTION OF TolR INTO THE TolQ PORE

Recent structures of ExbB-ExbD and MotA-MotB provide insight into how the N-termini of dimeric ExbD and MotB bind within their respective pentameric pores. Using Rosetta and models of

ExbB-ExbD and MotA-MotB as a guide, we generated a model of the TolQ-TolR stator complex (**Figure 3**). Similar to MotB and ExbD, the single TPHs of the TolR dimer are arranged parallel to each other, effectively creating a plug that would prevent free diffusion of hydronium ions through TolQ. Interactions that support assembly of the complex are largely localized to the TPHs of TolR within the TolQ pore. The structured periplasmic domain of TolR is located 20 Å away from TolQ and does not form interactions with the pore. In the 10 top-scoring Rosetta models of TolR, the periplasmic domain is located at different distances from TolQ, while the remainder of the stator complex remains largely unperturbed. This situation likely reflects the dynamic nature of the disordered linker sequence connecting the periplasmic domain of TolR to the TPHs.

The reliability of the TolQ-TolR complex model was strengthened by demonstrating its consistency with previous mutation and functional data. Early studies, which assumed the TPH was transmembrane, focused on characterizing its position relative to the TolQ helices (Kampfenkel and Braun, 1993; Vianney et al., 1994; Zhang et al., 2009, 2011), and delineating potential proton-trafficking pathways by site-directed mutagenesis (Goemaere et al., 2007). The positions of mutated essential residues that yielded an OM instability phenotype map to the interior of the TolQ pore (**Figure 3A**). Moreover, these residues are predominantly located within the upper region of the TolQ pore that interacts with the TPHs of the TolR dimer.

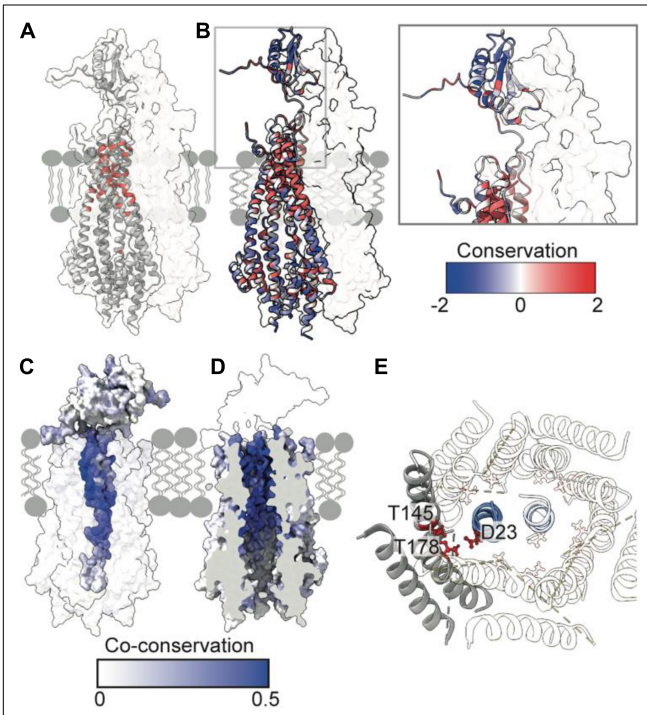


FIGURE 3 | Essential, conserved, and co-conserved stator residues map to the TolQR lumen. **(A)** *Red* identifies essential residues that confer membrane instability when substituted (Vianney et al., 1994; Goemaere et al., 2007; Zhang et al., 2011). Two TolQ monomers are shown in cartoon format with a single TolR monomer. **(B)** The relative conservation of TolQ-TolR residues, which was generated following alignment (Clustal Omega) of ten TolQ sequences from different species, indicates that the most conserved residues map to the top or bottom of the TolQ lumen. The most-conserved residues of TolR map to the transpore helix and β-strand two. **(C,D)** The TolQ-TolR co-conservation profile of individual residues as scored by RaptorX suggest that the TolR helix inserts into the center of the TolQ pore. Co-conserved TolR and TolQ residues are predominantly within the transpore helix and lumen, respectively. **(E)** A ring of highly conserved threonine residues (*red sticks*) within the transmembrane region of TolQ (T145 in helix 6 and T178 in helix 7) are proposed to stabilize protonated TolR D23 (*red sticks*), based on structures of the MotA-MotB and ExbB-ExbD complexes (Celia et al., 2019; Deme et al., 2020).

To identify regions of functional importance independently, sequence conservation of TolQ-TolR across 10 different species was calculated and mapped onto the TolQ-TolR model (**Figure 3B**). As expected, the most extensive sequence conservation was observed within the lumen of the TolQ pentamer rather than its exterior. Highly conserved residues were clustered at the upper and lower extremities of the pore, corresponding to the binding site for the TolR TPHs and a conserved electronegative region within the pentameric pore complex (**Figures 1J**, **3B**), respectively. For TolR, the most highly conserved residues mapped to the TPH and β2 (**Figure 3B**).

To differentiate between raw conservation and inter-subunit co-conservation, residue contact probabilities within the TolQ-TolR complex were scored with RaptorX (Zeng et al., 2018), and the highest pairwise score of individual residues mapped accordingly (**Figures 3C,D**). These computational data show that the residues with the highest co-conservation scores map to the luminal face of TolQ helix 7 (85% of the top 20 predicted contacts) and the TolR TPH (**Figures 3C,D**), supporting the proposed trans-pore insertion of TolR. The strongest co-conservation observed was between TolR V27-TolQ L175 (0.54), which are located on the same face within 9 Å of each other in our TolQ-TolR model. Similarly, the essential residue TolR D23, which is suggested to play a role in proton trafficking (Cascales et al., 2001; Goemaere et al., 2007), was highly co-conserved with TolQ T178 (0.50), and these residues are situated 4–5 Å of each other in the TolQ-TolR model (**Figure 3E**). TolQ T145 was previously suggested to play a role in PMF transduction (Goemaere et al., 2007), and it is also co-conserved with TolR D23, but with a lower probability (0.24) (**Figure 3E**). These aspartate and threonine residues are highly conserved across homologous stator systems (Braun and Herrmann, 1993), in accordance with the putative proton-conducting mechanisms proposed for MotA-MotB and ExbB-ExbD (Celia et al., 2019; Deme et al., 2020; Santiveri et al., 2020; Hu et al., 2021). TolR D23 is likely protonated (or coordinates a hydronium ion) and is stabilized by adjacent threonine residues before conformational changes result in rotation of TolQ relative to TolR, concomitant with proton release to the cytoplasm. As well as being both essential and co-conserved, the adjacent position of TolR D23 and TolQ T145/178 in the TolQ-TolR model, and their conservation across homologous stators, supports their proposed roles in proton trafficking and stabilization. Taken together, these sequence conservation and mutation analyses support structural models in which the TolR dimer inserts into

the TolQ pentamer, and protonation of TolR D23 is stabilized by a conserved threonine ring in TolQ.

TolA FORMS AN ELONGATED HELICAL HAIRPIN THAT COULD SPAN THE PERIPLASM

TolA is essential for bridging the TolQ-TolR-TolA complex from the IM through the periplasm to the OM. By doing so, it generates a connection from the stator to TolB and its complex with Pal. TonB, which forms a complex with ExbB-ExbD, is functionally equivalent to TolA. Low sequence conservation, especially in the regions that are thought to span the periplasm, suggests TolA and TonB are analogs lacking a common ancestor (Braun and Herrmann, 1993), although this is disputed (Witty et al., 2002). TolA is divided into three distinct domains (TolA I-III); an N-terminal domain anchoring the complex in the IM (TolA I), an elongated domain which forms an extended structure that spans the periplasm (TolA II), and a third, globular domain required for interactions at the OM (TolA III) (**Figure 4A**; Levengood et al., 1991; Levengood-Freyermuth et al., 1993). Although only limited structural data exists for TolA I and TolA II, the structure of TolA III from *E. coli* has been solved both in isolation and in complex with binding partner peptides, including bacteriophage proteins and colicins (Lubkowski et al., 1999; Lorenz et al., 2011; Ford et al., 2012; Li et al., 2012). TolA III forms a compact domain made up of three β-strands and three α-helices (**Figure 4B**). This domain arrangement is conserved across several species (**Figure 4B**). The extended structure of *Pseudomonas aeruginosa* TolA III reveals that helix three extends further than is observed in the *E. coli* structure (**Figure 4B**). SAXS models of TolA II-III confirm the predicted elongated structure of TolA II and combined with sequence-based secondary structure predictions and circular dichroism data, indicates that this domain likely forms a helical hairpin (Levengood et al., 1991; Witty et al., 2002). Although *ab initio* models and SAXS data are consistent with TolA II existing as an extended helical hairpin, TolA II likely exhibits both a helical hairpin ground state and a PMF-energized state where TolA II extends through holes in the PG to reach the OM. The conformational transitions within TolA

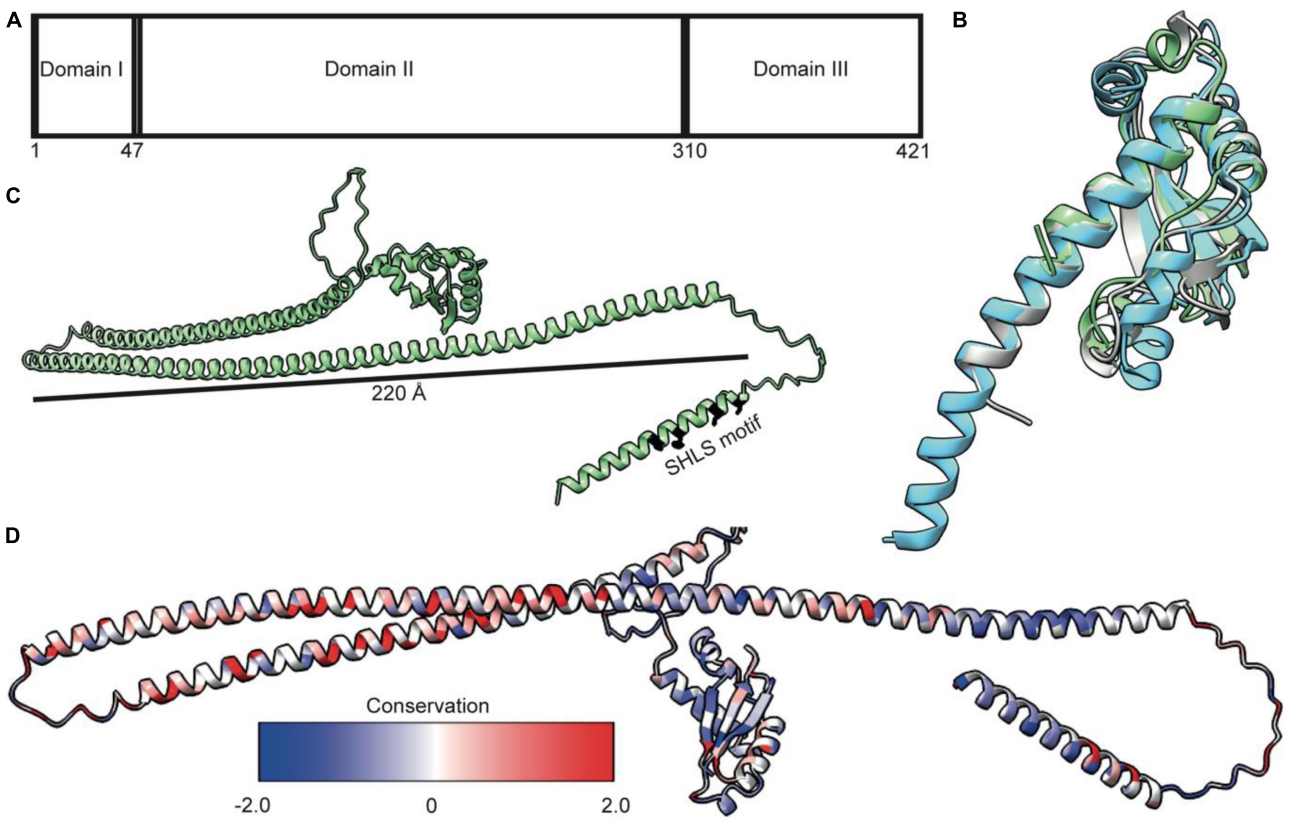


FIGURE 4 | TolA is a largely helical protein with three distinct domains. **(A)** TolA contains three annotated domains: domain I is the transmembrane helix, domain II is an elongated helical hairpin, and domain III is a small globular protein. Numbering is based on the *E. coli* sequence. **(B)** Structural overlay of TolA III from *P. aeruginosa* (*cyan*, PDB ID 1LR0) and *V. cholerae* (*gray*, PDB ID 4G7X) with the equivalent domain from *E. coli* (*green*, PDB ID 1S62) (RMSD of 1.3 and 2.0, respectively) showing that, although poorly conserved (20 and 25%, respectively), the domains have near identical folds. **(C)** The AlphaFold model of TolA from *E. coli.* The central domain II is predicted to form a helical hairpin that is 220 Å in length, which is long enough to span the periplasm. **(D)** Sequences of nine TolA proteins from different species were aligned in Clustal Omega, and sequence conservation was mapped onto the *E. coli* TolA structure within ChimeraX. Conserved residues are largely located within the C-terminal end of the helical hairpin of domain II. Residues in domains I and III are less conserved.

II have been shown to be PMF-dependent, with TolA I also required for energy transduction to the OM (Germon et al., 2001). This conclusion is supported by data that show tethering of TolA to the OM by colicins, bound at the OM but unable to translocate, restricts its diffusion in the inner membrane. However, upon abolition of the PMF, TolA exhibits unrestricted diffusion, suggesting that non-energized TolA cannot reach the OM (Rassam et al., 2018). Together, these data imply that energy dependent state transitions of TolA are an essential element of force transduction in Tol-Pal.

AlphaFold (Jumper et al., 2021) models of TolA from *P. aeruginosa* and *E. coli* (**Figure 4C**) show a single transmembrane helix within TolA I that is separated from TolA III by a helical hairpin that constitutes TolA II. The structures predicted by AlphaFold are consistent with the experimentally determined models for TolA III (**Figures 4B,C**). The hairpin structure of *P. aeruginosa* TolA II is 130 Å in length, whereas in *E. coli*, TolA II is 220Å in length, which is almost the entire width of the periplasm (250–300 Å) (Asmar et al., 2017). TolA sequences from nine Gram-negative bacteria show that most sequences are similar in the number of residues, with conserved residues located primarily within the helical hairpin structure of TolA II rather than in TolA I or TolA III (**Figure 4D**). This arrangement could suggest that TolA II interacts with other proteins through this domain, or that these residues are merely essential for ensuring that the helical hairpin structure forms to maintain the relative distance of TolA III from the IM. The C-terminal end of TolA II (residues 280–313) has previously been shown to bind the soluble periplasmic protein CpoB/YbgF; (Krachler et al., 2010). CpoB is not essential in *E. coli*, but its expression is tightly co-regulated within the *tol-pal* operon. CpoB binds TolA adjacent to the TolB-binding site of TolA III. It contains a number of so-called tetratricopeptide repeats (TPRs) that are typically found in protein-protein interaction hubs (D'Andrea and Regan, 2003). CpoB interacts with both TolA and the PG-synthase PBP1B (Gray et al., 2015), suggesting that TolA interactions with CpoB at the cell septum are temporally and spatially coordinated with the PG-remodeling complex PBP1B-LpoB. TolA was also found to interact with PBP1B directly, but this interaction was abrogated upon deletion of TolA I, suggesting that either energization is required for this interaction or that the binding site of PBP1B is within TolA I (Gray et al., 2015).

TolQ-TolR-TolA COMPLEX ASSEMBLY SUGGESTS THAT THE TolA TRANSMEMBRANE HELIX INSERTS INTO A TolQ GROOVE ON THE EXTERIOR OF THE TolQ PENTAMER

It has been suggested that TolA I associates with TolQ-TolR via an SHLS motif (**Figure 4C**), which was first identified in TonB, where it is essential both for stator association and PMF transduction (Karlsson et al., 1993; Koebnik et al., 1993). The SHLS motif denotes a non-consecutive, four-residue sequence composed of two serines, a histidine, and a leucine residue, which are located in the transmembrane helix of TonB and TolA. These residues are well conserved across species and are essential for activity. In *E. coli* TolA, this motif is composed of residues S18, H22, L29 and S33. Based on homology with the Ton system, in which maintenance of the position of SHLS residues is essential for ExbB binding (Larsen and Postle, 2001), it is reasonable to assume that this motif plays a similar role in the TolQ-TolA complex. In TonB, the unilateral geometry of S16 and H20 in the SHLS motif is essential for function (Larsen et al., 1994, 1999; Germon et al., 2001; Larsen and Postle, 2001). To date, very limited structural information is available for the TolQ-TolR-TolA complex. We used Rosetta to generate a low-energy model of TolQ-TolR-TolA (**Figure 5A**). In this model, TolA I sits parallel to the helices of TolQ, packed within a groove on the exterior of the pentamer structure (**Figure 5A**). The hydrophobic profile of the exterior of the TolQ-TolR-TolA complex (**Figure 5B**) shows that the position of TolA relative to TolQ creates a continuous hydrophobic

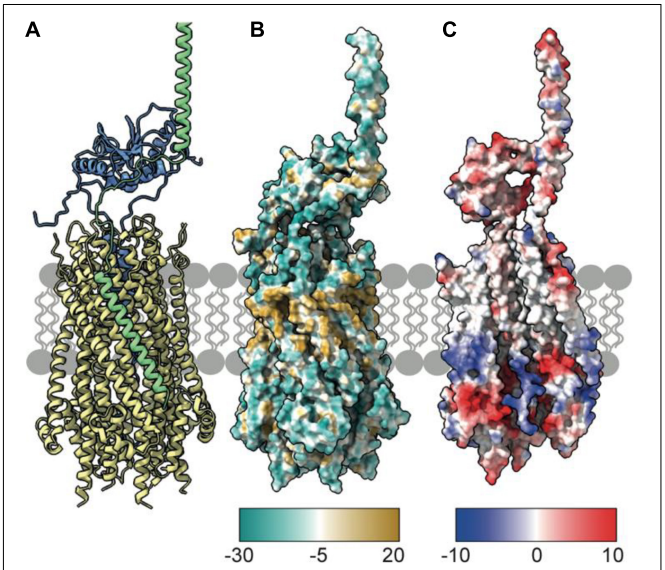


FIGURE 5 | TolA packs against the TolQ pentamer to form the TolQRA complex. **(A)** The Rosetta model of the TolQ-TolR-TolA complex from *E. coli* was generated following placement of full length TolA, taken from the AlphaFold database, within 10 Å of the TolQ-TolR complex (**Figure 2**). A series of Rosetta docking, and refinement steps were run to generate the lowest energy model shown. TolA (*green*) packs against the TolQ pentamer (*yellow*) with the transmembrane helix of TolA placed in a parallel arrangement within the exterior helices of TolQ. The TolR dimer sits above TolQ with its transpore helices packed within the TolQ pore. The model suggests that TolR is in close proximity to the hairpin (domain II) of TolA. **(B)** Hydrophobicity map of the TolQ-TolR-TolA complex shows a hydrophobic (*gold*) belt around the middle of the TolQ-TolA complex. This depiction is consistent with this region residing in the IM. **(C)** Electrostatic properties of the TolQ-TolR-TolA complex are displayed with chains B and C from TolQ hidden to show the charge within the pore. The extreme N-terminus of TolR is electropositive, complementing the electronegative charge within the pore. A similar charge-coupling is seen between the transmembrane helix of TolA and the exterior of TolQ. The TolQ-TolR-TolA model is available as a PDB file from associated **Supplementary Material**.

belt around the complex that would be amenable for insertion within the IM. The flexible N-terminal domain of TolR is anchored in the TolQ pore through electrostatic matching (**Figure 5C**) between the electronegative pore of TolQ and the electropositive charge at the extreme N-terminus of TolR. The position of TolA relative to TolQ and TolR also contributes some charge-matched regions (**Figure 5C**). It seems likely that charge complementarity plays a role in the assembly of the TolQ-TolR-TolA complex. Analogous charge matching is observed in both the Mot and Ton systems.

Our model of TolQ-TolR-TolA suggests that TolA I is oriented parallel to the TolQ helices, placing the SHLS motif between adjacent TolQ monomers (**Figure 6A**). In previous suppressor mutagenesis studies exploiting inactive TolA SHLS mutations, TolQ suppressor mutants were identified at G26, I29 and A30, respectively (Germon et al., 1998). The suppressor mutation sites are adjacent to TolA I within the model (**Figure 6A**). A co-conservation analysis between TolQ and truncated TolA (residues 1–100) yielded the highest scores for residues on the face of TolA I that are in contact with TolQ helix 2 (**Figures 6B,C**), corroborating the predicted position of TolA I. As expected, residues within the SHLS motif were highly co-conserved. The top twenty predicted inter-residue contacts were found exclusively within the hydrophobic region of TolQ helix 2, suggesting that this region constitutes the TolQ-TolA binding interface. TolA I also exhibits co-conservation with the TolQ pore-forming helices 6–7; cysteine-scanning data suggest that these helices undergo dynamic, PMF-dependent conformational rearrangements (Zhang et al., 2011), which might indicate transient contacts with TolA during TolQ rotation.

TolB INTERACTS WITH TolA AND Pal AT THE OUTER MEMBRANE

Force-transduction by the TolQ-TolR-TolA complex through the cell envelope has thus far been demonstrated only for the import of the bacteriocin colicin E9 (Francis et al., 2021), not for its physiological function of dissociating the TolB-Pal complex. TolB is a soluble periplasmic protein that interacts with TolA, Pal and colicins (Clavel et al., 1998; Walburger et al., 2002; Loftus et al., 2006). TolB has two domains, an N-terminal α/β domain and a C-terminal six-bladed β-propeller domain (Loftus et al., 2006; Bonsor et al., 2009; Zhang et al., 2010; Szczepaniak et al., 2020a). Interactions with binding partners requires conformational cycling between distinct states of TolB (Bonsor et al., 2007, 2009), which favor protein specific binding. Here, we focus on TolB interactions with TolA and Pal.

TolA III interacts with the disordered N-terminus of TolB. Yeast two-hybrid studies are consistent with residues 301–421 of TolA III forming a complex with the N-terminal 119 amino acids of TolB (Walburger et al., 2002). More recently, the solution NMR structure of a TolAIII-TolB (residues 22–34) complex has been reported (Szczepaniak et al., 2020a). It revealed that the proteins interact through β-strand augmentation in which the C-terminal helix of TolA III is displaced, exposing

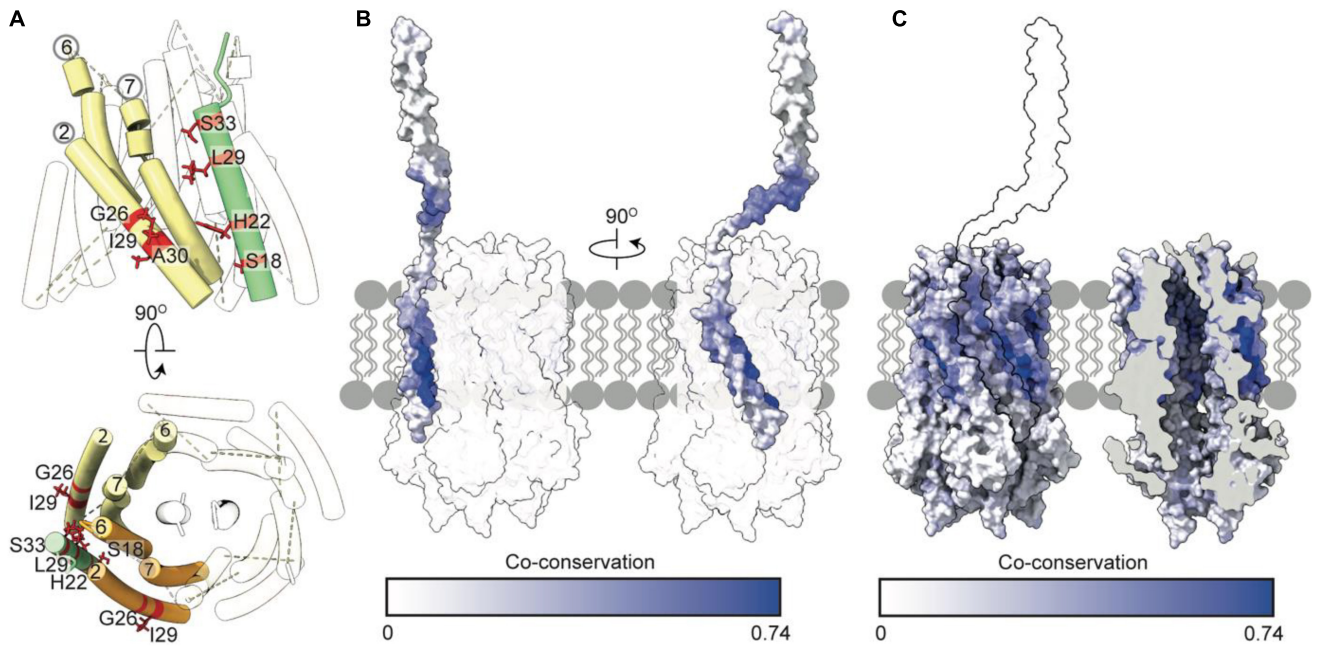


FIGURE 6 | *Tol-pal* suppressor and co-conservation analysis suggest the transmembrane helix of TolA docks within a groove formed by two TolQ helices. **(A)** The organization of TolQ helices (numbered) relative to the TolA transmembrane helix (*green*) within the TolQ-TolA model. Individual TolQ monomers are labeled in *yellow* and *orange*, respectively. The position of the TolA SHLS motif and suppressor mutations identified previously in TolQ (G26, I29 and A30 helix 2, labeled *red*) (Germon et al., 1998). **(B,C)** Maximum co-conservation scores of TolQ-TolA from RaptorX output mapped onto the TolQ-TolA model. The face of the TolA transmembrane helix in contact with TolQ in the model is strongly co-conserved. The TolQ helix 2 groove shows high co-conservation with the transmembrane helix of TolA (*yellow* outline).

the TolB-binding site. This interaction is analogous to that observed between TonB and the TonB boxes of TonB-dependent transporters (TBDTs). TBDT TonB boxes are short sequences of ∼8 residues that bind TonB through β-strand augmentation. Despite the low sequence conservation between TolA and TonB, the C-terminal domain of these proteins has the same fold and both exploit β-strand augmentation to facilitate binding to their respective partners.

When TolB is complexed with Pal, its N-terminus is buried, precluding interaction with TolA. Pal is a periplasmic protein attached to the inner leaflet of the OM through an N-terminal lipoyl tether. Like Lpp and OmpA, Pal binds to non-crosslinked stem peptides of PG, while simultaneously remaining bound to the OM. During cell division, Pal is recruited to division sites through interactions with TolB. TolB-binding and PG-binding sites overlap on Pal. Therefore, TolB association with Pal blocks its ability to bind PG, enhancing Pal diffusion in the OM and allowing for Pal recruitment to the division septum where TolQ-TolR-TolA is already localized (Bonsor et al., 2007; Szczepaniak et al., 2020a).

The structure of Pal is similar to that of other PG-binding proteins such as TolR, MotB, and ExbD, with a α/β sandwich fold where the PG- binding cleft is formed by the loops that connect elements of secondary structure. TolB is in conformational equilibrium between a compact state favored by its association with Pal, in which its N-terminus is buried between its two domains, and a relaxed state in which its N-terminus is free to bind TolA. A ternary TolA-TolB-Pal complex can also form, and it is on this complex that the TolQ-TolR stator is thought to exert force (Bonsor et al., 2007; Szczepaniak et al., 2020a,b). The release of Pal from TolB has been proposed to occur via a mechanism analogous to that of the unplugging of TBDTs by ExbB-ExbD-TonB. When TolA binds TolB, it effectively pulls TolB away from Pal to the inner periplasm through holes in the PG, thereby spatially segregating TolB from Pal to prevent immediate re-association. The role of TolB-Pal and TolB-TolA interactions in the function of the Tol-Pal system during cell division has been reviewed previously (Szczepaniak et al., 2020b).

PROTON MOTIVE FORCE TRANSDUCTION BY TolQ-TolR-TolA LIKELY FACILITATES TolA EXTENSION

The mechanism by which the Tol-Pal system generates force to drive TolB-Pal dissociation at the OM remains elusive. It is likely that a series of sequential PMF-dependent conformational transitions are transmitted through the periplasm. The key proteins required for formation of an energy transducing complex are TolQ, TolR, TolA, TolB and Pal, the last of which is not directly energized. The stoichiometry of the TolQ-TolR-TolA complex has not been explicitly demonstrated but is likely to be similar to Mot and Ton (**Figure 7A**; Celia et al., 2016, 2019; Deme et al., 2020; Santiveri et al., 2020). The free diffusion

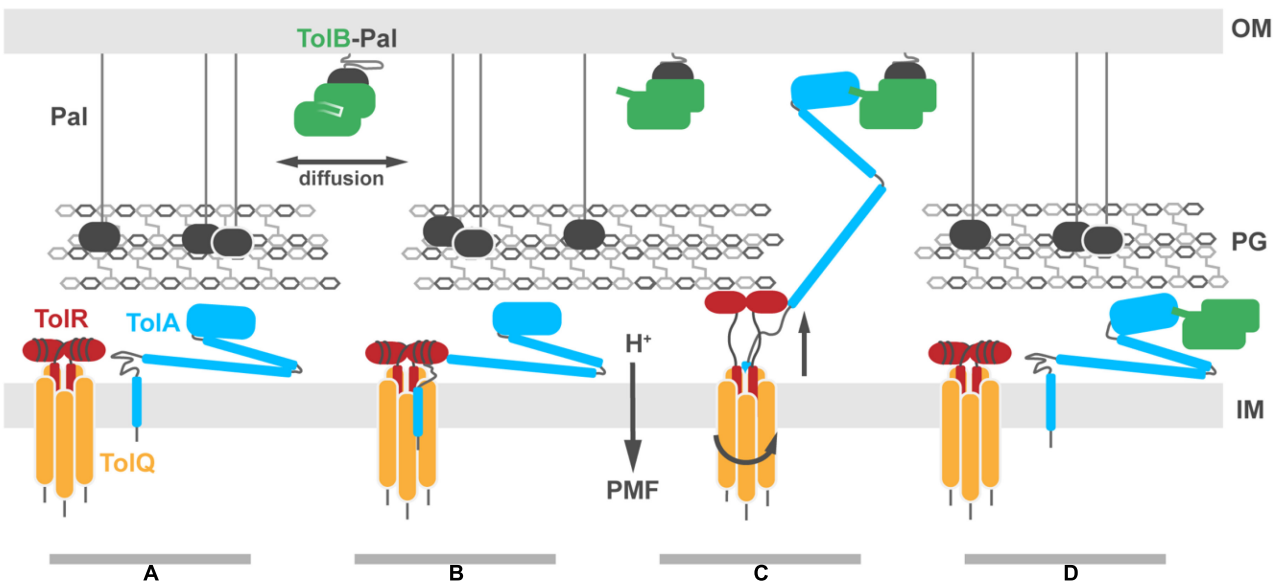


FIGURE 7 | Putative model for Tol-Pal force transduction through the cell envelope. **(A)** The TolQ-TolR stator and TolA diffuse freely within the IM. The abundant OM lipoprotein Pal is predominantly bound to the PG, stabilizing its connection to the OM. A sub-population of Pal molecules are bound to TolB. This binding blocks association of those Pal molecules with PG, enhancing their diffusion in the OM. **(B)** TolA associates with the TolQ-TolR stator, inserting between monomers of TolQ. **(C)** In response to protonation of stator residues, TolR extends and binds the PG layer, allowing rotation of the TolQ helices, which in turn drives extension of the TolA helical hairpin through pores in the PG layer. The C-terminal domain of TolA associates with the N-terminus of TolB in its complex with Pal. **(D)** Deprotonation of stator residues drive retraction of the TolR periplasmic domain away from the PG. Relaxation of the TolA helical hairpin toward the IM could be either through coupling to this structural change or refolding of the hairpin, following dissociation of TolA from the stator (as shown in the panel). We speculate that retraction of the TolA hairpin provides the driving force for dissociating TolB-Pal complexes at the OM and pulling TolB below the PG layer. The figure does not show recruitment of the TolQ-TolR-TolA complex to the divisome which concentrates Pal deposition at division sites to stabilize the invaginating OM.

of TolA in the IM (Gerding et al., 2007; Petiti et al., 2019; Szczepaniak et al., 2020a), suggests that multiple TolAs might bind a single stator complex. However, the estimated copy number of TolA (400–800 copies per cell) (Levengood et al., 1991) is 4–5× lower than that of TolR (Mueller et al., 1993), suggesting it is more likely that a single TolA is bound per stator complex (**Figure 7B**). TolA likely associates with the TolQ-TolR stator following 2D diffusion in the IM, with its long helical hairpin and globular domains (TolA II and TolA III) positioned below the PG (**Figures 7A,B**). This view is consistent with the observation that TolA-GFP exhibits unrestricted Brownian motion in the IM unless it forms a complex with the OM by reaching through the PG (Rassam et al., 2018). Our models and co-conservation analysis show that TolA could interact with both TolQ and TolR simultaneously to drive the initial assembly of the complex (**Figure 7B**). It is currently unclear whether TolA interacts with a strand-swapped dimer or an open PG-binding conformation of TolR. However, the PMF-dependent transition of TolR between these two dimer states is likely to be integral to force transduction.

Once the TolQ-TolR-TolA complex has formed, proton flux through the stator drives conformational changes in both TolR and TolA, possibly through a combination of rotary and piston-like motions. Protease-accessibility and immunoblotting experiments have suggested that TolA undergoes extensive structural rearrangements in response to the PMF. These arise from interactions of TolA I with the TolQ-TolR stator (Germon et al., 2001). Homologs, including MotA-MotB and ExbB-ExbD, are proposed to be rotary stator motors. Since TolQ is a related stator, we suggest that during rotation it could distort the geometry of TolA I, facilitating extension of the TolA II helical hairpin (**Figure 7C**). In conjunction with rotation of TolQ, TolR must also undergo conformational changes within the disordered sequence connecting the TPH to its periplasmic domain. The corresponding region in ExbD has been shown to undergo PMF-dependent conformational change suggesting force transduction facilitates conformational rearrangements of the periplasmic domain (Ollis et al., 2012). The electronegative charge at the cytoplasmic side of the TolQ lumen is not at an equivalent position around the lumen. Thus, as TolQ rotates, the electropositive N-terminus of TolR must rearrange to maintain charge matching between TolQ and TolR and to minimize charge repulsion between TolR monomers. This would result in an up-and-down piston motion that could propagate through TolR, resulting in an upward extension of the periplasmic domain that would allow for binding to the PG (**Figure 7C**). The distance from the disordered sequence connecting the TPH of TolR to the structured periplasmic domain is sufficient to reach the PG, ∼75 Å away. A similar extension has been proposed for MotB (Kojima et al., 2009; O'Neill et al., 2011).

If TolR exhibits a preference for binding non-crosslinked PG, it could bias the position of the TolQ-TolR stator toward pores in the PG. Assuming this were the case, TolR binding to PG would necessarily guide TolA II through the same hole during PMF-dependent extension (**Figure 7C**). Extended TolA would then be in a position for TolA III to bind TolB within the TolB-Pal complex at the OM (**Figure 7C**). The force-dependent step could then be either through PMF-driven deformation of TolA II by the TolQ-TolR stator or simple refolding of TolA II, following dissociation from the stator. Retraction of TolA II through the PG layer would bring TolB with it, thereby dissociating the TolB-Pal complex (**Figure 7D**).

Overall, the combination of new tools for predicting protein folds, modeling techniques, and integration of experimental data culminate in the model of TolQ-TolR-TolA presented here. This model supports the position of the TolR TPH within the lumen of the TolQ pentamer, and it includes a proposed TolQ-TolA interface within the plane of the IM, facilitated by charge and hydrophobicity matching. To integrate this model into the cell envelope and reconcile the PMF-dependence of both the conformational rearrangements of TolA and of the interactions of TolA with the OM, we posit that in its non-energized state TolA is localized below the PG layer, with PMF-energized TolQ-TolR required to guide TolA II to the outer periplasm, enabling TolA III to bind TolB-Pal in the OM.

OUTSTANDING QUESTIONS

Stabilization of the OM during cell division by Tol-Pal is facilitated by PMF-dependent structural rearrangements of the proteins involved. TolA exists predominantly in a compact state between the IM and the PG layer, a hypothesis based on structural and microscopy data (Rassam et al., 2018; Szczepaniak et al., 2020a). In this model, TolA does not reach the OM unless energized by the TolQ-TolR stator, which leads to conformational rearrangements in TolA II and extension across the periplasm through pores in the PG. Upon binding the N-terminus of TolB, the cycle reverses, returning TolA II to the inner membrane attached to its TolB cargo. Such a model invokes a multitude of further questions regarding the nature of the energized and non-energized states of TolA and how these structures are linked to the extension and retraction of the TolA II helical hairpin. Furthermore, there is the question of how the extension of TolA is coordinated with formation of the TolQ-TolR-TolA complex, with proton flux, and with the rotation of the TolQ-TolR stator.

Data on MotA-MotB and ExbB-ExbD suggest that the TolR dimer is the origin of rotation, but little can be inferred currently about how this rotation affects the conformation of TolA. The likely insertion of the TolA transmembrane helix into the groove between the outer TolQ helices begs additional questions of stoichiometry, affinity, and regulation. Does TolA play an active role as a receptor for proton flux, or is its energization a by-product of rotary motion and insertion between TolQ helices? Although H22 within TolA I has been suggested to be involved in the pathway of proton flux because it is essential for Tol-Pal function, based on our model it seems more likely that H22 simply contributes to the TolQ-binding interface. This is consistent with the Ton-system in which mutagenesis studies of H20 of the TonB SHLS motif suggest that the conserved histidine is of structural importance, rather than serving as a proton acceptor (Larsen et al., 2007; Postle et al., 2010; Swayne and Postle, 2011; Ollis et al., 2012). Consistent with the rotary motion

of TolQ-TolA being important for function, *in vivo* fluorescence anisotropy experiments of N-terminal GFP-TonB fusions have highlighted restricted diffusion and PMF-dependent rotation of the TonB transmembrane helix (Jordan et al., 2013). This likely occurs because TonB binds ExbB in a manner analogous to TolA binding TolQ, suggesting that rotation of stator complexes is the cornerstone of the energization mechanism in both cases.

Our model assumes that TolR is the stationary component about which TolQ rotates, and that it is spatially and temporally fixed by its association with PG. This assumption raises the question of how PG binding is modulated. It is known that TolQ-TolR and TolA freely diffuse in the IM and are independently recruited to the septal ring (Gerding et al., 2007; Petiti et al., 2019; Szczepaniak et al., 2020a). This trafficking of TolQ-TolR and TolA to the septum depends on the -remodeling of PG and the activity of FtsN and its interactors (e.g., FtsWI) rather than on direct interaction of TolR and TolA with FtsN (Gerding et al., 2007; Hale et al., 2021). This suggests that the local composition of PG plays a role in TolQ-TolR-TolA localization, either through the function of intermediary trafficking proteins or the preferential retention of the complex through direct Tol-PG interactions.

The parallels between the Tol and Ton systems extend beyond the structural similarities of the stator complexes. The SHLS motif is present in both TolA and TonB, and exchange of this sequence motif between the effectors subsequently establishes interactions with the opposite stator complex (Braun and Herrmann, 1993). TonB has a central domain that is substantially different from TolA II; it is predicted to be unstructured and proline rich. This suggests that these effectors span the periplasm by different mechanisms yet interact with their respective stators in a homologous fashion. Characterizing how stator rotation facilitates conformational rearrangements in TolA and TolR represents the next step in understanding the mechanism by which this PMF-dependent system transduces force across the periplasm to drive stabilization of the OM.

DATA AVAILABILITY STATEMENT

The data supporting the findings of the study are available in the associated **Supplementary Material** and are available upon request from the corresponding author.

AUTHOR CONTRIBUTIONS

MW and DW-J: data acquisition. MW, DW-J, and CK: writing – original draft review and editing. All authors contributed to the article and approved the submitted version.

FUNDING

The work was funded by a European Research Council Advanced Grant (742555; OMPorg) and a Biotechnology and Biological Science Research Council Project Grant (BB/V008056/1) to CK and a Wellcome Trust Doctoral Training Grant (224898) to DW-J.

ACKNOWLEDGMENTS

We are indebted to Joanna Szczepaniak (Oxford) for guidance and advice. We are also grateful to Connor Sharp for guidance on co-conservation analyses.

SUPPLEMENTARY MATERIAL

The Supplementary Material for this article can be found online at: https://www.frontiersin.org/articles/10.3389/fmicb.2022.852176/full#supplementary-material

RaptorX Co-conservation files and model PDB files are available in **Supplementary Material**.

REFERENCES

Asmar, A. T., Ferreira, J. L., Cohen, E. J., Cho, S.-H., Beeby, M., Hughes, K. T., et al. (2017). Communication across the bacterial cell envelope depends on the size of the periplasm. *PLoS Biol.* 15:e2004303. doi: 10.1371/journal.pbio.2004303

Bernadac, A., Gavioli, M., Lazzaroni, J. C., Raina, S., and Lloubes, R. (1998). *Escherichia coli* tol-pal mutants form outer membrane vesicles. *J. Bacteriol.* 180, 4872–4878. doi: 10.1128/JB.180.18.4872-4878.1998

Bonsor, D. A., Grishkovskaya, I., Dodson, E. J., and Kleanthous, C. (2007). Molecular Mimicry Enables Competitive Recruitment by a Natively Disordered Protein. *J. Am. Chem. Soc.* 15, 4800–4807. doi: 10.1021/ja070153n

Bonsor, D. A., Hecht, O., Vankemmelbeke, M., Sharma, A., Krachler, A. M., Housden, N. G., et al. (2009). Allosteric beta-propeller signalling in TolB and its manipulation by translocating colicins. *EMBO J.* 28, 2846–2857. doi: 10.1038/emboj.2009.224

Braun, V., and Herrmann, C. (1993). Evolutionary relationship of uptake systems for biopolymers in *Escherichia coli*: cross-complementation between the TonB-ExbB-ExbD and the TolA-TolQ-TolR proteins. *Mol. Microbiol.* 8, 261–268. doi: 10.1111/j.1365-2958.1993.tb01570.x

Cascales, E., Buchanan, S. K., Duché, D., Kleanthous, C., Lloubès, R., Postle, K., et al. (2007). Colicin biology. *Microbiol. Mol. Biol. Rev.* 71, 158–229.

Cascales, E., Gavioli, M., Sturgis, J. N., and Lloubes, R. (2000). Proton motive force drives the interaction of the inner membrane TolA and outer membrane pal proteins in *Escherichia coli*. *Mol. Microbiol.* 38, 904–915. doi: 10.1046/j.1365-2958.2000.02190.x

Cascales, E., Lloubes, R., and Sturgis, J. N. (2001). The TolQ-TolR proteins energize TolA and share homologies with the flagellar motor proteins MotA-MotB. *Mol. Microbiol.* 42, 795–807. doi: 10.1046/j.1365-2958.2001.02673.x

Celia, H., Botos, I., Ni, X., Fox, T., De Val, N., Lloubes, R., et al. (2019). Cryo-EM structure of the bacterial Ton motor subcomplex ExbB–ExbD provides information on structure and stoichiometry. *Commun. Biol.* 2:358.

Celia, H., Noinaj, N., Zakharov, S. D., Bordignon, E., Botos, I., Santamaria, M., et al. (2016). Structural insight into the role of the Ton complex in energy transduction. *Nature* 538, 60–65. doi: 10.1038/nature19757

Clavel, T., Germon, P., Vianney, A., Portalier, R., and Lazzaroni, J. C. (1998). TolB protein of *Escherichia coli* K-12 interacts with the outer membrane peptidoglycan-associated proteins Pal, Lpp and OmpA. *Mol. Microbiol.* 29, 359–367. doi: 10.1046/j.1365-2958.1998.00945.x

Connolley, L., Szczepaniak, J., Kleanthous, C., and Murray S. M. (2021). The quantitative basis for the redistribution of immobile bacterial lipoproteins to division septa. *PLoS Comput. Biol.* 17:e1009756. doi: 10.1371/journal.pcbi.1009756

D'Andrea, L. D., and Regan, L. (2003). TPR proteins: the versatile helix. *Trends Biochem. Sci.* 28, 655–662. doi: 10.1016/j.tibs.2003.10.007

Deme, J. C., Johnson, S., Vickery, O., Aron, A., Monkhouse, H., Griffiths, T., et al. (2020). Structures of the stator complex that drives rotation of the bacterial flagellum. *Nat. Microbiol.* 5, 1553–1564. doi: 10.1038/s41564-020-0788-8

Deprez, C., Lloubès, R., Gavioli, M., Marion, D., Guerlesquin, F., and Blanchard, L. (2005). Solution structure of the E.coli TolA C-terminal domain reveals conformational changes upon binding to the phage g3p N-terminal domain. *J. Mol. Biol.* 346, 1047–1057. doi: 10.1016/j.jmb.2004.12.028

Egan, A. J. F. (2018). Bacterial outer membrane constriction. *Mol. Microbiol.* 107, 676–687. doi: 10.1111/mmi.13908

Ford, C. G., Kolappan, S., Phan, H. T. H., Waldor, M. K., Winther-Larsen, H. C., and Craig, L. (2012). Crystal Structures of a CTXφ pIII Domain Unbound and in Complex with a *Vibrio cholerae* TolA Domain Reveal Novel Interaction Interfaces*. *J. Biol. Chem.* 287, 36258–36272. doi: 10.1074/jbc.M112.403386

Francis, M.-L. R., Webby, M. N., Housden, N. G., Kaminska, R., Elliston, E., Chinthammit, B., et al. (2021). Porin threading drives receptor disengagement and establishes active colicin transport through *Escherichia coli* OmpF. *EMBO J.* 40:e108610. doi: 10.15252/embj.2021108610

Fung, J., MacAlister, T. J., and Rothfield, L. I. (1978). Role of murein lipoprotein in morphogenesis of the bacterial division septum: phenotypic similarity of lkyD and lpo mutants. *J. Bacteriol.* 133, 1467–1471. doi: 10.1128/jb.133.3.1467-1471.1978

Fung, J. C., MacAlister, T. J., Weigand, R. A., and Rothfield, L. I. (1980). Morphogenesis of the bacterial division septum: identification of potential sites of division in lkyD mutants of *Salmonella* typhimurium. *J. Bacteriol.* 143, 1019–1024. doi: 10.1128/jb.143.2.1019-1024.1980

Gerding, M. A., Ogata, Y., Pecora, N. D., Niki, H., and de Boer, P. A. (2007). The trans-envelope Tol-Pal complex is part of the cell division machinery and required for proper outer-membrane invagination during cell constriction in *E. coli*. *Mol. Microbiol.* 63, 1008–1025. doi: 10.1111/j.1365-2958.2006.05571.x

Germon, P., Clavel, T., Vianney, A., Portalier, R., and Lazzaroni, J. C. (1998). Mutational analysis of the *Escherichia coli* K-12 TolA N-terminal region and characterization of its TolQ-interacting domain by genetic suppression. *J. Bacteriol.* 180, 6433–6439. doi: 10.1128/JB.180.24.6433-6439.1998

Germon, P., Ray, M. C., Vianney, A., and Lazzaroni, J. C. (2001). Energy-dependent conformational change in the TolA protein of *Escherichia coli* involves its N-terminal domain, TolQ, and TolR. *J. Bacteriol.* 183, 4110–4114. doi: 10.1128/JB.183.14.4110-4114.2001

Goemaere, E. L., Cascales, E., and Lloubes, R. (2007). Mutational analyses define helix organization and key residues of a bacterial membrane energy-transducing complex. *J. Mol. Biol.* 366, 1424–1436. doi: 10.1016/j.jmb.2006.12.020

Gray, A. N., Egan, A. J. F., Van't Veer, I. L., Verheul, J., Colavin, A., Koumoutsi, A., et al. (2015). Coordination of peptidoglycan synthesis and outer membrane constriction during *Escherichia coli* cell division. *eLife* 4:e07118. doi: 10.7554/eLife.07118

Hale, C. A., Persons, L., and de Boer, P. A. J. (2021). Recruitment of the TolA protein to cell constriction sites in *Escherichia coli* via three separate mechanisms, and a critical role for FtsWI activity in recruitment of both TolA and TolQ. *J. Bacteriol.* 204:e0046421. doi: 10.1128/JB.00464-21

Hu, H., Santiveri, M., Wadhwa, N., Berg, H. C., Erhardt, M., and Taylor, N. M. I. (2021). Structural basis of torque generation in the bi-directional bacterial flagellar motor. *Trends Biochem. Sci.* 47, 160–172. doi: 10.1016/j.tibs.2021.06.005

Johnson, S., Furlong, E. J., Deme, J. C., Nord, A. L., Caesar, J. J. E., Chevance, F. F. V., et al. (2021). Molecular structure of the intact bacterial flagellar basal body. *Nat. Microbiol.* 6, 712–721. doi: 10.1038/s41564-021-00895-y

Jordan, L. D., Zhou, Y., Smallwood, C. R., Lill, Y., Ritchie, K., Yip, W. T., et al. (2013). Energy-dependent motion of TonB in the Gram-negative bacterial inner membrane. *Proc. Natl. Acad. Sci. U. S. A.* 110, 11553–11558. doi: 10.1073/pnas.1304243110

Jumper, J., Evans, R., Pritzel, A., Green, T., Figurnov, M., Ronneberger, O., et al. (2021). Highly accurate protein structure prediction with AlphaFold. *Nature* 596, 583–589. doi: 10.1038/s41586-021-03819-2

Kampfenkel, K., and Braun, V. (1993). Membrane topologies of the TolQ and TolR proteins of *Escherichia coli*: inactivation of TolQ by a missense mutation in the proposed first transmembrane segment. *J. Bacteriol.* 175, 4485–4491. doi: 10.1128/jb.175.14.4485-4491.1993

Karlsson, M., Hannavy, K., and Higgins, C. F. (1993). A sequence-specific function for the N-terminal signal-like sequence of the TonB protein. *Mol. Microbiol.* 8, 379–388. doi: 10.1111/j.1365-2958.1993.tb01581.x

Khatib, F., Cooper, S., Tyka, M. D., Xu, K., Makedon, I., Popovic, Z., et al. (2011). Algorithm discovery by protein folding game players. *Proc. Natl. Acad. Sci. U. S. A.* 108, 18949–18953. doi: 10.1073/pnas.1115898108

Kleanthous, C. (2010). Swimming against the tide: progress and challenges in our understanding of colicin translocation. *Nat. Rev. Microbiol.* 8, 843–848. doi: 10.1038/nrmicro2454

Koebnik, R., Bäumler, A. J., Heesemann, J., Braun, V., and Hantke, K. (1993). The TonB protein of Yersinia enterocolitica and its interactions with TonB-box proteins. *Mol. Gen. Genet. MGG* 237, 152–160. doi: 10.1007/BF00282796

Kojima, S., Imada, K., Sakuma, M., Sudo, Y., Kojima, C., Minamino, T., et al. (2009). Stator assembly and activation mechanism of the flagellar motor by the periplasmic region of MotB. *Mol. Microbiol.* 73, 710–718. doi: 10.1111/j.1365-2958.2009.06802.x

Krachler, A. M., Sharma, A., Cauldwell, A., Papadakos, G., and Kleanthous, C. (2010). TolA modulates the oligomeric status of YbgF in the bacterial periplasm. *J. Mol. Biol.* 403, 270–285. doi: 10.1016/j.jmb.2010.08.050

Larsen, R. A., Deckert, G. E., Kastead, K. A., Devanathan, S., Keller, K. L., and Postle, K. (2007). His(20) provides the sole functionally significant side chain in the essential TonB transmembrane domain. *J. Bacteriol.* 189, 2825–2833. doi: 10.1128/JB.01925-06

Larsen, R. A., and Postle, K. (2001). Conserved residues Ser(16) and His(20) and their relative positioning are essential for TonB activity, cross-linking of TonB with ExbB, and the ability of TonB to respond to proton motive force. *J. Biol. Chem.* 276, 8111–8117. doi: 10.1074/jbc.M007479200

Larsen, R. A., Thomas, M. G., and Postle, K. (1999). Protonmotive force, ExbB and ligand-bound FepA drive conformational changes in TonB. *Mol. Microbiol.* 31, 1809–1824. doi: 10.1046/j.1365-2958.1999.01317.x

Larsen, R. A., Thomas, M. G., Wood, G. E., and Postle, K. (1994). Partial suppression of an *Escherichia coli* TonB transmembrane domain mutation (delta V17) by a missense mutation in ExbB. *Mol. Microbiol.* 13, 627–640. doi: 10.1111/j.1365-2958.1994.tb00457.x

Lazzaroni, J. C., Germon, P., Ray, M. C., and Vianney, A. (1999). The Tol proteins of *Escherichia coli* and their involvement in the uptake of biomolecules and outer membrane stability. *FEMS Microbiol. Lett.* 177, 191–197. doi: 10.1111/j.1574-6968.1999.tb13731.x

Levengood, S. K., Beyer, W. F. Jr., and Webster, R. E. (1991). TolA: a membrane protein involved in colicin uptake contains an extended helical region. *Proc. Natl. Acad. Sci. U. S. A.* 88, 5939–5943. doi: 10.1073/pnas.88.14.5939

Levengood-Freyermuth, S. K., Click, E. M., and Webster, R. E. (1993). Role of the carboxyl-terminal domain of TolA in protein import and integrity of the outer membrane. *J. Bacteriol.* 175, 222–228. doi: 10.1128/jb.175.1.222-228.1993

Li, C., Zhang, Y., Vankemmelbeke, M., Hecht, O., Aleanizy, F. S., Macdonald, C., et al. (2012). Structural evidence that colicin A protein binds to a novel binding site of TolA protein in *Escherichia coli* periplasm. *J. Biol. Chem.* 287, 19048–19057. doi: 10.1074/jbc.M112.342246

Loftus, S. R., Walker, D., Mate, M. J., Bonsor, D. A., James, R., Moore, G. R., et al. (2006). Competitive recruitment of the periplasmic translocation portal TolB by a natively disordered domain of colicin E9. *Proc. Natl. Acad. Sci. U. S. A.* 103, 12353–12358. doi: 10.1073/pnas.0603433103

Lorenz, S. H., Jakob, R. P., Weininger, U., Balbach, J., Dobbek, H., and Schmid, F. X. (2011). The filamentous phages fd and IF1 use different mechanisms to infect *Escherichia coli*. *J. Mol. Biol.* 405, 989–1003. doi: 10.1016/j.jmb.2010.11.030

Lubkowski, J., Hennecke, F., Pluckthun, A., and Wlodawer, A. (1999). Filamentous phage infection: crystal structure of g3p in complex with its coreceptor, the C-terminal domain of TolA. *Structure* 7, 711–722. doi: 10.1016/s0969-2126(99)80092-6

Maguire, J. B., Haddox, H. K., Strickland, D., Halabiya, S. F., Coventry, B., Griffin, J. R., et al. (2021). Perturbing the energy landscape for improved packing during computational protein design. *Proteins* 89, 436–449. doi: 10.1002/prot.26030

Mueller, J. E., Bryk, M., Loizos, N., and Belfort, M. (1993). "Homing endonucleases," in *Nucleases*, 2nd Edn, eds S. M. Linn, R. S. Lloyd, and R. J. Roberts (Cold Spring Harbor: Cold Spring Harbor Laboratory Press), 111–143.

Nagel de Zwaig, R., and Luria, S. E. (1967). Genetics and physiology of colicin-tolerant mutants of *Escherichia coli*. *J. Bacteriol.* 94, 1112–1123. doi: 10.1128/jb.94.4.1112-1123.1967

Nikaido, H. (2003). Molecular basis of bacterial outer membrane permeability revisited. *Microbiol. Mol. Biol. Rev.* 67, 593–656. doi: 10.1128/MMBR.67.4.593-656.2003

Ollis, A. A., Kumar, A., and Postle, K. (2012). The ExbD Periplasmic Domain Contains Distinct Functional Regions for Two Stages in TonB Energization. *J. Bacteriol.* 194, 3069–3077. doi: 10.1128/JB.00015-12

O'Neill, J., Xie, M., Hijnen, M., and Roujeinikova, A. (2011). Role of the MotB linker in the assembly and activation of the bacterial flagellar motor. *Acta Crystallogr. D Biol. Crystallogr.* 67, 1009–1016. doi: 10.1107/S0907444911041102

Parsons, L. M., Grishaev, A., and Bax, A. (2008). The periplasmic domain of TolR from *Haemophilus influenzae* forms a dimer with a large hydrophobic groove: NMR solution structure and comparison to SAXS data. *Biochemistry* 47, 3131–3142. doi: 10.1021/bi702283x

Petiti, M., Serrano, B., Faure, L., Lloubes, R., Mignot, T., and Duche, D. (2019). Tol Energy-Driven Localization of Pal and Anchoring to the Peptidoglycan Promote Outer-Membrane Constriction. *J. Mol. Biol.* 431, 3275–3288. doi: 10.1016/j.jmb.2019.05.039

Postle, K., Kastead, K. A., Gresock, M. G., Ghosh, J., and Swayne, C. D. (2010). The TonB dimeric crystal structures do not exist *In vivo*. *mBio* 1, e00307–10.

Rassam, P., Long, K. R., Kaminska, R., Williams, D. J., Papadakos, G., Baumann, C. G., et al. (2018). Intermembrane crosstalk drives inner-membrane protein organization in *Escherichia coli*. *Nat. Commun.* 9:1082. doi: 10.1038/s41467-018-03521-4

Roujeinikova, A. (2008). Crystal structure of the cell wall anchor domain of MotB, a stator component of the bacterial flagellar motor: implications for peptidoglycan recognition. *Proc. Natl. Acad. Sci. U. S. A.* 105, 10348–10353. doi: 10.1073/pnas.0803039105

Santiveri, M., Roa-Eguiara, A., Kühne, C., Wadhwa, N., Hu, H., Berg, H. C., et al. (2020). Structure and Function of Stator Units of the Bacterial Flagellar Motor. *Cell* 183, 244–257.e16. doi: 10.1016/j.cell.2020.08.016

Sturgis, J. (2001). Organisation and evolution of the tol-pal gene cluster. *J. Mol. Microbiol. Biotechnol.* 3, 113–122.

Sun, T. P., and Webster, R. E. (1986). fii, a bacterial locus required for filamentous phage infection and its relation to colicin-tolerant tolA and tolB. *J. Bacteriol.* 165, 107–115. doi: 10.1128/jb.165.1.107-115.1986

Swayne, C., and Postle, K. (2011). Taking the *Escherichia coli* TonB transmembrane domain "offline"? Nonprotonatable Asn substitutes fully for TonB His20. *J. Bacteriol.* 193, 3693–3701. doi: 10.1128/JB.05219-11

Szczepaniak, J., Holmes, P., Rajasekar, K., Kaminska, R., Samsudin, F., Inns, P. G., et al. (2020a). The lipoprotein Pal stabilises the bacterial outer membrane during constriction by a mobilisation-and-capture mechanism. *Nat. Commun.* 11:1305. doi: 10.1038/s41467-020-15083-5

Szczepaniak, J., Press, C., and Kleanthous, C. (2020b). The multifarious roles of Tol-Pal in Gram-negative bacteria. *FEMS Microbiol. Rev.* 44, 490–506.

Vianney, A., Lewin, T. M., Beyer, W. F. Jr., Lazzaroni, J. C., Portalier, R., and Webster, R. E. (1994). Membrane topology and mutational analysis of the TolQ protein of *Escherichia coli* required for the uptake of macromolecules and cell envelope integrity. *J. Bacteriol.* 176, 822–829. doi: 10.1128/jb.176.3.822-829.1994

Walburger, A., Lazdunski, C., and Corda, Y. (2002). The Tol/Pal system function requires an interaction between the C-terminal domain of TolA and the N-terminal domain of TolB. *Mol. Microbiol.* 44, 695–708. doi: 10.1046/j.1365-2958.2002.02895.x

Weigand, R. A., and Rothfield, L. I. (1976). Genetic and physiological classification of periplasmic-leaky mutants of *Salmonella* typhimurium. *J. Bacteriol.* 125, 340–345. doi: 10.1128/jb.125.1.340-345.1976

Weigand, R. A., Vinci, K. D., and Rothfield, L. I. (1976). Morphogenesis of the bacterial division septum: a new class of septation-defective mutants. *Proc. Natl. Acad. Sci. U. S. A.* 73, 1882–1886. doi: 10.1073/pnas.73.6.1882

Witty, M., Sanz, C., Shah, A., Grossmann, J. G., Mizuguchi, K., Perham, R. N., et al. (2002). Structure of the periplasmic domain of *Pseudomonas aeruginosa* TolA: evidence for an evolutionary relationship with the TonB transporter protein. *EMBO J.* 21, 4207–4218. doi: 10.1093/emboj/cdf417

Wojdyla, J. A., Cutts, E., Kaminska, R., Papadakos, G., Hopper, J. T., Stansfeld, P. J., et al. (2015). Structure and function of the *Escherichia coli* Tol-Pal stator protein TolR. *J. Biol. Chem.* 290, 26675–26687. doi: 10.1074/jbc.M115.671586

Yakhnina, A. A., and Bernhardt, T. G. (2020). The Tol-Pal system is required for peptidoglycan-cleaving enzymes to complete bacterial cell division. *Proc. Natl. Acad. Sci. U. S. A.* 117, 6777–6783. doi: 10.1073/pnas.1919267117

Zeng, H., Wang, S., Zhou, T., Zhao, F., Li, X., Wu, Q., et al. (2018). ComplexContact: a web server for inter-protein contact prediction using deep learning. *Nucleic Acids Res.* 46, W432–W437. doi: 10.1093/nar/gky420

Zhang, X. Y. Z., Goemaere, E. L., Seddiki, N., Célia, H., Gavioli, M., Cascales, E., et al. (2011). Mapping the Interactions between *Escherichia coli* TolQ Transmembrane Segments*. *J. Biol. Chem.* 286, 11756–11764. doi: 10.1074/jbc.m110.192773

Zhang, X. Y. Z., Goemaere, E. L., Thomé, R., Gavioli, M., Cascales, E., and Lloubés, R. (2009). Mapping the Interactions between *Escherichia coli* Tol Subunits: ROTATION OF THE TolR TRANSMEMBRANE HELIX*. *J. Biol. Chem.* 284, 4275–4282. doi: 10.1074/jbc.M805257200

Zhang, Y., Li, C., Vankemmelbeke, M. N., Bardelang, P., Paoli, M., Penfold, C. N., et al. (2010). The crystal structure of the TolB box of colicin A in complex with TolB reveals important differences in the recruitment of the common TolB translocation portal used by group A colicins. *Mol. Microbiol.* 75, 623–636. doi: 10.1111/j.1365-2958.2009.06808.x

Conflict of Interest: The authors declare that the research was conducted in the absence of any commercial or financial relationships that could be construed as a potential conflict of interest.

Publisher's Note: All claims expressed in this article are solely those of the authors and do not necessarily represent those of their affiliated organizations, or those of the publisher, the editors and the reviewers. Any product that may be evaluated in this article, or claim that may be made by its manufacturer, is not guaranteed or endorsed by the publisher.

Copyright © 2022 Webby, Williams-Jones, Press and Kleanthous. This is an open-access article distributed under the terms of the Creative Commons Attribution License (CC BY). The use, distribution or reproduction in other forums is permitted, provided the original author(s) and the copyright owner(s) are credited and that the original publication in this journal is cited, in accordance with accepted academic practice. No use, distribution or reproduction is permitted which does not comply with these terms.

frontiers | Frontiers in Microbiology

MINI REVIEW
published: 26 April 2022
doi: 10.3389/fmicb.2021.803720

How Did the Archaellum Get Its Rotation?

Davi Ortega[1]* *and Morgan Beeby*[2]*

[1] Koan Labs, São Paulo, Brazil, [2] Department of Life Sciences, Imperial College London, London, United Kingdom

How new functions evolve fascinates many evolutionary biologists. Particularly captivating is the evolution of rotation in molecular machines, as it evokes familiar machines that we have made ourselves. The archaellum, an archaeal analog of the bacterial flagellum, is one of the simplest rotary motors. It features a long helical propeller attached to a cell envelope-embedded rotary motor. Satisfyingly, the archaellum is one of many members of the large type IV filament superfamily, which includes pili, secretion systems, and adhesins, relationships that promise clues as to how the rotating archaellum evolved from a non-rotary ancestor. Nevertheless, determining exactly how the archaellum got its rotation remains frustratingly elusive. Here we review what is known about how the archaellum got its rotation, what clues exist, and what more is needed to address this question.

Keywords: archaellum/archaea/archaellum motor complex, propulsive nanomachines, archaeal flagella, genomics, biophysics, *in situ* structural biology, molecular evolution

OPEN ACCESS

Edited by:
Michael Manson,
Texas A&M University, United States

Reviewed by:
Ben Berks,
University of Oxford, United Kingdom

***Correspondence:**
Davi Ortega
davi@koan-labs.com
Morgan Beeby
mbeeby@imperial.ac.uk
orcid.org/0000-0001-6413-9835

Specialty section:
This article was submitted to Microbial Physiology and Metabolism, a section of the journal Frontiers in Microbiology

Received: *28 October 2021*
Accepted: *20 December 2021*
Published: *26 April 2022*

Citation:
Ortega D and Beeby M (2022) How Did the Archaellum Get Its Rotation? Front. Microbiol. 12:803720. doi: 10.3389/fmicb.2021.803720

HOW DOES ROTARY MOTION EVOLVE IN MOLECULAR MACHINES?

How do molecular machines evolve new roles? Macroscopic structures such as wings or eyes have evolved from simpler limbs or photoreceptors. In many cases, evolution of new functions in such macroscopic structures involved co-option of a pre-existing feature for the new role. Gould and Vrba coined the phrase *exaptation* to define this process, distinguishing it from *adaptation,* in which a pre-existing feature evolves to become more beneficial in its current role. Lightweight feathered wings, for example, existed in nascent forms before exaptation for flight (Gould and Vrba, 1982).

How such processes operate at the molecular scale remains less well understood. Nevertheless, it appears that at the molecular scale new functions also result from exaptation of existing underlying mechanisms instead of radical genesis of fully formed new machines. For example, rotary nanomachines used by cells for propulsion demonstrate exaptation of rotary mechanisms (Beeby et al., 2020). The best known such machine is the bacterial flagellum, which rotates a multi-micron filament as a rotary helical propeller to generate thrust. Bacterial flagella are believed to have exapted the intrinsic rotary mechanism of a family of rotary ion channels (the ExbBD/TolQR family, discussed elsewhere in this special issue), to drive rotation of a large axial ring, cogwheel-style, that in turn rotates an extracellular helical propeller (Chang et al., 2020; Deme et al., 2020; Santiveri et al., 2020). Better understanding of how this exaptation occurred, however, is frustrated by the absence of contemporary flagellar relatives that diverged prior to the evolution of rotation, leaving the evolutionary path to rotation speculative (Abby and Rocha, 2012; Beeby et al., 2020).

If the emergence of novelty in molecular machines involves exaptation, evolution of rotary motors suggests that rotary function should be a nascent function of ancestral protein components.

Four decades ago, Roger Hendrix suggested that rotation may be inherent to symmetry mismatched protein subcomplexes (Hendrix, 1978): the phase shifts in binding interactions around the interaction surface of two symmetry-mismatched cyclic subcomplexes will reduce the activation barrier to the small rotations required to achieve an identical–albeit rotated–set of interactions. In other words, unless active measures are taken to prevent rotation, rotation may be inevitable in such cases. Hendrix based his thesis on symmetry mismatch in phages, and symmetry mismatch was subsequently implicated as important for function of the bacterial flagellum (Thomas et al., 1999), ATP synthase (Pogoryelov et al., 2005), Clp proteases (Ripstein et al., 2020), kinetochore movement along microtubules (Westermann et al., 2006), and DNA translocases (Liu et al., 2015).

Curiously, rotation is not as frequently seen as we anticipated. Since Hendrix published his work, the phage portal protein has been shown not to rotate (Hugel et al., 2007), the protease ClpAP has been shown to function without rotation (Kim et al., 2020), and diverse symmetry-mismatched secretion systems have been shown to have architectures that preclude rotation (Umrekar et al., 2021a). Together, this suggests that strategies such as the sophisticated interlocking of different symmetries in phages (Fang et al., 2020) may have evolved to preclude the potential side-effect of inter-subcomplex rotation (Liu et al., 2014). If this assumption is the case, how might a protein machine overcome a selectively detrimental state to exapt an intrinsic rotary mechanism?

"How" is a nebulous word, and we use it to capture diverse questions: has exaptation played a role in the evolution of rotary protein machines? How many mutations are required to switch from a non-rotary interface to a rotary interface? What selective pressures exist to retain a protein complex in a non-rotary or rotary state? What structural features implement the retention of one or the other state (for example, symmetry adaptor domains, proteins that mediate stoichiometry matching, or promiscuous inter-subunit binding interfaces)? Do (or must) selectively metastable "gateway" evolutionary intermediates exist that facilitate the evolutionary pathway from non-rotary to rotary function? Such questions remain broadly unanswered, in part because we lack a model system in which to ask them.

THE ARCHAELLUM: AN EXCELLENT CASE STUDY OF THE EVOLUTION OF A ROTARY MOTOR

A possible model system to study emergence of rotation in molecular machines is the "archaellum" (previously known as the "archaeal flagellum"), whose diverse non-rotary contemporary relatives provide clues to its evolution (Albers and Jarrell, 2018). Archaella are members of the type IV filament (TFF) superfamily, a family of otherwise non-rotary machines that includes type II secretion systems, type IVa pili, type IVb pili, and various adhesin pili (Berry and Pelicic, 2015; Beeby, 2019; Denise et al., 2019), but feature additional proteins apparently associated with torque generation (**Figure 1**). Like bacterial flagella, archaella spin a filament to form a helical propeller that generates thrust for cell propulsion.

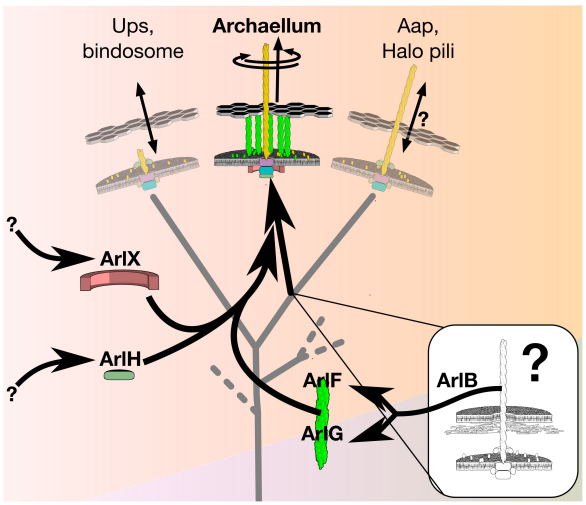


FIGURE 1 | The archaellum is a rotary motor that evolved from a non-rotary ancestor. The archaellum descends from a clade of the type IV filament superfamily that produced adhesive pili. Evolution of rotary motion included paralogous duplication of its filament protein, ArlB, to form the putative stator ArlFG, recruitment of ArlH from an unknown source as putative timer protein to switch from assembly to rotation, and recruitment of ArlX (or, in some species, ArlCDE) from an unknown source as a putative stator scaffold. The details of these recruitments, and how they affected the function of intermediate states, however, remains unclear.

Although the archaellum is less well-known than other rotary motors, its simplicity makes it an excellent system for studying the evolution of rotary function. The simplest archaellum, from *Sulfolobus acidocaldarius,* features just seven proteins. A multimicron-long extracellular filament of ArlB assembles on a platform composed of transmembrane ArlJ and cytoplasmic ArlI and ArlH; paralogs ArlF and ArlG likely span the pseudo-periplasm, while ArlX may mediate complex formation between ArlHIJ to ArlFG. (Note that archaellar proteins have recently been renamed "Arl" from "Fla/Flg" to prevent confusion with bacterial flagellar proteins Pohlschroder et al., 2018).

The ArlHIJ complex lies at the heart of the archaellum. Transmembrane ArlJ features two conserved cytoplasmic domains (Ghosh and Albers, 2011), dimerizes, and likely interacts with the cytoplasmic ATPase, ArlI, a cyclic hexamer that is the sole energy source of the complex. Curiously, ArlI powers both archaellum assembly and rotation, and it is a conserved member of the same ATPase family used across other members of the TFF family. These ATPases drive filament assembly in all TFF superfamily members; some family members also feature paralogs that can retract the filament; some family members have multiple paralogs capable of retraction with different forces (Chlebek et al., 2019; Talà et al., 2019). Beneath ArlI lies ArlH, which features ATP-binding motifs but has not been shown to be an ATPase (Hanson and Whiteheart, 2005; Chaudhury et al., 2016). ArlH has a RecA/RAD51-like fold related to the circadian clock protein KaiC (Chaudhury et al., 2016;

Meshcheryakov and Wolf, 2016), suggesting a timer function implicated in triggering a switch in ArlI between its two roles in assembly and rotation.

ArlB forms the archaellar filament, which coils to form a helical propeller when rotated by the archaellar motor (Poweleit et al., 2016; Daum et al., 2017; Meshcheryakov et al., 2019). This filament is assembled atop ArlJ using energy from ArlI's ATP hydrolysis activity. The ArlB filament is a compact helix assembled around a bundle of hydrophobic N-terminal α-helices. The head and N-terminal helix interact with six or eight neighboring protomers to assemble a strong and relatively rigid filament.

As with all rotary motors, productive rotation must depend upon a static stator component that the rotor component can rotate relative to. In the case of the archaellum, ArlF and ArlG have been implicated to form this stator (Banerjee et al., 2015). Both localize to the archaeal pseudo-periplasm; ArlG forms a helical filament that is probably capped by S-layer-anchored ArlF; deletion of either gene or abolition of S-layer binding abolishes rotation (Tsai et al., 2020).

The final component of the archaellum is an enigmatic cytoplasmic protein complex. In the model crenarchaeon *S. acidocaldarius,* ArlX, a protein with a transmembrane helix, forms 30 nm-wide cyclic oligomers (Banerjee et al., 2012, 2013). Other species instead feature a complex of ArlCDE. These lack predicted transmembrane helices but feature sequence motifs that evoke ArlX, although whether ArlCDE and ArlX are homologs remains to be seen. For brevity, for the remainder of this text we use "ArlX" as shorthand to denote both ArlX and ArlCDE. Little more is known about the role or location of ArlX.

What Is Known About the Mechanism of Archaellar Rotation?

Rotary motors rotate a rotor component against a stator component. In many, including human-made motors, the ATP synthase, and the bacterial flagellar motor, the energized component is integral to the stator, harnessing an energy source to drive rotation of the passive rotor. It remains unclear whether the archaellar energized component is part of the stator or rotor, however, and it is unclear for many components which rotate and which remain static–except for the S-layer-anchored ArlFG complex and rotating ArlB filament (Shahapure et al., 2014; Kinosita et al., 2016). While it follows that ArlJ, the assembly platform for ArlB, is contiguous with the archaellar filament to prevent the ArlB filament from detaching and diffusing away, *in situ* structures of related type IVa pili suggested that the ArlJ homolog could rotate against the pilus (Chang et al., 2016). The ArlJ:ArlI or ArlI:ArlH interfaces are candidates for intersubunit rotations because ArlI homologs undergo 60° rotations of conformational states, suggesting that this might be converted into physical rotation by pushing against ArlJ or ArlH. Indeed, conflicting evidence for the oligomeric state of ArlH *in situ* highlights the possibility of symmetry mismatch-mediated rotation between ArlI, ArlH, ArlJ, or ArlX. Nevertheless, ArlI, ArlH, and ArlX interact, suggesting they form a contiguous complex (Chaudhury et al., 2016), and ArlX is destabilized in the absence of ArlJ, suggesting that it is a structural component associated with the core of the motor. These insights hint that the rotor:stator interface may instead lie between ArlX and ArlFG; conformational changes in ArlI resulting from ATP hydrolysis could be communicated via ArlX to exert force against an interface with ArlFG, resulting in ArlFG being the stator and ArlX, ArlH, ArlI, ArlJ, and ArlB being the rotor. Nevertheless, ArlX would also provide an obvious structure to anchor a ring of ArlFG stator units. Understanding the location of this elusive interface, and identifying the mechanism of torque generation, is crucial to understanding where the archaellum got its rotation.

Direct observations of archaellum rotation provide some clues to the underlying mechanism (Alam and Oesterhelt, 1984; Shahapure et al., 2014). Archaella rotate both clockwise and counterclockwise but do not extend or retract during rotation. The torque produced by the archaellar motor is of the magnitude expected from ATP hydrolysis by a single hexameric ATPase (Iwata et al., 2019): the estimated torque required to rotate the archaellum one full turn would require hydrolysis of 12 ATP molecules, suggesting that two of the hexameric ArlI ATPase subunits are active at any one time, which coincides with the dimeric nature of ArlJ (Iwata et al., 2019). This, in turn, corresponds to detection of 60° steps in archaellar rotation in both directions (Kinosita et al., 2016), although a confounding observation is that the archaellum also rotates in 36° steps in both directions.

The Current Model for How the Archaellum Got Its Rotation

Understanding the evolutionary steps required to bridge the gap between a non-rotary ancestor to a rotary archaellum may be within our reach. Two phylogenetic studies of the TFF family provide first clues into how the archaellum evolved (Makarova et al., 2016; Denise et al., 2019). The more recent study assumed that archaellar components are organized in gene clusters in order to annotate TFF family members across bacteria and archaea, revealing that archaella diverged from a non-retracting pilus clade of the TFF family that includes Aap pili, halo pili, UV-inducible pili and bindosomes (Denise et al., 2019), suggesting the non-rotary ancestor of the archaellum assembled such a pilus. Archaella differ from this putative ancestor in three ways: first, their ATPase can generate torque; second, their ATPase can switch from assembly to torque generation; and third, they feature a stator complex against which to exert this torque. These differences involved gain of ArlF, ArlG, ArlH, and ArlX.

Naively, the biggest step would have been the first: to evolve an ATPase that exerts torque. It may be, however, that the intrinsic rotation of conformational states in the hexameric AAA + ATPase family was exapted for rotation of the rotor. It has even been suggested that all TFF ATPases rotate while extending the pilus (Campos et al., 2013) due to a symmetry mismatch between the hexameric ATPase and the helical pilus, suggesting that TFF ATPases rotate within the cytoplasm while the pilus extends. This, however, may be a red herring, as it holds that assembly is integral to rotation; the archaellum, meanwhile, can still rotate after assembly has halted.

What is required, then, is the second step: evolution of a stator complex to anchor to the cell superstructure to exapt the rotation of ArlI to rotate the pilus. Curiously, the probable stator proteins ArlF and ArlG are paralogs of the filament protein ArlB (Banerjee et al., 2015; Tsai et al., 2020). ArlF and ArlG share a fold and binding interfaces with ArlB, although ArlG forms an open helix, unlike the more rigid closed ArlB filament (Umrekar et al., 2021b). Although superficially dissimilar, closer inspection reveals that ArlG protomers still retain a subset, but not all, of the inter-protomer interactions of ArlB protomers, resulting in loss of lateral interactions and fewer ArlG protomers incorporating into the helix. Such an open helix of the ArlG filament will be more flexible than the tightly interconnected ArlB filament and could facilitate elastic storage of the energy burst from ATP hydrolysis. ArlX may couple the ATPase to the stator complexes.

The remaining step, functional switching of the ATPase from assembly to rotation, may not have been essential, as a rotating pilus that continues to extend, while wasteful, would still generate thrust. Switching from assembly to rotation may have initially been achieved by chance, and later enhanced by adding a dedicated ArlH timer. Indeed, because measuring the length of the archaellar filament is difficult, a timer may have been easier to evolve than a ruler.

WHAT IS NEEDED TO UNDERSTAND HOW THE ARCHAELLUM GOT ITS ROTATION?

More Information on Diversity That Might Reveal the Evolutionary Path to Rotation

Understanding how the archaellum evolved to rotate will benefit from the most comprehensive possible view of (meta)genomic diversity to understand contemporary variants and to ascertain whether any proto-archaellum "missing links" exist. Earlier studies lacked the current wealth of (meta)genomic data available, or assumed that all archaellum components cluster together in a genome (Makarova et al., 2016; Denise et al., 2019). Their sequence models can serve as a foundation for future focused studies across the breadth of genomic diversity (Parks et al., 2021) and can be updated to generate more sensitive models. False positives can be removed by iteratively removing proteins established to function elsewhere. Whether an identified TFF is an archaellum can also be suggested based on the presence of a class F1 chemosensory system (Wuichet and Zhulin, 2010), which appears to signal exclusively to archaella in the Archaea (Briegel et al., 2015). Most chemosensory proteins are easy to detect and unique to the chemosensory pathway.

A phylogeny derived from concatenated alignments of ubiquitous components of only archaella and close relatives will allow us to understand sequence changes during evolution and, ideally, "missing links" that lack one of the proteins exclusive to archaella. Should such a missing link be discovered, it will be valuable in illuminating the evolutionary steps taken to form the first fully fledged contemporary archaellum. Such missing links, however, are notoriously elusive, and they have still not been discovered for analogous, intensively studied machines like the bacterial flagellum (Beeby et al., 2020). Absence of these intermediary steps is similar to gaps in fossil records (Gould and Eldredge, 1993) and is suggestive of punctuated evolution, in which the first rotary archaellum rapidly (almost instantaneously on the evolutionary timescale) adapted to form an archaellum that already resembled that of contemporary *S. acidocaldarius*. Anecdotal support of this may come from the (admittedly problematic) use of core functionally invariant components as molecular timekeepers. For example, selective pressure on the prepilin peptidase, ArlK (Bardy and Jarrell, 2002), may not have changed in the transition to becoming an archaellum from a pilus, making ArlK a potential chronometer against which to assess rapid punctuated evolution of other components.

The diversity in bacterial flagella was unanticipated until they were imaged (Chen et al., 2011). Similarly, archaella may also have such unanticipated diversity. Comparative genomics may highlight variants of archaella and predict novel components. Consistent operon co-occurrence of two genes is a strong indicator of functional interaction of their products (Overbeek et al., 1999) and may suggest novel archaellum components. Similarly, curated phylogenetic profiles of protein families can highlight consistent cross-genome co-occurrences of protein families that are candidates for novel archaellum components (Pellegrini et al., 1999).

More Information on the Mechanism of Rotation

To understand how archaellar rotation evolved, it will be crucial to understand the mechanism of rotation. Obtaining atomic models of the archaellum in different conformational states is now conceivable given recent advances of *ex situ* and *in situ* cryoEM and structure prediction (Baek et al., 2021; Jumper et al., 2021). The best candidate for such structural work is likely to involve electron cryotomography with subtomogram averaging of the archaellum from *Pyrococcus furiosus,* which has proved to be the most tractable system for *in situ* archaellar imaging (Daum et al., 2017). More data collected using contemporary hardware will be required to push to the ∼8 Å-resolutions required to position α-helices.

By combining such structural snapshots of the machinery in action with biophysical studies and molecular dynamic simulations, it may be possible to parameterize a predictive molecular model of torque generation. Biophysical measurements will require high temporal and spatial resolution of torque and speed to identify steps and torques, mapped to different motor conformations using correlated structural and cellular techniques. Perturbations to mechanical output in mutants will provide more information about the roles of subcomponents. For example, the recent determination of the structure of the ArlG filament suggests that it acts as a stator and as an elastic storage device for the energy released during ATP hydrolysis (Umrekar et al., 2021b). Would a more rigid ArlG filament change the mechanical output of the motor by making steps more abrupt?

Understanding these results will ultimately also require us to understand which components rotate and which remain static, a goal that will require sophisticated imaging of live cells to detect rotation of different archaellar labeled subcomponents. Combining this with high resolution subtomogram averages of functional archaella *in situ* will enable mapping of conformational states to show what rotates and what does not.

More Information on the Origin of Rotation: Was It an Exaptation of Intrinsic Type IV Filament Rotation?

Is rotation intrinsic to TFFs, and was it exapted for rotation in archaella? Success in understanding which proteins rotate and which remain static may be extended to components of other TFF members to test whether proteins that rotate in archaella also rotate in other family members. Alternatively, a mutant could be created that binds or crosslinks (using, e.g., cysteines or unnatural amino acids) components to the cell body to create a surrogate for a stator complex to see if this results in pilus rotation.

Ultimately, the acid test of our theories will be whether we can recapitulate the evolutionary events we infer. First steps will be to "break" the archaellum in targeted components so that it no longer rotates and to identify suppressor mutations that restore motility. What is required for this? More extensive efforts may generate plausible ancestral states using ancestral sequence-reconstruction techniques to timepoints along the evolution of the contemporary archaellum and attempt to recapitulate the subsequent steps using strong lab-based selective pressure. Yet more ambitious would be to attempt to evolve an archaellum analog from a contemporary TFF superfamily member.

CONCLUDING REMARKS

The time is ripe for us to make substantial advances in understanding how rotation emerged in a molecular machine. The archaellum is a rotary motor that is uniquely simple (with many fewer components than all other rotary motors except the ExbBD family), easy to assay (with a long filament whose rotation is easier to monitor than complexes such as ExbBD), and phylogenetically well-understood (with many non-rotary cousins), making it an ideal case study of the emergence of rotation. Recent and continued advances in genomics, biophysics, and structural biology suggest that the archaellum is poised to become the first rotary machine whose evolution we understand.

AUTHOR CONTRIBUTIONS

Both authors conceived, wrote, and edited the manuscript.

FUNDING

This work was supported by the Human Frontiers Science Programme (grant no. RGP0028/2021) to MB.

REFERENCES

Abby, S. S., and Rocha, E. P. C. (2012). The non-flagellar type III secretion system evolved from the bacterial flagellum and diversified into host-cell adapted systems. *PLoS Genet.* 8:e1002983. doi: 10.1371/journal.pgen.1002983

Alam, M., and Oesterhelt, D. (1984). Morphology, function and isolation of halobacterial flagella. *J. Mol. Biol.* 176, 459–475. doi: 10.1016/0022-2836(84)90172-4

Albers, S.-V., and Jarrell, K. F. (2018). The archaellum: an update on the unique archaeal motility structure. *Trends Microbiol.* 26, 351–362. doi: 10.1016/j.tim.2018.01.004

Baek, M., DiMaio, F., Anishchenko, I., Dauparas, J., Ovchinnikov, S., Lee, G. R., et al. (2021). Accurate prediction of protein structures and interactions using a three-track neural network. *Science* 373, 871–876. doi: 10.1126/science.abj8754

Banerjee, A., Ghosh, A., Mills, D. J., Kahnt, J., Vonck, J., and Albers, S. V. (2012). FlaX, a unique component of the crenarchaeal archaellum, forms oligomeric ring-shaped structures and interacts with the motor ATPase FlaI. *J. Biol. Chem.* 287, 43322–43330. doi: 10.1074/jbc.M112.414383

Banerjee, A., Neiner, T., Tripp, P., and Albers, S. V., (2013). Insights into subunit interactions in the Sulfolobus acidocaldarius archaellum cytoplasmic complex. *FEBS J.* 280, 6141–6149. doi: 10.1111/febs.12534

Banerjee, A., Tsai, C.-L., Chaudhury, P., Tripp, P., Arvai, A. S., Ishida, J. P., et al. (2015). FlaF is a β-Sandwich protein that anchors the archaellum in the archaeal cell envelope by binding the S-Layer protein. *Structure* 23, 863–872. doi: 10.1016/j.str.2015.03.001

Bardy, S. L., and Jarrell, K. F. (2002). FlaK of the archaeon *Methanococcus maripaludis* possesses preflagellin peptidase activity. *FEMS Microbiol. Lett.* 208, 53–59. doi: 10.1016/S0378-1097(01)00579-1

Beeby, M. (2019). Evolution of a family of molecular Rube Goldberg contraptions. *PLoS Biol.* 17:e3000405. doi: 10.1371/journal.pbio.3000405

Beeby, M., Ferreira, J. L., Tripp, P., Albers, S.-V., and Mitchell, D. R. (2020). Propulsive nanomachines: the convergent evolution of archaella, flagella and cilia. *FEMS Microbiol. Rev.* 44, 253–304. doi: 10.1093/femsre/fuaa006

Berry, J.-L., and Pelicic, V. (2015). Exceptionally widespread nanomachines composed of type IV pilins: the prokaryotic Swiss Army knives. *FEMS Microbiol. Rev.* 39, 134–154. doi: 10.1093/femsre/fuu001

Briegel, A., Ortega, D. R., Huang, A. N., Oikonomou, C. M., Gunsalus, R. P., and Jensen, G. J. (2015). Structural conservation of chemotaxis machinery across Archaea and Bacteria. *Environ. Microbiol. Rep.* 7, 414–419. doi: 10.1111/1758-2229.12265

Campos, M., Cisneros, D. A., Nivaskumar, M., and Francetic, O. (2013). The type II secretion system – a dynamic fiber assembly nanomachine. *Res. Microbiol.* 164, 545–555. doi: 10.1016/j.resmic.2013.03.013

Chang, Y., Zhang, K., Carroll, B. L., Zhao, X., Charon, N. W., Norris, S. J., et al. (2020). Molecular mechanism for rotational switching of the bacterial flagellar motor. *Nat. Struct. Mol. Biol.* 27, 1041–1047. doi: 10.1038/s41594-020-0497-2

Chang, Y.-W., Rettberg, L. A., Treuner-Lange, A., Iwasa, J., Søgaard-Andersen, L., and Jensen, G. J. (2016). Architecture of the type IVa pilus machine. *Science* 351:aad2001. doi: 10.1126/science.aad2001

Chaudhury, P., Neiner, T., D'Imprima, E., Banerjee, A., Reindl, S., Ghosh, A., et al. (2016). The nucleotide-dependent interaction of FlaH and FlaI is essential for assembly and function of the archaellum motor. *Mol. Microbiol.* 99, 674–685. doi: 10.1111/mmi.13260

Chen, S., Beeby, M., Murphy, G. E., Leadbetter, J. R., Hendrixson, D. R., Briegel, A., et al. (2011). Structural diversity of bacterial flagellar motors. *EMBO J.* 30, 2972–2981. doi: 10.1038/emboj.2011.186

Chlebek, J. L., Hughes, H. Q., Ratkiewicz, A. S., Rayyan, R., Wang, J. C.-Y., Herrin, B. E., et al. (2019). PilT and PilU are homohexameric ATPases that coordinate to retract type IVa pili. *PLoS Genet.* 15:e1008448. doi: 10.1371/journal.pgen.1008448

Daum, B., Vonck, J., Bellack, A., Chaudhury, P., Reichelt, R., Albers, S. V., et al. (2017). Structure and in situ organisation of the *Pyrococcus furiosus* archaellum machinery. *eLife Sci.* 6:e27470. doi: 10.7554/eLife.27470

Deme, J., Johnson, S., Vickery, O., Muellbauer, A., Monkhouse, H., Griffiths, T., et al. (2020). Structures of the stator complex that drives rotation of the bacterial flagellum. *bioRxiv* [preprint] doi: 10.1101/2020.05.12.089201

Denise, R., Abby, S. S., and Rocha, E. P. C. (2019). Diversification of the type IV filament superfamily into machines for adhesion, protein secretion, DNA uptake, and motility. *PLoS Biol.* 17:e3000390. doi: 10.1371/journal.pbio.3000390

Fang, Q., Tang, W.-C., Tao, P., Mahalingam, M., Fokine, A., Rossmann, M. G., et al. (2020). Structural morphing in a symmetry-mismatched viral vertex. *Nat. Commun.* 11:1713. doi: 10.1038/s41467-020-15575-4

Ghosh, A., and Albers, S.-V. (2011). Assembly and function of the archaeal flagellum. *Biochem. Soc. Trans.* 39, 64–69. doi: 10.1042/BST0390064

Gould, S. J., and Eldredge, N. (1993). Punctuated equilibrium comes of age. *Nature* 366, 223–227. doi: 10.1038/366223a0

Gould, S. J., and Vrba, E. S. (1982). Exaptation-A missing term in the science of form. *Paleobiology* 8, 4–15.

Hanson, P. I. and Whiteheart, S. W., (2005). AAA+ proteins: have engine, will work. *Nat. Rev. Mol. Cell Biol.* 6, 519–529. doi: 10.1038/nrm1684

Hendrix, R. W. (1978). Symmetry mismatch and DNA packaging in large bacteriophages. *Proc. Natl. Acad. Sci. U.S.A.* 75, 4779–4783. doi: 10.1073/pnas.75.10.4779

Hugel, T., Michaelis, J., Hetherington, C. L., Jardine, P. J., Grimes, S., Walter, J. M., et al. (2007). Experimental test of connector rotation during DNA packaging into bacteriophage φ29 capsids. *PLoS Biol.* 5:e59. doi: 10.1371/journal.pbio.0050059

Iwata, S., Kinosita, Y., Uchida, N., Nakane, D., and Nishizaka, T. (2019). Motor torque measurement of *Halobacterium salinarum* archaellar suggests a general model for ATP-driven rotary motors. *Commun. Biol.* 2, 1–6. doi: 10.1038/s42003-019-0422-6

Jumper, J., Evans, R., Pritzel, A., Green, T., Figurnov, M., Ronneberger, O., et al. (2021). Highly accurate protein structure prediction with AlphaFold. *Nature* 596, 583–589. doi: 10.1038/s41586-021-03819-2

Kim, S., Zuromski, K. L., Bell, T. A., Sauer, R. T., and Baker, T. A. (2020). ClpAP proteolysis does not require rotation of the ClpA unfoldase relative to ClpP. *eLife* 9:e61451. doi: 10.7554/eLife.61451

Kinosita, Y., Uchida, N., Nakane, D., and Nishizaka, T. (2016). Direct observation of rotation and steps of the archaellum in the swimming halophilic archaeon *Halobacterium salinarum*. *Nat. Microbiol.* 1:16148. doi: 10.1038/nmicrobiol.2016.148

Liu, N., Chistol, G., and Bustamante, C. (2015). Two-subunit DNA escort mechanism and inactive subunit bypass in an ultra-fast ring ATPase. *eLife* 4:e09224. doi: 10.7554/eLife.09224

Liu, S., Chistol, G., Hetherington, C. L., Tafoya, S., Aathavan, K., Schnitzbauer, J., et al. (2014). A Viral packaging motor varies its DNA rotation and step size to preserve subunit coordination as the capsid fills. *Cell* 157, 702–713. doi: 10.1016/j.cell.2014.02.034

Makarova, K. S., Koonin, E. V., and Albers, S. V. (2016). Diversity and evolution of type IV pili systems in Archaea. *Front. Microbiol.* 7:667. doi: 10.3389/fmicb.2016.00667

Meshcheryakov, V. A., and Wolf, M. (2016). Crystal structure of the flagellar accessory protein FlaH of *Methanocaldococcus jannaschii* suggests a regulatory role in archaeal flagellum assembly. *Protein Sci.* 25, 1147–1155. doi: 10.1002/pro.2932

Meshcheryakov, V. A., Shibata, S., Schreiber, M. T., Villar-Briones, A., Jarrell, K. F., Aizawa, S.-I., et al. (2019). High-resolution archaellum structure reveals a conserved metal-binding site. *EMBO Rep.* 20:e46340. doi: 10.15252/embr.201846340

Overbeek, R., Fonstein, M., D'Souza, M., Pusch, G. D., and Maltsev, N. (1999). Use of contiguity on the chromosome to predict functional coupling. *In Silico Biol. (Gedrukt)* 1, 93–108.

Parks, D. H., Chuvochina, M., Rinke, C., Mussig, A. J., Chaumeil, P.-A., and Hugenholtz, P. (2021). GTDB: an ongoing census of bacterial and archaeal diversity through a phylogenetically consistent, rank normalized and complete genome-based taxonomy. *Nucleic Acids Res.* 50, D785–D794. doi: 10.1093/nar/gkab776

Pellegrini, M., Marcotte, E. M., Thompson, M. J., Eisenberg, D., and Yeates, T. O. (1999). Assigning protein functions by comparative genome analysis: protein phylogenetic profiles. *Proc. Natl. Acad. Sci. U.S.A.* 96, 4285–4288. doi: 10.1073/pnas.96.8.4285

Pogoryelov, D., Yu, J., Meier, T., Vonck, J., Dimroth, P., and Muller, D. J. (2005). The c15 ring of the Spirulina platensis F-ATP synthase: F1/F0 symmetry mismatch is not obligatory. *EMBO Rep.* 6, 1040–1044. doi: 10.1038/sj.embor.7400517

Pohlschroder, M., Pfeiffer, F., Schulze, S., and Halim, M. F. A. (2018). Archaeal cell surface biogenesis. *FEMS Microbiol. Rev.* 42, 694–717. doi: 10.1093/femsre/fuy027

Poweleit, N., Ge, P., Nguyen, H. H., Loo, R. R. O., Gunsalus, R. P., and Zhou, Z. H. (2016). CryoEM structure of the *Methanospirillum hungatei* archaellum reveals structural features distinct from the bacterial flagellum and type IV pili. *Nat. Microbiol.* 2, 16222–16222. doi: 10.1038/nmicrobiol.2016.222

Ripstein, Z. A., Vahidi, S., Houry, W. A., Rubinstein, J. L., and Kay, L. E. (2020). A processive rotary mechanism couples substrate unfolding and proteolysis in the ClpXP degradation machinery. *eLife* 9:e52158. doi: 10.7554/eLife.52158

Santiveri, M., Roa-Eguiara, A., Kühne, C., Wadhwa, N., Hu, H., Berg, H. C., et al. (2020). Structure and function of stator units of the bacterial flagellar motor. *Cell* 183, 244–257.e16. doi: 10.1016/j.cell.2020.08.016

Shahapure, R., Driessen, R. P. C., Haurat, M. F., Albers, S. V., and Dame, R. T. (2014). The archaellum: a rotating type IV pilus. *Mol. Microbiol.* 91, 716–723. doi: 10.1111/mmi.12486

Talà, L., Fineberg, A., Kukura, P., and Persat, A. (2019). *Pseudomonas aeruginosa* orchestrates twitching motility by sequential control of type IV pili movements. *Nat. Microbiol.* 4:774. doi: 10.1038/s41564-019-0378-9

Thomas, D. R., Morgan, D. G., and DeRosier, D. J. (1999). Rotational symmetry of the C ring and a mechanism for the flagellar rotary motor. *Proc. Natl. Acad. Sci. U.S.A.* 96, 10134–10139. doi: 10.1073/pnas.96.18.10134

Tsai, C.-L., Tripp, P., Sivabalasarma, S., Zhang, C., Rodriguez-Franco, M., Wipfler, R. L., et al. (2020). The structure of the periplasmic FlaG–FlaF complex and its essential role for archaellar swimming motility. *Nat. Microbiol.* 5, 216–225. doi: 10.1038/s41564-019-0622-3

Umrekar, T. R., Cohen, E., Drobnič, T., Gonzalez-Rodriguez, N., and Beeby, M. (2021a). CryoEM of bacterial secretion systems: a primer for microbiologists. *Mol. Microbiol.* 115, 366–382. doi: 10.1111/mmi.14637

Umrekar, T. R., Winterborn, Y. B., Sivabalasarma, S., Brantl, J., Albers, S.-V., and Beeby, M. (2021b). Evolution of archaellum rotation involved invention of a stator complex by duplicating and modifying a core component. *Front. Microbiol.* 12:773386. doi: 10.3389/fmicb.2021.773386

Westermann, S., Wang, H.-W., Avila-Sakar, A., Drubin, D. G., Nogales, E., and Barnes, G. (2006). The Dam1 kinetochore ring complex moves processively on depolymerizing microtubule ends. *Nature* 440, 565–569. doi: 10.1038/nature04409

Wuichet, K., and Zhulin, I. B. (2010). Origins and diversification of a complex signal transduction system in prokaryotes. *Sci. Signal.* 3:ra50. doi: 10.1126/scisignal.2000724

Conflict of Interest: The authors declare that the research was conducted in the absence of any commercial or financial relationships that could be construed as a potential conflict of interest.

Publisher's Note: All claims expressed in this article are solely those of the authors and do not necessarily represent those of their affiliated organizations, or those of the publisher, the editors and the reviewers. Any product that may be evaluated in this article, or claim that may be made by its manufacturer, is not guaranteed or endorsed by the publisher.

Copyright © 2022 Ortega and Beeby. This is an open-access article distributed under the terms of the Creative Commons Attribution License (CC BY). The use, distribution or reproduction in other forums is permitted, provided the original author(s) and the copyright owner(s) are credited and that the original publication in this journal is cited, in accordance with accepted academic practice. No use, distribution or reproduction is permitted which does not comply with these terms.

frontiers in Microbiology

REVIEW
published: 21 March 2022
doi: 10.3389/fmicb.2022.848597

Towards Elucidating the Rotary Mechanism of the Archaellum Machinery

*João Nuno de Sousa Machado[1,2], Sonja-Verena Albers[1,2] and Bertram Daum[3,4]**

[1]Molecular Biology of Archaea, Faculty of Biology, Institute of Biology II, University of Freiburg, Freiburg, Germany, [2]Spemann Graduate School of Biology and Medicine, University of Freiburg, Freiburg, Germany, [3]Living Systems Institute, University of Exeter, Exeter, United Kingdom, [4]College of Life and Environmental Sciences, University of Exeter, Exeter, United Kingdom

Motile archaea swim by means of a molecular machine called the archaellum. This structure consists of a filament attached to a membrane-embedded motor. The archaellum is found exclusively in members of the archaeal domain, but the core of its motor shares homology with the motor of type IV pili (T4P). Here, we provide an overview of the different components of the archaellum machinery and hypothetical models to explain how rotary motion of the filament is powered by the archaellum motor.

Keywords: archaea, archaellum motor, cell motility, type IV pili, archaella, molecular motors

OPEN ACCESS

Edited by:
Michael Manson,
Texas A&M University, United States

Reviewed by:
Damien Paul Devos,
Andalusian Center for Development Biology (CSIC), Spain
Jerry Eichler,
Ben-Gurion University of the Negev, Israel

***Correspondence:**
Bertram Daum
b.daum2@exeter.ac.uk

Specialty section:
This article was submitted to Microbial Physiology and Metabolism, a section of the journal Frontiers in Microbiology

Received: *04 January 2022*
Accepted: *23 February 2022*
Published: *21 March 2022*

Citation:
de Sousa Machado JN, Albers S-V and Daum B (2022) Towards Elucidating the Rotary Mechanism of the Archaellum Machinery. Front. Microbiol. 13:848597. doi: 10.3389/fmicb.2022.848597

INTRODUCTION

Rotary nanomachines play an essential role in virtually all living cells. A particularly famous example is the ubiquitous ATP synthase, which converts a proton gradient into ATP by rotary catalysis (Itoh et al., 2004). Other gyrating molecular machines, such as flagella, gliding motors, and archaella, drive cellular propulsion (Berg, 2003; Albers and Jarrell, 2015; Shrivastava et al., 2015).

Among these propulsive molecular machines, the archaellum is particularly interesting, considering its evolutionary history. The archaellum is part of a superfamily of molecular machines called type IV filaments (TFF), which include pili [e.g., type IV pili (T4P)] and secretion systems [e.g., type II secretion (T2SS); Berry and Pelicic, 2015]. While some T4P drive cellular motility through cycles of extension and retraction (Mattick, 2002), the archaellum is the only known member of the TFF superfamily with a rotating filament.

In this review, we summarise the current knowledge about the biophysics and structure of the archaellum machinery and present a hypothetical model describing its mechanism.

THE *ARL* OPERON

Archaella are found across various archaeal phyla, from the relatively well-characterised Euryarchaeota and Crenarchaeota to less understood organisms, such as the putative ectosymbionts of the DPANN superphylum (Jarrell et al., 2021). The biogenesis of a functional archaellum requires the expression of 7–15 genes, which are usually organised in a cluster—the *arl* operon—plus a membrane-embedded aspartic acid protease, often encoded elsewhere in the chromosome (Desmond et al., 2007; Pohlschröder et al., 2018; Jarrell et al., 2021). The aspartic acid protease ArlK/PibD is essential for motility, as it is responsible for cleavage of the class III signal

peptide from the filament-forming archaellin subunits (Bardy and Jarrell, 2002, 2003; Albers et al., 2003). The archaellins are usually encoded by gene(s) at the start of the *arl* cluster, with the remaining genes in the cluster coding for proteins of the archaellum motor complex (**Figure 1**). The motor complex consists of the ATPase ArlI, which powers the assembly and rotation of archaella; a putative switch protein ArlH (Reindl et al., 2013; Chaudhury et al., 2018); ArlJ, a polytopic membrane-embedded platform protein (Ghosh and Albers, 2011); and the pseudoperiplasmic stator proteins ArlF and ArlG (Banerjee et al., 2015; Tsai et al., 2020; Umrekar et al., 2021). In Crenarchaeota, a predicted membrane protein called ArlX is thought to form a cytosolic ring that serves as a scaffold for the motor (Banerjee et al., 2012). In Euryarchaeota, ArlX is likely replaced by ArlCDE and in Thaumarchaeota by a yet to be identified protein (Desmond et al., 2007; Jarrell et al., 2021).

Apart from the proteins directly involved in archaellum biogenesis, a subset of archaea belonging to Euryarchaeota or Thaumarchaeota is equipped with a chemotaxis sensory system (Briegel et al., 2015). The absence of chemotaxis in Crenarchaeota has been suggested to be correlated with the lack of *arlC/D/E* genes in this phylum (Albers and Jarrell, 2018). The chemotaxis genes in archaea resemble those found in Bacteria and, in fact, their origin appears to be the result of horizontal gene transfer (HGT). An archaeal-specific protein CheF provides the link between the bacteria-like chemotaxis machinery and the archaellum motor complex (Schlesner et al., 2009; Briegel et al., 2015).

THE ARCHAELLUM FILAMENT

The archaellum machinery consists of a helical filament driven by a motor complex. Even before the formal definition of the domain Archaea, researchers described the filament as a rotating structure that allowed for both forward and reverse movement in *Halobacterium salinarum* (Alam and Oesterhelt, 1984; Woese et al., 1990; Marwan et al., 1991). This filament can rotate

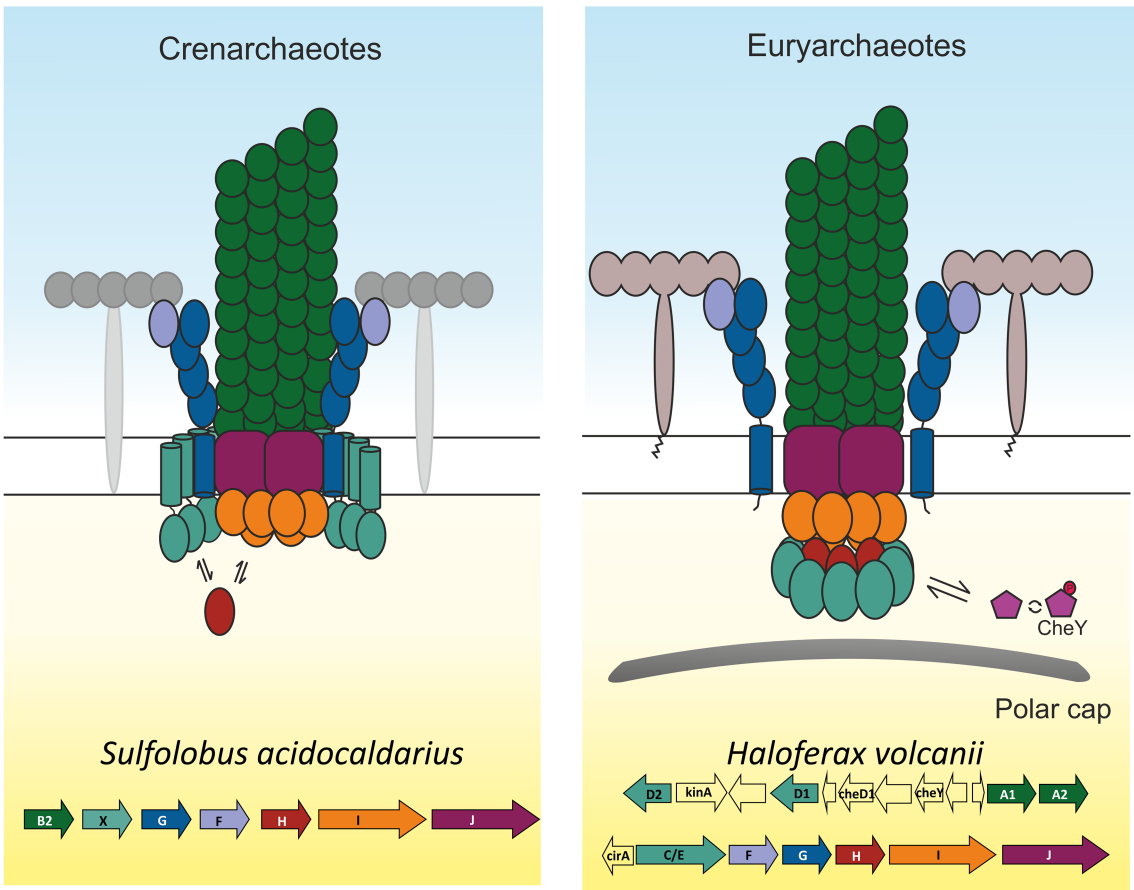


FIGURE 1 | The archaellum machinery in Cren- and Euryarchaeota. The structural proteins of the archaellum are encoded by genes organised in the *arl* cluster. The *arl* cluster differs between Crenarchaeota and Euryarchaeota in three main aspects: Crenarchaeota usually encode a single archaellin, with multiple present in the euryarchaeal arl cluster; the order of the genes *arlF* and *arlG* is different between the two phyla. The gene *arlX* is present only in Crenarchaeota and is replaced with *arlCDE* in Euryarchaeota (Desmond et al., 2007). ArlCDE in Euryarchaeota is thought to be linked to the chemotaxis machinery. ArlCDE is absent in Crenarchaeota, which also lack chemotaxis. The pre-archaellin peptidase PibD/ArlK is also essential for archaella biogenesis, but this gene is frequently found elsewhere in the genome. Upon expression of the cluster, the archaellum motor complex self assembles at the membrane.

either clock- or counter-clockwise, maintaining a chiral super-helical structure regardless of the direction of rotation (Marwan et al., 1991; Kinosita et al., 2016). Clockwise rotation of the archaellum enables the cell to swim forward, while anticlockwise rotation propels the cell backwards.

The archaellum filament consists of helically organised proteins called archaellins. Archaellins are tadpole shaped proteins with a hydrophobic N-terminal tail and a hydrophilic, β-sheet-rich globular C-terminus (**Figure 2**). The hydrophobic N-termini of the archaellins form the core of the filament, while the (often N-glycosylated) C-termini face outwards (Poweleit et al., 2016; Daum et al., 2017; Meshcheryakov et al., 2019; Gambelli et al., 2021). The N- and C-termini are coupled by a flexible hinge region, which allows each archaellum to change its shape in bending and twisting archaella. In addition, the hydrophobic tail domains are able to slide and rotate past each other, adding to the flexibility of the filament (Gambelli et al., 2021).

In many species, the *arl* operon encodes multiple archaellins, which are likely the result of gene duplication events. These duplicates are usually not redundant, even in cases where their deletion does not result in defective archaellum biogenesis. For instance, in the halophile *Haloarcula marismortui* the two archaellins ArlA and ArlB are ecoparalogs, each forming a filament better adapted to different salinity conditions (Syutkin et al., 2014, 2019). In some other organisms, all archaellin homologues are necessary for the synthesis of functional archaella. This suggests that—at least in some archaea—different archaellins make up different parts of the archaellum.

Take the example of *H. salinarum*: this organism encodes five archaellin genes belonging either to the *arlA* (*arlA1* and *arlA2*) or *arlB* (*arlB1-3*) families (Gerl and Sumper, 1988; Gerl et al., 1989). Deletion of the *arlA* and *arlB* genes results in cells without archaella (Tarasov et al., 2000). In cells where only the *arlA* or the *arlB* gene is deleted, archaella still form. However, these cells show significantly hampered motility, indicating that both archaellins are important for proper archaellar function (Tarasov et al., 2000). Even within the *arlA* family there seems to be no redundancy: when only *arlA2* was disrupted in *H. salinarum*, the cells expressed only straight (rather than curved) filaments, resulting in decreased motility (Tarasov et al., 2000). Deleting *arlA1* and *arlA2* in *H. salinarum* resulted in a mutant that expressed only the archaellins *arlB1-3*. These cells formed short, curved filaments, corroborating the notion that these archaellins may form the cell-proximal region of the archaellum filament (Tarasov et al., 2000). Methanococcales also seem to assemble archaella in which some of the archaellins are minor components of the filament, forming hook-like, specialised structures in the cell-proximal region (Kalmokoff et al., 1988; Bardy et al., 2002).

In *Methanococcus voltae*, the minor archaellin ArlA is distributed along the filament (Bardy et al., 2002). Although disrupting *arlA* does not abolish archaella synthesis, it does decrease motility in this organism, suggesting an unknown, important function for this minor archaellin (Jarrell et al., 1996). *Pyrococcus furiosus*, which possesses the genes *arlB0*, *arlB1*, and *arlB2*, has an archaellum filament which appears to consist mostly of ArlB0, with ArlB1 and ArlB2 possibly localising to the ends of the filament (Näther-Schindler et al., 2014; Daum et al., 2017). Most recently, it has been shown that the archaellum filament of *Methanocaldococcus villosus* consists of two alternating subunits—ArlB1 and ArlB2 (Gambelli et al., 2021). A third archaellin (AlrB3) is encoded in the genome and it is not found in the main part of the filament, again suggesting a role in forming a terminal structure.

THE ARCHAELLUM MOTOR COMPLEX

The rotation of the archaellum is driven by a motor complex that is embedded in the archaeal cell envelope. Analogous to the bacterial flagellum, the archaellar motor complex must have two components: a rotor and a stator. Torque is generated at the interface of a moving rotor and a stator that forms the bearing of the motor. In the flagellum, the stators MotA/MotB (or, in some species, PomA and PomB) also function as ion channels that convert an ion-motive force across the membrane into a conformational change, which in turn drives the rotation of the motor rings (Hu et al., 2021). As there is currently not a clear understanding of how the different protein components of the archaellum cooperate to generate torque, the identity and function of its motor and stator components is not fully understood. Here, we assess the structural, biochemical, and biophysical knowledge of the archaellum in order to present an informed guess at possible rotation mechanisms of the archaellum motor complex. A summary of structures solved for components of the archaellum machinery is shown in **Figure 2**.

The Motor ATPase ArlI

ArlI is the only *bona fide* ATPase encoded in the *arl* operon. The enzymatic activity of ArlI from the archaeal species *Saccharolobus solfataricus* (formerly *Sulfolobus solfataricus*; Sakai and Kurosawa, 2018), *Sulfolobus acidocaldarius*, and *P. furiosus* has been characterised *in vitro* (Albers and Driessen, 2005; Ghosh et al., 2011; Chaudhury et al., 2016, 2018). As the only protein capable of hydrolysing ATP, ArlI is the sole candidate for powering the assembly and bidirectional rotation of the archaellum filament. The dual role of ArlI has been reinforced by the finding that the first 29 residues of *Sa*ArlI are essential for filament rotation but not for its assembly (Reindl et al., 2013). Despite being a soluble protein, ArlI is membrane-associated, and indeed tetraether lipids increase the ATPase activity of this protein (Albers and Driessen, 2005; Ghosh et al., 2011; Reindl et al., 2013). A structure with 2 Å resolution of *S. acidocaldarius* ArlI has resulted in the identification of an N-terminal three-helix bundle that is essential for the localisation of ArlI to the cell membrane (Reindl et al., 2013).

Monomeric ArlI has two distinct domains. These two domains are separated by a hinge, which confers some flexibility between them (Reindl et al., 2013; Mancl et al., 2016). Homology between ArlI and ATPases involved in T4P assembly and retraction hinted that ArlI might form hexameric oligomers (Berry and Pelicic, 2015), as later confirmed *in vitro* (Ghosh et al., 2011; Reindl et al., 2013; Chaudhury et al., 2018; **Figure 2**).

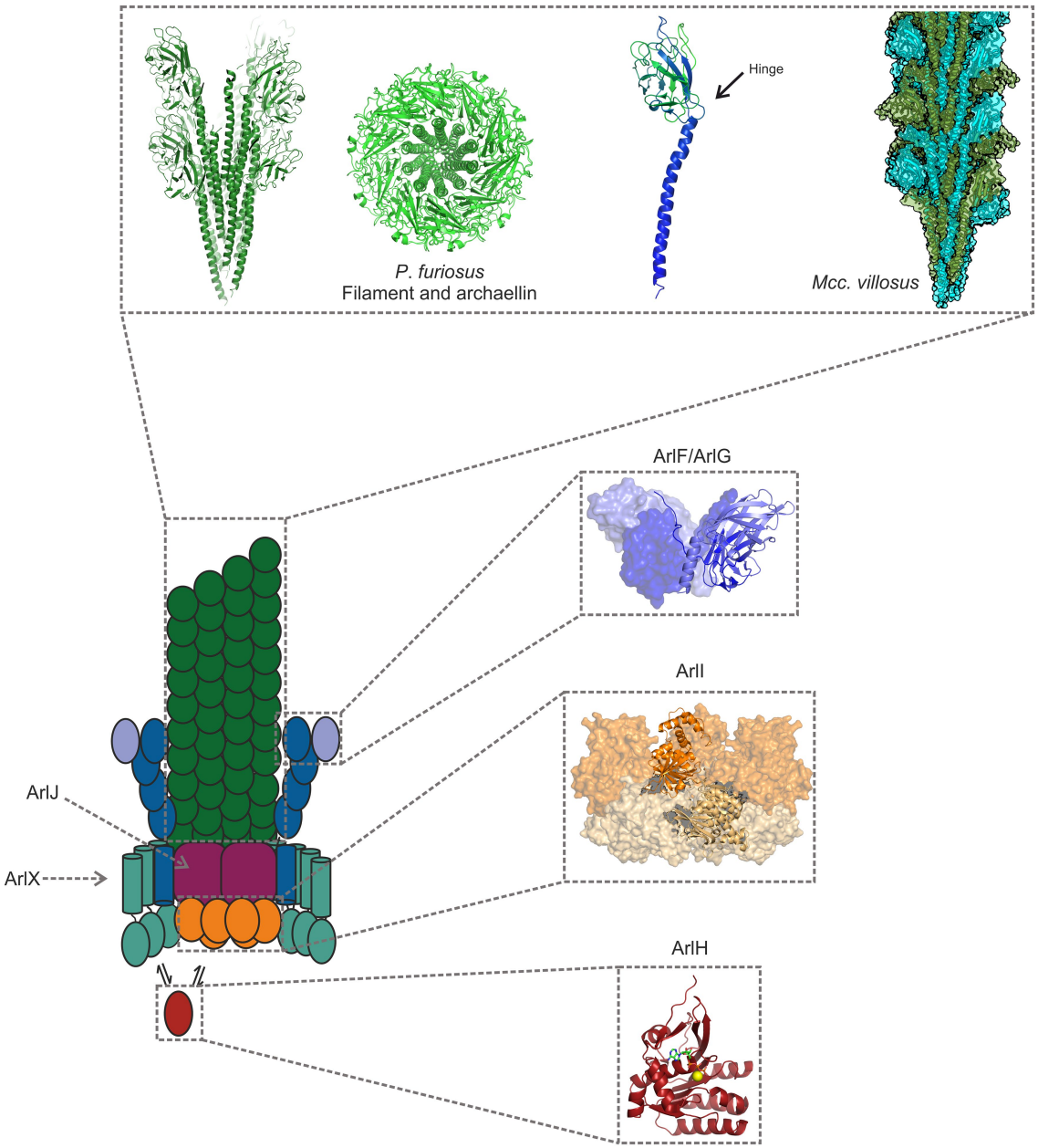


FIGURE 2 | Model of the archaellum machinery. The filament consists of tadpole shaped archaellins (left), with an N-terminal α-helical tail and a β-sheet rich, globular head domain. The hydrophobic tails make up the core of the archaellum, while the hydrophilic heads face the filament's exterior (Poweleit et al., 2016; Daum et al., 2017; Meshcheryakov et al., 2019; Gambelli et al., 2021). Two filaments are shown in the figure: one from *Pyrococcus furiosus*, and another from *Methanocaldococcus villosus* (PDB-7OFQ), a heteropolymeric filament. ArlG forms a filament that spans the pseudoperiplasm and that is tightly anchored to the S-layer by a heterotetramer consisting of ArlG and ArlF (Banerjee et al., 2015; Tsai et al., 2020; Umrekar et al., 2021). ArlI is the hexameric ATPase, which localises to the cytosolic side of the plasma membrane, probably owing to its interaction with the platform protein ArlJ, whose structure has not yet been determined (Reindl et al., 2013). ArlH is an auto-kinase that interacts with ArlI, modulating its activity and perhaps controlling when the ATPase assembles or rotates the filament (Chaudhury et al., 2016; Sousa Machado et al., 2021). The filament structure has been obtained from *P. furiosus* (5O4U; Daum et al., 2017), and the remaining structures from *Sulfolobus acidocaldarius* proteins 5TUG (Tsai et al., 2020); 4IHQ (Reindl et al., 2013); and 4YDS (Chaudhury et al., 2016).

Hexamerisation was found to be ATP-dependent, but ArlI from *P. furiosus* forms hexamers even without prior addition of this nucleotide (Mancl et al., 2016; Chaudhury et al., 2018). The X-ray structure of *S. acidocaldarius* ArlI shows a hexamer with 2-fold symmetry (Reindl et al., 2013), in which two protomers adopt an open, and the remaining four a closed, conformation. This is in line with biochemical evidence from ArlI from *P. furiosus* (Chaudhury et al., 2018): when MANT-ATP (a fluorescent analogue of ATP) is titrated in a reaction mixture containing ArlI, saturation is achieved when the concentration

of MANT-ATP equals one third that of ArlI, indicating that only two ATP-binding pockets are available (Chaudhury et al., 2018).

The structure of ArlI from *S. acidocaldarius* has allowed the modelling of the conformational changes that occur in the hexamer upon ATP binding, hydrolysis, and product release. These molecular motions include a rotation of inter-subunit blocks, which comprise the N-terminus of one protomer in close interaction with the C-terminus of a neighboring protomer. This motion likely drives the insertion of archaellin subunits during filament biosynthesis and facilitates filament rotation (Reindl et al., 2013). These conformational changes are possibly relayed across the cell membrane by the protein ArlJ. ArlI needs to be switchable so that it can promote either archaellin insertion during filament growth or rotation of a mature filament. ArlH is the protein that may provide this switch.

The Platform Protein ArlJ

The *arlJ* gene encodes a polytopic membrane protein homologous to the bacterial genes *pilC* and *gspF* belonging to the T4P and T2SS, respectively (Peabody et al., 2003). There is little experimental information about this protein except for it being essential for archaella assembly (Thomas et al., 2002; Chaban et al., 2007; Lassak et al., 2012). Bioinformatics predicts that ArlJ contains 7–9 transmembrane domains and conserved cytosolic loops (Thomas et al., 2001a; Ghosh and Albers, 2011). These cytosolic loops are rich in positively charged amino acids, which may interact with the negatively charged N-termini of ArlI (Ghosh and Albers, 2011). In *S. acidocaldarius*, ArlJ is unstable in the absence of ArlX, indicating that the two proteins interact (Lassak et al., 2012). ArlJ is presumably a platform protein during assembly and acts as a rotor that provides torque to the assembled archaellum filament (Jarrell et al., 2021). Notably, the homologous PilC protein has been suggested to rotate during extension and retraction of Type 4 pili (Chang et al., 2016), a mechanism which could conceivably have been adapted for the rotation of a filament during evolution. Moreover, it is possible that ArlJ interacts with the transmembrane domain of the putative stator subunit ArlG, which would be essential for ArlJ to act as a rotary component of the archaellum machinery.

The Putative Regulator Protein ArlH

ArlH is an ATP-binding protein that is essential for archaella biogenesis (Thomas et al., 2001b; Lassak et al., 2012; Chaudhury et al., 2016; Li et al., 2020), but its mode of action remains largely unknown. Two experimentally determined ArlH structures are currently available, one from the crenarchaeon *S. acidocaldarius* and another from the euryarchaeon *Methanocaldococcus jannaschii* (Chaudhury et al., 2016; Meshcheryakov and Wolf, 2016). The two structures are similar. Both show a RecA fold consisting of a β-sheet sandwiched between α-helices. ArlH belongs to the KaiC-like ATPases, a group of proteins widespread in Archaea. Archaeal KaiC-like ATPases are homologous with the well characterised cyanobacterial KaiC, which has a central role in the regulation of the circadian rhythm in these organisms (Johnson et al., 2017; Makarova et al., 2017). ArlH binds ATP, which is required for the biogenesis of the archaellum filament, presumably because only ATP-bound ArlH is able to stimulate the ATPase activity of ArlI (Chaudhury et al., 2016, 2018).

ArlH itself does not hydrolyse ATP (Chaudhury et al., 2016, 2018; Meshcheryakov and Wolf, 2016). Instead, ArlH exhibits auto-phosphorylation activity (Sousa Machado et al., 2021). ArlH has been shown to interact with other archaellum motor components, including ArlI (Chaudhury et al., 2016, 2018; Sousa Machado et al., 2021), ArlX (Banerjee et al., 2013; Chaudhury et al., 2016), and ArlCDE (Li et al., 2020). Phosphorylation of ArlH seems to influence both its oligomerisation and how it interacts with ArlI: the interaction between ArlI and ArlH is strongest when ArlH is not phosphorylated, and under these circumstances, ArlH adopts a hexameric form (Sousa Machado et al., 2021). When ArlH autophosphorylates, the hexameric oligomer disassembles from the ArlI/ArlH complex (Sousa Machado et al., 2021). It has been hypothesised that this is the signal that switches the archaellum machinery from filament assembly to filament rotation. As ArlH has been shown to interact with ArlX/ArlCDE, it may remain bound to these proteins after phosphorylation and dissociation from ArlI (Banerjee et al., 2013; Li et al., 2020).

The Putative Stators ArlFG

ArlF and ArlG are both periplasmic components of the archaellum motor complex. On the level of structure and sequence, both proteins show key similarities with archaellins, despite lacking the signal peptide that is characteristic for the latter (Tsai et al., 2020). Biochemical data indicate that ArlF interacts with S-layer proteins, which suggests a role for ArlF in anchoring the motor complex to the cell surface (Banerjee et al., 2015). Later, it was found that ArlG is secreted to the periplasm after being processed, but it was also seen that the processing of ArlG is not dependent on PibD/ArlK (Tsai et al., 2020). ArlG forms filaments, which can be capped by a heterotetramer formed by two ArlG and two ArlF protomers. These observations led to a model in which an ArlG filament spans the pseudoperiplasm, at which point an ArlF/ArlG heterotetramer connects the filament with the S-layer (Tsai et al., 2020; Umrekar et al., 2021). The role of these proteins is likely 2-fold; the ArlF/ArlG complex provides a scaffold around the motor complex, allowing for the rotation of the archaellar filament without cellular disruption. In addition, ArlF and ArlG act as a stator against which the motor rotates (Umrekar et al., 2021). The S-layer does not seem to be essential for the assembly of the archaellum filament, as *Sulfolobus islandicus* cells lacking an S-layer still synthesise archaella. However, these archaella are unable to rotate (Tsai et al., 2020).

The Cytosolic Ring ArlX

The *arlX* gene encodes a predicted membrane protein with a single α-helical transmembrane domain. ArlX is essential for archaella biogenesis (Banerjee et al., 2012; Lassak et al., 2012). The cytosolic domain of *S. acidocaldarius* ArlX (*Sa*ArlXc)

has been purified and shown to form an oligomeric ring structure with variable diameter, averaging 30 nm (Banerjee et al., 2012). Moreover, ArlXc was shown to interact with the cytosolic components of the *S. acidocaldarius* archaellum motor complex, ArlI and ArlH, with the latter localising inside the ring formed by ArlX (Banerjee et al., 2012; Chaudhury et al., 2016). Genetic data suggest that ArlX is stabilised by archaellins and ArlJ (Lassak et al., 2012). In combination, these data suggest that ArlX forms a stabilising ring around a central complex consisting of ArlJ, ArlI, and ArlH (Banerjee et al., 2012). In the same study, it was also suggested that ArlX may have a stator-like role in the archaellum motor complex (Banerjee et al., 2012).

ArlCDE and the Polar Cap

ArlC/D/E are thought to replace ArlX in the motor complexes of non-crenarchaeal species. Despite its possibly analogous role to ArlX, ArlC, D, and E lack the transmembrane domain found in ArlX. ArlC, D, and E are frequently found as fusion (e.g., ArlDE or ArlCDE), indicating that they are functionally interdependent and physically interact, which has been experimentally demonstrated for ArlCE and ArlD of *Haloferax volcanii* (Ng et al., 2006; Makarova et al., 2016; Li et al., 2020).

ArlCDE have been shown to interact directly with CheF, presumably because ArlCDE act as a switch complex that regulates motor activity upon chemoreceptor activation (Schlesner et al., 2009; Li et al., 2020). The interaction of ArlCDE with the core motor complex seems to be mediated by ArlH, as recently shown in *H. volcanii* (Li et al., 2020). CryoET of the motor complex from *P. furiosus* has led to the suggestion that ArlCDE (in this organism, ArlC and ArlDE) form a cytosolic ring around ArlI and ArlH. Furthermore, ArlC and ArlDE might interact with a cytosolic structure called the polar cap (Briegel et al., 2017; Daum et al., 2017). This polar cap is a cone-shaped, sheet-like and most likely proteinaceous structure that co-localises with the archaellated cell pole. The polar cap appears to be a hallmark of Euryarchaeota and was observed in early electron microscopy studies (Koval and Jarrell, 1987; Gongadze et al., 1993; Kupper et al., 1994). Until recently, the polar cap was assumed to correspond to chemosensory arrays (Briegel et al., 2015). Detailed analysis of the archaellum motor complex in *P. furiosus* and *Thermococcus kodakarensis* by cryogenic electron tomography (CryoET; Briegel et al., 2017; Daum et al., 2017) revealed that the polar cap is closely associated with the archaellum motor, suggesting that both may be physically and functionally linked.

Various functions have been suggested for the polar cap. For example, the polar cap may act as an organising centre that ensures the polar organisation of the archaellar bundle. In addition, it has been proposed that the polar cap may serve as a cytoplasmic anchor for archaella motor complexes in the absence of a membrane anchor in the putative ArlCDE stator (Briegel et al., 2017; Daum et al., 2017; Jarrell et al., 2021). Lastly, as chemosensory arrays have been observed to associate with the polar cap, it may be that the polar cap forms a relay between chemoreceptors and the archaellar motors.

Models Derived From CryoET

Despite various pieces of evidence about how the subunits of the archaellum motor interact with each other, the structure of the assembled machinery remains largely elusive. In 2017, a first three-dimensional *in situ* map of the motor complex in context with the archaellum filament, the S-layer, and the polar cap was published (Daum et al., 2017). The map showed the motor as a bell-shaped complex that projects from the cell membrane into the cytoplasm. This central complex is connected to a surrounding cytosolic ring, which itself does not appear to be connected to the cell membrane. By fitting the atomic model of ArlI from *S. acidocaldarius* and a 6-fold symmetric model of ArlH into the map, a structure for an ArlI-ArlH double-ring complex was suggested (Daum et al., 2017). In this model, ArlI attaches to the membrane *via* its N-terminal protrusions, while ArlH is associated with the opposite surface of the molecule.

Because of its position, its connection with the ArlI-ArlH complex, and its similarity with cryoEM maps of ArlX, it was suggested that the cytosolic ring may correspond to ArlC,D/E (Daum et al., 2017) This ring was not seen in tomograms of *T. kodakarensis* (Briegel et al., 2017), which could either be a consequence of species-specific variation of the archaellum motor architecture as seen in bacteria (Rossmann and Beeby, 2018), flexibility of the ring complex, or differences in the sample preparation method.

The motor complex is juxtaposed to the polar cap, suggesting a physical connection between them. However, because of limitations in resolution, no connections between polar cap and archaellum motor were resolved. Similarly, the membrane-embedded protein ArlJ and the potential ArlF/G stator subunits were not discernible.

THE BIOPHYSICS OF THE ARCHAELLUM MOTOR

Various biophysical parameters of archaellum filament rotation have been calculated for the motor of the halophiles *H. salinarum* and *H. volcanii* (Kinosita et al., 2016, 2020; Iwata et al., 2019). Both these organisms harbour the putative switch complex ArlCDE, a chemotaxis system and, at least for *H. salinarum*, a polar cap (Kupper et al., 1994). In the first detailed biophysical analysis of the rotating archaellum, the motor appeared to be stepping at 60°–36° intervals (6–10 steps per revolution; Kinosita et al., 2016). The number of steps during the revolution of a molecular motor can be correlated with the rotary mechanism. As described below, the ATPase that powers the archaellum forms a hexamer (Ghosh et al., 2011; Reindl et al., 2013; Chaudhury et al., 2018). The discrete 60° steps could thus correspond to the hydrolysis of one ATP molecule per monomer, with the hydrolysis of six ATP molecules per revolution. The ~36° steps, on the other hand, were hypothesised to be either associated with the hypothetical presence of 9–10 monomers of the modulator ArlH in the motor complex (as observed by Chaudhury et al., 2016), or motor slippage. Recent evidence suggests that ArlH forms a hexamer in the motor

(Sousa Machado et al., 2021), indicating the 9–10 stoichiometry of ArlH observed in previous single particle cryoEM data (Chaudhury et al., 2016) may have been an artefact of sample preparation. A more recent calculation indicated that the torque output of *H. salinarum* archaella is 160 pN.nm regardless of its load (Iwata et al., 2019). This torque value allowed the energy per revolution to be determined at 1,000 pJ, which is approximately twice the energy released by the hydrolysis of six molecules of ATP. This study suggested that more than six molecules of ATP are hydrolysed per revolution, and a model to account for this observation was proposed. According to this model, the membrane protein ArlJ is assumed to have *n*-fold symmetry, in which specific portions of ArlJ are in contact with *n* active sites of the ATPase ArlI. Each rotation step would therefore result in the hydrolysis of *n* ATP molecules simultaneously. By considering a motor composed of $ArlJ_2$:$ArlI_6$—which is likely, based on research on the platform protein of other TFF (Karuppiah et al., 2010; Bischof et al., 2016; Chang et al., 2016; Van Putte et al., 2018)—12 molecules of ATP would be hydrolysed per revolution. The energy released from the hydrolysis of these molecules would then result in a motor efficiency of ~100%. Other symmetries of ArlJ are also possible, with higher *n* resulting in lower motor efficiency.

Experiments on the archaellum of *H. volcanii* resulted in similar torque and energy values (Kinosita et al., 2020). The *in situ* enzymatic activity of ArlI from *P. furiosus* was found to be too low to allow for the required turnover of ATP to rotate the filament—a surprising finding given that the activity of ArlI from *P. furiosus* is reported to be 250 times higher than that measured for the ArlI of *S. acidocaldarius* (Ghosh et al., 2011; Chaudhury et al., 2018; Kinosita et al., 2020). The function of ArlI could be stabilised and stimulated *in vivo* in the presence of other motor components, as suggested by Kinosita et al. (2020). The calculations determining the number of ATP molecules hydrolysed per revolution according to the estimated torque assume a certain value of free energy per ATP molecule (Kinosita et al., 2020). Since free energy depends on temperature, it is also possible that calculations based on standard free energy of hydrolysis do not translate appropriately for hyperthermophilic organisms.

AlphaFold PREDICTIONS OF THE MOTOR CORE COMPLEX

The core of the archaellum motor is formed by the ATPase ArlI and the platform protein ArlJ, an architecture likely similar to that of other TFFs (Denise et al., 2020).

Despite the lack of biochemical and structural data on ArlJ—which was also not observed in the CryoETs—it is currently possible to predict the overall organisation of this core with the aid of AlphaFold-predicted structures of ArlJ (Jumper et al., 2021). The structure of ArlJ was predicted for *S. acidocaldarius* and for *P. furiosus*, and the resulting structures were compared with the AlphaFold-predicted ArlJ structure of *Mcc. jannaschii* available in UniProt. Overall, the three ArlJ homologs share a similar predicted structure (**Figure 3**). However, compared to ArlJ of *S. acidocaldarius*, the euryarchaeotic homologs (*P. furiosus* and *Mcc. jannaschii*) show an N-terminal extension. Alignment of ArlJ primary sequences has previously resulted in the identification of conserved cytosolic loops (Ghosh and Albers, 2011). These loops are rich in often conserved lysines and arginines, which are positively charged at the approximately neutral cytoplasmic pH. Based on the positive-inside rule for the topology of membrane proteins (von Heijne, 1992) and the putative interaction surface mediating ArlJ and ArlI interaction (Ghosh and Albers, 2011; Reindl et al., 2013), it is likely that this region faces the cytoplasm and interfaces with ArlI. These observations are in accordance with the TMHMM-predicted cytosolic, transmembrane, and extracellular regions, which are differentially coloured in the models in **Figure 3** (Sonnhammer et al., 1998; Krogh et al., 2001). Alphafold 2 was used to predict ArlJ from *S. acidocaldarius* and *P. furiosus* as a dimer, resulting in a heart-shaped structure (**Figure 4**). Calculating the hydrophobicity and charge distribution suggest the position of the membrane (**Figure 4**), as well as a putative electrostatic interface between ArlJ and ArlI (**Figure 5**). The relative orientation of ArlJ and ArlI suggests how a dimeric ArlJ may interact simultaneously with two monomers of ArlI. This has potential implications for the mechanism of archaellum rotation, as we explore below. The predicted structure shows a cleft between the two ArlJ monomers. It is conceivable that this cleft could serve as a lateral gate for incoming archaellins. Clamshell-like conformational changes within the ArlJ dimer could then facilitate the transfer of archaellins into the growing filament. However, it remains elusive how the mature archaellum filament remains anchored by the ArlJ dimer post assembly.

MODELS FOR A ROTATING ARCHAELLUM

Much information has been gathered about the individual components of the archaellum over the past years (see Jarrell et al., 2021, for a comprehensive review), but due to limited resolution of the available structures (Briegel et al., 2017; Daum et al., 2017), as well as incomplete biochemical understanding of the machinery, it is not yet possible to build a convincing and comprehensive mechanistic model to explain how the archaellum rotates. In particular, the positions and stoichiometry of some if its component proteins, such as ArlJ, ArlF, AlrG, and ArlCDE are currently unknown.

The first issue to tackle while devising possible mechanisms for archaella rotation is establishing, which archaellar components remain static and which ones move. According to the current models (Jarrell et al., 2021), ArlF and ArlG can be safely assumed to act as stators because the ArlG filament is capped by an ArlGF tetramer that is tightly bound to the S-layer (Banerjee et al., 2015; Tsai et al., 2020). Conversely, ArlJ is predicted to localise at the interface between the ATPase ArlI and the filament; therefore, ArlJ must be able to rotate in order to convey torque to the filament. Beyond this, it is more difficult to predict whether the remaining subunits of the

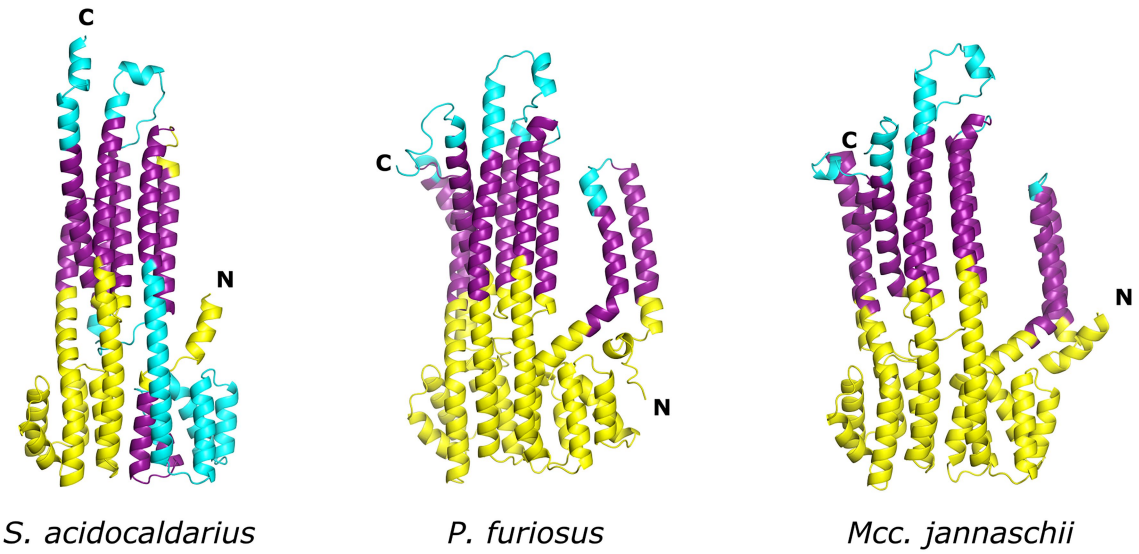


FIGURE 3 | Structure of ArlJ homologues predicted with AlphaFold. AlphaFold (Jumper et al., 2021) predictions of ArlJ from homologs of *Sulfolobus acidocaldarius*, *Pyrococcus furiosus*, and *Methanocaldococcus jannaschii*. Transmembrane regions were predicted with TMHMM. The cytosolic, transmembrane, and extracellular regions are, respectively, coloured yellow, purple, and cyan.

machinery rotate or not. Thus, we propose two possible hypotheses that start from the assumption that ArlJ is a rotor and ArlFG are stators.

In the first hypothesis (Hypothesis A, **Figure 6**), we consider that all proteins remain static with the exception of ArlJ. The N-terminus of ArlI interacts with the cytosolic loops of ArlJ. Assuming that ArlI is a hexamer and ArlJ is a dimer, two opposite monomers of ArlI interact each with an ArlJ monomer, as suggested in the model in **Figure 5**. This interaction is favoured when the two FlaI monomers are in the open state. Upon ATP hydrolysis, a conformational change occurs (Reindl et al., 2013), which transfers the ArlJ loops to the subsequent ArlI monomers that will change to the open state. Upon repeated ATP binding and hydrolysis, these conformational changes cycle through the otherwise static ArlI hexamer. The sequential binding and resulting transfer of ArlJ to the two open ArlI monomers therefore results in rotation of the ArlJ dimer, which in turn drives the rotation of the filament (**Figure 6**).

In the second hypothesis (Hypothesis B, **Figure 6**), both ArlJ and ArlI rotate. In this scenario, ArlI and ArlJ bind tightly, independent of the catalytic state of ArlI. ArlI is surrounded by either ArlX (in Crenarchaeota) or ArlCDE (in Euryarchaeota), and it interacts loosely with this ring. The conformational changes induced by ATP-hydrolysis result in the C-termini of opposing ArlI monomers pushing outwards and against the ArlX/ArlCDE ring, generating torque that results in rotational movement of ArlI, and consequently of ArlJ and the attached filament (**Figure 6**). For both hypotheses, the torque is assumed to be generated by the sequential rotary mechanism of ATP hydrolysis in the ArlI ring, as proposed for PilB/PilF, the ATPase that drives the assembly of T4P in *Thermus thermophilus* (Mancl et al., 2016).

Although the function of ArlH remains largely elusive, it has been proposed that this protein is involved in switching the archaellum machinery between filament assembly and rotation. ArlH is essential for archaella assembly (Thomas et al., 2001b; Lassak et al., 2012), but there are no data regarding its relevance for the rotation of the filament, suggesting that ArlH is only essential for archaella assembly. This possibility is supported by the observation that upon autophosphorylation, ArlH ceases to interact with ArlI (Sousa Machado et al., 2021).

According to Hypothesis A (**Figure 6**), ArlH may determine how ArlI interacts with ArlJ. In its unphosphorylated state, ArlH would promote an ArlI-ArlJ complex that catalyses filament assembly. Upon autophosphorylation, ArlH would be ejected from the ArlI-ArlJ complex (or perhaps remain attached to ArlX/ArlCDE). Dislocation of ArlH would in turn switch the ArlI-ArlJ complex from assembly to rotation mode. The corollary of this hypothesis is that filament assembly would last for as long as it takes for ArlH to autophosphorylate and that the kinetics of this process determines the length of the filament. Assuming that during archaellum assembly the filament does not rotate, ArlH may also function as a brake. ArlH remains bound to ArlCDE in close proximity to the motor, as has been reported for *H. volcanii* (Li et al., 2020); if ArlH can be dephosphorylated, it would be able to re-associate with ArlI, stopping the motor and possibly resulting in a switch in the direction of rotation to regulate forwards and backwards swimming motion.

Hypothesis B also suggests a mechanism for archaellum assembly. Here, un-phosphorylated ArlH would connect ArlI firmly to ArlCDE/ArlX, preventing the rotation of the ATPase. In this configuration, the conformational changes within the ArlI hexamer may cause and up-and-down motion in ArlJ,

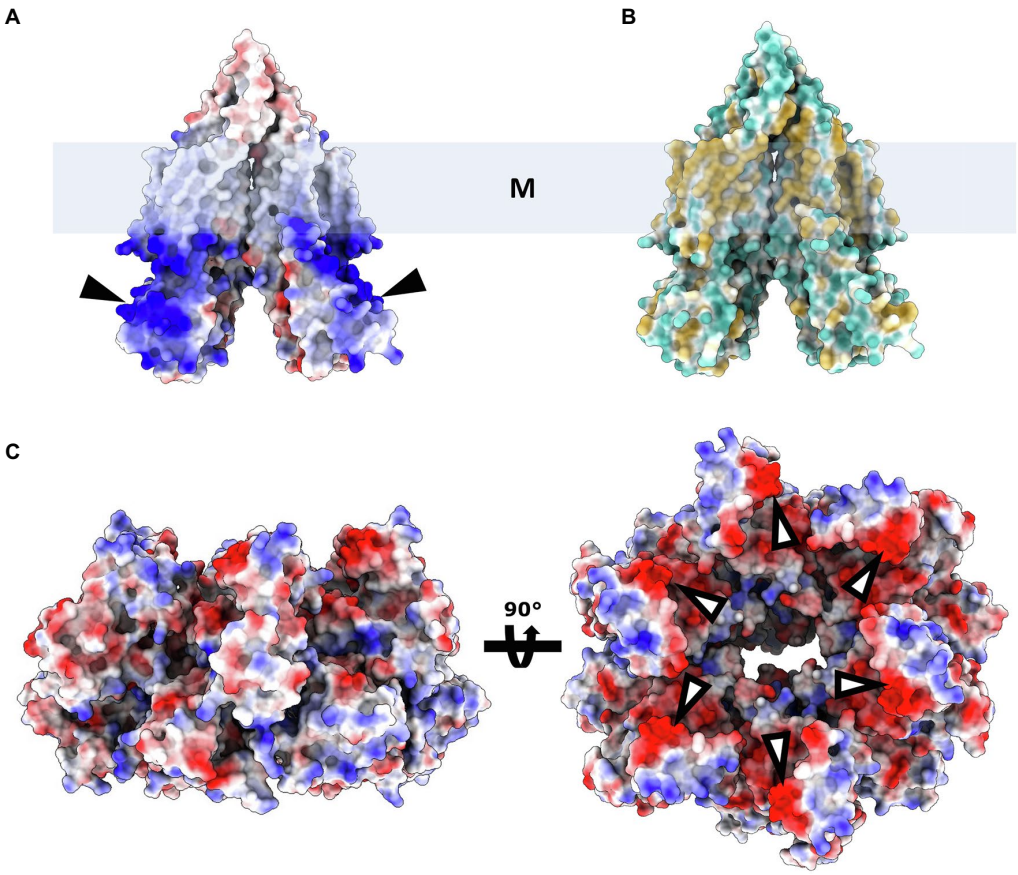


FIGURE 4 | ArlJ modelled as a dimer. **(A)**, surface representation of electrostatic potential (red, negative; white, neutral; and blue, positive local charges). **(B)**, surface representation of ArlJ coloured by hydrophobicity (blue, hydrophilic; yellow, hydrophobic). The position of the membrane (represented by the box M) can be inferred from the location of the hydrophobic belt **(B)**. According to the positive-inside rule, the positively charged domains **(A)** are likely located in the cytoplasm. **(C)**, ArlI (PDB-4IHQ) surface representation coloured by electrostatic potential. The complementary local charges in ArlJ and ArlI (black and white arrows, respectively) hint at electrostatic interactions between both proteins.

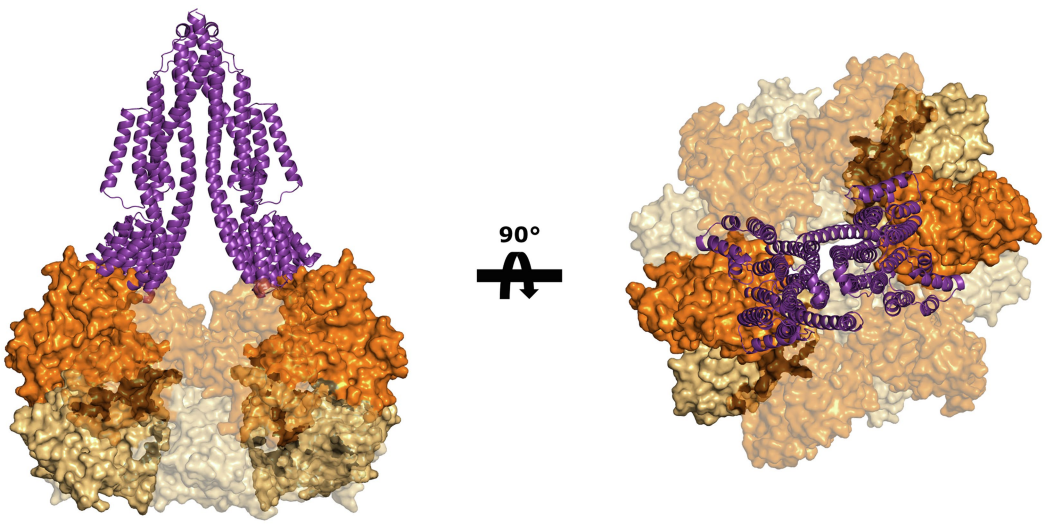


FIGURE 5 | Putative interaction between ArlJ and ArlI. The charge complementarity between the N-terminus of ArlI (PDB-4IHQ) and the cytosolic domain of the AlphaFold prediction of the ArlJ dimer from *S. acidocaldarius* suggests how the two proteins may interact. The model is shown in side view (left) and as seen from the pseudo-periplasm (right). In the model (highlighted), which would have important consequences for the mechanism of rotation.

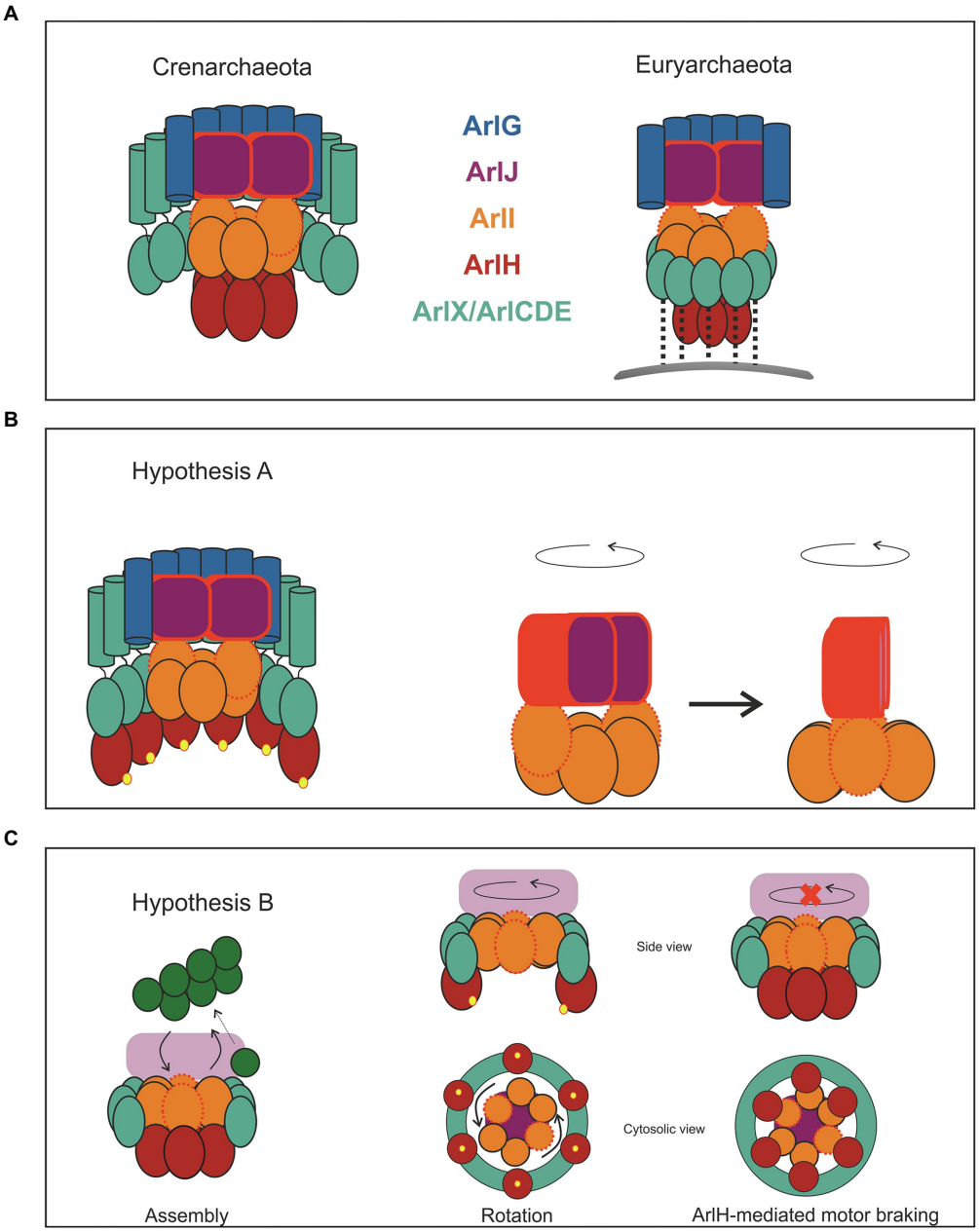


FIGURE 6 | Two hypotheses for archaellum rotation. Despite the differences between the crenarchaeal and euryarchaeal motor, we suggest two hypotheses for the rotary motion of this motor, which are applicable to both phyla. **(A)** Two schemes representing the crenarchaeal and the euryarchaeal motors. The motor is primed for archaella synthesis when ArlH is interacting with ArlI. Once ArlH is phosphorylated (represented by yellow spheres), this protein is either ejected from the motor complex or remains bound to ArlX or ArlCDE. In **(B,C)**, only the crenarchaeal motor is shown for simplicity. In hypothesis A, only ArlJ rotates. ArlJ, likely as a dimer, has high affinity for ArlI subunits in open conformation (red, dotted outline) and binds only weakly to ArlI subunits in the closed conformation. ATP hydrolysis causes ArlI subunits to switch from the closed to the open conformation, so sequential ATP hydrolysis causes subunits of closed and open conformation to cyclically go through the otherwise static hexamer. The binding preference of ArlJ to the open conformation of ArlI thus causes ArlJ to rotate by 60 degrees for each ATP hydrolysis step. The rotation of ArlJ thus causes the gyration of the filament. In **(B)**, both ArlI and ArlJ rotate. The side and bottom views of the motor are shown for clarity. The sequential ATP hydrolysis-induced conformational changes within ArlI push against the ArlX or ArlCDE stators, relax, and push again. The repetition of this process results in ArlI rotation. ArlI tightly interacts with ArlJ, causing it to rotate, which in turn transmits torque to the filament. Through the interaction of ArlH with ArlI **(A,B)** the conformational changes in ArlI result in piston-like motions in ArlJ, which push archaellins from the membrane into the growing filament. In **(B)** we show how ArlH may act as a motor brake: when ArlH is dephosphorylated (presumably by an unknown factor), this protein interacts once more with ArlI. Since ArlI, ArlH, and ArlX/CDE form now a triple complex, ArlI is unable to rotate against the ArlX/CDE surface.

scooping archaellin monomers from the membrane and inserting them into the growing filament.

CONCLUSION

Recent years have seen increased research into the archaellum machinery, with a particular focus on solving the structures of its components (Reindl et al., 2013; Banerjee et al., 2015; Chaudhury et al., 2016; Meshcheryakov and Wolf, 2016; Poweleit et al., 2016; Briegel et al., 2017; Daum et al., 2017; Tsai et al., 2020; Gambelli et al., 2022). Despite all of these efforts, a high-resolution structure of the entire machinery has so far not been achieved, meaning that the molecular mechanism of the archaellum remains largely unknown. However, drawing on accumulating knowledge about its structural components and with the aid of novel structural prediction algorithms, it is possible to piece together a picture about the rotary mechanism of the archaellum. We hope that the working models that we propose in this review will guide and fuel future research that will ultimately lead to a full understanding of this fascinating molecular machine.

AUTHOR CONTRIBUTIONS

JS created the models for archaellum rotation and predicted the topology of the ArlJI complex. BD predicted the structures of ArlJ with AlphaFold-2. JS, S-VA, and BD discussed and contributed to the proposed models and wrote the manuscript. All authors contributed to the article and approved the submitted version.

FUNDING

JS was supported by the Collaborative Research Centre SFB1381 funded by the Deutsche Forschungsgemeinschaft (DFG, German Research Foundation)—Project-ID 403222702—SFB1381. This study was supported in part by the Excellence Initiative of the German Research Foundation (GSC-4, Spemann Graduate School) and in part by the Ministry for Science, Research and Arts of the State of Baden-Wuerttemberg. BD was funded by the European Research Council (ERC) under the European Union's Horizon 2020 Research and Innovation Programme (grant agreement No 803894).

REFERENCES

Alam, M., and Oesterhelt, D. (1984). Morphology, function and isolation of halobacterial flagella. *J. Mol. Biol.* 176, 459–475. doi: 10.1016/0022-2836(84)90172-4

Albers, S.-V., and Driessen, A. J. M. (2005). Analysis of ATPases of putative secretion operons in the thermoacidophilic archaeon *Sulfolobus solfataricus*. *Microbiology* 151, 763–773. doi: 10.1099/mic.0.27699-0

Albers, S.-V., and Jarrell, K. F. (2015). The archaellum: how archaea swim. *Front. Microbiol.* 6:23. doi: 10.3389/fmicb.2015.00023

Albers, S.-V., and Jarrell, K. F. (2018). The archaellum: an update on the unique archaeal motility structure. *Trends Microbiol.* 26, 351–362. doi: 10.1016/j.tim.2018.01.004

Albers, S.-V., Szabó, Z., and Driessen, A. J. M. (2003). Archaeal homolog of bacterial type IV prepilin signal peptidases with broad substrate specificity. *J. Bacteriol.* 185, 3918–3925. doi: 10.1128/JB.185.13.3918-3925.2003

Banerjee, A., Ghosh, A., Mills, D. J., Kahnt, J., Vonck, J., and Albers, S.-V. (2012). FlaX, a unique component of the crenarchaeal archaellum, forms oligomeric ring-shaped structures and interacts with the motor ATPase FlaI. *J. Biol. Chem.* 287, 43322–43330. doi: 10.1074/jbc.M112.414383

Banerjee, A., Neiner, T., Tripp, P., and Albers, S.-V. (2013). Insights into subunit interactions in the *Sulfolobus acidocaldarius* archaellum cytoplasmic complex. *FEBS J.* 280, 6141–6149. doi: 10.1111/febs.12534

Banerjee, A., Tsai, C.-L., Chaudhury, P., Tripp, P., Arvai, A. S., Ishida, J. P., et al. (2015). FlaF is a β-sandwich protein that anchors the archaellum in the archaeal cell envelope by binding the S-layer protein. *Structure* 23, 863–872. doi: 10.1016/j.str.2015.03.001

Bardy, S. L., and Jarrell, K. F. (2002). FlaK of the archaeon *Methanococcus maripaludis* possesses preflagellin peptidase activity. *FEMS Microbiol. Lett.* 208, 53–59. doi: 10.1111/j.1574-6968.2002.tb11060.x

Bardy, S. L., and Jarrell, K. F. (2003). Cleavage of preflagellins by an aspartic acid signal peptidase is essential for flagellation in the archaeon *Methanococcus voltae*. *Mol. Microbiol.* 50, 1339–1347. doi: 10.1046/j.1365-2958.2003.03758.x

Bardy, S. L., Mori, T., Komoriya, K., Aizawa, S.-I., and Jarrell, K. F. (2002). Identification and localization of flagellins FlaA and FlaB3 within flagella of *Methanococcus voltae*. *J. Bacteriol.* 184, 5223–5233. doi: 10.1128/JB.184.19.5223-5233.2002

Berg, H. C. (2003). The rotary motor of bacterial flagella. *Annu. Rev. Biochem.* 72, 19–54. doi: 10.1146/annurev.biochem.72.121801.161737

Berry, J.-L., and Pelicic, V. (2015). Exceptionally widespread nanomachines composed of type IV pilins: the prokaryotic Swiss Army knives. *FEMS Microbiol. Rev.* 39, 134–154. doi: 10.1093/femsre/fuu001

Bischof, L. F., Friedrich, C., Harms, A., Søgaard-Andersen, L., and van der Does, C. (2016). The type IV pilus assembly ATPase PilB of *Myxococcus xanthus* interacts with the inner membrane platform protein PilC and the nucleotide-binding protein PilM. *J. Biol. Chem.* 291, 6946–6957. doi: 10.1074/jbc.M115.701284

Briegel, A., Oikonomou, C. M., Chang, Y., Kjær, A., Huang, A. N., Kim, K. W., et al. (2017). Morphology of the archaellar motor and associated cytoplasmic cone in *Thermococcus kodakaraensis*. *EMBO Rep.* 18, 1660–1670. doi: 10.15252/embr.201744070

Briegel, A., Ortega, D. R., Huang, A. N., Oikonomou, C. M., Gunsalus, R. P., and Jensen, G. J. (2015). Structural conservation of chemotaxis machinery across Archaea and bacteria: structure of archaeal chemoreceptor arrays. *Environ. Microbiol. Rep.* 7, 414–419. doi: 10.1111/1758-2229.12265

Chaban, B., Ng, S. Y. M., Kanbe, M., Saltzman, I., Nimmo, G., Aizawa, S.-I., et al. (2007). Systematic deletion analyses of the *fla* genes in the flagella operon identify several genes essential for proper assembly and function of flagella in the archaeon, *Methanococcus maripaludis*. *Mol. Microbiol.* 66, 596–609. doi: 10.1111/j.1365-2958.2007.05913.x

Chang, Y.-W., Rettberg, L. A., Treuner-Lange, A., Iwasa, J., Sogaard-Andersen, L., and Jensen, G. J. (2016). Architecture of the type IVa pilus machine. *Science* 351:aad2001. doi: 10.1126/science.aad2001

Chaudhury, P., Neiner, T., D'Imprima, E., Banerjee, A., Reindl, S., Ghosh, A., et al. (2016). The nucleotide-dependent interaction of FlaH and FlaI is essential for assembly and function of the archaellum motor. *Mol. Microbiol.* 99, 674–685. doi: 10.1111/mmi.13260

Chaudhury, P., van der Does, C., and Albers, S.-V. (2018). Characterization of the ATPase FlaI of the motor complex of the *Pyrococcus furiosus* archaellum and its interactions between the ATP-binding protein FlaH. *PeerJ* 6:e4984. doi: 10.7717/peerj.4984

Daum, B., Vonck, J., Bellack, A., Chaudhury, P., Reichelt, R., Albers, S.-V., et al. (2017). Structure and in situ organisation of the *Pyrococcus furiosus* archaellum machinery. *eLife* 6:e27470. doi: 10.7554/eLife.27470

Denise, R., Abby, S. S., and Rocha, E. P. C. (2020). The evolution of protein secretion systems by co-option and tinkering of cellular machineries. *Trends Microbiol.* 28, 372–386. doi: 10.1016/j.tim.2020.01.005

Desmond, E., Brochier-Armanet, C., and Gribaldo, S. (2007). Phylogenomics of the archaeal flagellum: rare horizontal gene transfer in a unique motility structure. *BMC Evol. Biol.* 7:106. doi: 10.1186/1471-2148-7-106

Gambelli, L., Isupov, M.N., Conners, R., McLaren, M., Bellack, A., Gold, V., et al. (2021). New insights into the architecture and dynamics of archaella biorxiv [Preprint]. doi: 10.1101/2021.10.01.462426

Gerl, L., Deutzmann, R., and Sumper, M. (1989). Halobacterial flagellins are encoded by a multigene family. Identification of all five gene products. *FEBS Lett.* 244, 137–140. doi: 10.1016/0014-5793(89)81179-2

Gerl, L., and Sumper, M. (1988). Halobacterial flagellins are encoded by a multigene family. Characterization of five flagellin genes. *J. Biol. Chem.* 263, 13246–13251. doi: 10.1016/S0021-9258(18)37697-X

Ghosh, A., and Albers, S. (2011). Assembly and function of the archaeal flagellum. *Biochem. Soc. Trans.* 39, 64–69. doi: 10.1042/BST0390064

Ghosh, A., Hartung, S., van der Does, C., Tainer, J. A., and Albers, S.-V. (2011). Archaeal flagellar ATPase motor shows ATP-dependent hexameric assembly and activity stimulation by specific lipid binding. *Biochem. J.* 437, 43–52. doi: 10.1042/BJ20110410

Gongadze, G. M., Kostyukova, A. S., Miroshnichenko, M. L., and Bonch-Osmolovskaya, E. A. (1993). Regular proteinaceous layers of *Thermococcus stetteri* cell envelope. *Curr. Microbiol.* 27, 5–9. doi: 10.1007/BF01576826

Hu, H., Santiveri, M., Wadhwa, N., Berg, H. C., Erhardt, M., and Taylor, N. M. I. (2021). Structural basis of torque generation in the bi-directional bacterial flagellar motor. *Trends Biochem. Sci.* 47, 160–172. doi: 10.1016/j.tibs.2021.06.005

Itoh, H., Takahashi, A., Adachi, K., Noji, H., Yasuda, R., Yoshida, M., et al. (2004). Mechanically driven ATP synthesis by F1-ATPase. *Nature* 427, 465–468. doi: 10.1038/nature02212

Iwata, S., Kinosita, Y., Uchida, N., Nakane, D., and Nishizaka, T. (2019). Motor torque measurement of *Halobacterium salinarum* archaellar suggests a general model for ATP-driven rotary motors. *Commun. Biol.* 2:199. doi: 10.1038/s42003-019-0422-6

Jarrell, K. F., Albers, S.-V., and de Sousa Machado, J. N. (2021). A comprehensive history of motility and archaellation in Archaea. *FEMS Microbiol. Ecol.* 2:xtab002. doi: 10.1093/femsmc/xtab002

Jarrell, K. F., Bayley, D. P., Florian, V., and Klein, A. (1996). Isolation and characterization of insertional mutations in flagellin genes in the archaeon *Methanococcus voltae*. *Mol. Microbiol.* 20, 657–666. doi: 10.1046/j.1365-2958.1996.5371058.x

Johnson, C. H., Zhao, C., Xu, Y., and Mori, T. (2017). Timing the day: what makes bacterial clocks tick? *Nat. Rev. Microbiol.* 15, 232–242. doi: 10.1038/nrmicro.2016.196

Jumper, J., Evans, R., Pritzel, A., Green, T., Figurnov, M., Ronneberger, O., et al. (2021). Highly accurate protein structure prediction with AlphaFold. *Nature* 596, 583–589. doi: 10.1038/s41586-021-03819-2

Kalmokoff, M. L., Jarrell, K. F., and Koval, S. F. (1988). Isolation of flagella from the archaebacterium *Methanococcus voltae* by phase separation with triton X-114. *J. Bacteriol.* 170, 1752–1758. doi: 10.1128/jb.170.4.1752-1758.1988

Karuppiah, V., Hassan, D., Saleem, M., and Derrick, J. P. (2010). Structure and oligomerization of the *PilC* type IV pilus biogenesis protein from *Thermus thermophilus*. *Proteins Struct. Funct. Bioinform.* 78, 2049–2057. doi: 10.1002/prot.22720

Kinosita, Y., Mikami, N., Li, Z., Braun, F., Quax, T. E. F., van der Does, C., et al. (2020). Motile ghosts of the halophilic archaeon, *Haloferax volcanii*. *Proc. Natl. Acad. Sci.* 117, 26766–26772. doi: 10.1073/pnas.2009814117

Kinosita, Y., Uchida, N., Nakane, D., and Nishizaka, T. (2016). Direct observation of rotation and steps of the archaellum in the swimming halophilic archaeon *Halobacterium salinarum*. *Nat. Microbiol.* 1:16148. doi: 10.1038/nmicrobiol.2016.148

Koval, S. F., and Jarrell, K. F. (1987). Ultrastructure and biochemistry of the cell wall of *Methanococcus voltae*. *J. Bacteriol.* 169, 1298–1306. doi: 10.1128/jb.169.3.1298-1306.1987

Krogh, A., Larsson, B., von Heijne, G., and Sonnhammer, E. L. L. (2001). Predicting transmembrane protein topology with a hidden markov model: application to complete genomes. *J. Mol. Biol.* 305, 567–580. doi: 10.1006/jmbi.2000.4315

Kupper, J., Marwan, W., Typke, D., Grünberg, H., Uwer, U., Gluch, M., et al. (1994). The flagellar bundle of *Halobacterium salinarium* is inserted into a distinct polar cap structure. *J. Bacteriol.* 176, 5184–5187. doi: 10.1128/jb.176.16.5184-5187.1994

Lassak, K., Neiner, T., Ghosh, A., Klingl, A., Wirth, R., and Albers, S.-V. (2012). Molecular analysis of the crenarchaeal flagellum. *Mol. Microbiol.* 83, 110–124. doi: 10.1111/j.1365-2958.2011.07916.x

Li, Z., Rodriguez-Franco, M., Albers, S., and Quax, T. E. F. (2020). The switch complex ArlCDE connects the chemotaxis system and the archaellum. *Mol. Microbiol.* 114, 468–479. doi: 10.1111/mmi.14527

Makarova, K. S., Galperin, M. Y., and Koonin, E. V. (2017). Proposed role for KaiC-like ATPases as major signal transduction hubs in archaea. *mBio* 8, e01959–e01917. doi: 10.1128/mBio.01959-17

Makarova, K. S., Koonin, E. V., and Albers, S.-V. (2016). Diversity and evolution of type IV pili systems in archaea. *Front. Microbiol.* 7:667. doi: 10.3389/fmicb.2016.00667

Mancl, J. M., Black, W. P., Robinson, H., Yang, Z., and Schubot, F. D. (2016). Crystal structure of a type IV Pilus assembly ATPase: insights into the molecular mechanism of PilB from *Thermus thermophilus*. *Structure* 24, 1886–1897. doi: 10.1016/j.str.2016.08.010

Marwan, W., Alam, M., and Oesterhelt, D. (1991). Rotation and switching of the flagellar motor assembly in Halobacterium halobium. *J. Bacteriol.* 173, 1971–1977. doi: 10.1128/jb.173.6.1971-1977.1991

Mattick, J. S. (2002). Type IV Pili and twitching motility. *Annu. Rev. Microbiol.* 56, 289–314. doi: 10.1146/annurev.micro.56.012302.160938

Meshcheryakov, V. A., Shibata, S., Schreiber, M. T., Villar-Briones, A., Jarrell, K. F., Aizawa, S., et al. (2019). High-resolution archaellum structure reveals a conserved metal-binding site. *EMBO Rep.* 20:e46340. doi: 10.15252/embr.201846340

Meshcheryakov, V. A., and Wolf, M. (2016). Crystal structure of the flagellar accessory protein FlaH of *Methanocaldococcus jannaschii* suggests a regulatory role in archaeal flagellum assembly. *Protein Sci.* 25, 1147–1155. doi: 10.1002/pro.2932

Näther-Schindler, D. J., Schopf, S., Bellack, A., Rachel, R., and Wirth, R. (2014). *Pyrococcus furiosus* flagella: biochemical and transcriptional analyses identify the newly detected flaB0 gene to encode the major flagellin. *Front. Microbiol.* 5:695. doi: 10.3389/fmicb.2014.00695

Ng, S. Y. M., Chaban, B., and Jarrell, K. F. (2006). Archaeal flagella, bacterial flagella and type IV Pili: a comparison of genes and posttranslational modifications. *J. Mol. Microbiol. Biotechnol.* 11, 167–191. doi: 10.1159/000094053

Peabody, C. R., Chung, Y. J., Yen, M.-R., Vidal-Ingigliardi, D., Pugsley, A. P., and Saier, M. H. Jr. (2003). Type II protein secretion and its relationship to bacterial type IV pili and archaeal flagella. *Microbiology* 149, 3051–3072. doi: 10.1099/mic.0.26364-0

Pohlschröder, M., Pfeiffer, F., Schulze, S., and Halim, M. F. A. (2018). Archaeal cell surface biogenesis. *FEMS Microbiol. Rev.* 42, 694–717. doi: 10.1093/femsre/fuy027

Poweleit, N., Ge, P., Nguyen, H. H., Loo, R. R. O., Gunsalus, R. P., and Zhou, Z. H. (2016). CryoEM structure of the *Methanospirillum hungatei* archaellum reveals structural features distinct from the bacterial flagellum and type IV pili. *Nat. Microbiol.* 2:16222. doi: 10.1038/nmicrobiol.2016.222

Reindl, S., Ghosh, A., Williams, G. J., Lassak, K., Neiner, T., Henche, A.-L., et al. (2013). Insights into FlaI functions in archaeal motor assembly and motility from structures, conformations, and genetics. *Mol. Cell* 49, 1069–1082. doi: 10.1016/j.molcel.2013.01.014

Rossmann, F. M., and Beeby, M. (2018). Insights into the evolution of bacterial flagellar motors from high-throughput *in situ* electron cryotomography and subtomogram averaging. *Acta Crystallogr. Sect. Struct. Biol.* 74, 585–594. doi: 10.1107/S2059798318007945

Sakai, H. D., and Kurosawa, N. (2018). *Saccharolobus caldissimus* gen. Nov., sp. nov., a facultatively anaerobic iron-reducing hyperthermophilic archaeon isolated from an acidic terrestrial hot spring, and reclassification of *Sulfolobus solfataricus* as *Saccharolobus solfataricus* comb. nov. and *Sulfolobus shibatae* as *Saccharolobus shibatae* comb. nov. *Int. J. Syst. Evol. Microbiol.* 68, 1271–1278. doi: 10.1099/ijsem.0.002665

Schlesner, M., Miller, A., Streif, S., Staudinger, W. F., Müller, J., Scheffer, B., et al. (2009). Identification of Archaea-specific chemotaxis proteins which interact with the flagellar apparatus. *BMC Microbiol.* 9:56. doi: 10.1186/1471-2180-9-56

Shrivastava, A., Lele, P. P., and Berg, H. C. (2015). A rotary motor drives Flavobacterium gliding. *Curr. Biol.* 25, 338–341. doi: 10.1016/j.cub.2014.11.045

Sonnhammer, E. L., von Heijne, G., and Krogh, A. (1998). A hidden Markov model for predicting transmembrane helices in protein sequences. *Proc. Int. Conf. Intell. Syst. Mol. Biol.* 6, 175–182.

Sousa Machado, J. N., Vollmar, L., Schimpf, J., Chaudhury, P., Kumariya, R., Does, C., et al. (2021). Autophosphorylation of the KaiC-like protein ArlH inhibits oligomerization and interaction with ArlI, the motor ATPase of the archaellum. *Mol. Microbiol.* 116, 943–956. doi: 10.1111/mmi.14781

Syutkin, A. S., Pyatibratov, M. G., Galzitskaya, O. V., Rodríguez-Valera, F., and Fedorov, O. V. (2014). *Haloarcula marismortui* archaellin genes as ecoparalogs. *Extremophiles* 18, 341–349. doi: 10.1007/s00792-013-0619-4

Syutkin, A. S., Wolferen, M., Surin, A. K., Albers, S., Pyatibratov, M. G., Fedorov, O. V., et al. (2019). Salt-dependent regulation of archaellins in *Haloarcula marismortui*. *Microbiologyopen* 8:e00718. doi: 10.1002/mbo3.718

Tarasov, V. Y., Pyatibratov, M. G., Tang, S.-L., Dyall-Smith, M., and Fedorov, O. V. (2000). Role of flagellins from A and B loci in flagella formation of *Halobacterium salinarum*. *Mol. Microbiol.* 35, 69–78. doi: 10.1046/j.1365-2958.2000.01677.x

Thomas, N. A., Bardy, S. L., and Jarrell, K. F. (2001a). The archaeal flagellum: a different kind of prokaryotic motility structure. *FEMS Microbiol. Rev.* 25, 147–174. doi: 10.1111/j.1574-6976.2001.tb00575.x

Thomas, N. A., Mueller, S., Klein, A., and Jarrell, K. F. (2002). Mutants in *flaI* and *flaJ* of the archaeon *Methanococcus voltae* are deficient in flagellum assembly. *Mol. Microbiol.* 46, 879–887. doi: 10.1046/j.1365-2958.2002.03220.x

Thomas, N. A., Pawson, C. T., and Jarrell, K. F. (2001b). Insertional inactivation of the flaH gene in the archaeon *Methanococcus voltae* results in non-flagellated cells. *Mol. Gen. Genomics.* 265, 596–603. doi: 10.1007/s004380100451

Tsai, C.-L., Tripp, P., Sivabalasarma, S., Zhang, C., Rodriguez-Franco, M., Wipfler, R. L., et al. (2020). The structure of the periplasmic FlaG–FlaF complex and its essential role for archaellar swimming motility. *Nat. Microbiol.* 5, 216–225. doi: 10.1038/s41564-019-0622-3

Umrekar, T. R., Winterborn, Y. B., Sivabalasarma, S., Brantl, J., Albers, S.-V., and Beeby, M. (2021). Evolution of archaellum rotation involved invention of a stator complex by duplicating and modifying a core component. *Front. Microbiol.* 12:773386. doi: 10.3389/fmicb.2021.773386

Van Putte, W., De Vos, T., Van Den Broeck, W., Stahlberg, H., Kudryashev, M., and Savvides, S.N. (2018). Inner-membrane GspF of the bacterial type II secretion system is a dimeric adaptor mediating pseudopilus biogenesis. biorxiv [Preprint]. doi: 10.1101/435982

von Heijne, G. (1992). Membrane protein structure prediction. *J. Mol. Biol.* 225, 487–494. doi: 10.1016/0022-2836(92)90934-C

Woese, C. R., Kandler, O., and Wheelis, M. L. (1990). Towards a natural system of organisms: proposal for the domains Archaea, bacteria, and Eucarya. *Proc. Natl. Acad. Sci.* 87, 4576–4579. doi: 10.1073/pnas.87.12.4576

Conflict of Interest: The authors declare that the research was conducted in the absence of any commercial or financial relationships that could be construed as a potential conflict of interest.

Publisher's Note: All claims expressed in this article are solely those of the authors and do not necessarily represent those of their affiliated organizations, or those of the publisher, the editors and the reviewers. Any product that may be evaluated in this article, or claim that may be made by its manufacturer, is not guaranteed or endorsed by the publisher.

Copyright © 2022 de Sousa Machado, Albers and Daum. This is an open-access article distributed under the terms of the Creative Commons Attribution License (CC BY). The use, distribution or reproduction in other forums is permitted, provided the original author(s) and the copyright owner(s) are credited and that the original publication in this journal is cited, in accordance with accepted academic practice. No use, distribution or reproduction is permitted which does not comply with these terms.

frontiers | Frontiers in Microbiology

REVIEW
published: 16 June 2022
doi: 10.3389/fmicb.2022.864006

CryoEM Reveals the Complexity and Diversity of ATP Synthases

Gautier M. Courbon [1,2] *and John L. Rubinstein* [1,2,3]*

[1] *Molecular Medicine Program, The Hospital for Sick Children, Toronto, ON, Canada,* [2] *Department of Medical Biophysics, The University of Toronto, Toronto, ON, Canada,* [3] *Department of Biochemistry, The University of Toronto, Toronto, ON, Canada*

During respiration, adenosine triphosphate (ATP) synthases harness the electrochemical proton motive force (PMF) generated by the electron transport chain (ETC) to synthesize ATP. These macromolecular machines operate by a remarkable rotary catalytic mechanism that couples transmembrane proton translocation to rotation of a rotor subcomplex, and rotation to ATP synthesis. Initially, x-ray crystallography, nuclear magnetic resonance (NMR) spectroscopy, and cross-linking were the only ways to gain insights into the three-dimensional (3D) structures of ATP synthases and, in particular, provided ground-breaking insights into the soluble parts of the complex that explained the catalytic mechanism by which rotation is coupled to ATP synthesis. In contrast, early electron microscopy was limited to studying the overall shape of the assembly. However, advances in electron cryomicroscopy (cryoEM) have allowed determination of high-resolution structures, including the membrane regions of ATP synthases. These studies revealed the high-resolution structures of the remaining ATP synthase subunits and showed how these subunits work together in the intact macromolecular machine. CryoEM continues to uncover the diversity of ATP synthase structures across species and has begun to show how ATP synthases can be targeted by therapies to treat human diseases.

Keywords: ATP synthase, cryoEM, protein, structure, membrane, bioenergetics

OPEN ACCESS

Edited by:
Jun Liu,
Yale University, United States

Reviewed by:
Anna Lapashina,
Lomonosov Moscow State University, Russia
Alfredo Cabrera-Orefice,
Radboud University Nijmegen Medical Centre, Netherlands

***Correspondence:**
John L. Rubinstein
john.rubinstein@utoronto.ca

Specialty section:
This article was submitted to Microbial Physiology and Metabolism, a section of the journal Frontiers in Microbiology

Received: *27 January 2022*
Accepted: *30 March 2022*
Published: *16 June 2022*

Citation:
Courbon GM and Rubinstein JL (2022) CryoEM Reveals the Complexity and Diversity of ATP Synthases. Front. Microbiol. 13:864006. doi: 10.3389/fmicb.2022.864006

INTRODUCTION

In eukaryotes and aerobic bacteria, the synthesis of most of the cell's adenosine triphosphate (ATP) is accomplished by the combined activities of the electron transport chain (ETC) and ATP synthase. Reduced nicotinamide adenine dinucleotide (NADH) produced by glycolysis, fatty acid oxidation, and the Krebs cycle, as well as succinate from the Krebs cycle, are oxidized by the integral membrane protein complexes of the ETC. Electrons pass between the complexes *via* the intermediate electron carriers quinone and cytochrome *c* before ultimately being used to reduce oxygen to water. Within some of the ETC complexes, these redox reactions are coupled to proton translocation across the membrane, either from the mitochondrial matrix to the mitochondrial intermembrane space in eukaryotes or from the cytoplasm to the periplasm or extracellular environment in bacteria. This activity establishes an electric field ($\Delta\psi$) and an ion gradient (ΔpH) that result in a proton motive force (PMF) across the membrane. In the final step of oxidative phosphorylation, ATP synthases

harness the PMF to synthesize ATP from adenosine diphosphate (ADP) and inorganic phosphate (Pi). The hydrolysis of this ATP is then used by a multitude of enzymes as an energy source to catalyze energetically unfavorable reactions. Significant structural knowledge of ATP synthase subunits and subcomplexes was obtained through pioneering efforts with x-ray crystallography (Abrahams et al., 1994; Stock et al., 1999; Dickson et al., 2006). This work provided insight mostly, though not exclusively, into the structure of the soluble region of the enzyme. Early electron cryomicroscopy (cryoEM) was limited to fitting crystal structures together, like pieces of a puzzle, to form a "mosaic model" of intact ATP synthases (Rubinstein et al., 2003; Lau et al., 2008; Baker et al., 2012). More recently, as described in this review, cryoEM has provided high-resolution structural knowledge for the missing pieces of the puzzle and offered a detailed picture of how intact ATP synthases work. These studies continue to reveal the complexity and diversity of ATP synthases across species.

OVERALL STRUCTURES OF ATP SYNTHASES

F-type ATP synthases are multi-subunit complexes consisting of a catalytic F_1 region and a membrane-embedded F_O region (**Figure 1**). Electron microscopy first detected the F_1 regions of ATP synthases protruding from mitochondrial membranes like lollipops in images of specimens prepared with heavy metal salt stain (Fernández-Morán, 1962; Kagawa and Racker, 1966a,b). The F_1 region catalyzes ATP synthesis but can also hydrolyze ATP under some conditions. F_1 is composed of three pairs of α and β subunits that form a ring around a central stalk consisting of subunits γ, δ, and ε in eukaryotes, or subunits γ and ε (a δ homolog) in prokaryotes (Walker et al., 1982, 1985; Abrahams et al., 1994; Stock et al., 1999; Gibbons et al., 2000). ATP synthesis or hydrolysis in the F_1 region is coupled to rotation of the central stalk within the $\alpha_3\beta_3$ hexamer. This central stalk is firmly attached to a ring of membrane-embedded c subunits that form part of the F_O region (Stock et al., 1999; Jiang et al., 2001; Seelert et al., 2003). In bacteria, the remainder of the F_O region consists of subunit a and a transmembrane α helix from each of two b subunits. Subunit a functions with the c ring to allow proton translocation while the two b subunits form a peripheral stalk that prevents F_1 and F_O from rotating relative to each other when the central stalk and c ring turn. In chloroplasts and some bacteria, this peripheral stalk is formed by a bb′ heterodimer rather than a b_2 homodimer. In mitochondrial ATP synthases, such as the enzyme from *Saccharomyces cerevisiae*, F_O includes subunits a, e, f, g, i/j (sometimes called 6.8PL in mammals), k (DAPIT in mammals), 8 (A6L in mammals), and a transmembrane portion of subunit b. The yeast peripheral stalk is formed from subunits b, d, h (known as F_6 in mammals), and the oligomycin sensitivity conferral protein (OSCP) (Liu et al., 2015; He et al., 2018). The number of c subunits in the c ring varies among species, with bacteria possessing between 9 (Preiss et al., 2015) and 15 (Pogoryelov et al., 2009) copies, yeast having 10 c subunits (Stock et al., 1999), and all animals proposed to have eight c subunits (Watt et al., 2010). Proton translocation through the interface of subunits a and c induces c ring rotation, which rotates subunit γ within the $\alpha_3\beta_3$ hexamer and drives ATP synthesis.

SIMULTANEOUS DEVELOPMENT OF ELECTRON MICROSCOPY AND STRUCTURAL MODELS OF ATP SYNTHASES

Developments in electron microscopy have contributed increasingly to the understanding of the structure and function of ATP synthases. After realizing that coupling of F_1 and F_O activities requires a peripheral stalk structure (Engelbrecht and Junge, 1997), electron microscopy of negatively stained ATP synthase particles from a variety of species revealed a faint feature corresponding to the stalk in two-dimensional (2D) class average images (Böttcher et al., 1998, 2000; Wilkens and Capaldi, 1998; Karrasch and Walker, 1999). This structure became clearly visible in three-dimensional (3D) maps with the advent of single-particle cryoEM methods for membrane proteins, which were initially limited to 20–30 Å resolution (Rubinstein et al., 2003; Lau et al., 2008). These early cryoEM structures relied on the availability of relatively stable cryospecimen holders for microscopes and highly coherent field emission electron sources, which are required to provide contrast in defocused images of protein complexes. However, the detective quantum efficiency of the photographic film used with microscopes remained relatively low, limiting the resolution of 3D reconstructions. Despite this limitation, cryoEM revealed density for the F_1 region, the peripheral stalk, the c ring, and a large region of density corresponding to the additional membrane protein subunits of the mitochondrial ATP synthase, most of which had unknown functions at the time. Perhaps most importantly, the structure of subunit a, which works together with the c ring to couple proton translocation to rotation, remained unknown. Advances in electron tomography revealed the 3D arrangement of mitochondrial ATP synthases in dimer ribbons (Strauss et al., 2008; Davies et al., 2011) that had previously been observed in freeze-etch electron microscopy (Allen et al., 1989). Gradual improvements in specimen preparation and image analysis allowed cryoEM of ATP synthases and related complexes at 10–20 Å resolution (Baker et al., 2012; Benlekbir et al., 2012; Lau and Rubinstein, 2012). However, this resolution still fell short of the 7–8 Å resolution needed to reliably detect α-helices in structures or the better than 4 Å resolution needed to detect amino acid side chains.

The development of direct detector device (DDD) cameras for electron microscopes led to a sudden increase in the resolution attainable by cryoEM (McMullan et al., 2016). This technology improved the resolution to 6–8 Å, which revealed highly tilted α-helices from the a subunit in contact with the c ring in both ATP synthases (Allegretti et al., 2015; Zhou et al., 2015; Sobti et al., 2016) and the related proton-pumping eukaryotic vacuolar-type (V-type) ATPases (Zhao et al., 2015). This progress coincided with solution of a crystal structure of a bacterial ATP synthase at comparable resolution (Morales-Rios et al., 2015).

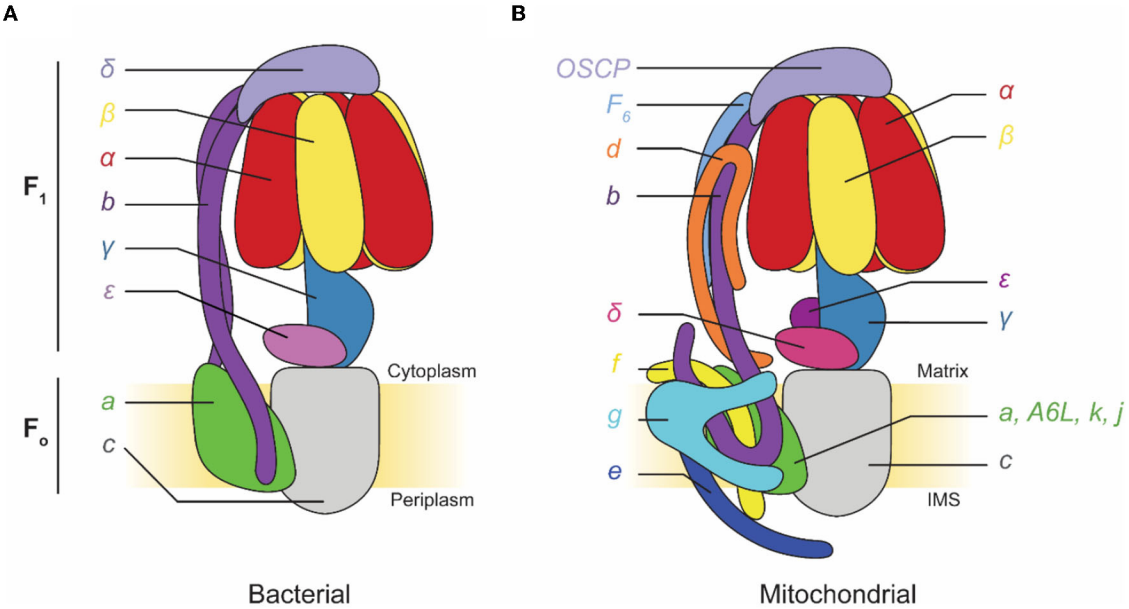


FIGURE 1 | Subunit composition of commonly studied adenosine triphosphate (ATP) synthases. **(A)** Cartoon of a bacterial ATP synthase. Based on Guo et al. (2019). **(B)** Cartoon of a mammalian mitochondrial ATP synthase. IMS, intermembrane space.

DYNAMICS OF ATP SYNTHASES

Although falling short of the 3–4 Å resolution needed to build atomic models, cryoEM with both field emission sources and DDD cameras gave rise to the study of ATP synthase dynamics by cryoEM (**Figure 2**). Three catalytic nucleotide-binding sites in the F_1 region are located at the interface of each αβ pair, primarily within the β subunits (Abrahams et al., 1994). These catalytic sites were termed as β_{TP} ("ATP-bound"), β_{DP} ("ADP-bound"), and β_E ("Empty"), based on their nucleotide content in the first crystal structure of the F_1 region. The structure of the bovine F_1 region supported the earlier prediction of a rotary catalytic mechanism in which each nucleotide-binding site of ATP synthase cycles between the three different catalytic states *via* rotation of the central stalk relative to the $\alpha_3\beta_3$ ring (Boyer, 1997). This rotation was observed experimentally by fluorescence microscopy using fluorescent actin filaments attached to the γ subunits of immobilized F_1 complexes (Noji et al., 1997). Fluorescence studies also revealed that the ATPase cycle can be divided into three distinct 120° steps, which is consistent with the pseudo 3-fold symmetry of the F_1 catalytic region (Yasuda et al., 1998).

The coexistence of these conformations in purified enzyme preparations complicates structural analysis by cryoEM, but also allows the possibility of direct visualization of the rotary cycle at a structural level. Methods to separate protein conformations that exist simultaneously in solution had been applied previously to ribosomes, viruses, and DNA helicases (Valle et al., 2002; Yang et al., 2002; Heymann et al., 2003; Gao et al., 2004; Scheres et al., 2007) but DDDs provided the signal-to-noise ratios in images needed to do this computational separation for ATP synthases and V-ATPases (Zhao et al., 2015; Zhou et al., 2015). The structures of rotational states show with striking clarity how rotor rotation within the $\alpha_3\beta_3$ hexamer drives the conformational transition between each of the three 120° catalytic steps (**Figure 2A**; Zhao et al., 2015; Zhou et al., 2015; Sobti et al., 2016; Hahn et al., 2018; Guo et al., 2019). Movies made from interpolation between rotational states suggest remarkable flexibility in the enzyme, allowing it to twist and deform to accommodate the symmetry mismatch between the 3-fold symmetric F_1 region and the higher symmetry in the c ring within the F_O region.

High-speed fluorescence microscopy subsequently detected the existence of F_1 substeps during the catalytic cycle, dividing each 120° step into a short ∼40° step and long ∼80° step (**Figures 2B,C**; Yasuda et al., 2001; Bilyard et al., 2013; Martin et al., 2014). With limiting amounts of ATP, the dwell preceding the ∼80° step becomes longer, while the dwell preceding the ∼40° step remains the same (Yasuda et al., 2001). This observation suggests that the ∼80° step is induced by ATP binding (the "binding dwell") while the ∼40° step is independent of ATP concentration and coincides with catalysis (the "catalytic dwell") (Yasuda et al., 2001). While the catalytic dwell conformation was detected in the earliest crystallographic structures, structural evidence for the F_1 binding dwell was first determined two decades later (Sobti et al., 2021). These structures confirmed the existence of a structurally distinct catalytic dwell and binding dwell, with a 44° rotation of the rotor during the ATP hydrolysis stroke and a 76° rotation during ATP binding at one site and product release from another site. The substep composition of catalytic cycles can differ between organisms (Zarco-Zavala et al., 2020). Notably, single-molecule and x-ray

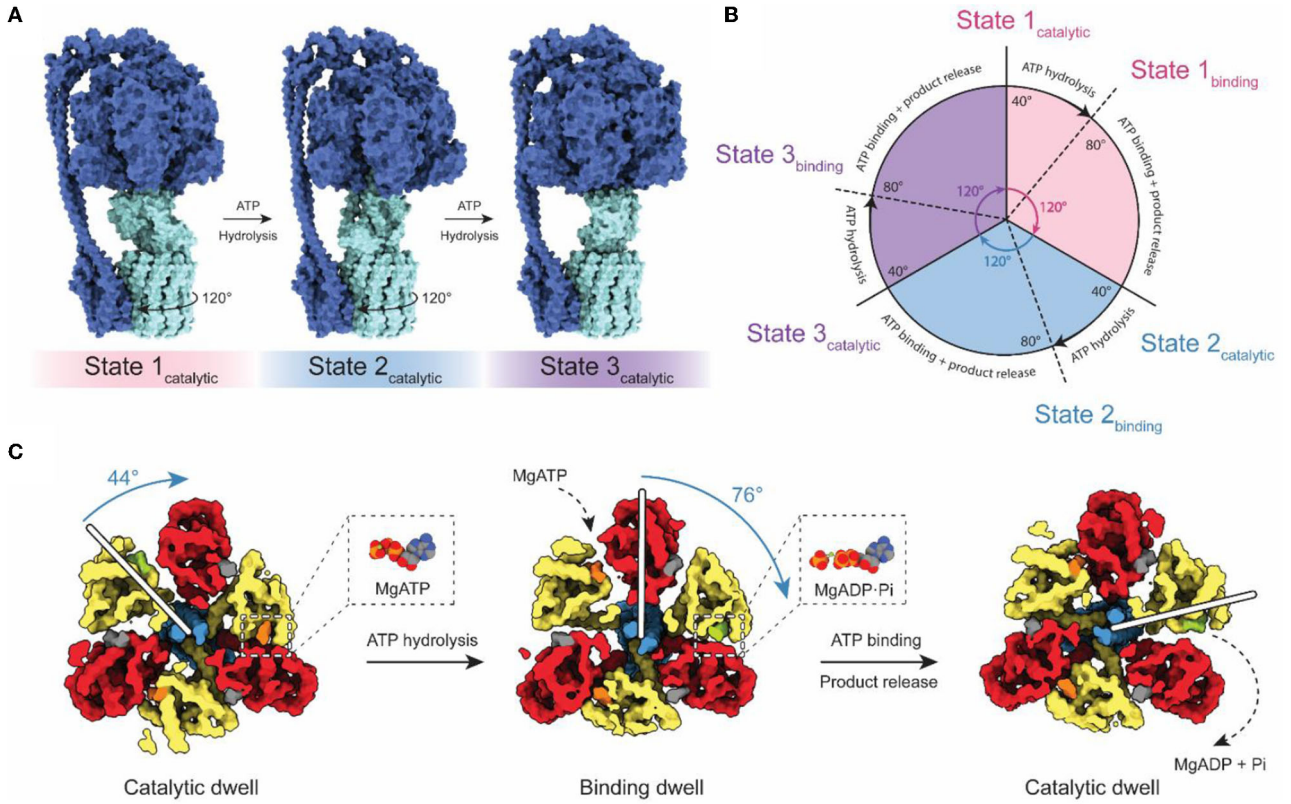


FIGURE 2 | Rotary catalytic mechanism of ATP synthase. **(A)** Atomic model of *Bacillus* PS3 ATP synthase showing the three main rotational states (PDB: 6N2Y, 6N30, and 6N2Z) (Guo et al., 2019). The light blue parts of the complex rotate relative to the dark blue parts. The direction of rotation during ATP hydrolysis is indicated. **(B)** Diagram of the catalytic cycle of the F_1 region during ATP hydrolysis. **(C)** Structures of the *Bacillus* PS3 F_1 complex catalytic substeps (PDB: 7L1R and 7L1Q) (Sobti et al., 2021). White bars represent the angle of the γ subunit. ATP, ADP, and non-catalytic nucleotides are colored orange, green, and dark gray, respectively. Based on Sobti et al. (2021).

crystallographic data have shown that mammalian ATP synthases possess an additional substep interpreted as a pre-phosphate release state (Suzuki et al., 2014; Bason et al., 2015). However, this state has not been observed in bacterial or yeast ATP synthases by either single-molecule experiments or structural studies.

HIGH-RESOLUTION STRUCTURES OF THE F_O REGION OBTAINED BY CHEMICAL OR COMPUTATIONAL ISOLATION FROM F_1

While providing movies of the conformational changes of ATP synthases during rotary catalysis, cryoEM maps at 6–8 Å resolution are not sufficient to build atomic models of subunits in the F_O region. These maps could be combined with evolutionary covariance (Marks et al., 2011), a technique central to the success of recent protein structure prediction methods (Senior et al., 2020), to determine the a subunit fold (Zhou et al., 2015; Schep et al., 2016). However, they lacked the high-resolution detail needed to determine amino acid side chain orientations, which cryoEM with a DDD can provide for other proteins (Cao et al., 2013; Bai et al., 2015a). One hypothesis for the limited resolution in ATP synthase structures was that conformational heterogeneity of the enzyme blurs the structure even following computational separation of the different rotary states. In support of this hypothesis, structure determination of the membrane-embedded V_O region of V-ATPase following physiological separation of V_1 and V_O reached a resolution of 3.9 Å, sufficient to build an atomic model of that complex (Mazhab-Jafari et al., 2016). Based on this idea, a first high-resolution structure of the F_O region was determined by chemically separating F_1 from F_O with sodium bromide before structure determination. This approach allowed the construction of an atomic model for the dimeric yeast F_O complex more than 20 years after the first high-resolution F_1 structure (Guo et al., 2017).

Computational separation of regions of a protein structure that move relative to each other offers an alternative method for gaining high-resolution insights into flexible proteins (Bai et al., 2015b). This method allows a computational equivalent of chemical separation, in which the structures of different parts of the enzyme can be determined at high resolution independently and then fit together to generate an overall composite high-resolution map. These techniques include separation of

conformations with maximum-likelihood classification (Scheres et al., 2007), selection of an area within a 3D map for high-resolution refinement, and signal subtraction to eliminate the contribution of regions outside the mask during particle image alignment. The combination of these evolving computational methods for 3D classification and focused refinement in software packages such as Relion (Scheres, 2012), Frealign/cisTEM (Grigorieff, 2016), and cryoSPARC (Punjani et al., 2017) allowed for high-resolution insights into the F_O regions of chloroplasts (Hahn et al., 2018), bacteria (Guo et al., 2019), algae (Murphy et al., 2019), mammalian mitochondria (Spikes et al., 2020), and protozoan mitochondria (Mühleip et al., 2019, 2021; Flygaard et al., 2020). High-resolution structures of F_O regions revealed a similar topology of residues important for proton translocation in both ATP synthase and V-type ATPase a subunits (Mazhab-Jafari et al., 2016; Schep et al., 2016). The structures show two offset proton half-channels in subunit a that allow the passage of protons to and from the c ring (**Figure 3**; Vik and Antonio, 1994; Junge et al., 1997). Protons are carried between the half-channels by conserved acidic residues in the c subunits, with rotation of the ring taking the proton from one half-channel, through the hydrophobic environment of the lipid bilayer, and to the second half-channel before its release. A conserved arginine in subunit a produces a positive charge on the surface of the a subunit where it contacts the c ring. This arginine residue prevents a short circuit in which protons can pass from one half-channel to the other without inducing ring rotation.

CRYOEM REVEALS THE DIVERSITY OF ATP SYNTHASES

The newfound ability to routinely determine high-resolution structures of ATP synthases has revealed remarkable diversity in these essential enzymes (**Figure 4**). While bacterial and chloroplast ATP synthases are monomeric, the mitochondrial enzyme forms higher-order oligomers. One area in which diversity between species occurs is the way in which monomers of ATP synthases assemble into larger dimers and dimer ribbons in mitochondria. CryoEM of an algal ATP synthase from *Polytomella* sp. (Klusch et al., 2017; Murphy et al., 2019) revealed a large and rigid peripheral stalk structure with numerous algae-specific subunits that results in the complex purifying in dimeric form even with relatively harsh detergents (Dudkina et al., 2005). In contrast, in yeast dimerization is mediated by fragile interactions between subunits e, k, i/j and a (Guo et al., 2017). In addition to determining the structures and identities of corresponding subunits in yeast and mammalian F_O regions (Hahn et al., 2016; Vinothkumar et al., 2016; Guo et al., 2017; Srivastava et al., 2018; Spikes et al., 2020), cryoEM of mammalian ATP synthases has allowed definition of the structure of higher-order contacts in dimer ribbons. A structure of a mammalian ATP synthase tetramer from porcine heart (Gu et al., 2019) was interpreted with insights from structures of a mammalian ATP synthase monomer isolated from ovine heart (Pinke et al., 2020) and of a mammalian ATP synthase dimer from bovine heart (Spikes et al., 2020). This analysis revealed that two inhibitory factor 1 (IF1) proteins link two dimers, with the dimer–dimer interaction stabilized by the N-terminal portions of subunits k and g above the membrane, and subunit e within the membrane. These mammalian ATP synthase structures also show that the C-terminal region of subunit e points toward the c ring within the monomer (Gu et al., 2019; Pinke et al., 2020; Spikes et al., 2020).

The diversity of enzyme architecture is perhaps most strikingly illustrated by recent structures of mitochondrial ATP synthases from *Euglena gracilis* of the phylum Euglenozoa (Mühleip et al., 2019), the intracellular parasitic protozoan *Toxoplasma gondii* of the phylum Apicomplexa (Mühleip et al., 2021), and the ciliated protozoan *Tetrahymena thermophila* of the phylum Ciliophora (Flygaard et al., 2020). These structures reveal highly elaborated enzymes with numerous additional subunits that influence monomer–monomer interactions, which in turn can lead to different oligomerization and cristae structures. These enzymes produce remarkable arrangements ranging from stable dimers that induce discoid cristae in Euglenozoa (Mühleip et al., 2019), tetramers that assemble into helical rows to induce the formation of tubular cristae in Ciliophora (Mühleip et al., 2016; Flygaard et al., 2020), and even hexamers that assemble into larger pentagonal pyramids to induce bulb-shaped cristae in Apicomplexa (Mühleip et al., 2021). Although in each case additional ATP synthase subunits and modifications of core subunits reveal *how* the enzyme shapes cristae, it remains unclear *why* cristae adopt these different shapes, and what physiological advantage the different cristae morphologies confer. Consequently, the specific roles of these additional subunits and of the diversity of mitochondrial membrane morphologies are a rich area of investigation.

A second area of diversity in the ATP synthase structure relates to how ATP hydrolysis is inhibited in different species in the absence of a PMF. In mammals and yeast, this role is filled by IF1, which binds and inhibits the enzyme upon PMF collapse (Cabezón et al., 2003). The structure of the chloroplast ATP synthase (Hahn et al., 2018) showed that the γ subunit contains a double-hairpin that acts as a redox sensor, where oxidation of a disulfide bond can prevent ATP hydrolysis. In many bacteria, the ε subunit can insert into the $\alpha_3\beta_3$ hexamer to block ATP hydrolysis (Cingolani and Duncan, 2011; Gu et al., 2019; Sobti et al., 2019). Inhibition of ATP hydrolysis appears to be achieved by subunit ζ in *Paraccocus denitrificans* (Morales-Rios et al., 2015; García-Trejo et al., 2016; Varghese et al., 2018), while in mycobacteria extensions from the α subunits interact with the γ subunits to block rotation and ATP hydrolysis (Guo et al., 2021).

While F-type ATP synthases are found in all eukaryotes and are the most common type of ATP synthase in eubacteria, there exist related proton-driven rotary ATP synthases that more closely resemble eukaryotic V-ATPases. Found in archaea and a few eubacteria, these enzymes are known either as prokaryotic V-ATPases, A-ATPases, or in our preferred nomenclature, V/A-ATPases. V/A-ATPases resemble eukaryotic proton-pumping V-type ATPases but have two instead of three peripheral stalks and lack the additional collar subunits found in V-ATPases (Bernal and Stock, 2004; Lau and Rubinstein, 2010; Muench et al., 2011). Further, like F-type

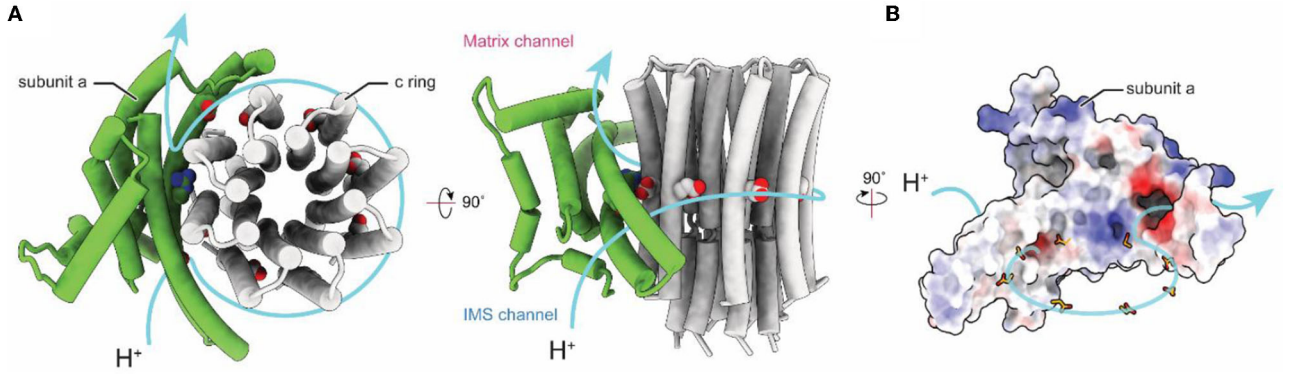


FIGURE 3 | Proton translocation in ATP synthase. **(A)** Proton path (blue arrow) through the interface between the a and c subunits of the F_O region of bovine ATP synthase (PDB: 6ZPO) (Spikes et al., 2020). The conserved arginine in subunit a and acidic residues in the c ring are shown as space filling models. **(B)** Electrostatic surface of bovine subunit a, with positively and negatively charged surfaces colored blue and red, respectively.

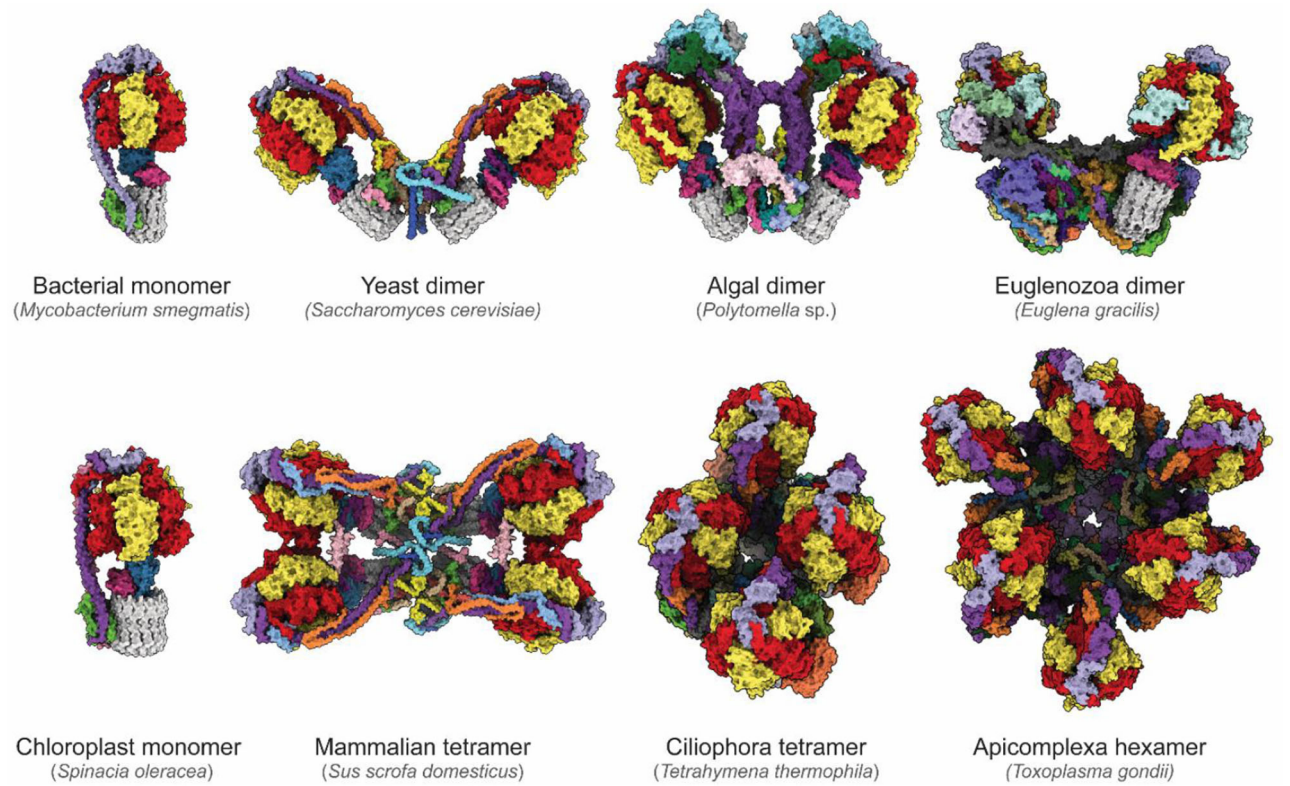


FIGURE 4 | Diversity of ATP synthases. Atomic models of ATP synthases from diverse species. Homologs of subunits α, β, γ, δ, ε, and c are colored red, yellow, blue, pink, purple, and gray, respectively. From the left to right, top to bottom: *Mycobacterium smegmatis* (PDB: 7JG5) (Guo et al., 2021), *Saccharomyces cerevisiae* dimer (PDB: 6B8H) (Guo et al., 2017), *Polymotella* sp. dimer (PDB: 6RD4) (Murphy et al., 2019), *Euglena gracilis* dimer (PDB: 6TDU) (Mühleip et al., 2019), *Spinacia oleracea* (PDB: 6FKF) (Hahn et al., 2018), *Sus scofa domesticus* tetramer (PDB: 6J5K, 6ZNA) (Gu et al., 2019; Spikes et al., 2020), *Tetrahymena thermophila* tetramer (PDB: 6YNZ) (Flygaard et al., 2020), and *Toxoplasma gondii* hexamer (PDB: 6TML) (Mühleip et al., 2021).

ATP synthases, these complexes do not appear to be regulated by the reversible dissociation mechanism that controls V-ATPase activity (Kane, 1995; Sumner et al., 1995). V/A-ATPases can function as ATP synthases, driven by protons or other ions, or as ion pumps (Muench et al., 2011). V/A-ATPases have been subjected to extensive structural analysis by x-ray crystallography, negative stain EM, and cryoEM (Boekema et al., 1999; Bernal and Stock, 2004; Murata et al., 2005; Numoto et al., 2009; Lau and Rubinstein, 2010, 2012; Lee et al., 2010). Similar to F-type ATP synthase, cryoEM has allowed computational separation of rotational states and elucidation of the a subunit fold by evolutionary covariance analysis (Schep et al., 2016), with

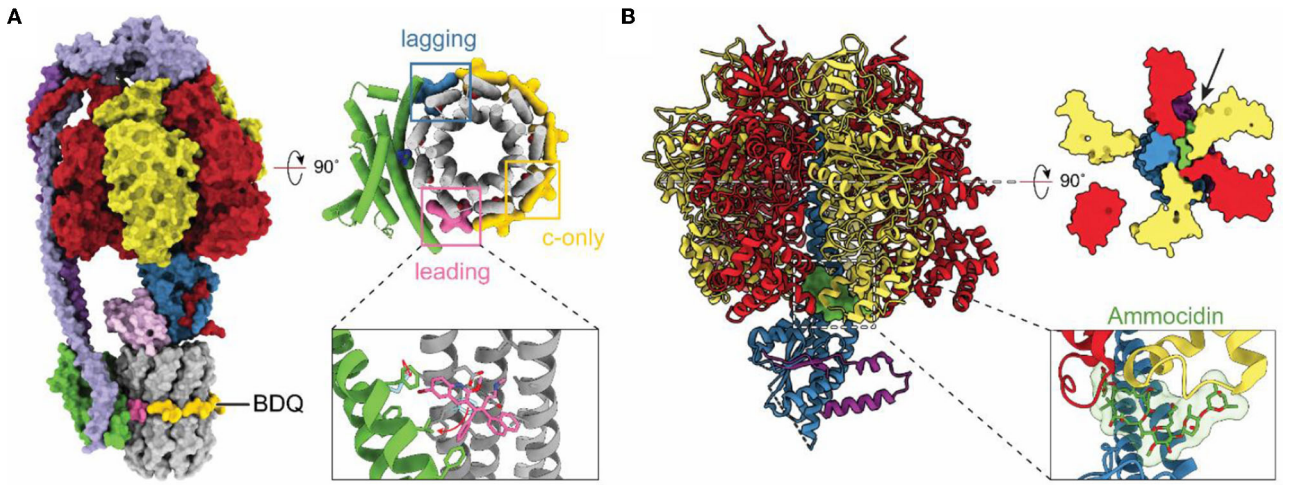


FIGURE 5 | Structures of drug-bound ATP synthases. **(A)** Atomic model of *M. smegmatis* ATP synthase bound to the tuberculosis (TB) drug bedaquiline (BDQ) (PDB: 7JGC) (Guo et al., 2021). Bedaquiline binds at five c-only sites (yellow), a leading site (pink), and a lagging site (blue) in the F_O region of the enzyme. Red arrows indicate the movement of residues upon bedaquiline binding. **(B)** Atomic model of *S. cerevisiae* ATP synthase F_1 region bound to Ammocidin (PDB: 7MD2) (Reisman et al., 2021). Ammocidin (green) binds at the rotor–stator interface (black arrow).

subsequent high-resolution structures revealing further details of the catalytic mechanism (Zhou and Sazanov, 2019; Kishikawa et al., 2022).

CRYOEM GUIDES NEW THERAPIES

With resolution in cryoEM rivaling or surpassing x-ray crystallography, cryoEM has become an option for investigating how drug molecules interact with ATP synthases in biomedically important forms of the enzyme. The structure of a mycobacterial ATP synthase (Guo et al., 2021) revealed the binding site and conformational changes induced in the enzyme by the compound bedaquiline (**Figure 5A**), an antibiotic that has revolutionized the treatment of drug-resistant tuberculosis (TB) (Cohen, 2017). Earlier crystallographic studies had already shown how bedaquiline interacts with the ATP synthase c ring (Preiss et al., 2015), but cryoEM with the intact enzyme revealed numerous contacts between the drug and subunit a that explain the drug's high affinity binding and efficacy as a treatment for TB. The structure of an ATP synthase from another major bacterial pathogen, *Acinetobacter baumannii*, has also been determined (Demmer et al., 2021). *A. baumannii* is part of ESKAPE, a group of bacteria that are a leading cause of nosocomial infections and show alarming levels of drug resistance (Oliveira et al., 2020). As ATP synthases are essential for the growth of *A. baumannii* in rich medium (Wang et al., 2014; Gallagher et al., 2015) these structural studies may aid in the development of new antibiotics. The structures of other ATP synthases from biomedically important pathogens have also been determined. These include *T. gondii*, which causes toxoplasmosis and is a model for the plasmodium species that causes malaria (Mühleip et al., 2021). In *Toxoplasma gondii*, disruption of ATP synthase has been shown to affect parasite viability (Huet et al., 2018). Similarly, ATP synthase in *Plasmodium* spp. has been shown to be essential in the mosquito phase of the parasite, with its disruption blocking malaria transmission (Sturm et al., 2015). Finally, the human ATP synthase itself has been identified as a target for cancer therapies with the realization that the glycomacrolides apoptolidin and ammocidin, which display selective cytotoxicity toward transformed cells, inhibit the enzyme (Reisman et al., 2021). The structure of the yeast ATP synthase bound to ammocidin revealed how the compound binds to the F_1 region to block enzyme activity (**Figure 5B**; Reisman et al., 2021).

CONCLUSIONS

It has been 60 years since electron microscopy first detected the structures within mitochondrial membranes that would come to be known as ATP synthase. In that time, the capabilities of electron microscopy have expanded from low-resolution imaging of cell ultrastructure to the determination of atomic-resolution structures of macromolecular assemblies such as ATP synthase. Today, cryoEM is revealing the fundamental mechanisms that all ATP synthases have in common, the diversity of ATP synthases throughout biology, and the insights necessary for developing ATP synthase targeting compounds to be used as therapeutics.

AUTHOR CONTRIBUTIONS

JR and GC wrote the manuscript and prepared figures. Both authors contributed to the article and approved the submitted version.

FUNDING

This study was supported by the Ontario Graduate Scholarship (GC) and Canada Research Chairs (JR).

REFERENCES

Abrahams, J. P., Leslie, A. G. W., Lutter, R., and Walker, J. E. (1994). Structure at 2.8 Â resolution of F1-ATPase from bovine heart mitochondria. *Nature* 370, 621–628. doi: 10.1038/370621a0

Allegretti, M., Klusch, N., Mills, D. J., Vonck, J., Kuhlbrandt, W., and Davies, K. M. (2015). Horizontal membrane-intrinsic alpha-helices in the stator a-subunit of an F-type ATP synthase. *Nature* 521, 237–240. doi: 10.1038/nature14185

Allen, R. D., Schroeder, C. C., and Fok, A. K. (1989). An investigation of mitochondrial inner membranes by rapid-freeze deep-etch techniques. *J. Cell Biol.* 108, 2233–2240. doi: 10.1083/jcb.108.6.2233

Bai, X.-C., Rajendra, E., Yang, G., Shi, Y., and Scheres, S. H. W. (2015b). Sampling the conformational space of the catalytic subunit of human g-secretase. *eLife* 4, e11182. doi: 10.7554/eLife.11182

Bai, X.-C., Yan, C., Yang, G., Lu, P., Sun, L., Zhou, R., et al. (2015a). An atomic structure of human gamma-secretase. *Nature* 212, 212–217. doi: 10.1038/nature14892

Baker, L. A., Watt, I. N., Runswick, M. J., Walker, J. E., and Rubinstein, J. L. (2012). Arrangement of subunits in intact mammalian mitochondrial ATP synthase determined by cryo-EM. *Proc. Natl. Acad. Sci. U.S.A.* 109, 11675–11680. doi: 10.1073/pnas.1204935109

Bason, J. V., Montgomery, M. G., Leslie, A. G. W., and Walker, J. E. (2015). How release of phosphate from mammalian F1-ATPase generates a rotary substep. *Proc. Natl. Acad. Sci. U.S.A.* 112, 6009–6014. doi: 10.1073/pnas.1506465112

Benlekbir, S., Bueler, S. A., and Rubinstein, J. L. (2012). Structure of the vacuolar-type ATPase from *Saccharomyces cerevisiae* at 11-Å resolution. *Nat. Struct. Mol. Biol.* 19, 1356–1362. doi: 10.1038/nsmb.2422

Bernal, R. A., and Stock, D. (2004). Three-dimensional structure of the intact thermus thermophilus H+-ATPase/synthase by electron microscopy. *Structure* 12, 1789–1798. doi: 10.1016/j.str.2004.07.017

Bilyard, T., Nakanishi-Matsui, M., Steel, B. C., Pilizota, T., Nord, A. L., Hosokawa, H., et al. (2013). High-resolution single-molecule characterization of the enzymatic states in *Escherichia coli* F1-ATPase. *Philos. Trans. R. Soc. B Biol. Sci.* 368, 20120023. doi: 10.1098/rstb.2012.0023

Boekema, E. J., van Breemen, J. F. L., Brisson, A., Ubbink-Kok, T., Konings, W. N., and Lolkema, J. S. (1999). Connecting stalks in V-type ATPase. *Nature* 401, 37–38. doi: 10.1038/43369

Böttcher, B., Bertsche, I., Reuter, R., and Gräber, P. (2000). Direct visualisation of conformational changes in EF0F1 by electron microscopy11. *J. Mol. Biol.* 296, 449–457. doi: 10.1006/jmbi.1999.3435

Böttcher, B., Schwarz, L., and Gräber, P. (1998). Direct indication for the existence of a double stalk in CF0F111. *J. Mol. Biol.* 281, 757–762. doi: 10.1006/jmbi.1998.1957

Boyer, P. D. (1997). The ATP synthase—a splendid molecular machine. *Annu. Rev. Biochem.* 66, 717–749. doi: 10.1146/annurev.biochem.66.1.717

Cabezón, E., Montgomery, M. G., Leslie, A. G. W., and Walker, J. E. (2003). The structure of bovine F1-ATPase in complex with its regulatory protein IF1. *Nat. Struct. Biol.* 10, 744–750. doi: 10.1038/nsb966

Cao, E., Liao, M., Cheng, Y., and Julius, D. (2013). TRPV1 structures in distinct conformations reveal activation mechanisms. *Nature* 504, 113–118. doi: 10.1038/nature12823

Cingolani, G., and Duncan, T. M. (2011). Structure of the ATP synthase catalytic complex (F(1)) from *Escherichia coli* in an autoinhibited conformation. *Nat. Struct. Mol. Biol.* 18, 701–707. doi: 10.1038/nsmb.2058

Cohen, J. (2017). Easier cure for resistant TB. *Science* 355, 677. doi: 10.1126/science.355.6326.677

Davies, K. M., Strauss, M., Daum, B., Kief, J. H., Osiewacz, H. D., Rycovska, A., et al. (2011). Macromolecular organization of ATP synthase and complex I in whole mitochondria. *Proc. Natl. Acad. Sci. U.S.A.* 108, 14121–14126. doi: 10.1073/pnas.1103621108

Demmer, J. K., Phillips, B. P., Uhrig, O. L., Filloux, A., Allsopp, L. P., Bublitz, M., et al. (2021). Structure of ATP synthase from ESKAPE pathogen *Acinetobacter baumannii*. *Sci. Adv.* 8:eabl5966. doi: 10.1126/sciadv.abl5966

Dickson, V. K., Silvester, J. A, Fearnley, I. M., Leslie, A. G. W., and Walker, J. E. (2006). On the structure of the stator of the mitochondrial ATP synthase. *EMBO J.* 25, 2911–2918. doi: 10.1038/sj.emboj.7601177

Dudkina, N. V., Heinemeyer, J., Keegstra, W., Boekema, E. J., and Braun, H.-P. (2005). Structure of dimeric ATP synthase from mitochondria: an angular association of monomers induces the strong curvature of the inner membrane. *FEBS Lett.* 579, 5769–5772. doi: 10.1016/j.febslet.2005.09.065

Engelbrecht, S., and Junge, W. (1997). ATP synthase: a tentative structural model. *FEBS Lett.* 414, 485–491. doi: 10.1016/S0014-5793(97)00997-6

Fernández-Morán, H. (1962). Cell-Membrane ultrastructure. *Circulation* 26, 1039–1065. doi: 10.1161/01.CIR.26.5.1039

Flygaard, R. K., Mühleip, A., Tobiasson, V., and Amunts, A. (2020). Type III ATP synthase is a symmetry-deviated dimer that induces membrane curvature through tetramerization. *Nat. Commun.* 11, 5342. doi: 10.1038/s41467-020-18993-6

Gallagher, L. A., Ramage, E., Weiss, E. J., Radey, M., Hayden, H. S., Held, K. G., et al. (2015). Resources for genetic and genomic analysis of emerging pathogen *Acinetobacter baumannii*. *J. Bacteriol.* 197, 2027–2035. doi: 10.1128/JB.00131-15

Gao, H., Valle, M., Ehrenberg, M., and Frank, J. (2004). Dynamics of EF-G interaction with the ribosome explored by classification of a heterogeneous cryo-EM dataset. *J. Struct. Biol.* 147, 283–290. doi: 10.1016/j.jsb.2004.02.008

García-Trejo, J. J., Zarco-Zavala, M., Mendoza-Hoffmann, F., Hernández-Luna, E., Ortega, R., and Mendoza-Hernández, G. (2016). The inhibitory mechanism of the ζ subunit of the F1FO-ATPase nanomotor of paracoccus denitrificans and related α-proteobacteria. *J. Biol. Chem.* 291, 538–546. doi: 10.1074/jbc.M115.688143

Gibbons, C., Montgomery, M. G., Leslie, A. G. W., and Walker, J. E. (2000). The structure of the central stalk in bovine F1-ATPase at 2.4 Å resolution. *Nat. Struct. Biol.* 7, 1055–1061. doi: 10.1038/80981

Grigorieff, N. (2016). Frealign: an exploratory tool for single-particle Cryo-EM. *Methods Enzymol.* 579, 191–226. doi: 10.1016/bs.mie.2016.04.013

Gu, J., Zhang, L., Zong, S., Guo, R., Liu, T., Yi, J., et al. (2019). Cryo-EM structure of the mammalian ATP synthase tetramer bound with inhibitory protein IF1. *Science* 364, 1068–1075. doi: 10.1126/science.aaw4852

Guo, H., Bueler, S. A., and Rubinstein, J. L. (2017). Atomic model for the dimeric FO region of mitochondrial ATP synthase. *Science* 358, 936–940. doi: 10.1126/science.aao4815

Guo, H., Courbon, G. M., Bueler, S. A., Mai, J., Liu, J., and Rubinstein, J. L. (2021). Structure of mycobacterial ATP synthase bound to the tuberculosis drug bedaquiline. *Nature* 589, 143–147. doi: 10.1038/s41586-020-3004-3

Guo, H., Suzuki, T., and Rubinstein, J. L. (2019). Structure of a bacterial ATP synthase. *eLife* 8, e43128. doi: 10.7554/eLife.43128

Hahn, A., Parey, K., Bublitz, M., Mills, D. J., Zickermann, V., Vonck, J., et al. (2016). Structure of a complete ATP synthase dimer reveals the molecular basis of inner mitochondrial membrane morphology. *Mol. Cell* 63, 445–456. doi: 10.1016/j.molcel.2016.05.037

Hahn, A., Vonck, J., Mills, D. J., Meier, T., and Kuhlbrandt, W. (2018). Structure, mechanism, and regulation of the chloroplast ATP synthase. *Science* 360, eaat4318. doi: 10.1126/science.aat4318

He, J., Ford, H. C., Carroll, J., Douglas, C., Gonzales, E., Ding, S., et al. (2018). Assembly of the membrane domain of ATP synthase in human mitochondria. *Proc. Natl. Acad. Sci. U.S.A.* 115, 2988–2993. doi: 10.1073/pnas.1722086115

Heymann, J. B., Cheng, N., Newcomb, W. W., Trus, B. L., Brown, J. C., and Steven, A. C. (2003). Dynamics of herpes simplex virus capsid maturation visualized by time-lapse cryo-electron microscopy. *Nat. Struct. Biol.* 10, 334–341. doi: 10.1038/nsb922

Huet, D., Rajendran, E., van Dooren, G. G., and Lourido, S. (2018). Identification of cryptic subunits from an apicomplexan ATP synthase. *eLife* 7, e38097. doi: 10.7554/eLife.38097.024

Jiang, W., Hermolin, J., and Fillingame, R. H. (2001). The preferred stoichiometry of c subunits in the rotary motor sector of Escherichia coli ATP synthase is 10. *Proc. Natl. Acad. Sci. U.S.A.* 8, 4966–4971. doi: 10.1073/pnas.081424898

Junge, W., Lill, H., and Engelbrecht, S. (1997). ATP synthase: an electrochemical ransducer with rotatory mechanics. *Trends Biochem. Sci.* 22, 420–423. doi: 10.1016/S0968-0004(97)01129-8

Kagawa, Y., and Racker, E. (1966a). Partial resolution of the enzymes oxidative phosphorylation X. Reconstruction of oligomycin-sensitive adenosine triphosphatase. *J. Biol. Chem.* 241, 2467–2474. doi: 10.1016/S0021-9258(18)96641-X

Kagawa, Y., and Racker, E. (1966b). Partial resolution of the enzymes catalyzing oxidative phosphorylation: X. Correlation of morphology and

function in submitochondrial particles. *J. Biol. Chem*. 241, 2475–2482. doi: 10.1016/S0021-9258(18)96642-1

Kane, P. M. (1995). Disassembly and reassembly of the yeast vacuolar H(+)-ATPase *in vivo*. *J. Biol. Chem*. 270, 17025–17032. doi: 10.1016/S0021-9258(17)46944-4

Karrasch, S., and Walker, J. E. (1999). Novel features in the structure of bovine ATP synthase. *J. Mol. Biol*. 290, 379–384. doi: 10.1006/jmbi.1999.2897

Kishikawa, J., Nakanishi, A., Nakano, A., Saeki, S., Furuta, A., Kato, T., et al. (2022). Structural snapshots of V/A-ATPase reveal the rotary catalytic mechanism of rotary ATPases. *Nat. Commun*. 13, 1213. doi: 10.1038/s41467-022-28832-5

Klusch, N., Murphy, B. J., Mills, D. J., Yildiz, Ö., and Kühlbrandt, W. (2017). Structural basis of proton translocation and force generation in mitochondrial ATP synthase. *eLife* 6, e33274. doi: 10.7554/eLife.33274.027

Lau, W. C. Y., Baker, L. A., and Rubinstein, J. L. (2008). Cryo-EM structure of the yeast ATP synthase. *J. Mol. Biol*. 382, 1256–1264. doi: 10.1016/j.jmb.2008.08.014

Lau, W. C. Y., and Rubinstein, J. L. (2010). Structure of intact *Thermus thermophilus* V-ATPase by cryo-EM reveals organization of the membrane-bound V(O) motor. *Proc. Natl. Acad. Sci. U.S.A*. 107, 1367–1372. doi: 10.1073/pnas.0911085107

Lau, W. C. Y., and Rubinstein, J. L. (2012). Subnanometre-resolution structure of the intact *Thermus thermophilus* H+-driven ATP synthase. *Nature* 481, 214–218. doi: 10.1038/nature10699

Lee, L. K., Stewart, A. G., Donohoe, M., Bernal, R. A., and Stock, D. (2010). The structure of the peripheral stalk of *Thermus thermophilus* H+-ATPase/synthase. *Nat. Struct. Mol. Biol*. 17, 373–378. doi: 10.1038/nsmb.1761

Liu, S., Charlesworth, T. J., Bason, J. V., Montgomery, M. G., Harbour, M. E., Fearnley, I. M., et al. (2015). The purification and characterization of ATP synthase complexes from the mitochondria of four fungal species. *Biochem. J*. 468, 167–175. doi: 10.1042/BJ20150197

Marks, D. S., Colwell, L. J., Sheridan, R., Hopf, T., a., Pagnani, A., et al. (2011). Protein 3D structure computed from evolutionary sequence variation. *PLoS ONE* 6, e28766. doi: 10.1371/journal.pone.0028766

Martin, J. L., Ishmukhametov, R., Hornung, T., Ahmad, Z., and Frasch, W. D. (2014). Anatomy of F1-ATPase powered rotation. *Proc. Natl. Acad. Sci. U.S.A*. 111, 3715–3720. doi: 10.1073/pnas.1317784111

Mazhab-Jafari, M. T., Rohou, A., Schmidt, C., Bueler, S. A., Benlekbir, S., Robinson, C. V., et al. (2016). Atomic model for the membrane-embedded VO motor of a eukaryotic V-ATPase. *Nature* 539, 118–122. doi: 10.1038/nature19828

McMullan, G., Faruqi, A. R., and Henderson, R. (2016). Direct electron detectors. *Methods Enzymol*. 579, 1–17. doi: 10.1016/bs.mie.2016.05.056

Morales-Rios, E., Montgomery, M. G., Leslie, A. G. W., and Walker, J. E. (2015). Structure of ATP synthase from *Paracoccus denitrificans* determined by X-ray crystallography at 4.0 Å resolution. *Proc. Natl. Acad. Sci. U.S.A*. 112, 13231–13236. doi: 10.1073/pnas.1517542112

Muench, S. P., Trinick, J., and Harrison, M. A. (2011). Structural divergence of the rotary ATPases. *Q. Rev. Biophys*. 44, 311–356. doi: 10.1017/S0033583510000338

Mühleip, A., Kock Flygaard, R., Ovciarikova, J., Lacombe, A., Fernandes, P., Sheiner, L., et al. (2021). ATP synthase hexamer assemblies shape cristae *of Toxoplasma mitochondria*. *Nat. Commun*. 12, 120. doi: 10.1038/s41467-020-20381-z

Mühleip, A., McComas, S. E., and Amunts, A. (2019). Structure of a mitochondrial ATP synthase with bound native cardiolipin. *eLife* 8, e51179. doi: 10.7554/eLife.51179

Mühleip, A. W., Joos, F., Wigge, C., Frangakis, A. S., Kühlbrandt, W., and Davies, K. M. (2016). Helical arrays of U-shaped ATP synthase dimers form tubular cristae in ciliate mitochondria. *Proc. Natl. Acad. Sci. U.S.A*. 113, 8442–8447. doi: 10.1073/pnas.1525430113

Murata, T., Yamato, I., Kakinuma, Y., Leslie, A. G., and Walker, J. E. (2005). Structure of the rotor of the V-Type Na+-ATPase from *Enterococcus hirae*. *Science* 308, 654–659. doi: 10.1126/science.1110064

Murphy, B. J., Klusch, N., Langer, J., Mills, D. J., Yildiz, Ö., and Kühlbrandt, W. (2019). Rotary substates of mitochondrial ATP synthase reveal the basis of flexible F1-Fo coupling. *Science* 364, eaaw9128. doi: 10.1126/science.aaw9128

Noji, H., Yasuda, R., Yoshida, M., and Kinosita, K. (1997). Direct observation of the rotation of F1-ATPase. *Nature* 386, 299–302. doi: 10.1038/386299a0

Numoto, N., Hasegawa, Y., Takeda, K., and Miki, K. (2009). Inter-subunit interaction and quaternary rearrangement defined by the central stalk of prokaryotic V1-ATPase. *EMBO Rep*. 10, 1228–1234. doi: 10.1038/embor.2009.202

Oliveira, D. M. P. D., Forde, B. M., Kidd, T. J., Harris, P. N. A., Schembri, M. A., Beatson, S. A., et al. (2020). Antimicrobial resistance in ESKAPE pathogens. *Clin. Microbiol. Rev*. 33, e00181–e00119. doi: 10.1128/CMR.00181-19

Pinke, G., Zhou, L., and Sazanov, L. A. (2020). Cryo-EM structure of the entire mammalian F-type ATP synthase. *Nat. Struct. Mol. Biol*. 27, 1077–1085. doi: 10.1038/s41594-020-0503-8

Pogoryelov, D., Yildiz, O., Faraldo-Gomez, J. D., and Meier, T. (2009). High-resolution structure of the rotor ring of a proton-dependent ATP synthase. *Nat. Struct. Mol. Biol*. 16, 1068–1073. doi: 10.1038/nsmb.1678

Preiss, L., Langer, J. D., Yildiz, Ö., Eckhardt-Strelau, L., Guillemont, J. E. G., Koul, A., et al. (2015). Structure of the mycobacterial ATP synthase Fo rotor ring in complex with the anti-TB drug bedaquiline. *Sci. Adv*. 1, e1500106. doi: 10.1126/sciadv.1500106

Punjani, A., Rubinstein, J. L., Fleet, D. J., and Brubaker, M. A. (2017). cryoSPARC: algorithms for rapid unsupervised cryo-EM structure determination. *Nat. Methods* 14, 290–296. doi: 10.1038/nmeth.4169

Reisman, B. J., Guo, H., Ramsey, H. E., Wright, M. T., Reinfeld, B. I., Ferrell, P. B., et al. (2021). Apoptolidin family glycomacrolides target leukemia through inhibition of ATP synthase. *Nat. Chem. Biol*. 18, 360–367. doi: 10.1038/s41589-021-00900-9

Rubinstein, J. L., Walker, J. E., and Henderson, R. (2003). Structure of the mitochondrial ATP synthase by electron cryomicroscopy. *EMBO J*. 22, 6182–6192. doi: 10.1093/emboj/cdg608

Schep, D. G., Zhao, J., and Rubinstein, J. L. (2016). Models for the a subunits of the *Thermus thermophilus* V/A-ATPase and *Saccharomyces cerevisiae* V-ATPase enzymes by cryo-EM and evolutionary covariance. *Proc. Natl. Acad. Sci. U.S.A*. 113, 3245–3250. doi: 10.1073/pnas.1521990113

Scheres, S. H. W. (2012). RELION: implementation of a Bayesian approach to cryo-EM structure determination. *J. Struct. Biol*. 180, 519–530. doi: 10.1016/j.jsb.2012.09.006

Scheres, S. H. W., Gao, H., Valle, M., Herman, G. T., Eggermont, P. P. B., Frank, J., et al. (2007). Disentangling conformational states of macromolecules in 3D-EM through likelihood optimization. *Nat. Methods* 4, 27–29. doi: 10.1038/nmeth992

Seelert, H., Dencher, N. A., and Müller, D. J. (2003). Fourteen protomers compose the oligomer III of the proton-rotor in spinach chloroplast ATP synthase. *J. Mol. Biol*. 333, 337–344. doi: 10.1016/j.jmb.2003.08.046

Senior, A. W., Evans, R., Jumper, J., Kirkpatrick, J., Sifre, L., Green, T., et al. (2020). Improved protein structure prediction using potentials from deep learning. *Nature* 577, 706–710. doi: 10.1038/s41586-019-1923-7

Sobti, M., Ishmukhametov, R., Bouwer, J. C., Ayer, A., Suarna, C., Smith, N. J., et al. (2019). Cryo-EM reveals distinct conformations of *E. coli* ATP synthase on exposure to ATP. *Elife* 8, e43864. doi: 10.7554/eLife.43864

Sobti, M., Smits, C., Wong, A. S., Ishmukhametov, R., Stock, D., Sandin, S., et al. (2016). Cryo-EM structures of the autoinhibited *E. coli* ATP synthase in three rotational states. *eLife* 5, e21598. doi: 10.7554/eLife.21598

Sobti, M., Ueno, H., Noji, H., and Stewart, A. G. (2021). The six steps of the complete F1-ATPase rotary catalytic cycle. *Nat. Commun*. 12, 4690. doi: 10.1038/s41467-021-25029-0

Spikes, T. E., Montgomery, M. G., and Walker, J. E. (2020). Structure of the dimeric ATP synthase from bovine mitochondria. *Proc. Natl. Acad. Sci. U.S.A*. 117, 23519–23526. doi: 10.1073/pnas.2013998117

Srivastava, A. P., Luo, M., Zhou, W., Symersky, J., Bai, D., Chambers, M. G., et al. (2018). High-resolution cryo-EM analysis of the yeast ATP synthase in a lipid membrane. *Science* 360, eaas9699. doi: 10.1126/science.aas9699

Stock, D., Leslie, A. G. W., and Walker, J. E. (1999). Molecular architecture of the rotary motor in ATP synthase. *Science* 286, 1700–1705. doi: 10.1126/science.286.5445.1700

Strauss, M., Hofhaus, G., Schröder, R. R., and Kühlbrandt, W. (2008). Dimer ribbons of ATP synthase shape the inner mitochondrial membrane. *EMBO J*. 27, 1154–1160. doi: 10.1038/emboj.2008.35

Sturm, A., Mollard, V., Cozijnsen, A., Goodman, C. D., and McFadden, G. I. (2015). Mitochondrial ATP synthase is dispensable in blood-stage *Plasmodium berghei* rodent malaria but essential in the mosquito phase. *Proc. Natl. Acad. Sci. U.S.A*. 112, 10216–10223. doi: 10.1073/pnas.1423959112

Sumner, J. P., Dow, J. A., Earley, F. G., Klein, U., Jager, D., and Wieczorek, H. (1995). Regulation of plasma membrane V-ATPase activity by dissociation of peripheral subunits. *J Biol Chem* 270, 5649–5653. doi: 10.1074/jbc.270.10.5649

Suzuki, T., Tanaka, K., Wakabayashi, C., Saita, E., and Yoshida, M. (2014). Chemomechanical coupling of human mitochondrial F1-ATPase motor. *Nat. Chem. Biol.* 10, 930–936. doi: 10.1038/nchembio.1635

Valle, M., Sengupta, J., Swami, N. K., Grassucci, R. A., Burkhardt, N., Nierhaus, K. H., et al. (2002). Cryo-EM reveals an active role for aminoacyl-tRNA in the accommodation process. *EMBO J.* 21, 3557–3567. doi: 10.1093/emboj/cdf326

Varghese, F., Blaza, J. N., Jones, A. J. Y., Jarman, O. D., and Hirst, J. (2018). Deleting the IF1-like ζ subunit from *Paracoccus denitrificans* ATP synthase is not sufficient to activate ATP hydrolysis. *Open Biol.* 8, 170206. doi: 10.1098/rsob.170206

Vik, S. B., and Antonio, B. J. (1994). A mechanism of proton translocation by F1F0 ATP synthases suggested by double mutants of the a subunit. *J. Biol. Chem.* 269, 30364–30369. doi: 10.1016/S0021-9258(18)43822-7

Vinothkumar, K. R., Montgomery, M. G., Liu, S., and Walker, J. E. (2016). Structure of the mitochondrial ATP synthase from *Pichia angusta* determined by electron cryo-microscopy. *Proc. Natl. Acad. Sci. U.S.A.* 113, 12709–12714. doi: 10.1073/pnas.1615902113

Walker, J. E., Fearnley, I. M., Gay, N. J., Gibson, B. W., Northrop, F. D., Powell, S. J., et al. (1985). Primary structure and subunit stoichiometry of F1-ATPase from bovine mitochondria. *J. Mol. Biol.* 184, 677–701. doi: 10.1016/0022-2836(85)90313-4

Walker, J. E., Runswick, M. J., and Saraste, M. (1982). Subunit equivalence in *Escherichia coli* and bovine heart mitochondrial F1F0 ATPases. *FEBS Lett.* 146, 393–396. doi: 10.1016/0014-5793(82)80960-5

Wang, N., Ozer, E. A., Mandel, M. J., and Hauser, A. R. (2014). Genome-Wide identification of acinetobacter baumannii genes necessary for persistence in the lung. *mBio* 5, e01163–14. doi: 10.1128/mBio.01163-14

Watt, I. N., Montgomery, M. G., Runswick, M. J., Leslie, A. G., and Walker, J. E. (2010). Bioenergetic cost of making an adenosine triphosphate molecule in animal mitochondria. *Proc. Natl. Acad. Sci. U.S.A.* 107, 16823–16827. doi: 10.1073/pnas.1011099107

Wilkens, S., and Capaldi, R. A. (1998). ATP synthase's second stalk comes into focus. *Nature* 393, 29. doi: 10.1038/29908

Yang, S., Yu, X., Vanloock, M. S., Jezewska, M. J., Bujalowski, W., Egelman, E. H., et al. (2002). Flexibility of the meric helicasrings : structural asymmetry in the DnaB hexae. *J. Mol. Biol.* 321, 839–849. doi: 10.1016/S0022-2836(02)00711-8

Yasuda, R., Noji, H., Kinosita, K., and Yoshida, M. (1998). F1-ATPase is a highly efficient molecular motor that rotates with discrete 120° steps. *Cell* 93, 1117–1124. doi: 10.1016/S0092-8674(00)81456-7

Yasuda, R., Noji, H., Yoshida, M., Kinosita, K., and Itoh, H. (2001). Resolution of distinct rotational substeps by submillisecond kinetic analysis of F1-ATPase. *Nature* 410, 898–904. doi: 10.1038/35073513

Zarco-Zavala, M., Watanabe, R., McMillan, D. G. G., Suzuki, T., Ueno, H., Mendoza-Hoffmann, F., et al. (2020). The 3 × 120° rotary mechanism of *Paracoccus denitrificans* F1-ATPase is different from that of the bacterial and mitochondrial F1-ATPases. *Proc. Natl. Acad. Sci. U.S.A.* 117, 29647–29657. doi: 10.1073/pnas.2003163117

Zhao, J., Benlekbir, S., and Rubinstein, J. L. (2015). Electron cryomicroscopy observation of rotational states in a eukaryotic V-ATPase. *Nature* 521, 241–245. doi: 10.1038/nature14365

Zhou, A., Rohou, A., Schep, D. G., Bason, J. V., Montgomery, M. G., Walker, J. E., et al. (2015). Structure and conformational states of the bovine mitochondrial ATP synthase by cryo-EM. *eLife* 4, e10180. doi: 10.7554/eLife.10180.049

Zhou, L., and Sazanov, L. A. (2019). Structure and conformational plasticity of the intact *Thermus thermophilus* V/A-type ATPase. *Science* 365, eaaw9144. doi: 10.1126/science.aaw9144

Conflict of Interest: The authors declare that the research was conducted in the absence of any commercial or financial relationships that could be construed as a potential conflict of interest.

Publisher's Note: All claims expressed in this article are solely those of the authors and do not necessarily represent those of their affiliated organizations, or those of the publisher, the editors and the reviewers. Any product that may be evaluated in this article, or claim that may be made by its manufacturer, is not guaranteed or endorsed by the publisher.

Copyright © 2022 Courbon and Rubinstein. This is an open-access article distributed under the terms of the Creative Commons Attribution License (CC BY). The use, distribution or reproduction in other forums is permitted, provided the original author(s) and the copyright owner(s) are credited and that the original publication in this journal is cited, in accordance with accepted academic practice. No use, distribution or reproduction is permitted which does not comply with these terms.

frontiers | Frontiers in Microbiology

REVIEW
published: 06 May 2022
doi: 10.3389/fmicb.2022.904084

How Does F_1-ATPase Generate Torque?: Analysis From Cryo-Electron Microscopy and Rotational Catalysis of Thermophilic F_1

Hiroyuki Noji and Hiroshi Ueno*

Department of Applied Chemistry, Graduate School of Engineering, The University of Tokyo, Tokyo, Japan

The F_1-ATPase is a rotary motor fueled by ATP hydrolysis. Its rotational dynamics have been well characterized using single-molecule rotation assays. While F_1-ATPases from various species have been studied using rotation assays, the standard model for single-molecule studies has been the F_1-ATPase from thermophilic *Bacillus* sp. PS3, named TF_1. Single-molecule studies of TF_1 have revealed fundamental features of the F_1-ATPase, such as the principal stoichiometry of chemo-mechanical coupling (hydrolysis of 3 ATP per turn), torque (approximately 40 pN·nm), and work per hydrolysis reaction (80 pN·nm = 48 kJ/mol), which is nearly equivalent to the free energy of ATP hydrolysis. Rotation assays have also revealed that TF_1 exhibits two stable conformational states during turn: a binding dwell state and a catalytic dwell state. Although many structures of F_1 have been reported, most of them represent the catalytic dwell state or its related states, and the structure of the binding dwell state remained unknown. A recent cryo-EM study on TF_1 revealed the structure of the binding dwell state, providing insights into how F_1 generates torque coupled to ATP hydrolysis. In this review, we discuss the torque generation mechanism of F_1 based on the structure of the binding dwell state and single-molecule studies.

Keywords: F_1-ATPase, molecular motor, single-molecule analysis, structure, chemo-mechanical coupling, torque

OPEN ACCESS

Edited by:
Tom Duncan,
Upstate Medical University,
United States

Reviewed by:
Masamitsu Futai,
Iwate Medical University, Japan
Yasuyuki Kato-Yamada,
Rikkyo University, Japan

****Correspondence:***
Hiroyuki Noji
hnoji@g.ecc.u-tokyo.ac.jp

Specialty section:
This article was submitted to Microbial Physiology and Metabolism, a section of the journal Frontiers in Microbiology

Received: *25 March 2022*
Accepted: *22 April 2022*
Published: *06 May 2022*

Citation:
Noji H and Ueno H (2022) How Does F_1-ATPase Generate Torque?: Analysis From Cryo-Electron Microscopy and Rotational Catalysis of Thermophilic F_1. Front. Microbiol. 13:904084. doi: 10.3389/fmicb.2022.904084

INTRODUCTION

The F_1-ATPase is the catalytic core of the F_oF_1 ATP synthase. F_oF_1 ATP synthase is the ubiquitous rotary motor enzyme, which is found in the membranes of mitochondria, chloroplasts, and bacteria (Hisabori et al., 2013; Junge and Nelson, 2015; Sielaff et al., 2018; Kuhlbrandt, 2019). When isolated from the F_o component, which is embedded in the lipid membrane, F_1 acts as an ATP-driven motor that rotates the central subunit of the rotor against the stator ring by using free energy derived from ATP hydrolysis (Noji et al., 2017). The chemo-mechanical coupling between ATP hydrolysis and rotation of F_1 is reversible; when the rotation is forcibly reversed, F_1 catalyzes ATP synthesis reaction (Rondelez et al., 2005). This reversible feature discriminates F_1 from other molecular motors. However, it should be noted that there are

arguments on whether F_1 synthesizes ATP exactly following the reverse reaction pathway for ATP hydrolysis in the whole F_oF_1 complex under ATP synthesis conditions (Vinogradov, 2019). The minimum structure that functions as a rotary motor is the $\alpha_3\beta_3\gamma$ subcomplex, which is composed of the $\alpha_3\beta_3$ stator ring and the rotor γ subunit. The $\alpha_3\beta_3$ ring possesses three catalytic reaction sites at the α–β interfaces. Most of the catalytic residues are in the β subunit, which undergoes large conformational transitions coupled with the catalytic reactions.

The kinetics and physicochemical properties of F_1 rotation have been well studied in single-molecule rotation assays (Watanabe et al., 2010; Noji et al., 2017). All of the F_1-ATPases investigated so far show counterclockwise rotation when viewed from the F_o side, suggesting that the fundamental mechanism of the chemo-mechanical coupling of F_1 is highly conserved among species (Konno et al., 2006; Bilyard et al., 2013; Suzuki et al., 2014; Steel et al., 2015; McMillan et al., 2016; Kobayashi et al., 2020; Zarco-Zavala et al., 2020). Since the rotation assay was established (Noji et al., 1997), the $\alpha_3\beta_3\gamma$ subcomplex of F_1-ATPase from thermophilic *Bacillus* sp. PS3, which we hereafter call TF_1 for simplicity, has been intensively studied to reveal fundamental features of the chemo-mechanical coupling reaction of the F_1-ATPase. Such features include a unitary step size (120°), a coupling stoichiometry of hydrolysis of 3 ATP molecules per turn, a generation of torque against viscous friction (approximately 40 pN·nm), and a high reversibility of the reaction that results in a high efficiency of energy conversion (Yasuda et al., 1998; Rondelez et al., 2005; Hayashi et al., 2010; Toyabe et al., 2011).

Figure 1A shows our proposed reaction scheme for rotary catalysis by TF_1 (Watanabe et al., 2010). Each β subunit completes a single ATP hydrolysis coupled with a single γ rotation. The unitary rotation step is 120° rotation, which is divided into 80° and 40° substeps, initiated after the binding dwell and catalytic dwell, respectively; TF_1 undergoes three binding dwells and three catalytic dwells in a single 360° rotation of γ. Each 80° substep is triggered after ATP binding, and the 40° substep is initiated after hydrolysis of bound ATP. TF_1 also conducts product-releasing reactions associated with the binding and catalytic dwells; ADP is released at the end of the binding dwell or during the 80° substep, and inorganic phosphate (Pi) is released during the catalytic dwell. The temperature-sensitive (TS) reaction, which is considered to be a conformational rearrangement of the β subunit before or after ATP binding, was also found to occur at a binding angle before the 80° substep (Enoki et al., 2009). Thus, TF_1 conducts multiple reactions in each dwell: ATP binding, ADP release, the TS reaction during the binding dwell, and ATP hydrolysis and Pi release during the catalytic dwell. The rotational position of the γ subunit is defined as 0° for one of the β subunits in the ATP-waiting state at the binding angle; this is shown in the uppermost panel in the scheme. This β subunit then hydrolyzes the bound ATP into ADP and Pi at +200°, releases ADP at +240°, and releases Pi at +320°. The TS reaction is suggested to occur at 0°. Note that the other two β subunits follow the same reaction process, although their reaction phases always differ by +120° or +240°.

TF_1 has two stable conformational states during catalysis: the binding dwell and the catalytic dwell. Other types of F_1 have also been reported to have binding and catalytic dwells (Bilyard et al., 2013; Suzuki et al., 2014; Steel et al., 2015; McMillan et al., 2016; Kobayashi et al., 2020). The exception is F_1 from *Paracoccus denitrificans*, which shows binding and catalytic dwells at the same angles (Zarco-Zavala et al., 2020). It is worth mentioning that mammalian mitochondrial F_1's show the third short dwell (Suzuki et al., 2014; Kobayashi et al., 2020), suggesting the additional stable conformational state in mammalian F_1's. Since the first crystal structure of F_1 was published (Abrahams et al., 1994), many different F_1 structures have been determined under a wide variety of conditions. Most of them, irrespective of species, represent the catalytic dwell state or its related states including the transition states and the inhibited states, in which two of the three β subunits assume a closed form (C) with a bound nucleotide (ADP or ATP analog). The helical C-terminal domain of the β subunit swings inward in the C conformation, seemingly pushing the γ subunit. The third β subunit assumes an open form (O), generally without a bound nucleotide, although some structures have shown bound ADP (Menz et al., 2001) or the Pi analog thiophosphate (Bason et al., 2015). This feature is well conserved among the structures of F_1 in the catalytic dwell state or its related states. As a result, the angular orientation of the γ subunit is not significantly different among these structures within the 40° substep (Okazaki and Takada, 2011). Thus, although the F_1 structures show three conformational states of the β subunit in the catalytic dwell (at 80°, 200°, and 320°), the remaining three states of the binding dwell (at 0°, 120°, and 240°) have not been available.

CRYO-EM ANALYSIS OF TF_1 IN THE BINDING DWELL STATE

To determine the structure of TF_1 in the binding dwell state, structural analysis of the mutant TF_1 (βE190D) at a low temperature was conducted using cryogenic electron microscopy (cryo-EM; Sobti et al., 2021). In this analysis, TF_1 complexes were incubated with MgATP at the low temperature of 10°C to keep the molecules in the binding dwell state while waiting for the TS reaction. A previous single-molecule study revealed that the βE190D mutant has an exceptionally long dwell at the binding dwell angle while waiting for the TS reaction to occur (Enoki et al., 2009). For comparison, the structure of the mutant F_1 at 28°C was also determined, at which temperature the catalytic dwell state is predominant. Cryo-EM analysis of the mutant TF_1 at 28°C showed a structure corresponding to the catalytic dwell state with the C-C-O conformation of β. Although the 28°C structure was almost identical to the catalytic dwell structures of other types of F_1, one difference was that ADP was bound to β in the O conformation, as discussed later. The structure of F_1 obtained at 10°C showed distinctive conformations of the β subunit; two of the β subunits adopted intermediate conformations between O and C, while the third one assumed a C conformation. The β subunit in the C conformation bound ATP, representing a

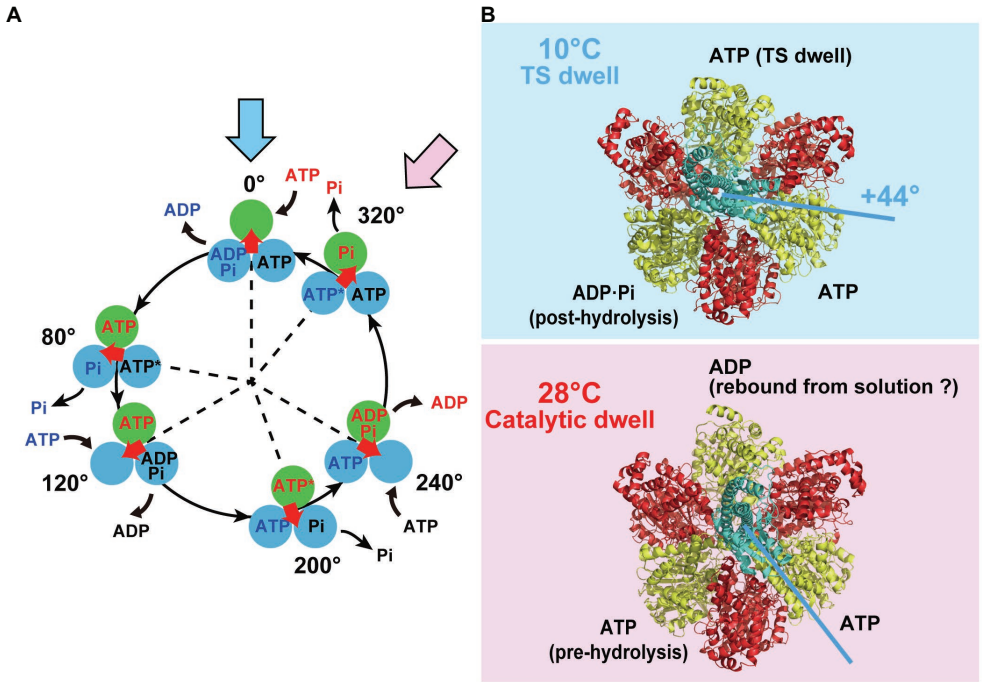


FIGURE 1 | Reaction scheme and cryo-EM structures of TF_1. **(A)** Reaction scheme of TF_1. Three circles represent catalytic states of the β subunit, and the arrow at the center indicates the orientation of the γ subunit. Blue and pink arrows indicate a binding dwell state and a catalytic dwell state, respectively. **(B)** The cryo-EM structures of TF_1 obtained at 10°C (highlighted in blue) or at 28°C (highlighted in red). The 10°C and 28°C structures represent the binding dwell state paused by temperature-sensitive reaction and the catalytic dwell state paused by hydrolysis reaction, respectively. The α, β, and γ subunits are represented in red, yellow, and cyan, respectively.

120° state according to the reaction scheme (**Figure 1A**). The β subunits in intermediate conformations were half-opened (HO) or half-closed (HC). The HO β subunit bound ADP and Pi, thus representing the post-hydrolysis form that should be in the 240° state. The HC β subunit had a weakly bound ATP with fewer interacting residues; it should correspond to the 0° state. The resultant arrangements of the 0°, 120°, and 240° states in the F_1 complex are consistent with the expected arrangements. Moreover, when the 10°C structure was compared to the catalytic dwell structure obtained at 28°C, the γ subunit was rotated by +44° from the catalytic dwell state (**Figure 1B**). This result agrees with the +40° rotation from the catalytic dwell state to the binding dwell state expected from single-molecule studies. Thus, cryo-EM analysis of βE190D TF_1 at 10°C provides the first structural information about F_1 in the binding dwell state.

TORQUE GENERATION MECHANISM

The structure of the binding dwell state enabled us to identify six conformational states of the β subunit along the reaction scheme, as shown in **Figure 2**. Based on this scheme, we now examine the conformational transitions of the β subunit revealed by cryo-EM analyses, focusing on a single pair of β and γ subunits. We then discuss the possible molecular mechanism of torque generation, using all of the available data. Here, the angle represents the angular position of the γ subunit during 360° rotation against the β subunit in the pair, where the origin, 0°, is defined as the angle at which β is in the 0° state, paused at the binding angle.

The 0° state in the HC conformation represents the state after association with ATP and before TS. The transition from −40° (=320°) to 0° induces a change from the O to the HC conformation, which is accompanied by a twisting motion of the C-terminal domain of the β subunit. The second large conformational transition is observed in the transition from 0 to 80°, which induces the HC to C transition, which causes a "push" of the C-terminal domain of the β subunit toward the off-axis bulge of the γ subunit. The transitions from 80 to 120° and 120 to 200° do not involve obvious conformational changes in the β subunit. The third large conformational transition is during the C to HO transition from 200 to 240°. This is the "pull back" motion of the C-terminal domain of the β subunit from the axis of the γ subunit. The final conformational transition is during the HO to O transition from 240 to 320°. This involves a "twist back" motion of the C-terminal domain of the β subunit. Thus, the series of conformational transitions of the β subunit in the course of a single turnover of ATP hydrolysis can be explained as a "twist" (−40–0°), a "push" (0–80°), a "pull back" (200–240°), and a "twist back" (240–320°) motions.

The first conformational transition, the "twist" motion, is seemingly driven by binding of ATP. Because the binding dwell structure before ATP association is not yet known, it is not

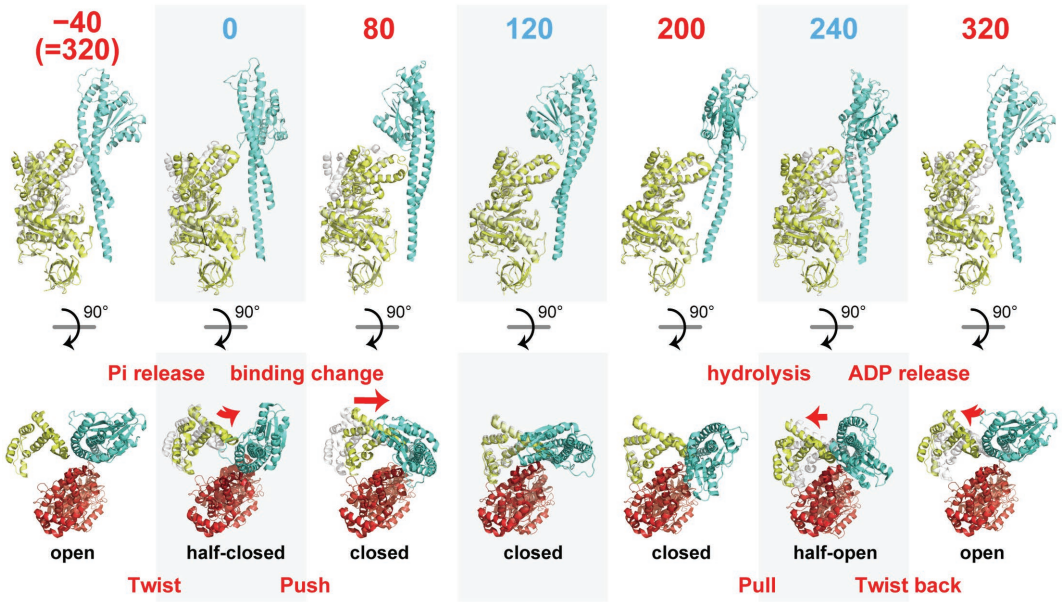


FIGURE 2 | Sequential images of the conformational states of the β subunit. αβ-pairs are superimposed on the N-terminal domain (β2-82) of the β subunit. The upper row shows the conformations of a pair of β (yellow) and γ subunits (cyan) viewed from the side. The numbers indicate the angle position of the γ subunit along the reaction scheme in **Figure 1A** where 0° is defined as the angle for ATP association. The lower row represents the positions of the C-terminal domains (after P356) of the β subunit (yellow) with the α (red) and γ subunits (blue) viewed from the top. The gray portion shows the structure of the β subunit before one reaction state for comparison purposes.

clear whether the twist motion is induced by association with ATP at 0° or by the 40° substep rotation before ATP association. In the former case, the β subunit conducts the twist motion without driving the rotation of γ, and the twist motion is not directly involved in torque generation. In the latter case, the direct cause of the twist motion is not ATP binding but rather another reaction, such as Pi release or a conformational rearrangement not coupled with a particular catalytic reaction. A single-molecule study by Masaike et al. (2008) supports the former model. They observed the rotation of a fluorophore attached to a helix of the C-terminal domain of the β subunit and found no obvious difference between the 320 and 0° states (Masaike et al., 2008). Thus, it is likely that the binding dwell structure before ATP association corresponds to the O conformation and the twist motion is triggered by ATP association but not directly coupled with γ rotation.

The "push" motion that occurs from 0 to 80° should be responsible for torque generation. In this conformational transition, the β subunit swings its C-terminal domain toward the axis of the γ subunit, enveloping the bound ATP. **Figure 3** shows a close-up view of the structure around the catalytic site. In comparison with the structure of the 0° state, the structure of the 80° state shows tighter associations of the bound ATP with the surrounding catalytic residues. In particular, Arg365 of the α subunit (αR365) and R191 of the β subunit (βR191) shift their position toward the phosphate group of ATP in the 80° state. In addition, the p-loop around βG161 approaches the phosphate group of ATP in the 80° state. These features are consistent with the findings of a single-molecule manipulation study that showed that TF_1 exponentially increased affinity to ATP by 235-fold during rotation by 60° (Watanabe et al., 2011). The torque generated by this affinity change is estimated at 21–54 pN·nm, indicating that the affinity change is the major torque-generating event in the 80° substep. This mechanism of torque generation upon the affinity change is also consistent with the binding-change mechanism proposed by Boyer, who suggested that the proton motive force (PMF) is used mainly to loosen the affinity of the catalytic site for ATP during ATP synthesis (Boyer, 2000). Thus, tightening the affinity for ATP is the major torque-generating step in the rotation of F_1 driven by ATP hydrolysis.

The third conformational transition, the C-HO transition from 200 to 240°, is associated with hydrolysis of the bound ATP, as the bound nucleotide switches from ATP in the 200° state to ADP and Pi in the 240° state. Many studies have revealed that ATP is hydrolyzed in the 200° state. Because the βE190D mutant is significantly retarded in the rate of ATP hydrolysis (Shimabukuro et al., 2003), it is very reasonable to see ATP bound in the 200° state. Thus, 240° represents the post-hydrolysis state. **Figure 3** shows a clear difference in the residues associating with Pi, such that αArg365 and βR191 undergo a positional shift to separate from the phosphate group of ADP. Although not shown in the figure, the α–β interface opens slightly during the C-HO transition. The aforementioned single-molecule manipulation study also demonstrated that the equilibrium constant of the hydrolysis state (ADP + Pi) against the synthesis state (ATP) increases with rotation (Watanabe et al., 2011), indicating the contribution of hydrolysis for torque

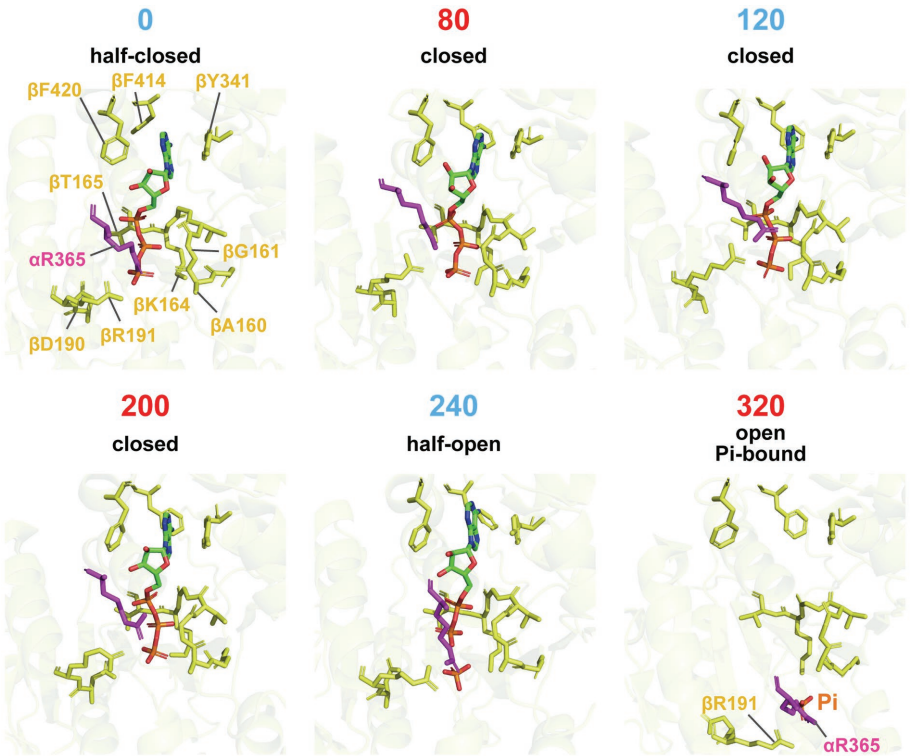


FIGURE 3 | Close-up structures of catalytic sites on the β subunit. Residues around the nucleotides of each conformational state from 0° to 320°, superimposed on residues (β163-165, β190, β191, β341, β414, and β420), are shown in stick representation. αR365 is shown in magenta. Note that the Pi-bound structure is used for the 320° conformation.

generation. However, the estimated torque (4–17 pN·nm) is significantly lower than that made possible by the change in affinity for ATP (Watanabe et al., 2011; Noji et al., 2017).

The molecular mechanism for the fourth conformational transition, the HO-O transition from 240 to 320°, must also be considered. The reaction scheme shown in **Figure 1A**, which suggests that ADP is released during this transition, is based on other structural analyses that show no bound nucleotides in the 320° state (Abrahams et al., 1994; Bowler et al., 2007) and simultaneous observations of rotation and the association/dissociation of fluorescently labeled nucleotides (Nishizaka et al., 2004; Adachi et al., 2007). However, ADP was bound in the 320° state in the catalytic dwell structure of TF_1. Considering that this structure was obtained in the presence of 10 mM ATP at 28°C, it is likely that ADP rebinds to the β subunit in the 320° state. **Figure 3** shows the 320° conformation of the Pi-bound structure of TF_1 obtained in medium containing 100 mM Pi and no nucleotides (Sobti et al., 2021). The exact determination of the catalytic state at 320° requires further investigation.

The 320 to 360° rotation corresponds to the −40 to 0° rotation. As mentioned above, it is likely that the twist motion during the O-HC transition is not directly coupled with γ rotation. Several studies have indicated that the 320 to 360° rotation is coupled with Pi release from the 320° state. The cryo-EM structure of TF_1 in the catalytic dwell state in the presence of Pi supports this model, showing Pi bound in the 320° state, as seen in the crystal structures of bovine or yeast mitochondrial F_1 (Kabaleeswaran et al., 2006; Bason et al., 2015). Kinetic analysis of rotation in the presence of Pi suggests that Pi release is the second major torque-generating step in F_1 in addition to the change in affinity for ATP (Adachi et al., 2007). A comprehensive analysis of the crystal structure suggests that Pi release is coupled with opening of the α–β interface (Okazaki and Takada, 2011). Further structural analysis will be required to elucidate the torque generation mechanism upon Pi release. In this regard, it is worth noting that the cryo-EM structure of TF_1 in the 320° state with bound Pi reveals a putative Pi exit channel in the β subunit. This model awaits experimental and theoretical verification.

REMAINING ISSUES

The cryo-EM structures of TF_1 provide several important insights into the molecular mechanism by which F_1 couples a catalytic reaction to torque generation. However, cryo-EM study on the mutant TF_1 also highlights several important issues that must be addressed. One is the molecular mechanism of the conformational entrapment of the β subunit in HC state that leads TS dwell. The current structural information in addition to previous single-molecule studies are not sufficient

to deduce this mechanism. Molecular dynamics simulation of TF_1 starting from TS dwell could address this point. Another issue is the structure of the 0° state before ATP association. The structure, once known, will resolve whether the β subunit assumes a conformation different from the HC state before ATP association and also show what type of conformational change is coupled with Pi release. Further structural analysis of TF_1 in its catalytic dwell state will be required to determine the point at which ADP is released. The cryo-EM study also provides a new way to address the structural basis of F_1 allostery. TF_1 is sufficiently stable to maintain the $\alpha_3\beta_3$ ring structure even when the γ subunit is removed. A previous study using high-speed atomic force microscopy showed that the isolated $\alpha_3\beta_3$ ring still possesses allostery (Uchihashi et al., 2011); the β subunits in the $\alpha_3\beta_3$ ring show sequential power-stroking motions, demonstrating that the fundamental allostery of F_1 originates from the $\alpha_3\beta_3$ structure. Currently, only the nucleotide-free structure of $\alpha_3\beta_3$ has been reported, in which all of the β subunits are in the O state. A cryo-EM approach would allow structural analysis of the $\alpha_3\beta_3$ ring with bound nucleotides, which should break the structural symmetry of the ring and provide important insights into the basis of the fundamental allostery of the $\alpha_3\beta_3$ ring. A more fundamental question arising from a comprehensive point of view is the generality of the findings; how well the molecular mechanism of torque generation learned from the studies on TF_1 is conserved among other F_1's. Considering the many common features found in the structure and rotation dynamics, it seems that the fundamental mechanism should be conserved across species. However, some points would be diverse to meet physiological requirements. In this context, it would be very intriguing to analyze how the torque generation mechanism is conserved or diverse between F_1- and V_1-ATPase. The manner of the conformational transition as well as the torque generation mechanism of binding-change process of V_1-ATPase were reported to be different from those of F_1, and even different among V_1-ATPase's (Imamura et al., 2005; Arai et al., 2013; Tirtom et al., 2013; Iida et al., 2019; Singharoy et al., 2019; Kishikawa et al., 2022). Therefore, more comprehensive investigation on the torque generation mechanism of V_1 is required.

AUTHOR CONTRIBUTIONS

HN and HU contributed to the conceptualization, review, and editing. HN wrote the original draft of the manuscript. All authors have contributed to the manuscript and approved the submitted version.

FUNDING

This work was supported in part by a Grant-in-Aid for Scientific Research on Innovation Areas (JP19H05380 and JP21H00388 to HU), Grant-in-Aids for Scientific Research (S; JP19H05624 to HN) from the Japan Society for the Promotion of Science, and JST CREST, Japan (JPMJCR19S4 to HN).

ACKNOWLEDGMENTS

We thank and acknowledge Meghna Sobti and Alastair G. Stewart for helpful discussions.

REFERENCES

Abrahams, J. P., Leslie, A. G., Lutter, R., and Walker, J. E. (1994). Structure at 2.8 A resolution of F1-ATPase from bovine heart mitochondria. *Nature* 370, 621–628. doi: 10.1038/370621a0

Adachi, K., Oiwa, K., Nishizaka, T., Furuike, S., Noji, H., Itoh, H., et al. (2007). Coupling of rotation and catalysis in F(1)-ATPase revealed by single-molecule imaging and manipulation. *Cell* 130, 309–321. doi: 10.1016/j.cell.2007.05.020

Arai, S., Saijo, S., Suzuki, K., Mizutani, K., Kakinuma, Y., Ishizuka-Katsura, Y., et al. (2013). Rotation mechanism of Enterococcus hirae V1-ATPase based on asymmetric crystal structures. *Nature* 493, 703–707. doi: 10.1038/nature11778

Bason, J. V., Montgomery, M. G., Leslie, A. G., and Walker, J. E. (2015). How release of phosphate from mammalian F1-ATPase generates a rotary substep. *Proc. Natl. Acad. Sci. U. S. A.* 112, 6009–6014. doi: 10.1073/pnas.1506465112

Bilyard, T., Nakanishi-Matsui, M., Steel, B. C., Pilizota, T., Nord, A. L., Hosokawa, H., et al. (2013). High-resolution single-molecule characterization of the enzymatic states in Escherichia coli F1-ATPase. *Philos. Trans. R. Soc. Lond. Ser. B Biol. Sci.* 368:20120023. doi: 10.1098/rstb.2012.0023

Bowler, M. W., Montgomery, M. G., Leslie, A. G., and Walker, J. E. (2007). Ground state structure of F1-ATPase from bovine heart mitochondria at 1.9 A resolution. *J. Biol. Chem.* 282, 14238–14242. doi: 10.1074/jbc.M700203200

Boyer, P. D. (2000). Catalytic site forms and controls in ATP synthase catalysis. *Biochim. Biophys. Acta* 1458, 252–262. doi: 10.1016/s0005-2728(00)00077-3

Enoki, S., Watanabe, R., Iino, R., and Noji, H. (2009). Single-molecule study on the temperature-sensitive reaction of F1-ATPase with a hybrid F1 carrying a single beta(E190D). *J. Biol. Chem.* 284, 23169–23176. doi: 10.1074/jbc.M109.026401

Hayashi, K., Ueno, H., Iino, R., and Noji, H. (2010). Fluctuation theorem applied to F1-ATPase. *Phys. Rev. Lett.* 104:218103. doi: 10.1103/PhysRevLett.104.218103

Hisabori, T., Sunamura, E., Kim, Y., and Konno, H. (2013). The chloroplast ATP synthase features the characteristic redox regulation machinery. *Antioxid. Redox Signal.* 19, 1846–1854. doi: 10.1089/ars.2012.5044

Iida, T., Minagawa, Y., Ueno, H., Kawai, F., Murata, T., and Iino, R. (2019). Single-molecule analysis reveals rotational substeps and chemo-mechanical coupling scheme of Enterococcus hirae V1-ATPase. *J. Biol. Chem.* 294, 17017–17030. doi: 10.1074/jbc.RA119.008947

Imamura, H., Takeda, M., Funamoto, S., Shimabukuro, K., Yoshida, M., and Yokoyama, K. (2005). Rotation scheme of V1-motor is different from that of F1-motor. *Proc. Natl. Acad. Sci. U. S. A.* 102, 17929–17933. doi: 10.1073/pnas.0507764102

Junge, W., and Nelson, N. (2015). ATP synthase. *Annu. Rev. Biochem.* 84, 631–657. doi: 10.1146/annurev-biochem-060614-034124

Kabaleeswaran, V., Puri, N., Walker, J. E., Leslie, A. G., and Mueller, D. M. (2006). Novel features of the rotary catalytic mechanism revealed in the structure of yeast F1 ATPase. *EMBO J.* 25, 5433–5442. doi: 10.1038/sj.emboj.7601410

Kishikawa, J., Nakanishi, A., Nakano, A., Saeki, S., Furuta, A., Kato, T., et al. (2022). Structural snapshots of V/A-ATPase reveal the rotary catalytic mechanism of rotary ATPases. *Nat. Commun.* 13:1213. doi: 10.1038/s41467-022-28832-5

Kobayashi, R., Ueno, H., Li, C. B., and Noji, H. (2020). Rotary catalysis of bovine mitochondrial F1-ATPase studied by single-molecule experiments. *Proc. Natl. Acad. Sci. U. S. A.* 117, 1447–1456. doi: 10.1073/pnas.1909407117

Konno, H., Murakami-Fuse, T., Fujii, F., Koyama, F., Ueoka-Nakanishi, H., Pack, C. G., et al. (2006). The regulator of the F1 motor: inhibition of

rotation of cyanobacterial F1-ATPase by the epsilon subunit. *EMBO J.* 25, 4596–4604. doi: 10.1038/sj.emboj.7601348

Kuhlbrandt, W. (2019). Structure and mechanisms of F-type ATP synthases. *Annu. Rev. Biochem.* 88, 515–549. doi: 10.1146/annurev-biochem-013118-110903

Masaike, T., Koyama-Horibe, F., Oiwa, K., Yoshida, M., and Nishizaka, T. (2008). Cooperative three-step motions in catalytic subunits of F(1)-ATPase correlate with 80 degrees and 40 degrees substep rotations. *Nat. Struct. Mol. Biol.* 15, 1326–1333. doi: 10.1038/nsmb.1510

McMillan, D. G., Watanabe, R., Ueno, H., Cook, G. M., and Noji, H. (2016). Biophysical characterization of a thermoalkaliphilic molecular motor with a high stepping torque gives insight into evolutionary ATP synthase adaptation. *J. Biol. Chem.* 291, 23965–23977. doi: 10.1074/jbc.M116.743633

Menz, R. I., Walker, J. E., and Leslie, A. G. (2001). Structure of bovine mitochondrial F(1)-ATPase with nucleotide bound to all three catalytic sites: implications for the mechanism of rotary catalysis. *Cell* 106, 331–341. doi: 10.1016/s0092-8674(01)00452-4

Nishizaka, T., Oiwa, K., Noji, H., Kimura, S., Muneyuki, E., Yoshida, M., et al. (2004). Chemomechanical coupling in F1-ATPase revealed by simultaneous observation of nucleotide kinetics and rotation. *Nat. Struct. Mol. Biol.* 11, 142–148. doi: 10.1038/nsmb721

Noji, H., Ueno, H., and McMillan, D. G. G. (2017). Catalytic robustness and torque generation of the F1-ATPase. *Biophys. Rev.* 9, 103–118. doi: 10.1007/s12551-017-0262-x

Noji, H., Yasuda, R., Yoshida, M., and Kinosita, K. Jr. (1997). Direct observation of the rotation of F1-ATPase. *Nature* 386, 299–302. doi: 10.1038/386299a0

Okazaki, K., and Takada, S. (2011). Structural comparison of F1-ATPase: interplay among enzyme structures, catalysis, and rotations. *Structure* 19, 588–598. doi: 10.1016/j.str.2011.01.013

Rondelez, Y., Tresset, G., Nakashima, T., Kato-Yamada, Y., Fujita, H., Takeuchi, S., et al. (2005). Highly coupled ATP synthesis by F1-ATPase single molecules. *Nature* 433, 773–777. doi: 10.1038/nature03277

Shimabukuro, K., Yasuda, R., Muneyuki, E., Hara, K. Y., Kinosita, K. Jr., and Yoshida, M. (2003). Catalysis and rotation of F1 motor: cleavage of ATP at the catalytic site occurs in 1 ms before 40 degree substep rotation. *Proc. Natl. Acad. Sci. U. S. A.* 100, 14731–14736. doi: 10.1073/pnas.2434983100

Sielaff, H., Duncan, T. M., and Borsch, M. (2018). The regulatory subunit epsilon in *Escherichia coli* FOF1-ATP synthase. *Biochim. Biophys. Acta Bioenerg.* 1859, 775–788. doi: 10.1016/j.bbabio.2018.06.013

Singharoy, A., Chipot, C., Ekimoto, T., Suzuki, K., Ikeguchi, M., Yamato, I., et al. (2019). Rotational mechanism model of the bacterial V1 motor based on structural and computational analyses. *Front. Physiol.* 10:46. doi: 10.3389/fphys.2019.00046

Sobti, M., Ueno, H., Noji, H., and Stewart, A. G. (2021). The six steps of the complete F1-ATPase rotary catalytic cycle. *Nat. Commun.* 12:4690. doi: 10.1038/s41467-021-25029-0

Steel, B. C., Nord, A. L., Wang, Y. M., Pagadala, V., Mueller, D. M., and Berry, R. M. (2015). Comparison between single-molecule and X-ray crystallography data on yeast F-1-ATPase. *Sci. Rep.* 5:8773. doi: 10.1038/srep08773

Suzuki, T., Tanaka, K., Wakabayashi, C., Saita, E., and Yoshida, M. (2014). Chemomechanical coupling of human mitochondrial F1-ATPase motor. *Nat. Chem. Biol.* 10, 930–936. doi: 10.1038/nchembio.1635

Tirtom, N. E., Okuno, D., Nakano, M., Yokoyama, K., and Noji, H. (2013). Mechanical modulation of ATP-binding affinity of V1-ATPase. *J. Biol. Chem.* 288, 619–623. doi: 10.1074/jbc.M112.420729

Toyabe, S., Watanabe-Nakayama, T., Okamoto, T., Kudo, S., and Muneyuki, E. (2011). Thermodynamic efficiency and mechanochemical coupling of F1-ATPase. *Proc. Natl. Acad. Sci. U. S. A.* 108, 17951–17956. doi: 10.1073/pnas.1106787108

Uchihashi, T., Iino, R., Ando, T., and Noji, H. (2011). High-speed atomic force microscopy reveals rotary catalysis of rotorless F1-ATPase. *Science* 333, 755–758. doi: 10.1126/science.1205510

Vinogradov, A. D. (2019). New perspective on the reversibility of ATP synthesis and hydrolysis by FoxF1-ATP synthase (hydrolase). *Biochemistry* 84, 1247–1255. doi: 10.1134/S0006297919110038

Watanabe, R., Iino, R., and Noji, H. (2010). Phosphate release in F1-ATPase catalytic cycle follows ADP release. *Nat. Chem. Biol.* 6, 814–820. doi: 10.1038/nchembio.443

Watanabe, R., Okuno, D., Sakakihara, S., Shimabukuro, K., Iino, R., Yoshida, M., et al. (2011). Mechanical modulation of catalytic power on F1-ATPase. *Nat. Chem. Biol.* 8, 86–92. doi: 10.1038/nchembio.715

Yasuda, R., Noji, H., Kinosita, K. Jr., and Yoshida, M. (1998). F1-ATPase is a highly efficient molecular motor that rotates with discrete 120 degree steps. *Cell* 93, 1117–1124. doi: 10.1016/s0092-8674(00)81456-7

Zarco-Zavala, M., Watanabe, R., McMillan, D. G. G., Suzuki, T., Ueno, H., Mendoza-Hoffmann, F., et al. (2020). The 3 x 120 degrees rotary mechanism of Paracoccus denitrificans F1-ATPase is different from that of the bacterial and mitochondrial F1-ATPases. *Proc. Natl. Acad. Sci. U. S. A.* 117, 29647–29657. doi: 10.1073/pnas.2003163117

Conflict of Interest: The authors declare that the research was conducted in the absence of any commercial or financial relationships that could be construed as potential conflicts of interest.

Publisher's Note: All claims expressed in this article are solely those of the authors and do not necessarily represent those of their affiliated organizations, or those of the publisher, the editors and the reviewers. Any product that may be evaluated in this article, or claim that may be made by its manufacturer, is not guaranteed or endorsed by the publisher.

Copyright © 2022 Noji and Ueno. This is an open-access article distributed under the terms of the Creative Commons Attribution License (CC BY). The use, distribution or reproduction in other forums is permitted, provided the original author(s) and the copyright owner(s) are credited and that the original publication in this journal is cited, in accordance with accepted academic practice. No use, distribution or reproduction is permitted which does not comply with these terms.

frontiers | Frontiers in Microbiology

TYPE Review
PUBLISHED 23 August 2022
DOI 10.3389/fmicb.2022.965620

Check for updates

OPEN ACCESS

EDITED BY
Tom Duncan,
Upstate Medical University,
United States

REVIEWED BY
Michael Boersch,
University Hospital Jena,
Germany
Masamitsu Futai,
Iwate Medical University,
Japan

*CORRESPONDENCE
Wayne D. Frasch
frasch@asu.edu

SPECIALTY SECTION
This article was submitted to Microbial Physiology and Metabolism, a section of the journal Frontiers in Microbiology

RECEIVED 09 June 2022
ACCEPTED 26 July 2022
PUBLISHED 23 August 2022

CITATION
Frasch WD, Bukhari ZA and Yanagisawa S (2022) F_1F_O ATP synthase molecular motor mechanisms. *Front. Microbiol.* 13:965620. doi: 10.3389/fmicb.2022.965620

COPYRIGHT
© Frasch, Bukhari and Yanagisawa. This is an open-access article distributed under the terms of the Creative Commons Attribution License (CC BY). The use, distribution or reproduction in other forums is permitted, provided the original author(s) and the copyright owner(s) are credited and that the original publication in this journal is cited, in accordance with accepted academic practice. No use, distribution or reproduction is permitted which does not comply with these terms.

F_1F_O ATP synthase molecular motor mechanisms

Wayne D. Frasch*, Zain A. Bukhari and Seiga Yanagisawa

School of Life Sciences, Arizona State University, Tempe, AZ, United States

The F-ATP synthase, consisting of F_1 and F_O motors connected by a central rotor and the stators, is the enzyme responsible for synthesizing the majority of ATP in all organisms. The F_1 $(\alpha\beta)_3$ ring stator contains three catalytic sites. Single-molecule F_1 rotation studies revealed that ATP hydrolysis at each catalytic site (0°) precedes a power-stroke that rotates subunit-γ 120° with angular velocities that vary with rotational position. Catalytic site conformations vary relative to subunit-γ position (β_E, empty; β_D, ADP bound; β_T, ATP-bound). During a power stroke, β_E binds ATP (0°–60°) and β_D releases ADP (60°–120°). Ärrhenius analysis of the power stroke revealed that elastic energy powers rotation *via* unwinding the γ-subunit coiled-coil. Energy from ATP binding at 34° closes β_E upon subunit-γ to drive rotation to 120° and forcing the subunit-γ to exchange its tether from β_E to β_D, which changes catalytic site conformations. In F_1F_O, the membrane-bound F_O complex contains a ring of c-subunits that is attached to subunit-γ. This c-ring rotates relative to the subunit-a stator in response to transmembrane proton flow driven by a pH gradient, which drives subunit-γ rotation in the opposite direction to force ATP synthesis in F_1. Single-molecule studies of F_1F_O embedded in lipid bilayer nanodisks showed that the c-ring transiently stopped F_1-ATPase-driven rotation every 36° (at each c-subunit in the c_{10}-ring of *E. coli* F_1F_O) and was able to rotate 11° in the direction of ATP synthesis. Protonation and deprotonation of the conserved carboxyl group on each c-subunit is facilitated by separate groups of subunit-a residues, which were determined to have different pKa's. Mutations of any of any residue from either group changed both pKa values, which changed the occurrence of the 11° rotation proportionately. This supports a Grotthuss mechanism for proton translocation and indicates that proton translocation occurs during the 11° steps. This is consistent with a mechanism in which each 36° of rotation the c-ring during ATP synthesis involves a proton translocation-dependent 11° rotation of the c-ring, followed by a 25° rotation driven by electrostatic interaction of the negatively charged unprotonated carboxyl group to the positively charged essential arginine in subunit-a.

KEYWORDS

F_1F_o ATP synthase, F_1 ATPase, single-molecule studies, rotary molecular motor, torque

The F-type, A-type, and V-type family of rotary molecular motors

The F_1F_O ATP synthase (Figure 1), which is found in all animals, plants, and eubacteria, provides the largest source of ATP that fuels most cellular processes (Spetzler et al., 2012; Kühlbrandt, 2019). The F_1F_o complexes use a non-equilibrium proton gradient (or Na^+ gradient in some organisms) to drive the ATP/ADP•Pi concentration ratio far from equilibrium. Most cellular processes use ATP as an energy source, which returns the concentration ratio toward equilibrium upon hydrolysis. Consistent with its vital role to life on earth, evolutionary variations of F_1F_O are now known that enable life forms to survive in a wide variety of environmental conditions. Complete structures of F_1F_O have now been determined from a variety of organisms. Although the identity of rotor and stator subunits in each motor is largely the same, variations in activity-altering loop regions are present in some subunits, and F_1F_O from some species contain additional unique subunits. For example, additional subunits in mammalian facilitate the formation of F_1F_O dimers. The F-type ATP synthases are also members of an extended family of rotary motors that include archaeal A-type (A_1A_O) ATP-synthases, prokaryotic A/V-type ATP synthases, as well as prokaryotic and eukaryotic vacuolar V-type ATPases (V_1V_O) that hydrolyze ATP to generate a transmembrane proton gradient. All share a common core of structural features that are embodied in F_1F_O from *E. coli* (EcF_1F_O).

The F_1F_O ATP synthases are comprised of two rotary molecular motors (the F_1 and F_O complexes) that are attached by their rotors and their stators (Figure 2). The F_O motor, which is embedded in bioenergetic membranes, uses a non-equilibrium transmembrane chemiosmotic proton gradient (or a Na^+ gradient) known as a proton-motive force (pmf), to power clockwise (CW) rotation of its ring of c-subunits relative to stator subunits a and b as viewed from the *E. coli* periplasm. These subunits contribute to the peripheral stalk bound to one side of the F_1 $(\alpha\beta)_3$-subunit ring, which collectively serve as the stators of both motors. The F_1 motor is a peripheral protein complex that in eukaryotes is exposed to the mitochondrial matrix or the chloroplast stroma. In bacteria such as *E. coli*, F_1 is exposed to the cytoplasm. Extending through the core of the $(\alpha\beta)_3$-ring, the F_1 subunit-γ forms a central stalk that, with subunit-ε, docks to the c-ring of F_O. The F_1 motor is capable of catalyzing ATP hydrolysis-driven CCW rotation that pumps protons across the membrane to create a proton gradient. However, a variety of regulatory mechanisms have evolved in different organisms to minimize hydrolysis, which can be a wasteful process.

The F_1 complex can be purified from the membrane and studied as an ATPase independently from F_O. Each αβ–heterodimer comprises a catalytic site where most of the catalytic residues reside on subunit-β. Three additional non-catalytic binding sites are present at the alternate αβ interfaces where residues on subunit-α contribute to nucleotide binding.

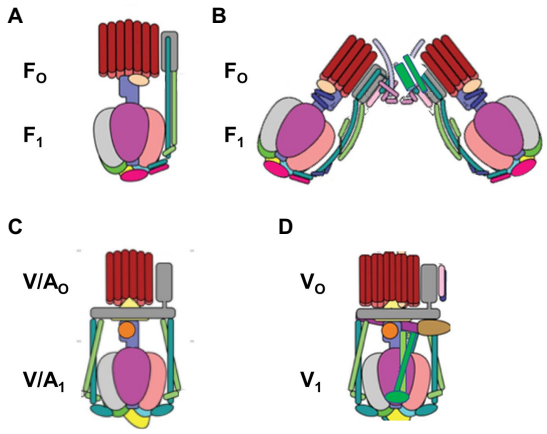


FIGURE 1
Structural variations among the family of rotary ATP synthases and ATPases that are coupled to transmembrane proton, or rarely sodium, gradients. **(A)** F-type ATP synthases in bacteria and plant chloroplasts (pdb-IDs 6OQR and 6FKF). **(B)** F-type ATP synthases in mitochondria (pdb-ID 6B8H). **(C)** V-type ATPases in some bacteria such as *E. hirae* and V/A-type ATP synthases in archaebacteria (pdb-ID 6R0Z) **(D)** V-type ATPases in vacuoles (pdb-ID 3J9V). V-type motors are incapable of synthesizing ATP and are used to pump protons to create a transmembrane pH gradient.

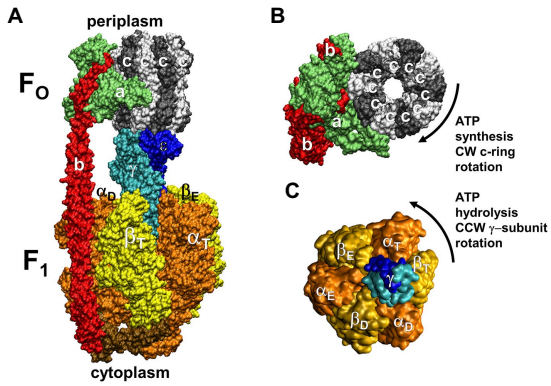


FIGURE 2
Subunit composition of EcF_1F_O (pdb-ID 6OQR) from the side **(A)**, of F_O from the periplasm **(B)**, and of solubilized F_1 **(C)** from the periplasm (pdb-ID 3OAA). Peripheral stalk, b-subunits; central stalk, γ– and ε–subunits; rotor subunits, γ–, ε–subunits and the c-ring; catalytic sites, β-subunits; proton-translocating half-channels, subunit-a. Each c-subunit carries one proton between subunit-a half-channels during rotation.

The binding-change/alternating site hypothesis

The alternating site (or binding-change) mechanism of ATP synthesis was proposed to explain the results of experiments that measured isotope exchange among the substrates (ADP and Pi) and products (ATP and H_2O) as a function of nucleotide concentration (Boyer and Kohlbrenner, 1981; O'Neal and

Boyer, 1984). This mechanism posited that the binding of ADP and Pi at one catalytic site induces a conformation change of all three catalytic sites to create an environment in which the equilibrium constant of tightly bound substrates and products at a second site approaches unity. It was estimated that interconversion of substrates and products at this latter site can occur up to 400 times prior to product release and suggested that energy from the pmf was required to induce a conformational change that enabled the release of product ATP from one site while ATP synthesis at another site could occur without significant energy input. It was proposed that this was possible because, at any moment, the three catalytic sites were in different conformations and that rotation of subunit-γ forces successive conformational changes of each site.

Evidence of coordinated, sequential catalytic site conformations changes

Early evidence supporting the binding-change hypothesis was obtained when VO^{2+} was used as a functional surrogate for Mg^{2+} in F_1 purified from *Spinacia oleracea* chloroplasts (*So*CF_1) (Frasch, 2000a,b). Nucleotides bind to the F_1 catalytic and non-catalytic sites as a complex with Mg^{2+} (Abrahams et al., 1994), which serves as a cofactor for ATP hydrolysis. The VO^{2+} studies revealed that the conformations of the three catalytic sites are staggered, and that they all change in a concerted, sequential manner through the three conformations (when ATP binds to the lowest affinity site). Methods had been established to replace the Mg^{2+}-nucleotide bound specifically to each of three sites in the $(\alpha\beta)_3$-ring of *So*CF_1 (Bruist and Hammes, 1981). Catalytic Site-3 can bind Mg-ATP or Mg-ADP with μM affinity, which can be depleted *via* gel filtration. Non-catalytic Site-2 binds only Mg-ATP that will not dissociate even after extensive catalytic turnover, but can be depleted as the result of partial unfolding *via* ammonium sulfate precipitation in the presence of EDTA. Site-1 contains tightly bound Mg-ADP that is not dissociated by extensive dialysis or gel filtration but can be exchanged for Mg-ADP or Mg-ATP in the medium after removal of subunit-ε. A third catalytic site was also known to contain very tightly bound Mg-ATP.

Although these studies preceded the first F_1 crystal structure, the distances between these nucleotide binding sites and between specifically labeled cysteines on *So*CF_1 had been determined by FRET measurements (Richter et al., 1985). Because *So*CF_1 ATPase activity is latent until a disulfide bond on subunit-γ is reduced, each catalytic site could be specifically filled with a VO^{2+}nucleotide, and then catalysis-dependent changes could be followed upon activation with dithiothreitol. Rates of VO^{2+}-dependent and Mg^{2+}-dependent chloroplast F_1F_O ATP synthesis were comparable, and the VO^{2+}-dependent F_1-ATPase activity was higher than that observed with either Mg^{2+}, Mn^{2+}, or Ca^{2+} (Houseman et al., 1994a).

Vanadyl is composed of the metal V(IV) double-bonded to oxygen that results in a molecule with a net charge of 2+ (Figure 3). Like Mg^{2+}, the ligands of VO^{2+} adopt an octahedral configuration with four equatorial ligands and one axial ligand that is *trans* to the oxo group. Vanadyl serves as a sensitive probe of the nucleotide-binding environment of the catalytic sites because each functional group (e.g., phosphate, carboxyl, hydroxyl) coordinated at the equatorial positions contributes independently and quantitatively to the magnitude of the values that define the Electron Paramagnetic Resonance (EPR) spectrum.

The binding of VO^{2+}-ATP to non-catalytic Site-2 gave rise to an EPR spectrum designated Species-A (Frasch et al., 1992; Houseman et al., 1994a, 1995a). Filling the low affinity catalytic Site-3 of latent *So*CF_1 with VO^{2+}-ADP or VO^{2+}-ATP resulted in an EPR spectrum containing two EPR species, designated B and C, where the former predominated. *So*CF_1-ATPase is susceptible to inhibition when the metal cofactor binds in the absence of nucleotide (Frasch and Sharp, 1985; Haddy et al., 1985, 1987, 1989). Species B was also observed when VO^{2+} was bound to latent *So*CF_1 in the absence of nucleotide indicating that this was the cofactor-inhibited conformation in the latent state. Activation of *So*CF_1 containing VO^{2+}-ADP bound to Site-3 resulted in the conversion of species-B to species-C, indicating that the metal ligands had changed (Houseman et al., 1994b, 1995a,b). When VO^{2+}-ATP was bound to Site-3, activation not only caused the elimination of Species B, but also formed species-D in addition to species-C, where species-D was the predominant conformation. Species-D represents the environment of VO^{2+}-ATP in the tight catalytic site conformation. Thus, consistent with the Binding-Change Mechanism, the binding of VO^{2+}-ATP to the low affinity site enabled a large fraction of the enzyme molecules in the sample to change its conformation to the high affinity conformation.

Exchanging VO^{2+}-ADP for the Mg-ADP bound to medium affinity catalytic Site-1 resulted in the formation of EPR species-E and -F, where the EPR values of the latter were close to that of VO^{2+} bound in the absence of nucleotide (Chen et al., 2000). Because the Mg-ADP from this site can only be exchanged after activation of F_1 by removal of subunit-ε, the environment that gives rise to species-E represents the third conformation of the catalytic site. These experiments demonstrated that, at any one time, the metal-nucleotide complex bound to the three catalytic sites are in different conformations, and that the binding of Mg-ATP to the empty site induces the conformations of all three sites to change to that of its successor. Consistent with the Binding-Change mechanism, the concerted conformational changes of EPR species in the three catalytic sites is C → D, D → E, E → F, where in F, nucleotide had dissociated (Frasch, 2000a,b). Based on their binding affinities and positions measured by FRET, these EPR species are analogous to ATPase-driven conformational changes now known as $\beta_E \rightarrow \beta_T$, $\beta_T \rightarrow \beta_D$, and $\beta_D \rightarrow \beta_E$.

Prior to the identification of Mg^{2+} ligands *via* protein crystallography, metal cofactor ligands at chloroplast F_1 catalytic sites were identified by effects on the EPR spectra of bound VO^{2+}-nucleotides from site-directed mutations of *Chlamydomonas reinhardtii* (Hu et al., 1995, 1996, 1999; Chen et al., 1999; Chen and Frasch, 2001; Crampton et al., 2001).

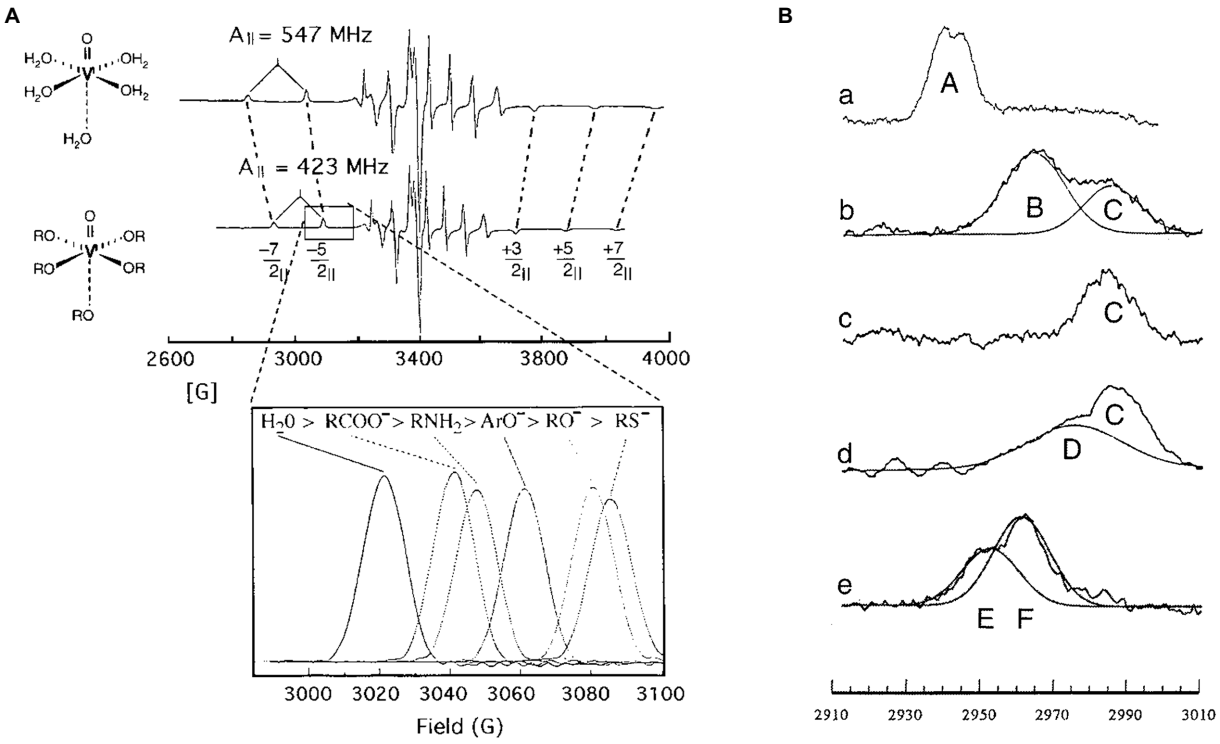


FIGURE 3
Sequential conformational changes of vanadyl-nucleotides bound to specific F_1-ATPase catalytic sites demonstrate the F_1 binding-change mechanism. **(A)** Equatorial ligands determine ^{51}V-hyperfine Parameters of VO^{2+}. EPR spectra of VO^{2+} with water (top) or hydroxyl groups (bottom) as equatorial ligands. The parallel transitions ($-7/2_{||}$, $-5/2_{||}$, $+3/2_{||}$, $+5/2_{||}$, and$+7/2_{||}$) that are not superimposed with perpendicular transitions are identified. Inset: dependence of the $-5/2_{||}$ transition on the type of equatorial ligands. **(B)** The $-5/2_{||}$ transition(s) of VO^{2+} bound to *So*F_1 as: (a) VO^{2+}–ATP at latent Site-2, (b) VO^{2+}–ADP bound to latent Site-3, (c) VO^{2+}–ADP bound to activated Site-3, (d) VO^{2+}–ATP bound to activated site 3; and (e) VO^{2+}–ATP bound to Site 1 using *So*F_1–ε. This figure was modified from Frasch (2000a,b) with permission of the publisher.

Although structures of the *Clamydomonas* chloroplast F_1 complex are not yet available, recent structures of *So*CF_1 are consistent with the composition of the amino acid sidechains and phosphate oxygens that comprise coordination environment of the metal cofactor obtained from VO^{2+} EPR spectroscopy.

Structural evidence correlating catalytic site occupancy and subunit-γ asymmetry

The 1BMF (PDB-IDs are used here throughout) structure of *Bos taurus* F_1 (*Bt*F_1) provided the first details of the asymmetric relationship of subunit-γ to the surrounding $(\alpha\beta)_3$-ring, which resulted in the three conformations of the catalytic sites (Abrahams et al., 1994). The α and β subunits, which have closely similar folds, alternate in the ring such that each αβ-heterodimer comprises a catalytic site (Figure 4). Each of these subunits contains a β-barrel "crown" domain, a helical "lever" domain, and a nucleotide-binding domain where, in the β-subunits, ATP is synthesized or hydrolyzed. The crown domains abut to stabilize the catalytic site conformations. The adenine rings of the nucleotides bind to the lever domain *via* π–π stacking with aromatic residues while the nucleotide phosphates bind to the catalytic domain *via* the P-loop such that the γ-phosphate of ATP faces the carboxyl residue that serves as the catalytic base.

Due to the asymmetric interactions of subunit-γ with the ring, the three catalytic sites adopt different conformations (Abrahams et al., 1994). One catalytic site contains bound Mg-ATP (β_T), the second site contains Mg-ADP (β_D), while the third site is empty (β_E). Each of the three non-catalytic sites contains bound Mg-ATP. These conformations were consistent with the VO^{2+}-nucleotide studies (Frasch, 2000a,b). The most obvious difference between the conformations of the three β-subunits is that, in the absence of Mg-nucleotide (β_E), the lever domain is open and extends away from the catalytic domain, whereas it is closed in the β_T and β_D conformations.

Subunit–γ consists of: (i) a globular "foot" domain that protrudes from the $(\alpha\beta)_3$-ring and docks with subunit-ε and the c-ring of F_O; (ii) an antiparallel coiled-coil domain that extends through the core of the $(\alpha\beta)_3$-ring; and (iii) a singular α–helix at the C-terminal end known as the tip. The $(\alpha\beta)_3$-ring contacts subunit-γ at three locations. *First*, the ends of the six α– and β–lever domains, which in *Ec*F_1 β–subunits contain the D_{372}IIA sequence, surround and contact the γ-coiled-coil proximal to the globular foot domain. The globular domain of subunit-γ, extends over the closed levers of β_T and β_D and away

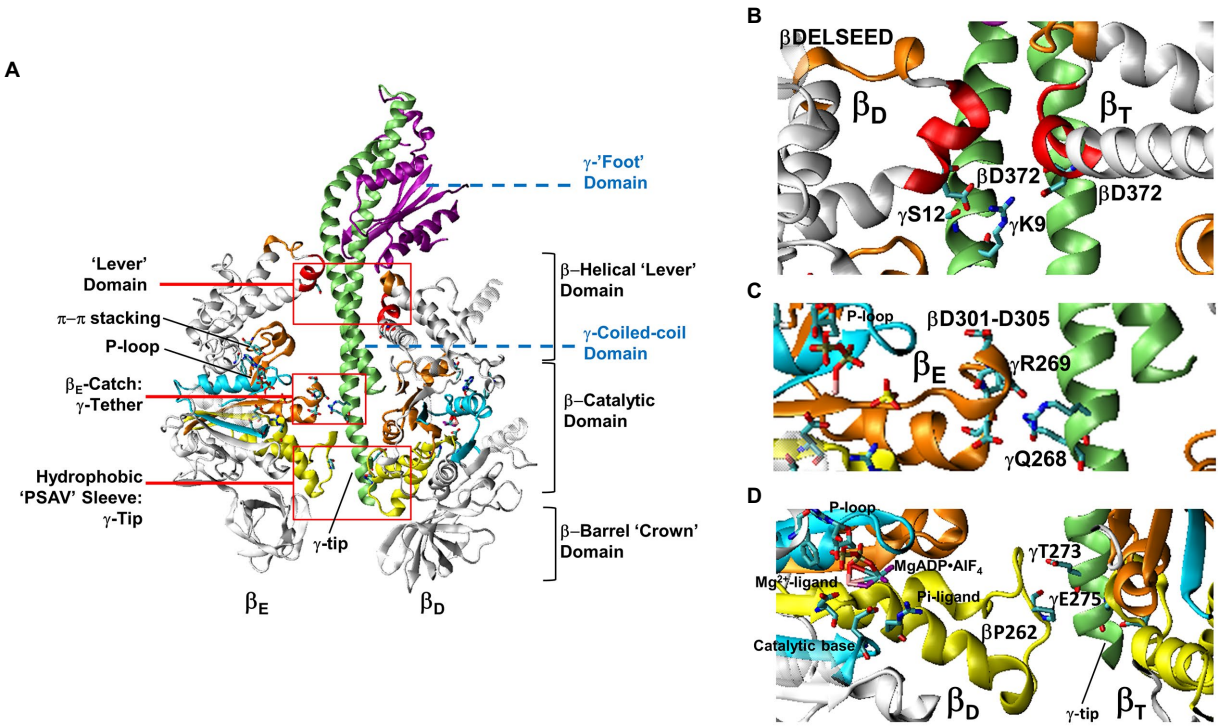


FIGURE 4
Domain composition of F_1 showing the relationship between Mg-nucleotide binding motifs and the stator-rotor interfaces. **(A)**. Cross-section of F_1 showing the relationship between the β_E and β_D-subunit conformations and subunit-γ. Red boxes are detailed in **(B–D)** showing subunit-γ and catalytic site interfaces. **(B)**. Interactions between the β_D and β_T-subunit Lever domains and subunit-γ. **(C)**. Electrostatic interactions between the β_E-Catch loop and γ-subunit tether residues. **(D)**. The short β_D and β_T-subunit helices that connect the Mg^{2+} and Pi ligands of bound MgADP•AlF_n transition state analogs with the hydrophobic sleeve surrounding the C-terminal tip of subunit-γ. Images show *Bt*F_1 structure pdb-ID 1H8E labeled with equivalent *Ec*F_1 residue numbers to show the location of bound MgADP•AlF_n.

from that of β_E. *Second*, at the end of the γ-coiled-coil distal from the foot, conserved γ–tether residues (*Ec*F_1-γR268 and γQ269) form strong electrostatic interactions with conserved β_E–"catch loop" residues (*Ec*F_1-βD301, βD302, βT304 and βD305). *Third*, the γC-terminal tip residues pass through a hydrophobic sleeve formed by loops of the six α– and β–catalytic domains.

Evidence demonstrating F_1 ATP hydrolysis-dependent subunit-γ Rotation

Although the conformations of the three catalytic sites were staggered, and changed conformations in a concerted, sequential manner, this may have occurred without subunit-γ rotation. Evidence supporting subunit-γ rotation with *Ec*F_1 was first obtained by mutation βD380C, a point where only one β-subunit could form a disulfide with subunit-γC87 (Duncan et al., 1995). Dissociation of the disulfide crosslinked subunits and reconstitution with ^{35}S-labeled β-subunits was followed by disulfide reduction. After ATP hydrolysis, and subsequent crosslinking, the radioactivity of the crosslinked product increased indicating that ATPase activity had randomized the position of the unlabeled β-subunit relative to subunit-γ, consistent with ATP hydrolysis-driven rotation of subunit-γ within the $(\alpha\beta)_3$-ring. Similar experiments demonstrated rotation with *Ec*F_1F_O (Zhou et al., 1996).

Rotational motion of subunit-γ by at least 200°, as the result of ATP hydrolysis, was also observed in *So*CF_1 using the technique of polarized absorption relaxation after photobleaching by modifying γC322 with eosin maleimide and immobilizing the *So*CF_1 on DEAD-A50 Sephadex (Sabbert et al., 1996). The rotational orientations of the subunit-γ bound eosin in the immobilized *So*CF_1 were evenly distributed prior to a 5 ns polarized light flash, which photobleached the subset of eosin aligned with the direction of polarization. Photobleaching changed the extent of light absorption by eosin (that was probed with continuous 520 nm polarized light) *vs.* time after the flash. This initially reported the fraction of eosin molecules that were photobleached by the laser pulse, but diminished *vs.* time due to *So*CF_1 ATPase-dependent subunit-γ rotation.

Single-molecule studies of *Geobacillus stearothermophilus* F_1 (*Gs*F_1), previously known as thermophilic *Bacillus* Sp. *PS3* F_1, demonstrated that ATP hydrolysis induced 360° rotation of subunit-γ (Noji et al., 1997). Here, F_1 was immobilized on a Ni-NTA-coated cover slip by six his-tags on the β–subunit N-terminus that positioned the subunit-γ globular domain distal from the cover slip. Biotinylation of γS107C this globular domain

enabled attachment of a 1 μm to 3 μm fluorescently labeled actin filament *via* streptavidin (Müller et al., 2002). As viewed from the foot of subunit-γ, ATPase-dependent counterclockwise (CCW) rotation was observed in discrete 120° steps with a CCD camera at 30 frames sec^{-1}. Single-molecule FRET experiments of EcF_1F_O in membrane vesicles confirmed CCW rotation during ATP hydrolysis, and demonstrated clockwise (CW) rotation during ATP synthesis (Diez et al., 2004).

When ATPase-dependent rotation was monitored using a 40 nm gold bead as a visible probe and rotation data of GsF_1 was collected at 8000 fps, 120° rotational stepping was observed at saturating ATP, which were separated by 2 ms dwells with a kinetic profile that indicated the presence of two successive 1 ms steps (Yasuda et al., 2001). This was designated the catalytic dwell because the duration of the first kinetic step of the dwell was extended by ATPγS (adenosine 5′-[γ-thio]triphosphate) or by mutation of catalytic base residue βE190D, which each slow ATP hydrolysis. The increase in duration of the second kinetic step with Pi indicated that Pi release ends the catalytic dwell and rotation resumes. At ATP concentrations that limited the rate of ATPase activity, a second ATP-binding dwell was observed 30°–40° after the catalytic dwell. The duration of this dwell varied inversely with ATP concentration.

Quantitation of tryptophan fluorescence quenching as a function of ATP binding to EcF_1 established that the affinity of the three catalytic sites differed by several orders of magnitude (Weber et al., 1993) consistent with the nucleotide affinities of $SoCF_1$ (Bruist and Hammes, 1981). Subsequent EcF_1 tryptophan fluorescence studies using ITP, which binds with lower affinity than ATP, showed that two catalytic sites always contain bound nucleotide, and that ATP binding to the third site induces catalysis (Weber and Senior, 1997, 2001). This 3-site mechanism was confirmed in single-molecule rotation studies using fluorescent Cy3-ATP, which showed that the ATP that bound to a catalytic site at 0° remained bound for 240°–320° during forced rotation of a magnetic bead probe by an external magnet (Adachi et al., 2007). However, these experiments were unable to resolve the precise rotational position of ADP release.

Use of gold nanorods to measure F_1 ATPase-driven rotational power strokes

The single-molecule rotation studies with actin filaments and gold beads provided important information regarding the rotational positions of the catalytic dwell and the ATP-binding dwell. However, as the result of limitations on the frame rate at which rotational data could be acquired, and precision of the rotational position during an ATPase-driven power stroke, information was scarce concerning the periods between the dwells when subunit-γ was in the process of rotating. As a result, the rotation appeared to occur as a discontinuous function between dwell positions.

To capture subunit-γ rotation between dwells, the intensity of polarized light scattered from a gold nanorod (AuNR) was measured by a single-photon counting avalanche photodiode (Spetzler et al., 2006; Hornung et al., 2011). Identification of AuNR attached to rotating F_1 in the presence of 1 mM MgATP were initially identified in a field of view of the microscope through a polarizing lens with a color camera at 50 fps (Figure 5). At this data acquisition rate, rotating AuNR blinked red and green as the long and short axes, respectively, became aligned with the polarizer. In contrast, the color did not change for any AuNR that was not rotating. Single-molecule F_1-ATPase-dependent AuNR rotation was then interrogated by aligning it with a 100 μm pinhole that eliminated all light except that which was scattered from the selected AuNR (Hornung et al., 2011). The scattered light was then passed through a polarizing filter mounted on a rotational stage, a high wavelength pass filter to eliminate all but red light that was focused onto a single-photon counting avalanche photodiode (Perkin-Elmer SPCM-AQR-15). The detector had a dark count of ~50 photons/s with a temporal resolution of 50 ns.

The intensity of light scattered from a AuNR changes in a sinusoidal manner as a function of the rotary position of the AuNR relative to the plane of polarization with minimal and maximal intensities separated by 90° (Spetzler et al., 2006). The distribution of scattered red light intensities from a single AuNR immobilized to the surface of a microscope slide as a function of the rotational position of the polarizing filter is shown in Figures 6A,B (Ishmukhametov et al., 2010). At each rotary position of the polarizer, the scattered light intensity is sampled 3,520 times under conditions comparable to that used to measure rotation of single F_1 ATPase molecular motors. This sample number was used because it corresponds to the average number of F_1-ATPase power stroke events during a 5 s or 50 s data acquisition period for a given F_1 molecule or F_1F_O molecule rotation measurement, respectively, when data is collected at 100 kHz (equivalent to 100,000 fps). The scattered light intensity from the AuNR varied between maximum and minimum values of 2,500 and 500 photons. The difference between these values comprises a dynamic range of ~2000 photons per sample, which determines the sensitivity of the measurement. This was the minimum dynamic range used to measure rotation, while the average range was ~3,000 per sample. Thus, calculation of the error from these data represents an upper limit in a rotation data set acquired from rotation of a single F_1 molecule. The distribution of light intensities scattered from the AuNR was smaller at polarization angles in which the intensity was at a minimum than the distribution at maximum intensities. The standard error in the measurements at each rotary position of the polarizer varied between 0.02° and 0.12° degrees as calculated from the minimum and maximum intensity values (Figure 6C).

Polarizer Rotation Measurements show 120° step rotations at saturating Mg-ATP. In a polarizer rotation measurement (PRM), the variation of intensity of red light scattered from a nanorod attached to a single F_1 molecule in the presence of saturating MgATP was observed as a function of the stepped rotation of the polarizer by 10°, in 5 s intervals, at a data sampling rate of 1 kHz (Spetzler et al., 2006). This low data acquisition speed reports the positions of the three catalytic dwells because subunit-γ rotation

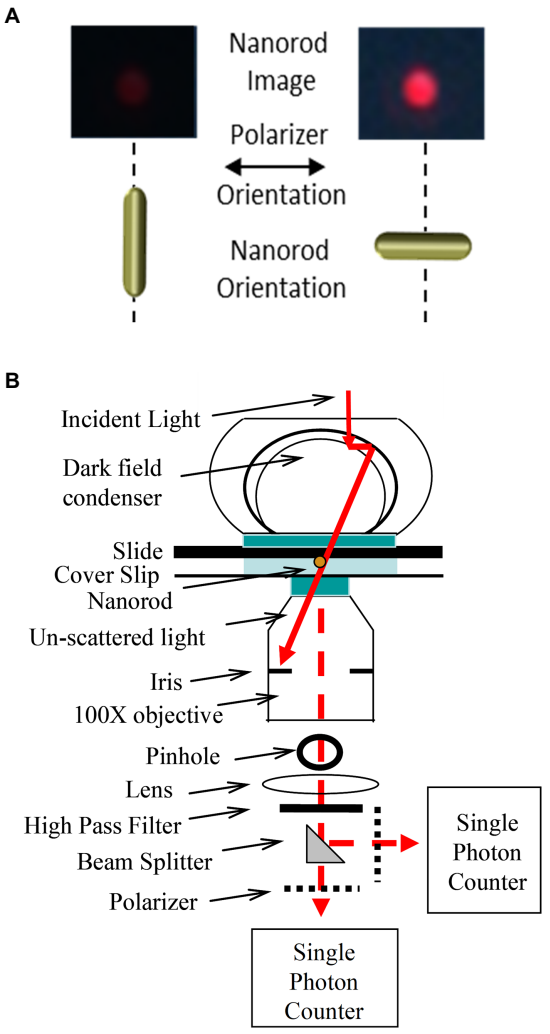


FIGURE 5
Use of scattered red light intensity from a 75 × 35nm gold nanorod (AuNR) to measure rotation at the nanoscale. **(A)**. Color image of AuNR-scattered light viewed by dark-field microscopy through a high pass filter to eliminate all but red light and a polarizer filter when the long axis of the AuNR is perpendicular and parallel to the plane of polarization. **(B)**. Dark-field microscope design to record changes of scattered red light intensity vs. time from a single AuNR capable of determining the direction of rotation using a beam splitter to divert half of the photons through a second polarizer set at a rotational position that will reach a maximum light intensity before the first if the AuNR is rotating counterclockwise (CCW). This figure has been modified from that in Hornung et al. (2011).

during the power stroke typically occurs too fast (μsec time scale) for the detector to capture most of the intermediate rotational AuNR positions (Figures 6D,E). Each dwell contributes a peak in the distribution of the histogram at a given set angle of the polarizer. When viewed as a series of histograms of light intensities at each of 36 polarizer angles covering 360°, three offset sinusoidal curves in scattered light intensities were observed from a nanorod attached to the actively rotating drive shaft of a single F_1-ATPase. Because the dependence of light intensity versus AuNR orientation relative to the axis of the polarizer is sinusoidal, the three offset sinusoidal curves in the histogram indicates rotation occurs in 120° power strokes separated by catalytic dwells.

For a given F_1, the spacing between the three sinusoidal curves in a PRM is sensitive to the tilt of the rotation axis of subunit-γ from orthonormal to the microscope cover slip. Given that the data acquisition speed is set at 1 kHz, the variation in intensity of catalytic dwells *vs.* the rotary position of the polarizer indicates that catalytic dwells are shorter at some positions. When light intensity is observed in the space between the three sinusoidal curves, the angular velocity of the power stroke is slow enough to be captured by the 1 kHz data acquisition speed. To date, the three off-set sinusoidal intensity curves observed by PRMs, which are indicative of three successive 120° power strokes, have been observed with *Ec*F_1 (Spetzler et al., 2006; Sielaff et al., 2016), *Gs*F_1 (Sielaff et al., 2016), and *Mycobacterium smegmatis* F_1 (*Ms*F_1) (Ragunathan et al., 2017), as well as with the *Methanocarcina mazei Gö1* A_1-ATPase (*Mm*A_1) (Sielaff et al., 2016).

Rotation temporarily stopped by ε-subunit or Mg-ADP inhibition. Rotation catalyzed by *Ec*F_1 is subject to intermittent inhibition by the C-terminal helical domain of subunit-ε (εCTH) or by Mg-ADP, each of which can last for seconds (Sekiya et al., 2010; Shah et al., 2013). These inhibitions are independent processes, where the former results from the extension of the εCTH along the coiled-coil during the catalytic dwell that competes with the possible transition into the Mg-ADP inhibited state (Shah et al., 2013). In all single-molecule AuNR rotation assays, substrate was added as a 2:1 ratio of ATP:Mg^{2+}, which is known to minimize the occurrence of Mg-ADP inhibition (Hyndman et al., 1994; Kato et al., 1995). About 25 and 50% of the molecules in a given field of view were observed to rotate in the presence of MgATP and MgGTP, respectively (York et al., 2007). This difference is explained by the fact that hydrolysis of GTP is less sensitive to this type of inhibition (Hyndman et al., 1994). In comparison, ~5% of the F_1-ATPase molecules are observed to rotate using a gold bead assay, which is likely because observation of rotation requires precession of the bead around the axis of rotation (Yasuda et al., 1998).

During a PRM assay, inhibition by subunit-ε or Mg-ADP is evident by the temporary conversion of the three off-set sinusoidal intensity curves to a single intensity curve (Figure 6F) that lasts until inhibition is relieved and rotation resumes. Inhibition by Mg-ADP occurs at catalytic dwell positions (Hirono-Hara et al., 2001; Sekiya et al., 2010; Bilyard et al., 2013), and pauses can last ~30 s in *Gs*F_1 (Hirono-Hara et al., 2001). Using the AuNR assay, the average catalytic dwell duration with saturating 1 mM MgATP was 8.3 ms for an *Ec*F_1 preparation with a k_{cat} of 130 s^{-1}, which was measured by an ensemble ATPase coupled assay (Spetzler et al., 2006). This k_{cat} value corresponds to 7.7 ms per ATP hydrolyzed, which was comparable to the average dwell duration for all dwells including the long dwells that result from ε-subunit or Mg-ADP inhibition. The duration of *Ec*F_1 catalytic dwells averaged ~2 ms during periods that where extended inhibition dwells were absent

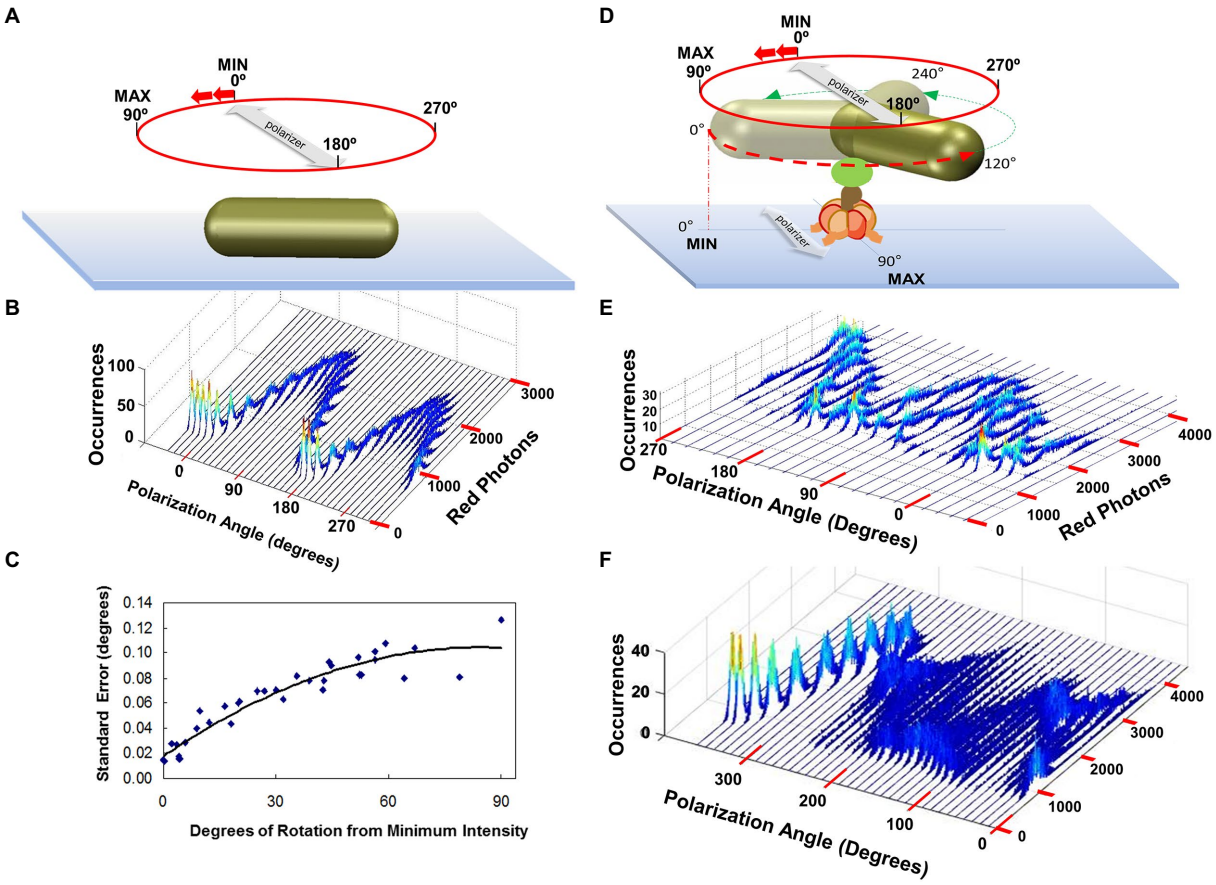


FIGURE 6
Polarizer Rotation Measurements (PRM) to determine rotational position measurement error and to show F_1-ATPase-dependent 120° step rotations. **(A)** PRM measurement of a nonrotating AuNR attached directly to the cover slip. Red photons scattered from the AuNR were measured in 5s intervals at a data sampling rate of 1kHz (1,000 fps) at each 10° stepped rotational position of the polarizer. **(B)** PRM-dependent distribution of photons scattered from the non-rotating AuNR of **A** vs. rotary position of the polarizer. **(C)** Standard error of the AuNR rotary position vs. degrees of rotation from the minimum intensity calculated from **B**. This error is equivalent to that obtained from a data set of 3,250 power strokes. **(D)** PRM measurement of a AuNR attached to an actively rotating subunit-γ of the F_1-ATPase in the presence of saturating ATP concentrations. **(E)** PRM-dependent distribution of photons scattered from the non-rotating AuNR of **A** vs. rotary position of the polarizer. **(F)** PRM when the AuNR is attached to actively rotating F_1 subunit-γ, which stops rotating at polarizer angle 260°, likely due to subunit-ε inhibition. This figure was reconfigured from Spetzler et al. (2006), Ishmukhametov et al. (2010), Sielaff et al. (2016).

(Nakanishi-Matsui et al., 2006), which are comparable to those observed with *Gs*F_1 (Shimabukuro et al., 2003).

Resolution of F_1 rotary power stroke positions between catalytic dwells. The charge-coupled device used to quantify the number of photons scattered from a single AuNR has a 50 nsec time resolution. Consequently, to obtain light intensity measurements at 1 kHz, the number of photons measured were binned in successive 1 ms intervals. Due to the brightness of the AuNR with the light source used, it was possible to resolve F_1ATPase-driven rotational position *vs.* time when scattered light intensity was sampled at rates as high as 400 kHz, corresponding to 2.5 μs per data point (Spetzler et al., 2006).

These measurements were the first to reveal details of the position of the F_1 axle as it rotated between catalytic dwells (Martin et al., 2014). To accomplish this, the changes in intensity of AuNR scattered light from a rotating F_1 molecule measured by the avalanche photodiode is examined for the minimum and maximum scattered light intensity difference *vs.* time (Hornung et al., 2011). The polarizer is then rotated to maximize this difference, which aligns the polarizer with the short axis of the AuNR, such that the light intensity is at a minimum during one of the three catalytic dwells. As a result, the light intensity increases from a minimum during the subsequent power stroke, which passes through a maximum intensity upon rotation by 90°, then decreases in intensity until the next catalytic dwell begins at 120° (Figure 7A). A power stroke is defined here by the rotation of subunit-γ between catalytic dwells. During the second power stroke, the intensity passes through the minimum but not through the maximum, and during the third, the intensity first passes through the maximum upon rotating 30° and returns to the minimum intensity as a 360° rotation is completed.

After collecting a data set for 5 s from each F_1 molecule at 200 kHz, rotation events that began at a minimum and passed through a maximum were collected for further analysis

(Spetzler et al., 2006). Data sets were analyzed that each comprised ~3000 of these 120 degree power strokes, which undergo F_1 ATPase-dependent rotation in the absence of subunit-epsilon and/or Mg-ADP inhibition.

EcF_1-ATPase-dependent rotation is CCW. To determine whether *Ec*F_1 rotated exclusively CCW when actively hydrolyzing ATP, a beam splitter was placed in the path of scattered the red light scattered from a rotating AuNR and each beam was directed through a separate polarizer and photon counter for quantification (Spetzler et al., 2009). The polarizers were set a different rotary positions such that the direction of AuNR rotation was determined by the photon counter that measured the maximum intensity of scattered light first (Figure 7B). All *Ec*F_1 molecules examined rotated almost exclusively CCW for the length of the measurements, during which subunit-γ completed ~200 revolutions equivalent to a total of 600 consecutive power strokes (Figure 7C). Similar CCW rotation has been observed with *Gs*F_1 during ATP hydrolysis (Noji et al., 1997).

Average torque generated by EcF_1 during a power stroke. Torque is a measure of the ability of a motor to rotate against an opposing load. To measure the average torque during a power stroke, the load on *Ec*F_1 was increased by varying the viscous drag on the AuNR attached to subunit-γ (Hornung et al., 2008). The effects of drag *vs.* the time required to rotate between catalytic dwells, and the duration of these dwells in the presence of saturating (1 mM) Mg-ATP was then determined (Spetzler et al., 2009). To vary viscous drag, rotation was compared when subunit-γ was attached to a AuNR with dimensions of 73 × 35 nm, 87 × 36 nm, 90 × 46 nm, and 91 × 45 nm. Although the latter two were of similar dimensions, the former had a rectangular profile, while the latter had rounded ends. The effects of load on *Ec*F_1 rotation were also measured when viscous drag was varied by the addition of polyethylene glycol 400 (PEG-400). The viscosity of the buffers containing PEG-400 (vol/vol) were measured directly, and the data were used to calculate the shear stress *vs.* shear rate. The linear dependence between these parameters indicated that the assay buffer containing PEG-400 behaves as a Newtonian fluid. As a result, the PEG-400 molecules are too small to be pulled along by the rotating AuNR, and do not make secondary nonlinear contributions to the drag.

When any of the three smallest AuNR were bound to subunit-γ, the average time for the power stroke to rotate 90° from the end of the catalytic dwells (transition time) was constant (~275 μs) until the load on the motor reached 4 aN nm ms (Spetzler et al., 2009). This indicated that the velocity of the rotation between catalytic dwells was not limited by viscous drag on the AuNR under these conditions, but instead by the intrinsic rate-limiting properties of the *Ec*F_1 motor. At higher viscosities, the transition time increased proportional to the drag (Figure 8). However, the duration of the catalytic dwell and the ensemble measurement the turnover time (k_{cat}) of ATPase-activity increased proportionately with drag on the motor at loads <4 aN nm ms. At higher loads the proportional increase in catalytic dwell time changed concurrent with the dependence of average transition time *vs.* drag. This strongly suggests that the rate of ATP hydrolysis and/or Pi release, which occur during the catalytic dwell (Spetzler et al., 2009), involves motion of subunit-γ that is dampened by the imposed load.

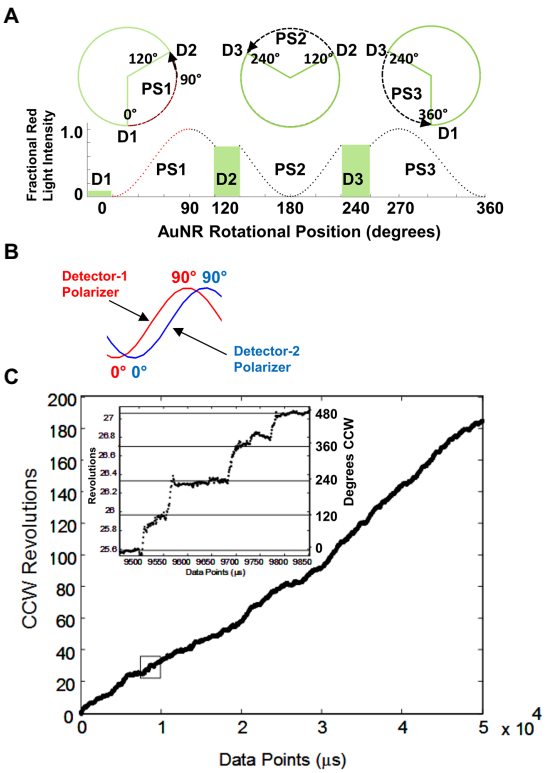


FIGURE 7
(A) Changes in AuNR scattered red light intensity during one complete revolution involving three consecutive power strokes (PS) and three consecutive catalytic dwells (D) separated by exactly 120° when, prior to data collection, the polarizer is rotated such that scattered light intensity is at a minimum during catalytic dwell-1 (D1). **(B)** Rotational off-set of polarizer positions when two detectors are used to observe the direction of rotation. **(C)** Counterclockwise rotation observed by *Ec*F_1-ATPase-dependent rotation calculated from two detectors with off-set polarizer positions with data acquired at 10kHz in the presence of 1mM $MgCl_2$ and 2mM ATP. (Inset) Detail of the rotational stepping of the boxed region. Horizontal lines show the 120° dwell positions. This figure was reconfigured from Spetzler et al. (2009).

Torque was calculated using the 91 × 45 nm nanorods that imposed significant drag on the rotation in the absence of PEG-400 (Hornung et al., 2008). The drag coefficient was determined directly by measuring the amount of angular change of individual AuNR that were suspended near, but not attached to the surface of a microscope slide in the absence of *Ec*F_1, which enabled calculation of the diffusion coefficient. Using Einstein's relation, the diffusion coefficient was used to determine the drag coefficient.

The average torque generated by *Ec*F_1 varied as a function of viscous load on the AuNR, which averaged 63 ± 8 pN nm (Hornung et al., 2008). A statistically equivalent torque value of 56 ± 6 pN nm was obtained with *Ec*F_1 (Junge et al., 2009), and of

50 ± 6 pN nm with *Ec*F_1F_O (Pänke et al., 2001), using the extent of deformation of an actin filament attached to the rotor. Torque values of ~80 pN nm and 40–50 pN nm for *Gs*F_1 were estimated from actin filament (Yasuda et al., 1998) and duplex bead rotation rates (Usukura et al., 2012).

Rotor-Stator contact points contribute to F_1-ATPase activity and rotation. The mechanism in which the energy generated by the consumption of ATP is used to power subunit-γ rotation, and conversely, the means that by which rotation powered by F_O acts upon the catalytic sites in the $(\alpha\beta)_3$-ring to synthesize ATP continues to be the focus of intense investigation. The interactions between the $(\alpha\beta)_3$-ring and subunit-γ responsible for F_1-ATPase-powered rotation have alternatively emphasized electrostatic interactions (Mukherjee and Warshel, 2011, 2015), steric interactions (Koga and Takada, 2006; Pu and Karplus, 2008), or an elastic spring mechanism between the stator and rotor (Czub and Grubmüller, 2011). The results described here indicate that all these interactions contribute to the rotation mechanism.

Mutations that alter interactions of charged and polar groups between subunit-γ and the $(\alpha\beta)_3$-ring were examined to assess their contributions to catalytic activity and ATPase-dependent rotation (Greene and Frasch, 2003; Boltz and Frasch, 2005, 2006; Lowry and Frasch, 2005). These included the $(\alpha\beta)_3$-hydrophobic sleeve that surrounds the tip comprised of the C-terminal helical extension beyond the coiled-coil, the β_E-catch loop electrostatic interactions with the γ-tether residues on the C-terminal helix of the coiled-coil distal from the foot, and the $(\alpha\beta)_3$-lever domains that surround the γ-subunit coil-coil proximal to the globular foot domain.

The hydrophobic sleeve. The subunit-γ C-terminal tip consists of a single α–helix that extends 17–19 amino acids (depending on species) through the $(\alpha\beta)_3$-hydrophobic sleeve. The β-subunit loops of the sleeve contain the conserved PSAV motif, where βP262 in *Ec*F_1 constrains the mobility of the loop (Figure 4D). The β_D and β_T loops contact the final 12 and 13 residues of the tip, respectively, while the β_E-loop contacts subunit-γ 9 and 15 residues from the C-terminus. Residues γE275 and γT273 are the only polar groups in the γC-terminal tip that pass through the hydrophobic sleeve.

Single-site *Ec*F_1 mutations of βP262 and βV265 in the PSAV loops, and mutations of γE275 and γT273 in the subunit-γ tip were made to determine their impact on enzymatic function (Boltz and Frasch, 2005). The γT273D and γE275D mutations increased purified *Ec*F_1 ATPase activity >1.5-fold, increased ATPase-dependent proton gradient formation by *Ec*F_1F_O in inverted membranes measured by ACMA quenching, and increased ATP synthesis measured by growth on succinate. Conversely, mutants βP262G, γT273A, and γT273V decreased *Ec*F_1 ATPase activity by ~2 orders of magnitude, abolished ATPase-dependent proton gradient formation by *Ec*F_1F_O in inverted membranes, and decreased ATP synthase measured by growth on succinate.

The ATPase activity of *Ec*F_1 is inactivated by the binding of the transition state analog MgADP•AlF_n that forms over a period of ~240 min upon addition of Mg-ADP, $AlCl_3$, and NaF (Boltz and Frasch, 2005). Mutations γT273A, γT273V, and βP262G decreased the rate of *Ec*F_1 ATPase inactivation due to the binding of MgADP•AlF_n, where the latter mutation increased the rate by 3 orders of magnitude. Conversely, mutations γT273D and γE275D increased the rate of inactivation by MgADP•AlF_n consistent with the increase in catalytic activity of the enzyme.

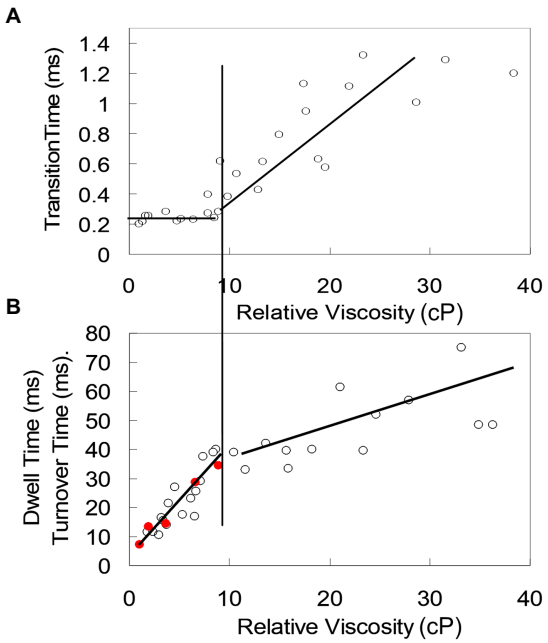


FIGURE 8
Interdependence of catalytic dwell duration, ATPase activity, and average transition time (time required for the power stroke to rotate 90°) as a function of load on the *Ec*F_1 motor. **(A)** Transition time vs. viscosity. **(B)** Catalytic dwell duration (○) and ensemble ATPase activity measured as k_{cat} (●) vs. viscosity. Load on the motor was varied by increasing concentration of PEG-400, which increased the viscous drag on the AuNR attached to subunit-γ. At loads <4 aN nm ms (vertical line between **A** and **B**), transition time is constant (not load-limited) while catalytic dwell time and k_{cat} show the same proportional increase with drag. At loads >4 aN nm, both transition time and catalytic dwell time increase proportionately with load. These data were reconfigured from those in Spetzler et al. (2009).

These studies (Boltz and Frasch, 2005) were the first to show that specific interactions between subunits-γ and -β are linked to ATP hydrolysis and ATP synthesis. Catalytic residues βD242 and βR246 in *Ec*F_1, which serve as a Mg^{2+} ligand and bind Pi upon hydrolysis of ATP, respectively, are connected to the PSAV loop *via* a short α-helix. In the "transition state" *Bt*F_1 structure 1H8E (Menz et al., 2001), γE275 and γT273 form hydrogen bonds to the backbone of βV265 of catalytic sites β_T and β_D, respectively, that both contain the bound transition state analog MgADP•AlF_4^-. Consequently, the mutations examined were found to either increase or decrease the ability to form the transition state that results in ATP hydrolysis.

The Catch Loop. In the β_E conformation, a strong electrostatic interaction exists between carboxyl residues in the "catch loop"

with residues of the γ-subunit tether at the end of coiled-coil that are separated from the tip residues that pass through the hydrophobic sleeve by several amino acids (Figure 4C). This electrostatic interaction exists in every F_1 structure solved to date. Consequently, this interaction identifies the β_E conformation of the motor, despite differences in its nucleotide occupancy or the open or closed position of the β-lever domain.

Selective mutations of individual *Ec*F_1 residues that diminished or eliminated electrostatic interactions between the β_E-conformation catch loop (residues 301–305) and the subunit-γ tether (γR268, γQ269) were also found to dramatically decrease ATPase activity of purified F_1 (Greene and Frasch, 2003). Of these, βD302V, βD305V, βD305S, abolished F_1-ATPase activity. The ATPase activity of the conservative βD305E mutation, which retained a carboxyl group, as well as βD302T, and γQ269L decreased by ~2 orders of magnitude, while that of γR268L decreased 10-fold from that of WT.

In the β_T and β_D conformations, catch loop residues βD302 and βD305 form electrostatic interactions with residues αR283, from the respective α_T and α_D-subunits, while catch loop βD301 residues form electrostatic interactions with β_TR323 and β_DR323. Mutation αR282E eliminated ATPase activity while αR282Q and βR323K decreased it by ~10-fold (Boltz and Frasch, 2006).

Mutations that eliminated ATP synthase activity as measured by growth on succinate included γQ269L, βD301E, βD305V, βD305S, and βD305E, while mutants γR268L, βD301V, βD301T, βD301N, βD302V, and βD302T decreased the growth rate several fold (Greene and Frasch, 2003; Boltz and Frasch, 2006). These results clearly showed that these electrostatic interactions are extremely important for ATPase activity, and perhaps are essential for *Ec*F_1F_O to catalyze ATP synthesis. Based on these results, these residues were proposed to act as an escapement mechanism that insures tight coupling of substrate binding to the concerted conformational changes during the alternating site mechanism (Greene and Frasch, 2003), which essential for all motors and clocks. During F_1 ATPase-driven rotation, ATP binding would trigger release of the β_E-catch allowing CCW rotation of subunit-γ, which induces the subunit-γ tether to connect with the β_T catch such that $\beta_E \rightarrow \beta_T$, $\beta_T \rightarrow \beta_D$, and $\beta_D \rightarrow \beta_E$.

The β-Levers. The $(\alpha\beta)_3$-lever domains that surround the γ-subunit coil-coil are comprised of a helix-turn-helix (Figure 4B). The *Ec*F_1 βD_{372}IIA sequence motif at the C-end of the first helix of each β-lever contact γ-coiled-coil residues proximal to the γ-globular foot domain. This motif is followed by the DELSEED sequence in the β-lever turn, which does not contact subunit-γ, and has been shown not to contribute significantly to the rotational or catalytic mechanism (Hara et al., 2000).

The effects of mutations of *Ec*F_1 residues of β-lever residue βD372V, and γ–subunit contacts γK9I, γS12A and double mutation γK9I/S12A were examined for their impact on enzymatic function (Lowry and Frasch, 2005). Mutants βD372V, γS12A and γK9I/S12A reduced ATP synthase activity by 2 orders of magnitude as measured by growth on succinate. Mutations βD372V, γK9I, γS12A and γK9I/S12A all abolished the ability of F_1F_O to catalyze ATPase-dependent proton pumping. In contrast, γK9I and γK9I/S12A decreased ATPase activity 2-fold, while those of γS12A and βD372V was essentially unchanged from that of WT. This shows that, while these mutations do not decrease ATPase activity in the absence of a load, the presence of a pmf (which applies an opposing load) decreases the ATPase rate significantly. In other words, these mutations decrease the ATPase-dependent torque significantly.

The results that demonstrate that the interactions of subunit-γ with both the hydrophobic bearing (Boltz and Frasch, 2005) and the catch loop (Greene and Frasch, 2003; Boltz and Frasch, 2006) contribute significantly to the F_1-ATPase catalytic mechanism have been confirmed by studies of the effects of subunit-γ truncation mutants on rotation and catalysis (Furuike et al., 2008; Hossain et al., 2008). In these single-molecule studies, truncation of the γC-terminus by as few as 14 residues decreased ATPase activity significantly. Deletion of 17 residues, which made the subunit-γ tip too short to extend through the hydrophobic sleeve, decreased ATPase activity by an order of magnitude. Elimination of the γ-subunit tether by a 21-residue truncation decreased ATPase activity by 2 orders of magnitude and resulted in a 2-fold decrease in torque.

The number of molecules with truncations of ≥35 residues of the γC-terminus with a truncation of the γN-terminus to match the length of the coiled-coil had ATPase activities almost 3 orders of magnitude lower than WT (Furuike et al., 2008; Hossain et al., 2008). The F_1 molecules that were observed to rotate became exceedingly rare (fewer than 1 per field of view) with movements that primarily stumbled forward and backward rather than rotating. It is noteworthy that an F_1 molecule can occasionally appear to be catalyzing ATPase-dependent rotation, but the movement is the result of a loose attachment of the His-tags to the surface of the cover slip.

It is likely that the inability of molecules to rotate that contain truncations of ≥35 residues result from deletions of the section of the coiled-coil that interact with the β-lever. The β_T-DIIA lever motif contacts γC-helix residues γ252 and γ256, and β_D-DIIA contacts γN-helix residues γK9 and γS12 when *Ec*F_1 is not in the ε-subunit inhibited state. A 35-residue truncation deletes both γ252 and γ256. The position that the β_E-DIIA lever contacts the γ-coiled-coil varies among F_1 structures. Example subunit-γ contacts with the β_E-DIIA using *Ec*F_1 numbering include: γN-helix-γ15 and γ17, "transition state" structure 1H8E (Menz et al., 2001); γN-helix-γ25, "ground state" as well as "hydrolysis dwell" structures 2JDI and 7L1R (Bowler et al., 2007; Sobti et al., 2021); γC-helix-γ243 and γ244, structure 4ASU (Rees et al., 2012); γC-helix-γ227-γ228, "ε-inhibited" structure 3OAA (Cingolani and Duncan, 2011); and γC-helix-γ231, "ADP-binding" structure 7L1Q (Sobti et al., 2021).

In addition to showing that both the hydrophobic sleeve and the catch loop interactions were important for catalysis and rotation, these results also confirmed that the catch loop interaction is responsible for one half of the torque generated by F_1. This suggests that the other half is derived from the β-lever

interactions with subunit-γ. The results that demonstrate that the interactions between subunit-γ and the β-lever DIIA motif (Lowry and Frasch, 2005) contribute significantly to the *Ec*F_1-ATPase catalytic mechanism have been confirmed by studies of the effects of mutants *Gs*F_1 that truncated portions of the β-lever that included the DI of the DIIA motif on rotation and catalysis (Usukura et al., 2012). These truncations decreased the rate of ATP synthesis by ~10-fold and significantly decreased the ability of F_1F_O to catalyze ATPase-dependent proton pumping in inverted membranes. The truncations also decreased torque generated by the F_1-ATPase by 2-fold. The ATPase activity of the *Gs*F_1 motors in the absence of viscous load was not very different from WT. However, in the presence of a load such as rotating large beads and/or pumping protons to create a pmf, the decrease in torque was apparent.

These results closely replicate the effects of *Ec*F_1 β-lever βD372V and the complimentary mutations of one of its contact sites on subunit-γ (Lowry and Frasch, 2005). Taken together with the results of mutations that demonstrate that contribution of the interactions between the catch loop and the subunit-γ tether, clearly half of the torque is generated by the β-lever interaction and half of the torque is generated by the catch loop interaction, while the hydrophobic sleeve interaction is contributes significantly to the rate of transition state formation for ATP hydrolysis.

Although their data show that the tip and the coiled-coil of subunit-γ make significant contributions to the production of torque, Hossain et al., 2006, 2008 concluded that neither helix in the coiled-coil region of the axle of F_1-ATPase plays a significant role in torque production. Other more radical chimera of F_1 have been observed to rotate in some manner (Mnatsakanyan et al., 2009; Kohori et al., 2011; Chiwata et al., 2014). However, more work is required to clarify what insight these chimeric complexes can provide to the mechanism of the F_1 ATPase and intact F_1F_O.

F_1 and A_1 ATPase Power Stroke Angular Velocities vs. Rotational Position. Using AuNR rotation data collected at 200 kHz, the angular velocity of *Ec*F_1 was measured as a function of rotational position during the power stroke in the presence of 1 mM Mg-ATP (Martin et al., 2014). After collecting 5 s of data from each molecule, the power strokes that started at a minimum scattered light intensity at the end of the catalytic dwell (0°) and passed through a maximum intensity upon rotating 90° were collected, and the rotational position *vs.* time for each power stroke was determined for the entire 120° of rotation. This was accomplished using arcsine square root functions to convert light intensity to rotational position (Figure 9A).

Maximum and minimum scattered light intensities were defined as those from the highest and lowest 5th percentile, respectively (Spetzler et al., 2006; Hornung et al., 2011). This aligned the power strokes and minimized phase shift when averaging the data from many power strokes and set the same minimum and maximum intensity values for any one molecule. Average angular velocities (ω) of all power strokes acquired at each rotary position were binned and averaged for every 3° of rotation.

The resulting profile of angular velocity *vs.* degrees of rotation during the F_1-ATPase power stroke showed that the angular velocity is not constant and undergoes a series of accelerations and decelerations during continuous counterclockwise rotation between catalytic dwells at saturating Mg-ATP (Martin et al., 2014). Due to the low drag imposed on the motor by a 75 × 35 nm AuNR, the velocity changes during the power stroke result from limitations in the rotation rate imposed by the internal mechanism of the motor. The power stroke of *Ec*F_1 subsequent to the catalytic dwell was divided into two distinct phases. Phase-1 (designated as 0° to 60°) is when ATP binding occurs. Phase-2 (designated as 60° to 120°) is when ADP release occurs.

The small error bars were possible because the angular velocity at each rotary position in Figure 9B is the average of >72,000 power strokes from 22 *Ec*F_1 molecules (Martin et al., 2014). The designation that the rotary position of the catalytic dwell is 0° resulted from the necessity to align the polarizer with the AuNR prior to data collection. It is important to note that once the power strokes were aligned in this manner for a given F_1 molecule, the power strokes analyzed at the end of the data set remained aligned with those collected at the beginning at the data set shortly after the polarizer was aligned so that the scattered light from the AuNR was at a minimum during the prior catalytic dwell of the power strokes. The data set of rotation information collected from a given F_1 molecule includes a total of ~9,000 power strokes of which ~3,000 power strokes were analyzed, which remained aligned with the polarizer the entire duration of data collection. The ability to resolve the changes in angular velocity *vs.* rotational position from data acquired from many F_1 molecules that were all aligned with the polarizer in the same way clearly demonstrate that the rotary position of the catalytic dwell is a constant from which the power stroke proceeds for 120°.

Closely similar profiles of angular velocity *vs.* degrees of rotation have been observed in power strokes of *Gs*F_1, and *Ms*F_1, as well as with *Mm*A_1 (Sielaff et al., 2016; Ragunathan et al., 2017). Consequently, several steps in the molecular mechanism to drive ATPase-dependent rotation must be shared among this diverse family of motors. It is noteworthy that the angular velocity during Phase-1 is almost 30% slower for *Gs*F_1 and *Mm*A_1 than that of *Ec*F_1. This suggests that the conversion of ATP binding into angular velocity is more efficient for *Ec*F_1 than for the thermophilic and archaeal rotary motors. Differences in substrate binding affinity and the drag imposed on subunit-γ by the inner surface of the $(\alpha\beta)_3$-ring may explain these effects. The slower angular velocities of *Gs*F_1 than observed with *Ec*F_1 are consistent with the lower torque generated by the former motor.

The F_1-ATPase has been postulated to operate at 100% efficiency based on the high values of torque (Yasuda et al., 1998; Kinosita et al., 2000, 2004). A consequence of 100% efficiency is

10.3389/fmicb.2022.965620

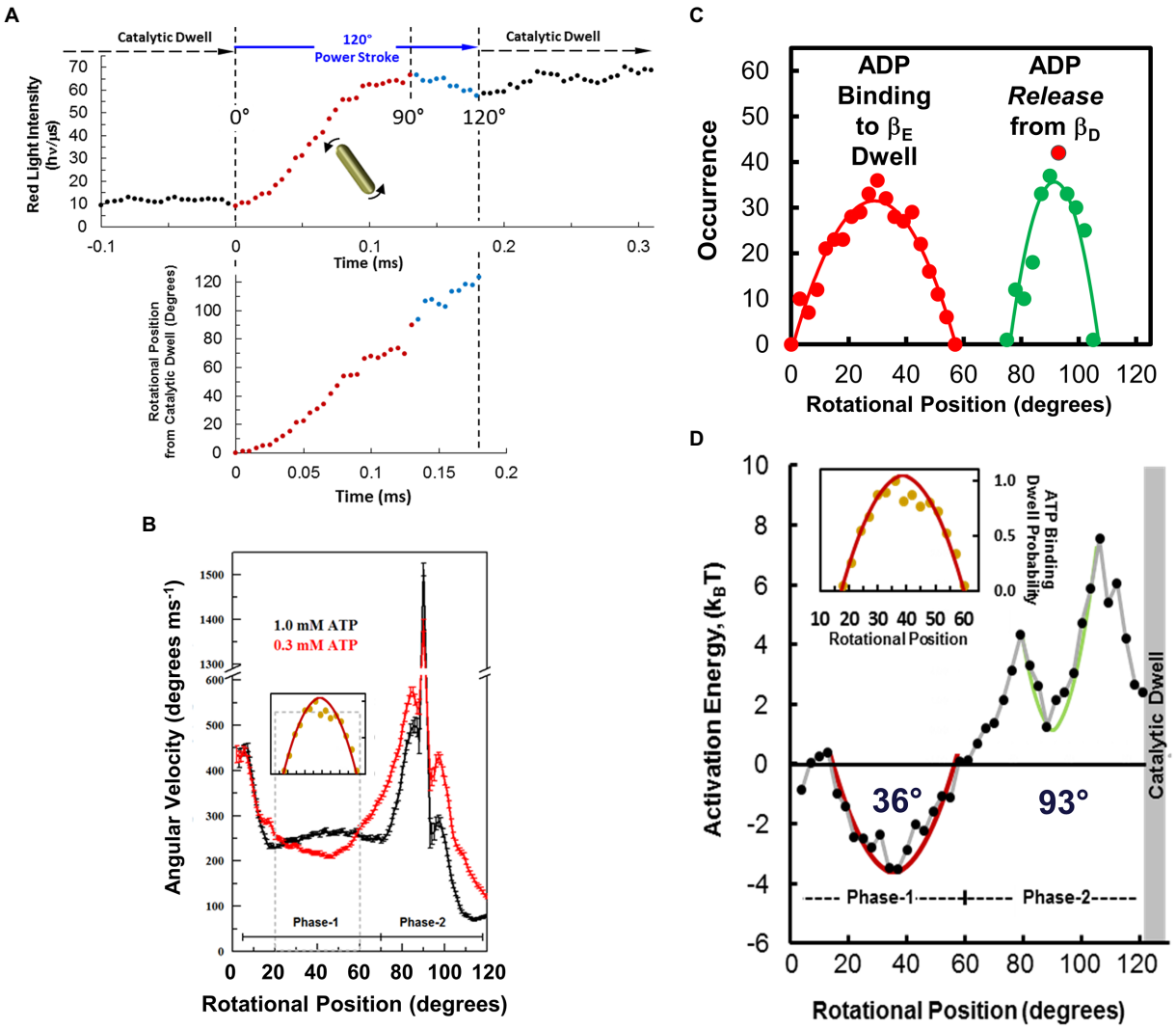


FIGURE 9
Measuring F_1-ATPase power stroke angular velocity vs. rotary position from red light intensity of a rotating AuNR collected at 200kHz (200,000 fps). **(A)**. Example of changes in scattered light intensity vs. time during an *Ec*F_1 power stroke in saturating 1mMMg-ATP. This power stroke occurred subsequent to the catalytic dwell, which had been set to a minimum light intensity by rotating the polarizer prior to data collection. Power stroke rotational position vs. time was calculated from scattered light intensity using Eq. 1 (red) and Eq. 2 (blue). **(B)**. Average power stroke angular velocity vs. rotational position of *Ec*F_1 ATPase-driven γ-subunit rotation binned for every 3° of rotation from the end of the catalytic dwell, which was designated as 0° in the presence of saturating 1mMMg-ATP (black) and 0.3mMMg-ATP (red). Inset: Distribution of ATP-binding dwells vs. rotational position in the presence of 0.3mMMg-ATP, which is proportional to the decrease in average angular velocity vs. rotational position at 0.3mMMg-ATP. **(C)**. Distributions of ADP-binding dwells (red) and ADP-dependent velocity decreases (green) vs. rotational position of the power stroke at 1.0mM MgATP and 3mM MgADP. **(D)**. Activation energy of the *Ec*F_1-ATPase power stroke vs. rotational position at 1mMMg-ATP, 10μMMg-ADP and 10μM Pi. Energy stored vs. extent of twist of a torsion spring with spring constants, κ=50 k_BT rad^{-2} (red) and κ=150 k_BT rad^{-2} (green) from equilibrium positions of 34° and 93°, respectively. Inset: Distribution of ATP-binding dwells vs. rotational position from B. This figure was reconfigured using data from Martin et al. (2014, 2018), Sielaff et al. (2016).

that the angular velocity must be constant during the rotation between dwells (Wang and Oster, 1998). The observed accelerations and decelerations during the power stroke provide evidence that the F_1-ATPase is not 100% efficient at saturating concentrations of ATP.

The angular velocity profile of the F_1 power stroke during Phase-2 (Martin et al., 2014) correlates well with the trajectory of γ-subunit position derived by targeted molecular dynamics simulations (Pu and Karplus, 2008). This correlation supports the mechanism in which rotation during the final 85° of the power stroke is powered by van der Waals repulsive forces from Mg-ATP binding-dependent movement of the β_E-lever domain pushing against the γ-subunit as the lever closes. Comparison of catalytic subunit-β conformations show that the lever domain closes upon subunit-γ when ATP binds *via* π–π stacking of the adenine ring with aromatic residues at the base of the β-lever domain and by electrostatic interactions between the nucleotide triphosphates with P-loop residues in the β-catalytic domain. The affinity of the

residues on these domains for Mg-ATP decreases the distance between them upon substrate binding.

Effects of ATP binding on F_1 power stroke velocity and ATP-binding dwells. Decreases in ITP-dependent angular velocity observed during Phase-1, a substrate with lower affinity than ATP to *Ec*F_1, provided the first direct evidence that angular velocity depends on substrate binding affinity (Martin et al., 2014). When *Ec*F_1 rotation was examined by the AuNR assay, rate-limiting ATP concentrations significantly decreased the average Phase-1 angular velocity between 20°–60°. This decrease resulted from the occurrence of ATP-binding dwells between these rotational positions that approximated a hyperbolic distribution with a maximum at ~36° (Figure 9B **inset**).

The distribution of *Ec*F_1 ATP-binding dwell positions using the AuNR assay, which provides precise measurements of rotational position, indicates that an ATP-binding dwell can occur over a distribution of rotational positions during Phase-1 of the power stroke that was comparable to the decreases that resulted from ITP binding (Martin et al., 2014). This range of positions fits well with the distribution of *Gs*F_1 ATP-binding dwell measured using a 40 nm gold bead (Yasuda et al., 2001). It was concluded that ATP-binding dwells occur at ~40° after the catalytic dwell in *Gs*F_1 under comparable conditions based on measurements in which the centroid position of a ~ 300 nm diameter diffraction limited image from a 40 nm diameter gold bead (Yasuda et al., 2001). The 40° position was the average of the observed distribution, which was thought to result from the error in the measurement. Consequently, it was concluded that at limiting ATP, subunit-γ can rotate beyond 40° without an ATP binding dwell only if ATP has become bound before it reaches that rotational position (the just-in-time binding hypothesis). Otherwise, subunit-γ must wait for ATP to bind before it can rotate beyond 40°. The comparable distribution of the occurrence of *Ec*F_1 ATP-binding dwells (Martin et al., 2014) conflicts with the just-in-time hypothesis and instead suggest that interruption of rotation during Phase-1 at limiting ATP can occur for a variety of reasons that may be specific to each rotational position between 20°–60°. However, in all cases, the interruption of the power stroke is relieved by the binding of ATP.

The power stroke angular velocity profile *vs.* rotational position of *Mm*A_1 was not altered by rate-limiting concentrations of ATP and did not give rise to ATP-binding dwells during Phase-1 (Sielaff et al., 2016). Although the V_1-ATPase from *Enterococcus hirae* V_1V_O (*Eh*V_1) showed both ATP-binding and catalytic dwells (Iida et al., 2019), the *Paracoccus denitrificans Pd*F_1, and V/A_1-ATPase from the bacterial V/A-type ATP synthase of *Thermus thermophilus* (*Tt*V/A_1) did not exhibit an ATP-binding dwell at rate-limiting ATP concentrations (Furuike et al., 2011; Zarco-Zavala et al., 2020), suggesting that ATP binding of these rotary motors occurs at the same rotary position as the catalytic dwell.

The subunit composition of *Mm*A_1 and for the *Tt*V_1 and *Eh*V_1 is A_3B_3DF, where rotor subunits D and F form a helical coiled-coil that extends into the core of the $(AB)_3$-ring. The γ-subunit, which serves as the rotor in *Ec*F_1 and *Gs*F_1, is comprised of a coiled-coil domain from α-helices that are connected by a globular domain, which may restrict the motion of the rotor relative to that of the A-type rotor. Understanding the differences in sequence and mobility of the F-type and A-type rotors is anticipated to provide important insight concerning the basis for the occurrence and variation in rotary position of ATP-binding dwells.

Effects of elevated ADP concentrations on EcF_1 ATPase-dependent rotation. Elevated ADP concentrations were found to affect *Ec*F_1 ATPase-dependent rotation in two ways (Martin et al., 2014). First, the presence of ADP suppressed the Phase-1 angular velocity by ~30%, which occurred as the result of an increase in dwells that lasted between 300 μs and 450 μs. These MgADP dwells were maximal at ~36° subsequent to the catalytic dwell (Figure 9C) with a distribution that was comparable to ATP-binding dwells (Figure 9D **inset**). The similarity between *Ec*F_1 Phase-1 ADP-inhibition dwells and ATP-binding dwells indicates competitive binding of ADP with ATP for β_E, the empty catalytic site (Martin et al., 2014). Second (Figure 9C), elevated ADP concentrations also decreased the average Phase-2 angular velocity with a distribution of rotary positions between 78° and 110° with a maximum of ~93° where there was also an increase in dwells of comparable duration to those during Phase-1 (Martin et al., 2014). These changes during Phase-2 were proportional to the increase in ADP concentration in solution. This inhibition is consistent with a mass action-dependent decrease in the ability of ADP to be released from the β_D catalytic site at elevated ADP concentrations. It is noteworthy that these ADP dependent dwells are unrelated to what is referred to as Mg-ADP inhibition, which occurs during the catalytic dwell and lasts up to 30 s (Hirono-Hara et al., 2001; Sekiya et al., 2010; Bilyard et al., 2013). By comparison, *Mm*A_1 did not exhibit either ADP-inhibition dwells or show any decreases in the angular velocity of the power stroke during either Phase-1 or Phase-2 in the presence of ADP concentrations as high as 250 μM (Sielaff et al., 2016). These results provide further support for the conclusion that for this A-type ATPase, ATP binds to the β_E conformation, and ADP dissociates from β_D conformation during the catalytic dwell.

Energetics of EcF_1 ATPase-dependent Rotation. The thermodynamic parameters of the *Ec*F_1-ATPase power stroke were derived by Årrhenius analysis of the dependence of angular velocity *vs.* rotational position, as a function of temperature, in the presence of saturating Mg-ATP where $\Delta\mu_{ATP} = -31.25\ k_BT$ (Martin et al., 2018). The temperatures examined ranged from 16.3°C to 44.6°C. The *Ec*F_1-ATPase is believed to remain stable over this temperature range since Årrhenius plots of ensemble ATPase measurements remain linear as high as 55°C. At all temperatures examined, the angular velocity profiles contained a similar pattern of accelerations and decelerations *vs.* rotational position and differed from each other only in the magnitude of angular velocities at various rotary positions.

The angular velocity changed inversely with temperature during most of the first 60° of rotation after the catalytic dwell (Martin et al., 2018). As a result, the activation energy (E_a) values derived from these Årrhenius plots were negative during Phase-1

of the power stroke and reached a minimum of −3.5 k_BT after rotation by 34° from the catalytic dwell. As rotation continued beyond 34°, E_a values increased to zero at 61°, at which point the angular velocity did not change significantly as a function of temperature (Figure 9D). The E_a continued to increase during Phase-2 of the power stroke, reaching the first maximum of 4.3 k_BT at 79° when subunit-γ rotation was accelerating. At 93°, E_a reached a local minimum of 1.3 k_BT, and then increased again to a maximum of 7.5 k_BT at 106° during the final deceleration as subunit-γ approached the next catalytic dwell.

Negative E_a values indicate that the energy used for work during Phase-1 rotation is of entropic origin, which is characteristic of elastic energy (Mark et al., 1993; Bustamante et al., 1994), and is commonly observed in long biological polymers such as a protein coiled-coil (Wolgemuth and Sun, 2006; Neukirch et al., 2008). Twisting a coiled-coil away from its equilibrium position stores elastic energy that can serve as an entropic spring capable of mechanical work when it unwinds (Panyukov and Rabin, 2000). This is thought to occur because fewer conformations are possible when a coiled-coil is twisted, which reduces the entropy significantly (Treloar, 1975). Allowing a coiled-coil to return to its untwisted equilibrium position exerts a restoring force as the number of possible conformations, and the associated entropy, increase.

The negative E_a values during Phase-1 varied with a hyperbolic dependence, indicative of energy derived from the extent of twisting of a coiled-coil from equilibrium (Martin et al., 2018). The axle of the rotary subunit-γ is a long helical coiled-coil that extends through the core of the $(\alpha\beta)_3$-ring. Assuming that the negative E_a values resulted only from compliance of this coiled-coil, the negative hyperbolic E_a values were fit to $U = \frac{1}{2}(\kappa\phi^2)$, where U is the amount of stored potential energy as a function of ϕ, the angle of twist of the coiled-coil from its equilibrium position in radians and κ, the spring constant. Using the minimum E_a value of 34°, the best fit of the data was achieved with a spring constant of 50 $k_BT \cdot rad^{-2}$ (205 $pN \cdot nm \cdot rad^{-2}$). The E_a values between 79° and 106° that had a local minimum at 88° were also fit to a plot of energy stored in a torsion spring that fit best with $\kappa = 150$ $k_BT \cdot rad^{-2}$.

It is noteworthy that the inverse of the distribution of the rotary position where ATP-binding dwells occur correlates well with the hyperbolic dependence of the negative E_a values observed during Phase-1 (Martin et al., 2018). Likewise, the inverse of the distribution of rotary positions where elevated ADP concentrations suppress angular velocities also correlated with the hyperbolic decrease in E_a values during Phase-2 that has a local minimum at 93° (Figures 9C,D). These correlations are consistent with a mechanism in which ATP binds to β_E over a range of rotational positions during Phase-1 with a maximal probability of binding at 36°, and where dissociation of ADP from β_E occurs over a range of rotational positions during Phase-2 with a maximum probability of ~93°.

The presence of tethers between subunit-γ and the $(\alpha\beta)_3$-ring that give rise to torsional elastic springs (Saita et al., 2015) have been observed at the same rotary positions as those reported by Årrhenius analysis of the power stroke (Martin et al., 2018). The springs designated I and II were observed at the same rotary positions as those which we reported to occur when ATP bound and ADP dissociated, while the third occurred during the catalytic dwell. These were measured by the forced rotation of a magnetic particle attached to subunit-γ using an external magnet. Although the use of magnetic force to control the rotational position of subunit-γ revealed the existence of these torsional springs, the limits imposed by the magnetic force eliminated the ability to determine the contributions of these springs to the mechanism of the power stroke.

Atomistic simulations of the F_1 torsional elasticity in conjunction with the $(\alpha\beta)_3$-ring identified two pair of harmonically coupled subunit-γ coiled-coil segments that had spring constants of 85 and 134 $k_BT \cdot rad^{-2}$ (Czub and Grubmüller, 2011). These spring constants are similar to 50 and 150 $k_BT \cdot rad^{-2}$ experimentally observed by Årrhenius analysis of the power stroke (Martin et al., 2018). These γ-coiled-coil segments correspond to the same locations where the β-subunit catch loop and lever domains interact with subunit-γ, consistent with the elastic coupling mechanism.

The free energy of activation ($\Delta G^{\ddagger}$) profile of the *Ec*F_1-ATPase power stroke and its enthalpic ($\Delta H^{\ddagger}$) and entropic ($T\Delta S^{\ddagger}$) components were derived from the Årrhenius analysis (Martin et al., 2018). The enthalpy of activation, which is proportional to E_a, was also negative during Phase-1. The $\Delta G^{\ddagger}$, determined from $\Delta G^{\ddagger} = \Delta H^{\ddagger} - T\Delta S^{\ddagger}$, was positive throughout the power stroke because these values were dominated by the entropy of activation ($T\Delta S^{\ddagger}$).

The thermodynamic values derived for the beginning and end of the power stroke (Martin et al., 2018) are consistent with those values derived for the catalytic dwell from single-molecule measurements of *Ec*F_1 and *Gs*F_1 (Sekiya et al., 2010; Adachi et al., 2012; Watanabe et al., 2014). During the catalytic dwell, ATP hydrolysis precedes Pi release, which starts the power stroke. The $\Delta G^{\ddagger}$ for ATP hydrolysis from *Gs*F_1 is comparable to the value at the end of the *Ec*F_1 power stroke, while the $\Delta G^{\ddagger}$ for Pi release in *Gs*F_1 is only slightly higher than that observed at the start of the *Ec*F_1 power stroke. Although the $\Delta G^{\ddagger}$ values of *Gs*F_1 for Pi release and ATP hydrolysis correspond to those at the start and end of the *Ec*F_1 power stroke, the $\Delta H^{\ddagger}$ and $T\Delta S^{\ddagger}$ values from which they were derived differ significantly between the F_1 from these species. This suggests that the underlying processes that occur during the catalytic dwell and power stroke differ substantially.

The $\Delta G^{\ddagger}$ profile *vs.* rotational position is inversely proportional to the angular velocity during the power stroke (Martin et al., 2018). This makes sense because higher angular velocities correspond to lower free energy of activation barriers. The maximum $\Delta G^{\ddagger}$ value of 22.6 k_BT was observed as the power stroke reached 120°, which was the point at which the catalytic dwell began. At all rotational positions, the available energy $\Delta\mu_{ATP}$ (−31.25 k_BT), which was derived from the ATP/ADP•Pi

concentration ratio, was greater than required to overcome the energy barrier of the power stroke ($\Delta G^{\ddagger}$) used in the experiments. The efficiency of *Ec*F_1 calculated from the $-\Delta G^{\ddagger}/\Delta\mu_{ATP}$ ratio ranged from 62% to a maximum of 72% at 120°. These efficiencies were determined using the AuNR assay under conditions in which the velocity of rotation was not limited by a significant opposing force. Investigations that concluded that *Gs*F_1 operates with 100% efficiency (Yasuda et al., 1998; Kinosita et al., 2000, 2004) were based on calculations of the ratio of useful work, where "useful work" is defined as the average angular velocity against a rate-limiting opposing force. Operating against a near-stall force is known to increase efficiency of molecular motors including F_1 (Bustamante et al., 2004).

The elastic coupling power stroke mechanism of F_1-ATPase powered rotation

The elastic coupling mechanism is based on single-molecule experiments of *Ec*F_1 ATPase-driven rotation (Martin et al., 2014, 2018), the effects of mutations that altered electrostatic interactions between subunit-γ and the $(\alpha\beta)_3$-ring (Greene and Frasch, 2003; Boltz and Frasch, 2005, 2006; Lowry and Frasch, 2005), as well as available F_1 structures including those shown in Figure 10.

During the catalytic dwell at 0° (Figure 10A), the γ–subunit coiled-coil is tightly wound (Martin et al., 2014) where torsion on the coiled-coil is maintained by restraints at both ends. The restraint that is distal from the globular subunit-γ foot domain is composed of the β_E-catch loop (β_ED301–D305) and subunit-γ tether (γR268, γQ269) electrostatic interactions (Greene and Frasch, 2003), while the proximal restraint is derived from the closed positions of the six lever domains of the $(\alpha\beta)_3$-ring (Lowry and Frasch, 2005).

The catalytic dwell ends after ATP hydrolysis at the β_D-site and Pi release at the β_E-site (Figure 10B). This opens the β_E and β_D lever domains and allows the γ-coiled-coil to unwind at the start of Phase-1 of the power stroke. During this phase, which is characterized by negative activation energies (Martin et al., 2018), the β_E-catch loop remains attached to the subunit-γ tether such that only the subunit-γ foot domain rotates (Figures 10B,C). Rotation is observed because the AuNR is attached to the foot domain.

The binding of ATP can occur during Phase-1 between 20° to 60°, but most commonly at ~36° (Figures 10C,D), which coincides with the rotary position when activation energy reaches a minimum during the power stroke (Martin et al., 2014, 2018). The energy that powers Phase-2 of the power stroke is then derived from ATP binding to β_E, which depends upon the K_D of ATP for the β_E catalytic site *vs.* rotary position. The binding of ATP triggers the closure of the β_E-lever domain and, using van der Waals repulsive forces to push against and rotate the γ-subunit (Pu and Karplus, 2008; Martin et al., 2014), powers Phase-2 of the power stroke (Figure 10E).

ATP binding also induces the transfer of the γ–subunit tether from the β_E-catch loop to the β_D-catch loop (Figure 10D). As a result, the γ-coiled-coil rewinds, and the entire γ-subunit rotates during Phase-2. This is a pivotal step in the binding-change mechanism because it induces the conformational changes of the three catalytic sites $\beta_D \rightarrow \beta_E$, $\beta_E \rightarrow \beta_T$, and $\beta_T \rightarrow \beta_D$ (Greene and Frasch, 2003; Martin et al., 2018).

Dissociation of ADP (Figure 10E) occurs during Phase-2 between 78° to 110° with a maximum of ~93° (Martin et al., 2014). At the beginning of the power stroke, this ADP was bound to β_D. However, due to the catch loop induced $\beta_D \rightarrow \beta_E$, the dissociating ADP is bound to the newly formed β_E that has lower affinity for ADP. Consequently, during Phase-2 of the power stroke, the newly formed β_T and β_D sites each contain bound ATP, while the newly formed β_E site contains bound Pi. In response, the β-lever domains close upon the γ-coiled-coil, trapping it in the twisted, tightly wound conformation that stores torsional energy to be used for the subsequent power stroke (Martin et al., 2018). Consistent with this energy storage mechanism, ATPase activity is severely impacted by mutations that disturb either the interaction between β_E–catch loop and γ–tether (Greene and Frasch, 2003; Boltz and Frasch, 2006) or that between the β-lever DIIA motif and γ-coiled-coil (Lowry and Frasch, 2005). Disturbing either of these interactions also decreases the torque during a power stroke by about one half (Furuike et al., 2008; Hossain et al., 2008; Usukura et al., 2012).

In all F_1 structures determined to date, the β_E–catch loop is engaged with the γ–tether. When structures are aligned using β_E residues 5 to 50 of the β-barrel "crown" domain, the difference in rotational position of subunit-γ at the position of the catch loop is minimal. However, the γ–subunit foot domain rotational position varies by as much as 53°, which due to the catch loop-tether attachment, can only happen as the result of unwinding the γ-coiled-coil consistent with the Elastic Coupling Mechanism. Assigning the catalytic dwell at 0° (Figures 10A,F) to ground state *Bt*F_1 structures 2JDI and 4YXW (Bowler et al., 2007; Bason et al., 2015), unwinding the coiled-coil results in rotation of the subunit-γ foot domain by 26°, 30°, and 40° represented by the Mg^{2+}-dissociated structure 4ASU (Figure 10B), the *Ec*F_1 subunit-ε inhibited *Ec*F_1 structure 3OAA (Figure 10C), and temperature-sensitive *Gs*F_1 mutant structure 7L1Q (Figure 10D), respectively (Cingolani and Duncan, 2011; Rees et al., 2012; Sobti et al., 2021), while that of ADP release at 107° (Figure 10E) is represented by pre-product release state *Bt*F_1 structure 1H8E (Menz et al., 2001).

Although the β_E-catch loop and γ-tether are attached in all structures, the γ-tether residues are pulled increasingly toward the β_D-catch loop as the coiled-coil unwinds. Upon rotation of the γ-foot by 40° (*Gs*F_1 structure 7L1Q), the EcF_1 equivalent of γR269 has broken free of the β_E-catch loop now faces the β_D-Catch loop, while αR283 is positioned to form an electrostatic interaction with the β_E-Catch loop, validating this mechanism

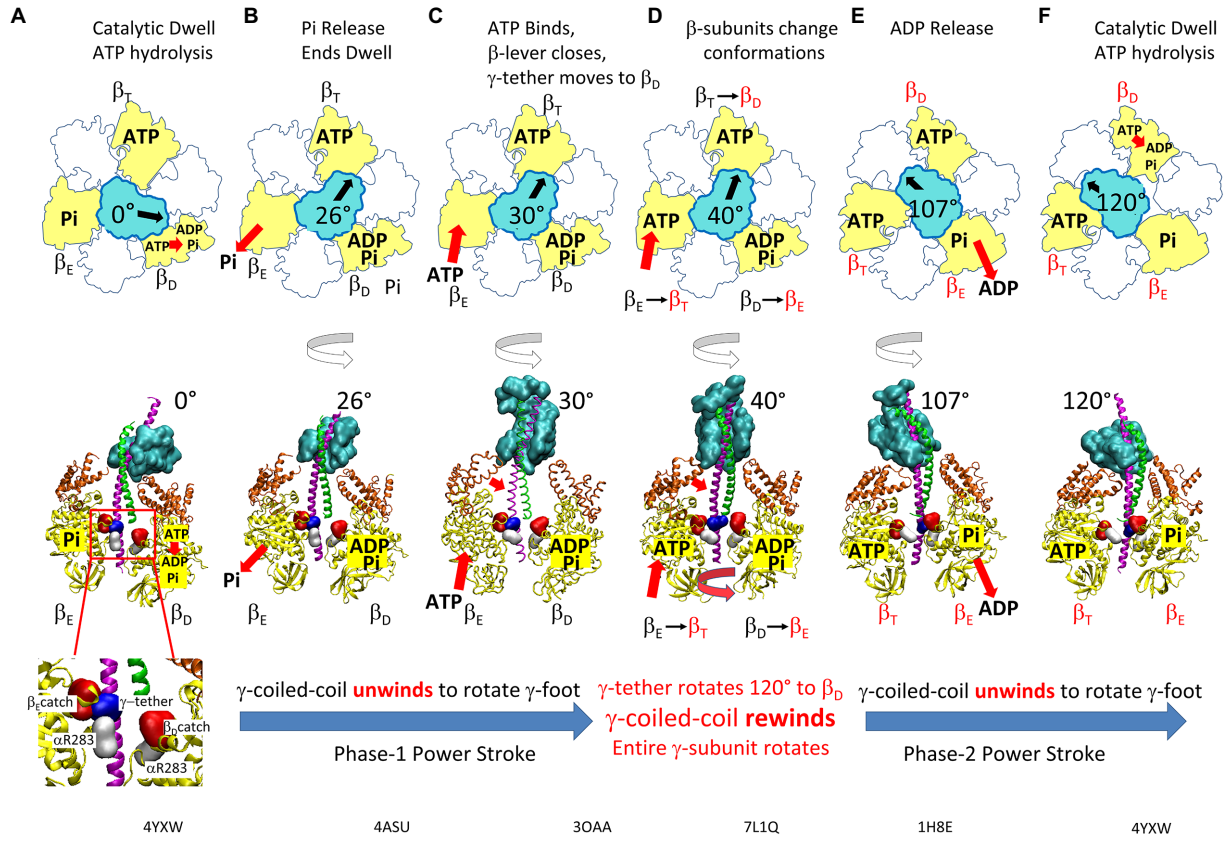


FIGURE 10
Elastic Coupling Mechanism of the F_1-ATPase Power Stroke. **(A)** Catalytic dwell where ATP hydrolysis occurs at β_D. Inset: residues of the β_E- and β_D- catch loops (red), the γ-tether (blue), and aR283 (white). **(B)** Pi release from β_D initiates Phase-1 power stroke using torsion energy from tightly wound γ-coiled-coil to rotate γ-foot. **(C)** As γ-coiled-coil unwinds, ATP binds β_E from 20°–50° (optimally 34°) to force β-lever closed and rotate γ-foot further. **(D)** γ-tether moves from β_E-catch loop to β_D-catch to rotate γ-coiled-coil 120° and rewind it to initiate Phase-2 power stroke. This initiates catalytic site conformational changes $\beta_E \rightarrow \beta_T$, $\beta_T \rightarrow \beta_D$, and $\beta_D \rightarrow \beta_E$. **(E)** Release of ADP upon $\beta_D \rightarrow \beta_E$ occurs from 78°–110° (optimally 93°). **(F)** Catalytic dwell state after γ-foot rotates 120°. Structures corresponding to the indicated γ-foot rotation positions are *Bt*F_1 4YXW at 0° **(A)** and 120° **(F)**, *Bt*F_1 4ASU at 26° **(B)**, EcF_1 3OAA at 30° **(C)**, GsF_1 7L1Q at 40°**(D)**, and *Bt*F_1 1H8E at 110° **(E)**. Top view structures as viewed from γ-foot, while side view structures omitted α-subunits and the rear β-subunit for clarity. White, α-subunits; yellow, β-subunits; orange, β-levers; cyan, γ-subunit foot; green and pink, γ-coiled-coil. This figure was modified from that in Martin et al. (2018).

(Greene and Frasch, 2003; Boltz and Frasch, 2006; Martin et al., 2014, 2018). Thus, the exchange of the γ-tether residues from the β_E-catch loop to the β_D-catch loop defines the rotational position at which the binding-change conformational changes occur (i.e., $\beta_E \rightarrow \beta_T$, $\beta_T \rightarrow \beta_D$, and $\beta_D \rightarrow \beta_E$).

The rotary position of the γ-foot in *Bt*F_1 structure 1H8E (Menz et al., 2001), which is 13° CW from structures 2JDI and 4YXW, is consistent with the ADP release occurring late in Phase-2 of the power stroke (Martin et al., 2014). This structure was proposed to be the conformation just prior to release of bound ADP (Menz et al., 2001), since all three catalytic sites contain bound nucleotide and β_E contains ADP and sulfate, the Pi analog. Since Phase-2 of the power stroke occurs after the exchange of the γ-tether from the β_E-catch to the β_D-catch and its associated conformational changes, the bound ADP and sulfate are in the β_E-conformation, newly formed after binding-change. It is noteworthy that the other two catalytic sites each contain the transition state analog MgADP•AlF_n, which suggests that ATP hydrolysis may begin during Phase-2 of the power stroke.

Elastic Coupling in F_1F_O. The exchange of the subunit-γ tether from the β_E catch loop to that of β_D was proposed to act as an escapement mechanism to insure tight coupling of substrate binding to the concerted conformational changes during the alternating site mechanism (Greene and Frasch, 2003). The need for an escapement mechanism is of particular importance in F_1F_O to ensure that pmf-driven c-ring rotation only occurs upon ADP and Pi binding to the empty catalytic site. In this mechanism, ADP and Pi binding triggers the release of the β_E catch loop, which allows the subunit-γ tether to rotate CW and form electrostatic interactions with β_D. This in turn changes the conformations of all three catalytic sites to promote ATP release from β_T.

Measurements of hydrogen/deuterium exchange kinetics of backbone amide groups of F_1F_O support the role of the subunit-γ tether/catch loop interaction as an F_1F_O escapement mechanism (Vahidi et al., 2016). This exchange rate, which depends upon

transient H-bond fluctuations in secondary structure, exhibited a pmf-dependent increase specifically in the 16-residue α-helical segment containing the subunit-γ tether residues. The increased exchange rate did not occur in a burst, indicating that the pmf had not caused this α-helical segment to become disordered. Consequently, this is an indication of transient torsional strain that results as the catch loop restrains subunit-γ rotation in F_1 relative to pmf-driven c-ring rotation in F_O.

Several cryo-EM F_1F_O structures show the c-ring in multiple rotary positions relative to F_O subunit-a in the stator even though the overall rotary position of subunit-γ in F_1 remains unchanged (Murphy et al., 2019). This is possible because subunit-δ, which attaches the peripheral stalk to F_1, has flexed to accommodate the differences in rotary positions of the F_O and F_1 rotors. Given the contribution of elastic energy of subunit-γ to the ATPase activity of purified F_1 (Martin et al., 2018), it is anticipated that the ability of the γ-coiled-coil to twist in F_1F_O would be significantly dampened, which should decrease ATPase activity. However, this remains to be examined. It is noteworthy that the α-helical segment containing the subunit-γ tether to the Catch Loop does show signs of torsional strain in *Sc*F_1F_O structures where the c-ring has rotated by multiple c-subunits relative to the stator (Guo and Rubinstein, 2022) consistent with the results of hydrogen/deuterium exchange kinetics (Vahidi et al., 2016).

Divergence of F_1, A_1 and V/A_1 ATPase-dependent rotation mechanisms

The power strokes of *Ec*F_1, *Gs*F_1, *Ms*F_1, and *Mm*A_1 have closely similar profiles of angular velocity *vs.* degrees of rotation (Sielaff et al., 2016; Ragunathan et al., 2017), which support similar rotational mechanisms. The *Ec*F_1 elastic coupling mechanism (Martin et al., 2014, 2018) has recently been shown to be used by *Gs*F_1 as well based on cryo-EM structures (Sobti et al., 2021). This includes supporting evidence that ADP dissociates from β_D ~93° after the catalytic dwell. As a result, the *Gs*F_1 rotary mechanism has been recently revised (Sobti et al., 2021) to align with that of *Ec*F_1.

The *Enterococcus hirae* V_1-ATPase (*Eh*V_1) showed dwells separated by 40° and 80° rotational steps that appear similar to *Ec*F_1 and *Gs*F_1 (Iida et al., 2019). However, the dwell prior to the 40° step of *Eh*V_1 involves ATP hydrolysis, Pi release and ATP binding, while the dwell prior to the 80° step involves release of ADP. *Paracoccus denitrificans Pd*F_1 (Zarco-Zavala et al., 2020), *Tt*V/A_1-ATPase (Furuike et al., 2011), and *Mm*A_1 (Sielaff et al., 2016) did not give rise to ATP-binding dwells separate from the catalytic dwells. This suggests that the rotary position for ATP binding to these rotary motors occurs at the same rotary position as that at which ATP hydrolysis and Pi release occur. The rotary position of the ATP-binding dwell of *Homo sapiens* F_1 (*Hs*F_1) and *Bt*F_1 occurs 30° and 40° after the catalytic dwell, respectively, and Pi is released 95° after the catalytic dwell (Suzuki et al., 2014; Kobayashi et al., 2020). The underlying mechanistic reasons that the ATP synthases from these organisms differ in the rotational positions for these steps are currently not understood.

Single-molecule rotation of F_1F_O embedded in lipid bilayer nanodiscs

Single-molecule studies have been difficult for membrane-bound molecular motors like F_1F_O where proton transport across a lipid bilayer is used to synthesize ATP. These problems were circumvented by embedding the F_O portion of *Ec*F_1F_O into a lipid bilayer nanodisc that has been shown to provide a good model for lipid bilayers (Ishmukhametov et al., 2010). The nanodisc are large enough to allow the incorporation of the F_O complex and a few hundred lipid molecules yet are on the same scale as the F_1F_O complex, which is required for single-molecule studies (Figure 11C).

Assembly of stable nanodisc-F_1F_O complexes from membrane scaffold protein (MSP) and detergent-solubilized ATP synthase was verified by 2D electrophoresis where the first nondenaturing gel dimension contained one prominent band (Ishmukhametov et al., 2010). This band contained both MSP and all F_1F_O subunits when separated in the second denaturing gel dimension. When F_1F_O was incorporated into nanodisc, the initial ATPase activity after purification was 1.5-fold higher than the detergent solubilized protein and did not decline significantly after the preparation had been at 25°C for 8 h. DCCD inhibited ATPase activity by 85%, indicating that there was strong coupling between hydrolysis and proton transport. By comparison, ATPase activity of detergent solubilized F_1F_O lost all activity and aggregated within a few hours at room temperature.

The mutation c2∇C was made to the c-subunit, which inserted a cysteine residue at position-2 in the c-subunit to a cys-free *Ec*F_1F_O that was used for biotinylation (Ishmukhametov et al., 2010). An AuNR was then attached to the ten biotins on the c-ring after the nanodisc-F_1F_O complexes (hereafter F_1F_O) were attached to the cover slip *via* his-tags at the F_1 β-subunit N-terminus for single-molecule studies to examine ATPase-driven rotation when scattered red light intensity was acquired at 5 μsec intervals. ATPase-dependent rotation of F_1F_O molecules was measured at 1 mM Mg-ATP, 50 μM ADP, and 50 μM Pi at pH 8.0 (Ishmukhametov et al., 2010). This saturating concentration of ATP was used because under these conditions, F_1-ATPase-driven rotation events occur in continuous 120° power strokes between catalytic dwells that are not interrupted by ATP-binding dwells. Prior to data collection, the polarizer was rotated to align the AuNR so that the scattered red light intensity was at a minimum at one of the three catalytic dwells and the intensity of the subsequent power stroke increased through a maximum scattered light intensity upon rotation at 90°. Scattered light intensity *vs.* time was then collected from the AuNR attached to a given F_1F_O molecule for 50 s during which ~3,520 power stroke events were

monitored. The rotational position during each power stroke was determined *vs.* time using *Eq. 1*.

Two populations of F_1F_O power strokes were observed (Ishmukhametov et al., 2010). The power strokes of one population rotated continuously comparable to that observed with purified F_1-ATPase-driven CCW rotation, which required ~200 μs to rotate 90° (Figure 12A). The other population of molecules took much longer to complete a power stroke, due to the appearance of what were designated transient dwells (TDs). Since the average transient dwell duration was ~150 μs, the total time required to rotate 90° in the presence of transient dwells was ~650 μs. Under these conditions, TDs were present in ~22% of power strokes examined, of which about 70% were able to rotate the c-ring in the CW direction against the torque generated by the F_1 power stroke. The extent of these ATP synthase direction rotations during these dwells averaged 11° and did not exceed 36° (Yanagisawa and Frasch, 2017, 2021).

Due to the sinusoidal dependence of scattered light intensity *vs.* rotational position, the first 90° of each power stroke was examined for the presence of TDs when light intensity increased from a minimum through a maximum. For power strokes that contained TDs, an average of ~2.5 TDs occurred during the 90° of rotation examined. Measurements of both the rotational spacing of TDs and the average number of TDs translate to ~10 transient dwells for each complete 360° revolution of the c_{10}-ring, or one TD per c-subunit. This indicated that TDs result from an interaction between subunit-a and each successive c-subunit during rotation. These data also showed that rotational stepping events that skip one or two c-subunits were a rare occurrence.

Transient dwells were eliminated from F_1F_O power strokes by a mutation to subunit-a (a∇14) that inserted 14 amino acids into subunit-a (Ishmukhametov et al., 2010). This mutation, which did not alter F_1F_O assembly, subunit composition or ATPase activity, was not susceptible to DCCD inhibition, and inverted membranes containing this mutant were unable to catalyze ATPase-dependent proton translocation. The results from this mutation indicated that TDs arise from the periodic interaction between subunit-a and each successive c-subunit in the c-ring.

Viscosity dependence of transient dwell formation

Increasing the drag on the AuNR by changing the viscosity from 0.9 cP (without PEG400) to 1.8 cP (15% PEG400) did not decrease the average angular velocity of the F_1F_O ATPase-dependent power strokes (Ishmukhametov et al., 2010) as was also observed with purified F_1 (Spetzler et al., 2009). However, concurrent with the viscosity-dependent decrease in average angular velocity between 1.8 cP and 4.3 cP, the abundance of TD-containing power strokes increased from 27 to >80%. At viscosities that exceeded 7.5 cP, the angular velocity of the F_1F_O-ATPase-dependent power strokes were too slow to observe a difference in the rate caused by the presence of TDs. In contrast, none of the power strokes from F_1F_O molecules containing the subunit-a∇14 insert exhibited transient dwells regardless of the PEG400 concentration.

To observe the distribution of F_1F_O power strokes that contain TDs, rotation data from each molecule was collected for a total of 50 s in ten 5s data sets and the percent of power strokes containing TDs were binned into 10% increments (Martin et al., 2015). Data sets were collected from ~50 molecules, which allowed the distribution of the percent of TDs per data set to be determined. These distributions showed the same average increase in the percent of TDs *vs.* viscosity observed by that obtained from the average of all power strokes. At a viscosity of 4.3 cP, the distribution of TDs per data set had a single maximum of ~85% with very few data sets of <50%. The distribution of the cD61G mutant was clearly bifurcated with local maxima of ~20 and 90%. This suggested that at high viscosities, TDs can originate from the proton translocation-dependent process involving c-ring rotation, and by a second interaction that was independent of proton translocation. Similar results were observed with mutations cR210G and cR210L that removed the guanidinium group thought to displace the proton into the output channel of subunit-a.

The highly conserved subunit-a residue aE196 was identified as a participant in output channel proton translocation based on observations that aE196Q and aE196L mutations: (1) showed similar decreases in TDs per data set to that of cD61G at elevated viscosity where the distribution was bifurcated into local maxima of 30 and 60%; (2) decreased ATP synthase activity by 11- and 15-fold; and (3) increased NADH-dependent ACMA quenching in inverted *E. coli* membrane vesicles similar to the effects of cD61G. This was the first residue to be identified as a component of an F_O proton output channel (Martin et al., 2015).

The average transient dwell duration was ~200 μs at 1.8 cP, which decreased to ~50 μs at 5.5 cP. The decrease in dwell duration was compensated by slower power stroke velocities at high PEG400 concentrations such that the power stroke velocity was too slow to distinguish changes in velocity that resulted from the existence of TDs (Ishmukhametov et al., 2010).

The increase in the abundance of TD-containing power strokes at pH 8.0 and viscosities >1.8 cP *vs.* PEG400 correlated with the subset of *Ec*F_1F_O molecules subjected to loads exceeding ~1.4 pN ms as the result of the drag on the AuNR (Ishmukhametov et al., 2010). Molecules subject to drag exceeding the 1.4 pN ms threshold had power stroke angular velocities observed at viscosities between 1.8 and 5.5 cP, which corresponded to molecules with velocities less than 220° ms^{-1}. Since the interaction responsible for TD formation occurs every ~36° (i.e., between subunit-a and each c-subunit), the time constant for TD formation is ~160 μs. Thus, any molecule that rotates 36° in <163 μs does not exhibit transient dwells. Given the dependence of TD duration on viscosity, these results indicate that the time constant for the termination of the interaction is ~175 μs, which is independent of

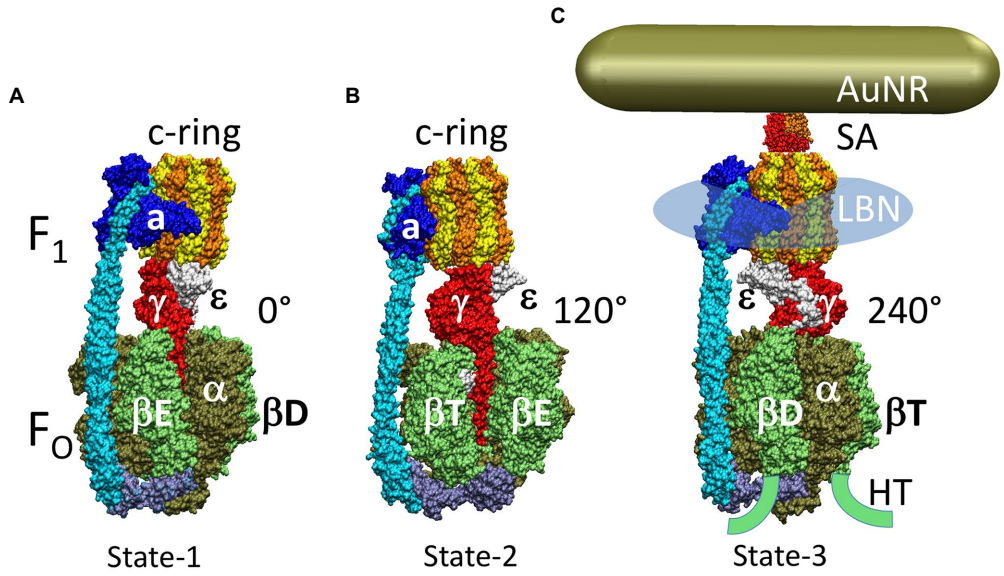


FIGURE 11
Cryo-EM structures of the three rotary states of *Ec*F_1F_O ATP synthase inhibited by ADP. **(A)** State-1 *Ec*F_1F_O structure 6OQU. **(B)** State-2, *Ec*F_1F_O structure 6OQV with rotor 120° CCW from A where subunit-α is not shown to reveal subunit−γ. **(C)** State-3 *Ec*F_1F_O structure 6WNR with rotor 240° CCW from A showing microscope slide assembly of F_1F_O embedded in a lipid bilayer nanodisk (LBN) for rotation measurements. His_6-tags (HT) on β-subunit C-termini enabled attachment to slide, while the AuNR coated with streptavidin (SA) bound to the biotinylated subunit-c ring. This figure was modified from Yanagisawa and Frasch, (2021).

viscosity, and the turnover time for the interaction between subunit-a and subunit-c is then ~338 μs.

At the slowest angular velocities of any given molecule, the subunit-a/subunit-c interaction forms after the c-ring rotated CCW only a few degrees. This interaction between the a/c subunits must then act as a leash that allows rotation to continue to a limit of ~36° after it forms (Ishmukhametov et al., 2010). The extent to which the c-ring rotates CCW after the 163 μs interaction formation time decreases as the angular velocity is slowed by increased load on the motor. For example, at viscosities between 3.0 cP and 5.5 cP, the interaction forms after the c-ring rotated ~31° and 21°, respectively. It is noteworthy that these time constants are specific for the viscosity-dependent interaction between subunit-a and each c-subunit in the c-ring, which were measured at pH 8.0 where there was evidence that the leash interaction had a proton-translocation-dependent component, and a proton-translocation independent component (Ishmukhametov et al., 2010; Martin et al., 2015). The viscosity of the aqueous spaces inside mitochondria is comparable to that which gives rise to the high occurrence of TDs that we observed. Of course, the F_1F_O inside mitochondria are not attached to an AuNR that slows c-ring rotation as the result of drag at these viscosities. However, it is possible that PEG400 may also affect rotation by dehydrating the protein. Dehydration could enhance the strength of hydrophobic subunit interactions that could contribute to the proton translocation independent leash, and slow the rate that protons enter and leave the subunit-a half-channels, which are necessary for proton-translocation-dependent TD formation.

pH dependent transient dwells and synthase-direction steps

The pH dependence of TD formation was examined in the absence of PEG400 (Yanagisawa and Frasch, 2017). The average occurrence of ~22% TDs per data set that was previously observed at pH 8.0 (Martin et al., 2015) was observed between pH 9.0 and pH 7.5 (Yanagisawa and Frasch, 2017). From pH 7.0 to pH 5.0, the percent of TDs increased to an average occurrence of ~50% at pH 5.0. This pH dependence was fit to a Henderson-Hasselbalch relationship, which indicated that the observed TDs resulted from proton-translocation-dependent events, which suggested that protonation of a group with a pKa of 6.3 was necessary to form a TD. However, the average changes in TD formation between pH values 6.0 and 7.5 did not fit well to the dependence on the protonation of a single group.

The TDs observed *vs.* pH during F_1F_O-ATPase-dependent power strokes share many similarities with those formed as the result of high viscosity (Yanagisawa and Frasch, 2017). TDs occur with an average periodicity of every ~36° throughout the power stroke, which did not change between pH 5.0 and 9.0 (Figure 12A) consistent with successive stepping of single c-subunits of the *E. coli* c_{10}-ring relative to subunit-a. The TDs also either stopped CCW rotation, or induced CW rotation against the force of the ATPase power stroke (synthase direction steps) (Figure 12A).

Differences between pH-dependent TDs (Yanagisawa and Frasch, 2017) and viscosity-dependent TDs (Martin et al., 2015) include the dwell duration time and the fraction of TDs that undergo synthase direction steps. The duration of proton-translocation-dependent TDs reached a maximum of ~158 μs at

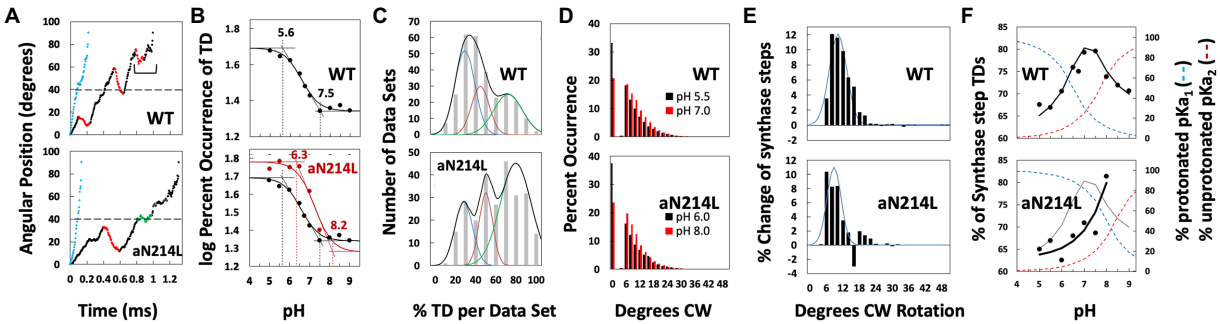


FIGURE 12
Characterization of F_O transient dwells (TDs) and ATP-synthase direction steps in WT and the subunit-a N214L mutant. **(A)** Example F_1F_O ATPase-dependent power strokes without TDs (blue), and power strokes with TDs that contain (red) or lack (green) ATP synthase direction c-ring rotation relative to subunit-a plotted as degrees of rotation where 0° is the catalytic dwell and ATP-binding and/or ADP-inhibition occurs at ~35°. Brackets indicate Brownian-type oscillations during a TD. **(B)** Average TDs per data set vs. pH showing pKa values for WT (black) and aN214L (red). **(C)**. Distributions at pH 6.0 of the percent of TDs per power stroke data set (gray bars) where each data set contained ~300 power strokes that were collected from ~50 different F_1F_O molecules, and data were binned in 10% increments. The data were fit to the sum of three Gaussians (black line) representing low (blue), medium (orange), and high (green) TD formation efficiencies. **(D)** Distribution of the extent of CW synthase-direction rotation during TDs at the low and high pH values where the percent of synthase-direction steps was maximum and minimum. **(E)** Gaussian distributions (blue) of the difference between low and high pH values from **D** in extent of CW synthase-direction step rotation. **(F)** Percent of TDs containing CW synthase-direction steps vs. pH where data were fit to the sum of Henderson–Hasselbalch curves (black) resulting from the fraction of protonated groups with pKa_1 (blue) and unprotonated groups with pKa_2 (red) vs. pH. This figure was modified from Yanagisawa and Frasch, (2021).

pH 8.0 and was at a minimum of ~118 μs at both pH 5.0 and pH 9.0. By contrast, the viscosity-dependent TD dwell durations at pH 8.0 decreased *vs.* viscosity from ~158 μs in aqueous medium to ~50 μs at viscosities of 5.5 cP. Importantly, the fraction of TDs that contained a synthase-direction step varied as a function of pH, with a maximum of 80% at ~pH 7.3, and minimum values of 67 and 71% at pH values of 5.5, and > 7.5, respectively. By contrast, the fraction of TDs containing synthase steps of ~70% in aqueous buffer at pH 8.0 did not change with viscosity.

Synthase steps can be Power strokes or Brownian Ratchets. A power stroke mechanism has been defined as the generation of a large free energy gradient over a distance comparable to the step size of the molecular motion so that transition to the forward position occurs nearly irreversibly (Hwang and Karplus, 2019). By contrast, in a Brownian ratchet mechanism the motor is thought to visit previous and forward positions through thermal motion, where stabilization in the forward position results in conformational changes triggered by the fuel processing event. Some synthase-direction steps rotated CW in a concerted, and apparently irreversible manner characteristic of a power stroke (Figure 12A), while others, as indicated by brackets in Figure 12A were observed to oscillate back and forth during the TD (Yanagisawa and Frasch, 2021). The TDs with oscillations most commonly occur late in the F_1 power stroke (~70–80°) and were more pronounced in all mutations examined except aN214L. Such oscillations are direct evidence of a Brownian ratchet mechanism and are likely the result of a close balance between the energy that powers the F_1-ATPase power stroke with the energy that powers synthase-direction rotation, which suggests that these mutations cause a decrease in the energy to power synthase-direction rotation.

TD formation efficiencies correlate with EcF_1F_O structural states. The distribution of the percent of TDs per data set determined at each pH did not fit to a single Gaussian curve (Yanagisawa and Frasch, 2017). These distributions had similarities to those obtained *vs.* viscosity. While the viscosity-dependent TD distributions were based on data from 25 F_1F_O molecules (~75,000 power strokes) at each viscosity, data was collected from ~50 F_1F_O molecules (~150,000 power strokes) at each pH to increase the resolution (Figure 12C). Good fits of the distributions at each pH fit were achieved by the sum of three Gaussian curves where the probability of forming transient dwells was low, medium, and high. The average values of TDs represented by each Gaussian curve increased inversely with pH. The Gaussian distribution with the highest probability of forming TDs increased by the greatest extent with an average value of 70% TDs per data set at pH 5.0. In several data sets, TDs were present in 100% of the power strokes.

Single particle cryo-EM structures of EcF_1F_O revealed three unique states that differed by the asymmetric rotary positions of central stalk subunits –γ and –ε relative to subunit-a and the peripheral stalk (Sobti et al., 2016). These are equivalent to the rotary positions of the drive shaft between the 120° ATPase-driven power strokes (Figures 11A–C). For each F_1F_O molecule examined (Yanagisawa and Frasch, 2017), only one of the three consecutive power strokes, which together comprise a complete 360° rotation, was analyzed for the presence of TDs. Thus, for every 51 F_1F_O molecules analyzed, it is likely that the power strokes specific to each of the three structural states was sampled by 17 molecules.

Due to asymmetry in EcF_1F_O between the three F_1 catalytic sites that rotate the γ–subunit axle in 120° power strokes with the

F_O c_{10}-ring that rotates in 36° steps concurrent with the transport of each proton, the c-ring will rotate 4 × 36° for one power stroke, and 3 × 36° for the other two. The positive and negative torsion on the c_{10}-ring from the elastic energy needed to accommodate the +14° and −14° misalignments between F_1 and F_O during two of the three power strokes was proposed to be responsible for the differences between the high and low probabilities of forming TDs relative to the medium TD-forming probability when the c-ring and the F_1 catalytic dwells are aligned (Yanagisawa and Frasch, 2017).

The results of the single-molecule AuNR *Ec*F_1F_O rotation studies, which showed the high, medium and low probabilities of TD formation, were compared to other single-molecule analyses of fluorescence video-microscopy of *Ec*F_1F_O rotation. For instance, analyses that used actin filaments, those that used Fōrster resonance energy transfer between pairs of fluorescent probes attached to the *Ec*F_1F_O stator and rotor that give rise to low, medium, and high FRET efficiencies, etc. (Sielaff et al., 2019). All three assays demonstrated differences among the three consecutive 120° power strokes that support the conclusion that the +14° and −14° misalignments between F_1 and F_O in two of the three structural states of the complex is compensated by internal elastic coupling between F_1 and F_O, which is responsible for the differences in efficiencies of the three rotary steps. The three structural states of *Ec*F_1F_O determined by cryo-EM differ in the rotary position of the c_{10}-ring relative to subunit-a by 108°, 108°, and 144° consistent with 3 protons translocated during two ATPase power strokes and 4 protons translocated during the third (Sobti et al., 2016). As a result of the asymmetric binding of subunits γ and ε to the c-ring, each c-subunit is unique such that aR210 is positioned adjacent to cD61 residues of adjacent c-subunits chains M and N in state 3 (*Ec*F_1F_O structure 5 T40), chains S and T in state 2 (*Ec*F_1F_O structure 5T4P), and chains P and Q in state 3 (*Ec*F_1F_O structure 5T4Q). During power stroke-1, c-subunits M, V, U, T rotate past subunit-a thereby translocating 4 protons, while in power stroke-2 and power stroke-3, c-subunits S, R, Q, and subsequently P, O, N rotate past subunit-a that each translocate 3 protons.

Each power stroke is also unique because a portion of subunit-γ must pass through the narrow gap created by the peripheral stalk during power stroke-1, and a portion of subunit-ε must pass through this gap during power stroke-3. However, power stroke-2 is not affected in this manner (Sobti et al., 2016). As the result of these structural differences, we postulated that the low, medium, and high probabilities of forming TDs using the AuNR rotation assay result from rotational transitions from structure 5T4O to 5T4P, from structure 5T4P to 5T4Q, and from structure 5T4Q to 5T4O, respectively (Sielaff et al., 2019).

pKa Values of Transient Dwells. The F_1F_O cryo-EM structures show that two c-subunits from the c-ring are in contact with subunit-a at a time (Sobti et al., 2016). During CW rotation in the ATP synthesis direction, the leading c-subunit must accept a proton from the input channel while the lagging c-subunit donates its proton to the output channel. The poor fit of the pH dependence of TD formation to a single Henderson-Hasselbalch equation for protonation of a group with a single pKa value suggested that this pH dependence resulted from both the protonation and deprotonation events that operated with different pKa values (Yanagisawa and Frasch, 2021).

Equations were used that define the pH dependence of enzyme inhibition kinetics (Cook and Cleland, 2007) to determine the pKa values precisely (Yanagisawa and Frasch, 2021). A TD occurs when subunit-a binds to the c-ring to stop F_1 ATPase-driven rotation temporarily, which can happen 3.6 times per F_1 power stroke. Kinetically, the duration of a 120° without TDs is ~260 μs, and the duration of a power stroke containing 3.6 TDs is ~720 μs, which represents a 64% decrease (inhibition) in the rotation rate. The average occurrence of TD formation for the three efficiencies of TD formation *vs.* pH were fit to these equations to determine the pKa values (Figure 12B). The average maximum value of 47.5% TD occurrence occurred at pH 5.0, which decreased with increasing pH until it plateaued at a minimum of ~22% at pH values >7.5. Observation of such a minimum value with increasing pH indicated that a TD can form as the result of the presence of an unprotonated group with a high pKa, but that the efficiency of TD formation increases with decreasing pH when a second group with a low pKa value becomes protonated. The equation that defines this relationship is based on a log function. As a result, when plotted as the log of the percent of TDs formed versus pH, the two pKa values were determined by the intersection of the pH-dependent increase in TD formation with the high and low plateaus (Figure 12B). In this manner, the pKa values of the groups that must be protonated and unprotonated to induce a TD were 5.6 and 7.5, respectively.

The proportions of TDs with synthase-direction steps depends on the proportion of both the high pKa and low pKa groups in the correct protonation state to enable proton transfer to and from the carboxyl groups of the leading and lagging c-subunits in the ring, respectively (Yanagisawa and Frasch, 2021). The subset of TDs that forced the c-ring to rotate CW (synthase-direction step) against the CCW force of F_1-ATPase rotation had a maximum of 80% at ~pH 7.3 and a minimum of 67% at pH 5.5. At pH values >7.5, the proportion of synthase-directions steps also decreased to 71% at pH 9.0. The pH dependencies of TDs with and without synthase-steps fit well to curves calculated from the proportions of the group with low and high pKa values that were protonated and unprotonated, respectively. Consequently, TDs that lacked a synthase-direction step reached a maximum of the low and high pH values examined when only the group with pKa_1 or with pK_2 were protonated and unprotonated, respectively. Conversely, the pH-dependence of TDs containing synthase-direction steps required the correct protonation from the groups with both high and low pKa values to enable proton transfer to and from the c-ring (Figure 12F).

Subunit-a mutations from either half-channel alter both high and low pKa values. E. coli subunit-a residues aN214, aE219, aH245, aQ252 of the synthase-direction proton input channel and

aE196 of the synthase-direction output channel were initially identified by site-directed mutagenesis studies by their impact on ensemble assays of ATP synthesis, ATP hydrolysis, and ATPase-dependent proton pumping activity. (Lightowlers et al., 1988; Vik et al., 1988; Howitt et al., 1990; Eya et al., 1991; Hartzog and Cain, 1994; Hatch et al., 1995; Fillingame and Steed, 2014; Martin et al., 2015). These groups were originally thought to function by directly transferring protons from one group to the next. Cryo-EM F_1F_O structures that revealed details of subunit-a confirmed that these residues are positioned along possible half-channels that are separated by aR210 (Martin et al., 2015; Zhou et al., 2015; Hahn et al., 2018; Pinke et al., 2020; Sobti et al., 2020) where the role of aR210 has been thought to be responsible for deprotonation of the proton from the lagging c-subunit carboxyl group sending the proton to the output channel. Alternatively, proton translocation through F_O has been postulated to occur *via* a Grotthuss mechanism where the input and output channel residues are hydrogen-bonded to a column of single water molecules that behave in a coherent manner to transfer protonic charge over long distances *via* rapid exchange of protons between H_3O and H_2O (Feniouk et al., 2004; Cukierman, 2006).

It was anticipated that if the subunit-a channel residues were directly transferring protons, then mutation of any of the known channel residues would impact the pKa of only the half-channel in which it is located. However, mutations aN214L, aQ252L, aE219L, aH245L, and aE196L each changed both the pKa values of both half-channels. For example, aN214L changed both the low and high pKa values associated with proton transfer to and from, respectively the c-ring (Figure 12B). This also changed the pH dependence of synthase-direction steps (Figure 12F), which depend on the sum of the proportion of protonated input channel residues with the low pKa, and the proportion of unprotonated output channel residues with the high pKa. Note that these pKa values do not represent a single amino acid sidechain, but the average of pKa's for the entire channel. In addition, mutation of any single residue did not completely eliminate the proton translocation-dependent synthase-direction steps.

These results strongly support a Grotthuss mechanism in F_O where simultaneous stepwise movement of protons distributed along water columns in the two half-channels communicate *via* rotation-dependent proton transfer to and from the leading and lagging c-ring cD61 carboxyls *in lieu of* transferring protons directly and independently (Yanagisawa and Frasch, 2021). In *E. coli*, the coherent behavior of the water columns enables the release of a proton to the cytoplasm concurrent from the output channel with each proton that enters the subunit-a *via* the input channel from the periplasm. This conclusion is also consistent with the fact that participating residues aS199, aN214, and aQ252 are polar but not ionizable, and distances between channel residues are too far apart for direct proton transfer but are positioned at distances able to support a water column. Although aQ252 is highly conserved, glycine or hydrophobic groups naturally occur at positions aN214 (e.g., *T. gondii, and T. thermophilus*), for aH245 (e.g., *M. phlei, T. thermophila, A. woodiii, T. gondii, I. tartaricus, F. nucleatum, and T. thermophilus*) and for aE219 (e. g. *T. thermophila, E. gracilis, B. pseudofirmus OF4, P. angusta, S. cerevisiae*, and *A. platensis PCC9438*). Such mutations can be tolerated if the primary role of these groups is to support a water column that transfers protons.

Recent *Polytomella*F_1F_O and *Bt*F_1F_O structures were of sufficient resolution to observe density near the input channel residues consistent with Grotthuss-type water molecules in this half-channel (Murphy et al., 2019; Spikes et al., 2020). Unidentified electron densities near subunit-a input channel residues in *Ec*F_1F_O structures also suggest the presence of bound waters (Sobti et al., 2020). The observation of a water column in both half-channels of the V_O complex (Roh et al., 2020) suggests that Grotthuss-based proton translocation is a commonly shared trait among the greater family of rotary ATPases.

A Grotthuss mechanism was first proposed to explain extremely high rates of F_O-dependent proton translocation across *R. capsulatus* membranes (Feniouk et al., 2004). The rates were so fast that an ~40 Å diameter Coulomb cage lined with charged and polar groups was proposed to be required to serve as a proton antenna to increase the delivery rated of protons from the aqueous solution to the entrance of the input channel water column (Wraight, 2006). A ~ 30 Å diameter funnel (Figure 13) lined with carboxylate and imidazole residues as the funnel narrows has been identified in *Ec*F_O (Yanagisawa and Frasch, 2021) where aE219, which was proposed to be the start of the Grotthuss column, is positioned at the apex of this funnel.

Proton translocation ATP synthase-direction steps rotate the c-ring 11° CW. The proportion of TDs with and without a synthase-direction step varied as a function of the pH (Figure 12D). In WT and aN214L, the minimum proportion of synthase-direction steps (black bars) was observed at the lower end of the pH scale of pH 5.5 and 6.0, respectively. Even at these low pH values, synthase-direction steps accounted for ~67% of all TDs in WT. The maximum proportion of synthase-direction steps (red bars) was observed at a neutral pH of 7.0 for WT and 8.0 for aN214L. In WT, a maximum of ~80% of TDs contained synthase-direction steps at pH 7.0, which was an increase of 13% from the minimum. (Yanagisawa and Frasch, 2017, 2021).

After subtracting the occurrence of the extent of synthase-direction step CW rotation at the pH when it was at a minimum (black bars) from that observed at its maximum (red bars), a Gaussian distribution of the increase in the extent of synthase-direction step CW rotation was observed (Figure 12E). These plots show the distributions of the extent of CW rotation during a synthase-direction step, for which the $11° \pm 3$ average values of CW rotation were not changed significantly by the mutations (Figure 12E). However, they did alter the pH dependence of the occurrence of synthase-direction steps in a manner that showed that these steps involved protonation and deprotonation of the leading and lagging c-subunits, respectively, of the c-ring (Figures 12B,F). The effects of the subunit-a mutations on the synthase-direction steps ruled out the possibility that these steps result from twisting the entire F_O relative to F_1. During a CCW

F_1-ATPase power stroke, TDs occur every 36°, which is equivalent to an interaction between subunit-a and each successive c-subunit in the *E. coli* c_{10}-ring. Since synthase-direction steps rotate by 11°, rotation by an additional 25° is required to advance the c-ring by one full c-subunit, which we observed in only 0.1% of the synthase-direction steps. Rotational sub-state structures (pdb-ID 6OQR and 6OQS) of ADP-inhibited *E. coli* F_1F_O that differ by a 25° rotation of the c-ring relative to subunit-a were obtained by cryo-EM (Sobti et al., 2020). Since advancing the c-ring by one c-subunit involves rotation by 36°, the difference between these sub-state structures also reveals information relevant to the 11° synthase-direction steps. Similar 11° and 25° rotational sub-states have also been observed with ADP-inhibited *Bt*F_1F_O and *Ms*F_1F_O (Zhou et al., 2015; Guo et al., 2021). In the latter, the binding of bedaquiline stabilizes a rotational sub-state that is either 25° CW or 8° CCW from the equivalent rotational state in the absence of the drug (Guo et al., 2021). The rotational position of the c-ring in cryo-EM structures of *Saccharomyces cerevisiae* *Sc*F_1F_O is also changed by ~9° when the inhibitor oligomycin is bound to F_O (Srivastava et al., 2018).

Alternating two-step mechanism of F_O-dependent synthase direction c-ring rotation

The alternating two-step mechanism to power synthase-direction c-ring rotation (Figure 14) is based on single-molecule rotation experiments of *Ec*F_1F_O (Ishmukhametov et al., 2010; Martin et al., 2015), the effects of mutations of residues involved in F_O translocation on the pH-dependence of rotation (Yanagisawa and Frasch, 2017, 2021), and available F_1F_O structures including *Ec*F_1F_O sub-state structures 6OQR (Figure 14B) and 6OQS (Figure 14C) that differ due to rotation of the c_{10}-ring relative to subunit-a by 25° (Sobti et al., 2020). Since rotation by a single c-subunit in the c_{10}-ring is 36°, an 11° sub-step is required to return the c-ring from that of 6OQS (Figure 14A) to its original position of 6OQR (Figure 14B). This is consistent with the 11° synthase-direction steps that occur every 36° in the *Ec*F_1F_O single-molecule studies (Yanagisawa and Frasch, 2017, 2021).

Several structural features of the *Ec*F_O motor, which are common to F-type ATP synthase, are relevant to the Alternating Two-step Mechanism of proton translocation-dependent c-ring rotation during ATP synthesis (Figures 13A, 14). Each c-subunit contains a carboxyl group that transports individual protons from the input channel to the output channel. Only two c-subunits in the ring contact subunit-a at a time, which are designated the leading (pink) and lagging (orange) for CW synthase-direction rotation. Leading and lagging carboxyls (subunit-cD61 in *E. coli*) are protonated and deprotonated by the respective input and output channels. The remaining carboxyl groups are protonated and rotate through the hydrophobic core of the membrane (yellow) until they reach the output channel. Positively charged aR210 is positioned adjacent to residues aN214 and aQ252 (green), which protonate the leading c-ring carboxyl group such that it can rotate away from subunit-a and into the hydrophobic lipid membrane. An aqueous vestibule (blue) that extends from aR210 to the initial output channel residues, aE196 and aS199, is formed by the interface between subunit-a and the c-ring. The vestibule is lined by subunit-a polar residues above and below the plane of rotation of the c-ring carboxyl groups, which aligns with aN214/aQ252 and aE196/aS199. Residues that provide a possible path for the output channel from aE196 to the cytoplasm include aQ181, aE177, and the subunit-a C-terminal carboxyl, which span this distance a ~ 4 Å intervals, consistent with that needed to stabilize a Grotthuss water channel. However, these are not conserved in several species.

STEP-1. *The 11° sub-step is powered by proton translocation to and from the subunit-a output and input channels from the lagging and leading cD61 carboxyls of the c-ring, respectively* (Figures 14A,B). In the 6OQS structure (Figure 14A), the lagging cD61 (orange) is 3.5 Å from the aS199 which enables proton transfer to aS199 and aE196 *via* bound water. The leading cD61 (pink) is 3.8 Å from the aR210-guanidinium, consistent with intervening water. This cD61 is also proximal to aN214 and aQ252, which positions it for protonation from the input channel *via* bound water. The pH-dependent 11° sub-step occurs upon proton transfer from water bound to aN214 and aQ252 to the leading cD61, and by proton transfer from the lagging cD61 to aS199 and aE196. Protonation from the input channel is vital to displace the unprotonated cD61 from the aR210 guanidinium, which eliminates the charge of cD61 to enable rotation into the hydrophobic lipid bilayer.

STEP-2. The 25° sub-step is powered by electrostatic attraction of the lagging cD61 carboxyl deprotonated in Step-1 to the aR210 guanidinium group (Figures 14B,C). Deprotonation of the lagging cD61 by aE196/aS199 in Step-1 decreases the distance between this carboxyl group and the aR210 guanidinium from ~11.5 Å to ~7.5 Å (Figure 14C). These distances are inconsistent with the long-held belief that the role of aR210 is to displace the proton from the lagging cD61. Instead, the electrostatic attraction between the now negatively charged lagging cD61 and aR210 enables the 25° sub-step, which decreases the distance between them from 7.5 to 3.8 Å.

The occurrence of TDs may appear to be stochastic, but their occurrence depends on the kinetics and the energetics of the system. Slowing the angular velocity of the F_1 ATPase-driven power stroke increases TD occurrence at pH 8.0 (a suboptimal pH), indicating that the ability to form a TD depends on the rate that an interaction can form between subunit-a and each c-subunit relative to the angular velocity of F_1-ATPase-driven rotation. Evidence supports the hypothesis that the energy for F_1-ATPase power strokes is derived from ATP binding-dependent closure of the β-subunit lever domain as it acts upon subunit-γ, which is initiated at ~36° after the catalytic dwell in *Ec*F_1 (Martin et al., 2014). Based on the K_D of ATP at 36° measured in *Gs*F_1, the energy available for the power stroke from ATP binding is ~13.5 k_BT (Adachi et al., 2012). Consequently, the F_O motor must have at least 13.5 k_BT available to cause a TD.

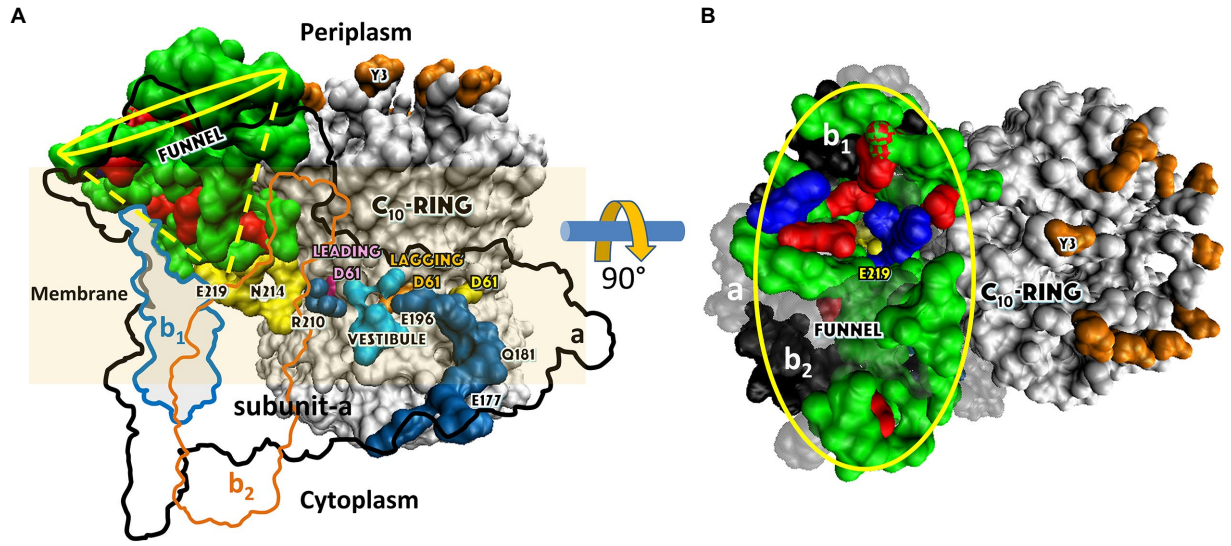


FIGURE 13
Aqueous Funnel of charged and polar groups can serve as an antenna to supply protons to the input channel. **(A)** Transmembrane view of *E. coli* F_O (pdb-ID 6OQR) showing the path of charged and polar residues across the membrane. Outlines indicate space occupied by hydrophobic residues in subunit-a (black line), subunit-b_1 (blue line), and subunit-b_2 (orange line). The inner surface of the Funnel, which is lined with polar residues and loop regions (green), acidic groups (red) and histidines (blue) from subunit-a and the subunit-b_1 N-terminus, is exposed to the periplasm at its wide end that narrows to aE219 (yellow) at the bottom. The input channel (yellow) extends from aE219 to aN214 and aQ252, which are proximal to aR210. Between aR210 and the Output Channel (dark blue) the leading (pink) and lagging (orange) cD61 groups rotate through a Vestibule lined above and below the cD61 rotation plane by polar sidechains (light blue) that decrease the dielectric constant of the vestibule from that of the lipid bilayer. A protonated cD61 exposed to the lipid bilayer (yellow) is also visible. **(B)** Periplasmic surface of F_O showing the interior surface of the Funnel (yellow oval) lined with charged and polar groups from subunit-a and subunit-b_1 as in **(A)** that narrows to aE219 (yellow) at the bottom where the input channel begins. Hydrophobic residues are shown of subunit-a (gray), subunits-b_1 and b_2 (black), and the c-ring (white). The cY3 sidechains (orange) are shown to indicate the orientation of the periplasmic surface of the c-ring. This figure was modified from Yanagisawa and Frasch, (2021).

Two single-molecule observations indicate that the energy available to cause a TD are close to 13.5 k_BT. *First*, TDs that occur early during F_1-ATPase-dependent rotation mostly lack oscillations consistent with power strokes. Thus, the energy available to form the TD is clearly greater than that which causes ATPase-dependent rotation. However, oscillations are observed much more often during TDs that occur late in the F_1-ATPase power stroke, which is consistent with a Brownian ratchet where the energy to drive F_O-dependent CW rotation is close to that available by F_1 to drive CCW rotation. *Second*, the low, medium, and high efficiencies of TD formation were attributed to torsional strain resulting from the asymmetry between 36° c_{10}-ring stepping, and the 120° F_1 power stroke. The torsional energy stored from the ±14° mismatch between F_1 and F_O amounts to only 0.4 k_BT (Yanagisawa and Frasch, 2021) calculated using the spring constant measured for *Ec*F_1F_O (Sielaff et al., 2008). The fact that such a small difference in energy can significantly alter the efficiency of TD formation supports the conclusion that the energy used by F_O to generate TDs is close to that of the F_1-ATPase power stroke.

The difference in pKa values between input and output channels measured by our single-molecule studies can provide as much as 4.4 k_BT that can be used to rotate the c-ring in the ATP synthase-direction (Yanagisawa and Frasch, 2021). The desolvation energy of the negatively charged carboxyl group of the lagging cD61 upon deprotonation generates 5.9 k_BT of energy (White and Whimley, 1999) because that charged moiety is excluded from the lipid bilayer into the aqueous vestibule. Conversely, the energy penalty of 0.8 k_BT needed to insert the leading protonated cD61 carboxyl into the lipid bilayer (White and Whimley, 1999) is avoided by its conversion to the closed and locked conformation in the c-ring (Pogoryelov et al., 2010). The energy of the electrostatic attraction of aR210 to the unprotonated lagging cD61 is highly dependent upon the distance between the charges and the dielectric constant, which is a measure of the hydrophobicity of the environment that ranges from 2 (lipid bilayer) to 80 (aqueous solvent).

If these groups were both directly in the lipid bilayer separated by 11.5 Å, their electrostatic interaction would be as much as 38.1 k_BT. Although we do not yet know how wet the vestibule is, a dielectric constant of 13 and an 11.5 Å aR210-cD61 distance results in 3.8 k_BT, which when summed with the other energy sources totals 14.1 k_BT without input of torsional energy. Since F_1-ATPase rotation from the catalytic dwell to the point that ATP binds is powered by no more than 4 k_BT (Martin et al., 2018), this explains why synthase-direction rotation near this rotational position typically has power stroke characteristics.

After the 25° rotation step when the unprotonated cD61-aR210 distance is 3.8 Å, the electrostatic energy is 11.4 k_BT or 73.8 k_BT when the dielectric constant is 13 or 2, respectively

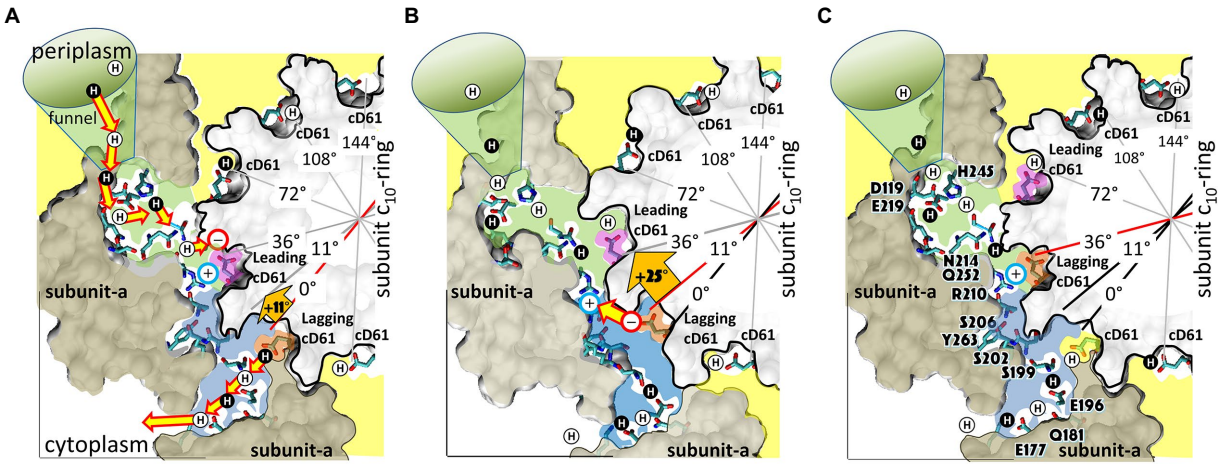


FIGURE 14
Alternating 11° and 25° sub-steps that power F_O c-ring ATP synthase direction rotation. **(A)** The pH-dependent 11° sub-step occurs when H^+ transfer from aN214/aQ25-bound water to the unprotonated leading cD61-carboxyl (pink), and from the protonated lagging cD61-carboxyl (orange) to aS199/aE196-bound water. Upon displacement from aR210 by protonation, leading cD61 adopts the closed conformation to enable rotation into the lipid bilayer (yellow). Due to coherent H^+ movement in the Grotthuss column, each H^+ entering the input channel (green) from the funnel causes a H^+ to exit the output channel (blue) to the cytoplasm. Rotation occurs when lagging cD61 is deprotonated because the negatively charged carboxyl moves in response to the decrease in hydrophobicity from the lipid bilayer to the water-containing vestibule (blue), and from the electrostatic attraction to aR210. This decreases the distance between the lagging cD61 carboxyl and the aR210-guanidinium from ~11.5Å to ~7.5Å. **(B)** The 25° sub-step occurs primarily from the electrostatic interaction between the lagging cD61 carboxy (orange) and the aR210 guanidinium. **(C)** Electrostatic attraction decreases the distance between orange cD61 and aR210 from ~7.5Å to ~3.5Å to complete a 36° stepwise c-ring rotation, which positions the orange cD61 to become the leading carboxyl for the next pH-dependent 11° sub-step. *E. coli* F_1F_O cryo-EM structures of rotary sub-states pdb-IDs 5OQS **(A,C)**, and 5OQR **(B)** are shown as cross-sections of F_O with hydrophobic resides of subunit-a (brown) and the c-ring (gray) along the plane defined by cD61 groups as viewed from the periplasm. Protons are alternately colored black and white to show the progression of proton transfer events. This figure was modified from Yanagisawa and Frasch, (2021).

(Yanagisawa and Frasch, 2021). Thus, in a strictly hydrophobic environment the electrostatic interaction would be far too strong for any rotation to occur. For sustained CW rotation during ATP synthesis, the sum of the energy inputs from the pKa differences, desolvation energies, and pmf must be enough to displace cD61-aR210 when separated by 3.8 Å.

Recently, all-atom free energy calculations of *Sc*F_O found independent evidence of the 11° sub-step (Marciniak et al., 2022), confirmed that the differences in pKa values bias c-ring rotation in the synthase direction, and revealed similar energetic contributions from desolvation energies and electrostatic interactions to that observed from our single-molecule studies (Yanagisawa and Frasch, 2021). In addition, Marciniak et al. (2022) found that the yeast equivalent of aR210 (aR176) dictates the direction of rotation, controls the protonation state of the proton-release site, and separates the two input and output channels. As a result, this arginine is necessary to avoid slippage between proton flux and the mechanical output to guarantee highly efficient energy conversion.

Substate structures of ScF_1F_O were recently solved by cryo-EM (Guo and Rubinstein, 2022) in which each of the three 120° F_1 rotational contained substates in which F_1 was either in the catalytic dwell position or the ATP-binding position, each of which was further distinguished by different F_O substates that differed by rotational single c-subunit stepping of its c_{10}-ring. Most of the torsional strain that resulted from these single c-subunit steps was taken up by the compliance of the peripheral stalk. The number of rotational c-subunit steps observed differed among the three F_1 states consistent with the low, medium, and high efficiency c-subunit stepping observed in the single-molecule studies (Yanagisawa and Frasch, 2017, 2021). Comparing the single-molecule studies and the new cryo-EM results will lead to a greater understanding of the molecular mechanism of ATP synthesis. More work is required to quantify the energetics of these sub-steps during ATP synthesis because, when understood in the context of steady-state pmf values, and the dissociation constants of ATP, ADP, and Pi versus rotary position, these energy contributions will determine the non-equilibrium ATP/ADP•Pi concentration ratio that can be maintained by F_1F_O at steady-state *in vivo*.

Frontiers of F_1F_O mechanisms and nanotechnology applications of molecular motors

Interest in using molecular motors including F_1 for nanotechnology applications began soon after single-molecule techniques were developed that enabled the visualization of molecular motor movements (Spetzler et al., 2007; York et al., 2008). This also sparked an interest in the design of synthetic

molecular motors inspired by the F_1-ATPase that has continued to grow. Designing a synthetic motor that rotates unilaterally by 360° by consuming a chemical fuel like that of F_1 remains a challenge and is still in its infancy (Mo et al., 2022). However, the possibilities inherent in the development of these new technologies underscore the importance of understanding the mechanism of the F-type ATP synthase at a detailed level.

The significant progress in understanding the molecular mechanisms of both the F_1 and F_O complexes has resulted from the development of new approaches to study the structure and function of these motors, of which several are described here. However, several important questions remain. A major unresolved question concerns the molecular basis for the differences among species in the rotary positions when the F_1-ATPase binds ATP, hydrolyzes it, and when products are released. This is a conundrum since the sequence homologies of the αβ-heterodimers are so high, particularly among the residues that contribute to the catalytic sites. Although twisting of the subunit-γ coiled-coil occurs and contributes significantly to the ATPase mechanism of purified F_1, the extent to which subunit-γ twisting contributes to the mechanism of ATP synthesis catalyzed by F_1F_O remains to be determined.

The reasons for the >2-fold species variations in c-ring sizes of F_O are also major unresolved questions. From a bioenergetics perspective, the energy requirements of 8 H^+ and 15 H^+ to make three ATPs in mitochondria and chloroplasts is significant and the underlying reasons for these differences are unexplained. This difference also raises questions about the molecular mechanism of F_O because c_8-rings and c_{15}-rings rotate 45° and 24°, respectively, with each proton translocated across the membrane. The residues that comprise the subunit-a input channel are mostly characterized. However, except for aE196 and aS199, residues that participate in the output channel are not well conserved and remain to be identified. Although there is good evidence that protons are transported across the membrane *via* a Grotthuss mechanism, input and output channels of ATP synthases that transport Na^+ must have specific adaptations that are not yet understood.

Author contributions

WF, ZB, and SY wrote the manuscript. WF conceived the work and obtained funding. All authors contributed to the article and approved the submitted version.

Funding

This work was funded by NIH R01GM097510 to WF, and from NSF-BII 2119963.

Conflict of interest

The authors declare that the research was conducted in the absence of any commercial or financial relationships that could be construed as a potential conflict of interest.

Publisher's note

All claims expressed in this article are solely those of the authors and do not necessarily represent those of their affiliated organizations, or those of the publisher, the editors and the reviewers. Any product that may be evaluated in this article, or claim that may be made by its manufacturer, is not guaranteed or endorsed by the publisher.

References

Abrahams, J., Leslie, G., Lutter, J., and Walker, J. (1994). Structure at 2.8 Å resolution of F_1-ATPase from bovine heart mitochondria. *Nature* 370, 621–628. doi: 10.1038/370621a0

Adachi, K., Oiwa, K., Nishizaka, T., Furuike, S., Noji, H., Itoh, H., et al. (2007). Coupling of rotation and catalysis in F_1-ATPase revealed by single-molecule imaging and manipulation. *Cell* 130, 309–321. doi: 10.1016/j.cell.2007.05.020

Adachi, K., Oiwa, K., Yoshida, M., Nishizaka, T., and Kinosita, K. (2012). Controlled rotation of F_1-ATPAse reveals differential and continuous binding changes for ATP synthesis. *Nat. Commun.* 3:1022. doi: 10.1038/ncomms2026

Bason, J. V., Montgomery, M., Leslie, A., and Walker, J. E. (2015). How release of phosphate from mammalian F_1-ATPase generates a rotary substep. *Proc. Natl. Acad. Sci. U. S. A.* 112, 6009–6014. doi: 10.1073/pnas.1506465112

Bilyard, T., Nakanishi-Matsui, M., Steel, B. C., Pilizota, T., Nord, A. L., Hosokawa, H., et al. (2013). *Phil. Trans. Royal Soc. B*, 368. doi: 10.1098/rstb.2012.0023

Boltz, K., and Frasch, W. D. (2005). Interactions of γT273 and γE275 with the β subunit PSAV segment that links the γ-subunit to the catalytic site Walker homology B aspartate are important to the function of *Escherichia coli* F_1F_o ATP synthase. *Biochemistry* 44, 9497–9506. doi: 10.1021/bi050070o

Boltz, K., and Frasch, W. D. (2006). Hydrogen bonds between the α and β subunits of the F_1-ATPase allow communication between the catalytic site and the interface of the β catch loop and the γ subunit. *Biochemistry* 45, 11190–11199. doi: 10.1021/bi052592+

Bowler, M. W., Montgomery, M. G., Leslie, A. G., and Walker, J. E. (2007). Ground state structure of F_1-ATPase from bovine heart mitochondria at 1.9 Å resolution. *J. Biol. Chem.* 282, 14238–14242. doi: 10.1074/jbc.M700203200

Boyer, P. D., and Kohlbrenner, W. E. (1981). "Energy coupling in photosynthesis," in *The present status of the binding-change mechanism and its relation to ATP formation by chloroplasts*. eds. B. R. Selman and S. Selman-Reimer (Amsterdam: Elsevier), 231–240.

Bruist, M. F., and Hammes, G. G. (1981). Further characterization of nucleotide binding sies on chloroplast coupling factor one. *Biochemistry* 20, 6298–6305. doi: 10.1021/bi00525a003

Bustamante, C., Chemla, Y. R., Forde, N. R., and Izhaky, D. (2004). Mechanical processes in biochemistry. *Annu. Rev. Biochem.* 73, 705–748. doi: 10.1146/annurev.biochem.72.121801.161542

Bustamante, C., Marko, J. F., Siggia, E. D., and Smith, S. (1994). Entropic elasticity of lambdaphage DNA. *Science* 265, 1599–1600. doi: 10.1126/science.8079175

Chen, W., and Frasch, W. D. (2001). Interaction of the catch-loop tyrosine Y317 with the metal at catalytic site 3 of *Chlamydomonas* chloroplast F_1-ATPase. *Biochemistry* 40, 7729–7735. doi: 10.1021/bi0105779

Chen, W., Hu, C.-H., Crampton, D. J., and Frasch, W. D. (2000). Characterization of the metal binding environment of catalytic site 1 of

chloroplast F_1-ATPase from *Chlamydomonas*. *Biochemistry* 39, 9393–9400. doi: 10.1021/bi000281n

Chen, W., LoBrutto, R., and Frasch, W. D. (1999). EPR spectroscopy of VO^{2+}-ATP bound to catalytic site 3 of chloroplast F_1-ATPase from *Chlamydomonas* reveals changes in metal ligation resulting from mutations to the phosphate-binding loop threonine (βT168). *J. Biol. Chem.* 274, 7089–7094. doi: 10.1074/jbc.274.11.7089

Chiwata, R., Kohori, A., Kawakami, T., Shiroguchi, K., Furuike, S., Adachi, K., et al. (2014). None of the rotor residues of F_1-ATPase are essential for torque generation. *Biophys. J.* 106, 2166–2174. doi: 10.1016/j.bpj.2014.04.013

Cingolani, G., and Duncan, T. M. (2011). Structural basis for inhibition of bacterial ATP synthase by subunit epsilon of the rotor stalk. *Nat. Struct. Mol. Biol.* 18, 701–707. doi: 10.1038/nsmb.2058

Cook, G., and Cleland, W. W. (2007). "Enzyme kinetics and mechanism," in *Fundamentals of Protein Structure and Function*. ed. E. Buxbaum (London: Garland Science), 325–364.

Crampton, D. J., LoBrutto, R., and Frasch, W. D. (2001). Identification of the P-loop lysine as a metal ligand in the absence of nucleotide at catalytic site 3 of chloroplast F_1-ATPase from *Chlamydomonas reinhardtii*. *Biochemistry* 40, 3710–3716. doi: 10.1021/bi002895y

Cukierman, S. (2006). Et tu, Grotthuss! and other unfinished stories. *Biochim. Biophys. Acta* 1757, 876–885. doi: 10.1016/j.bbabio.2005.12.001

Czub, J., and Grubmüller, H. (2011). Torsional elasticity and energetics of F_1-ATPase. *Proc. Natl. Acad. Sci. U. S. A.* 108, 7408–7413. doi: 10.1073/pnas.1018686108

Diez, M., Zimmermann, B., Börsch, M., Konig, M., Schweinberger, E., Steigmiller, S., et al. (2004). Proton-powered subunit rotation in single membrane-bound F_OF_1-ATP synthase. *Nature Struct. Mol. Biol.* 11, 135–141. doi: 10.1038/nsmb718

Duncan, T., Bulygin, V., Zhou, Y., Hutcheon, M., and Cross, R. (1995). Rotation of subunits during catalysis by *Escherichia coli* F_1-ATPase. *Proc. Natl. Acad. Sci. U. S. A.* 92, 10964–10968. doi: 10.1073/pnas.92.24.10964

Eya, S., Maeda, M., and Futai, M. (1991). Role of the carboxyl terminal region of H^+-ATPase (F_0F_1) *a* subunit from *Escherichia coli*. *Arch. Biochem. Biophys.* 284, 71–77. doi: 10.1016/0003-9861(91)90265-K

Feniouk, B., Koslova, M., Knorre, D., Cherepanov, D., Mulkidjanian, A., and Junge, W. (2004). The proton-driven rotor of ATP synthase: ohmic conductance (10 fS) and absence of voltage gating. *Biophys. J.* 86, 4094–4109. doi: 10.1529/biophysj.103.036962

Fillingame, R. H., and Steed, P. R. (2014). Half-channels mediating H^+ transport and the mechanism of gating in the F_O sector of *Escherichia coli* F_1F_O ATP synthase. *Biochim. Biophys. Acta* 1837, 1063–1068. doi: 10.1016/j.bbabio.2014.03.005

Frasch, W. D. (2000a). Vanadyl as a probe of the function of the F_1-ATPase-Mg^{2+} cofactor. *J. Bioenergetics and Biomembranes* 32, 539–546. doi: 10.1023/A:1005629427630

Frasch, W. D. (2000b). The participation of metals in the mechanism of the F_1-ATPase. *Biochim. Biophys. Acta* 1458, 310–325. doi: 10.1016/S0005-2728(00)00083-9

Frasch, W. D., and Sharp, R. R. (1985). Nucleotide binding to the chloroplast ATP synthase: effect on the proton spin-echo NMR spectrum. *Biochemistry* 24, 5454–5458. doi: 10.1021/bi00341a026

Frasch, W. D., LoBrutto, R., and Roskelley, A. (1992). Characterization of the metal ligands at nucleotide binding sites of CF1. *Res. Photosynth* II.8, 745–748.

Furuike, S., Hossain, M. D., Maki, Y., Adachi, K., Suzuki, T., Kohori, A., et al. (2008). Axle-less F_1-ATPase rotates in the correct direction. *Science* 319, 955–958. doi: 10.1126/science.1151343

Furuike, S., Nakano, M., Adachi, K., Noji, H., Kinosita, K., and Yokoyama, K. (2011). Resolving stepping rotation in *Thermus thermophilus* H^+-ATPase/synthase with an essentially drag-free probe. *Nat. Commun.* 2:233. doi: 10.1038/ncomms1215

Greene, M. D., and Frasch, W. D. (2003). Interactions between γR268, γQ269 and the β subunit catch-loop of *E. coli* F_1-ATPase are critical for catalytic activity. *J. Biol. Chem.* 278, 51594–51598. doi: 10.1074/jbc.M309948200

Guo, H., and Rubinstein, J. (2022). Structure of ATP synthase under strain during catalysis. *Nat. Commun.* 13:2232. doi: 10.1038/s41467-022-29893-2

Guo, H., Courbon, G. M., Bueler, S. A., Mai, J., Liu, J., and Rubinstein, J. L. (2021). Structure of mycobacterial ATP synthase bound to the tuberculosis drug bedaquiline. *Nature* 589, 143–147. doi: 10.1038/s41586-020-3004-3

Haddy, A. B., Frasch, W. D., and Sharp, R. R. (1985). Cooperative binding of manganese to the soluble chloroplast ATP synthase measured by NMR proton relaxation enhancement. *Biochemistry* 24, 7926–7930. doi: 10.1021/bi00348a012

Haddy, A. E., Frasch, W. D., and Sharp, R. R. (1989). Properties of the manganese(II) binding site in ternary complexes of Mn•ADP and Mn•ATP with chloroplast coupling factor 1: magnetic field dependence of solvent ^1H and ^2H NMR relaxation rates. *Biochemistry* 28, 3664–3669. doi: 10.1021/bi00435a007

Haddy, A., Sharp, R. R., and Frasch, W. D. (1987). Characterization of the Mn(II) binding site of chloroplast coupling factor one: proton magnetic relaxation field dependence. *Prog. Photosynth. Res.* 3, 119–122. doi: 10.1007/978-94-017-0516-5_26

Hahn, A., Vonck, J., Mills, D., Meier, T., and Kühlbrandt, W. (2018). Structure, mechanism, and regulation of the chloroplast ATP synthase. *Science* 360, eaat:4318. doi: 10.1126/science.aat4318

Hara, K. Y., Noji, H., Bald, D., Yasuda, R., Kinosita, K., and Yoshida, M. (2000). The role of the DELSEED motif of the b-subunit in rotation of F_1-ATPase. *J. Biol. Chem.* 275, 14260–14263. doi: 10.1074/jbc.275.19.14260

Hartzog, P. E., and Cain, B. D. (1994). Second-site suppressor mutations at glycine 218 and histidine 245 in the a subunit of F_1F_0 ATP synthase in Escherichia coli. *J. Biol. Chem.* 269, 32313–32317. doi: 10.1016/S0021-9258(18)31637-5

Hatch, L. P., Cox, G. B., and Howitt, S. M. (1995). The essential arginine residue at position 210 in the alpha subunit of the Escherichia coli ATP synthase can be transferred to position 252 with partial retention of activity. *J. Biol. Chem.* 270, 29407–29412. doi: 10.1074/jbc.270.49.29407

Hirono-Hara, Y., Noji, H., Muniyuki, E., Hara, K. Y., Yasuda, R., Kinosita, K., et al. (2001). Pause and rotation of F_1-ATPase during catalysis. *Proc. Natl. Acad. Sci. U. S. A.* 98, 13649–13654. doi: 10.1073/pnas.241365698

Hornung, T., Ishmukhametov, R., Spetzler, D., Martin, J., and Frasch, W. D. (2008). Determination of torque generation from the power stroke of *Escherichia coli* F_1-ATPase. *Biochim. Biophys. Acta- Bioenergetics* 1777, 579–582. doi: 10.1016/j.bbabio.2008.04.016

Hornung, T., Martin, J., Ishmukhametov, R., Spetzler, D., and Frasch, W. D. (2011). Microsecond resolution of single molecule rotation catalyzed by molecular motors. *Methods Mol. Biol.* 778, 273–289. doi: 10.1007/978-1-61779-261-8_18

Hossain, M. D., Furuike, S., Maki, Y., Adachi, K., Ali, M. Y., Huq, M., et al. (2006). The rotor tip inside a bearing of a thermophilic F_1-ATPase is dispensable for torque generation. *Biophys. J.* 90, 4195–4203. doi: 10.1529/biophysj.105.079087

Hossain, M. D., Furuike, S., Maki, Y., Adachi, K., Suzuki, T., Kohori, A., et al. (2008). Niether helix in the coiled-coil region of the axle of F_1-ATPase plays a significant role in torque production. *Biophys. J.* 95, 4837–4844. doi: 10.1529/biophysj.108.140061

Houseman, A. L. P., Bell, M. K., LoBrutto, R., and Frasch, W. D. (1995b). The participation of metals in the CF_1-ATPase mechanism. *Photosynthesis: from Light to Biosphere* 3, 127–130.

Houseman, A., LoBrutto, R., and Frasch, W. D. (1994b). The coordination of nucleotides to the metals at the M2 and M3 metal-binding sites of the spinach chloroplast F_1-ATPase. *Biochemistry* 33, 10000–10006. doi: 10.1021/bi00199a025

Houseman, A., LoBrutto, R., and Frasch, W. D. (1995a). Effects of nucleotides on the ligands of the metals at the M2 and M3 metal-binding sites of the spinach chloroplast F_1-ATPase. *Biochemistry* 34, 3277–3285. doi: 10.1021/bi00010a018

Houseman, A., Morgan, L., LoBrutto, R., and Frasch, W. D. (1994a). Characterization of ligands of a high affinity metal binding site in the latent chloroplast F_1-ATPase by EPR spectroscopy of bound VO^{2+}. *Biochemistry* 33, 4910–4917. doi: 10.1021/bi00182a020

Howitt, S. M., Lightowlers, R. N., Gibson, F., and Cox, G. B. (1990). Mutational analysis of the function of the a-subunit of the F_0F_1-APPase of *Escherichia coli*. *Biochim. Biophys. Acta* 1015, 264–268. doi: 10.1016/0005-2728(90)90030-8

Hu, C.-Y., Chen, W., and Frasch, W. D. (1999). Metal ligation by Walker homology B aspartate βD262 at site 3 of the latent but not activated form of the chloroplast F_1-ATPase from *Chlamydomonas reinhardtii*. *J. Biol. Chem.* 274, 30481–30486. doi: 10.1074/jbc.274.43.30481

Hu, C.-Y., Houseman, A. L. P., Morgan, L., Webber, A. N., and Frasch, W. D. (1995). Catalytic function of a vital carboxylate residue in the β subunit of the CF1-ATPase from Creinhardtii. *Photosynthesis: from Light to Biosphere* 3, 131–134. doi: 10.1007/978-94-009-0173-5_487

Hu, C.-Y., Houseman, A. L. P., Morgan, L., Webber, A. N., and Frasch, W. D. (1996). Catalytic and EPR studies of the E204Q mutant of the β subunit of the chloroplast F_1-ATPase from *Chlamydomonas reinhardtii*. *Biochemistry* 35, 12201–12211. doi: 10.1021/bi961105a

Hwang, W., and Karplus, M. (2019). Structural basis for power stroke vs. Brownian ratchet mechanisms of motor proteins. *Proc. Nat. Acad. Sci. USA* 116, 19777–19785. doi: 10.1073/pnas.1818589116

Hyndman, D. J., Milgrom, Y. M., Bramhall, E. A., and Cross, R. L. (1994). Nucleotide-binding sites on Escherichia coli F1-ATPase. Specificity of noncatalytic sites and inhibition at catalytic sites by MgADP. *J. Biol. Chem.* 269, 28871–28877. doi: 10.1016/S0021-9258(19)61988-5

Iida, T., Minigawa, Y., Ueno, H., Kawai, F., Murata, T., and Iino, R. (2019). Single-molecule analysis reaveals rotational substeps and chemo-mechanical coupling scheme of *enterococcus hirae* V_1-ATPase. *J. Biol. Chem.* 294, 17017–17030. doi: 10.1074/jbc.RA119.008947

Ishmukhametov, R., Hornung, T., Spetzler, D., and Frasch, W. D. (2010). Direct observation of stepped proteolipid ring rotation in *E. coli* F_oF_1-ATP synthase. *EMBO J.* 29, 3911–3923. doi: 10.1038/emboj.2010.259

Junge, W., Sielaff, H., and Engelbrecht, S. (2009). Torque generation and elastic power transmission in the rotary F_OF_1-ATPase. *Nature* 459, 364–370. doi: 10.1038/nature08145

Kato, Y., Sassayama, T., Muneyuki, E., and Yoshida, M. (1995). Analysis of time-dependent change of *Escherichia coli* F_1-ATPase activity and its relationship with apparent negative cooperativity. *Biochim. Biophys. Acta* 1231, 275–281. doi: 10.1016/0005-2728(95)00087-Y

Kinosita, K., Adachi, K., and Itoh, H. (2004). Rotation of F_1-ATPase: how an ATP-driven molecular machine may work. *Ann. Rev. Biophys. Biomol. Struct.* 33, 245–268. doi: 10.1146/annurev.biophys.33.110502.132716

Kinosita, K., Yasuda, R., Noji, H., and Adachi, K. (2000). A rotary molecular motor that can work at near 100% efficiency. *Philos. Trans. R. Soc. London B Biol. Sci.* 355, 473–489. doi: 10.1098/rstb.2000.0589

Kobayashi, R., Ueno, H., Li, C.-B., and Noji, H. (2020). Rotary catalysis of bovine mitochondrial F_1-ATPase studied by single-molecule experiments. *Proc. Natl. Acad. Sci. U. S. A.* 117, 1447–1456. doi: 10.1073/pnas.1909407117

Koga, N., and Takada, S. (2006). Folding-based molecular simulations reveal mechanism of the rotary motor F_1-ATPase. *Proc. Natl. Acad. Sci. U. S. A.* 103, 5367–5372. doi: 10.1073/pnas.0509642103

Kohori, A., Chiwata, R., Hossain, M. D., Furuike, S., Shiroguchi, K., Adachi, K., et al. (2011). Torque generation in F_1-ATPase devoid of the entire amino-terminal helix of the rotor that fills half of the stator orifice. *Biophys. J.* 101, 188–195. doi: 10.1016/j.bpj.2011.05.008

Kühlbrandt, W. (2019). Structure and mechanism of F-type ATP synthases. *Annu. Rev. Biochem.* 88, 515–549. doi: 10.1146/annurev-biochem-013118-110903

Lightowlers, R. N., Howitt, S. M., Hatch, L., Gibson, F., and Cox, G. B. (1988). The proton pore in the *Escherichia coli* F_oF_1-ATPase: substitution of glutamate by glutamine at position 219 of the alpha-subunit prevents F_o-mediated proton permeability. *Biochim. Biophys. Acta* 933, 241–248. doi: 10.1016/0005-2728(88)90031-X

Lowry, D., and Frasch, W. D. (2005). Interactions between βD372 and γ-subunit N-terminus residues γK9 and γS12 are important for ATP synthase activity catalyzed by the *E. coli* F_oF_1 ATP synthase. *Biochemistry* 44, 7275–7281. doi: 10.1021/bi047293j

Marciniak, A., Chodnicki, P., Hossain, K. A., Slabonska, J., and Czub, J. (2022). Determinants of directionality and efficiency of the ATP synthase F_O motor at atomic resolution. *J. Phys. Chem. Lett.* 13, 387–392. doi: 10.1021/acs.jpclett.1c03358

Mark, J. E., Eisenberg, A., Graessley, W. W., Mandelkern, L., and Koenig, J. L. (1993). *Physical Properties of Polymers*. American Chemical Society, (Washington, DC), *2nd Ed*.

Martin, J., Hornung, T., Ishmukhametov, R., Spetzler, D., and Frasch, W. D. (2018). Elastic coupling power stroke mechanism of the F_1-ATPase molecular motor. *Proc. Natl. Acad. Sci. U. S. A.* 115, 5750–5755. doi: 10.1073/pnas.1803147115

Martin, J., Hudson, J., Hornung, T., and Frasch, W. D. (2015). F_o-driven power stroke rotation occurs against the force of F_1ATPase-dependent rotation in the F_oF_1 ATP synthase. *J. Biol. Chem.* 290, 10717–10728. doi: 10.1074/jbc.M115.646430

Martin, J., Ishmukhametov, R., Hornung, T., Ahmad, Z., and Frasch, W. D. (2014). Anatomy of F_1-ATPase powered rotation. *Proc. Natl. Acad. Sci. U. S. A.* 111, 3715–3720. doi: 10.1073/pnas.1317784111

Menz, R. I., Walker, J. E., and Walker, J. E. (2001). Structure of bovine mitochondrial F_1-ATPase with nucleotide bound to all three catalytic sites: implications for the mechanism of rotary catalysis. *Cell* 106, 331–341. doi: 10.1016/S0092-8674(01)00452-4

Mo, K., Zhang, Y., Dong, Z., Yang, Y., Ma, X., Feringa, B. L., et al. (2022). Intrinsically unidirectional chemically fueled rotary molecular motors. *Nature*. doi: 10.1038/s41586-022-05033-0

Mnatsakanyan, N., Hook, J. A., Quisenberry, L., and Weber, J. (2009). ATP synthase with its gamma subunit reduced to the N-terminal helix can still catalyze ATP synthesis. *J. Biol. Chem.* 284, 26519–26525. doi: 10.1074/jbc.M109.030528

Mukherjee, S., and Warshel, A. (2011). Electrostatic origin of the mechanochemical rotary mechanism and the catalytic dwell of F_1-ATPase. *Proc. Natl. Acad. Sci. U. S. A.* 108, 20550–20555. doi: 10.1073/pnas.1117024108

Mukherjee, S., and Warshel, A. (2015). Dissecting the role of the γ-subunit in the rotary-chemical coupling and torque generation of F_1-ATPase. *Proc. Natl. Acad. Sci. U. S. A.* 112, 2746–2751. doi: 10.1073/pnas.1500979112

Müller, M., Pänke, O., Junge, W., and Engelbrecht, S. (2002). F_1-ATPase, the C-terminal end of subunit γ is not required for ATP hydrolysis-driven rotation. *J. Biol. Chem.* 277, 23308–23313. doi: 10.1074/jbc.M201998200

Murphy, B. J., Klusch, N., Langer, J., Mills, D. J., Yildiz, Ö., and Kühlbrandt, W. (2019). Rotary substates of mitochondrial ATP synthase reveal the basis of flexible F1-FO coupling. *Science* 364:eaaw9128. doi: 10.1126/science.aaw9128

Nakanishi-Matsui, M., Kashiwagi, S., Hosokawa, H., Cipriano, D. J., Dunn, S. D., Wada, Y., et al. (2006). Stochastic high-speed rotation of *Escherichia coli* ATP synthase F_1 sector: The ε subunit-sensitive rotation. *J. Biol. Chem.* 281, 4126–4131. doi: 10.1074/jbc.M510090200

Neukirch, S., Goriely, A., and Hausrath, A. C. (2008). Chirality of coiled coils: elasticity matters. *Phys. Rev. Lett.* 100:038105. doi: 10.1103/PhysRevLett.100.038105

Noji, H., Yasuda, R., Yoshida, M., and Kinosita, K. (1997). Direct observation of the rotation of F_1-ATPase. *Nature* 386, 299–302. doi: 10.1038/386299a0

O'Neal, C. C., and Boyer, P. D. (1984). Assessment of the rate of bound substrate interconversion and of ATP acceleration of product release during catalysis by mitochondrial adenosine triphosphatase. *J. Biol. Chem.* 259, 5761–5767. doi: 10.1016/S0021-9258(18)91079-3

Pänke, O., Cherepanov, D. A., Gumbiowski, K., Engelbrecht, S., and Junge, W. (2001). Viscoelastic dynamics of actin filaments coupled to rotary F-ATPase: angular torque profile of the enzyme. *Biophys. J.* 81, 1220–1233. doi: 10.1016/S0006-3495(01)75780-3

Panyukov, S., and Rabin, Y. (2000). Thermal fluctuations of elastic filaments with spontaneous curvature and torsion. *Phys. Rev. Lett.* 85, 2404–2407. doi: 10.1103/PhysRevLett.85.2404

Pinke, G., Zhou, L., and Sazanov, L. (2020). Cryo-EM structure of the entire mammalian F-type ATP synthase. *Nat. Struct. Molec. Bio.* 27, 1077–1085. doi: 10.1038/s41594-020-0503-8

Pogoryelov, D., Krah, A., Langer, J. D., Yildiz, Ö., Faraldo-Gómez, J. D., and Meier, T. (2010). Microscopic rotary mechanism of ion translocation in the F_O complex of ATP synthases. *Nat. Chem. Bio.* 6, 891–899. doi: 10.1038/nchembio.457

Pu, J., and Karplus, M. (2008). How subunit coupling produces the gamma-subunit rotary motion in F_1-ATPase. *Proc. Natl. Acad. Sci. U. S. A.* 105, 1192–1197. doi: 10.1073/pnas.0708746105

Ragunathan, R., Sielaff, H., Sundararaman, L., Biukovic, G., Sony, M., Manimekalai, S., et al. (2017). The uniqueness of subunit α of mycobacterial F-ATP synthases: An evolutionary variant for niche adaptation. *J. Biol. Chem.* 292, 11262–11279. doi: 10.1074/jbc.M117.784959

Rees, D., Montgomery, M., Leslie, A., and Walker, J. E. (2012). Structural evidence of a new catalytic intermediated in the pathway of ATP hydrolysis by F_1-ATPase from bovine heart mitochondria. *Proc. Natl. Acad. Sci. U. S. A.* 109, 11139–11143. doi: 10.1073/pnas.1207587109

Richter, M. L., Snyder, B., McCarty, R. E., and Hammes, G. G. (1985). Binding stoichiometry and structural mapping of the epsilon polypeptide of chloroplast coupling factor 1. *Biochemistry* 24, 5755–5763. doi: 10.1021/bi00342a011

Roh, S.-H., Shekhar, M., Pintilir, G., Chipot, C., Wilkens, S., Singaroy, A., et al. (2020). Cryo-EM and MD infer water-mediated proton transport and autoinhibition of VO complex. *Sci. Adv.* 6:eabb9605. doi: 10.1126/sciadv.abb9605

Sabbert, D., Engelbrecht, S., and Junge, W. (1996). Intersubunit rotation in active F-ATPase. *Nature* 381, 623–625. doi: 10.1038/381623a0

Saita, E.-I., Suzuki, T., Kinosita, K., and Yoshida, M. (2015). Simple mechanism whereby the F_1-ATPase motor rotates with near-perfect chemomechanical energy conversion. *Proc. Natl. Acad. Sci. U. S. A.* 112, 9626–9631. doi: 10.1073/pnas.1422885112

Sekiya, M., Hosokawa, H., Nakanashi-Matsui, M., Al-Shawi, M. K., Nakamoto, R. K., and Futai, M. (2010). Single molecule behavior of inhibited and active states of Escherichia coli ATP synthase F_1 rotation. *J. Biol. Chem.* 285, 40258–42067. doi: 10.1074/jbc.M110.176701

Shah, N. B., Hutcheon, M. L., Haarer, B. K., and Duncan, T. M. (2013). F_1-ATPase of *Escherichia coli*: The ε-inhibited state forms after ATP hydrolysis, is distinct form the ADP-inhibited state, and responds dynamically to catalytic site ligands. *J. Biol. Chem.* 288, 9383–9395. doi: 10.1074/jbc.M113.451583

Shimabukuro, K., Yasuda, R., Muneyuki, E., Hara, K., Kinosita, K., and Yoshida, M. (2003). Catalysis and rotation of F_1 motor: cleavage of ATP at the catalytic site occurs in 1 ms before 40 degree substep rotation. *Proc. Natl. Acad. Sci. U. S. A.* 100, 14731–14736. doi: 10.1073/pnas.2434983100

Sielaff, H., Martin, J., Singh, D., Biukovic, G., Grüber, G., and Frasch, W. D. (2016). Power stroke angular velocity profiles of archaeal A-ATP synthase versus thermophilic and mesophilic F-ATP synthase molecular motors. *J. Biol. Chem.* 291, 25351–25363. doi: 10.1074/jbc.M116.745240

Sielaff, H., Rennekamp, H., Wächter, A., Xie, H., Hilbers, F., Feldbauer, K., et al. (2008). Domain compliance and elastic power transmission in rotary F_OF_1-ATPase. *Proc. Natl. Acad. Sci. U. S. A.* 105, 17760–17765. doi: 10.1073/pnas.0807683105

Sielaff, H., Yanagisawa, S., Frasch, W., Junge, W., and Börsch, M. (2019). Structural asymmetry and kinetic limping of single rotary F-ATP synthases. *Molecules* 24, 504–529. doi: 10.3390/molecules24030504

Sobti, M., Smits, C., Wong, A. S. W., Ishmukhametov, R., Stock, D., Sandin, S., et al. (2016). Cryo-EM structures of the autoinhibited E. coli ATP synthase in three rotational states. *eLife* 5:21598. doi: 10.7554/eLife.21598

Sobti, M., Ueno, H., Noji, H., and Stewart, A. G. (2021). The six steps of the complete F_1-ATPase rotary catalytic cycle. *Nat. Commun.* 12:4690. doi: 10.1038/s41467-021-25029-0

Sobti, M., Walshe, J., Wu, D., Ishmukhametov, R., Zeng, Y. C., Robinson, C. V., et al. (2020). Cryo-EM structures provide insight into how *E. coli* F_1F_O ATP synthase accommodates symmetry mismatch. *Nat. Commun.* 11:2615. doi: 10.1038/s41467-020-16387-2

Spetzler, D., Ishmukhametov, R., Day, L. J., Hornung, T., Martin, J., and Frasch, W. D. (2009). Single molecule measurements of F_1-ATPase reveal an interdependence between the power stroke and the dwell duration. *Biochemistry* 48, 7979–7985. doi: 10.1021/bi9008215

Spetzler, D., Ishmukhametov, R., Hornung, T., Martin, J., York, J., Jin-Day, L., et al. (2012). "Photosynthesis: plastid biology, energy conversion and carbon assimilation. Advances in Photosynthesis and Respiration," in *Energy Transduction by the Two Molecular Motors of the F_1F_o ATP Synthase. Vol. 34.* eds. J. J. Eaton-Rye, B. C. Tripathy and T. D. Sharkey (Dordrecht, The Netherlands: Springer), 561–590.

Spetzler, D., York, J., Lowry, D., Daniel, D., Fromme, R., and Frasch, W. D. (2006). Microsecond time resolution of single molecule F_1-ATPase rotation. *Biochemistry* 45, 3117–3124. doi: 10.1021/bi052363n

Spetzler, D., York, J., Dobbin, C., Martin, J., Xiong, F., Ishmukhametov, R., et al. (2007). Recent developments of biomolecular motors as on-Chip devices using single molecule techniques. *Lab Chip* 7, 1633–1643. doi: 10.1039/b711066a

Spikes, T. E., Montgomery, M. G., and Walker, J. E. (2020). Structure of the dimeric ATP synthase from bovine mitochondria. *Proc. Natl. Acad. Sci. U. S. A.* 117, 23519–23526. doi: 10.1073/pnas.2013998117

Srivastava, A. P., Lou, M., Zhou, W., Symersky, J., Bai, D., Chambers, M. G., et al. (2018). High-resolution cryo-EM analysis of the yeast ATP synthase in a lipid membrane. *Science* 360:eaas9699. doi: 10.1126/science.aas9699

Suzuki, T., Tanaka, K., Wakabayashi, C., Saita, E.-I., and Yoshida, M. (2014). Chemomechanical coupling of human mitochondrial F1-ATPase motor. *Nature Chem. Biol.* 10, 930–936. doi: 10.1038/nchembio.1635

Treloar, L. R. G. (1975). *The Physics of Rubber Elasticity*. Oxford University Press, London.

Usukura, E., Suzuki, T., Furuike, S., Soga, N., Saita, E., Hisabori, T., et al. (2012). Torque generation and utilization in motor enzyme F_OF_1-ATP synthase: half-torque F_1 with short-sized pushrod helix and reduced ATP synthesis by half-torque F_OF_1. *J. Biol. Chem.* 287, 1884–1891. doi: 10.1074/jbc.M111.305938

Vahidi, S., Bi, Y., Dunn, S. D., and Konermann, L. (2016). Load-dependent destabilization of the g-rotor shaft in F_OF_1 ATP synthase revealed by hydrogen/deuterium-exchange mass spectrometry. *Proc. Natl. Acad. Sci USA* 113, 2412–2417. doi: 10.1073/pnas.1520464113

Vik, S., Cain, B., Chun, K., and Simoni, R. (1988). Mutagenesis of the a subunit of the F_1F_O-ATPase from *Escherichia coli*. Mutations at glu-196, pro-190, and ser-199. *J. Biol. Chem.* 263, 6599–6605. doi: 10.1016/S0021-9258(18)68683-1

Wang, H., and Oster, G. (1998). Energy transduction in the F_1 motor of ATP synthase. *Nature* 396, 279–282. doi: 10.1038/24409

Watanabe, R., Minagawa, Y., and Noji, H. (2014). Thermodynamic analysis of F_1-ATPase rotary catalysis using high-speed imaging. *Protein Sci.* 23, 1773–1779. doi: 10.1002/pro.2559

Weber, J., and Senior, A. E. (1997). Catalytic mechanism of F_1-ATPase. *Biochim. Biophys. Acta* 1319, 19–58. doi: 10.1016/S0005-2728(96)00121-1

Weber, J., and Senior, A. E. (2001). Bi-site catalysis in F_1-ATPase: does it exist? *J. Biol. Chem.* 276, 35422–35428. doi: 10.1074/jbc.M104946200

Weber, J., Wilke-Mounts, S., Lee, R. S., Grell, E., and Senior, A. E. (1993). Specific placement of tryptophan in the catalytic sties of *Escherichia coli* F_1-ATPase provides a direct probe of nucleotide binding: maximal ATP hydrolysis occurs with three sites occupied. *J. Biol. Chem.* 268, 20126–20133. doi: 10.1016/S0021-9258(20)80703-0

White, S., and Whimley, W. C. (1999). Membrane protein folding and stability: physical principals. *Ann. Rev. Biophys. Biomol. Struct.* 28, 319–365. doi: 10.1146/annurev.biophys.28.1.319

Wolgemuth, C. W., and Sun, S. X. (2006). Elasticity of alpha-helical coiled coils. *Phys. Rev. Lett.* 97:248101. doi: 10.1103/PhysRevLett.97.248101

Wraight, C. A. (2006). Chance and design-proton transfer in water, channels and bioenergetic proteins. *Biochim. Biophys. Acta* 1757, 886–912. doi: 10.1016/j.bbabio.2006.06.017

Yanagisawa, S., and Frasch, W. D. (2017). Protonation dependent stepped rotation of the F-type ATP synthase c-ring observed by single-molecule measurements. *J. Biol. Chem.* 292, 17093–17100. doi: 10.1074/jbc.M117.799940

Yanagisawa, S., and Frasch, W. D. (2021). pH-dependent 11° F1FO ATP synthase sub-steps reveal insight into the FO torque generating mechanism. *eLife* 10:e70016. doi: https://doi.org/10.7554/eLife.70016

Yasuda, K., Noji, H., Yoshida, M., Kinosita, K., and Itoh, H. (2001). Resolution of distinct rotational substeps by submillisecond kinetic analysis of F_1-ATPase. *Nature* 410, 898–904. doi: 10.1038/35073513

Yasuda, R., Noji, H., Kinosita, K. Jr., and Yoshida, M. (1998). F_1ATPase is a highly efficient molecular motor that rotates with discrete 120° steps. *Cell* 93, 1117–1124. doi: 10.1016/S0092-8674(00)81456-7

York, J., Spetzler, D., Hornung, T., Ishmukhametov, R., Martin, J., and Frasch, W. D. (2007). Abundance of *Escherichia coli* F_1-ATPase molecules observed to rotate via single-molecule microscopy with gold nanorod probes. *J. Bioenergetics Biomembranes* 39, 435–439. doi: 10.1007/s10863-007-9114-x

York, J., Spetzler, D., Xiong, F., and Frasch, W. D. (2008). Single molecule detection of DNA via sequence-specific links between F_1-ATPase motors and gold Nanorod sensors. *Lab Chip* 8, 415–419. doi: 10.1039/b716744j

Zarco-Zavala, M., Watanabe, R., McMillan, G. G., Suzuki, T., Ueno, H., Mendoza-Hoffmann, F., et al. (2020). The 3 x 120° rotary mechanism of *Paracoccus denitrificans* F_1-ATPase is different from that of the bacterial and mitochondrial F_1-ATPases. *Proc. Natl. Acad. Sci. U. S. A.* 117, 29647–29657. doi: 10.1073/pnas.2003163117

Zhou, A., Rohou, A., Schep, D. G., Bason, J. V., Montgomery, M. G., Walker, J. E., et al. (2015). Structure and conformational states of the bovine mitochondrial ATP synthase by cryo-EM. *eLife* 4:e10180. doi: 10.7554/eLife.10180

Zhou, Y., Duncan, T., Bulygin, V., Hutcheon, M., and Cross, R. (1996). ATP hydrolysis by membrane-bound *Escherichia coli* F_OF_1 causes rotation of the gamma subunit relative the beta subunits. *Biochim. Biophys. Acta* 1275, 96–100. doi: 10.1016/0005-2728(96)00056-4

frontiers | Frontiers in Microbiology

REVIEW
published: 16 June 2022
doi: 10.3389/fmicb.2022.872565

Rotational Mechanism of F_O Motor in the F-Type ATP Synthase Driven by the Proton Motive Force

Shintaroh Kubo[1*†] *and Shoji Takada*[2*†]

[1] Department of Anatomy and Cell Biology, McGill University, Montreal, QC, Canada, [2] Department of Biophysics, Graduate School of Science, Kyoto University, Kyoto, Japan

In F_OF_1 ATP synthase, driven by the proton motive force across the membrane, the F_O motor rotates the central rotor and induces conformational changes in the F_1 motor, resulting in ATP synthesis. Recently, many near-atomic resolution structural models have been obtained using cryo-electron microscopy. Despite high resolution, however, static information alone cannot elucidate how and where the protons pass through the F_O and how proton passage is coupled to F_O rotation. Here, we review theoretical and computational studies based on F_O structure models. All-atom molecular dynamics (MD) simulations elucidated changes in the protonation/deprotonation of glutamate—the protein-carrier residue—during rotation and revealed the protonation states that form the "water wire" required for long-range proton hopping. Coarse-grained MD simulations unveiled a free energy surface based on the protonation state and rotational angle of the rotor. Hybrid Monte Carlo and MD simulations showed how proton transfer is coupled to rotation.

Keywords: F_OF_1 ATP synthases, F_O motor, molecular dynamics simulations, coarse-grained model, Monte Carlo simulations

OPEN ACCESS

Edited by:
Tom Duncan,
Upstate Medical University,
United States

Reviewed by:
Jacek Czub,
Gdansk University of Technology, Poland
Abhishek Singharoy,
Arizona State University, United States

***Correspondence:**
Shintaroh Kubo
shintaroh.kubo@mail.mcgill.ca
Shoji Takada
takada@biophys.kyoto-u.ac.jp

† These authors have contributed equally to this work

Specialty section:
This article was submitted to Microbial Physiology and Metabolism, a section of the journal Frontiers in Microbiology

Received: *09 February 2022*
Accepted: *20 April 2022*
Published: *16 June 2022*

Citation:
Kubo S and Takada S (2022) Rotational Mechanism of F_O Motor in the F-Type ATP Synthase Driven by the Proton Motive Force. Front. Microbiol. 13:872565. doi: 10.3389/fmicb.2022.872565

INTRODUCTION

F_OF_1 ATP synthase, a ubiquitous enzyme that synthesizes most ATP in living cells, comprises two rotary motors: the membrane-embedded proton-driven F_O motor and the catalytic F_1 motor; these motors share the central rotor and peripheral stalk. The F_O motor harbors a ring-shaped c-subunit oligomer, which serves as the rotor, and an a-subunit (stator), which mediates proton transfer between the c-ring and outer membrane aqueous environment [matrix and intermembrane space (IMS) of mitochondrial ATP synthase]. The a-subunit possesses two half-channels [confirmed for bacterial, mitochondrial (Srivastava et al., 2018; Spikes et al., 2020), and chloroplast (Hahn et al., 2018) F_O motors]. One exchanges protons with IMS or outside the cell, and the other shuttles protons between the matrix and cytoplasm. Since these two half-channels are not directly connected, protons can only pass through the membrane *via* rotation of the c-ring. Therefore, the passage of protons through the membrane is coupled to the rotational motion of the c-ring (**Figure 1A**).

Recent cryo-electron microscopic (EM) studies have elucidated details of F_O rotary mechanisms. For instance, Klusch et al. (2017) confirmed that the two half-channels of the a-subunit harbor continuous spaces through which protons can pass from the matrix/IMS region to the key residues responsible for proton transport in the c-subunit. In the c-ring, the key residues for proton transport receive and pass protons *via* protonation and deprotonation,

respectively. Pogoryelov et al. (2010) elucidated the c-ring structure of F_O in *Spirulina platensis* and reported that the key residues are in a proton-locked conformation in the lipid membrane environment and in a proton-unlocked conformation in the hydrophilic environment, assuming an interface with the a-subunit. In addition, molecular dynamics (MD) simulations confirmed that these two states could move back and forth depending on the surrounding environment. Thus, high-resolution structures, together with MD simulations, have offered important insights into the proton pathway.

In the present review, we describe theoretical and computational studies aimed at clarifying the rotational mechanisms of the F_O motor in F_OF_1 ATP synthase. First, we present a chronological overview of the structural and theoretical studies on F_O. Next, we introduce a recent all-atom MD simulation study that examines how the conformation of side chains of the key residues changes depending on the protonation state and environment. All-atom MD simulations have provided substantial information on water molecule accessibility. The free energy profile of a transferring proton, including its pKa value, is briefly discussed. Then, we describe coarse-grained MD simulations, which allow for modeling large-scale dynamics. Coarse-grained MD simulations have revealed protonation state-dependent free energy surfaces. We explain a computational methodology to simulate proton transfer-coupled F_O rotation through a hybrid Monte Carlo/MD approach, which identified a preferred pathway in which two or three c-subunit key residues are deprotonated during a single rotational step. A recent biochemical experiment, together with the corresponding simulations, supports this view. Finally, we discuss the effects of a mutation of the conserved arginine of the a-subunit, the symmetry mismatch between F_O and F_1, and the coupling between side-chain reorientation of the c-subunit key residues and proton transfer-coupled F_O rotation.

OVERVIEW OF THEORETICAL MODELS OF THE F_O MOTOR

As the fundamental mechanism of proton transfer-driven F_O rotation, the model first proposed by Vik and Antonio (1994) has been widely accepted (**Figure 1A**). The model assumes the presence of two half-channels in F_O: one that shuttles protons from the IMS aqueous environment to the middle of the membrane, and the other that connects the middle of the membrane to the matrix-side aqueous environment. However, the two half-channels are not directly connected to the membrane. Instead, the end of each half-channel is close to a proton carrier amino acid in the middle of the F_O c-subunit such that the proton can be transferred between each half channel and the proton-carrier residue in the c-subunit. Importantly, the c-subunits connected to the two half-channels are not the same in the c-ring. Thus, for the proton to move across the membrane, c-ring rotation is obligatory. Vik and Antonio introduced various mutations in the half-channel residues on the cytoplasmic side of the a-subunit (aE219 in *Escherichia coli*) adjacent to the proton carrier acidic residue of the c-ring (cD61 in *E. coli*) and measured ATP hydrolysis-driven proton pump activity; the authors noted that the proton-accepting residue at the aE219 position is critical for proton transfer. Subsequently, Oster et al. extended the Vik and Antonio model to a quantitative mathematical model (Elston et al., 1998). In this model, the authors focused on switches in electrostatic attractions between protonated and deprotonated acidic residues of the c-ring (cD61 in *E. coli*) and the conserved arginine of the a-subunit (aR210 in *E. coli*), which serves key regulatory roles in enzyme function (**Figure 1B**, left). This model was also applied to sodium-transporting F_OF_1-ATPase, suggesting that it captures the universal nature of the F_O motor (Dimroth et al., 1999; Xing et al., 2004). Together, the results successfully explained the experimental data (Vik and Antonio, 1994), and many subsequent theoretical studies were based on these models. For example, Aksimentiev et al. used a low-resolution structure (Girvin et al., 1998; Rastogi and Girvin, 1999) which allowed for speculating the positional association between c-ring and a-subunit for their simulations. Consequently, in addition to distance, the angle of the c-ring relative to the conserved arginine of the a-subunit garnered attention, and their kinetic model was constructed to explain the experimental results (Aksimentiev et al., 2004). In summary, it was theoretically confirmed that the F_O motor achieves rotational motion by the kinetics of proton transfer and the associated effects of electrostatic interactions changing.

Then, cryo-EM revolutionized the resolution of structural information. In 2015, cryo-EM structural models of the F_O part were obtained at a resolution of ∼7 Å (Allegretti et al., 2015; Zhou et al., 2015). Interestingly, the a-subunit of F_O harbors two long helices within the membrane, which are highly tilted from the normal to the membrane surface, and the conserved arginine residue is located in the middle of these helices (**Figure 1C**). This structural model clearly support the half-channel model of Vik and Antonio (1994). Based on the structural information at that time, Warshel group performed coarse-grained MD simulations to evaluate the free energy surface depending on the rotation angle of the c-ring under fixed protonated/deprotonated conditions (Mukherjee and Warshel, 2011). In addition, more recent advances in cryo-EM allowed for obtaining the structure of F_O in mitochondrial, chloroplast, and bacterial ATP synthases at a resolution of ∼3–4 Å (Guo et al., 2017; Klusch et al., 2017; Hahn et al., 2018; Srivastava et al., 2018; Gu et al., 2019). With the higher resolution models, Warshel group re-performed similar coarse-grained MD simulations to more reliably evaluate the free energy surface (Bai and Warshel, 2019) because their earlier work assumed a different orientation of the a-subunit with respect to the c-ring. Moreover, Roh et al. (2020) and Marciniak et al. (2022) performed all-atom MD simulations to evaluate the free energy surface of F_O and V_O motors, respectively. We also performed hybrid Metropolis Monte Carlo (MC)/MD simulations of proton transfer-coupled F_O rotation, where proton transfer was mimicked by MC moves and the rotational motion of the F_O motor was simulated by MD (Kubo et al., 2020). This method is based on the constant-pH MD (Baptista et al., 2002; Mongan et al., 2004)

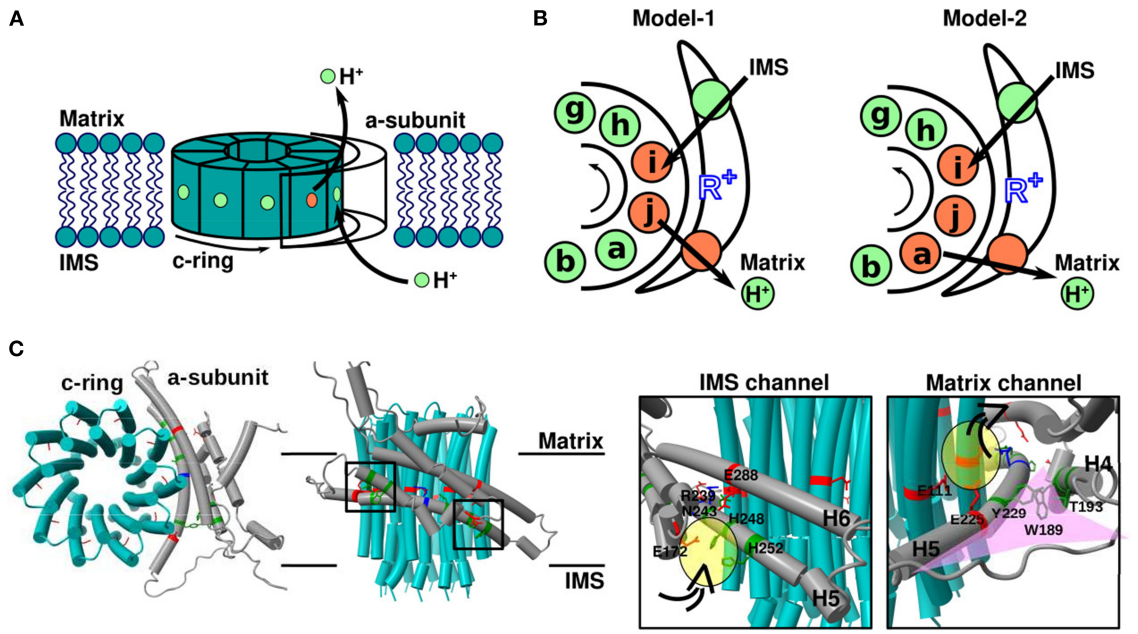


FIGURE 1 | Overview of the F_O motor. **(A)** Cartoon showing the geometry of the mitochondrial F_O motor. The rotational direction of the c-ring and movement of protons required for ATP synthesis are indicated. **(B)** Cartoons showing the mechanism of proton transfer between the a-subunit and c-ring. Green and orange spheres represent protonated (EH) and deprotonated (E^-) glutamate, respectively. Black arrows indicate the net proton flow during ATP synthesis. R^+ (blue) is a highly conserved arginine residue of the a-subunit. **(C)** Top (left) and side (middle) views of the mitochondrial F_O motor a-subunit (gray), and c-ring (cyan) (PDB ID: 6F36). Close-up (right) views of the square region in the middle cartoon. Representative residues with acidic, basic, and neutral side chains are indicated in red, blue, and green, respectively. The proton-carrier residue of c-subunit is cE111, the conserved arginine of a-subunit is aR239, and the representative residues of two half-channels are aE288 for the IMS channel and aE225 for the matrix channel. Water-accessible regions in the two half-channels, namely the IMS and matrix channels, are shown in yellow. The funnel-like space in the matrix channel is shown in pink.

and empirical valence bond (EVB) approaches (Kato et al., 2006; Olsson and Warshel, 2006), and similar approach, as called MCCE approach, used to study conformationally-dependent protonation states in Complex I (Khaniya et al., 2020). Note that as shown in **Figure 1B** (left), the proton-carrier residue in only one or two c-subunits can be deprotonated under rotation in the conventional model. For instance, Leone and Faraldo-Gómez (2016) predicted the possible c-ring rotational mechanism as follows: (1) only the *i*th c-subunit is deprotonated [denoted as DEP(c_i)]; (2) the protonated *j*th c-subunit releases protons to the matrix region; (3) c-ring rotates; (4) the *i*th c-subunit receives the proton from the IMS region; and (5) c-ring rotates and completes the 36° step rotation (Leone and Faraldo-Gómez, 2016). This mechanism can be represented as follows:

$$\mathrm{DEP}\,(c_i) \xrightarrow{\mathrm{deprot}} \mathrm{DEP}\,(c_i,\ c_j) \xrightarrow{\mathrm{rot}} \mathrm{DEP}\,(c_i,\ c_j) \xrightarrow{\mathrm{prot}} \mathrm{DEP}\,(c_j) \xrightarrow{\mathrm{rot}} \mathrm{DEP}\,(c_j)$$

In contrast, our MC/MD simulations (Kubo et al., 2020) and recent all-atom MD simulations (Marciniak et al., 2022) based on recent high-resolution structures suggested a new pathway, in which two or three c-subunits are simultaneously deprotonated under rotation, as shown in **Figure 1B** (right). This pathway can be described as follows:

$$\mathrm{DEP}\,(c_i,\ c_j) \xrightarrow{\mathrm{deprot}} \mathrm{DEP}\,(c_i,\ c_j,\ c_a) \xrightarrow{\mathrm{rot}} \mathrm{DEP}\,(c_i,\ c_j,\ c_a) \xrightarrow{\mathrm{prot}} \mathrm{DEP}\,(c_j,\ c_a) \xrightarrow{\mathrm{rot}} \mathrm{DEP}\,(c_j,\ c_a)$$

The results of our MC/MD simulations are described in greater detail below. Discrepancies between the two pathways may be due to the different species (the former was for F_O in *Polytomella* sp. and the latter for F_O in yeast). If two half-channels are close to each other, there is no space for an additional deprotonated c-subunit. Alternatively, these differences may arise from the resolution of the original cryo-EM maps (∼6.2 vs. 3.6 Å).

The hybrid MC/MD approach has many benefits for understanding mechanisms of molecular motors, in general. It can track conformational dynamics together with some elementary reactions, such as proton movements in the F_O motor. We have succeeded in theoretically reproducing the rotational motion of the F_O motor corresponding to the proton motion by combining MD and MC. Remarkably, the model that used the hybrid MC/MD approach rotated with a force equivalent to the torque confirmed in the experiment. However, it should be noted that these methods were based on many assumptions and have many limitations. Coarse-grained MD

does not take into account the side chains orientation, and the simulated time correspondence with the real time is not perfect. All-atom MD can solve these problems, but it is hard to handle the entire motion of a huge system such as a F_OF_1 motor at once because of the computational cost. The MC methods were able to treat the proton movement only empirically; nothing that is not designed happens. In principle, it is possible to handle the proton transfer by the hybrid quantum mechanics/molecular mechanics simulation, but the computational cost is way beyond the current reach. The hybrid MC/MD simulation we performed is a sort of compromise. Along this line, the constant-pH MD simulation is a closely related approach, in which protonation states in relevant amino acids are updated *via* MC processes. However, the commonly used constant-pH MD simulation allows appearance and disappearance of protons at any protonatable amino acids instead of considering the proton transfer from one site to the other. Thus, this cannot directly be used in the proton-transport study. This can be modified in a similar manner to the introduced hybrid MC/MD approach. Despite much room of improvement, the hybrid MC/MD approach has the advantage of being able to track proton and conformational motions with a high spatiotemporal resolution than experiments.

PROTON TRANSFER PATHWAY BASED ON ATOMIC-RESOLUTION STRUCTURE MODEL

Several high-resolution structural models have been obtained using cryo-EM, allowing unambiguous discussions on proton transfer pathways. Klusch et al. (2017) identified water-accessible channels in their mitochondrial ATP synthase structure model used the program Hollow (Ho and Gruswitz, 2008). Based on the water-accessible region and molecular model constructed from a map at 3.7 Å resolution, plausible proton transfer pathways across the membrane could be investigated. First, the pathway from the IMS to the c-ring involves the following two steps. (1) From the IMS aqueous environment, protons enter the a-subunit through the aqueous space around aE172, aH248, aH252, and aE288 (yellow oval in **Figure 1C**). (2) Then, protons pass through the space between aN243 (H5) and aE288 (H6), reaching the side chain of cE111 (chain-i in **Figure 1B**), which is protonated (the proton-carrier residue of the c-ring). The water-accessible region ends around aR239, which is a strictly conserved arginine residue of the a-subunit located between the two half-channels. Based on this pathway, aR239 plays a role in preventing direct proton jump between the two half-channels, which corresponds to proton leakage. Next, the pathway from the c-ring to the matrix-side aqueous space likely involves the following steps. (1) The proton-carrying cE111 (chain-a in **Figure 1B**) moves from the lipid-facing environment to the region that contacts the a-subunit (particularly H5) *via* c-ring rotation. (2) Then, cE111 releases the protons to exit into the matrix space. Because the side chain of aE225(H5) faces the c-ring and is expected to function as the end of the half-channel that reaches the matrix-side aqueous space, the proton passes from aE225 to the inside of the a-subunit and is released into the matrix space (yellow oval in **Figure 1C**). Notably, the orientation of the funnel-like space with H4–loop–H5 of the a-subunit with respect to the c-ring should be unaltered. Especially, it may be so essential for ATP synthase activity that H5 is positioned along the c-ring as discussed in (Klusch et al., 2017). For because residues aW189(H4), aT193(H4), and aY229(H5) are thought to contribute to maintaining the angle of the funnel-like tip, and mutations of these residues (or those present at the same position in other species) resulted in severe mitochondrial diseases (De Meirleir et al., 1995; Castagna et al., 2007; Cortés-Hernández et al., 2007). The mutations might cause wrong orientation of the H5 curvature along the c-ring, it would separate aE225 (matrix channel) from cE111 (proton carrier of the c-ring), and the distance between the c-ring and the channel will make it difficult for protons to transport. By the way, the subtlety of this pathway warrants discussion. Roh et al. (2020) identified a tightly bound lipid molecule in the cavity between the c-ring and a-subunit in the cytosol of the V_O motor (corresponding to the matrix side in the case of mitochondrial F_O). This tightly bound lipid molecule prevents the direct access of water molecules from the cytoplasm to the c-ring. It should be noted that V_O motor conformation has some notable difference from those of the F_O motor. For example, one of the c-subunits in the V_O is different from the others. Thus, it is not clear how well the mechanisms of Vo can be generalized to F_O. Therefore, it is unlikely that protons are directly released by the c-ring proton-carrying residues into the matrix-side aqueous space, as anticipated in Fo. Instead, the proton in the c-ring residue would be first transferred to the a-subunit proton-carrying residue, followed by release on the matrix side.

If atomic-resolution electron maps are available, water molecules can be directly traced to the channels. Roh et al. (2020) marked water molecules on a 2.7 Å map using the "Find Waters" routine available in Coot (Emsley et al., 2010) (blue dots in **Figure 2A**). The authors also performed all-atom MD simulations from a randomly arranged water molecule configuration and mapped the frequency of the water molecule positions (red spheres in **Figure 2A**). Thus, Coot mapping, in conjugation with all-atom MD simulations, is an effective method to evaluate where water molecules are released inside the water-accessible channel. The authors also found that water molecules reside between the half-channels and c-subunit, possibly enabling proton relay between the a- and c-subunits. Interestingly, the placement of relaying water molecules strongly depended on the protonation state of the proton-relaying residues; thus, the authors examined two different setups for the protonation states of glutamate. In the first setup, cE137 (the proton-carrying residue of the yeast V_O motor c-ring) was protonated and aE789 (the representative glutamate on the lumen side half-channel of the yeast V_O motor) was deprotonated (left panel in **Figure 2B**). In the second setup, the protonation states of the two glutamates were swapped (right panel in **Figure 2B**). A "water wire"—a single-file arrangement of water molecules—was stably formed between the protonated cE137 and the deprotonated aE789 (left panel in **Figure 2B**), but not in the other setup. Unidirectional transport of protons may occur through this wire.

Pogoryelov et al. (2010) illustrated the structure of proton-coupled c-ring in *S. platensis,* which gives structural insights

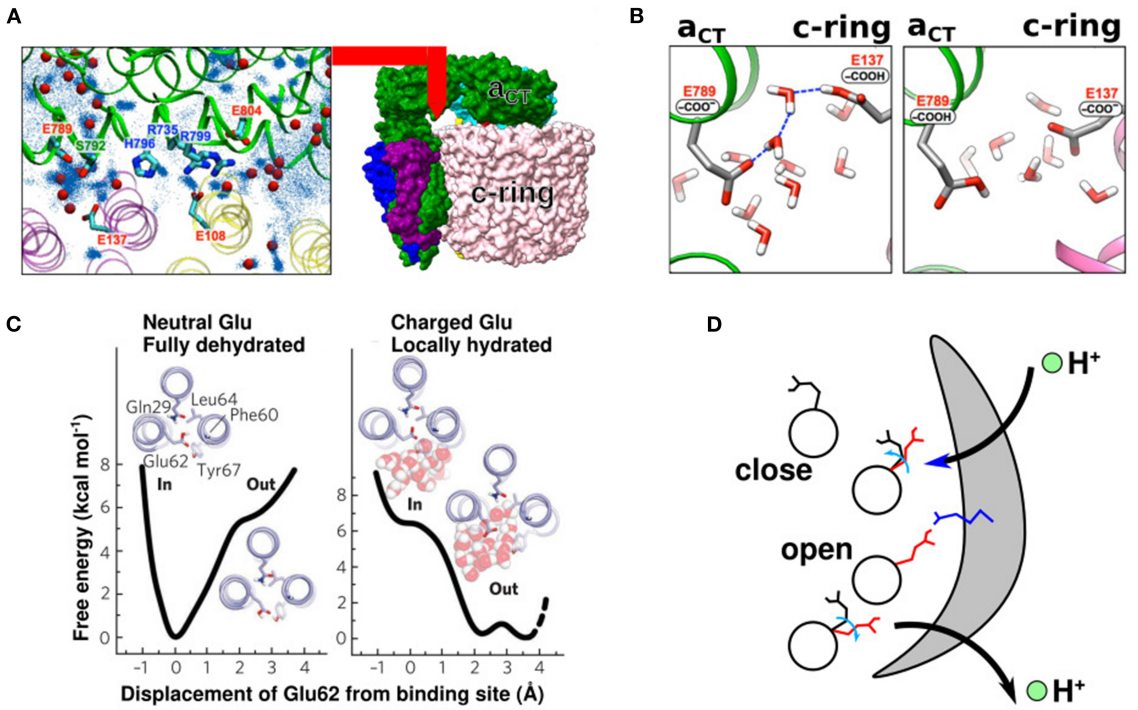


FIGURE 2 | Side-chain conformation coupled with the protonation states. **(A)** A 2.7 map of the V_O motor a-subunit (green) and c-ring (pink and yellow) (right panel). Water molecules near the interface between the α-subunit and c-ring (left panel). Red beads are defined by cryo-EM map and Coot function. Blue dots are defined by all-atom MD simulation (Roh et al., 2020) **(B)** Representative snapshot of all-atom MD simulation with protonated (left) and deprotonated (right) cE137. The left panel shows a water-wire (Roh et al., 2020) **(C)** Free energy surfaces of the closed Pogoryelov et al. (2010) and open conformations of cE62 in *S. platensis*. **(D)** Proton movement with changes in glutamate conformation. Black and red side chains indicate the closed and open glutamate conformation, respectively. Blue side chain indicates the highly conserved arginine of the a-subunit.

on the proton-transfer pathway. The side chains of the c-ring proton-carrier residues assume variable conformations depending on the protonation state and surrounding environment. Moreover, all-atom MD simulations confirmed that the orientation of the side chains of c-ring acidic proton-carrying residues changes depending on whether the residue faces the lipid membrane or a-subunit. When it faces the lipid membrane, the protonated side chain of the c-ring proton-carrier residue tends to face the inner side of the c-ring (proton-locked conformation) (left panel in **Figure 2C**). Meanwhile, when it faces the a-subunit, the deprotonated side chains face outward (deprotonated-extended conformation), facilitating proton transfer from the c-ring to the half-channels of the a-subunit (right panel in **Figure 2C**). These two conformations have also been reported in yeast V_O motors (Roh et al., 2020). Overall, the proton relay can be summarized as follows (**Figure 2D**). (1) The c-subunit glutamate in the membrane-facing region is protonated and exists in a closed state. (2) When it faces the a-subunit, it releases protons, undergoing deprotonation-coupled conformational change of the side chain to the open state. (3) When the deprotonated glutamate comes close to the other half-channel *via* c-ring rotation, it receives a proton, followed by a conformational change to the closed state. (4) Upon protonation, glutamate in the closed state enters the lipid-facing region.

FREE ENERGY PROFILES OF PROTONS AND pKa VALUES

ATP synthesis by the action of F_OF_1 ATP synthase is driven by the proton motive force, which is the sum of contributions from the proton concentration gradient and membrane electrical potential as pointed out by Mitchell (1961). For the former, the pH values on the IMS and matrix sides are ∼7.0 and 8.0, respectively, corresponding to a free energy difference of 2.3 k_BT. Typically, the mitochondrial membrane electrical potential is 150 mV, corresponding to 5.4 k_BT. Notably, Soga et al. (2012) found that the sum of the two factors, namely the contribution from the pH difference across the membrane and membrane electrical potential, rather than their individual contribution is relevant to ATP synthesis kinetics. This suggests that not only the thermodynamics, but also kinetics are largely controlled by the sum of the two contributions. Notably, Soga et al. (2012) used a bacterial ATP synthase that was engineered with a deletion of an endogenous inhibitory domain (epsilon subunit's C-terminal domain), so they eliminated another factor that might control kinetics *in vivo*.

To understand the free energy profile of proton transfer through the transport pathway, in addition to the overall driving force, another key factor is the intrinsic affinity of protons toward every proton carrier residue; this is quantified in terms of the

pKa value, which is proportional to the protonation free energy of the corresponding chemical group and calculated as $V_{pKa} = -(ln\ 10)\ k_B T\ pKa$.

Based on high-resolution structures, Srivastava et al. (2018) discussed the pKa values of glutamate residues of two half-channels in yeast ATP synthase (aE223 for the IMS channel and aE162 for the matrix channel) and the c-ring glutamate responsible for proton transport (cE59). If the pKa of glutamate is 5.0, the standard value in an aqueous solution as they mentioned in the paper, the difference in pH on the matrix side would be 3.0. Note, glutamate pKa value in water is, typically, treated around 4 (Tollinger et al., 2002). In this case, proton transfer from aE162 to the matrix side during the ATP synthesis reaction would be easy, although reverse proton transfer during ATP hydrolysis would be difficult. Thus, the authors inferred that the pKa values of glutamates and c-ring proton-carrier residues of the two half-channels should be ∼7.0. The pKa value of carboxylates shifted to ∼7.0 through glutamate–glutamate and histidine–glutamate interactions (Koeppe and Stroud, 1976; Root and Mackinnon, 1994; Morrill and MacKinnon, 1999; Harris and Turner, 2002). In addition, although the distance between the side chains of cE59 and aE223/aE162 was not small in their structure, they confirmed that it could be brought to ∼4 Å through specific c-ring rotation. Therefore, the authors speculated that c-ring rotation brings cE59 and aE223/aE162 closer, shifting the pKa value to near 7.0. In fact, as shown in **Figure 2D**, when the c-ring is close to the a-subunit, the orientation of its proton-carrier side chains changes in the direction in which the reaction is more likely to occur; therefore, the shift in pKa values is expected to occur at the same time. Most recently, Marciniak et al. (2022) calculated the shift in pKa values of glutamates using all-atom MD simulations and reported that pKa values of the matrix and IMS sites faced c-subunits' glutamates were ∼2 and 8, respectively. Of note, however, accurate *de novo* estimation of the pKa value is very challenging owing to its sensitivity to the local environments and approximations used.

FREE ENERGY PROFILES ALONG ROTARY ANGLES FOR GIVEN PROTONATION STATES

In previous sections, we discussed how the protonation and deprotonation of glutamates in the F_O motor are controlled by the environment, such as pKa, pH, and membrane potential, as well as physical interactions, such as whether they faces the a-subunit or lipid molecules. Now, we shall focus on the actual free energy of the F_O motor along the rotary angle. Recently, for some representative protonation states obtained from our MC/MD simulations (details are described later), we drew the free energy surfaces of different protonation states (**Figures 3A,B**) (Kubo et al., 2020). For each fixed protonation state, we performed coarse-grained MD simulations to obtain the free energy surface. Using these trajectories, we employed the Bennett acceptance ratio method (Bennett, 1976) and calculated the free energy differences among different protonation states. Based on the results, we illustrated the preferred proton transfer pathways for both ATP hydrolysis and ATP synthesis. Starting from the state in which the proton-carrying residues of the two c-subunits are deprotonated, we propose two plausible pathways of ATP synthesis: the deprotonation-first pathway (**Figure 3A**) and the protonation-first pathway (**Figure 3B**). We speculate that the deprotonation-first pathway occurs more frequently than the protonation-first pathway. Warshel group also obtained free energy surfaces using fixed protonated states and coarse-grained MD; Using Metropolis MC proton transfer approach (Vorobyov et al., 2016) to determine the protonation state of each c-subunit of the chloroplast ATP synthase F_O motor and determined the free energy surface for each angle of the c-ring (Bai and Warshel, 2019).

Using all-atom MD simulations, Roh et al. (2020) determined free energy surfaces for c-ring angles based on the yeast V_O motor structures they obtained. The authors selected a few representative residues for (de)protonation and rotated the c-ring for each protonation setup by adding a force to the residues. The string method was used to refine the pathway. Finally, 50 intermediate structures along the pathway were determined in a rotation of ∼14° and connected by successive all-atom MD simulations. Successive all-atom MD simulations revealed that the free energy surface of c-ring rotation showed five intermediate states (A to E) and a transition state (TS) between states C and D (**Figure 3C**). At the TS, c″E108 completely lost hydrogen bonds with aR735 and aR799 (**Figure 3D**). These contacts were maintained until state C. Thus, the loss of these connections is the rate-limiting step in the reaction. In addition, Marciniak et al. (2022) determined free energy surfaces depending on the c-ring rotational angle for the yeast F_O motor.

Technically, although coarse-grained MD simulations can easily sample various conformations, they are intrinsically less accurate. Meanwhile, while all-atom MD simulations are more accurate, they are limited in sampling for large molecular machines, such as ATP synthase. In a recent study (Unarta et al., 2021), the merits of the two approaches were combined: a wide range of structures sampled by coarse-grained MD simulations were back-mapped to all-atom models, followed by all-atom MD simulations.

PROTON TRANSFER-COUPLED F_O ROTATION

Furthermore, we investigated how proton transfer is dynamically coupled to c-ring rotation. The rotation of the F_O motor is realized through proton transfer between the two half-channels and the c-ring *via* protonation and deprotonation of their side chains. In particular, the electrostatic interaction between the conserved arginine residue of the a-subunit and the c-subunit acidic proton-carrying residue is thought to be important in driving the rotation of the F_O motor during ATP synthesis. However, how they are dynamically coupled remains unclear.

Recently, we performed hybrid Metropolis MC/MD simulations, where proton transfer was mimicked by an MC move and the rotational motion of the F_O motor was realized through MD simulations (**Figure 4A**) (Kubo et al., 2020). We

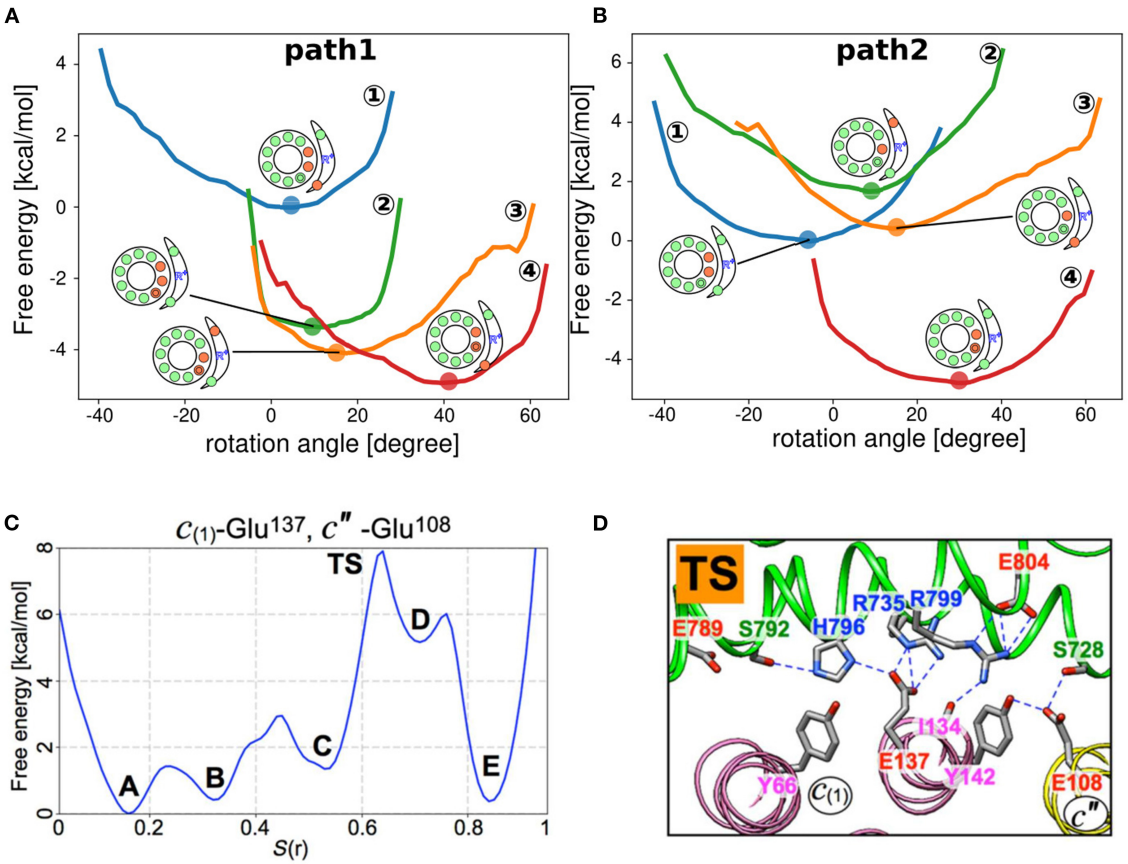


FIGURE 3 | Free energy surface based on the rotational angle. **(A,B)** Free energy surfaces of individual protonation states obtained from coarse-grained MD simulations (Kubo et al., 2020). "Path 1" and "Path 2" represent the deprotonation-first and the protonation-first pathways, respectively. **(C)** Free energy surface of the c-ring rotation in yeast V_O motor. Five local minima (A–E) and transition states (TS) (Roh et al., 2020). **(D)** Representative snapshot of the TS state in **(C)**. The a-subunit and c-ring interface is focused, with some polar residue side chains indicated with sticks. Blue dashed lines indicate hydrogen bonds (Roh et al., 2020).

conducted MD and MC steps alternatively; in the MD step, only the protein conformations were updated, while in the MC step, the protonation state for a fixed conformation was updated. In this section, we briefly describe the computational approach.

We used the yeast mitochondrial F_O structure (PDB ID: 6CP6) (Srivastava et al., 2018). Our simulation system comprised an a-subunit and 10 c-subunits, forming a c10-ring. The proton carrier residue in the c-subunit was cE59. In the IMS and matrix channels, the residues that directly transferred protons to and from the c-ring were aE223 and aE162, respectively. We defined these 12 glutamates (10 cE59 residues and 2 residues in the half-channels) as proton-carrier sites and dynamically updated their protonation states. Their protonation states are represented by a 12-dimensional vector $\{h_i^+\}$, where each element h_i^+ is either zero when protonated or one when deprotonated. For simulation, we assigned $-h_i^+$ charge to each glutamate.

The total energy function was defined as follows:

$$V_{total}(\mathrm{R},\ \mathrm{H}^+) = V_{non-es}\,(\mathrm{R}) + V_{es}(\mathrm{R},\ \mathrm{H}^+) + V_{pKa}\,(\mathrm{H}^+)$$

where R represents all protein structure coordinates. On the right-hand side, the first term is the protein interaction energy, except for electrostatic interactions, and it is, therefore, independent of the protonation state (H^+); the second term is the electrostatic interaction, which depends on both the conformation and protonation state; and the last term represents the intrinsic preference for protonation, corresponding to the intrinsic pKa, which is assumed to be independent of the conformation.

During the MD step, protein conformation dynamics were determined as V_{non-es} (R) and V_{es}(R, H^+). For V_{non-es} (R), we used a well-established structure-based model that maintains both c-ring and a-subunit structures (Li et al., 2014). This model uses a coarse-grained representation of proteins, where each amino acid is simplified as one bead located at the Cα position. V_{es}(R, H^+) includes two terms: the Coulomb interaction between any charged residue term V_C(R, H^+), and the membrane-environment term V_{mem}(R, H^+). The latter term approximates the electrostatic penalty to embed a charged residue, deprotonated glutamate in this case, into the lipid membrane environment. The simulations did not explicitly include lipid molecules. Instead, we assumed that the c-ring glutamate faces the lipid membrane not the a-subunit. When we reduced the lipid membrane area in the control simulation, rotation activity was markedly reduced, which suggests the

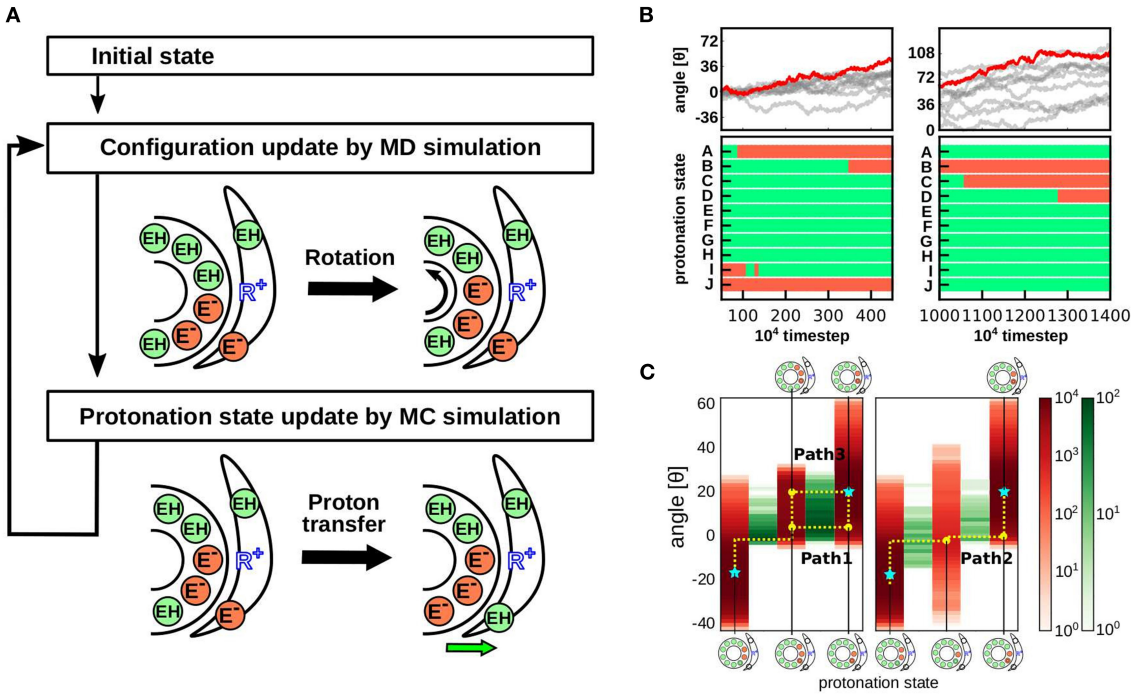


FIGURE 4 | Hybrid MC/MD simulation protocol and results. **(A)** Our hybrid MC/MD simulation protocol. We performed alternative short MC and MD simulations. **(B)** Representative trajectory of the cumulative c-ring rotational angle (top) and protonation state of each c-subunits (bottom). The bottom time courses are obtained from the red trajectory in the top panels. Protonated and deprotonated states are indicated in green and orange, respectively. **(C)** Protonation state distribution depends on the c-ring rotational angle. The rotational angle is indicated in red, and the proton transfer event at each angle is indicated in green (Kubo et al., 2020).

importance of the funnel-like structure of the matrix-side half-channel, corroborating the view put forth by Klusch et al. (2017). Approximation of the lipid membrane area can be refined using all-atom models. For instance, using the CHARMM-GUI membrane builder (Jo et al., 2008; Wu et al., 2014; Lee et al., 2016), lipid molecules can be explicitly placed around the F_O motor, the range within which lipids are present can be estimated, and the free energies of protonation/deprotonation can be obtained. In a recent study, Marciniak et al. (2022) reported this direction. Also, Novitskaia et al. (2019) used CHARMM-GUI membrane builder for evaluation of the number of lipid molecules inside c-ring.

The MC step begins with probabilistic selection of the protonation states of two glutamates in the a-subunit, namely aE223 and aE162, for yeast mitochondrial ATP synthase, followed by probabilistic proton transfer between the a-subunit and c-subunit glutamates. Here, an underlying assumption is that water molecules in the half-channels can move protons fast enough to equilibrate the protonation states of aE223 and aE162 for the IMS and matrix-side half-channels, respectively. The protonation energy for each residue can be calculated as follows:

$$\epsilon_{aE223} \equiv (ln10)\, k_B T \left(pH_{IMS} - pKa_{aE223}\right) - \Delta\Psi/2$$
$$\epsilon_{aE162} \equiv (ln10)\, k_B T \left(pH_{matrix} - pKa_{aE162}\right) + \Delta\Psi/2$$

The pH values of the IMS and matrix aqueous space were set to 7.0 and 8.0, respectively, and the membrane potential (Ψ) to 150 mV. As all glutamates are located near the center of the membrane bilayer, we assumed the electrical potential at that site to be $\Psi/2$. Accordingly, the local equilibrium probabilities of protonation at each site P_i can be calculated as follows:

$$P_i = \frac{\exp\left(-\epsilon_i/k_B T\right)}{1 + \exp\left(-\epsilon_i/k_B T\right)}$$

where i = aE223 or aE162; each MC phase begins with the probabilistic selection of the protonation states of aE223 and aE162 with these values.

Next, we realized probabilistic proton transfer between the c-subunit and a-subunit glutamates. For proton transfer between pairs, the following conditions must be satisfied: (1) only one glutamate molecule in each pair is protonated; (2) the two glutamates are close to each other; (3) they are located at an appropriate angle; and (4) they are not located across aR176, which is a highly conserved arginine in the a-subunit that separates the two half channels. The kinetic weight factor for the three last criteria can be given as follows:

$$w_{j \leftarrow i}(r,\, \theta) = f(r)\, g(\theta)\, h_{aR176}$$

where $f(r)$ is the decreasing function of the distance r between two glutamates; $g(\theta)$ is the function of angle θ between the two vectors that emulate the side chain conformation of the donor and acceptor; $g(\theta)$ assumes a Gaussian form centered

around the corresponding angle in the cryo-EM structure; and h_{aR176} represents the role of aR176 in preventing proton leakage between two half channels. We assumed that h_{aR176} was 0 when the proton donor and acceptor were located across aR176; otherwise, $h_{aR176} = 1$.

Using the kinetic weight factor $w_{j\leftarrow i}$, the probability of proton transfer from the i^{th} site to the j^{th} site can be given as follows:

$$p\left(\mathrm{H}^{+(before)} \rightarrow \mathrm{H}^{+(after)}\right) = (1 - e^{-k\tau w_{j\leftarrow i}})Min(1,\ \exp(-\Delta E/k_B T))$$

where E is the energy change upon proton transfer; k is the overall rate constant; and τ is the time step between MC trials. We set $\tau = 10^5$ MD steps. As the value of the overall rate constant of proton transfer k is unknown, we simply set $k\tau = 1$. $\mathrm{H}^{+}\left(before\right)$ and $\mathrm{H}^{+}\left(after\right)$ represent the protonation states before and after the proton transfer trial, respectively. Accordingly, energy change upon proton transfer can be given as follows:

$$\Delta E = V_{total}\left(\mathrm{R},\ \mathrm{H}^{+(after)}\right) - V_{total}\left(\mathrm{R},\ \mathrm{H}^{+(before)}\right)$$

where the second and third terms in V_{total} are relevant to proton transfer, and the last term $V_{pKa}\left(\mathrm{H}^{+}\right)$ represents the intrinsic propensity for protonation at each site (i.e., 2 half-channels and 10 c-subunits). In a previous study (Kubo et al., 2020), we set $pKa_{aE223} = 6.0$, $pKa_{aE162} = 9.0$, and $pKa_{cE59} = 8.0$, based on discussion by Srivastava et al. (2018). The reliability of these values was also examined using the pKa calculation tool PROPKA (Li et al., 2005). Note, the all parameter used in our previous study are listed in **Table 1**.

TABLE 1 | All parameter list tested in Kubo et al. (2020).

	Kubo et al. (2020)	Test in Kubo et al. (2020)
pH (IMS; aE223)	7.0	
pH (matrix; aE162)	8.0	7.0, 9.0
pKa (aE223)	6.0	
pKa (cE59)	8.0	
pKa (aE162)	9.0	8.0, 7.0
Membrane potential	150 mV (for cE59)	0, 300

TWO OR THREE C-SUBUNITS ARE DEPROTONATED DURING A SINGLE ROTATION STEP

Earlier theoretical models assume that after a proton is released from the c-subunit into the matrix, a single-step rotation of the c-ring is followed by the receipt of a proton from the IMS site to the same or the nearest neighbor c-subunit (Elston et al., 1998) (left panel in **Figure 1B**). In other words, during the cycle, the number of deprotonated proton-carrier residues in the c-subunit is between zero and two. Subsequently, high-resolution cryo-EM structures revealed the accurate position of the highly tilted α-subunit, suggesting that the deprotonated c-subunit is be immediately protonated in the next step (right panel in **Figure 1B**). In fact, our hybrid MC/MD simulations indicated that proton-carrier residues in the two c-subunits are simultaneously deprotonated in the ground state (**Figure 4B**). In addition, a recent study using all-atom MD simulation supports the presence of doubly deprotonated c-subunits (Marciniak et al., 2022).

Starting from the doubly deprotonated c-ring configuration, which occurs next: further deprotonation to the triple-deprotonated state (deprotonation-first pathway) or protonation to the single-protonated state (protonation-first pathway)? How is this coupled to c-ring rotation? Based on free energy profiles obtained from our simulations along the two scenarios (**Figures 3A,B**), the deprotonation-first pathway has a lower free energy cost, whereas the protonation-first pathway requires high free energy to achieve the single-protonated state. Interestingly, the deprotonation-first pathway was dominant in both ATP synthesis and hydrolysis. However, the proposed pathway does not fully consider the dynamical aspects of c-ring rotation coupled to proton transfer. Thus, through further dynamic hybrid MC/MD simulations, we obtained the most prominent pathway in the synthetic direction (**Figure 4C**) (Kubo et al., 2020), as follows:

$$\mathrm{DEP}\,(\mathrm{c}_1,\ \mathrm{c}_2)\ \theta\ \sim\ -18^\circ \xrightarrow{\mathrm{rot}} \mathrm{DEP}\left(\mathrm{c}_1,\ \mathrm{c}_2^\circ\right)\ \theta\ \sim\ -2^\circ \xrightarrow{\mathrm{deprot}}$$
$$\mathrm{DEP}\,(\mathrm{c}_1,\ \mathrm{c}_2,\ \mathrm{c}_3)\ \theta\ \sim\ -2^\circ \xrightarrow{\mathrm{rot}} \mathrm{DEP}\,(\mathrm{c}_1,\ \mathrm{c}_2,\ \mathrm{c}_3)\ \theta\ \sim\ 3^\circ \xrightarrow{\mathrm{prot}}$$
$$\mathrm{DEP}\,(\mathrm{c}_2,\ \mathrm{c}_3)\ \theta\ \sim\ -3^\circ \xrightarrow{\mathrm{rot}} \mathrm{DEP}\,(\mathrm{c}_2,\ \mathrm{c}_3)\ \theta\ \sim\ 18^\circ$$

In this pathway, mean c-ring rotational position in the double-deprotonated state $DEP\,(c_1,\ c_2)$ is at −18, with marked fluctuations (here, the reference of the angle is arbitrary; therefore, the change in angle rather than its absolute value is important). When the value fluctuates to −2, the third c-subunit c_3 releases a proton, resulting in the triple-deprotonated state $DEP\,(c_1,\ c_2,\ c_3)$, with relatively limited fluctuations. After a while, the c-subunit $c_1$receives a proton, followed by c-ring rotation to an angle of 18.

Currently, this pathway has not been directly confirmed by other studies. Although very challenging, direct observations of rotational motions together with proton transfer are warranted. However, a recent study demonstrating the coupling among neighboring c-subunits supports the involvement of a multiply deprotonated state, as described below (Mitome et al., 2022).

F_O-ASP MUTANTS EXHIBITED A CHARACTERISTIC DECREASE IN ACTIVITY

Proton transfer-coupled molecular simulations suggested that proton-carrier residues in two or three c-subunits are simultaneously deprotonated while the F_O motor rotates. Recently, we examined the coupling of multiple c-subunits in F_O through a collaborative study of biochemical assays and molecular simulations of mutant F_O motors (Mitome

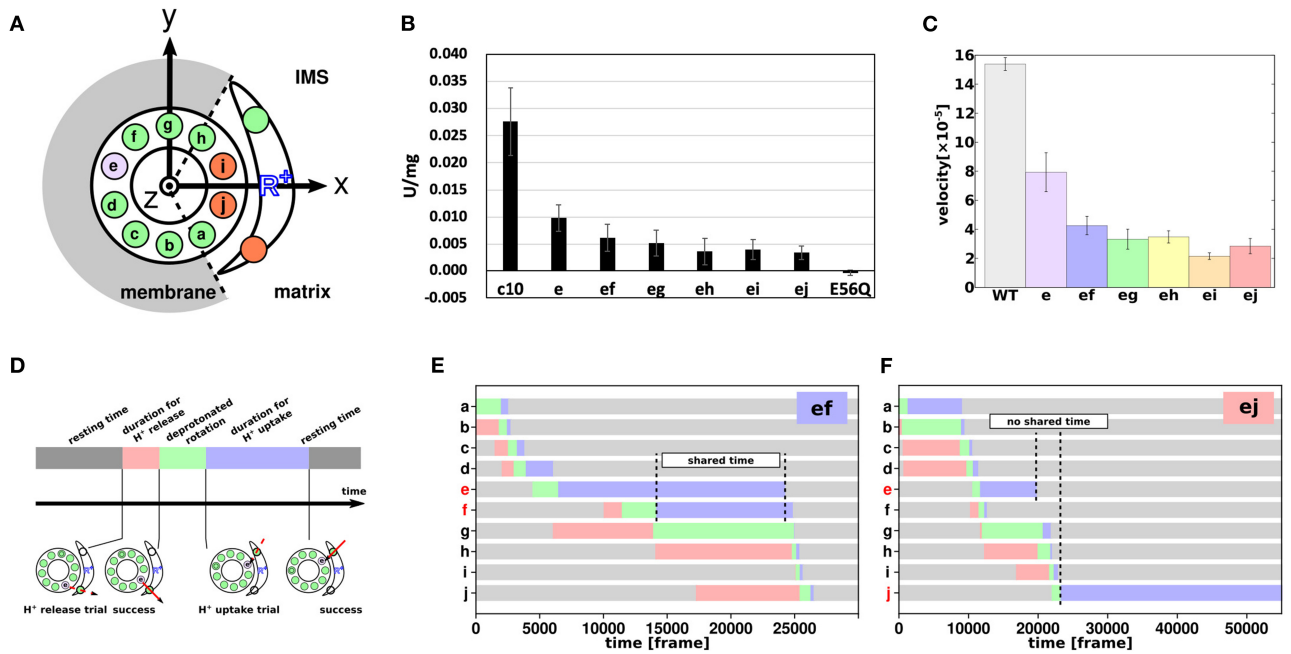


FIGURE 5 | Coupling among c-subunits for F_O rotation. **(A)** Schematic cartoon of the a-subunit and c-ring of the F_O motor. The 10 c-subunits are labeled a–j. Circles represent 10 glutamates of the c-ring and 2 glutamates of the IMS and matrix channels. Green and orange represent protonated and deprotonated states, respectively. Purple represent cE56D mutant c-subunit. **(B)** ATP synthesis driven by NADH oxidation. c10 is the wild-type (WT); e to ej are the results of cE56D mutants, and E56Q are the results of c10(E56Q)- F_OF_1. Bars represent standard error. **(C)** Average rotational velocities for WT and mutants in coarse-grained MC/MD simulations. Bars represent standard error. **(D)** Cartoon showing the four phases of proton transfer, namely the resting time (gray), proton release duration (red), deprotonated rotation (green), and proton uptake duration (blue). **(E,F)** Representative time course of durations for the double mutant "ef" in **(E)** and "ej" in **(F)** (Mitome et al., 2022).

et al., 2022). First, Mitome et al. (2004) built a genetically fused single-chain c-ring of *Bacillus* PS3 ATP synthase. In the single-chain c-ring, 10 c-subunits were labeled in the order "a" through "j" (**Figure 5A**). We then introduced a mutation of the proton-carrier cE56 to aspartic acid in a specific c-subunit of the single-chain c-ring. Due to its shorter side chain and lower pKa value, the cE56D mutation in the c-subunit "e" slowed down yet did not abolish ATP synthesis compared with the wildtype (c10 and "e" in **Figure 5B**). Furthermore, double mutants carrying cE56D mutations in two c-subunits exhibited further reduced ATP synthesis activity compared with the single mutants. Interestingly, the ATP synthesis activity in double mutants depended on the distance between the two mutated c-subunits. Specifically, among the five double mutants examined, the ones carrying mutations in the neighboring c-subunits ("ef") exhibited the highest ATP synthesis activity. The activity tended to decrease with increase in distance between the two mutated subunits. Motivated by this finding, we performed molecular simulations on the corresponding mutant of mitochondrial F_OF_1 ATP synthase that we had used earlier and found that the F_O rotation rate decreased as the distance between two mutation sites increased, which is consistent with the results of biochemical assays (**Figure 5C**). Although this experiment alone did not offer any direct mechanistic understanding, the corresponding simulations provided some clues. Briefly, four phases were defined for each c-subunit: resting time, proton release duration, deprotonated rotation, and proton uptake duration (**Figure 5D**). The time series of the 10 c-subunit protonation states was plotted based on the four phases defined. **Figures 5E,F** show the four phases of "ef", in which the neighboring "e" and "f" are mutated, and "ej", in which the farthest subunits "e" and "j" are mutated. The time for the most prolonged duration for proton uptake was markedly shared in "ef" (**Figure 5E**), but not in "ej" (**Figure 5F**). Thus, the farther apart the mutated c-subunits are, the less latency they share for protonation and the lower is their activity. Thus, the results of biochemical assays are consistent with the view that the proton-carrier residues in multiple c-subunits are simultaneously deprotonated, indicating coupling among the c-subunits.

MUTATION OF THE CONSERVED ARGININE OF THE A-SUBUNIT

As previously described, mutations of the c-subunit proton-carrier residues as well as of the a-subunit affect rotational activity of the F_O motor. The effect of mutation of the highly conserved aArg (aR176 in mitochondrial ATP synthase) was significant. From structural information, aArg is important for separating the two water-accessible regions beyond the two half-channels. In addition, Mitome et al. (2010) found that aArg mutation decreased ATPase activity and induced proton leakage. Thus, we tested leak events through simulations mimicking the aR176A mutation. We modeled the effect of the arginine mutation by replacing the factor h_{aR176} with unity. Consequently, both ATP

synthesis and hydrolysis were markedly suppressed. In particular, in the ATP hydrolysis pathway, protons leaked in the opposite direction. Proton leakage occurred both in ATP synthesis and hydrolysis during the waiting time for the c-subunit to receive protons (Kubo et al., 2020).

Using all-atom MD simulations, Marciniak et al. (2022) found that the aR176A mutation connects the two half channels such that water molecules can directly pass through, regardless of the c-ring rotation. The authors also noted similar results in the aR176K mutant, which may be due to the higher flexibility of the lysine side chain than that of the arginine side chain.

DISCUSSION ON HOW TO SOLVE THE SYMMETRY MISMATCH

As high-resolution cryo-EM structure models of the F_O motor, together with functional and theoretical information, offered a refined view of proton transfer-coupled F_O rotation, the next aspect to be refined was how F_O rotation is coupled to ATP synthesis. The fundamental mechanism of coupling has long been known; briefly, the F_O motor rotates the central rotor, which is shared with the F_1 motor. The rotation of the central rotor in F_1, the γ-subunit, induces a series of conformational changes in the F_1 stator, $\alpha_3\beta_3$, which drives ATP synthesis at the interface of the α-β-subunits. An obvious question that remains to be addressed is the symmetry mismatch. The F_1 motor exhibits 3-fold pseudo-symmetry in all species, whereas the F_O motor exhibits diverse pseudo-symmetries, ranging from 7- to 13-fold. First, the units of rotational steps in F_O and F_1 are not consistent. Furthermore, the symmetries of F_O and F_1 are coprime in many species, rendering the three unit steps of F_1 rotation unequal with respect to F_O rotation. How does ATP synthase solve this symmetry mismatch issue, realizing high efficiency of energy transduction? Some earlier studies have suggested various possibilities: the elastic torsion of the central rotor may contribute (Cherepanov et al., 1999; Pänke and Rumberg, 1999; Okazaki and Hummer, 2015); the torsion of the peripheral stalk, b-subunit, may be of central importance (Zhou et al., 2015; Guo et al., 2019); or the δ-subunit may absorb the symmetry mismatch (Murphy et al., 2019). Despite various notions, however, no consensus has been reached as yet.

Recently, we sought to elucidate the means of resolving this symmetry through coarse-grained MD simulations for the holo-complex of *Bacillus PS3* F_OF_1 ATP synthase (Kubo et al., 2021). In this study, instead of simulating proton transports in F_O, we mechanically rotated the c-ring with 10 c-subunits at 36°-steps, examining changes in the other parts of the holo-complex structures. Overall, the mismatches between angular positions favored by the F_1 and F_O motors were absorbed by combination of a number of elements, depending on the degree of mismatch. Distortion and twist of the central rotor, γ-subunit, can absorb some mismatches. Distortion of the peripheral stalk, b-subunit, results in the rotation of the F_1 stator, $\alpha_3\beta_3$, relative to the F_O stator, a-subunit. Furthermore, a comparative study of cryo-EM structure models among three species confirmed the results of MD simulations and elucidated significant deviation of the c-ring rotation angle from the one anticipated based on the symmetry (a multiple of 36°). Notably, in our simulations of the holo-complex, the F_O c-ring was forced to rotate at steps of 36° without room for fluctuation; thus, the deviation of the c-ring rotation from its symmetric position could not be observed using this design. However, our previous simulation of proton transfer-coupled F_O rotation revealed marked fluctuations in c-ring rotation (**Figures 3A,C**), which is consistent with the observation of c-ring rotation angle deviation from the ideal value. In the future, hybrid MC/MD simulations for proton transfer-coupled c-ring rotation should be performed on the holo-complex.

ATOMIC DETAILS OF THE ELEMENTARY PROCESS OF PROTON TRANSFER COUPLED TO SIDE CHAIN REORIENTATION OF KEY RESIDUES

As described above, the side chain of glutamates, the proton-carrier residues of the c-ring, assumes two distinct conformations depending on the surrounding environment: open and closed. Changes in conformation induces a pKa shift, and their conformation is important for bidirectional rotation. Thanks to remarkable advances in cryo-EM technology, atomic details of both conformations have already been revealed. In addition, free energy surfaces that depend on both the conformation and surrounding environment have already been estimated. In our MC/MD simulations using a coarse-grained model, we did not treat the side chain explicitly but set the angular relationship to mimic the effect of side chain reorientation.

In the future, more detailed proton transfer pathways and rotational mechanisms of F_O motors can be revealed through computational simulations more explicitly taking the orientation of side chains into account. Furthermore, it would be interesting to simulate the actual movement of protons; QM/MM simulations have been employed to explicitly mimic the actual motion of protons during photosynthesis. However, explicit investigations of proton transfer dynamics depending on the rotational motion and orientation of key glutamate side chains is expected to be challenging.

AUTHOR CONTRIBUTIONS

SK and ST conceived the project. SK made figures. Both authors were involved in the manuscript writing process. Both authors contributed to the article and approved the submitted version.

FUNDING

The study was supported partly by JSPS KAKENHI Grants JP21J00021 (SK), 20H05934 (ST) and 21H02441 (ST), and partly by JPMXP1020200101 as Program for Promoting Researches on the Supercomputer Fugaku (ST).

ACKNOWLEDGMENTS

We would like to thank Noriyo Mitome and Toru Niina for discussions throughout the collaboration.

REFERENCES

Aksimentiev, A., Balabin, I. A., Fillingame, R. H., and Schulten, K. (2004). Insights into the molecular mechanism of rotation in the Fo sector of ATP synthase. *Biophys. J.* 86, 1332–1344. doi: 10.1016/S0006-3495(04)74205-8

Allegretti, M., Klusch, N., Mills, D. J., Vonck, J., Kühlbrandt, W., and Davies, K. M. (2015). Horizontal membrane-intrinsic α-helices in the stator a-subunit of an F-type ATP synthase. *Nature* 521, 237–240. doi: 10.1038/nature14185

Bai, C., and Warshel, A. (2019). Revisiting the protomotive vectorial motion of F0-ATPase. *Proc. Natl. Acad. Sci. U. S. A.* 116, 19484–19489. doi: 10.1073/pnas.1909032116

Baptista, A. M., Teixeira, V. H., and Soares, C. M. (2002). Constant-pH molecular dynamics using stochastic titration. *J. Chem. Phys.* 117, 4184–4200. doi: 10.1063/1.1497164

Bennett, C. H. (1976). Efficient estimation of free energy differences from Monte Carlo data. *J. Comput. Phys.* 22, 245–268. doi: 10.1016/0021-9991(76)90078-4

Castagna, A. E., Addis, J., McInnes, R. R., Clarke, J. T. R., Ashby, P., Blaser, S., et al. (2007). Late onset leigh syndrome and ataxia due to a T to C mutation at bp 9,185 of mitochondrial DNA. *Am. J. Med. Genet. Part A* 143A, 808–816. doi: 10.1002/ajmg.a.31637

Cherepanov, D. A., Mulkidjanian, A. Y., and Junge, W. (1999). Transient accumulation of elastic energy in proton translocating ATP synthase. *FEBS Lett.* 449, 1–6. doi: 10.1016/S0014-5793(99)00386-5

Cortés-Hernández, P., Vázquez-Memije, M. E., and García, J. J. (2007). ATP6 homoplasmic mutations inhibit and destabilize the human F 1F0-ATP synthase without preventing enzyme assembly and oligomerization. *J. Biol. Chem.* 282, 1051–1058. doi: 10.1074/jbc.M606828200

De Meirleir, L., Seneca, S., Lissens, W., Schoentjes, E., and Desprechins, B. (1995). Bilateral striatal necrosis with a novel point mutation in the mitochondrial ATPase 6 gene. *Pediatr. Neurol.* 13, 242–246. doi: 10.1016/0887-8994(95)00184-H

Dimroth, P., Wang, H., Grabe, M., and Oster, G. (1999). Energy transduction in the sodium F-ATPase of Propionigenium modestum. *Proc. Natl. Acad. Sci. U. S. A.* 96, 4924–4929. doi: 10.1073/pnas.96.9.4924

Elston, T., Wang, H., and Oster, G. (1998). Energy transduction in ATP synthase. *Nature* 391, 185. doi: 10.1038/35185

Emsley, P., Lohkamp, B., Scott, W. G., and Cowtan, K. (2010). Features and development of Coot. *Acta Crystallogr. Sect. D Biol. Crystallogr.* 66, 486–501. doi: 10.1107/S0907444910007493

Girvin, M. E., Rastogi, V. K., Abildgaard, F., Markley, J. L., and Fillingame, R. H. (1998). Solution structure of the transmembrane H+-transporting subunit c of the F1F0 ATP synthase. *Biochemistry* 37, 8817–8824. doi: 10.1021/bi980511m

Gu, J., Zhang, L., Zong, S., Guo, R., Liu, T., Yi, J., et al. (2019). Cryo-EM structure of the mammalian ATP synthase tetramer bound with inhibitory protein IF1. *Science.* 364, 1068–1075. doi: 10.1126/science.aaw4852

Guo, H., Bueler, S. A., and Rubinstein, J. L. (2017). Atomic model for the dimeric FO region of mitochondrial ATP synthase. *Science.* 358, 936–940. doi: 10.1126/science.aao4815

Guo, H., Suzuki, T., and Rubinstein, J. L. (2019). Structure of a bacterial ATP synthase. *Elife* 8, 1–17. doi: 10.7554/eLife.43128

Hahn, A., Vonck, J., Mills, D. J., Meier, T., and Kuhlbrandt, W. (2018). Structure, mechanism, and regulation of the chloroplast ATP synthase. *Science.* 360, eaat4318. doi: 10.1126/science.aat4318

Harris, T. K., and Turner, G. J. (2002). Structural basis of perturbed pKa values of catalytic groups in enzyme active sites. *IUBMB Life* 53, 85–98. doi: 10.1080/15216540211468

Ho, B. K., and Gruswitz, F. (2008). HOLLOW: Generating accurate representations of channel and interior surfaces in molecular structures. *BMC Struct. Biol.* 8, 1–6. doi: 10.1186/1472-6807-8-49

Jo, S., Kim, T., Iyer, V. G., and Im, W. (2008). CHARMM-GUI: a web-based graphical user interface for CHARMM. *J. Comput. Chem.* 29, 1859–1865. doi: 10.1002/jcc.20945

Kato, M., Pisliakov, A. V., and Warshel, A. (2006). The barrier for proton transport in aquaporins as a challenge for electrostatic models: the role of protein relaxation in mutational calculations. *Proteins Struct. Funct. Bioinforma.* 64, 829–844. doi: 10.1002/prot.21012

Khaniya, U., Gupta, C., Cai, X., Mao, J., Kaur, D., Zhang, Y., et al. (2020). Hydrogen bond network analysis reveals the pathway for the proton transfer in the E-channel of *T. thermophilus* complex I. *Biochim. Biophys. Acta Bioenerg.* 1861, 1–22. doi: 10.1016/j.bbabio.2020.148240

Klusch, N., Murphy, B. J., Mills, D. J., Yildiz, Ö., and Kühlbrandt, W. (2017). Structural basis of proton translocation and force generation in mitochondrial ATP synthase. *Elife* 6, 1–16. doi: 10.7554/eLife.33274

Koeppe, R. E., and Stroud, R. M. (1976). Mechanism of hydrolysis by serine proteases: direct determination of the pka's of aspartyl-102 and aspartyl-194 in bovine trypsin using difference infrared spectroscopy. *Biochemistry* 15, 3450–3458. doi: 10.1021/bi00661a009

Kubo, S., Niina, T., and Takada, S. (2020). Molecular dynamics simulation of proton-transfer coupled rotations in ATP synthase FO motor. *Sci. Rep.* 10, 8225. doi: 10.1038/s41598-020-65004-1

Kubo, S., Niina, T., and Takada, S. (2021). F O-F 1 coupling and symmetry mismatch in ATP synthase resolved in every FO rotation step. *bioRxiv [Preprint]*. doi: 10.1101/2021.11.14.468453

Lee, J., Cheng, X., Swails, J. M., Yeom, M. S., Eastman, P. K., Lemkul, J. A., et al. (2016). CHARMM-GUI input generator for NAMD, GROMACS, AMBER, OpenMM, and CHARMM/OpenMM simulations using the CHARMM36 additive force field. *J. Chem. Theory Comput.* 12, 405–413. doi: 10.1021/acs.jctc.5b00935

Leone, V., and Faraldo-Gómez, J. D. (2016). Structure and mechanism of the ATP synthase membrane motor inferred from quantitative integrative modeling. *J. Gen. Physiol.* 148, 441–457. doi: 10.1085/jgp.201611679

Li, H., Robertson, A. D., and Jensen, J. H. (2005). Very fast empirical prediction and rationalization of protein pK a values. *Proteins Struct. Funct. Genet.* 61, 704–721. doi: 10.1002/prot.20660

Li, W., Wang, W., and Takada, S. (2014). Energy landscape views for interplays among folding, binding, and allostery of calmodulin domains. *Proc. Natl. Acad. Sci. U. S. A.* 111, 10550–10555. doi: 10.1073/pnas.1402768111

Marciniak, A., Chodnicki, P., Hossain, K. A., Slabonska, J., and Czub, J. (2022). Determinants of directionality and efficiency of the ATP synthase F o motor at atomic resolution. *J. Phys. Chem. Lett.* 13, 387–392. doi: 10.1021/acs.jpclett.1c03358

Mitchell, P. (1961). Coupling of phosphorylation to electron and hydrogen transfer by a chemi-osmotic type of mechanism. *Nature* 191, 144–148. doi: 10.1038/191144a0

Mitome, N., Kubo, S., Ohta, S., Takashima, H., Shigefuji, Y., Niina, T., et al. (2022). Cooperation among c- subunits of Fo F1- ATP synthase in rotation- coupled proton translocation. *Elife* 11, e69096. doi: 10.7554/eLife.69096

Mitome, N., Ono, S., Sato, H., Suzuki, T., Sone, N., and Yoshida, M. (2010). Essential arginine residue of the F_o - *a* subunit in F_o F_1 -ATP synthase has a role to prevent the proton shortcut without *c* -ring rotation in the F_o proton channel. *Biochem. J.* 430, 171–177. doi: 10.1042/BJ20100621

Mitome, N., Suzuki, T., Hayashi, S., and Yoshida, M. (2004). Thermophilic ATP synthase has a decamer c-ring: Indication of noninteger 10:3 H+/ATP ratio and permissive elastic coupling. *Proc. Natl. Acad. Sci.* 101, 12159–12164. doi: 10.1073/pnas.0403545101

Mongan, J., Case, D. A., and McCammon, J. A. (2004). Constant pH molecular dynamics in generalized Born implicit solvent. *J. Comput. Chem.* 25, 2038–2048. doi: 10.1002/jcc.20139

Morrill, J. A., and MacKinnon, R. (1999). Isolation of a single carboxyl-carboxylate proton binding site in the pore of a cyclic nucleotide-gated channel. *J. Gen. Physiol.* 114, 71–83. doi: 10.1085/jgp.114.1.71

Mukherjee, S., and Warshel, A. (2011). Electrostatic origin of the mechanochemical rotary mechanism and the catalytic dwell of F1-ATPase. *Proc. Natl. Acad. Sci. U. S. A.* 108, 20550–20555. doi: 10.1073/pnas.1117024108

Murphy, B. J., Klusch, N., Langer, J. D., Mills, D. J., Yildiz, Ö., and Kühlbrandt, W. (2019). Rotary substates of mitochondrial ATP synthase reveal the basis of flexible F1-Fo coupling. *Science.* 364, aaw9128. doi: 10.1126/science.aaw9128

Novitskaia, O., Buslaev, P., and Gushchin, I. (2019). Assembly of spinach chloroplast ATP synthase rotor ring protein-lipid complex. *Front. Mol. Biosci.* 6, e00135. doi: 10.3389/fmolb.2019.00135

Okazaki, K., and Hummer, G. (2015). Elasticity, friction, and pathway of γ-subunit rotation in F o F 1 -ATP synthase. *Proc. Natl. Acad. Sci.* 112, 10720–10725. doi: 10.1073/pnas.1500691112

Olsson, M. H. M., and Warshel, A. (2006). Monte Carlo simulations of proton pumps: On the working principles of the biological valve that controls proton pumping in cytochrome c oxidase. *Proc. Natl. Acad. Sci. U. S. A.* 103, 6500–6505. doi: 10.1073/pnas.0510860103

Pänke, O., and Rumberg, B. (1999). Kinetic modeling of rotary CF0F1-ATP synthase: storage of elastic energy during energy transduction. *Biochim. Biophys. Acta* 1412, 118–128. doi: 10.1016/S0005-2728(99)00059-6

Pogoryelov, D., Krah, A., Langer, J. D., Yildiz, Ö., Faraldo-Gómez, J. D., and Meier, T. (2010). Microscopic rotary mechanism of ion translocation in the F(o) complex of ATP synthases. *Nat. Chem. Biol.* 6, 891–899. doi: 10.1038/nchembio.457

Rastogi, V. K., and Girvin, M. E. (1999). Structural changes linked to proton translocation by subunit c of the ATP synthase. *Nature* 402, 263–268. doi: 10.1038/46224

Roh, S. H., Shekhar, M., Pintilie, G., Chipot, C., Wilkens, S., Singharoy, A., et al. (2020). Cryo-EM and MD infer water-mediated proton transport and autoinhibition mechanisms of Vo complex. *Sci. Adv.* 6, 1–11. doi: 10.1126/sciadv.abb9605

Root, M. J., and Mackinnon, R. (1994). Two identical noninteracting sites in an ion channel revealed by proton transfer. *Science.* 265, 1852–6. doi: 10.1126/science.7522344

Soga, N., Kinosita, K., Yoshida, M., and Suzuki, T. (2012). Kinetic equivalence of transmembrane ph and electrical potential differences in ATP synthesis. *J. Biol. Chem.* 287, 9633–9639. doi: 10.1074/jbc.M111.335356

Spikes, T. E., Montgomery, M. G., and Walker, J. E. (2020). Structure of the dimeric ATP synthase from bovine mitochondria. *Proc. Natl. Acad. Sci. U. S. A.* 117, 23519–23526. doi: 10.1073/pnas.2013998117

Srivastava, A. P., Luo, M., Zhou, W., Symersky, J., Bai, D., Chambers, M. G., et al. (2018). High-resolution cryo-EM analysis of the yeast ATP synthase in a lipid membrane. *Science.* 360, eaas9699. doi: 10.1126/science.aas9699

Tollinger, M., Forman-Kay, J. D., and Kay, L. E. (2002). Measurement of side-chain carboxyl pKa values of glutamate and aspartate residues in an unfolded protein by multinuclear NMR spectroscopy. *J. Am. Chem. Soc.* 124, 5714–5717. doi: 10.1021/ja020066p

Unarta, I. C., Cao, S., Kubo, S., Wang, W., Cheung, P. P.-H., Gaoe, X., et al. (2021). Role of bacterial RNA polymerase gate opening dynamics in DNA loading and antibiotics inhibition elucidated by quasi-Markov State Model. *Proc. Natl. Acad. Sci.* 118, 1–8. doi: 10.1073/pnas.2024324118

Vik, S. B., and Antonio, B. J. (1994). A mechanism of proton translocation by F1F0 ATP synthases suggested by double mutants of the a subunit. *J. Biol. Chem.* 269, 30364–30369. doi: 10.1016/S0021-9258(18)43822-7

Vorobyov, I., Kim, I., Chu, Z. T., and Warshel, A. (2016). Refining the treatment of membrane proteins by coarse-grained models. *Proteins Struct. Funct. Bioinforma.* 84, 92–117. doi: 10.1002/prot.24958

Wu, E. L., Cheng, X., Jo, S., Rui, H., Song, K. C., Dávila-Contreras, E. M., et al. (2014). CHARMM-GUI membrane builder toward realistic biological membrane simulations. *J. Comput. Chem.* 35, 1997–2004. doi: 10.1002/jcc.23702

Xing, J., Wang, H., Von Ballmoos, C., Dimroth, P., and Oster, G. (2004). Torque generation by the Fo motor of the sodium ATPase. *Biophys. J.* 87, 2148–2163. doi: 10.1529/biophysj.104.042093

Zhou, A., Rohou, A., Schep, D. G., Bason, J. V., Montgomery, M. G., Walker, J. E., et al. (2015). Structure and conformational states of the bovine mitochondrial ATP synthase by cryo-EM. *Elife* 4, e10180. doi: 10.7554/eLife.10180.049

Conflict of Interest: The authors declare that the research was conducted in the absence of any commercial or financial relationships that could be construed as a potential conflict of interest.

Publisher's Note: All claims expressed in this article are solely those of the authors and do not necessarily represent those of their affiliated organizations, or those of the publisher, the editors and the reviewers. Any product that may be evaluated in this article, or claim that may be made by its manufacturer, is not guaranteed or endorsed by the publisher.

Copyright © 2022 Kubo and Takada. This is an open-access article distributed under the terms of the Creative Commons Attribution License (CC BY). The use, distribution or reproduction in other forums is permitted, provided the original author(s) and the copyright owner(s) are credited and that the original publication in this journal is cited, in accordance with accepted academic practice. No use, distribution or reproduction is permitted which does not comply with these terms.

frontiers | Frontiers in Microbiology

REVIEW
published: 22 April 2022
doi: 10.3389/fmicb.2022.861855

F_1-ATPase Rotary Mechanism: Interpreting Results of Diverse Experimental Modes With an Elastic Coupling Theory

Sándor Volkán-Kacsó[1,2] and Rudolph A. Marcus[1]**

[1]Noyes Laboratory of Chemical Physics, California Institute of Technology, Pasadena, CA, United States, [2]Segerstrom Science Center, Azusa Pacific University, Azusa, CA, United States

OPEN ACCESS

Edited by:
Tom Duncan,
Upstate Medical University,
United States

Reviewed by:
Abhishek Singharoy,
Arizona State University,
United States
Kwangho Nam,
University of Texas at Arlington,
United States

***Correspondence:**
Sándor Volkán-Kacsó
svk@caltech.edu
Rudolph A. Marcus
ram@caltech.edu

Specialty section:
This article was submitted to Microbial Physiology and Metabolism, a section of the journal Frontiers in Microbiology

Received: 25 January 2022
Accepted: 28 March 2022
Published: 22 April 2022

Citation:
Volkán-Kacsó S and Marcus RA (2022) F_1-ATPase Rotary Mechanism: Interpreting Results of Diverse Experimental Modes With an Elastic Coupling Theory. Front. Microbiol. 13:861855. doi: 10.3389/fmicb.2022.861855

In this chapter, we review single-molecule observations of rotary motors, focusing on the general theme that their mechanical motion proceeds in substeps with each substep described by an angle-dependent rate constant. In the molecular machine F1-ATPase, the stepping rotation is described for individual steps by forward and back reaction rate constants, some of which depend strongly on the rotation angle. The rotation of a central shaft is typically monitored by an optical probe. We review our recent work on the theory for the angle-dependent rate constants built to treat a variety of single-molecule and ensemble experiments on the F_1-ATPase, and relating the free energy of activation of a step to the standard free energy of reaction for that step. This theory, an elastic molecular transfer theory, provides a framework for a multistate model and includes the probe used in single-molecule imaging and magnetic manipulation experiments. Several examples of its application are the following: (a) treatment of the angle-dependent rate constants in stalling experiments, (b) use of the model to enhance the time resolution of the single-molecule imaging apparatus and to detect short-lived states with a microsecond lifetime, states hidden by the fluctuations of the imaging probe, (c) treatment of out-of-equilibrium "controlled rotation" experiments, (d) use of the model to predict, without adjustable parameters, the angle-dependent rate constants of nucleotide binding and release, using data from other experiments, and (e) insights obtained from correlation of kinetic and cryo-EM structural data. It is also noted that in the case where the release of ADP would be a bottleneck process, the binding of ATP to another site acts to accelerate the release by 5–6 orders of magnitude. The relation of the present set of studies to previous and current theoretical work in the field is described. An overall goal is to gain mechanistic insight into the biological function in relation to structure.

Keywords: F1-ATPase, stepping rotation of F1-ATPase, rotary biomolecular motors, cryo-electron microscopy, single-molecule imaging, multi-state theory, ATP binding, concerted kinetics

INTRODUCTION

Fueled by the free energy of ATP hydrolysis, cellular nanomachinery works to realize functions, such as muscle contraction, cell motility, cell division, intracellular protein transport, wound healing, and DNA repair (McLaughlin et al., 2016; Saper and Hess, 2020 and references cited therein). These nanomachines are rotary motors (F- or V-ATPases), linear motors (myosins, kinesins, and dyneins), and revolving motors (viral packaging motors and DNA motor complexes; Guo et al., 2016; Tong and Bustamante, 2021), in which biological function arises from the interconversion of chemical free energy of ATP (or in some machines, GTP), hydrolysis/synthesis, and mechanical energy of conformational changes (Braig et al., 2000; Senior, 2007; Weber, 2010; Mukherjee and Warshel, 2011, 2015; Junge and Nelson, 2015). Single-molecule imaging is used to resolve the kinetic steps in relation to mechanical displacement, which is also stepwise (Noji et al., 1997; Yasuda et al., 2001; Nishizaka et al., 2004; Sakaki et al., 2005; Adachi et al., 2007, 2012; Sielaff et al., 2008, 2016; Spetzler et al., 2009; Watanabe et al., 2010; Sugawa et al., 2016; Miller et al., 2018).

In particular, the F-ATPase (ATP synthase) uses a proton concentration gradient across the mitochondrial membrane (or cell membrane in prokaryotes) to synthesize ATP from ADP and inorganic phosphate (Pi), an energetically uphill process, *via* a rotating shaft (Boyer, 1993; Weber and Senior, 1997), seen in the structure from **Figure 1** (Braig et al., 2000). F_1-ATPase is the water-soluble part of the F-ATPase, and it is the minimal subsystem that functions as a rotary motor. Single-molecule imaging experiments (Iino and Noji, 2013) in the Thermophilic Bacillus F_1-ATPase demonstrated that it converts chemical free energy from ATP hydrolysis into a stepping rotation of 80 and 40° substeps by a coordinated mechanism (Senior et al., 2002).

The stepping rotation of a single F_1-ATPase motor enzyme (**Figure 1**) proceeds on a timescale of milliseconds (or, under certain conditions, seconds), while the fluctuations during the transitions relax within micro- to nanoseconds. The stepping behavior involves a concerted mechanism involving a small molecule and the host subunits, which undergo conformational dynamics, driving the directional mechanical motion (e.g., rotation) and leading to the biological functions. The microsecond processes, present in F_1-ATPase and across all types of motors, have eluded detection in single-molecule imaging experiments and was only recently captured by atomistic computer simulations in kinesin (Hwang et al., 2017).

We review some recent theoretical works treating microsecond to second kinetics from single motors, at high and low ATP concentrations, applied to $-F_1$-ATPase from *Thermophilic Bacillus* (ThF1) and *Paracoccus denitrificans* (PdF1) in relation to their structure. The topics in the review are as follows: In the section "Relevance of single-molecule F1-ATPase experiments and theory to operation of FOF1 ATP synthase," we provide some arguments supporting the relevance for the function of the F-ATP synthase of the single-molecule experiments and theory. In the section "Use of data on ensemble studies to assist in predictions of single-molecule measurements," we review an elastic transfer theory of F_1-ATPases and its predictions of stalling experiments. In the section "Predictions of angle-dependent rate constants for binding and release in ThF1, using controlled rotation data at Low ATP concentrations," the use of theory to predict rate constants in slow, low ATP concentration, controlled rotation experiments in ThF1 is reviewed. In the section "Detection of an intermediate state related to ATP binding and ADP release, observed at high ATP concentrations," a related method using velocities to extract fast states in ThF1 is described. In the section "Behavior of the system in the dwell region using statistical methods and the forced diffusion equation to study the statistical mechanical properties," recent work on applying a velocity method to PdF1 to study shorter

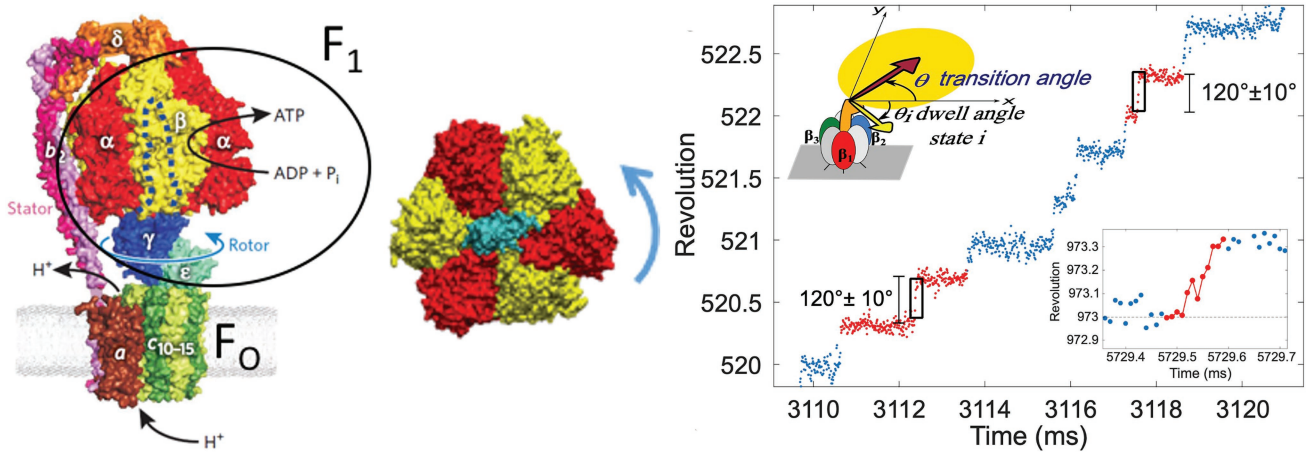


FIGURE 1 | F-ATPase structure showing the F1 and Fo components (left). F1-ATPase motor "transverse cross-section" view showing the central rotor in blue and α ring subunits in gold and β subunits in red (center). Example of a trajectory showing stepping rotation of F1-ATPase (right), as imaged by a probe in single molecule experiment (top inset). A transition is shown (red points) between two dwells (blue dots) in the lower inset. Figures were reproduced, with permission from Weber (2010) and Volkán-Kacsó et al. (2019).

time scales is reviewed. In the section "Comparison of kinetics and the structural behavior inferred from cryo-EM studies," the implications of the single-molecule elastic transfer theory for the kinetics-structure relation are discussed, with emphasis on recent Cryo-EM structures. In the section "Relation between mechanical motion and chemistry," a relation between single-molecule kinetic and chemistry is discussed from studies at low ATP concentration. In the section "Relation to other theoretical and computational work," our results are related to other theoretical and computational work in the field of single-molecule imaging of biomolecular motors.

RELEVANCE OF SINGLE-MOLECULE F_1-ATPASE EXPERIMENTS AND THEORY TO OPERATION OF F_OF_1 ATP SYNTHASE

The complete enzyme, F_OF_1 ATP Synthase, contains a number of subunits not present in single-molecule F_1-ATPase studies. In particular, it contains the in-membrane F_o assembly that includes the c subunits as well as a δ and ϵ subunit. In some bacteria, the ϵ subunit acts as a rachet to reduce the possibility of a back-reaction (García-Trejo, and Morales-Ríos, 2008), while in other systems like the mammalian F-ATPase the δ and ϵ subunits are incorporated into the globular section of the rotor shaft and they do not work as ratchets. The question naturally arises of the relevance experimental and theoretical studies of this truncated system, F_1-ATPase, which is the operation of the F_OF_1 system. A ratchet, for example, is not needed if the forward reaction is very downhill, and so is sometime operative and sometimes not.

The full F_0F_1 system also uses an acid–base reaction at the beginning and at the end of an offset channel in the F_O unit to cause a rotation of a central γ shaft in the F_1 (Bai and Warshel, 2019; Sielaff et al., 2019). In the single-molecule experiments, this rotation is accomplished instead by externally controlled rotation of the γ shaft (Adachi et al., 2000) or by performing stalling (Watanabe et al., 2012) or free rotation experiments (Adachi et al., 2007).

The successive proton jumps from position in the entrance channel to a (Bai and Warshel, 2019) carboxyl group in the nearest *c*-ring member causing a rotation to occur because it is sufficiently downhill or because the ratchet is used to inhibit the back reaction. Thereby, we have in the F_O-ATPase a stepped rotation. This stepped rotation is paralleled in the single-molecule controlled rotation experiments by collecting data on the occupation of successive cells in angle space of a size comparable to $360°/N$, where N is the number of *c* subunits in the F_O portion of the F_OF_1 ATP synthase. So, in this respect, these single-molecule experiments simulate the stepwise motion of the gamma shaft caused by the stepped acid base proton transfer reaction and their behavior. In this aspect, it is reasonable to infer that the single-molecule experiments in these controlled rotation experiments are relevant to those to the full enzyme. Inasmuch as the stalling experiments can be used to predict the controlled rotation experiment, as discussed in the section "Use of data on ensemble studies to assist in predictions of single-molecule measurements," in obtaining agreement with no adjustable parameters, the implication is that the stalling experiments are also relevant to providing insight into the kinetic behavior and parameters of the F_OF_1 ATP Synthase.

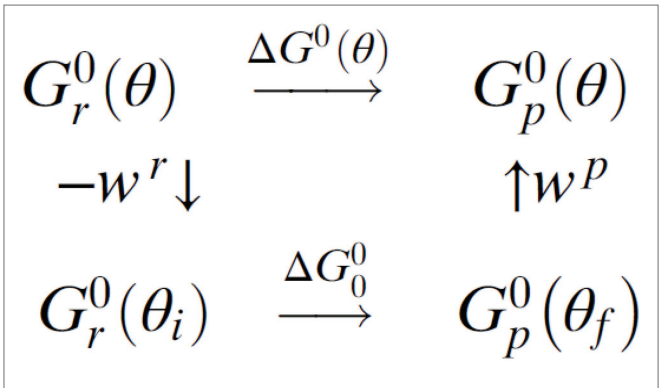
USE OF DATA ON ENSEMBLE STUDIES TO ASSIST IN PREDICTIONS OF SINGLE-MOLECULE MEASUREMENTS

Using ideas that originated in the 1960s in the transfer of atoms and groups, we applied them (Volkán-Kacsó and Marcus, 2015, 2016, 2017a) to the binding and release of ATP in single-molecule experiments in which the rotation angle is stalled or rotated at a constant angular velocity. In F1-ATPase, the dwell angles are angles of local stability and so they serve to identify initial and final states during a transition from one dwell to the next. A thermodynamic cycle (**Scheme 1**) provides a relationship between the free energies of a nucleotide binding when the angle of the rotor shaft is not constrained by the imaging probe, ΔG_0^0, and the binding free energy $\Delta G^0(\theta)$ at a constant rotor angle θ. If the free energies in the reactant and product spaces are denoted using indices r and p, and the stable dwell angles in these states by θ_i and θ_f, the thermodynamic cycle is:

Due to an elastic coupling of the probe to the stator ring that includes the rotor shaft (Sielaff et al., 2008), according to **Scheme 1**, keeping the system at a fixed angle θ would require an elastic energy, both when the system is in the reactant and product states,

$$w^r = \frac{k}{2}\left(\theta - \theta_i\right)^2 \text{and} w^p = \frac{k}{2}\left(\theta - \theta_f\right)^2 \quad (1)$$

Then, for the standard free energy of reaction it is found that (Volkán-Kacsó and Marcus, 2015),



SCHEME 1 | Thermodynamic cycle for the nucleotide binding step.

$$\begin{aligned}\Delta G^0\ \theta &= \Delta G_0^0 + w^p\ \theta - w^r\ \theta \\ &= \Delta G_0^0 - k\ \theta_f - \theta_i \left[\theta - \theta_f + \theta_i\ /2\right]\end{aligned} \quad (2)$$

The elastic terms for the reactants and products of an individual step in a subunit are given as a function of θ in equation (1), and, using a parabolic relation for the transfer process (Marcus, 1968, 1993; Marcus and Sutin, 1985), they yield an equation for the free energy barrier as a function of θ,

$$\Delta G*(\theta) = W^r + \left[\lambda + \Delta G^0(\theta)\right]^2 / 4\lambda \quad (3)$$

A work term W^r arises from the attachment of the ATP from solution to the exterior of the F_1-ATPase, and the standard free energy of reaction $\Delta G^0(\theta)$ is given as a function of θ in equation (2) (Volkán-Kacsó and Marcus, 2015). Stalling experiments provide the θ-dependent rate constants and equilibrium constants for the steps. The $\Delta G^0(\theta)$ is related to the θ-dependent equilibrium constant $K(\theta)$ for that step by $\Delta G^0(\theta) = -\ kT \ln K(\theta)$ and so $\ln K(\theta)$ for ATP binding/release is linear in θ, a result also seen in the experimental data in **Figure 2** (noting that the "k" in this equation is the Boltzmann constant). In passing, we note that equation (3), without the θ, has also been extensively applied to atom, ion, and group transfer reactions (Wolfe and Mitchell, 1981; Lewis and Hu, 1984; Lewis, 1986; Warren and Mayer, 2012).

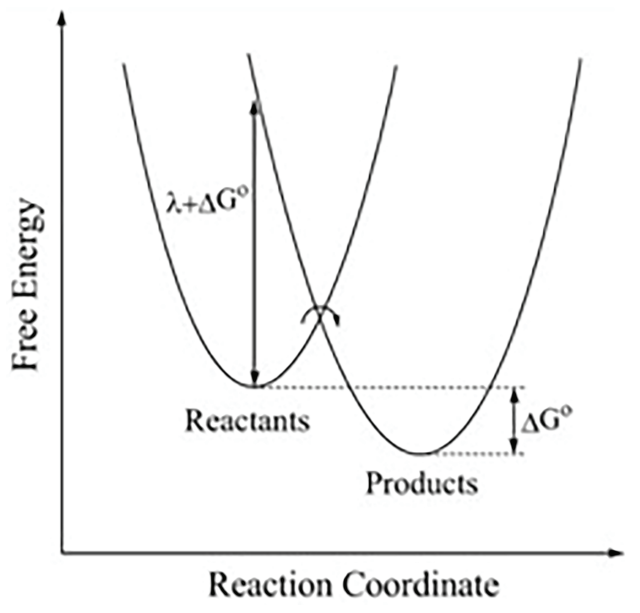


FIGURE 2 | Free energy curves for reactant and product states showing the definition of ΔG^0 and λ. These two parabolas are plotted vs. the reaction coordinate that describes the progress of the reaction. The transition state occurs at the intersection of the two parabolas, as also in Figure 1 in Marcus and Sutin (1985). For simplicity of presentation, some symbols and the labeling of work terms are omitted here.

We consider next the physical meaning of λ appearing in equations (2) and (3). The standard theory of chemical reaction rates, transition state theory (e.g., Glasstone et al., 1941; Truhlar et al., 1996), expresses the reaction rate constant in terms of a free energy barrier, which in the present application is given by equations (2) and (3) for each value of the rotation angle, θ. This free energy barrier to reaction depends on how downhill or uphill the reaction is, namely it depends on $\Delta G°$. It also depends on what is known as the reorganization energy, λ, in the electron transfer literature and depends on the work term w^r to bring the system from the dwell angle of the reactants θ_i to the angle θ, followed by the various internal changes to reach the transition state at that angle, and also on the work term w^p associated with reaching the dwell angle θ_f.

In **Figure 2**, λ is seen there to be the vertical difference of the products' and the reactants' free energy evaluated at the equilibrium distribution of coordinates of the reactants and their environment and corrected for the contribution of ΔG° at the given θ. One sees from equations (4–6) of Marcus and Sutin (1985) that λ depends on the magnitude of the changes and not on their sign. That is, the breaking of a hydrogen bond contributes the same amount to λ as the forming of a hydrogen bond. For example, in the case of an ATP entering a cleft in the ATPase, if one counts the number of hydrogen bonds of the ATP that are broken or formed, they contribute equally to λ. So, it will contain the sum of the free energies of these two quantities. Similarly, λ will contain the free energy changes due to other structural changes such as changes in dielectric polarization of the medium surrounding the charges regardless of sign, at any given rotation angle θ. In the particular case of electron transfer reactions (Marcus and Sutin, 1985), equations were given for λ that depends on the size of the reacting ions, the change in ionic charges of each reactant, the resulting changes in solvation, and the changes in bond lengths and angles, all of which accompany an electron transfer. In applying equation (3) for ΔG* to atom or group transfers, we note that they are topologically different from that of electron transfers. A result is that equation (3) is confined to the region $|\Delta G^0|/\lambda$ which is equal to or less than unity, outside a range termed the inverted region in electron transfer (Marcus and Sutin, 1985). In passing, we note that the quantity λ plays an important role in interpreting in physical chemical terms the extensive experimental data on the rates of electron transfer reactions. The ideas were further extended to bond breaking—bond-forming reactions, using a bond energy-bond order model (Marcus, 1968).

All of these remarks refer to the case where transition state theory and its quasi-equilibrium assumption for the formation of the transition state are applicable. There are some situations, particularly for some reactions that are ultrafast, where the rate constant depends also on a slow relaxation time of some key coordinate in adjusting to the new configurations. In this case, transition state theory, which assumes instead a quasi-equilibrium between the transition state and the reactants, requires modification. Details are given in the famous paper by Kramers in 1940 for systems treated one dimensionally (Kramers, 1940) and elaborated upon in numerous papers

since. An example of an elaboration involves the case where there are two coordinates to be considered, one of which is "fast" and the other of which is "slow" (Agmon and Hopfield, 1983; Sumi and Marcus, 1986) and contributed to by many authors. The applicability of this type of formalism to F_1-ATPase was suggested in Watanabe et al. (2013).

The Brønsted slope, or its counterpart in electrochemistry, the Tafel slope, is often used to provide mechanistic information on chemical reactions. Under certain conditions (constant λ), it gives insight into where the bottleneck to the reaction lies (the "transition state"), for example whether it is close to the reactants configuration (a slope close to zero) or close to the product's configuration (a slope close to unity) or in between (close to 0.5).

In the present system, the F1-ATPase, the Brønsted slope for ATP addition and ejection are close to 0.5, found both from interpreting stalling experiments (Adachi et al., 2012; Volkán-Kacsó and Marcus, 2015) and from a theoretical prediction using quantities from other independent ensemble and single-molecule experiments. Meanwhile, for the hydrolysis step it is close to unity (Adachi et al., 2012; Volkán-Kacsó and Marcus, 2017b), and correspondingly for the synthesis step it is close to zero, all of which provides mechanistic information.

The angle dependence of the hydrolysis reaction substep indicates, in the theory, elastic coupling of the reaction with conformational changes in the host subunit (Volkán-Kacsó and Marcus, 2017b), yielding a prediction that the hydrolysis substep produces a small rotation of about 15°. Atomistic simulations of the hydrolysis reaction (Dittrich et al., 2004) in the catalytic pocket support the coupling model. This coupling involves of an Arginine "finger," αR373, which can be displaced, thereby reducing the reaction free energy barrier. The arginine finger is part of the neighboring α subunit, and its displacement appears to be linked to the opening/closing of that α / β interface, as discussed later in the section "Relation to other theoretical and computational work."

Free energy simulations have been shown (Warshel et al., 1994) to be a promising tool for descriptions of Brønsted slopes of complex systems. We note that in other systems' dissociations in the gas phase, it was suggested (e.g., Wardlaw and Marcus, 1988) that the unimolecular dissociations often have a transition state with internal degrees of freedom similar to those of the separated products of the dissociating reactant. In Brønsted slope phrasing, these systems would also thereby have a Brønsted slope near unity.

Regarding the Brønsted slopes of unity for the hydrolysis reaction and correspondingly zero for the reverse reaction, ATP synthesis, independent information on the nature of the transition state for the hydrolysis can be obtained when the Michaelis–Menten expression for the rate constant is valid, using data at the high ATP concentration at different temperatures. When the resulting Arrhenius pre-exponential factor is large, much larger than 10^{13} s^{-1}, say $\sim 10^{16}$ s^{-1}, an argument can be given that the transition state's internal structure represents that of the products (c.f., Wardlaw and Marcus, 1988 and references cited therein) and hence would yield a Brønsted slope of unity. On the other hand, if the data show a pre-exponential factor at high ATP concentration approximately 10^{13} s^{-1} one can argue that typically, other things being equal, the transition state's internal structure likely resembles that of the reactants, and so would correspond to the Brønsted slope of zero. We plan to investigate this issue further using both ensemble and single molecule data.

However, because of solvational effects accompanying the formation of the transition state for the hydrolysis, further analysis is needed. The Arginine finger, mentioned earlier in this section, is displaced into the proximity of the γ phosphate group, in a configuration that stabilizes the free energy barrier for bond cleavage (Dittrich et al., 2004), and its role in the entropy of activation of the reaction and hence in affecting the pre-exponential factor of the hydrolysis needs to be considered. In passing, we note that from a quantitative point of view, if the reaction involves more than one step but if there is nevertheless a single bottleneck, only the standard free energy of that state relative to that of the reactants is needed for computation of the chemical reaction rate and its temperature dependence. Information about any other intermediate states plays no role.

PREDICTIONS OF ANGLE-DEPENDENT RATE CONSTANTS FOR BINDING AND RELEASE IN ThF1, USING CONTROLLED ROTATION DATA AT LOW ATP CONCENTRATIONS

Single-molecule experiments yielded rotation angle-dependent rate constants for ATP binding or Pi release in the ThF1 (Watanabe et al., 2012). Fluorescently labeled ATP and ADP were used to detect individual events of their binding and release. To treat and explain these data, an elastic chemo-mechanical model was proposed (Volkán-Kacsó and Marcus, 2015). In it, the molecular transfer of nucleotides occurs in tandem with a hinge bending or closing motion of the host subunit coupled to the rotation of the shaft.

Subsequently, the theory was used to predict, without adjustable parameters, the exponential angular dependence of ATP binding/release rate constants (Volkán-Kacsó and Marcus, 2016), seen in **Figure 3**. We note that in the theoretical treatment, the effects of the relatively long-imaging frame times were taken into account by allowing binding/release processes to occur within an imaging frame, resulting in missed events in the single-molecule trajectories.

Controlled rotation experiments performed on the F_1-ATPase mimic, to some degree, the conditions of rotational catalysis in the whole F_OF_1-ATPase, by enforcing the rotation in the ATP synthesis direction. If the enforced rotation is slow compared to the relaxation of the protein structure, the reaction kinetics in the F1-ATPase is described in this quasi-static condition by angle-dependent rate constants, which translate to time-dependent rate constants (Volkán-Kacsó and Marcus, 2016). When the discrete stepping of the Fo part is considered, the compliant structure of the rotor shaft was assumed to have

an effect of smoothing out the rotation velocity (Oster and Wang, 2000; Panke et al., 2001); therefore, the framework of steps with angle-dependent rate constants becomes applicable to the rotation of the F_OF_1-ATPase.

DETECTION OF AN INTERMEDIATE STATE RELATED TO ATP BINDING AND ADP RELEASE, OBSERVED AT HIGH ATP CONCENTRATIONS

Recently, the theory was used as a basis for detecting an intermediate state (Volkán-Kacsó et al., 2019). The method relies on the analysis of angular jumps, a measure of the instantaneous velocity of rotation, detected by a nanoscale probe attached to the rotor shaft of the ThF1 motor. The method of using the angle-dependent velocity of the rotation for the analysis of rotation in F_1-ATPase was first proposed by Frasch and co-workers, who monitored fast single-molecule rotation using polarization spectroscopy with a nanorod probe thereby achieving high temporal resolution (Spetzler et al., 2009). In a recent work, Frasch and coworkers found evidence in single-molecule rotation experiments of a large power-stroke associated with the ADP release. In this section, we discuss our findings (Volkán-Kacsó et al., 2019) using a multistate model of a short-lived state in ThF1, likely before the ADP release. These finding support Frasch's conclusions, namely that about half of the 80° substep is due to a power stroke provided by the release of ADP, the other half being a result of ATP binding (to another subunit). A multistate model, which is consistent with a previously established rotation scheme (Watanabe et al., 2010) of sequential steps, was utilized. This constraining information was applied (Volkán-Kacsó et al., 2019) to an earlier model (Oster and Wang, 2000) to treat the imaging probe as (1) a Brownian particle of diffusion coefficient D elastically coupled to the stator ring *via* an elastic rotor shaft of spring constant κ_r, where (2) the potential minimum θ_i could "switch" according to angle-dependent forward and back rate constants, $k_f(\theta)$ and $k_b(\theta)$. The resulting equations for the angle- and time-dependent probability density $\rho_i(\theta,t)$ for each state i are (Volkán-Kacsó et al., 2019),

$$\frac{\partial \rho_i}{\partial t} = D\frac{\partial}{\partial \theta}\left[\beta\kappa_r\ \theta-\theta_i\ \rho_i\right]+D\frac{\partial^2\rho_i}{\partial\theta^2} -\left[k_{f,i}\ \theta\ +k_{b,i-1}\ \theta\ \right]\rho_i+k_{f,i-1}\ \theta\ \rho_{i-1}+k_{b,i}\ \theta\ \rho_{i+1} \quad (4)$$

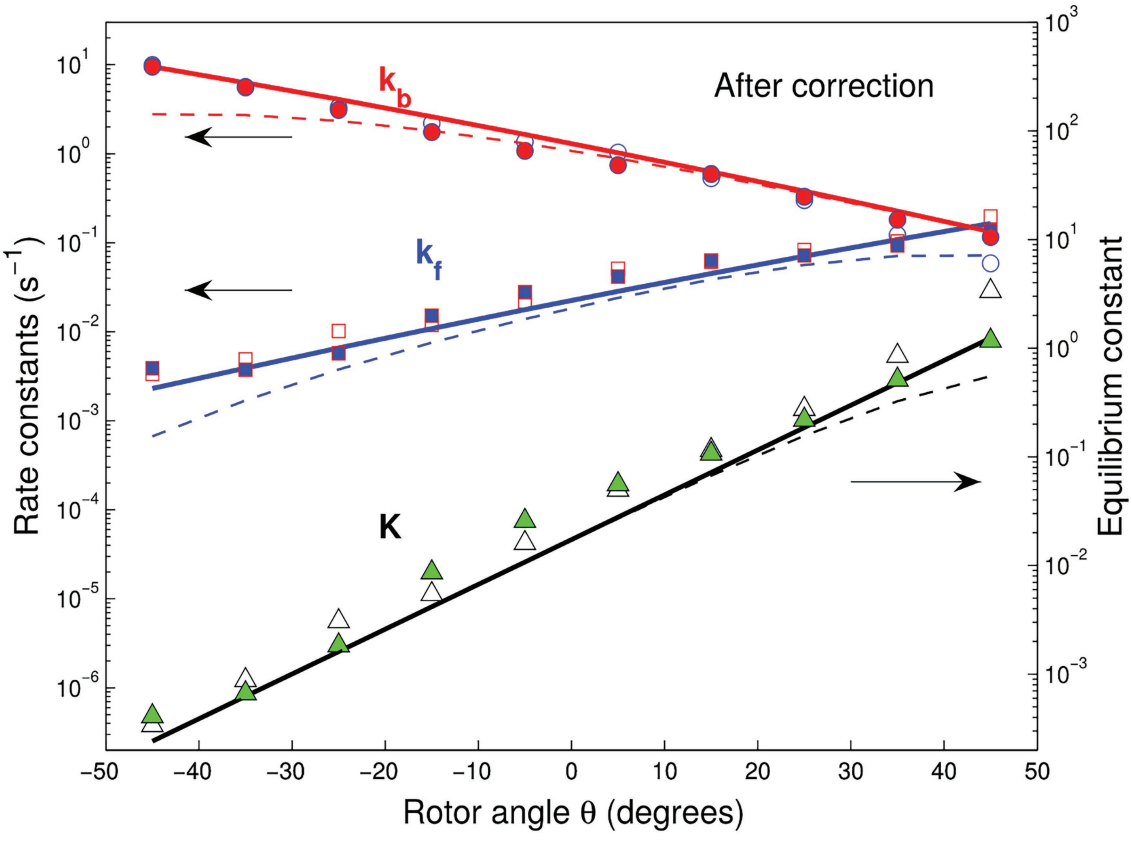


FIGURE 3 | Binding (forward) and release (back) rate and equilibrium rate constants vs. θ angle for Cy3-ATP in the presence (solid squares, circles, and triangles) and absence of Pi (open symbols) in solution. The experimental data of Adachi et al. corrected for missed events are compared with their theoretically predicted counterparts (solid lines). Dashed lines show the data without corrections. The figure is reproduced from Volkán-Kacsó and Marcus (2016).

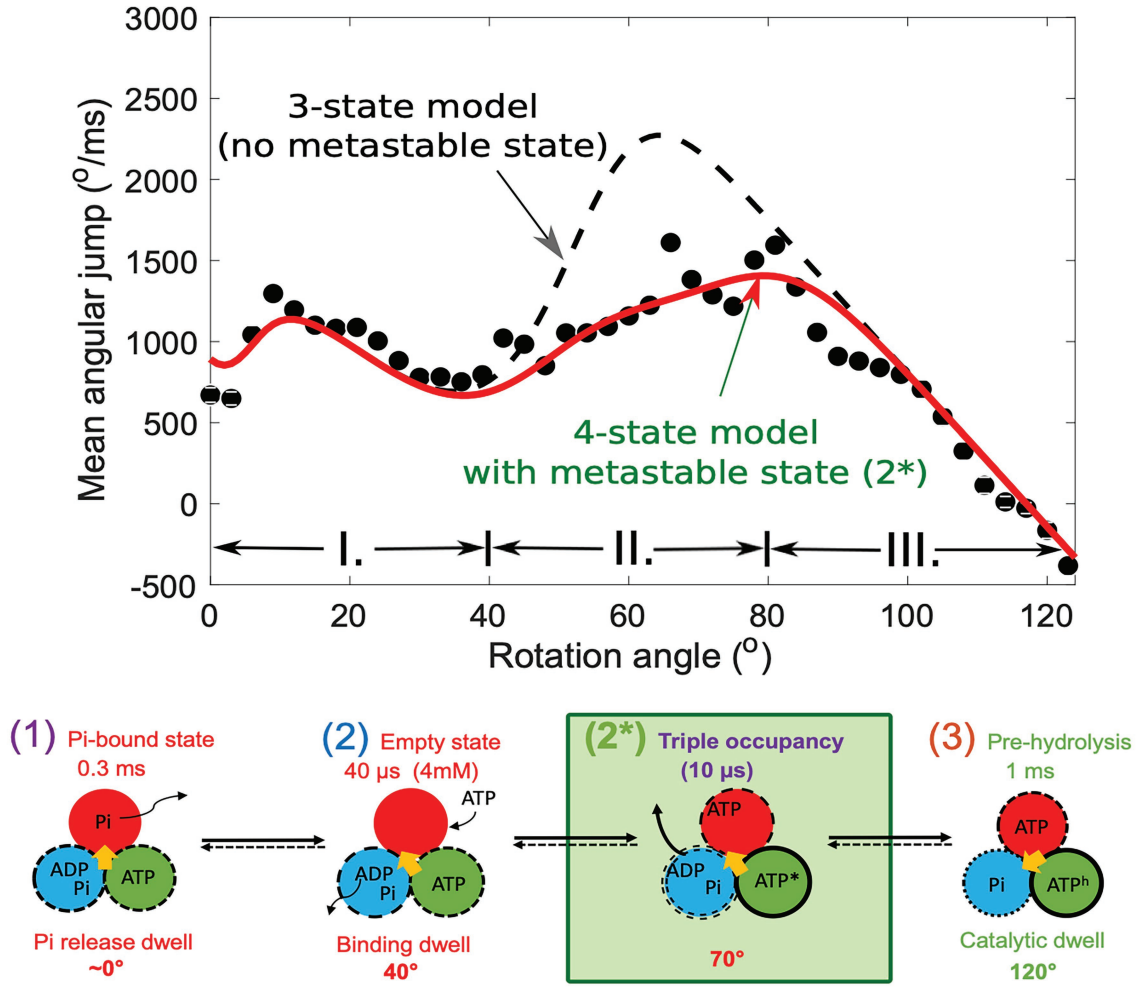


FIGURE 4 | Mean angular jump as a function of rotation angle (top) in fast rotation trajectories. Black dots indicate experimental points, the dashed line shows the predictions from a three-state model, and the continuous line was calculated assuming a fourth state. It is a three-occupancy state. The ATP* and ATP^h indicate that the ATP in the pocket is in different environments sue to conformational changes in their host subunits. The figure was reproduced from Volkán-Kacsó et al. (2019).

When the motor is found in a given state I, it is subject to an elastic restoring force, acting so as to restore the system to the dwell angle of that state. A key quantity used is the jump $\Delta\theta$ in the trajectories, i.e., the change in the angular position from one imaging frame to the next. This jump, when divided by the imaging frame time Δt, yields an estimate for the instantaneous velocity,

$$\upsilon(t) = \left.\frac{\Delta\theta}{\Delta t}\right|_t = \frac{\theta(t+\Delta t) - \theta(t)}{\Delta t} \tag{5}$$

The mean velocity, now as a function of the rotation angle, $v(\theta)$, can be calculated from averaging over jump events in an angular bin. When $v(\theta)$ is also calculated using a 3- or 4-state model and compared with the experimental velocity (**Figure 4**), it was found that a fourth state was needed to accurately describe the experiment. In **Figure 3**, the dashed line shows that a 3-state model would predict a large "hump" in the velocity (or jump) which is not seen in the experimental data. A slow-down of the rotation then is induced by the presence of a short-lived fast state, state 2* in the scheme in **Figure 4**.

The method thereby revealed a metastable state with a 12-μs lifetime after ATP binding and before ADP release. The detected fast state is similar to a three-occupancy Walker X-ray crystallography structure in which all active sites are occupied by nucleotides. It was concluded that ADP release is accelerated 10,000 times by ATP binding to another subunit, removing a bottleneck that would otherwise prevent the efficient function of the biological motor. We note that this conclusion from theoretical analysis correlates well with results of the original ensemble kinetics experiments that reported such cooperative acceleration (Grubmeyer et al., 1982). Both ATP binding and the induced ADP release are associated with large 40° powerstrokes, which is consistent with conclusion in a recent work by Frasch and coworkers (Martin et al., 2018).

BEHAVIOR OF THE SYSTEM IN THE DWELL REGION USING STATISTICAL METHODS AND THE FORCED DIFFUSION EQUATION TO STUDY THE STATISTICAL MECHANICAL PROPERTIES

The spring constant is related to the width of the Brownian fluctuations in the dwells by a simple expression. The SD σ (measured in radians) yields a spring constant in units of $pN{\cdot}nm$ (Sielaff et al., 2008),

$$\kappa_m = 4.1/\sigma^2 \tag{6}$$

where σ is found *via* fitting the histograms with Gaussians. If the relaxation time τ of the system is comparable or faster than the imaging time Δt, the width of the Gaussians is artificially narrowed, so a correction is applicable (Volkán-Kacsó et al., 2019),

$$\kappa_r = 2\left[\frac{\tau}{\Delta t} - \frac{\tau^2}{\Delta t^2}\left(1 - e^{-\Delta t/\tau}\right)\right]\kappa_m. \tag{7}$$

To utilize dwells from all three subunits in the same analysis, a correction to the trajectories was applied to correct for any tilt of the rotor axis, which yielded a more symmetric set of angular distributions for the 120° steps, seen in **Figure 4**. Then, the elastic spring constant for ThF1 was found to be about 70 pN nM. In contrast, in recent investigation, we yielded wider fluctuations in PdF1 (Zarco-Zavala et al., 2020) corresponding to a smaller spring constant, in the range of 25–35 pN nM. We note that different trajectories yielded somewhat different values for the spring constant.

The harmonic elastic response of the rotor shaft extends to a remarkably large displacement in PdF1 trajectories, displacements of 60°–70° in both clockwise and counterclockwise directions, as evidenced by linear velocity-angle dependence. In the Brownian regime, the average velocity is proportional to the restoring force; hence, a linear dependence on the rotation angle displacement relative to the dwell angle is indicative of a harmonic spring response. The slope of the velocity line in the dwell agrees with that at the end of the transition, thereby indicating that in the second part of the transition the system has already jumped to the next dwell and the probe is relaxing to the new energy minimum.

A comparison of molecular ratchet vs. power stroke mechanism was discussed in a recent perspective (Hwang and Karplus, 2019). For the full chemo-mechanical cycle of the F_1-ATPase, it is likely that both mechanisms play a role. For example, the binding and release of the nucleotides are events associated with large conformational changes in the host domains, indicative of a power-stroke mechanism. The substep of the ATP hydrolysis in the pocket is energetically neutral, yet they also produce a small step of about 10° (Volkán-Kacsó and Marcus, 2018), which may indicate a ratcheting mechanism: the hydrolysis substep seems to gate the subsequent energetically downhill Pi release step from the neighboring pocket, thereby providing a directionality for the rotation. Hwang and Karplus also point out that the molecular mechanism of the elastic response of twisted or deformed protein structure in the motors has not been found in simulations. So, the emergent harmonic behavior seen in experimental single-molecule fluctuation data in various F_1-ATPase species requires further investigation using Cryo-EM structure-based atomistic simulations. Warshel and co-workers have shown using free energy simulations that the detailed mechanism of the proton gradient-induced step-like kinetics of the Fo-ATPase is complex and involves the displacement of multiple key residues (Bai and Warshel, 2019). These mechanisms appear to have the qualities of both power stroke and Brownian ratchet-like unidirectional processes.

COMPARISON OF KINETICS AND THE STRUCTURAL BEHAVIOR INFERRED FROM Cryo-EM STUDIES

Unidirectional (counter clockwise when viewed from the site where the F_o would be) rotation of the F1-ATPase γ shaft in unconstrained (free) rotation experiments was first demonstrated using fluorescent filaments attached to the rotor shaft (Noji et al., 1997) and later confirmed in numerous single-molecule imaging experiment using beads and nanoparticles as probes. The unidirectionality was later suggested to be "encoded" in the structure of the stator ring subunits, when the conformational kinetics of rotorless F_1-ATPase was imaged in high-speed AFM experiments (Uchihashi et al., 2011).

To address the structural basis mechanism of the directed rotation in the F_1-ATPase, we consider the X-ray crystallography (Braig et al., 2000; Menz et al., 2001) and more recent Cryo-EM structures (Guo and Rubinstein, 2018; Sobti et al., 2021). We first note that an interplay of molecule transfer and diffusion-controlled regimes was suggested in an earlier study (Volkán-Kacsó and Marcus, 2016) of the controlled rotation experiments (Adachi et al., 2012; Watanabe et al., 2012). In the study, a theory of the time-dependent kinetics is developed for the angle-dependent lifetimes of the observed nucleotide binding and release events. The system is at all times driven by an external torque and so it is out of equilibrium, which is reminiscent of earlier force-ramp pulling experiments (Hummer and Szabo, 2010). A turnover in the ATP-binding rate constants vs. rotor angle plot is seen in **Figure 5A**, as the closing of the binding channel continues beyond 80°.

It was suggested (Volkán-Kacsó and Marcus, 2016) that the ATP transits the channel at the $\alpha - \beta$ subunit interface (**Figure 5C**) by a transfer mechanism, after an initial docking of the ATP to the outside of the F_1-ATPase. Features from X-Ray crystallography structures (Braig et al., 2000;

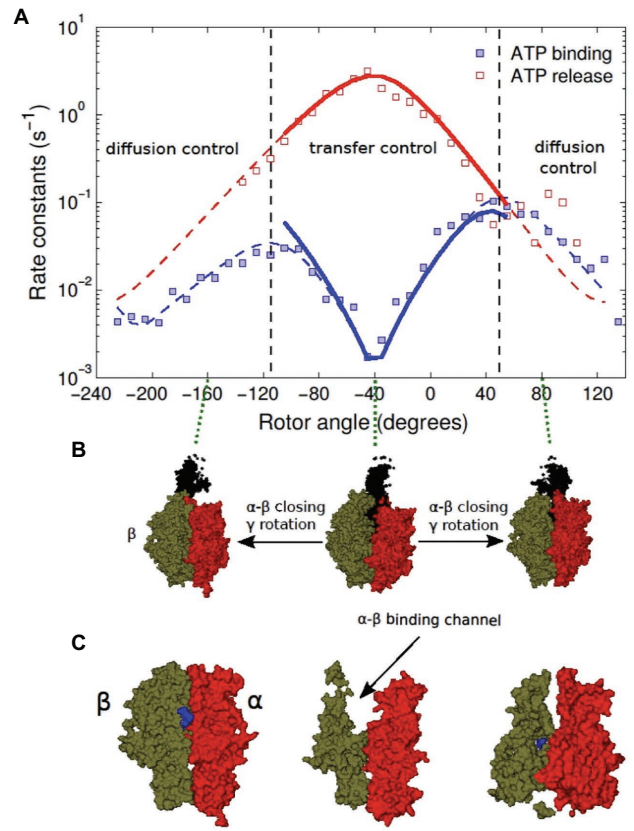


FIGURE 5 | (A) Reported binding and release rate constants vs. controlled rotation angle for fluorescent ATP in the presence of Pi in solution. The reported uncorrected experimental data (squares) are compared with theoretical counterparts (solid lines) by calculating missed events and also correcting for an error due to replacing the time in the empty state T_0 by the total time T. Dashed lines show a fit to the experimental data. **(B)** F_1-ATPase structure at three different rotor angles with β subunits in green, α subunits in red and the γ subunit in black. **(C)** Cutaway of the three structures (PDB:1H8E) revealing the binding channel at the α−β interface and its narrowing as the rotor angle is changed. The figure was reproduced with permission from Volkán-Kacsó and Marcus (2017b).

Menz et al., 2001) supported this mechanism that relates the opening/closing of channels, rotation of the shaft and the entering/exiting of nucleotides.

In the reaction scheme, the transfer reaction determines the angle dependence in the θ-region from about −45° to +45° where stalling and controlled rotation experiments overlap. In a transfer mechanism, a cleft closes upon the transfer of an ATP molecule into an "internal" binding pocket formed at the interface between neighboring α and β subunits. A cross section of the barrel structure of the stator ring and rotor shaft is shown in **Figure 5** for an open and a closed cleft. In these X-ray crystallography structures, the binding channel is formed by the two subunits and it appears to close upon the binding of an ATP molecule. At angles outside of ±50° or so, the binding channel leading to the binding pocket (**Figure 6C**) closes as the rotor is moved in the positive direction (**Figure 6B**). This inference was recently verified in Cryo-EM structures, which were assigned to dwells in the active kinetic cycle of the F_1-ATPase motor (Guo and Rubinstein, 2018). This narrowing of the channel retards the diffusion process so that diffusion becomes the rate-limiting step during binding. The rotation of shaft, opening/closing of the channel, and displacement of the nucleotides are related as follows, using current structure and kinetic data:

1. Rotating the shaft either counterclockwise or clockwise starting from −40° induces a closing of the β subunit which accelerates binding. This behavior is consistent with the spontaneous forward rotation induced by binding of ATP in free rotation experiments occurring in a θ-range to the right of −40° (from 0 to 80°).
2. Rotating the γ rotor towards −40° either clockwise or counterclockwise induces an opening of the β subunit, which accelerates ADP (or ATP) release. This result is consistent with the spontaneous forward rotation induced by the release of ADP in free rotation experiments occurring in a θ-range to the left of −40° (from −20 to −40°).
3. When rotation induces an increased narrowing of the channel, diffusion becomes the bottleneck process and closing of the channel slows down both binding and release processes. So, approaching the most closed conformation (at +140°) in either clockwise or counterclockwise direction will slow down the binding and release of nucleotides in free rotation experiments.

The unidirectionality of the rotation then is due to the specific angular ranges where the rotation-driving (power-stroke) event occurs: binding of ATP in the −40 to 40° range drives the shaft *forward*, release of ADP (at another site) in the next 40° range dominates and drives the rotation *forward* (ADP release in the 280°–320° range in the other site induces closing and forward rotation, as seen in **Figures 5C, 6**). Finally, the remaining 40° rotation *forward* is presumably driven by Pi release and to a small extent the ATP hydrolysis step. We note that recently a role of the ϵ subunit was revealed in accelerating product ATP release when the motor rotates in the synthesis direction (Watanabe et al., 2018).

In a recent kinetic modeling by Dill and coworkers (Wagoner and Dill, 2019), a minimal two-state model was employed to discuss the question of efficiency vs. speed in the molecular motors. Their model could be extended by using a kinetic scheme in which the rate constants depend on a generalized structural slow coordinate, such as the angle of the rotor shaft or a hinge structure that opens and closes upon nucleotide binding.

RELATION BETWEEN MECHANICAL MOTION AND CHEMISTRY

In the section "Use of data on ensemble studies to assist in predictions of single molecule measurements," we discussed

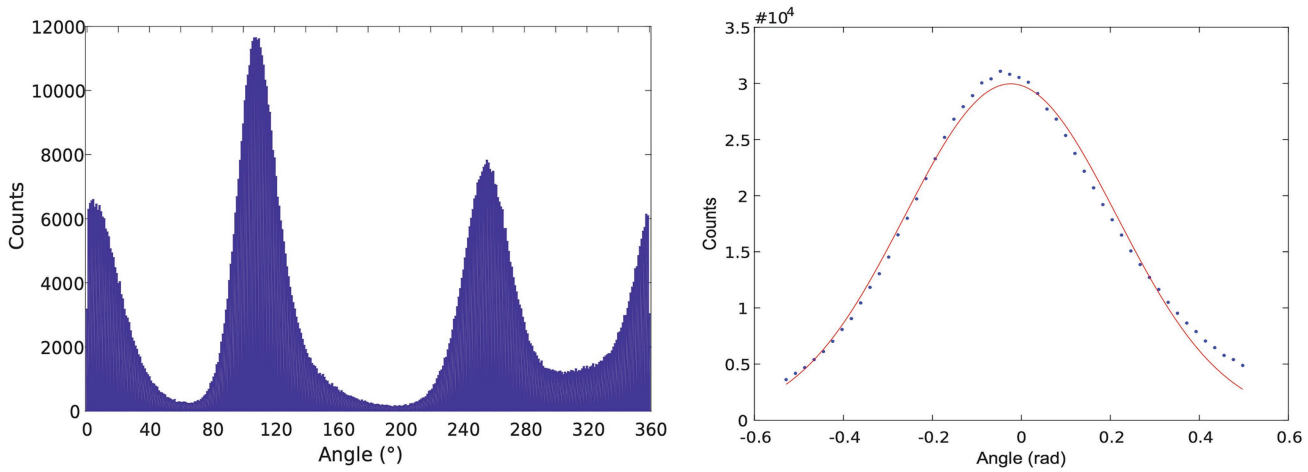


FIGURE 6 | Left: Histogram of angular positions in the dwells from ThF1 rotation trajectories. Right: Consolidated histogram of all three subunits after selecting for "high-quality" dwells. More recently, a correction method was developed for treating the asymmetry between subunits using a tilting algorithm. The figure was reproduced from Volkán-Kacsó et al. (2019).

angle-dependent rate constants for individual steps. From them, occupation probability density profiles can also be calculated. In itself, the rate constants data do not actually explain the connection between the mechanical motion and the chemical reactions. Further insight into the latter is obtained from additional observations related to these rate constant data, by comparing population densities. It was found from studies where the typical total occupancy in the three sites was no larger than unity (Volkán-Kacsó and Marcus, 2017a) that there nevertheless was a correlation between the probability of exit of an ADP and the probability, in another subunit, of entrance of an ATP even though, as mentioned, the total occupation probability of the three sites was not greater than unity.

The probability of ATP binding early in the cycle was correlated with the probability density of an ADP escape some 240° later. It was inferred therefore that the correlation of the two events is inherent in the correlated structural behavior of the clefts from different subunits and did not require actual occupation of both clefts for the correlation to occur. So, the correlation between an ATP binding and ADP release at another site occurs more or less simultaneously. It implies that if computations with a correct force field are undertaken one does not require occupancy for there to be a correlation between the behavior opening (closing) of an ATP site and that closing (opening) of an ADP site. Both the γ shaft and the individual α and β subunits have asymmetric shapes and when they are in contact rolling over each other during the rotation: there is a correlated behavior whereby while one cleft is opening the other is closing. There is predicted in this way to be an approximate conservation of total unoccupied volume in the three empty clefts during the rotation.

We also note that comparing the various single-molecule experiments on F_1-ATPase with the actual enzyme F_oF_1-ATP synthase the single-molecule experiment of the controlled rotation type resembles most closely the behavior of the actual F_oF_1 enzyme since both have a constant rotation rate, the one in the ATP synthase being discretized in the form of successive proton transfers to the c-ring members while the one in the single molecule experiment being continuous.

RELATION TO OTHER THEORETICAL AND COMPUTATIONAL WORK

A probabilistic approach to treat a discrete stepping model of the rotary motor F1-ATPase as observed using a microbead optical probe was pioneered by Oster and Wang (2000). In an early version of the model, all combinations of 64 possible kinetic states were considered, and a discrete numerical method was developed for solving the Fokker–Planck equations in an attempt to treat the full cycle of the chemo-mechanical coupling. In a theoretical work assuming a simpler, sequential kinetics, Junge and co-workers proposed an elastic mechanical coupling between the rotation of the F_O and the F_1 (Panke et al., 2001). The latter resolved the puzzle of efficient motor function when the number of subunits in the $\alpha_3\beta_3$ barrel (F_1 part) is not commensurate with that of subunits in the C-ring (F_O part).

Alternatively, a Langevin dynamics approach has the advantage of generating simulated trajectories, which can then be subjected to the same analysis as experimental single-molecule trajectories. Langevin simulations were used to simulate a discrete-state model with rotation angle-dependent switching potentials, modeled after single-molecule experiments (Watanabe et al., 2013). Langevin dynamics was also used with potentials derived from electrostatic free energy calculations based on atomistic structure (Mukherjee and Warshel, 2011).

Single-molecule imaging provides time-dependent observations of the motors at an individual motor level. They introduce

observables that were not considered when traditional statistical thermodynamics was developed for ensembles that describe the bulk system. F_1-ATPase proved to be a robust "model system" for the development of new stochastic tools suitable for single-molecule experiments. An example is "fluctuation theorems" used to extract steady-state observations from fluctuating single-molecule observation in the context of discrete-state models (Andrieux and Gaspard, 2006; Astumian, 2007), including experiments in which single molecules were driven out of equilibrium by time-dependent pulling forces (Hummer and Szabo, 2010) or torques (Volkán-Kacsó and Marcus, 2016).

Together with single-molecule experiments that revealed the concerted kinetics, the early theoretical works were the precursors of the elastic molecule transfer model of angle-dependent rates in the steps in the active chemo-mechanical pathway of F1-ATPase rotation. In practical applications, relating the stochastic behavior to experimentally observable trajectories requires an additional (painstaking) data analysis step. An approach used in our studies is to remain close to the experiments, in the present case performing the data analysis of fluctuating trajectories to extract experimentally observable quantities, such as histograms, velocities, and correlation functions from the single-molecule data (Volkán-Kacsó and Marcus, 2021). Then, using the theoretical models, the theoretical counterpart of these observable quantities was derived and used to predict or fit experimental single-molecule data.

The atomic resolution of the F_1-ATPase structure in various nucleotide occupancy conditions and conformational states (Walker, 2013) triggered several studies using computer simulations. The cleavage reaction during hydrolysis in the tightly closed binding pocket was simulated using an embedded quantum-classical method (Dittrich et al., 2004). In these studies, the overall conformation of the host subunits was unchanged during the transition from ATP to a cleaved ADP and Pi. Even so, the coupling between chemistry and conformation was demonstrated: They found that an arginine "finger," if in close proximity to the bond being ruptured, reduces the reaction free energy barrier, thereby accelerating the reaction. Conversely, in a conformation where the arginine is not close to the bond, the reaction proceeds an order of magnitude more slowly (Dittrich et al., 2004).

The relation of structure, as revealed by X-ray crystallography, and function, as revealed in rotation experiment, has been pursued also by atomistic computational methods. In an early study of the conformational change in the ring subunits leading to a rotation of the shaft, it was revealed by steered molecular dynamics simulations that the closure of the subunit hinges induced a 80/40 degree stepping rotation (Pu and Karplus, 2008). Simulations with accurate electrostatic modeling yielded a 2-dimensional free energy profile, concluding that a minimum energy path results in the 80/40 substeps (Mukherjee and Warshel, 2011). Large conformational changes of hinge-bending of individual β subunits leading to rotation of the γ shaft were studied with all-atom force-field free energy calculations (Ito et al., 2011). The free energy profiles calculated along interpolated structure between open and closed structures in the presence or absence of ATP yielded quadratic-like profiles which are consistent with the energy relation from equation (3) used in the elastic transfer theory for the ATP binding step in the kinetic scheme from **Figure 3**.

In the theoretical study that revealed a short-lived state in the transitions between subsequent dwells (Volkán-Kacsó et al., 2019), the state is predicted to be a three-occupancy state in which one of the sites will release an ADP molecule within about 10 ms. Large-scale simulations can be used to test this prediction of nucleotide release. The displacement of nucleotides and Pi in the binding pockets is coupled with conformational changes in the structure. Molecular dynamics simulations were used to estimate the diffusion constant for Pi diffusion in the channel (Hummer, 2005). The diffusion of the Pi molecule in unbiased MD simulations induced a significant conformational change in the host subunit (Okazaki and Hummer, 2013). The Pi release on the scheme from **Figure 3**. occurs after the release of ADP, and the work by Hummer's team suggests that the protonation state of the Pi might play a key role in its delayed release: a doubly charged Pi, i.e., HPO_4^{2-}, was found to be tightly bound in the catalytic pocket, as opposed to a singly charged $H_2PO_4^-$.

There is a rapidly growing body of structures resolved for various species of rotary motors, including the V-ATPase family. The experimental groups of Murata, Wilkens, and Rubinstein have reported in recent years structures relevant to the kinetic mechanism of V-ATPase (Arai et al., 2013; Oot et al., 2016; Ueno et al., 2018; Abbas et al., 2020). Given the similarity in the $\alpha_3\beta_3$ rings of the F- and V-ATPases, it is conceivable that the mechanism of accelerated ADP release induced by the binding of ATP to another subunit was conserved over eons of evolution, even as their different functions arose, e.g., V-ATPases, as opposed to certain F-ATPases are not reversible, they are proton pumps that cannot synthesize ATP. The theoretical and computational study of a hypothetical universal mechanism for the allosteric nucleotide binding-release mechanism in rotary motors should be pursued.

AUTHOR CONTRIBUTIONS

SV-K and RM planned and performed the research and wrote the manuscript. All authors contributed to the article and approved the submitted version.

FUNDING

This work was supported by the Office of the Naval Research and the James W. Glanville Foundation.

ACKNOWLEDGMENTS

We would like to acknowledge the helpful discussions of the Cryo-EM and related data with Ricardo Matute and the helpful analysis of Nayree Panossian, Oganes Khatchikian, and Nathan Suiter of the temperature-dependent and single-molecule kinetic data of Watanabe and Noji (2014).

REFERENCES

Abbas, Y. M., Wu, D., Bueler, S. A., Robinson, C. V., and Rubinstein, J. L. (2020). Structure of V-ATPase from the mammalian brain. *Science* 367, 1240–1246. doi: 10.1126/science.aaz2924

Adachi, K., Oiwa, K., Nishizaka, T., Furuike, S., Noji, H., Itoh, H., et al. (2007). Coupling of rotation and catalysis in F1-ATPase revealed by single molecule imaging and manipulation. *Cell* 130, 309–321. doi: 10.1016/j.cell.2007.05.020

Adachi, K., Oiwa, K., Yoshida, M., Nishizaka, T., and Kinosita, K. Jr. (2012). Controlled rotation of the F1-ATPase reveals differential and continuous binding changes for ATP synthesis. *Nat. Commun.* 3:1022. doi: 10.1038/ncomms2026

Adachi, K., Yasuda, R., Noji, H., Itoh, H., Harada, Y. S., Yoshida, M., et al. (2000). Stepping rotation of F1-ATPase visualized through angle-resolved single-fluorophore imaging. *Proc. Natl. Acad. Sci. U. S. A.* 97, 7243–7247. doi: 10.1073/pnas.120174297

Agmon, N., and Hopfield, J. J. (1983). Transient kinetics of chemical reactions with bounded diffusion perpendicular to the reaction coordinate: Intramolecular processes with slow conformational changes. *J. Chem. Phys.* 78, 6947–6959. doi: 10.1063/1.444643

Andrieux, D., and Gaspard, P. (2006). Fluctuation theorems and the nonequilibrium thermodynamics of molecular motors. *Phys. Rev. E* 74:011906. doi: 10.1103/PhysRevE.74.011906

Arai, S., Saijo, S., Suzuki, K., Mizutani, K., Kakinuma, Y., Ishizuka, Y., et al. (2013). Rotation mechanism of enterococcus hirae V1-ATPase based on asymmetric crystal structures. *Nature* 493, 703–707. doi: 10.1038/nature11778

Astumian, R. D. (2007). Design principles for Brownian molecular machines: how to swim in molasses and walk in a hurricane. *Phys. Chem. Chem. Phys.* 9, 5067–5083. doi: 10.1039/b708995c

Bai, C., and Warshel, A. (2019). Revisiting the protomotive vectorial motion of Fo-ATPase. *Proc. Natl. Acad. Sci. U. S. A.* 116, 19484–19489. doi: 10.1073/pnas.1909032116

Boyer, P. D. (1993). The binding change mechanism for ATP synthase—some probabilities and possibilities. *Biochim. Biophys. Acta* 1140, 215–250. doi: 10.1016/0005-2728(93)90063-L

Braig, K., Menz, R. I., Montgomery, M. G., Leslie, A. G., and Walker, J. E. (2000). Structure of bovine mitochondrial F1-ATPase inhibited by Mg2+ADP and aluminium fluoride. *Structure* 8, 567–573. doi: 10.1016/S0969-2126(00)00145-3

Dittrich, M., Hayashi, S., and Schulten, K. (2004). ATP hydrolysis in the TP and DP catalytic sites of F1 –ATPase. *Biophys. J.* 87, 2954–2967. doi: 10.1529/biophysj.104.046128

García-Trejo, J. J., and Morales-Ríos, E., (2008). Regulation of the F1F0-ATP synthase rotary Nanomotor in its monomeric-bacterial and Dimeric-mitochondrial forms. *J. Biol. Phys.* 34, 197–212. doi: 10.1007/s10867-008-9114-z

Glasstone, S., Laidler, K. J., and Eyring, H. (1941). *The Theory of Rate Processes*. New York: McGraw-Hill Book Company.

Grubmeyer, C., Cross, R. L., and Penefsky, H. S. (1982). Mechanism of ATP hydrolysis by beef heart mitochondrial ATPase. Rate enhancements resulting from cooperative interactions between multiple catalytic sites. *J. Biol. Chem.* 257, 12101–12105.

Guo, P., Noji, H., Yengo, C. M., Zhao, Z., and Grainge, I. (2016). Biological nanomotors with a revolution, linear, or rotation motion mechanism. *Microbiol. Mol. Biol. Rev.* 80, 161–186. doi: 10.1128/MMBR.00056-15

Guo, H., and Rubinstein, J. L. (2018). Cryo-EM of ATP synthases. *Curr. Op. Struct. Biol.* 52, 71–79. doi: 10.1016/j.sbi.2018.08.005

Hummer, G. (2005). Position-dependent diffusion coefficients and free energies from Bayesian analysis of equilibrium and replica molecular dynamics simulations. *New J. Phys.* 7, 34–40. doi: 10.1088/1367-2630/7/1/034

Hummer, G., and Szabo, A. (2010). Free energy profiles from single-molecule pulling experiments. *Proc. Natl. Acad. Sci. U. S. A.* 107, 21441–21446. doi: 10.1073/pnas.1015661107

Hwang, W., and Karplus, M. (2019). Structural basis for power stroke vs. Brownian ratchet mechanisms of motor proteins. *Proc. Natl. Acad. Sci. U. S. A.* 116, 19777–19785.

Hwang, W., Lang, M. J., and Karplus, M. (2017). Kinesin motility is driven by subdomain dynamics. *elife* 6:e28948. doi: 10.7554/eLife.28948

Iino, R., and Noji, H. (2013). Operation mechanism of FoF1-adenosine triphosphate synthase revealed by its structure and dynamics. *IUBMB Life* 65, 238–246. doi: 10.1002/iub.1120

Ikeguchi, M., Ueno, J., Sato, M., and Kidera, A. (2005). Protein structural change upon ligand binding: linear response theory. *Phys. Rev. Lett.* 94:078102. doi: 10.1103/PhysRevLett.94.078102

Ito, Y., Oroguchi, T., and Ikeguchi, M. (2011). Mechanism of the conformational change of the F1-ATPase β subunit revealed by free energy simulation. *J. Am. Chem. Soc.* 133, 3372–3380. doi: 10.1021/ja1070152

Junge, W., and Nelson, N. (2015). ATP synthase. *Annu. Rev. Biochem.* 84, 631–657. doi: 10.1146/annurev-biochem-060614-034124

Kleinekathofer, U., Isralewitz, B., Dittrich, M., and Schulten, K. (2011). Domain motion of individual F1-ATPase β-subunits during unbiased molecular dynamics simulations. *J. Phys. Chem. A* 115, 7267–7274. doi: 10.1021/jp2005088

Kramers, H. A. (1940). Brownian motion in a field of force and the diffusion model of chemical reactions. *Physica* 7, 284–304. doi: 10.1016/S0031-8914(40)90098-2

Lewis, E. S. (1986). Application of the Marcus equation to methyl transfers. *J. Phys. Chem.* 90, 3156–3159.

Lewis, E. S., and Hu, D. D. (1984). Methyl transfers. 8. The Marcus equation and transfers between Arsenesulfonates. *J. Am. Chem. Soc.* 106, 3292–3296. doi: 10.1021/ja00323a038

Marcus, R. A. (1968). Theoretical relations among rate constants, barriers, and Brønsted slopes of chemical reactions. *J. Phys. Chem.* 72, 891–899. doi: 10.1021/j100849a019

Marcus, R. A. (1993). Electron transfer reactions in chemistry. Theory and experiment. *Rev. Mod. Phys.* 65, 599–610.

Marcus, R. A., and Sutin, N. (1985). Electron transfers in chemistry and biology. *Biochim. Biophys. Acta* 811, 265–322. doi: 10.1016/0304-4173(85)90014-X

Martin, J. L., Ishmukhametov, R., Spetzler, D., Hornung, T., and Frasch, W. D. (2018). Elastic coupling power stroke mechanism of the F1-ATPase molecular motor. *Proc. Natl. Acad. Sci. U. S. A.* 115, 5750–5755. doi: 10.1073/pnas.1803147115

McLaughlin, R. T., Diehl, M. R., and Kolomeisky, A. B. (2016). Collective dynamics of processive cytoskeletal motors. *Soft Matter* 12, 14–21. doi: 10.1039/C5SM01609F

Menz, R. I., Walker, J. E., and Leslie, A. G. W. (2001). Structure of bovine mitochondrial F1-ATPase with nucleotide bound to All three catalytic sites: implications for the mechanism of rotary catalysis. *Cell* 106, 331–341. doi: 10.1016/S0092-8674(01)00452-4

Miller, H., Zhou, Z., Shepherd, J., Wollman, A. J. M., and Leake, M. C. (2018). Single-molecule techniques in biophysics: a review of the progress in methods and applications. *Rep. Prog. Phys.* 81:024601. doi: 10.1088/1361-6633/aa8a02

Mukherjee, S., and Warshel, A. (2011). Electrostatic origin of the mechanochemical rotary mechanism and the catalytic dwell of F1-ATPase. *Proc. Natl. Acad. Sci. U. S. A.* 108, 20550–20555. doi: 10.1073/pnas.1117024108

Mukherjee, S., and Warshel, A. (2015). Dissecting the role of the γ-subunit in the rotary chemical coupling and torque generation of F1-ATPase. *Proc. Natl. Acad. Sci. U. S. A.* 112, 2746–2751. doi: 10.1073/pnas.1500979112

Nishizaka, T., Oiwa, K., Noji, H., Kimura, S., Muneyuki, E., Yoshida, M., et al. (2004). Chemomechanical coupling in F1-ATPase revealed by simultaneous observation of nucleotide kinetics and rotation. *Nat. Struct. Mol. Biol.* 11, 142–148. doi: 10.1038/nsmb721

Noji, H., Yasuda, R., Yoshida, M., and Kinosita, K. Jr. (1997). Direct observation of the rotation of F1-ATPase. *Nature* 386, 299–302. doi: 10.1038/386299a0

Okazaki, K., and Hummer, G. (2013). Phosphate release coupled to rotary motion of F_1-ATPase Proc. *Proc. Natl. Acad. Sci. U. S. A.* 110, 16468–16473. doi: 10.1073/pnas.1305497110

Oot, R., Kane, P. M., Berry, E. A., and Wilkens, S. (2016). Crystal structure of yeast V1-ATPase in the autoinhibited state. *EMBO* 35, 1694–1706. doi: 10.15252/embj.201593447

Oster, G., and Wang, H. (2000). Reverse engineering a protein: the mechanochemistry of ATP synthase. *Biochim. Biophys. Acta* 1458, 482–510. doi: 10.1016/S0005-2728(00)00096-7

Panke, O., Cherepanov, D. A., Gumbiowski, K., Engelbrecht, S., and Junge, W. (2001). Viscoelastic dynamics of actin filaments coupled to rotary F-ATPase: angular torque profile of the enzyme. *Biophys. J.* 81, 1220–1233. doi: 10.1016/S0006-3495(01)75780-3

Pu, J., and Karplus, M. (2008). How subunit coupling produces the gamma-subunit rotary motion in F1-ATPase. *Proc. Natl. Acad. Sci.* 105, 1192–1197. doi: 10.1073/pnas.0708746105

Sakaki, N., Shimo-Kon, R., Adachi, K., Itoh, H., Furuike, M. E. H., Yoshida, M., et al. (2005). One rotary mechanism for F1-ATPase over ATP concentrations from millimolar down to nanomolar. *Biophys. J.* 88, 2047–2056. doi: 10.1529/biophysj.104.054668

Saper, G., and Hess, H. (2020). Synthetic systems powered by biological molecular motors. *Chem. Rev.* 120, 288–309. doi: 10.1021/acs.chemrev.9b00249

Senior, A. E. (2007). ATP synthase: motoring to the finish line. *Cell* 130, 220–221. doi: 10.1016/j.cell.2007.07.004

Senior, A. E., Nadanaciva, S., and Weber, J. (2002). The molecular mechanism of ATP synthesis by F1F0-ATP synthase, Biophys. *Biochim. Acta.* 1553, 188–211.

Sielaff, H., Martin, J., Singh, D., Biukovic, G., Grueber, G., and Frasch, W. D. (2016). Power stroke angular velocity profiles of archaeal A-ATP synthase versus thermophilic and mesophilic F-ATP synthase molecular motors. *J. Biol. Chem.* 291, 25351–25363. doi: 10.1074/jbc.M116.745240

Sielaff, H., Rennekamp, H., Engelbrecht, S., and Junge, W. (2008). Functional halt positions of rotary FOF1-ATPase correlated with crystal structures. *Biophys. J.* 95, 4979–4987. doi: 10.1529/biophysj.108.139782

Sielaff, H., Yanagisawa, S., Frasch, W. D., Junge, W., and Börsch., M., (2019). Structural asymmetry and kinetic limping of single rotary F-ATP synthases. *Molecules* 24:504. doi: 10.3390/molecules24030504

Sobti, M., Ueno, H., Noji, H., and Stewart, A. G. (2021). The six steps of the complete F1-ATPase rotary catalytic cycle. *Nat. Commun.* 12:4690. doi: 10.1038/s41467-021-25029-0

Spetzler, D., Ishmukhametov, R., Hornung, T., Day, L. J., Martin, J., and Frasch, W. D. (2009). Single molecule measurements of F1-ATPase reveal an interdependence between the power stroke and the dwell duration. *Biochemist* 48, 7979–7985. doi: 10.1021/bi9008215

Sugawa, M., Okazaki, K.-I., Kobayashi, M., Matsui, T., Hummer, G., Masaike, T., et al. (2016). F1-ATPase conformational cycle from simultaneous single-molecule FRET and rotation measurements. *Proc. Natl. Acad. Sci. U. S. A.* 113, E2916–E2924. doi: 10.1073/pnas.1524720113

Sumi, H., and Marcus, R. A. (1986). Dynamical effects in electron transfer reactions. *J. Chem. Phys.* 84, 4894–4914. doi: 10.1063/1.449978

Tong, A. B., and Bustamante, C. (2021). Helical inchworming: a novel translocation mechanism for a ring ATPase. *Biophys. Rev.* 13, 885–888. doi: 10.1007/s12551-021-00883-w

Truhlar, D. G., Garrett, B. C., and Klippenstein, S. J. (1996). Current status of transition-state theory. *J. Phys. Chem.* 100, 12771–12800. doi: 10.1021/jp953748q

Uchihashi, T., Iino, R., Ando, T., and Noji, H. (2011). High-speed atomic force microscopy reveals rotary catalysis of rotorless F1-ATPase H. *Science* 333, 755–758. doi: 10.1126/science.1205510

Ueno, H., Suzuki, K., and Murata, T. (2018). Structure and dynamics of rotary V1 motor. *Cell. Mol. Life Sci.* 75, 1789–1802. doi: 10.1007/s00018-018-2758-3

Volkán-Kacsó, S., Le, L. Q., Zhu, K. C., Su, H., and Marcus, R. A. (2019). Method to extract multiple states in F1-ATPase rotation experiments from jump distributions. *Proc. Natl. Acad. Sci. U. S. A.* 116, 25456–25461. doi: 10.1073/pnas.1915314116

Volkán-Kacsó, S., and Marcus, R. A. (2015). Theory for rates, equilibrium constants, and Brønsted slopes in F1-ATPase single molecule imaging experiments. *Proc. Natl. Acad. Sci. U. S. A.* 112, 14230–14235. doi: 10.1073/pnas.1518489112

Volkán-Kacsó, S., and Marcus, R. A. (2016). Theory of controlled rotation experiments, predictions, tests and comparison with stalling experiments in F1-ATPase. *Proc. Natl. Acad. Sci. U. S. A.* 113, 12029–12034. doi: 10.1073/pnas.1611601113

Volkán-Kacsó, S., and Marcus, R. A. (2017a). Theory of long binding events in single molecule controlled rotation experiments on F1-ATPase. *Proc. Natl. Acad. Sci. U. S. A.* 114, 7272–7277. doi: 10.1073/pnas.1705960114

Volkán-Kacsó, S., and Marcus, R. A. (2017b). What can be learned about the enzyme ATPase from single molecule studies of its subunit F1? *Qart. Rev. Biophys.* 50:e14. doi: 10.1017/S0033583517000129

Volkán-Kacsó, S., and Marcus, R. A. (2018). "Free, stalled, and controlled rotation single molecule experiments on F1-atpase and their relationships," in *Photosynthesis and Bioenergetics*. eds. J. Barber and A. V. Ruban (Singapore: World Scientific Publishing Co.), 35–53.

Volkán-Kacsó, S., and Marcus, R. A. (2021). "Single molecule studies of a biological motor F1-ATPase: interplay of experiment, analytic theory and computation," in *Computational Materials, Chemistry, and Biochemistry: From Bold Initiatives to the Last Mile. Springer Series in Materials Science*. eds. S. Shankar, R. Muller, T. Dunning and G. H. Chen, vol. *284* (Cham: Springer)

Wagoner, J. A., and Dill, K. A. (2019). Mechanisms for achieving high speed and efficiency in biomolecular machines. *Proc. Natl. Acad. Sci. U. S. A.* 116, 5902–5907. doi: 10.1073/pnas.1812149116

Walker, J. E. (2013). The ATP synthase: the understood, the uncertain and the unknown. *Biochem. Soc. Trans.* 41, 1–16. doi: 10.1042/BST20110773

Wardlaw, D. M., and Marcus, R. A. (1988). On the statistical theory of Unimolecular processes. *Adv. Chem. Phys.* 70, 231–263.

Warren, J. J., and Mayer, J. M. (2012). "Application of the marcus cross relation to hydrogen atom transfer/proton-coupled electron transfer reactions", in *Proton-Coupled Electron Transfer: A Carrefour of Chemical Reactivity Traditions.* eds. S. Formosinho and M. Barroso (The Royal Society of Chemistry), 1–31.

Warshel, A., Schweins, T., and Fothergill, M. (1994). Linear free energy relationships in enzymes. Theoretical analysis of the reaction of Tyrosyl-tRNA Synthetase. *J. Am. Chem. Soc.* 116, 8437–8442. doi: 10.1021/ja00098a001

Watanabe, R., Genda, M., Kato-Yamada, Y., and Noji, H. (2018). Essential role of the ε subunit for reversible chemo-mechanical coupling in F1-ATPase. *Biophys. J.* 114, 178–187. doi: 10.1016/j.bpj.2017.11.004

Watanabe, R., Hayashi, K., Ueno, H., and Noji, H. (2013). Catalysis-enhancement via rotary fluctuation of F1-ATPase. *Biophys. J.* 105, 2385–2391. doi: 10.1016/j.bpj.2013.09.050

Watanabe, R., Iino, R., and Noji, H. (2010). Phosphate release in F1-ATPase catalytic cycle follows ADP release. *Nat. Chem. Biol.* 6, 814–820. doi: 10.1038/nchembio.443

Watanabe, R., and Noji, H. (2014). Timing of inorganic phosphate release modulates the catalytic activity of ATP-driven rotary motor protein. *Nat. Commun.* 5:3486. doi: 10.1038/ncomms4486

Watanabe, R., Okuno, D., Sakakihara, S., Shimabukuro, K., Iino, R., Yoshida, M., et al. (2012). Mechanical modulation of catalytic power on F1-ATPase. *Nat. Chem. Biol.* 8, 86–92. doi: 10.1038/nchembio.715

Weber, J. (2010). Structural biology: toward the ATP synthase mechanism. *Nat. Chem. Biol.* 6, 794–795. doi: 10.1038/nchembio.458

Weber, J., and Senior, A. E. (1997). Catalytic mechanism of F1-ATPase. *Biochim. Biophys. Acta* 1319, 19–58. doi: 10.1016/S0005-2728(96)00121-1

Wolfe, S., and Mitchell, D. J. (1981). Theoretical studies of SN2 transition states. 2. Intrinsic barriers, rate-equilibrium relationships, and the Marcus equation. *J. Am. Chem. Soc.* 103, 7694–7696. doi: 10.1021/ja00415a069

Yasuda, R., Noji, H., Yoshida, M., Kinosita, K. Jr., and Itoh, H. (2001). Resolution of distinct rotational substeps by submillisecond kinetic analysis of F1-ATPase. *Nature* 410, 898–904. doi: 10.1038/35073513

Zarco-Zavala, M., Watanabe, W., McMillan, D. G. G., Suzuki, T., Ueno, H., Mendoza-Hoffmann, F., et al. (2020). The 3 × 120° rotary mechanism of *Paracoccus denitrificans* F1-ATPase is different from that of the bacterial and mitochondrial F1-ATPases. *Proc. Natl. Acad. Sci.* 117, 29647–29657. doi: 10.1073/pnas.2003163117

Conflict of Interest: The authors declare that the research was conducted in the absence of any commercial or financial relationships that could be construed as a potential conflict of interest.

Publisher's Note: All claims expressed in this article are solely those of the authors and do not necessarily represent those of their affiliated organizations, or those of the publisher, the editors and the reviewers. Any product that may

be evaluated in this article, or claim that may be made by its manufacturer, is not guaranteed or endorsed by the publisher.

Copyright © 2022 Volkán-Kacsó and Marcus. This is an open-access article distributed under the terms of the Creative Commons Attribution License (CC BY). The use, distribution or reproduction in other forums is permitted, provided the original author(s) and the copyright owner(s) are credited and that the original publication in this journal is cited, in accordance with accepted academic practice. No use, distribution or reproduction is permitted which does not comply with these terms.

Advantages of publishing in Frontiers

OPEN ACCESS
Articles are free to read for greatest visibility and readership

FAST PUBLICATION
Around 90 days from submission to decision

HIGH QUALITY PEER-REVIEW
Rigorous, collaborative, and constructive peer-review

TRANSPARENT PEER-REVIEW
Editors and reviewers acknowledged by name on published articles

Frontiers
Avenue du Tribunal-Fédéral 34
1005 Lausanne | Switzerland

Visit us: www.frontiersin.org
Contact us: frontiersin.org/about/contact

REPRODUCIBILITY OF RESEARCH
Support open data and methods to enhance research reproducibility

DIGITAL PUBLISHING
Articles designed for optimal readership across devices

FOLLOW US
@frontiersin

IMPACT METRICS
Advanced article metrics track visibility across digital media

EXTENSIVE PROMOTION
Marketing and promotion of impactful research

LOOP RESEARCH NETWORK
Our network increases your article's readership